Rotation-induced mixing and thermohaline instability in low- and intermediate-mass stars. Consequences on the Galactic evolution of light elements.

Nadège Lagarde

To cite this version:

Nadège Lagarde. Rotation-induced mixing and thermohaline instability in low- and intermediate-mass stars. Consequences on the Galactic evolution of light elements.. Solar and Stellar Astrophysics [astro-ph.SR]. University of Geneva, 2012. English. NNT : . tel-00754970

HAL Id: tel-00754970
https://theses.hal.science/tel-00754970

Submitted on 20 Nov 2012

Université de Genève
Département d'astronomie

Faculté des Sciences
Professeure Corinne Charbonnel

Rotation-induced mixing and thermohaline instability in low- and intermediate-mass stars.

Consequences on the Galactic evolution of light elements.

Thèse

présentée à la Faculté des sciences de l'Université de Genève
pour obtenir le grade de Docteur ès sciences,
mention Astronomie et Astrophysique

par

Nadège Lagarde

de

Pujols sur Dordogne (France)

Thèse N° 4433

Genève
Observatoire de Genève
2012

UNIVERSITÉ
DE GENÈVE
FACULTÉ DES SCIENCES

Doctorat ès sciences
Mention astronomie et astrophysique

Thèse de *Madame Nadège LAGARDE*

intitulée :

" Rotation-induced Mixing and Thermohaline Instability in Low- and Intermediate-mass stars. Consequences on the Galactic Evolution of Light Elements "

La Faculté des sciences, sur le préavis de Madame C. CHARBONNEL, professeure associée et directrice de thèse (Département d'astronomie), Messieurs G. MEYNET, professeur ordinaire (Département d'astronomie), S. UDRY, professeur ordinaire (Département d'astronomie), P. EGGENBERGER, docteur (Département d'astronomie), J.-P. ZAHN, docteur (LUTH – Observatoire de Paris – Meudon, France), et Madame C. CHIAPPINI, docteure (Leibniz-Institut für Astrophysik – Potsdam, Germany), autorise l'impression de la présente thèse, sans exprimer d'opinion sur les propositions qui y sont énoncées.

Genève, le 15 juin 2012

Thèse - 4433 -

Le Doyen, Jean-Marc TRISCONE

N.B. - La thèse doit porter la déclaration précédente et remplir les conditions énumérées dans les "Informations relatives aux thèses de doctorat à l'Université de Genève".

Contents

List of Figures v

List of Tables vii

Résumé ix

Remerciements xi

Publications related to this thesis xiii

1 Introduction 1
- 1.1 General context 1
- 1.2 Overview of the thesis 2

2 Evolution and nucleosynthesis : Standard predictions 5
- 2.1 Pre-Main sequence 7
- 2.2 Main sequence 7
- 2.3 The sub-giant branch 10
- 2.4 Red Giant Branch 14
- 2.5 He-burning phase 19
- 2.6 The Asymptotic Giant Branch 19
  - 2.6.1 The early-AGB phase 19
  - 2.6.2 TP-AGB phase 21
- 2.7 Summary 25

3 Observations : Keys to constrain stellar evolution 27
- 3.1 Abundance indicators 27
- 3.2 Carbon isotopic ratio and nitrogen 28
  - 3.2.1 Open clusters 28
  - 3.2.2 Fields stars 31
- 3.3 Lithium A(Li) and Beryllium A(Be) 36
  - 3.3.1 Open clusters : IC 4651, M67, Hyades 37
  - 3.3.2 Globular clusters : NGC 6397 38
  - 3.3.3 Field stars 39
- 3.4 Oxygen isotopic ratio and Sodium 40
- 3.5 ^{3}He case 42
- 3.6 Summary 43

4 From parametric to hydrodynamic computations. 53
4.1 Parametrized prescriptions for transport processes of nucleides 53
4.2 Rotation-induced mixing 54
4.2.1 Physical description of rotation 54
4.2.2 Effect of rotation induced-mixing on chemical species 57
4.3 Thermohaline instability 58
4.3.1 Physical mechanism in laboratory 58
4.3.2 Thermohaline instability in astrophysical context 60
4.3.3 Thermohaline instability in stellar interior of RGB stars 62
4.3.4 Hydrodynamic simulations of thermohaline mixing 65
4.3.5 Effect of different prescriptions on the diffusion coefficient 67
4.3.6 Preliminary hydrodynamic study 71

5 Thermohaline mixing and rotation-induced mixing 81
5.1 STAREVOL code and input physics of stellar models 81
5.1.1 Basic inputs with STAREVOL 81
5.1.2 Transport processes in radiative zones 84
5.2 Beryllium abundances in the open cluster IC 4651. 85
5.3 Low- and intermediate-mass solar metallicity stars up to the end of the AGB 97
5.4 Grid of stellar models and asymptotic asteroseismic quantities 116

6 Cosmic evolution of ^{3}He from the Big Bang to present day 133
6.1 The “^{3}He problem” 133
6.2 Yields of ^{3}He for low- and intermediate-mass stars 135
6.3 Evolution of light elements in the Galaxy 149

7 Conclusions and perspectives 163
7.1 Results 163
7.2 Future perspectives 164

Conference’s proceedings 167

Bibliography 225

List of Figures

2.1 Theoretical evolutionary tracks in the Hertzsprung Russel diagram for all our standard models computed with the code STAREVOL. 6
2.2 Effects of mass at solar metallicity and of metallicity on evolutionary tracks in the HR diagram for standard models. 7
2.3 Central temperature as a function of central density for the standard models at $Z_\odot$. 8
2.4 Evolution of stellar structure of a standard 1.5 $M_\odot$ model at solar metallicity. 9
2.5 Abundance profiles as a function of coordinate in mass, at the main sequence turn off, for the 1.5 $M_\odot$ and 6.0 $M_\odot$ models at $Z_\odot$and Z=0.0001. 10
2.6 Temperature profiles at the turn off, at the BUMP luminosity, and at the RGB tip for $1.5M_\odot$ at Z=0.014 and Z=0.0001. 11
2.7 Maximum depth in mass of the convective envelope relative to the total stellar mass reached during first and second dredge-up as a function of initial stellar mass and for different metallicities. 12
2.8 Carbon isotopic ratio at the end of the first dredge-up as a function of initial stellar mass for different value of metallicity (Z=0.014, 0.004, 0.002 and 0.0001). 13
2.9 Theoretical evolution of carbon isotopic ratio and $^{12}C/^{14}N$ at the stellar surface as a function of luminosity for stellar models of various masses at Z=0.002 and Z=0.014 from the main sequence up to the early AGB. 14
2.10 Theoretical evolution of ^3He at the stellar surface as a function of luminosity for stellar models of various masses at Z=0.002 and Z=0.014 from the main sequence up to the early AGB. 15
2.11 Theoretical evolution of A(Li) and A(Be) at the stellar surface as a function of luminosity for stellar models of various masses at Z=0.002 and Z=0.014 from the main sequence up to the early AGB. 16
2.12 Theoretical evolution of $^{16}O/^{17}O$ and $^{16}O/^{18}O$ at the stellar surface as a function of luminosity for stellar models of various masses at Z=0.002 and Z=0.014 from the main sequence up to the early AGB. 17
2.13 Abundance profiles as a function of δM for our $1.5M_\odot$ standard model at solar metallicity before the bump luminosity. 18
2.14 The evolution of the stellar luminosity around the bump as a function of time for our 1.5 $M_\odot$ at solar metallicity. 18
2.15 Evolution of the surface abundances of ^3He and ^{14}N (in mass fraction), of A(Li), and of the carbon and oxygen isotopic ratios as a function of stellar luminosity for the 1.5 $M_\odot$ models at two metallicities (Z=0.014 and Z=0.0001) computed with standard prescriptions, are shown up to the RGB tip. 20
2.16 Structure of an AGB star. 21

2.17 Evolution during the (4th and 5th) pulses and interpulse for 1.5 $M_\odot$ at $Z_\odot$ of the internal structure in mass (Kippenhahn diagram) ; of the stellar radius ; and of the nuclear luminosity associated with hydrogen (LH) and helium (LHe). 22
2.18 The TP-AGB phase of a 1.5 $M_\odot$ standard model at solar metallicity : evolution of stellar luminosity, effetive temperature, total mass, the surface abundances of A(Li), ^{3}He, carbon isotopic ratio, $^{12}C/^{14}N$, $^{16}O/^{17}O$ and $^{16}O/^{18}O$. 23
2.19 Theoretical evolution of the temperature at the base of convective envelope, and of the same chemical species as Fig. 2.18 for our 6.0 $M_\odot$ standard model at solar metallicity. 24

3.1 Evolution of the surface carbon isotopic ratio as a function of stellar luminosity. Observations along the evolutionary sequence of the open cluster M67 are from Gilroy & Brown (1991). 29
3.2 Observations of carbon isotopic ratio in evolved stars of open clusters as a function of turn-off mass of the host cluster. 30
3.3 Carbon isotopic ratios for the old disk giants. *Figure from Charbonnel et al. (1998a)* 32
3.4 Carbon isotopic ratio as a function of metallicity and M_V for field stars. *Figures from Charbonnel & Do Nascimento (1998)* 33
3.5 Observations of carbon isotopic ratio in evolved low metallicity, and low mass-fields stars. 34
3.6 Nitrogen abundance against stellar luminosity for stars observed by Carretta et al. (2000) (*Figure from Carretta et al. (2000)*), and observations of nitrogen in field stars by Gratton et al. (2000). 34
3.7 Carbon isotopic ratio in field giant stars as a function of stellar mass. . . . 35
3.8 The Li and Be abundances for stars in the open cluster IC 4651, as a function of effective temperature. 36
3.9 Li abundance as a function of effective temperature in two open clusters : M67 and Hyades. 37
3.10 Lithium observation in NGC 6397 as a function of effective temperature. . . 38
3.11 Positions in the HR diagram of our large sample of field giant stars with metallicities around solar metallicity, and with Li determinations. 39
3.12 A(Li) as a function of effective temperature for the same sample than in figure 3.11. 40
3.13 Oxygen abundance as a function of stellar luminosity for field stars sample. 41
3.14 Evolution of sodium ratio as a function of turn-off mass for the sample of Galactic open clusters, and as a function of stellar luminosity for field stars sample. 41
3.15 Observations of $^3He/H$ in NGC3242 as a function of the progenitor mass. . 42
3.16 Evolution of several chemical species as a function of luminosity in metal-poor field stars. *Figure from Gratton et al. (2000).* 44

4.1 Chemical structure at the turnoff of the 1.5 $M_\odot$ star computed for different initial rotation velocities. 58
4.2 Evolution of the surface abundances of five chemical species as a function of stellar luminosity for the 1.5 $M_\odot$ models at solar metallicity computed with standard prescriptions and including rotation-induced mixing. 59
4.3 Schematic vue of thermohaline mixing 60

4.4 The viscosity, thermal and haline diffusivity, the Prandtl number, and the inverse Lewis number for our 1.25 $M_\odot$ model at $Z_\odot$ as a function of δM. . . 64
4.5 Evolutionary track of the 1.25 $M_\odot$ model computed with thermohaline mixing only. 66
4.6 Diffusion coefficient of thermohaline convection as a function of δM at various evolution points on the RGB for different prescriptions. 67
4.7 *From top to bottom :* Profiles of the abundances (in mass fraction) of H, ^{3}He and of thermohaline diffusion coefficient at various evolution points on the RGB (at L= 65, 94, 113, 123 $L_\odot$). The abscissa is the scaled mass coordinate δ M that allows a blow up of the region of interest (δM=0 at the base of the HBS and δM=1 at the base of the convective envelope). The solid lines correspond to prescription by Denissenkov (2010) (at at L=65, 94, 113, and 123 $L_\odot$ with orange, black, red, and blue line reaspectively) and the black dashed line to prescription by Charbonnel & Lagarde (2010a) at log L/$L_\odot$=2 (or L=94 $L_\odot$). 68
4.8 1.25 $M_\odot$ model with thermohaline mixing (no rotation) 69
4.9 1.25 $M_\odot$ model with thermohaline mixing (no rotation) following prescription of Denissenkov (2010) 70

6.1 Standard galactic evolution of ^{3}He/H in the solar neighborhood and its distribution along the galactic disc predicted by the standard prescription at the present time 134

List of Tables

3.1 References for the abundance studies in Galactic open clusters used in the comparisons with model predictions. 30
3.2 Observations of chemical abundances for open clusters from the literature. 45
3.3 Observations of chemical abundances for globular clusters from the literature. 48
3.4 Observations of chemical abundances for field stars from the literature. . . 50

4.1 Comparison between ocean, hydrodynamic simulations and stellar parameters 65

Résumé

La théorie classique de l'évolution stellaire propose une évolution simple de l'helium-3 (^{3}He) dans la Galaxie, dominée par une grande production de cet isotope par les étoiles de faible masse (Iben 1967; Rood 1972; Rood et al. 1976; Dearborn et al. 1996a; Weiss et al. 1996). Dans les étoiles ayant une masse initiale M $\lesssim$ 2-2.5 M$_\odot$, l'^{3}He est produit tout d'abord au cours de la combustion du deuterium sur la pré-séquence principale et ensuite par combustion de l'hydrogène (chaines pp) sur la séquence principale. Ce nouvel ^{3}He est ensuite "dragué" dans l'enveloppe convective pendant le premier "dredge-up". En accord avec les modèles classiques, cet isotope est préservé pendant les phases suivantes de l'évolution et est restitué au milieu interstellaire par de forts vents de matière ainsi que lors de l'éjection de la nébuleuse planétaire. Par conséquent, la quantité d'^{3}He dans la Galaxie aurait dû fortement augmenter depuis le moment originel de l'Univers.

Cependant les résultats des observations de ^{3}He dans les régions HII montrent des abondances similaires à celles observées pour le Soleil, ainsi que pour le système solaire (météorites, le sol et les roches lunaires, le vent solaire, l'atmosphère de Jupiter) et ne présentent aucun signe d'un enrichissement en ^{3}He depuis 12 milliards d'années. C'est ce qui est appelé le "problème de l'^{3}He". De plus, les modèles classiques d'évolution stellaire prédisent un rapport isotopique du carbone élevé dans les géantes rouges, contrairement aux observations faites dans les amas ouverts montrant une valeur très faible (Gilroy & Brown 1991; Luck 1994; Smiljanic et al. 2009).

Le mélange thermohaline a été récemment identifié comme le mécanisme pouvant gouverner la composition des atmosphères des étoiles géantes rouges de faible masse (Charbonnel & Zahn 2007b). Cette instabilité double-diffusive, très bien connue dans les océans, se développe dans les étoiles géantes rouges en présence d'une inversion du gradient de poids moléculaire due à la réaction ^{3}He(^{3}He,2p)^{4}He au sommet de la coquille de combustion de l'hydrogène. Elle prend la forme de ce que l'on appelle des "doigts de sel". En effet, cette réaction convertit deux particules en trois, et diminue ainsi le poids moléculaire moyen (Ulrich 1972). L'instabilité thermohaline prend place après le premier dredge-up quand l'étoile se trouve sur la branche des géantes rouges à la luminosité du bump.

Au cours de cette thèse, nous avons calculé une grille de modèles stellaires à différentes masses et métallicités, avec les prescriptions du modèle standard et en incluant le mélange thermohaline ainsi que le mélange induit par rotation, tout au long de l'évolution, de la pré-séquence principale à la phase des pulses thermiques. Nous avons pour cela utilisé le code STAREVOL. A l'aide de cette grille de modèles, incluant pour la première fois le mélange thermohaline et le mélange induit par rotation, nous avons étudié les effets de ces deux processus de transport sur la stucture, ainsi que sur les abondances en surface des étoiles de faible masse et de masse intermédiaire. Afin de valider nos modèles, nous les

avons comparés aux abondances observées dans les étoiles d'amas et du champ.

Nous avons alors montré que le mélange thermohaline change les abondances de surface de l'^{3}He, du ^{7}Li, du carbone, et de l'azote dans les étoiles de faible masse, à partir de la luminosité du bump. Ce qui est en accord avec les observations dans les amas, et les étoiles du champ (Charbonnel & Lagarde 2010a). Par ailleurs, nous avons montré que l'abondance en ^{3}He est fortement diminuée par le mélange thermohaline sur la branche des géantes rouges, bien que les étoiles de faible masse restent des producteurs d'^{3}He. La contribution de ces étoiles à l'évolution galactique de l'^{3}He est donc fortement réduite contrairement à ce qui était prédit par les modèles standards. Pour les étoiles de masse intermediaire, nous avons montré que le mélange thermohaline permettait une production de lithium ainsi qu'une faible diminution de l'abondance en ^{3}He pendant la phase des pulses thermiques. Les “yields” de lithium restent, cependant, négatifs et ne contribuent donc pas à l'enrichissement de la Galaxie. De plus, le mélange induit par la rotation modifie la structure chimique interne des étoiles de la séquence principale, et permet au mélange thermohaline de se produire à une luminosité plus faible sur la branche des géantes rouges.

Nous avons donc conclu que le mélange thermohaline est le processus de transport dominant dans les géantes rouges de faible masse gouvernant ainsi la composition chimique de leur atmosphère ($M \lesssim 2.0\ M_\odot$). En outre, nos résultats montrent que l'efficacité du mélange thermohaline croît quand la masse et la métallicité de l'étoile diminuent. Le mélange induit par la rotation explique les abondances de surface des étoiles plus massives ($M > 2.0\ M_\odot$). Ces résultats sont présentés dans Smiljanic et al. (2010), Charbonnel & Lagarde (2010a), Lagarde et al. (2011), et Lagarde et al. (2012a).

Nous avons étudié, ensuite, les effets du mélange thermohaline et du mélange induit par la rotation sur l'évolution chimique de la Galaxie, et plus particulièrement sur l'évolution des éléments légers tels que l'^{3}He, le deuterium et l'^{4}He. En effet, nous avons inclu ces nouveaux yields (D, ^{3}He, ^{4}He) dans le code d'évolution chimique de la Galaxie (Matteucci & Francois 1989). Pour cette étude, nous avons comparé ces nouvelles prescriptions avec leurs valeurs primordiales, et les abondances déduites des observations de différentes régions de la Galaxie (milieu interstellaire local, regions HII). Les modèles d'évolution chimique de la Galaxie tenant compte des effets du mélange thermohaline et du mélange induit par la rotation reproduisent très bien les abondances observées du deuterium, de l'^{3}He, et de l'^{4}He dans la Galaxie. Nous avons montré que le mélange thermohaline est le seul processus physique connu jusqu'à présent qui permet de résoudre le “problème de l'^{3}He” discuté depuis longtemps dans la littérature (Lagarde et al. 2012b).

Durant ces dernières années un grand nombre d'observations astérosismiques a été obtenu, et en particulier la détection et la caractérisation des oscillations de type solaire dans un grand nombre de géantes rouges (*CoRoT* et *Kepler*). La confrontation entre ces observations et les modèles stellaires s'avère être indispensable afin d'améliorer l'approche théorique de l'évolution stellaire. C'est dans ce but que nous avons étudié les signatures de la rotation et du mélange thermohaline, ainsi que l'effet de la masse et de la métallicité de l'étoile sur des grandeurs astérosismiques observées. Utilisant nos nouvelles grilles de modèles, nous avons montré que le mélange induit par rotation avait un impact direct sur les paramètres globaux astérosismiques. Néanmoins, l'instabilité thermohaline ne peut pas être caractérisé par ces paramètres astérosismiques, bien que ces effets puissent être identifiés par des études spectroscopiques (Lagarde et al. 2012a).

Remerciements

Ecrire une thèse en astronomie : un rêve d'enfant exaucé ! Mais cette belle aventure n'a été possible qu'avec la participation de plusieurs personnes.

Dans un premier lieu, je tiens à exprimer ma profonde gratitude au Prof. Corinne Charbonnel pour m'avoir donné l'opportunité d'effectuer mon travail de doctorat dans son groupe de recherche, et m'avoir proposé ce voyage au coeur des étoiles... Je tiens aussi à la remercier pour sa disponibilité à toute heure (jour et nuit), son amour du métier et sa motivation dans le travail, qu'elle transmet très facilement. Résumer en quelques lignes quatre années de thèse avec Corinne serait réducteur autant d'un point de vue scientifique, pour ses nombreux conseils, que d'un point de vue personnel, pour les liens amicaux que nous avons tissés durant ces années. Alors tout simplement : un grand MERCI pour tout !!

Je remercie ensuite les membres du jury pour le temps consacré à lire mon travail de doctorat. Merci à Jean-Paul Zahn et Cristina Chiappini pour avoir fait le déplacement jusqu'à Genève.

Je tiens ensuite à remercier la "Charbonnel's team", en commençant par Ana Palacios, ma grande soeur scientifique, pour sa disponibilité et ses bons conseils ; ainsi que Thibaut Decressin, mon grand frère scientifique, pour sa patience face à mes questions. Je remercie aussi l'equipe d'évolution stellaire, en commençant par Georges Meynet, pour avoir accepté de faire partie des membres de mon jury ; Patrick Eggenberger pour les échanges "astérosismiques" et sa disponibilité pour apporter des réponses à mes questions de débutante ; ainsi que Sylvia Ekström pour sa bonne humeur communicative.

Je tiens à remercier Cristina Chiappini pour m'avoir fait confiance dans notre projet d'évolution chimique sur l'helium-3, pour nos échanges scientifiques et amicaux. Je tiens également à remercier Donatella Romano et Monica Tosi pour leur accueil chaleureux à l'Observatoire de Bologne, et les échanges scientifiques que nous avons pu avoir pendant le calcul des modèles d'évolution chimique de la Galaxie.

Merci aussi à Jean-Paul Zahn et François Lignières de m'initier à l'hydrodynamique depuis notre séjour à Santa Cruz, pour leur disponibilité et leur enthousiasme face à l'apparition de beaux champignons !!

Merci à mon collègue de bureau (307!), Stéphane, pour avoir supporté mes discussions avec mon ordinateur, mes moments de doute, mais aussi de joie (trop) communicative, et surtout pour son humour "quasi-cosmique" !! Merci aussi à Maxime pour les fous rire, et les pauses interminables... ! Merci à Stéphane, Maxime, Marine et Nahuel pour les soirées jeux autour d'un bon verre de vin (ou de porto blanc), qui remettent du baume au coeur. Un grand merci à Livia pour faciliter la vie administrative des doctorants, et pour sa bonne humeur. Plus généralement, merci au personnel et doctorants de l'Observatoire de Genève pour leur accueil chaleureux.

Thanks to Rebecca and Frances for their support in writing this thesis. Et merci à Andréa, Céline, Raphaël, Rebecca, Frances, Camille, Daphné, Elise, Marie-Laure, Carine, et Julien, scientifiques ou non, pour les coups de fil interminables, les soirées de retour à Bordeaux, les week-ends ski, et les réveillons mémorables !!

Merci à Nahuel pour m'avoir supporté, encouragé, reboosté, au quotidien, tout au long de ces années d'études. Ce soutien aura été un des plus importants, et des plus efficaces.

Je tiens aussi à remercier toute ma famille pour m'avoir encouragé. J'ai une pensée particulière pour Christiane, Eric, et Jaouad, toujours intéressés et présents. Enfin, je tiens à remercier mes parents pour m'avoir encouragé depuis mes 13 ans dans ce projet fou de devenir astronome ! Pour leur soutient sans faille, à tous les deux, tout au long de ces années. Et un merci tout particulier à ma soeur pour sa gentillesse et sa bonne humeur.

"Fais de ta vie un rêve, et d'un rêve une réalité"
Antoine de Saint-Exupéry

"Je ne crois pas que l'univers soit muet,
je crois plutôt que la science est dure d'oreille..."
Hubert Reeves

Publications related to this thesis

Refereed journals

- ”Beryllium abundances along the evolutionary sequence of the open cluster IC 4651 - New test for hydrodynamical stellar models”
  Smiljanic R. Pasquini P. Charbonnel C. and **Lagarde N.**, 2010, A&A, 510, A50.
- ”Thermohaline instability and rotation-induced mixing in low and intermediate-mass stars. I - Solar metallicity ”
  Charbonnel C. & **Lagarde N.**, 2010, A&A, 522, A10.
- ”Thermohaline instability and rotation-induced mixing. II - Yields of ^{3}He for low- and intermediate-mass stars”
  Lagarde N., Charbonnel C., Decressin T., Hagelberg J., 2011, A&A, 536, A28.
- ”Thermoahline instability and rotation-induced mixing. III - Grid of stellar models and asymptotic asteroseismic quantities fron the pre-main sequence up to AGB for low- and intermediate-mass stars at various metallicities.”
  Lagarde N., Decressin T., Charbonnel C., Egenberger P., Ekström S., and Palacios A., 2012, A&A, 543, A108
- ”Effects of thermohaline instability and rotation-induced mixing on the evolution of light elements in the Galaxy : D, ^{3}He, and ^{4}He”
  Lagarde N., Romano D., Charbonnel C., Tosi M., Chippini C., Matteucci F., 2012, A&A, 542, A62

Conference proceedings - Oral contribution

- ”Thermohaline instability and rotation induced mixing in low and intermediate-mass stars”
  Lagarde N. and Charbonnel C., Proceedings of the Annual meeting of the French Society of Astronomy and Astrophysics, SF2A 2009.
- ”Thermohaline mixing in stars and the long-standing ^{3}He problem”
  Charbonnel C. and **Lagarde N.**, Chemical Abundances in the Universe: Connecting First Stars to Planets, proceeding IAU Symposium 265.
- ”Thermohaline mixing in stars - Solving the long-standing ^{3}He problem”
  Charbonnel C. and **Lagarde N.**, 2010, Light elements in the Universe proceeding IAU Symposium 268.
- ”Thermohaline instability and rotation-induced mixing in low- and intermediate-mass stars”
  Lagarde N. and Charbonnel C., Proceedings of the Annual meeting of the French Society of Astronomy and Astrophysics, SF2A 2010.

- ”Thermohaline mixing in the small-Péclet number approximation”
  Lagarde N., Lignières F., and Zahn J.P., 2010 International Summer Institute for Modeling in Astrophysics.

- ”Impact of rotational mixing on the global and asteroseismic properties of red giants”
  Eggenberger, P. ; **Lagarde, N.** ; Charbonnel, C., 2011, workshop ”Red Giants as Probes of the Structure and Evolution of the Milky Way”

- ”Effects of rotation and thermohaline mixing in red giant stars”
  Charbonnel, C. ; **Lagarde, N.** ; Eggenberger, P. , 2011, workshop ”Red Giants as Probes of the Structure and Evolution of the Milky Way”

Conference proceedings - Poster contribution

- ”Beryllium abundances along the evolutionary sequence of the open cluster IC 4651”
  Smiljanic R. Pasquini P. Charbonnel C. and **Lagarde N.**, 2010, Light elements in the Universe proceeding IAU Symposium 268.

- ”Li survey in giant stars : Probing non-standard stellar physics”
  Lagarde N., Charbonnel C., Jasniewicz G., North P., Shetrone M., Hollek J., Smith V.V., 2010, Light elements in the Universe proceeding IAU Symposium 268.

Chapter 1

Introduction

1.1 General context

Stars are the building blocks of the Universe. Understanding their evolution is crucial to improve our knowledge from chemical properties of galaxies to the formation and evolution of planetary systems.

As shown by the initial mass function (e.g. Salpeter 1955; Scalo 1986; Kroupa 2001; Luhman et al. 2000), low- and intermediate-mass stars are the most numerous stars in our Galaxy. They form the dominant stellar component of our Galaxy and represent a very important astrophysical interest. In their advanced phases, these stars undergo important changes of their structure and chemical composition. Due to strong winds during the superwind phase, which leads to the emergence of planetary nebula, they contribute significantly to the enrichment of the interstellar medium and to the chemical evolution of galaxies. They have a rich nucleosynthesis, with a large part of enrichment in ^{4}He, and they dominate the production of ^{13}C, ^{14}N, and main s-process elements. We are interested here specifically in their contribution to the evolution of ^{3}He in the Galaxy.

Observations allow to constrain the modeling of low- and intermediate-mass stars. Interferometry, spectroscopy and spectropolarimetry are classical methods to get information about stellar mass, radius, rotation, magnetic activity and chemical abundances. Indeed, spectroscopic studies with the *Very Large Telescopes* (VLT) with powerful instruments such as the high-resolution optical spectrograph *Ultraviolet and Visual Echelle Spectrograph* (UVES), *the CRyogenic high-resolution InfraRed Echelle Spectrograph* (CRIRES), or the intermediate-resolution spectrograph *X-shooter*, allow to derive the global and chemical properties of the stars, stellar clusters, interstellar matter, galaxies, and intergalactic medium. The spectropolarimetric observations, for example with *NARVAL* (OMP) and *ESPADON* (CFHT), have underlined the existence of magnetic fields at the surface of low-mass red giant stars (e.g. Aurière et al. 2011). Moreover, infrared data can give informations about the signature of stellar mass loss (*VISIR* at VLT).

On the other hand, asteroseismology has emerged during the last decade, and is a powerful tool to investigate the internal stellar structure. *CoRoT* (Baglin et al. 2006), and *Kepler* (Borucki et al. 2010) missions have already observed a large sample of red giant stars wherein radial and non-radial solar-like oscillations can be detected. They have opened the possibility to probe the deep interior of low- and intermediate-mass stars. The most important breakthrough of the *CoRoT* and *Kepler* missions are the detection of non-radial oscillations in red giants, and mixed modes which contribute to the determination of the precise evolutionary phase of giant stars (Mosser et al. 2011). Moreover, the large number of stars observed with these missions allows the statistical analysis of red giants based on their pulsation properties (Miglio et al. 2009). The internal rotation can be accessed with seismology and it has been studied in red giant and in some subgiant stars (Beck et al. 2012, Deheuvels et al. in prep.). In addition, it has been shown that asteroseismology can keep in the study of magnetic activity by the detection of starspots (García et al. 2010). These missions provided an independent way to determine mass and radius of stars, and then better constraints on stellar evolution models.

1.2 Overview of the thesis

The classical stellar evolution model of low- and intermediate-mass stars have difficulties to reproduce observations. In particular spectroscopic observations underline the existence of abundance anomalies at the surface of many stars. Indeed, standard models do not explain stellar surface evolution of elements associated with hydrogen-burning like ^{7}Li, ^{3}He, C, O, N, and Na, especially along the red giant branch (RGB).

We study in details standard predictions from the pre-main sequence to the end of the thermal pulses phase. In this aim, we based our discussion in chapter 2, on a 1.5 $M_\odot$ model at solar metallicity, which corresponds to the mass domain where thermohaline mixing is efficient. We also discuss in this chapter, the metallicity and the mass effects on the chemical surface abundances all along the stellar evolution.
In chapter 3, we present an overview and a synthesis of numerous observational data available in the literature. To underline abundance anomalies, we also compared several of these abundances (^{7}Li, ^{9}Be, carbon isotopic ratios, nitrogen, oxygen isotopic ratios, and sodium) with our standard models.

Different transport processes have been proposed in literature to explain these abundance anomalies observed in red giant stars. More particularly, rotation-induced mixing has been investigated as a possible source of mixing on the RGB. It has been found that rotation-induced mixing has an impact on stellar structure and on the chemical surface abundances during the main sequence, but it does not explain abundance anomalies observed in red giants (Palacios 2002; Palacios et al. 2003, 2006).

In chapter 4, we present in details this transport process with thermohaline instability which has been proposed by Charbonnel & Zahn (2007b) to be a fundamental physical process in low-mass red giant stars. Since the last five years, thermohaline mixing has been discussed in different astrophysical contexts which are presented in chapter 4. In addition, to better constrain the diffusion coefficient of thermohaline instability, hydrodynamic studies have been already published trying to reach stellar conditions (Denissenkov 2010; Denissenkov & Merryfield 2011; Traxler et al. 2011a; Rosenblum et al. 2011), but remain too far from real conditions in stars. We also discuss these studies in chapter 4 and we present my preliminary hydrodynamic study of thermohaline instability.

Thermohaline mixing is then considered to be a good candidate to explain abundance anomalies in low-mass red giant stars, and should be tested in a large domain of mass and metallicity. In this aim, I computed, with the code STAREVOL, stellar evolutionary models including thermohaline instability and rotation-induced mixing at various metallicities and stellar masses. With this grid, including for the first time these two processes, I study their effects in low- and intermediate-mass stars on internal structure, stellar evolution, nucleosynthesis as well as asteroseismic and chemical properties (Chapter 5, and Charbonnel & Lagarde (2010a); Lagarde et al. (2011, 2012a)). To validate our results, we compare our models with observations of surface abundances in field and open clusters stars. For this purpose, we use the abundance evolution of lithium, beryllium (for example IC4651, Smiljanic et al. 2010), nitrogen, and carbon isotopic ratio in main sequence, sub-giants, and giants stars (Charbonnel & Lagarde 2010a, at solar metallicity).

In recent years, a large number of asteroseismic observations have been obtained for different kinds of stars. The comparison between models including a detailed description of transport processes in stellar interiors and asteroseismic constraints from the space missions *CoRoT* and *Kepler*, opens a new promising path for our understanding of stars. In the third part of chapter 5 (Lagarde et al. 2012b), we present signatures of rotation and thermohaline instability on the asteroseismic stellar properties that can be detected observationally. This comparison between asteroseismic observations and stellar models is then essential to improve the theoretical stellar evolution.

The predictions of these new stellar models including both thermohaline instability and rotation-induced mixing show that these two transport processes have an impact on the chemical composition of the material ejected by the star in the interstellar medium. In chapter 6, we quantify the effects of these processes on the production and destruction of ^{3}He over the lifetime of low- and intermediate-mass stars, which are classically considered to be net ^{3}He producers, and we compute yields of ^{3}He for various masses and metallicities (Lagarde et al. 2011). In this chapter, we also present the impact of these new yields on the evolution of light elements in our Galaxy, using the galactic chemical evolution code developed by D. Romano, C. Chiappini, M. Tosi, and F. Matteucci (Lagarde et al. 2012b), and we resolve the long-standing "^{3}He problem".

Chapter 2

Evolution and nucleosynthesis of low- and intermediate-mass stars : Standard predictions

In this thesis we are going focus on stars who end their lives as CO white dwarfs and have an initial mass typically lower than 6-8 $M_\odot$. Among these objects one can distinguish between low- and intermediate-mass stars, depending whether central helium burning ignites in degenerate ($M \leq 2.0$ - 2.5 $M_\odot$ at $Z_\odot$) or non-degenerate conditions. The aim of this chapter is to describe the evolution of the internal structure and of the global and chemical properties of these stars as predicted by the standard models from the pre-main sequence to the end of the thermal pulse phase. Our discussion is based on a grid of models we computed with the code STAREVOL for a large domain in mass and metallicity, and which is presented and compared with observations in different papers. Input physics used in the computation are presented in Lagarde et al (2012, Part III) and in Chapter 5. For the mass loss we use Reimers (1975) formula (from the beginning of central hydrogen burning up to central helium exhaustion), and Vassiliadis & Wood (1993) prescription (on asymptotic giant branch). In these standard models no transport mechanism other than convection is taken into account. Standard predictions will be compared with observations of surface abundances of low- and intermediate-mass stars in Chapter 3, which will help us to detect the signatures of different non-standard transport processes which will be studied in the following chapters. Non standard models including rotation-induced mixing and thermohaline instability will be presented in Chap. 4 and 5.

In the following we present our detailed predictions for a standard 1.5 $M_\odot$ model at solar metallicity, which belongs to the mass domain where thermohaline mixing is very efficient (see chap. 5). We will also discuss the effects of mass and metallicity on the abundance variations of different chemical elements along the evolution. The corresponding standard tracks are shown in the Hertzsprung Russel (HR) diagrams in figure 2.1.

The effects of stellar mass and metallicity on the evolution in the Hertzsprung Russel diagram are also illustrated in figure 2.2 for the 1.5 and 6.0 $M_\odot$ cases.

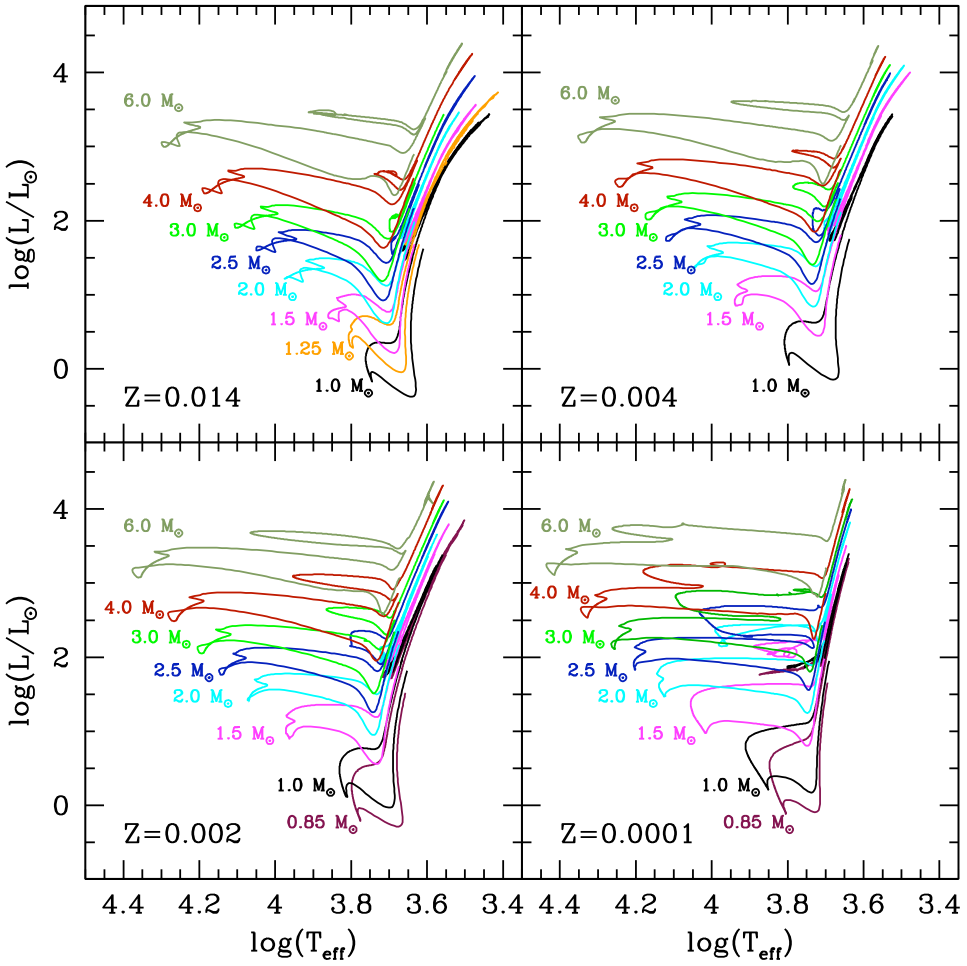

Figure 2.1: Theoretical evolutionary tracks in the Hertzsprung Russel diagram for all our standard models computed at four metallicities (Z$_\odot$ (top left panel), Z=0.004 (right top panel), Z=0.002 (bottom left panel), Z=0.0001 (bottom right panel)), from the pre-main sequence to the end of the asymptotic giant branch with the code STAREVOL. Adapted from Lagarde et al (2012, Paper III).

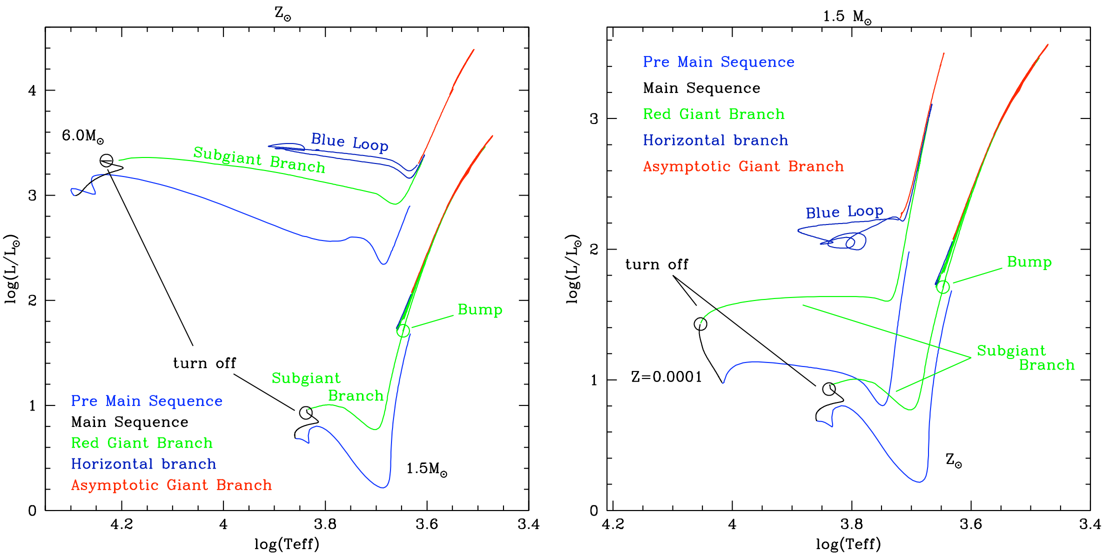

Figure 2.2: Evolutionary tracks in the HR diagram for standard models computed with STAREVOL. Effects of mass at solar metallicity *(left panel)* and of metallicity for 1.5 $M_\odot$ star *(right panel)*. Evolutionary phases are indicated by a colour label : Pre Main Sequence (lightblue), Main Sequence (black), Red Giant Branch (green), He-burning phase (blue), and Asymptotic giant branch (red). We also indicate the position of the subgiant branch and turn off.

2.1 Pre-Main sequence

We follow the evolution of stars along the Hayashi line without taking into account accretion. The star is then fully convective. During the so-called pre-main sequence, gravitational contraction is the main source of energy until stars ignite core hydrogen burning. On the pre-main sequence the central temperature (T_c) and density (ρ_c) increase (figure 2.3), together with the effective temperature while the stellar luminosity and radius decrease significantly. A radiative core appears and the convective envelope retreats in mass. Once T_c and ρ_c are sufficient nuclear reactions begin and the nuclear energy released by the central H-burning becomes dominant.

Before the arrival on the Zero Age Main Sequence (ZAMS), light elements are the only chemicals that are affected by nuclear reactions at relatively low internal temperature. In particular, the reaction D(p,γ)^{3}He occurs at a temperature of $\sim 10^6$K while the 1.5 $M_\odot$, $Z_\odot$ star is still convective. For [1.5 $M_\odot$, $Z_\odot$] model, at log ($L/L_\odot$) $\sim$ 1.4, ^{3}He surface abundance therefore increases from $2.83 \cdot 10^{-5}$ to 10^{-4} (in mass fraction, see Fig. 2.10).

When the central temperature is $\sim 2.5 \times 10^6$K, the star is still convective, and the lithium decreases at the surface.

2.2 Main sequence

During the main sequence the energy production is dominated by central hydrogen burning to helium. When the [1.5 $M_\odot$,$Z_\odot$] model arrives on the ZAMS, its convective core fulled up with hydrogen burning through the CNO cycle is surrounded by a radiative zone and a thin convective envelope. For less massive stars (the limit depending on metallicity), the convective core vanishes early on the main sequence when energy production is dominated

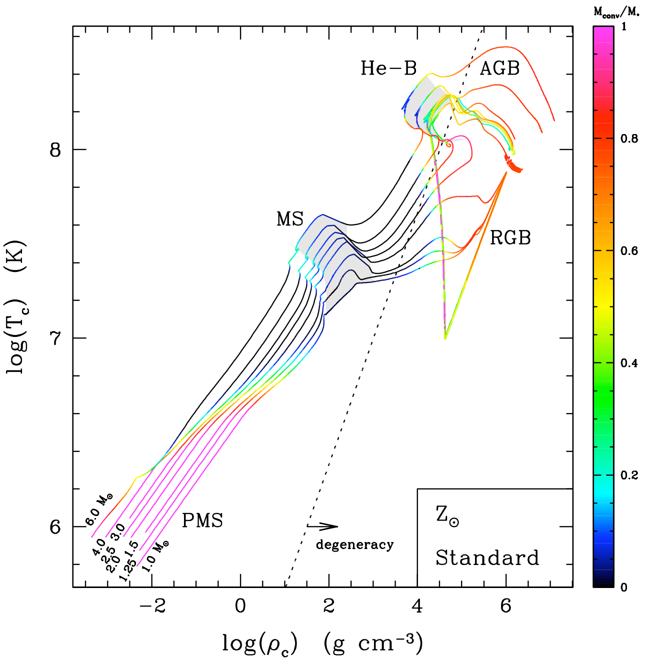

Figure 2.3: Central temperature as a function of central density for the standard models at Z$_\odot$. Colours indicate the mass of convective regions (convective core and/or convective envelope) over the total stellar mass (see colours indice on the right). Shaded regions indicate the phases of central hydrogen-burning (MS) and helium-burning (He-B). The dotted line shows roughly the separation between non-degeneracy and degeneracy of the electron gas ($\log(\mathrm{T}_c) = 5 + \frac{2}{3}\log(\rho_c)$).

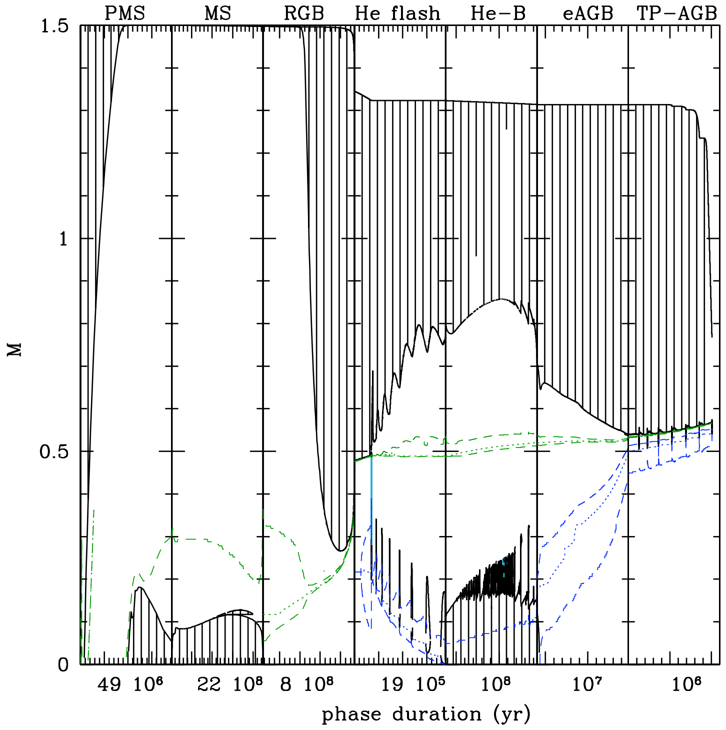

Figure 2.4: Evolution of stellar structure of a standard 1.5 $M_\odot$ model at solar metallicity (Kippenhahn diagram). The successive panels correspond to the Pre Main sequence (PMS), the Main Sequence (MS), the Red Giant Branch (RGB), the He flash, the central helium burning, early-AGB (eAGB), and the thermal pulses phase (TP-AGB). Convective regions (core and envelope) are shown with hachured regions. The hydrogen-burning shell and helium-burning shell are shown in green and blue respectively (in both cases, the dotted lines show the region of maximum nuclear energy production). The time given in abscissa below the panels correspond to the duration of each phase.

by the PP chains. Positions of stars on the main sequence (from ZAMS to turnoff) change relatively little during this long lasting phase (see Fig. 2.1 and 2.2).

In figure 2.1 , 2.2 and 2.3 we can see the effects of the stellar mass and metallicity on the evolutionary tracks and on the central temperature and density. The effective temperature and luminosity on the main sequence increase with increasing stellar mass and decreasing metallicity. As the proportion of metals is greater in the higher metallicity stars, the convective core is larger and persists during almost all of the main sequence. At the end of the hydrogen burning (turn off), only the envelope is convective.

Figure 2.5 depicts the chemical structure of the 1.5 $M_\odot$ and 6.0 $M_\odot$ models at Z=0.014 and Z=0.0001 at the end of central hydrogen burning. The most fragile elements lithium, beryllium, and boron burn by proton captures at relatively low temperature and are preserved only in the most external stellar layers (only Li is shown). During the main sequence H-burning through the pp-chains builds up a ^{3}He peak as a result of the competition between the production reactions (namely p(p, D) followed by D(p, ^{3}He)) and the destruction ones (i.e., ^{3}He(^{3}He, ^{4}He), ^{3}He(^{4}He, ^{7}Be)). Deeper inside the star the ^{13}C peak results from the competition between the ^{12}C(p,γ)^{13}N($\beta + \nu$)^{13}C and ^{13}C(p,γ)^{14}N reactions. ^{12}C and ^{16}O are partially converted into ^{14}N whose abundance profile presents a double plateau.

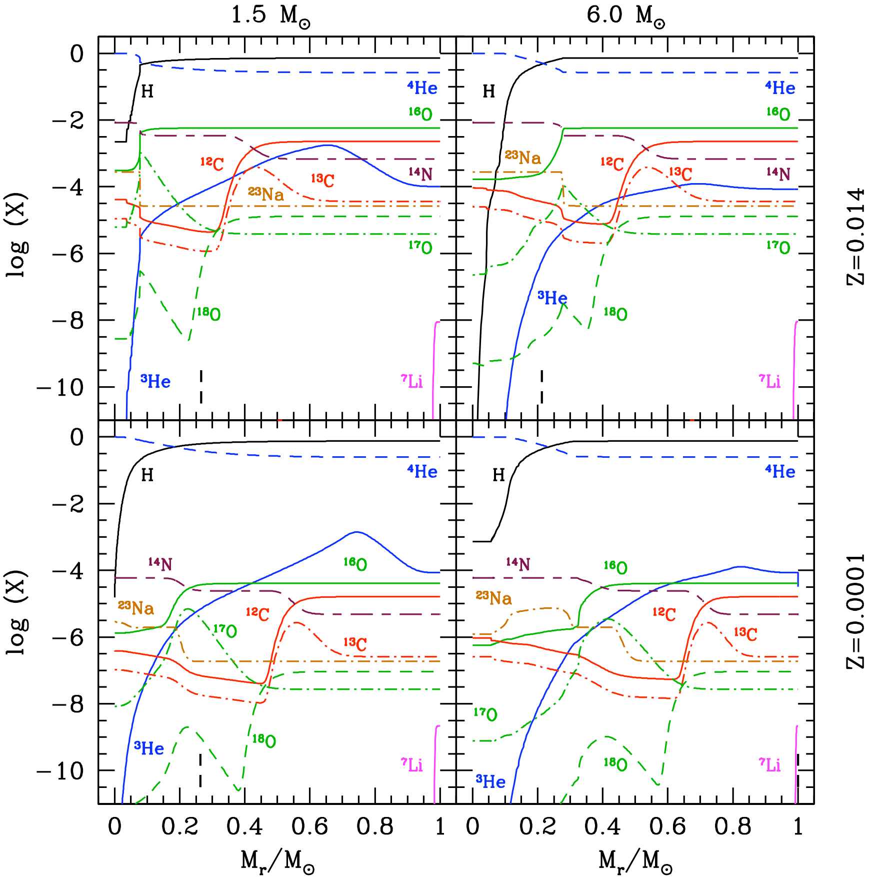

Figure 2.5: Abundance profiles as a function of coordinate in mass, at the main sequence turn off, for the 1.5 M$_\odot$ and 6.0 M$_\odot$ models (left and right respectively) at Z$_\odot$and Z=0.0001 (top and bottom respectively). The vertical dashed lines show, in all cases, the maximum depth reached by the convective envelope at its maximum extent during the first dredge-up.

ON cycling results in ^{18}O depletion and in the building up of a ^{17}O peak. In the very central regions, ^{23}Na is produced through proton captures by ^{22}Ne. The mass fraction of ^{4}He increases in the central regions, while that of hydrogen decreases.

The influence of the metallicity and stellar mass on the chemical structure at the turn-off is illustrated in figure 2.5. For a star of a given mass, an increase of the initial metallicity induces an increase of the interior opacity, and thus a decrease of the temperature (see Fig. 2.6), pressure, and density at a given depth inside the star. Consequently, the abundances profiles are shifted inward when the metallicity is higher and stellar mass is lower (see for exemple ^{13}C and ^{3}He peak). When the mass increases and metallicity decreases, the region of Li destruction is closer to the convective envelope where the temperature is higher (see Fig. 2.6).

2.3 The sub-giant branch

For low- and intermediate-mass stars, at the turn off point, the central temperature of the 1.5 M$_\odot$ model does not exceed ~25-28·10^{6}K, for Z= 0.014 and Z= 0.0001 respectively, which is insufficient to burn helium. Therefore at the end of the main sequence, the helium core is deprived of nuclear sources and becomes isothermal. As seen in figure 2.6, at solar

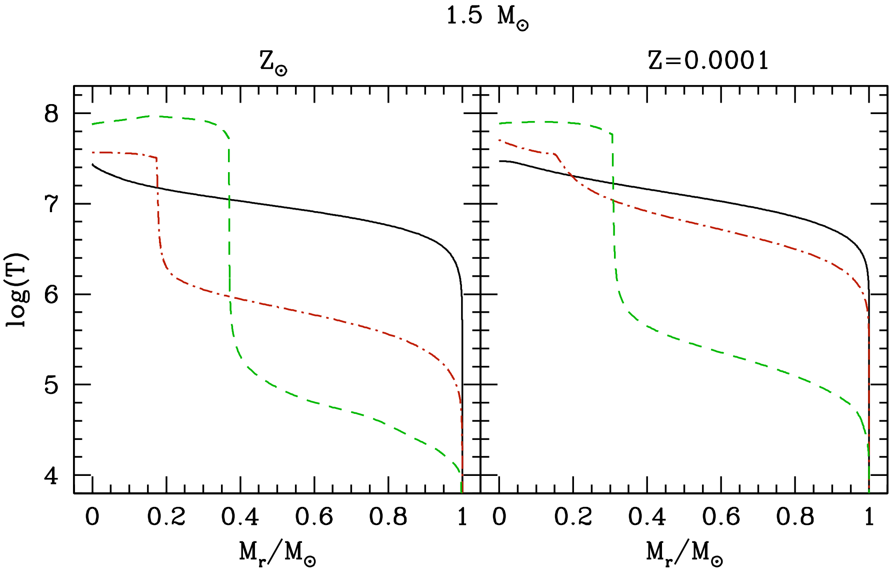

Figure 2.6: Temperature profiles at the turn off (solid black line), at the BUMP luminosity (red dashed-dotted lines), and at the RGB tip (dashed green lines) for $1.5 M_\odot$ at Z=0.014 and Z=0.0001.

metallicity during the Red Giant Branch (RGB), the temperature inside the core stays almost constant (red curve, left panel). The hydrogen burning migrates into a shell around the He core, which then grows in mass due to the nuclear burning in the shell. This H-burning phase in the shell continues until the core mass reaches ∼10% of the stellar mass which corresponds to the Schönberg Chandrasekhar limit. Then, the star experiences core contraction, which is accompagnied by an envelope inflation, and the star evolves rapidly toward the red giant branch. In the stellar core, electrons are degenerated. The transition from central to shell burning can be seen in Fig. 2.4 (green lines).

The convective envelope expands as a result of the core contraction and shell burning, and the effective temperature decreases while stellar luminosity stays almost constant. This phase is called the ”Sub giant branch” (SBG), when the stars cross HR diagram almost horizontally. This occurs at higher luminosity when the stellar mass increases and metallicity decreases (see Fig. 2.1 and 2.2). In low-mass star like the 1.5 M$_\odot$, Z$_\odot$ case, due to significant degeneracy, the helium core stays isothermal until the star reaches the tip of the RGB.

The first dredge-up

When the star expands after the turnoff and moves towards the RGB, its outer layers cool down, and external convection develops. The convective envelope grows in mass and deepens inside the star as indicated by the vertical dashed lines in Fig. 2.5 (see also third panel of Fig.2.4). This leads to the so-called *first dredge-up*, where the convective envelope dilutes the external convective stellar layers with hydrogen-processed material, resulting in a change of the surface abundances. As a consequence, the surface abundances of ^{7}Li, ^{9}Be, ^{12}C and ^{18}O decrease while those of ^{3}He, ^{4}He, ^{13}C, ^{14}N, and ^{17}O increase (see Fig. 2.10 and 2.11). Consequently, the isotopic ratios ^{12}C/^{13}C, ^{12}C/^{14}N, ^{16}O/^{17}O, and ^{18}O/^{16}O decrease at the surface (see Fig. 2.9 and 2.12). Figure 2.15 shows clearly these signatures of the first dredge-up at Log(L/L$_\odot$)∼ 0.8 and 1.6 for 1.5 M$_\odot$ stars at Z$_\odot$ and Z=0.0001 respectively.

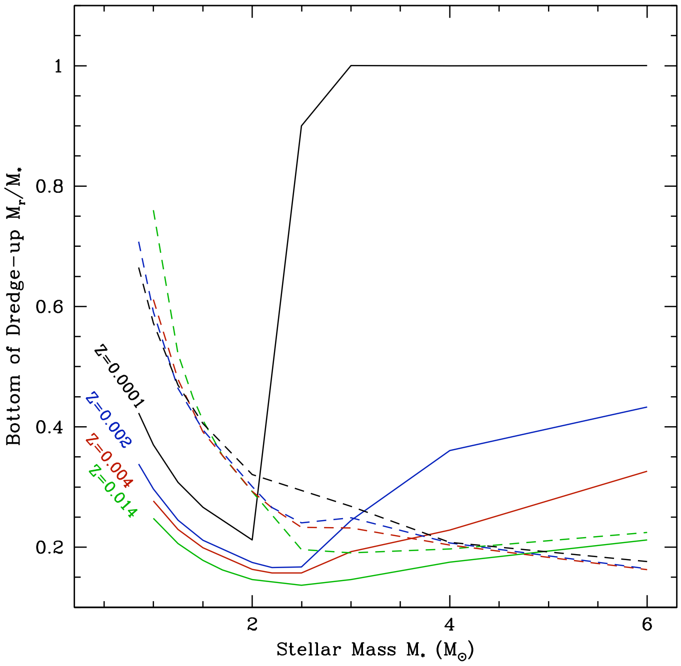

Figure 2.7: Maximum depth in mass of the convective envelope relative to the total stellar mass reached during first and second dredge-up (solid and dashed lines respectively) as a function of initial stellar mass and for different metallicities, as indicated by the colors of the curves. Standard models from Lagarde et al (2012).

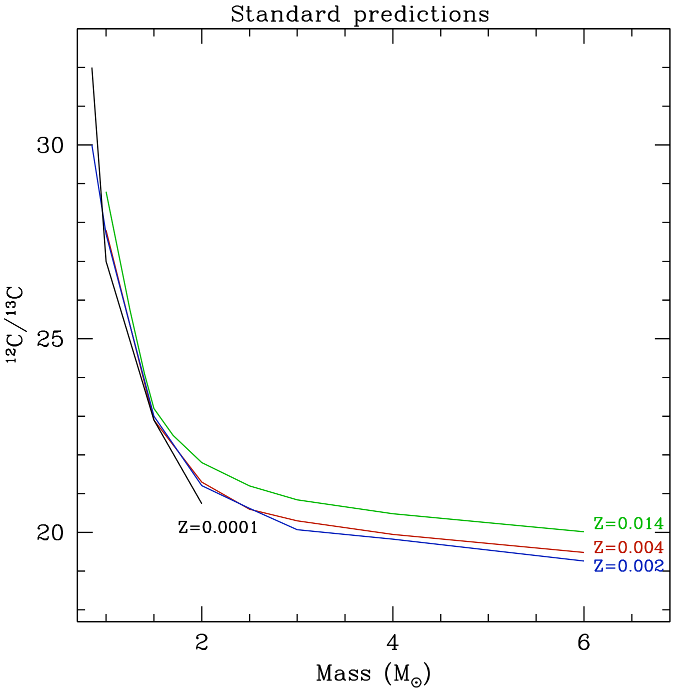

Figure 2.8: Carbon isotopic ratio at the end of the first dredge-up as a function of initial stellar mass for different value of metallicity (Z=0.014, 0.004, 0.002 and 0.0001). At Z=0.0001 we only show star undergoes a significant first dredge-up (see Fig.2.7). Standard models from Lagarde et al (2012).

The first dredge-up efficiency (in terms of maximum penetration depth of the convective envelope) decreases with decreasing metallicity as shown in Fig.2.7 (at $Z=10^{-4}$, no first dredge-up occurs for stars more massive than $\sim$ 3.0 $M_\odot$). Figure 2.8 shows the surface carbon isotopic ratio at the end of the first dredge-up as a function of initial stellar mass. We can deduce that the chemical variations during the first dredge-up depend on the initial stellar mass as well as on the metallicity (see e.g. Fig. 2.8 and 2.15).

Figure 2.9 shows the evolution of the carbon isotopic ratio at the surface as a function of luminosity for various initial stellar masses at two metallicities. For a given stellar mass, figure 2.9 shows that the depletion of $^{12}C/^{13}C$ begins at lower luminosity when metallicity increases. For a given stellar mass, the post dredge-up value of $^{12}C/^{13}C$ decreases when the metallcity decreases (see Fig. 2.8, and 2.9). This dependance is true for $^{12}C/^{14}N$, ^{3}He (Fig.2.10), A(Li)[1] and A(Be)[2] (see Fig. 2.11), as well as for oxygen isotopic ratios (see Fig. 2.12).

At a given metallicity, our mass range can be devide in two groups :

- For stars with $M \lesssim 2$-2.5 $M_\odot$ (for Z= 0.0001 and Z= 0.014 respectively), during the first dredge-up the convective envelope reaches deeper regions when the initial stellar mass increases (see Fig.2.7). This implies a decrease of the $^{12}C/^{13}C$ post dredge-up value when the initial stellar mass increases, as well as $^{12}C/^{14}N$, A(Li), A(Be), $^{16}O/^{17}O$, and $^{18}O/^{16}O$.

- For higher mass stars, the maximum expansion of the convective envelope during the

---

[1] $A(Li)=\log(\frac{X(Li)}{X(H)} \cdot \frac{A_H}{A_{Li}})+12$, with X(Li) the Lithium mass fraction

[2] $A(Be)=\log(\frac{X(Be)}{X(H)} \cdot \frac{A_H}{A_{Be}}+12$, with X(Be) the Beryllium mass fraction

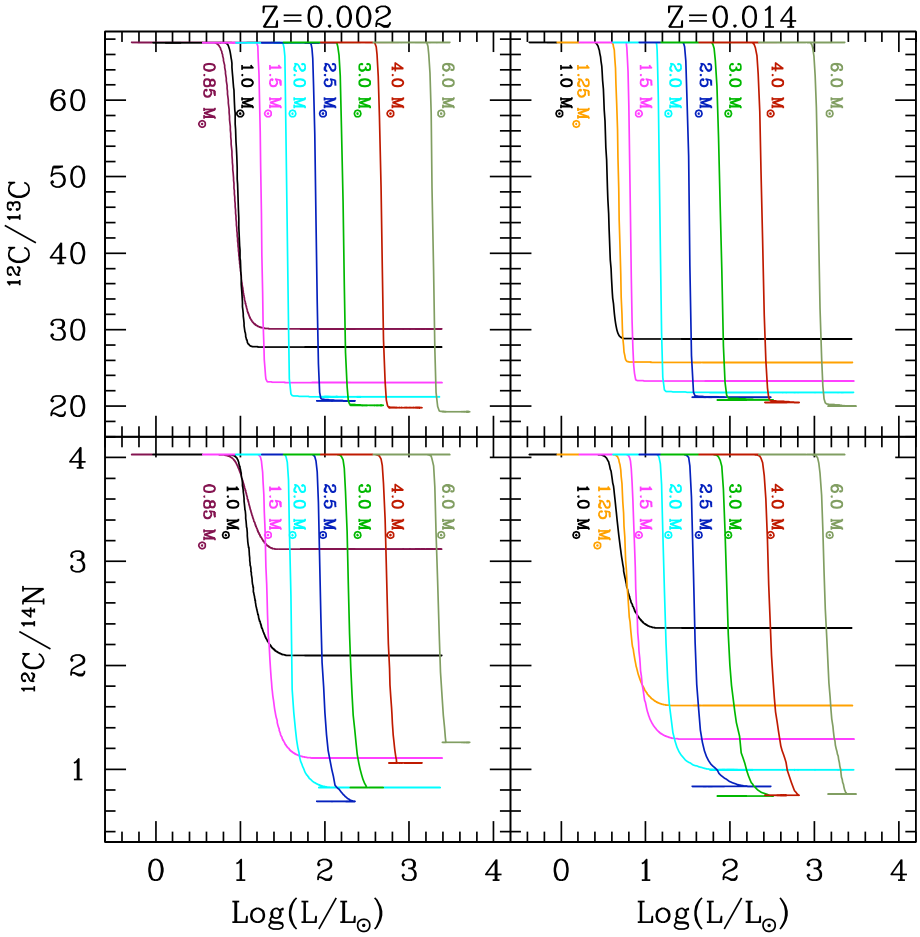

Figure 2.9: Theoretical evolution of carbon isotopic ratio (top panels) and $^{12}C/^{14}N$ (bottom panels) at the stellar surface as a function of luminosity for stellar models of various masses at Z=0.002 (left panel) and Z=0.014 (right panel) from the main sequence up to the early AGB.

first dredge-up is less important when initial stellar mass increases. This results in an almost constant $^{12}C/^{13}C$ when stellar mass increases, while it implies a decreases of $^{12}C/^{14}N$, A(Li), A(Be), $^{16}O/^{17}O$, and $^{18}O/^{16}O$.

From the subgiant branch to the RGB tip, the temperature at the base of the convective envelope is always insufficient to activate nuclear reactions. As a consequence, in standard models the only change in surface abundances is due to the first dredge-up on the subgiant branch ; after this episode the surface abundances remain constant all along the RGB once the convective envelope recedes.

2.4 Red Giant Branch

During the ascent of the Red Giant branch (RGB), the stellar effective temperature slightly decreases while the stellar luminosity and radii increase greatly with increasing core mass for low-mass stars (Fig. 2.1 and 2.2). On the other hand, the helium core grows in mass thanks to the hydrogen burning shell all along the RGB.

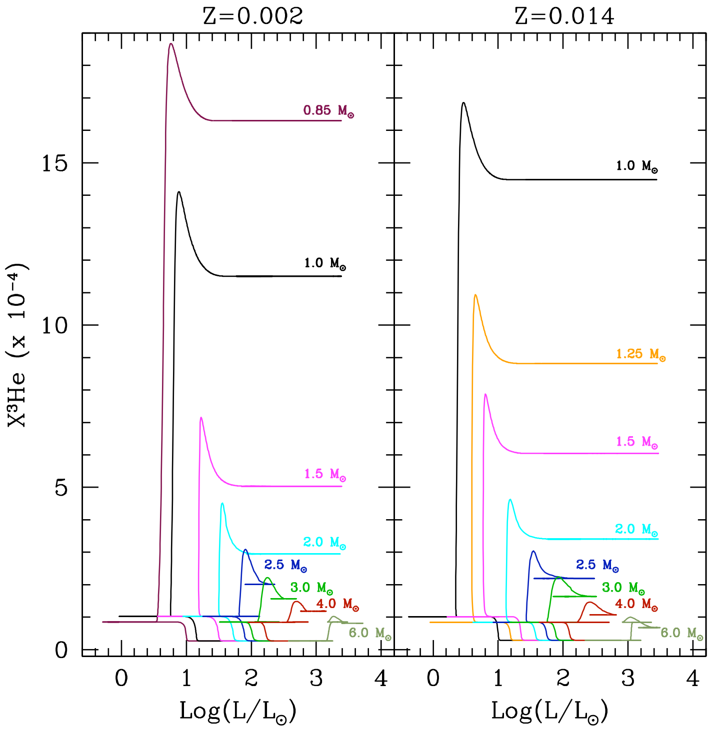

Figure 2.10: Same as Fig. 2.9 for the theoretical evolution of ^{3}He.

Figure 2.13 shows the abundance profiles of different chemical elements and the profile of the gradient of mean molecular weight (∇_μ) before the bump luminosity (see below for definition) as a function of δM for 1.5 M$_\odot$ at Z$_\odot$. The variable δM is a relative mass coordinate allowing for a blow-up of the radiative region above the Hydrogen Burning Shell (HBS). Namely,

$$\delta M = \frac{M_r - M_{HBS}}{M_{BCE} - M_{HBS}},$$

is equal to 1 at the base of the convective envelope M$_{BCE}$ (the Schwartschild criterium allows us to define it) and to 0 at the base of the HBS M$_{HBS}$ (which is chosen as the depth where the hydrogen mass fraction equals 10^{-10}).

As seen previously, during the first dredge-up, the convective envelope homogenizes a large fraction in mass of the star and builds a very steep gradient of molecular weight at its maximum penetration (dashed black line in Figure 2.13) between the He-enriched central layers and the homogeneous H-rich outer layers. This corresponds to the external peak at $\delta M \sim 0.95$ in ∇_μ profile in Figure 2.13. On the other hand, the deeper peak (at δM$\sim$0.05) matches the region where H is efficiently depleted by nuclear reactions in the HBS.

The bump luminosity

As seen in Figure 2.14, the monotonous increase of the stellar luminosity along the RGB momentarily stops when the hydrogen burning shell crosses the molecular weight barrier left behind by the first dredge-up. At that moment, indeed, the mean molecular weight of the HBS becomes smaller, which implies a decrease of the total stellar luminosity. This is the so-called **bump** in the luminosity function. When the region of nuclear energy

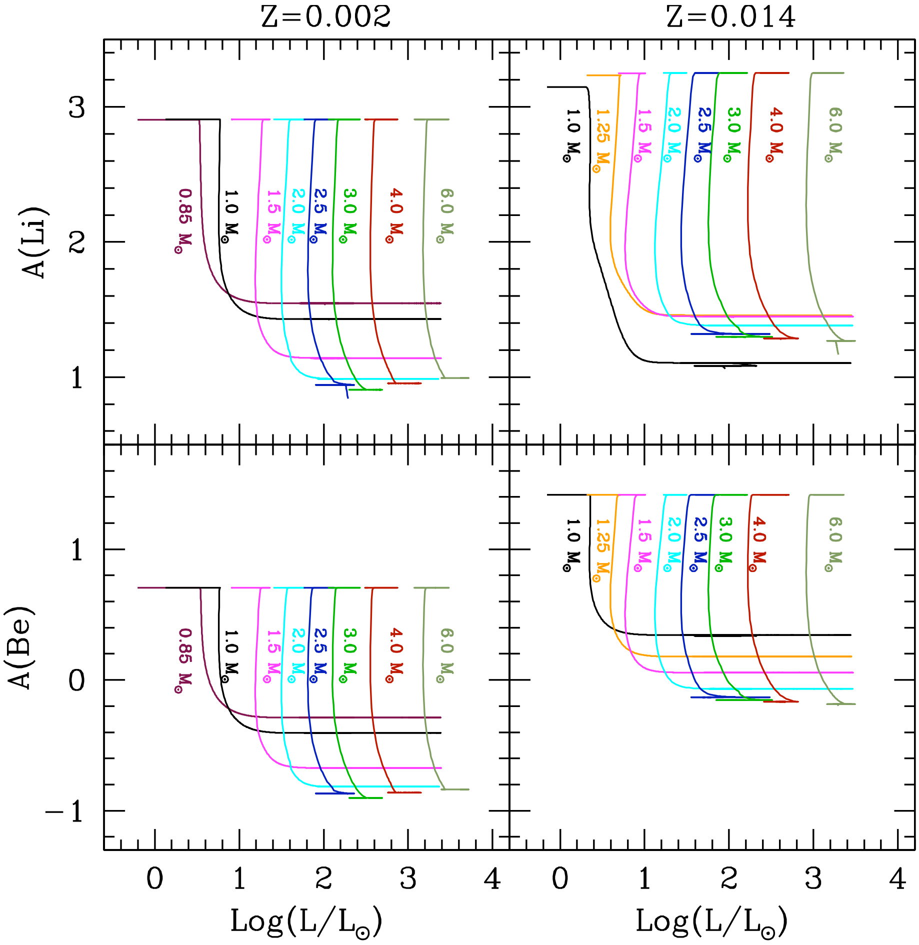

Figure 2.11: Same as Fig. 2.9 for the theoritecal evolution of A(Li) (top panels) and A(Be) (bottom panels).

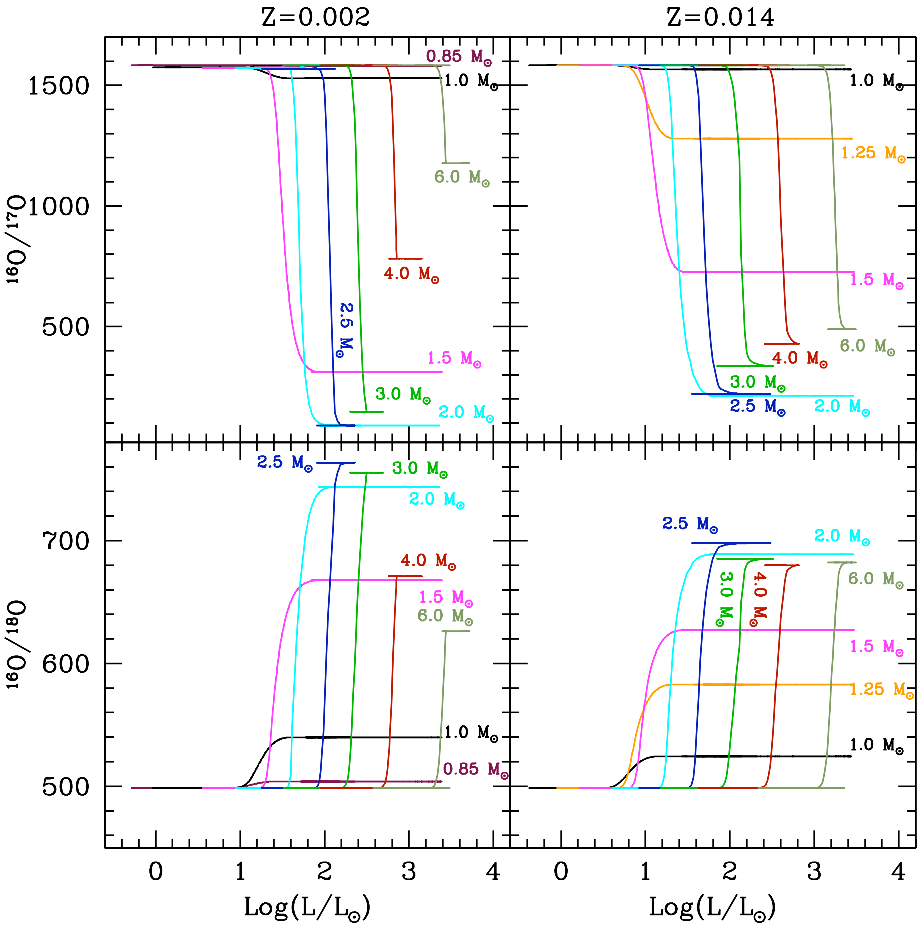

Figure 2.12: Same as Fig. 2.9 for the theoritecal evolution of $^{16}O/^{17}O$ (top panels) and $^{16}O/^{18}O$ (bottom panels).

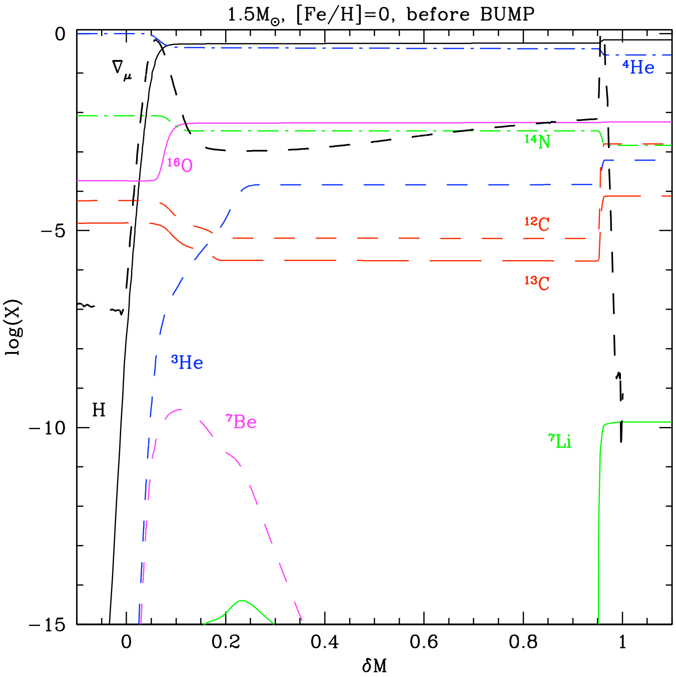

Figure 2.13: Abundance profiles as a function of δM for our $1.5 M_\odot$ standard model at solar metallicity before the bump luminosity. The gradient of mean molecular weight is represented by the black dashed line.

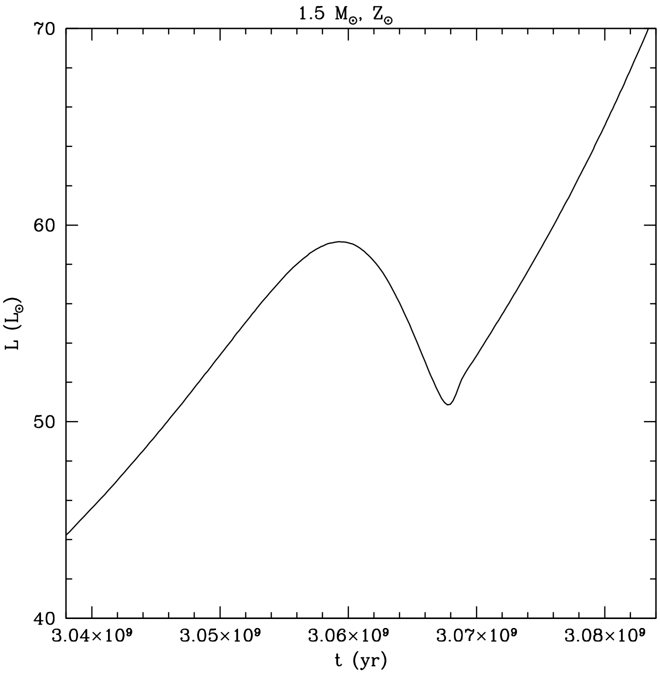

Figure 2.14: The evolution of the stellar luminosity around the bump as a function of time for our 1.5 $M_\odot$ at solar metallicity.

production has passed this discontinuity, the mean molecular weight slightly increases and the stellar luminosity increases again. The bump luminosity is indicated on Fig.2.15 by the asterisk at Log($L/L_\odot$)$\sim$ 1.7 and 2.7 for [1.5 $M_\odot$, $Z_\odot$] and [1.5 $M_\odot$, $Z=10^{-4}$] stars, respectively (see also Fig. 2.2).

Intermediate-mass stars are objects that ignite central helium-burning in a non-degenerate core at relatively low luminosity on the RGB, well before the HBS reaches the mean molecular weight discontinuity caused by the first dredge-up. Consequently, these objects do not go through the bump on their short ascend of the RGB.

Towards the RGB tip

After the bump, the HBS continues to move outwards (in mass), growing the mass core and increasing stellar luminosity. In low-mass stars ($M \lesssim 2.0$-2.5 $M_\odot$), an increase of the core temperature as a result of contraction is prevent by neutrino emission. Due to strong neutrinos cooling, the maximum temperature is not in the center but at a given depth $M_r\sim$ 0.17 $M_\odot$ for [1.5 $M_\odot$, $Z_\odot$] model (see Fig.2.6 green dashed line), where degeneracy is lower. Helium burning thus starts in the external layers of the core, where fusion reactions in degenerate medium are unstable, and produce a thermal runaway : **He flash**. The energy from the flash drives a new temporary convective layer (between convective envelope and radiative core), which rapidly dies out, increasing temperature at the center, and lifting degeneracy. Thereafter, a series of secondary flashes gradually lift the core degeneracy and allow the maximum temperature to reach at the center.

For higher initial mass stars ($M>2.0$ $M_\odot$ at $Z_\odot$), the core mass and temperature at the turnoff is higher, and the degeneracy is much weaker. The maximum temperature is then located at the center of the star, and helium ignites in non-degenerate conditions.

2.5 He-burning phase

After the violent helium flash and a serie of secondary He flashes, the star enters the phase of central He burning when He is converted into ^{12}C and ^{16}O in a convective core. The temperature of He-ignition depends on the density ($\propto \rho^{-2}$). Consequently, He ignition occurs at a slightly higher T_c when the stellar mass increases (see Fig. 2.3). This helium burning phase is shorter than the main sequence. Indeed, the duration of the He-burning phase is :

- For 1.5 $M_\odot$ star at $Z_\odot$, $t_{\rm HeB} \sim 1.06{\cdot}10^8$ yr (i.e. $\sim$ 4.6 % of the MS)
- For 1.5 $M_\odot$ star at $Z=10^{-4}$, $t_{\rm HeB} \sim 9.47{\cdot}10^7$ yr (i.e. $\sim$ 3.8% of the MS)
- For 6.0 $M_\odot$ at $Z_\odot$, $t_{\rm HeB} \sim 1.4{\cdot}10^7$ yr (i.e. $\sim$ 19% of the MS)

In the HR diagram this phase is known as "the clump".

2.6 The Asymptotic Giant Branch

2.6.1 The early-AGB phase

When helium is exhausted in the stellar center, He burning ignites in a shell surrounding the CO degenerate core (see sixth panel "e-AGB" on Fig. 2.4). The surface layers expand and the convective envelope deepens again. This leads to a second dredge-up in stars with

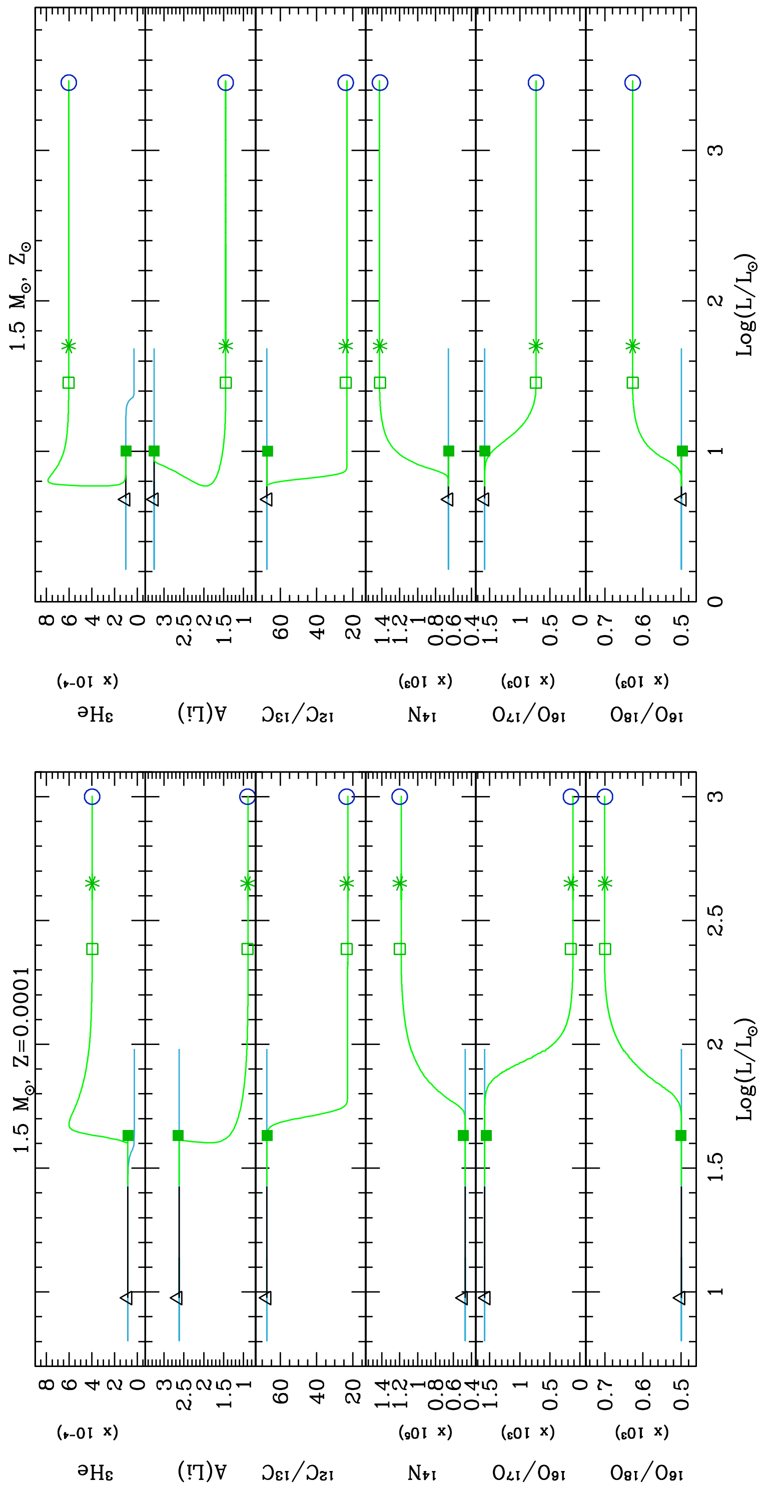

Figure 2.15: Evolution of the surface abundances of ^{3}He and ^{14}N (in mass fraction), of A(Li), and of the carbon and oxygen isotopic ratios as a function of stellar luminosity for the 1.5 M$_\odot$ models at two metallicities (Z=0.014 and Z=0.0001) computed with standard prescriptions, are shown up to the RGB tip. Evolutionary phases are indicated by the same colors than in figure 2.2. Main evolution steps are pointed out with different symbols : ZAMS (open triangle), first dredge-up (start/end ; full/open squares), BUMP luminosity (asterisk), RGB tip (open circle).

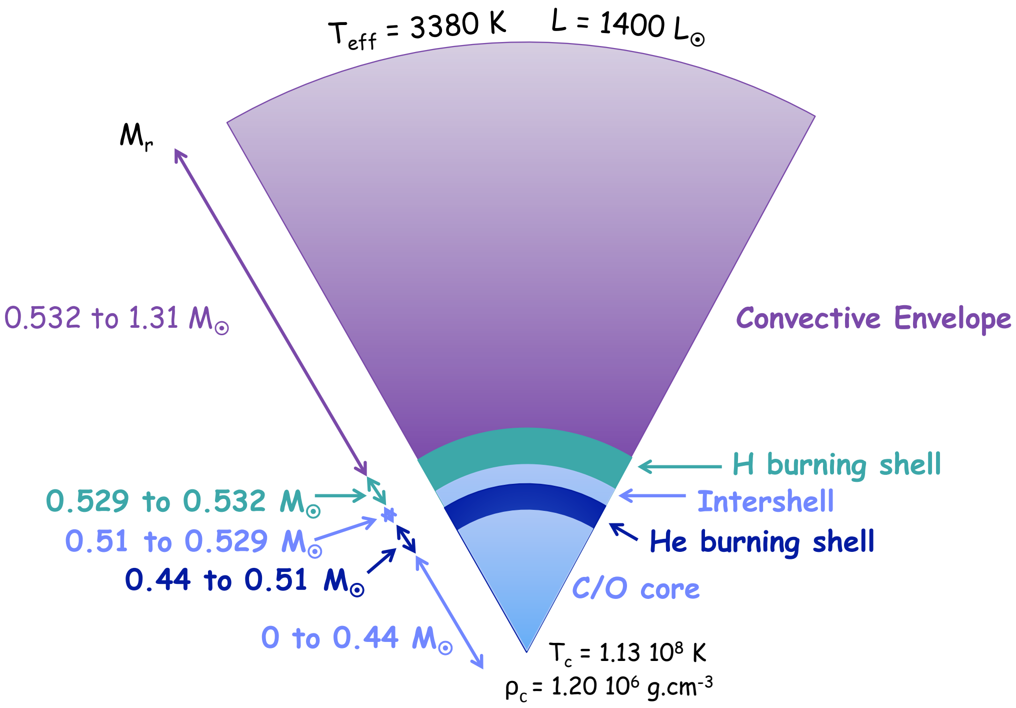

Figure 2.16: Structure of an AGB star. The coordinate in mass ($M_\odot$), the effective temperature, the luminosity at the surface, and central density and temperature are given for a 1.5 $M_\odot$ model at $Z_\odot$ at the end of the second dredge-up.

mass $M \geq 4.0\ M_\odot$(at $Z_\odot$) that induces a very modest decrease of the surface ^{3}He, ^{7}Li and $^{12}C/^{13}C$ when the star starts ascending the early-AGB. The maximum depth of the 2DUP as a function of stellar mass is presented by dashed lines in Fig 2.7.

2.6.2 TP-AGB phase

The TP-AGB phase represents the ultimate nuclearly active evolutionary stage of low- and intermediate-mass stars. AGB stars are composed of a degenerated core made of carbon and oxygen, surrounded by a thin helium burning shell where recurring instabilities take place : the thermal pulses (see below). This layer is surmounted by a radiative shell, the intershell, composed by the products of H burning and too cool to ignite helium. Above this intershell, hydrogen burns in thin layer. A second radiative zone separates the HBS from the convective envelope, which expands over 99% of the radius surrounding the nuclearly active regions. This structure of AGB stars is schematically illustrated in Fig.2.16.

TP-AGB stars are characterized by the developement of recurrent instabilities in the helium-burning shell, and by the alternate activation of H and He shells burning which are very close in mass and in radius. Figure 2.17 shows the evolution during a pulse-interpulse cycle of the nuclear luminosities associated with hydrogen and helium burning for our 1.5 $M_\odot$ model at solar metallicity. During the thermal pulse, energy comes from helium burning while during the interpulse the main source of energy is the hydrogen burning shell. During the interpulse, H-shell burning adds helium to the intershell layer, increasing its mass. The temperature and pressure of inactive He burning shell (HeBS) increase caused by core contraction until He ignites. Due to the thinness of He shell,

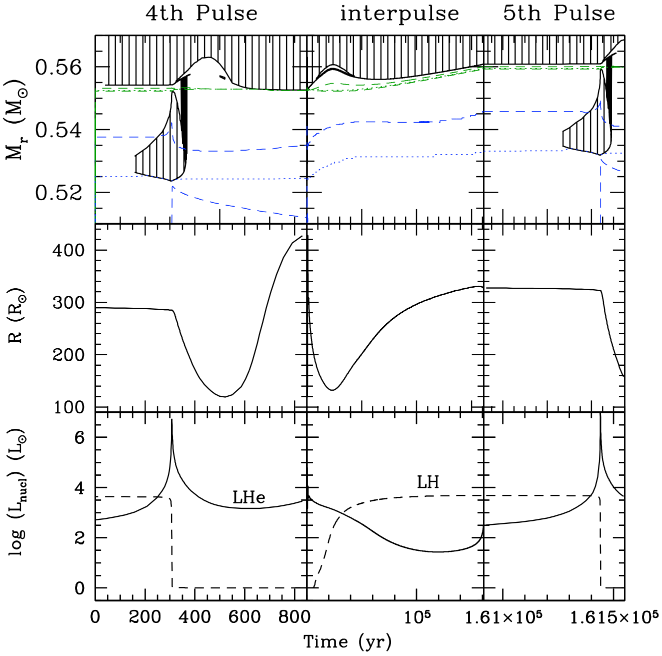

Figure 2.17: Evolution during the (4th and 5th) pulses and interpulse for 1.5 $M_\odot$ at $Z_\odot$ (from top to bottom panel) of the internal structure in mass (Kippenhahn diagram) ; of the stellar radius ; and of the nuclear luminosity associated with hydrogen (LH) and helium (LHe). The convective zones are hatched and the dashed lines represent the hydrogen and helium burning shell (green and blue respectively). The abscissa is the time from the beginning of the 4th pulse.

the ignition of helium is very unstable. Even if it expands, it is too thin to decrease the pressure exerted by the intershell. The energy liberated increases temperature, the nuclear energy production due to He-burning ($\epsilon(He) \propto T^{40}$) grows, T increases again, and then $\epsilon(He)$ amplifies. Due to the strong energy release, HeBS becomes convective and expands outwards. It is the thermal pulse.

This instability grows quickly and pushes the above layers outwards. The convective envelope slightly retracts and the HBS extinguishes. Without this important energy source, the star contracts (see stellar radius on Fig. 2.17). When the pulse reaches its maximum extension, the region between the nuclear region and the convective envelope is thin enough to evacuate the excess of energy created by the instability to the surface by convection. The instability dies out and the He burning is extinct again. The convective envelope moves inwards again inducing a small change of surface abundances, like a very low decrease of the surface abundance of carbon istopic ratio, $^{12}C/^{14}N$, A(Li), ^{3}He and oxygen isotopic ratios (see Fig. 2.18).

Figure 2.18 shows the evolution of luminosity, effective temperature, and total stellar mass along the TP-AGB for our 1.5 $M_\odot$, $Z_\odot$ standard model. Between each thermal pulse, the stellar radius and luminosity increase, while due to mass loss the total mass slowly decreases. AGB stars suffer a signicant mass loss rate, which depends a lot on the luminosity (e.g. Vassiliadis & Wood 1993). As the AGB stars become progressively bright (see Fig. 2.18), the mass loss rate also increases between each pulse, while it raises enormously during the pulse. This results in the total stellar mass to decrease by steps at this phase. The cycle of pulse-interpulse is repeated until the whole convective enve-

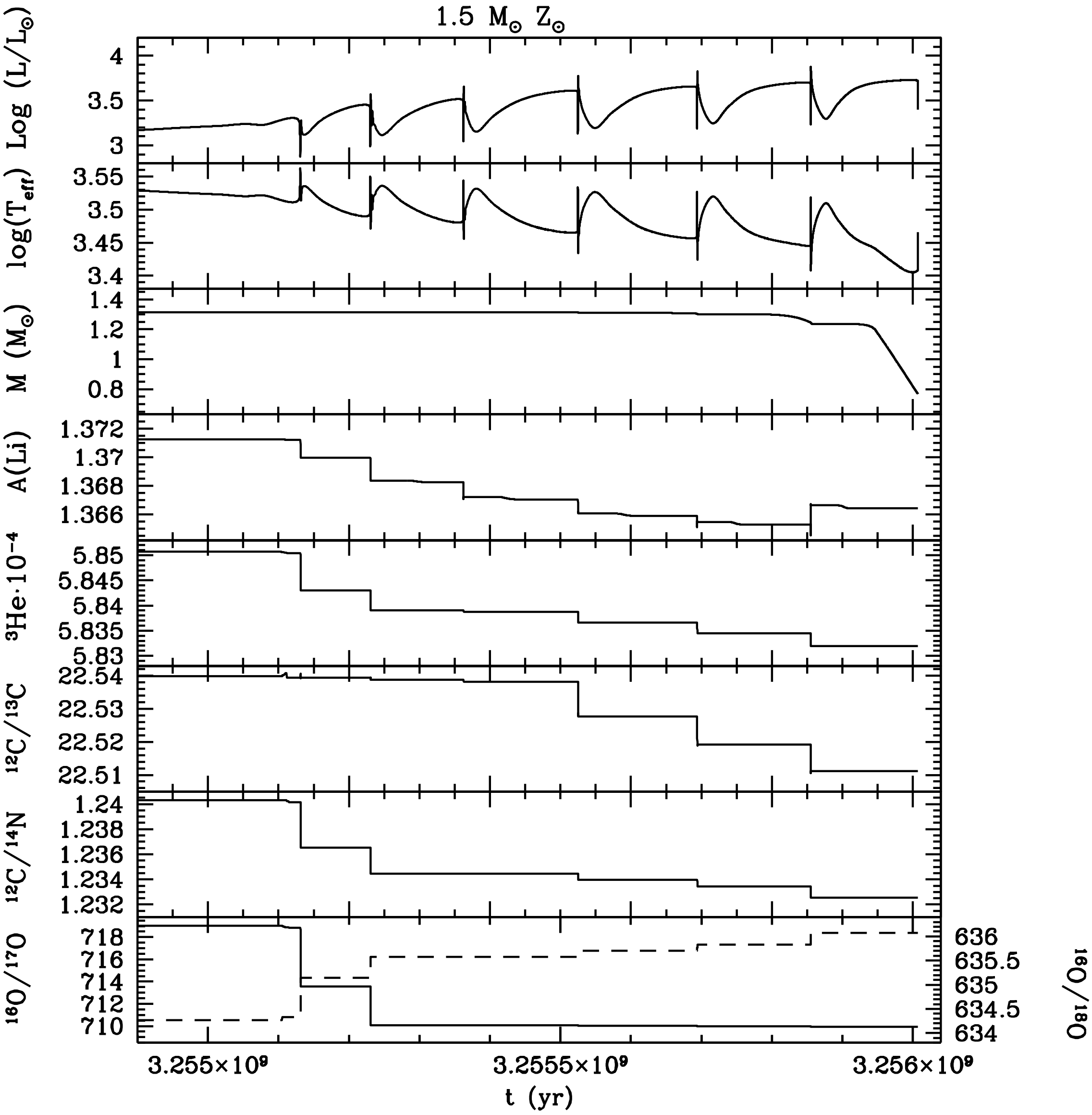

Figure 2.18: The TP-AGB phase of a 1.5 M$_\odot$ standard model at solar metallicity (from top to bottom) : evolution of stellar luminosity, effetive temperature, total mass, the surface abundances of A(Li), ^{3}He, carbon isotopic ratio, ^{12}C/^{14}N, ^{16}O/^{17}O (solid black line) and ^{16}O/^{18}O (dashed black line).

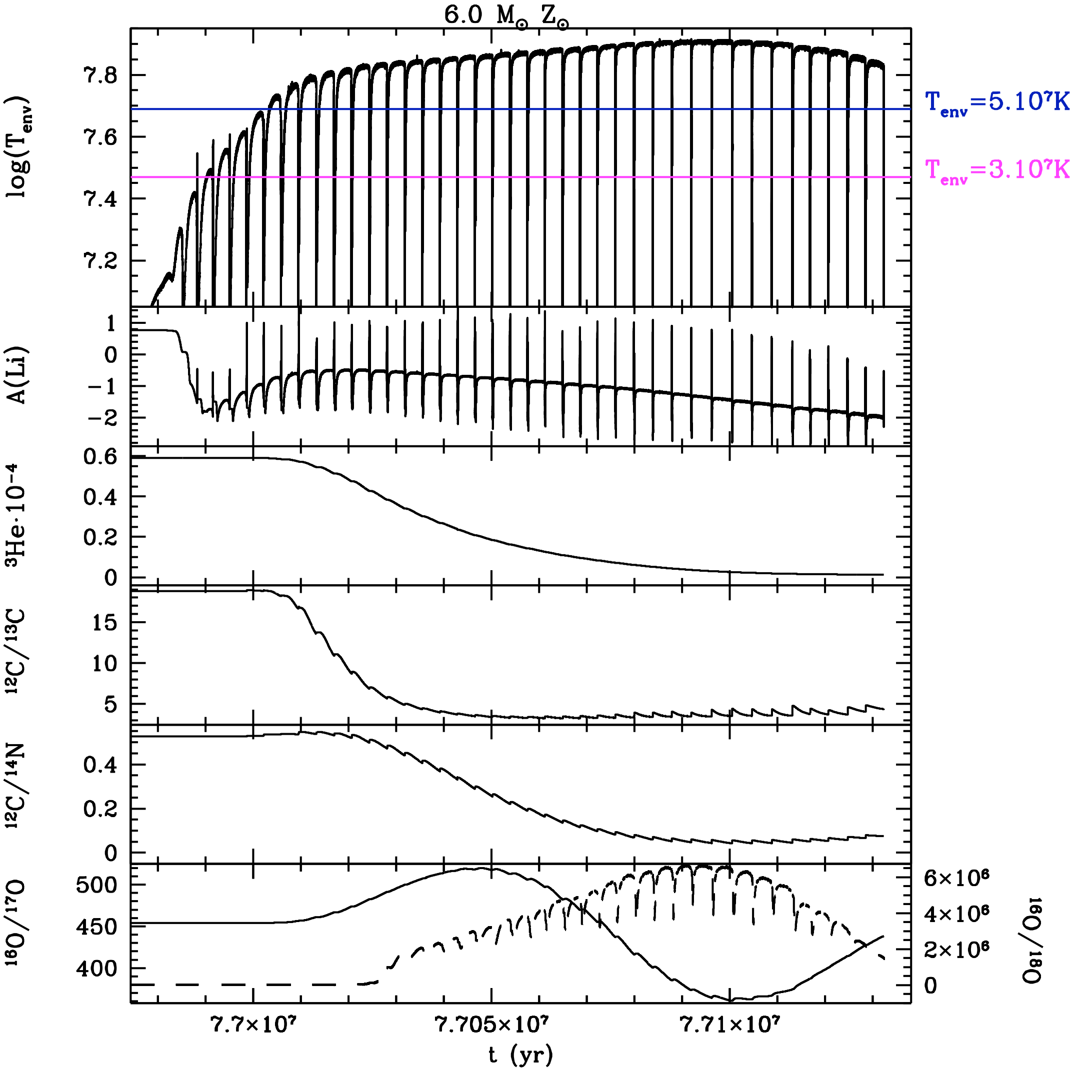

Figure 2.19: Theoretical evolution of the temperature at the base of convective envelope, and of the same chemical species as Fig. 2.18 for our 6.0 M$_\odot$ standard model at solar metallicity.

lope is gone. So the number of pulse for a given stellar mass depends on the mass loss rates.

In the massive stars (M$\geq$ $4M_\odot$) the temperature at the bottom of the convective envelope is sufficient to burn hydrogen. It is the Hot Bottom Burning (HBB). The products of H-burning are immediately mixed to the surface. Figure 2.19 presents the evolution of the same chemical species than in Fig.2.18 and the evolution of the temperature at the base of the convective envelope for our 6.0 M$_\odot$ standard model at solar metallicity. When the temperature at the base of the convective envelope reaches T$_{env}\gtrsim$ 3·10^{7}K, lithium-7 increases at the surface during the interpulse (see Fig. 2.19) by Cameron & Fowler (1971) mechanism, caused by HBB. In this process ^{7}Be is produced at the base of the envelope by PP cycle, transported by convection in cooler external region of the star, where it is destroyed by electron capture to form ^{7}Li. In addition, HBB implies a decrease of helium-3 at the surface during the interpulse (see Fig. 2.19). When the T$_{env}\gtrsim$ 5·10^{7}K, reactions of CNO cycle allow the building of ^{14}N with the destruction of ^{12}C, ^{13}C, ^{16}O, and ^{18}O. This results in a decrease of $^{12}C/^{13}C$ and $^{12}C/^{14}N$ (see Fig. 2.19). In addition, oxygen isotopic ratios follow the production and the destruction of ^{17}O.

On the other hand, when the convective envelope reaches deeper regions where layers that were occupied previously by the pulse (this is a critical point depending on convective parameters and mixing). It is so called the third dredge-up (3DUP). It allows to drive chemical elements from these deeper regions to the surface ; and induces a slightly increase of helium-3, and carbon isotopic ratios (see Fig. 2.19).

At the end of their life, the ejection of their envelope, due to stellar wind, leads to the emergence of a planetary nebula.

2.7 Summary

In this chapter, we presented the evolution of the internal structure and nucleosynthesis of the low- and intermediate-mass stars according to the standard model, from the pre-main sequence to the end of the thermal pulse phase. Our discussion was based on our grid of models computed for various masses at four metallicities, with STAREVOL. We illustrated our discussion with the evolution of our 1.5 $M_\odot$ standard model at $Z_\odot$ following its structure, global stellar parameters (luminosity, effective temperature,...), and chemical properties (with Li, Be, ^{3}He, and carbon and oxygen isotopic ratios). In addition, we discussed the effect of stellar mass and metallicity on these parameters.

We showed that standard theory predicts no change of chemical abundances until the first dredge-up. It modifies the surface composition of low- and intermediaite-mass stars due to dilution of the external convective stellar layers with hydrogen-processed material. The lithium and the carbon abundances as well as the carbon isotopic ratio decline, while the helium-3 and nitrogen abundances increase. The importance of these variations depends on initial stellar mass, and metallicity. After the first dredge-up, standard theory does not predict variations on the chemical surface abundances up to the early-AGB phase. At that point of the evolution, a star undergoes the second dredge-up which changes stellar chemical properties.

In the next chapter, we will present abundance anomalies in open and globular cluster stars as well as in field stars, to show the necessity of introducing a new extra-mixing which can explain these anomalies.

Chapter 3

Observations :
Keys to constrain stellar evolution

As we showed in the previous chapter, during the first dredge-up (1DUP; Iben 1967), the chemical composition of the stellar surface is modified when the deepening convective envelope mixes the external layers with hydrogen-processed material. Dilution then changes the surface abundances of helium-3, lithium, beryllium, boron, carbon, nitrogen, and eventually sodium, with modification amplitudes that strongly depend on the initial stellar mass and metallicity (e.g. Sweigart et al. 1989; Charbonnel 1994; Boothroyd & Sackmann 1999). Standard stellar evolution models predict no variation of chemical composition at the surface of red giant stars between the end of the first dredge-up and the RGB tip.

Numerous observations provide, however, compelling evidence of a non-canonical mixing process that occurs when low-mass stars reach the so-called bump in the luminosity function on the red giant branch (RGB) and further modifies the surface composition. In the following we review these so-called abundance anomalies in open and globular cluster stars (where masses, metallicities and age of stars can be estimated); as well as in field stars (for which Hypparcos parallaxes allows an accurate determination of the luminosity and of the evolutionnary phase). These data are extensively used in chap. 5 and in Charbonnel & Lagarde (2010a) to test our non-standard theoretical predictions.

A summary of existing data in open clusters (Table 3.6), in globular clusters (Table 3.3), and in the field stars (Table 3.6) is provided at the end of this chapter.

3.1 Abundance indicators

The observations that are relevant in this thesis and that we present in this chapter are abundances determinations of different elements at the surface of low- and intermediate-mass stars. We will not present observation techniques, nor methods for reducing photometric or spectroscopic data, but we will focus on the results.

The intensities of molecular bands as CH and CN are easier to access than the atomic lines in cool stars, but can be more difficult to interpret. They allow to deduce the abundance of carbon and nitrogen, by photometric adjustment (Briley et al. 2001), by adjusting synthetic spectra to observed spectra, or by the combination of the two previous techniques (Bell & Dickens 1980). Intensities and colors of the molecular bands CN and CH are then confronted with grids of atmosphere models calculated for different combinations of carbon, nitrogen, and oxygen abundances. To obtain the carbon abundance of a star, for exemple, we therefore speculate on the nitrogen, oxygen and ^{12}C/^{13}C abundances. However, the molecular bands like CN are more difficult to interpret. Indeed, the intensity of the CN molecular bands depends on variations in the number of carbon or nitrogen nuclei (i.e. an increase in the number of C nuclei or a reduction of those of N causes an increase of this intensity). The determination of nitrogen abundance with the CN molecular bands depends strongly on the carbon abundance. On the other hand, molecules of CH, NH, and OH give a direct estimation of the carbon, nitrogen, and oxygen abundances, while the carbon isotopic ratio is derived of fitting the ^{12}CN and ^{13}CN lines.

In most cases, the abundances of oxygen are deduced from the forbidden line [OI] at 6300 Å, for red giant stars. For hotter stars, the triplet OI, the transition lines OH in UV and in IR can also be use although they drive to different results. This results in discussions whether to use or not these lines.

3.2 Carbon isotopic ratio and nitrogen

As we have seen in the last chapter, the standard theory predicts that during the first dredge-up the convective envelope of low- and intermediate-mass stars reaches regions where ^{12}C was processed to ^{13}C and ^{14}N. As a consequence, the carbon isotopic ratio and ^{12}C/^{14}N decrease during this phase (from 70 to ∼20). Then the surface abundances stay constant until the second dredge-up occurs.

However observational data show a different reality as discussed below. The first observation of carbon isotopic ratio for 2 K-giants by Day et al. (1973) revealed much lower values of ^{12}C/^{13}C of 7.2±1.5 for Arcturus and 12±2 for αSerpentis. This discrepancy was confirmed by Lambert & Ries (1981) with observations of C, N, and O abundances in a sample of 32 G and K subgiant and giant stars. Indeed, the observed conversion of ^{12}C to ^{13}C and ^{14}N greatly exceeds the levels predicted by standard models ; the carbon isotopic ratio is then lower than in standard case.

3.2.1 Open clusters

The behavior of the carbon isotopic ratio is the best indicator of non-standard transport processes in evolved low-mass stars. This quantity has been determined in a large number of stars in Galactic open clusters.

Nineteen stars from M67 were observed and analysed by Brown (1987), in order to confirm observationaly the occurence of the first dredge-up, through variations of the abundances of carbon and nitrogen along the HR diagram. An indication was found in this study of variations of C/N abundance ratio in different stars (subgiants, giants, and clump stars) from M67. Then Gilroy (1989) and Gilroy & Brown (1991) studied M67 giants in oder to determine the carbon isotopic ratio which is displayed in figure 3.1 in subgiant, RGB, and clump stars of the open cluster M67 (turnoff mass ∼1.2 $M_\odot$) by Gilroy & Brown (1991). We also compared observations with our closest standard predictions of this turnoff mass (1.25 $M_\odot$ at solar metallicity). As expected, ^{12}C/^{13}C decreases (i.e. Log(L/$L_\odot$) ∼ 0.9) due to the first dredge-up. We can underline the dispersion of stars that have not yet reached the RGB bump (i.e., with Log(L/$L_\odot$) between ∼ 0.7 and 1.8), that might be induced by non-standard process during the main sequence. As we shall see indeed (see chap 5), a observed dispersion of the carbon isotopic ratio just after the turnoff can be attributed to rotation-induced mixing on the main sequence (see Fig. 16 of

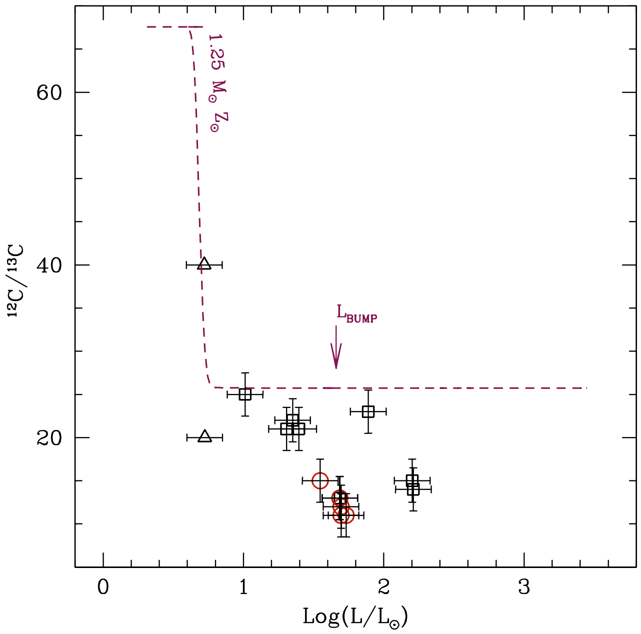

Figure 3.1: Evolution of the surface $^{12}C/^{13}C$ value as a function of stellar luminosity. Observations along the evolutionary sequence of the open cluster M67 are from Gilroy & Brown (1991). The triangles are for a subgiant star for which only a lower value could be obtained, while black squares and red circles correspond to true determination respectively RGB and clump stars.

Charbonnel & Lagarde (2010a) and Chap. 5). The brightest RGB stars (log(L/L$_\odot$)>2) as well as clump stars (red circles) have a carbon isotopic ratio lower than predicted by the standard model.
Tautvaišiene et al. (2000) re-investigated carbon isotopic ratio in M67 for six core helium-burning "clump" stars and three giants. There are seven stars in common with Gilroy (1989) and Gilroy & Brown (1991). Except for two stars (F84 and F170), $^{12}C/^{13}C$ ratios in Tautvaišiene et al. (2000) sample agree with $^{12}C/^{13}C$ abundances derived by Gilroy & Brown (1991), within errors of uncertainties.

Tautvaišienė et al. (2005) derived $^{12}C/^{13}C$ and C/N ratios for six bright giants and three core-helium burning clump stars in the open cluster NGC 7789 (M_{TO} = 1.6 M$_\odot$). They found $^{12}C/^{13}C$ ratios are very similar for all the stars investigated, contrary to $^{12}C/^{14}N$ ratios, which is different in the giants (mean $^{12}C/^{14}N = 1.9 \pm 0.5$) and in the clump stars (mean $^{12}C/^{14}N = 1.3 \pm 0.2$). However, carbon isotopic ratios were analysed by Sneden & Pilachowski (1986) for seven stars, in NGC 7789 among which two stars are in common with Tautvaišienė et al. (2005). They found $^{12}C/^{13}C$ in the range of 10-20 contrary to Tautvaišienė et al. (2005) who found $^{12}C/^{13}C$ between 7 and 11. Particularly, for two giants K501 and K669, Sneden & Pilachowski (1986) found a carbon isotopic ratio between 15 and 20 for both stars, while Tautvaišienė et al. (2005) found $^{12}C/^{13}C = 9 \pm 4$ (K501) and 11^{+7}_{-5} (K669). In a view of large error bars predicted by Tautvaišienė et al. (2005) and the disagreement with observations by Sneden & Pilachowski (1986), we could suggested that this underestimation of carbon isotopic by Tautvaišienė et al. (2005) is caused by observational reasons, and not by effects of He-core-flash as they proposed.

Table 3.1: References for the abundance studies in Galactic open clusters used in the comparisons with model predictions. Brown (1987): B87; Gilroy (1989): G89; Gilroy & Brown (1991): GB91; Mikolaitis et al. (2010): M10; Smiljanic et al. (2009): S09. The red turnoff masses given in the second column were estimated using the WEBDA database and Geneva isochrones.

open cluster	$M_{\rm redTO}$ ($M_\odot$)	$^{12}C/^{13}C$
M67	1.5	GB91
NGC 5822	2.14	S09
IC 4756	2.31	S09
NGC 6134	2.31	S09, M10
NGC 2447	2.74	S09
NGC 6633	2.74	S09
IC 2714	2.85	S09
NGC 3532	2.96	S09
NGC 6281	3.09	S09

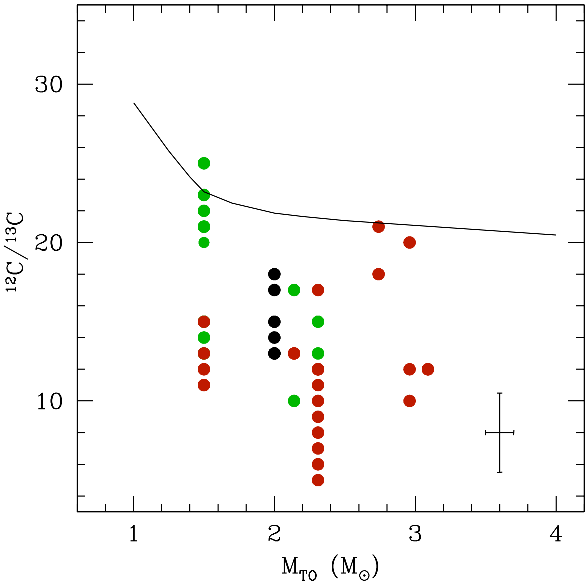

Figure 3.2: Observations of carbon isotopic ratio, $^{12}C/^{13}C$, in evolved stars of open clusters as a function of turn-off mass of the host cluster. Data by Smiljanic et al. (2009), Gilroy (1989), Gilroy & Brown (1991), and Mikolaitis et al. (2010) are shown with green circles for 1DUP/RGB stars, and with red circles for clump/early-AGB stars, while black circles are for stars with uncertain evolutionary status. A typical error bar is indicated. Our theoretical standard predictions of carbon isotopic ratio are shown at the tip of the RGB by a solid black line. *Adapted from Charbonnel & Lagarde (2010a).*

More recently, Smiljanic et al. (2009) derived the abundances of C, N, O and Na, as well as the $^{12}C/^{13}C$ ratio in a sample of 31 evolved stars, including red giants, clump giants, and early-AGB stars, in ten open clusters with turnoff masses from 1.7 to 3.1 $M_\odot$. In addition, Mikolaitis et al. (2010) and Mikolaitis et al. (2011) studied clump giant stars in two open clusters NGC 6134 and IC465, and determined C/N and $^{12}C/^{13}C$ ratios.

Figure 3.2 shows carbon isotopic ratios in open clusters as a function of the cluster's turnoff masses. The data shown in this figure are from Gilroy & Brown (1991) for M67, from Gilroy (1989) for NGC 752 (M_{TO} = 1.7 $M_\odot$), from the more recent study by Smiljanic et al. (2009) for nine open clusters with turnoff masses above 1.7 $M_\odot$ (IC 2714, IC 4756, NGC 2360, NGC 2447, NGC 3532, NGC 5822, NGC 6134, NGC 6281, NGC 6633), and from Mikolaitis et al. (2010) for NGC 6134 (M_{TO}= 2.31 $M_\odot$). Indications on the evolutionary status of the observed stars, when available, are given in the plot (green and red circles are for 1DUP/RGB stars, and clump/early-AGB stars respectively, while black circles are for stars with uncertain evolutionary status). Standard prediction of carbon isotopic ratio is shown at the tip of the RGB for Z=0.014. Table 3.1 summarizes open clusters used in this figure and their turnoff mass.

For lower mass stars (M$\leq$2.3 $M_\odot$) clump stars present low value of $^{12}C/^{13}C \lesssim 16$ contrary to standard models which predicted $^{12}C/^{13}C$ between 20 and 30. In addition, 1DUP/RGB stars (green symbols) can be divided in two groups, one with higher $^{12}C/^{13}C$ (between 20 and 26), and an other with lower value of $^{12}C/^{13}C$ (between 10 and 17). The first includes stars undergoing the first dredge-up episod, and the second one are stars have yet reached the BUMP luminosity.

3.2.2 Fields stars

Observational data in field stars are a good test for theoretical predictions when very precise bolometric magnitude value from HIPPARCOS parallaxes are available ; in that case, the luminosity, mass and evolutionary status of the stars can be derived accurately.

Charbonnel et al. (1998a) have assembled literature abundance data for Li, C, $^{12}C/^{13}C$ and N for five field stars with [Fe/H]$\simeq$-0.6. Figure 3.3 shows the carbon isotopic ratio from different references (see caption) including stars observed by Charbonnel and collaborators. An abrupt change in $^{12}C/^{13}C$ between $M_{bol} \sim 0.9$ and 0.5 is seen in this figure. Similarly to Fig. 3.1 for M67, carbon isotopic ratio decreases from value around 30, corresponding to the post dredge-up value, to values lower than 20. Note that Charbonnel et al. (1998a) have indicated the location of the bump (horizontal solid line) in the luminosity fonction of 47 Tuc. This confirms that an extra-mixing further decreases the $^{12}C/^{13}C$ in bright RGB stars.

That confirms the results obtained by Charbonnel & Do Nascimento (1998), who collected in the literature all the available observations of the carbon isotopic ratio in field and cluster giant stars as shown in figure 3.4 : $^{12}C/^{13}C$ decreases again after the bump luminosity ($M_V < 2$), while the standard models predict a value around 40. Charbonnel & Do Nascimento (1998) determined that 96% of low-mass stars do experience an extra-mixing process on the RGB. Moreover, this reduction of $^{12}C/^{13}C$ is more important when the metallicity is low (see figure 3.4).

Gratton et al. (2000) confirm abundances variations after the bump luminosity (indi-

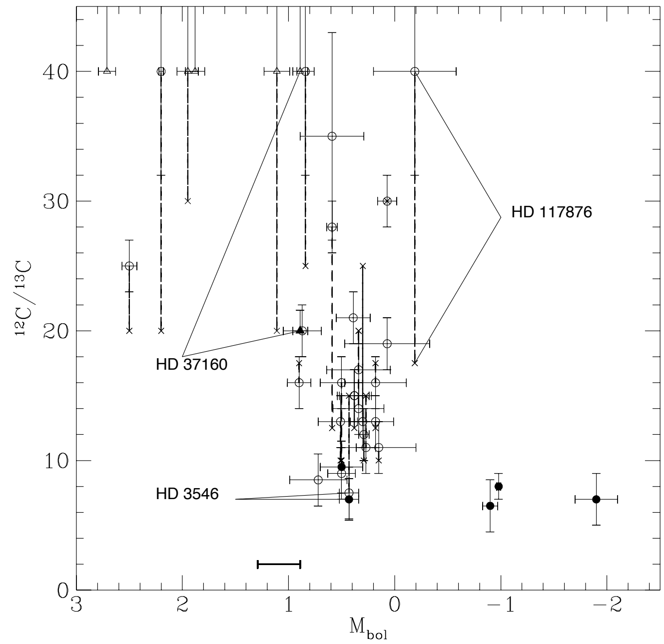

Figure 3.3: Carbon isotopic ratios for the old disk giants by Cottrell & Sneden (1986, ; crosses) and Shetrone et al. (1993, ; open circles and triangles). Charbonnel et al. (1998a) program stars are also shown (black circles and triangles). Observations for the same stars are connected by dashed lines. The absolute magnitudes are derived from the HIPPARCOS parallaxes. The horizontal line (at $M_{bol} \sim 1$) indicates the position of the bump in the luminosity function of 47 Tuc (King et al. 1985). *Figure from Charbonnel et al. (1998a).*

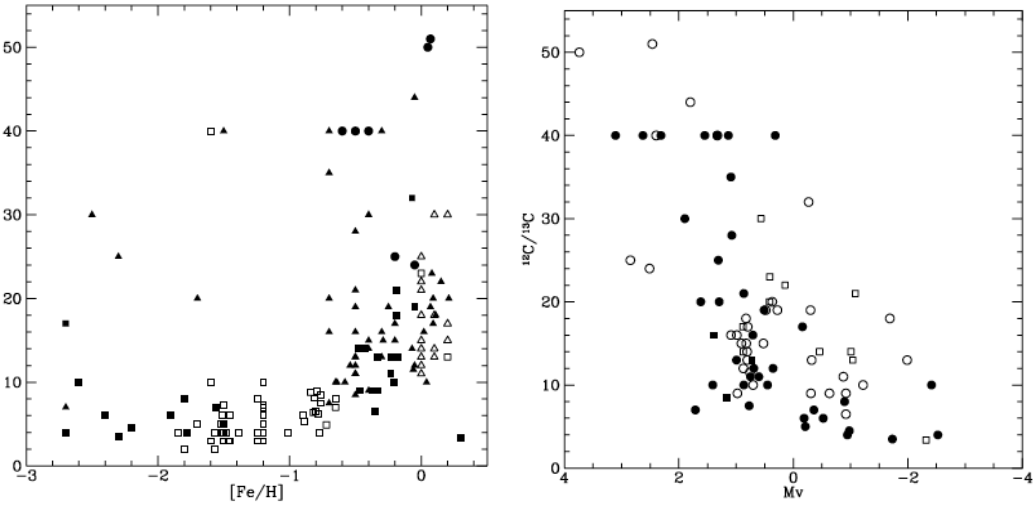

Figure 3.4: *Left panel :* Carbon isotopic ratio as a function of [Fe/H] for Charbonnel & Do Nascimento (1998) whole literature sample. The circles correspond to stars with M_V higher than 2, the triangles to stars with M_V between 0 and 2, and the squares to the brightest stars with M_V lower than 0. Black and white symbols relate respectively to field and cluster giants. *Right panel :* Carbon isotopic ratio as a function of M_V for field stars. The circles relate to single stars and the squares to binaries. Black and white symbols correspond to [Fe/H]≤-0.5 and [Fe/H] > -0.5 respectively. *Figures from Charbonnel & Do Nascimento (1998)*

cated by an arrow in Fig.3.5). Indeed figure 3.5 shows the carbon isotopic ratio determination in low-metallicity and low-mass field stars analyses by Gratton et al. (2000), compared to theoretical predictions of our standard 0.85 $M_\odot$ models at two metallicities (Z=0.002 and Z=0.0001). The depletion of carbon isotopic ratio at $\log(L/L_\odot)\sim1.8$ is clear.

In addition, figure 3.6 shows observations of nitrogen from Carretta et al. (2000) (left panel), and Gratton et al. (2000) (right panel). As figure 3.5, we compare in these figures our standard predictions for 0.85 $M_\odot$ at two metallicities which correspond to extreme metallicities of the sample. In this figure, we note a higher value of nitrogen in clump and the brightest RGB stars than in the less bright stars. These variations always occur near the bump luminosity ($\log(L/L_\odot) \sim 2$).

Figure 3.7 shows carbon isotopic ratios of giants stars in Galactic field by Tautvaišienė et al. (2010b) (-0.60<[Fe/H]<0.10). Standard predictions at the RGB tip for two metallicities (Z=0.014 and Z=0.004, i.e. [Fe/H]= 0 and -0.55) are shown by the solid black and blue lines respectively. The comparison between observations and theoretical predictions shows that the stars separate into two groups : one is first ascent giants (green symbols) which have a carbon isotopic ratio in agreement with the standard first dredge-up predictions ; the other is helium-core burning stars (red symbols) which have a carbon isotopic ratio altered by an extramixing.

On the other hand, we can find in literature chemical composition of the binary systems composed of two late-type chromospherically active fast rotating stars, one of which has already evolved off the main sequence. Tautvaišiene G., Barisevičius G., Berdyugina S., Chorniy Y. and Ilyin I., present in a series of four papers, a study of photospheric abundances in these stars (Barisevičius et al. 2010; Tautvaišienė et al. 2010a; Barisevičius

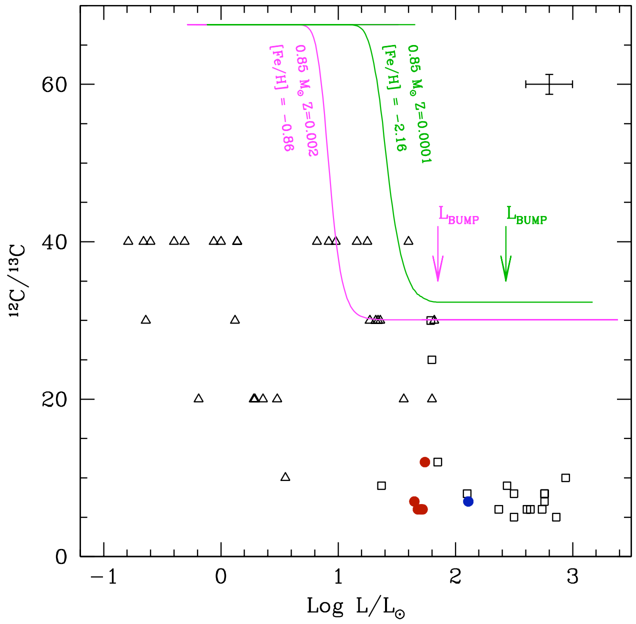

Figure 3.5: Observations of carbon isotopic ratio in evolved low metallicity, and low mass-fields stars by Gratton et al. (2000) (-2<[Fe/H]<-1). Black open squares (actual determinations) and triangles (lower limits) are for MS and RGB stars ; Red circles for clump stars and blue circle for AGB star. Our standard theoretical predictions for 0.85 $M_\odot$ stars at Z=0.0001 and Z=0.002 are shown by the solid green and magenta lines respectively.

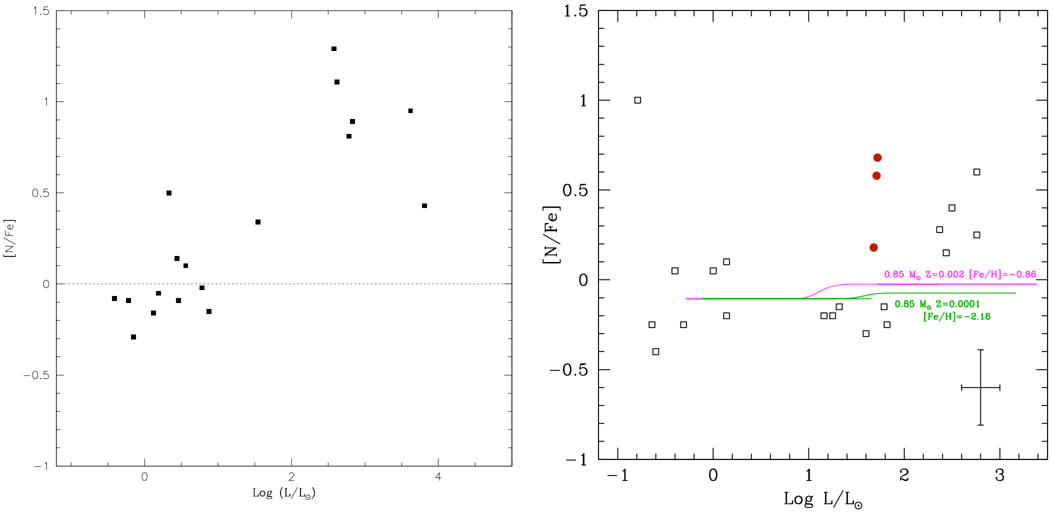

Figure 3.6: *Left panel :* The [N/Fe] ratios against stellar luminosity for stars observed by Carretta et al. (2000). *Figure from Carretta et al. (2000). Right panel :* Observations of nitrogen in field stars by Gratton et al. (2000) (-2<[Fe/H]<-1). Black squares (actual determinations) are for MS and RGB stars and red circles for clump stars. Our theoretical standard predictions for 0.85 $M_\odot$ stars at Z=0.0001 and Z=0.002 are shown in solid green and magenta lines respectively.

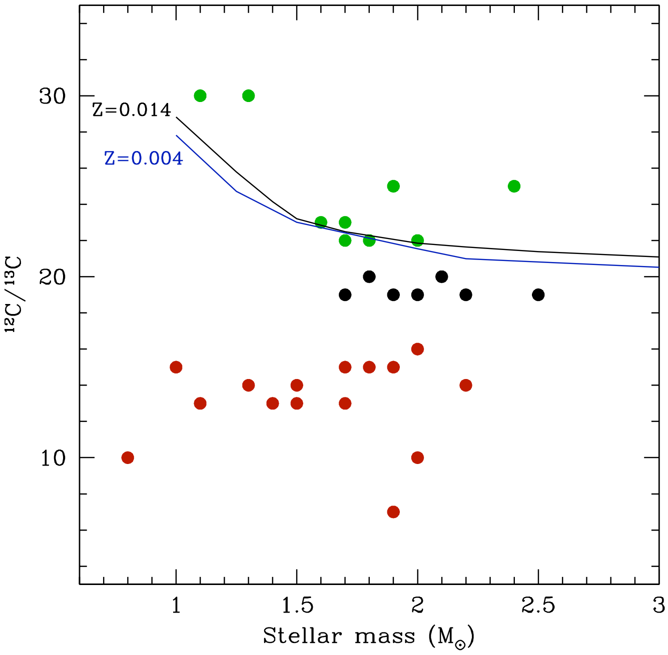

Figure 3.7: Carbon isotopic ratio in field giant stars as a function of stellar mass by Tautvaišienė et al. (2010b). First ascent giants are shown with green circles, while red circles show Helium core burning stars and black circles uncertain evolutionary states. Our theoretical standard predictions are shown at the tip of the RGB by the solid black and blue lines for Z=0.014 and Z=0.004 respectively.

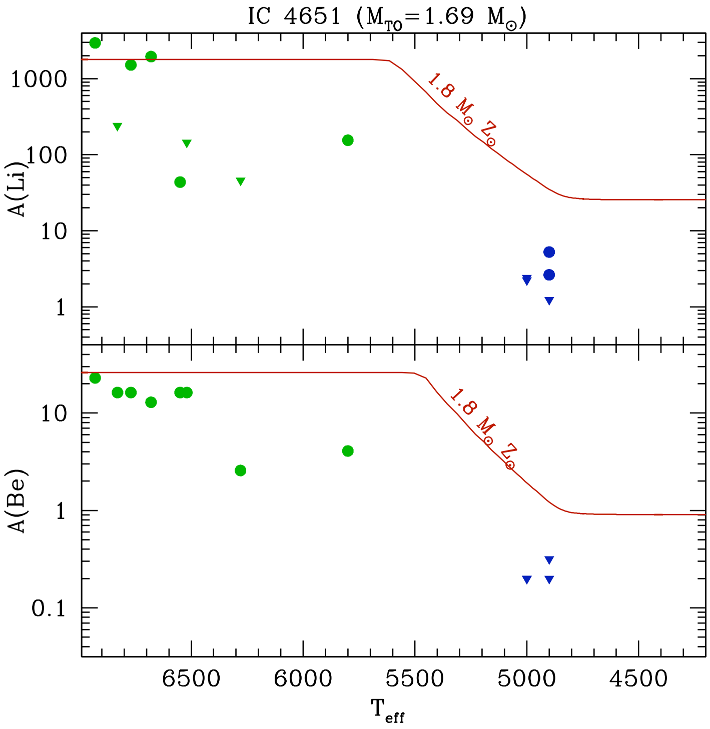

Figure 3.8: The Li (top panel) and Be (bottom panel) abundances for stars in the open cluster IC 4651, as a function of effective temperature, that depicts the evolutionnary phase. The turn-off stars and subgiants are shown in green while giants are shown in blue. Abundance determinations are shown by solid circles and upper limits by solid triangles. Li and Be observations are from Pasquini et al. (2004b) and Smiljanic et al. (2009) respectively. The red solid line represents standard prediction for our standard 2.0 M$_\odot$ at solar metallicity from main sequence to lower RGB.

et al. 2011; Tautvaišienė et al. 2011). In addition, Drake et al. (2011) present C and N abundances in λ And. They proposed that in low-mass chromospherically active fast rotating stars, the extra mixing is present earlier than at the bump luminosity in the red giant stars in non-active stars. In fact, λ And and 29 Draconis are more active stars, with a carbon isotopic ratio lower than standard predictions at the end of the first dredge-up. In addition, 33 Piscium has a negligible activity, and so has standard abundances.

3.3 Lithium A(Li) and Beryllium A(Be)

Lithium, and Beryllium are fragile elements destroyed at relatively low temperature (~2.5 10^6 K for Li and 3.5 10^6 K for Be) by proton capture. This is a sensitive and precious indicator of transport mechanisms of the chemical elements inside stars. Lithium and Beryllium are complementary, and they can be useful in the characterization of mixing mechanisms because they burn at different temperatures, i.e. at different depths in stellar interiors. In this section we follow the observed behaviour of the Li- and Be-abundance all along the evolution of low- and intermediate-mass stars.

Figures 3.8 to 3.12 show lithium abundances as a function of effective temperature for stars from main sequence to advanced phases (references are given in the captions). To allow a better understanding data are subdivided into three groups : (1) open clusters

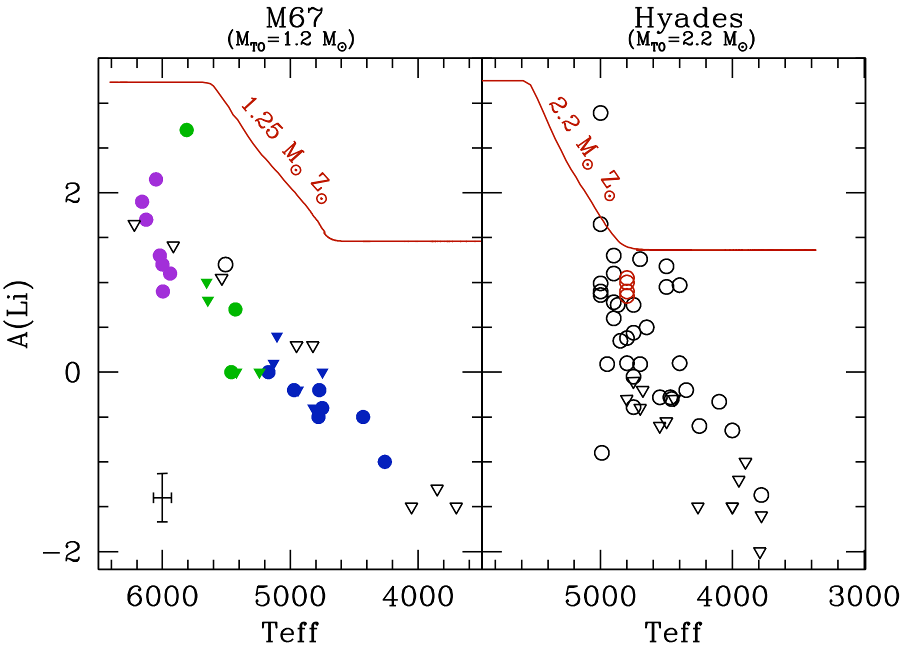

Figure 3.9: Li abundance as a function of effective temperature in two open clusters : M67 (left panel, M_{TO}=1.2 $M_\odot$) and Hyades (right panel, M_{TO}=2.2$M_\odot$). *Left panel :* Data from Canto Martins et al. (2011), Balachandran (1990), and Pilachowski et al. (1988). The purple, green, and blue symbols represent turn-off stars, subgiants, and giants respectively. Black symbols represent stars with doubtful evolutionary status. *Right panel :* Data from Lambert et al. (1980) (black symbols) and Gilroy (1989) (red symbols). In both panels abundance determinations are shown as circles and upper limits as triangles. We compare observations with our predictions from main sequence to lower RGB for our 1.25 $M_\odot$ and 2.2 $M_\odot$ standard models at solar metallicity.

(Fig. 3.8, 3.9) ; (2) globular clusters (Fig. 3.10) ; and (3) fields stars (Fig. 3.12).

3.3.1 Open clusters : IC 4651, M67, Hyades

Pasquini et al. (2004b) and Smiljanic et al. (2009) derived respectively Li and Be in stars sampling the main sequence and the red giant branches in order to investigate mixing mechanism along the whole evolutionary sequence.
Figure 3.8 shows the Li and Be abundances for this sample as a function of effective temperature. We compare observations in IC4651 (M_{TO}=1.69 $M_\odot$, Carretta et al. (2004)) with our closer (in mass) standard model : 1.8 $M_\odot$ at solar metallicity. The observed behaviour of Beryllium is found to follow that of Li. For turnoff and subgiant stars, observtions show Li and Be depletion, which is not predicted by standard models, as well as a non-negligible Li dispersion (green symbols, $T_{\rm eff} \gtrsim$5700 K). In addition, giant stars (blue symbols, $T_{\rm eff}$ ~5000K) present much lower Be and Li abundances, than predicted by the standard models after the so-called first dredge-up.

Figure 3.9 shows the observed dilution of Li during the first dredge-up along the subgiant branch of M67 (M_{TO}=1.2 $M_\odot$) and of the Hyades (M_{TO}=2.2 $M_\odot$). We also compare

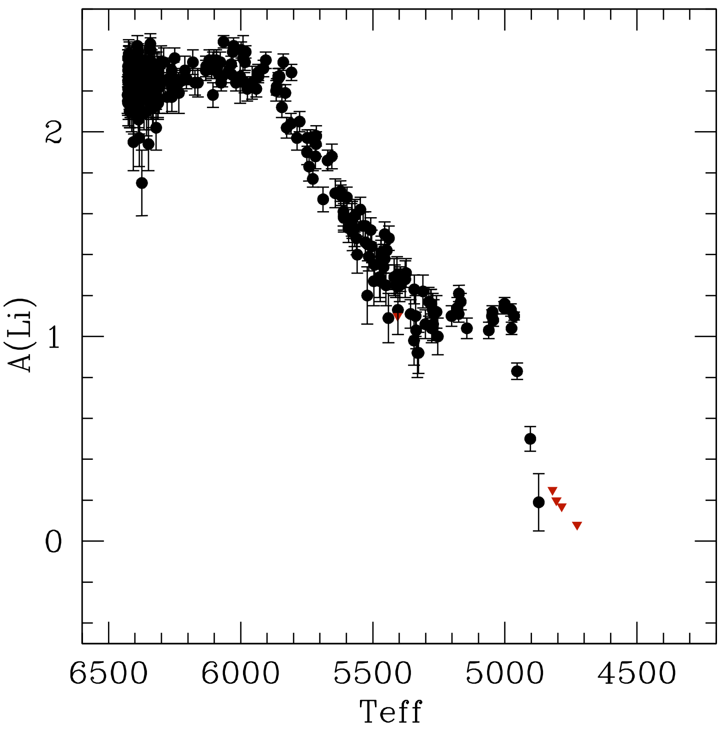

Figure 3.10: Lithium observation in NGC 6397 as a function of effective temperature. Upper limits are shown with red triangles. *Data from Lind et al. (2009).*

Li observations with standard predictions of the evolution of the surface abundance for our 1.25 $M_\odot$ and 2.2 $M_\odot$ models at solar metallicity. As in IC4651 (Fig. 3.8) a strong dispersion of Li abundance is observed among turnoff and subgiant stars, and the observations lie well below the standard predictions all along the evolution. ln addition we see that Li keeps dilution after the end of the first dredge-up for giant stars (at ∼4400 K in both panels). This Li depletion in bright RGB stars is not predicted by the standard theory which predicts no change in Li and Be abundances after the end of 1DUP on the early RGB.

This feature has been already discussed for Li in open clusters (IC4651, NGC 3680 Pasquini et al. 2004b, 2001, respectively) and also in field stars (Brown et al. 1989; Lèbre et al. 1999; do Nascimento et al. 2000; Palacios et al. 2003). This implies the presence of mixing during the main sequence or/and after the first dredge-up (see chap. 4).

3.3.2 Globular clusters : NGC 6397

Figure 3.10 shows the surface abundance of Li as a function of effective temperature for turnoff, subgiant and giant stars in the globular cluster NGC 6397 (Lind et al. 2009). The decrease of Li at ∼5900 K is due to the first dredge-up. However, the second episode of Li depletion at ∼5000 K is not predicted by standard theory ; it happens at the BUMP luminosity on the red giant branch.

In addition, D'Orazi & Marino (2010), D'Orazi et al. (2010), and Shen et al. (2010) report Li abundances for a sample of giants both below and above the RGB bump luminosity in the globular clusters NGC 6121 (M4), 47 Tuc, and NGC 6752, respectively. They

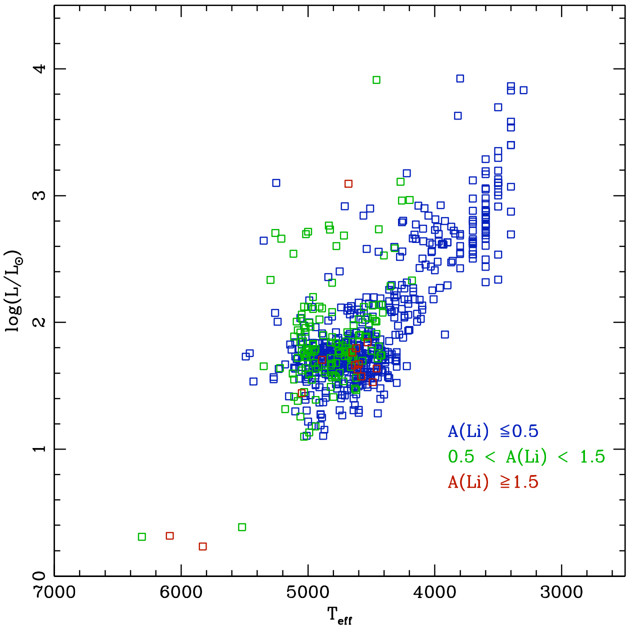

Figure 3.11: Positions in the HR diagram of our large sample of field giant stars (subgiants, RGB, and early-AGB stars) with metallicities around solar metallicity, and with Li determinations (Charbonnel et al. in prep.).

also show that Li tends to disappear as the stars reach the RGB bump luminosity.

3.3.3 Field stars

Here we use as additional constraints, Li observations that we performed for a large sample of 800 field giant stars (subgiant, RGB, and early-AGB stars) with -0.6<[Fe/H]<0.3. All sample stars have Hipparcos parallaxes so that their mass and evolutionary status could be relatively well determined (Charbonnel et al. in preparation). Figure 3.11 presents HR diagram of the complete sample with indication of lithium content.

Figure 3.12 shows the lithium content for all stars of the sample (left panel), and we pay particular attention to the solar metallicity (i.e. [Fe/H]=0 ; right panel) in order to focus on the same metallicity domain than open clusters. We determined the stellar mass of each star by interpolation between our standard models and observations in HR diagram. In figure 3.12 (right panel) we distinguished stars with respect to their mass (less or more massive than 2 M$_\odot$ in the left and right panels respectively). For the stars with initial masses lower than 2 M$_\odot$, Li properties are compared with standard predictions for the [1.5 M$_\odot$, Z$_\odot$] model, while for stars with initial masses higher, Li abundances are compared with standard predictions for [2.5 M$_\odot$, Z$_\odot$] model.

As underlined with previous figures (3.8, 3.9, and 3.10), these observations allow us to underline again several features (see Fig. 3.12):

- Standard models predict no Li depletion on the main sequence and a A(Li) at the end of the first dredge-up of the order of 1.5 and 1.3 for [1.5 M$_\odot$, Z$_\odot$] and [2.5 M$_\odot$, Z$_\odot$] models respectively, which is at odds with the data. A few stars (4000<T$_{eff}$ < 5500 K) have lower Li abundance than predicted by standard theory. This implies

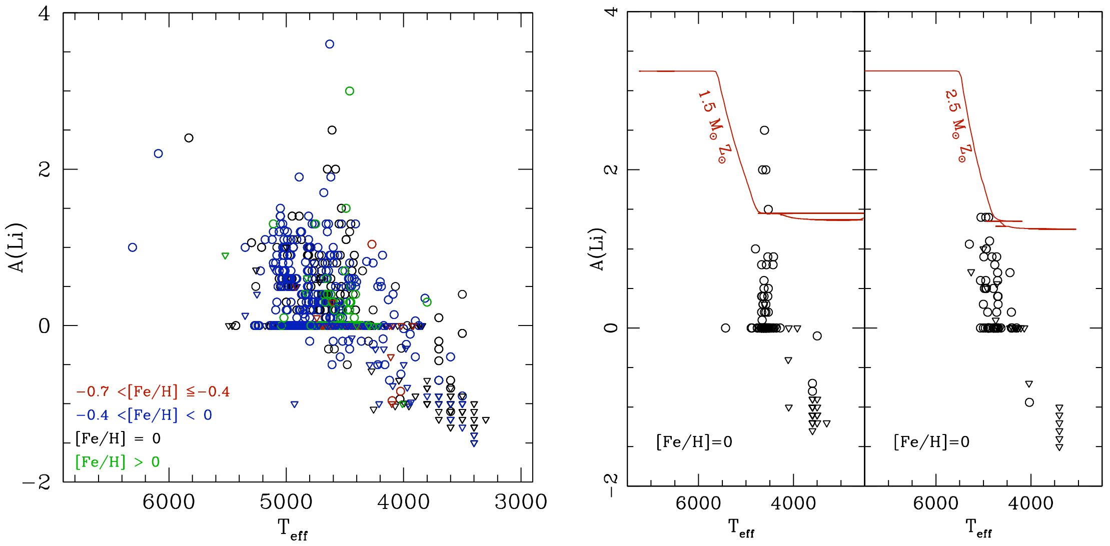

Figure 3.12: A(Li) as a function of effective temperature for the same sample than in figure 3.11. *Left panel :* Metallicities are shown with different colors. Triangles represent upper limits in Li abundance. *Right panel :* Lithium data for field evolved stars from the sample by Charbonnel et al. (in prep., see the text) that are segregated according to their mass (left and right panels include respectively sample stars with masses lower and higher than 2 $M_\odot$). Li detections and upper limits are shown by circles and triangles respectively. Our standard theoretical lithium evolution is shown from the ZAMS up to the end of the early-AGB for 1.5 $M_\odot$ and 2.5 $M_\odot$ at solar metallicity ([Fe/H=0]).

the presence of other mechanism allowing to explain them, as we have seen in Figure 3.8 (IC 4651).

- Then at $T_{\rm eff}$ ∼4200 K, the second depletion of Li abundance with a lot of Li upper limits for the brightest stars is not predicted by standard model. This feature implies the occurence of a second mixing inside the bright RGB stars which allow a decrease of the lithium at the surface.

3.4 Oxygen isotopic ratio and Sodium

Observations for oxygen and sodium in red giants are also available. We collected more recent observations by Gratton et al. (2000); Smiljanic et al. (2009); Mikolaitis et al. (2010); Hamdani et al. (2000); Jacobson et al. (2007, 2008, 2009) in figure 3.13 and 3.14 (for [O/Fe] and [Na/Fe] respectively).

[O/Fe] does not present evolution with the luminosity. However, a very important dispersion with the luminosity is shown in figure 3.13. Indeed this dispersion is important between -0.2 dex and 0.6 dex. It does not highlight the signature of an extra-mixing at the luminosity bump, which would affect only the lightest chemical elements.

In figure 3.14 we plot the [Na/Fe] ratio in open clusters as a function of cluster turnoff mass, for which carbon isotopic ratio has been determined (left panel), and in field stars by Gratton et al. (2000). Note that the observational data were reported to the solar Na

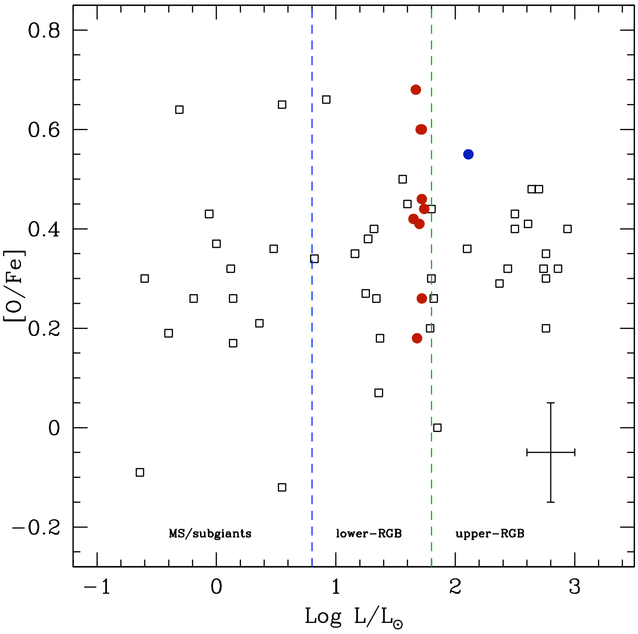

Figure 3.13: [O/Fe] ratio as a function of stellar luminosity for field stars sample observed by Gratton et al. (2000). Error bar is shown.

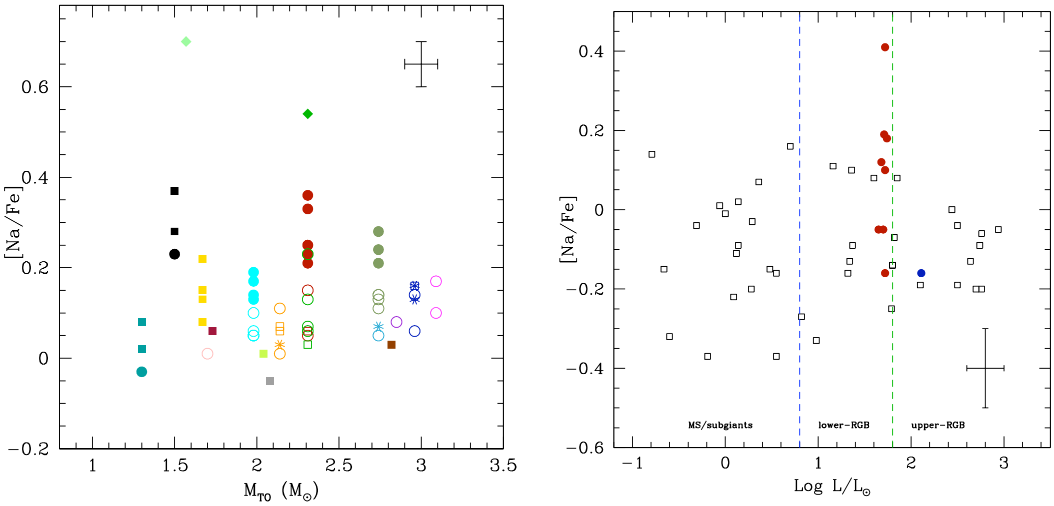

Figure 3.14: [Na/Fe] ratio as a function of turn-off mass *Left panel :* for the sample of Galactic open clusters, by Smiljanic et al. (2009, open symbols), Gilroy (1989), Gilroy & Brown (1991), Mikolaitis et al. (2010), Jacobson et al. (2007), Jacobson et al. (2008), Jacobson et al. (2009), and Hamdani et al. (2000). *Right panel :* [Na/Fe] ratio as a function of stellar luminosity for field stars sample observed by Gratton et al. (2000).

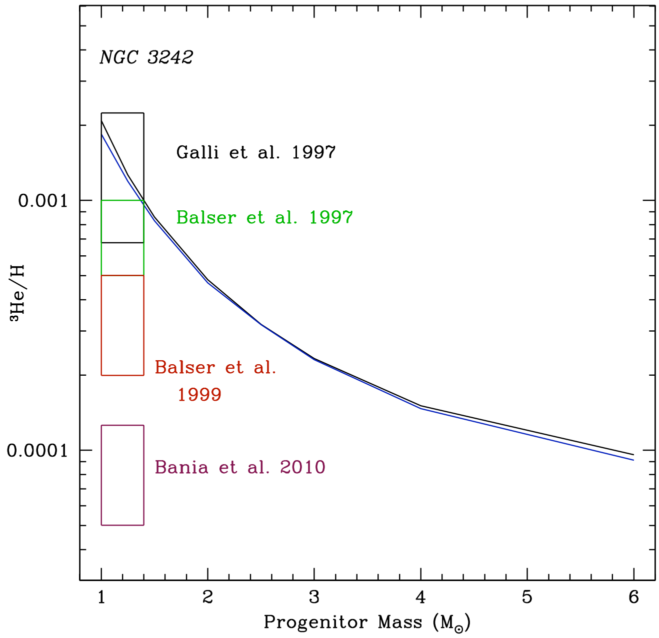

Figure 3.15: Observations of ^{3}He/H in NGC3242 (Galli et al. 1997; Balser et al. 1997, 1999b; Bania et al. 2010) as a function of the progenitor mass (from Palla et al. 2000). Standard predictions are shown at the tip of the RGB and after completion of the second dredge-up (black and blue lines respectively).

value from Asplund et al. (2005) we assume in the initial composition of our models[1]. Sodium shows also a large dispersion at all luminosities, [Na/Fe] varies between -0.05 and ∼0.64 in open clusters (presented in left panel of Fig. 3.14), and [Na/Fe] in field stars between -0.4 and 0.4 (right panel Fig. 3.14). Nevertheless, no change is visible during the ascent of the red giant branch for sodium abundance at the surface.

3.5 ^{3}He case

As discussed in Chapter 2, ^{3}He is produced in stars by deuterium combustion on the pre-main sequence, and through the PPI chain ^{2}D(^{1}H, γ)^{3}He on the main sequence. The standard theory predicts that the first dredge-up brings ^{3}He in the stellar convective envelope where it is preserved all along the advanced phases of evolution (see Chap. 2, Fig. 2.15). At the end of their evolution, low- and intermediate-mass stars become planetary nebulae, which should be enriched in ^{3}He as predicted by standard models.

Detecting ^{3}He$^+$ in the nebulae surrounding Planetary Nebulae (PNe) is a challenging experimental problem. Indeed, finding ^{3}He in PNe challenges the sensitivity limits of all existing radio telescopes because PNe nebula contain low quantity of gas ($\sim$ 1 M$_\odot$ for PNe against $\sim$ 100 to $\sim$1000 M$_\odot$ for HII region plasma). Balser D.S., Bania T.M., Rood R.T. observed ^{3}He towards six PNe (Rood et al. 1992; Balser et al. 1997, 1999b, 2006;

---

[1] Smiljanic et al. (2009) and Mikolaitis et al. (2010) adopted solar abundances recommended by Grevesse et al. (1993) (A(Na) = 6.33, A(Fe)=7.50), while Jacobson et al. (2007, 2008, 2009) and Hamdani et al. (2000) used solar abundances given by Anders & Grevesse (1989) (A(Na)=6.33). In Fig. 21 the observational data are reported to the solar abondances values we use in our computations (Asplund et al. 2005, A(Na)=6.20, and A(Fe) = 7.45).

Bania et al. 2010) that have been selected to maximize the likelihood of ^{3}He$^+$ detection, since upper limits would be difficult to interpret. These PNe have been selected to have indications in nebular gas of nuclear processing on the RGB or AGB. They are also rejected PNe with high He, N, or ^{13}C which indicate that the gas had undergone CNO processing and also ^{3}He depletion. This implies a bias in observations.

In figure 3.15, our standard predictions of ^{3}He abundance at the RGB tip and at the end of the second dredge-up are compared with observations of ^{3}He/H in NGC 3242 by Galli et al. (1997); Balser et al. (1997, 1999b); Bania et al. (2010). The abscissa is the progenitor mass derived by Palla et al. (2000) ; this quantity is highly uncertain as shown by the error bars. Balser et al. (1997) observed these six planetary nebulae, and found only one detection for NGC 3242 which have high helium-3 content (^{3}He/H=(5-10)$\cdot 10^{-4}$, see green square on fig.3.15), in agreement with standard models contrary to observations in HII regions which predict lower value of helium-3 (see Chapter 6). This planetary nebula is the only detection of helium-3 in agreement with standard models. It is therefore of particular importance to constrain theoretical models. However, Balser and collaborators do not have definitive detections in any other PNe. NGC 3242 has been reobserved by Balser et al. (1999b) and they confirmed their earlier detection of ^{3}He (^{3}He/H = (2-5)$\cdot 10^{-4}$, red square on Fig. 3.15). More recently, Bania et al. (2010) proposed new observations with different telescopes and they do not confirm previous result (Balser et al. 1999b, , see Fig. 3.15), finding a ^{3}He/H abundance is lower by a factor 4 in NGC 3242 (purple square on Fig. 3.15).

3.6 Summary

In this chapter, we presented the main observations of Li, Be, ^{3}He, C, N, O and Na abundances, in low- and intermediate-mass stars, in globular and open clusters, and in field stars, at various metallicities. Through comparison with predictions of standard stellar models, we underlined the abundances anomalies.

All of these observations depict evolution of lithium, carbon, and nitrogen abundances at the surface of giants stars together with carbon isotopic ratio, ^{12}C/^{13}C. As predicted by standard models (see Chapter 2), variations of surface abundances are observed in subgiant stars caused by the first dredge-up. However, the dispersion of chemical species observed in stellar luminosity and effective temperature for stars less luminous than the bump luminosity, which is not predicted by standard models, shows the presence of an extra-mixing which occurs during the early phases.

Then, the second variations of surface abundances occurs at the bump luminosity when the hydrogen burning shell crosses the discontinuity left behind by the convective envelope. These variations might be due to an extra mixing which occurs at this luminosity. Effect of this extra-mixing can be summarized with figure 3.16. Indeed it shows the evolution of lithium, carbon, nitrogen, oxygen and sodium in field stars observed by Gratton et al. (2000). At the bump luminosity ($\log(L/L_\odot)\sim 1.8$), Li, C, and carbon isotopic ration decrease while nitrogen increases, and oxygen and sodium stay constant.

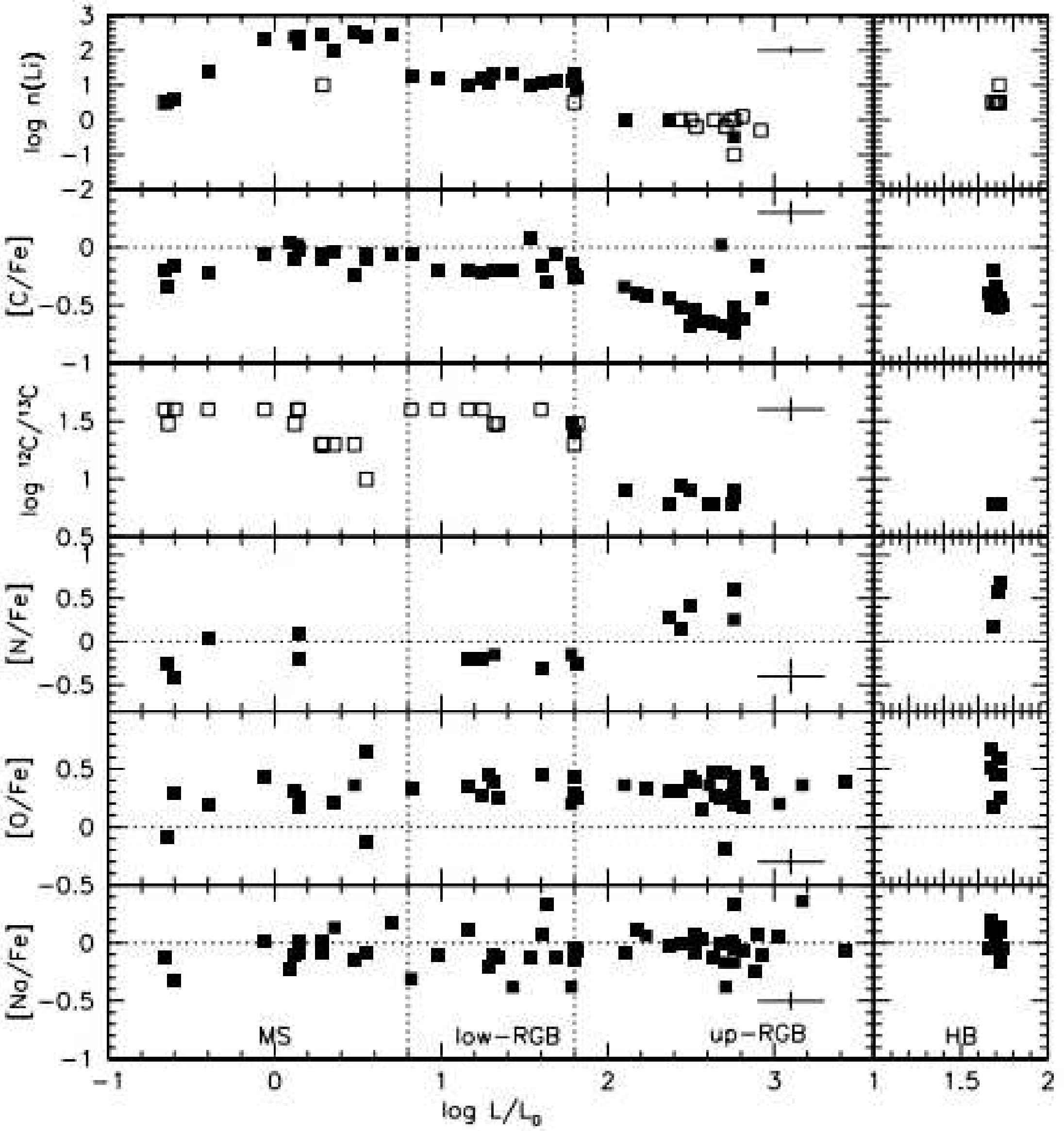

Figure 3.16: Run of the abundance of Li, of the abundance ratios [C/Fe], [N/Fe], [O/Fe] and [Na/Fe], and of the isotopic ratio $^{12}C/^{13}C$ with luminosity for stars with $-2 < [Fe/H] < -1$. Filled symbols are actual measures; arrows are upper (for Li) or lower (for $^{12}C/^{13}C$) limits.Typical error bars for the various quantities are shown. Dashed lines separate various evolutionary phases (MS and TO stars; lower-RGB stars; upper-RGB stars). Results for RHB stars are plotted separately for clarity. *Figure from Gratton et al. (2000).*

Table 3.2: Observations of chemical abundances for open clusters from the literature.

Open Cluster

References	Chemicals	Remarks
NGC 3680		
Pasquini et al. (2001)	Li	24 main sequence, subgiant and giant stars
Anthony-Twarog et al. (2009)	Li	53 stars
Smiljanic et al. (2009)	Na	M$_{red,TO}$= 1.70 M$_\odot$ log(t)=9.25,[Fe/H]=0.04 1 stars
M67		
Pilachowski et al. (1988)	Li	14 giant stars
Brown (1987)	C/N	Subgiants and giants
Gilroy (1989)	^{12}C/^{13}C	M$_{TO}$=1.2M$_\odot$,log(t)= 9.69 7 stars
Balachandran (1990)	Li	5 stars
Gilroy & Brown (1991)	^{12}C/^{13}C	From subgiants to clump stars. M$_{TO}$=1.2 M$_\odot$
Tautvaišiene et al. (2000)	C, N, O	M$_{TO}$=1.2 M$_\odot$; log(t)=5.10^9
	Na, Mg, ^{12}C/^{13}C, C/N	9 stars (3 giants and 6 clump stars)
Randich et al. (2002)	Li, Be	5 stars
Yong et al. (2005a)	Na	3 stars
Canto Martins et al. (2011)	Li	From TO stars to giant stars ; metallicity is given 27 stars
NGC 752		
Pilachowski et al. (1988)	Li	11 giant stars
Gilroy (1989)	^{12}C/^{13}C	- M$_{TO}$=1.6 M$_\odot$; log(t)= 9.30
	Li	6 stars
Stock 2		
Gilroy (1989)	^{12}C/^{13}C	- M$_{TO}$=2.8 M$_\odot$; log(t)= 8.60
	Li	2 stars
Tr 2		
Gilroy (1989)	^{12}C/^{13}C	- M$_{TO}$=4.5 M$_\odot$; log(t)= 7.95
	Li	1 star
NGC 1342		
Gilroy (1989)	^{12}C/^{13}C	- M$_{TO}$=3.1 M$_\odot$; log(t)= 8.48
	Li	1 star
NGC 1545		
Gilroy (1989)	^{12}C/^{13}C	- M$_{TO}$=2.8 M$_\odot$; log(t)= 8.60
	Li	1 star
Hyades		
Wallerstein et al. (1965)	Li	23 stars
Zappala (1972)	Li	41 stars
Lambert et al. (1980)	Li ^{12}C/^{13}C	- 50 G- and K- giants
Cayrel et al. (1984)	Li	12 MS stars
Gilroy (1989)	^{12}C/^{13}C	- M$_{TO}$=2.2 M$_\odot$; log(t)= 8.90
	Li	4 stars
Smiljanic (2012)	Na	3 stars
NGC 1662		
Gilroy (1989)	^{12}C/^{13}C	- M$_{TO}$=2.8 M$_\odot$; log(t)= 8.60
	Li	2 stars
NGC 1817		
Jacobson et al. (2009)	Na, [O/Fe]	- M$_{TO}$=2.82 M$_\odot$ 2 stars
NGC 1883		
Jacobson et al. (2009)	Na, [O/Fe]	- M$_{TO}$=2.08 M$_\odot$ 3 stars
NGC 2141		
Yong et al. (2005a)	Na, [O/Fe]	- 1star
Jacobson et al. (2009)	Na, [O/Fe]	- M$_{TO}$=1.73 M$_\odot$ 1 star
NGC 2158		
Jacobson et al. (2009)	Na, [O/Fe]	- M$_{TO}$=2.04 M$_\odot$ 1 star

Open Cluster - continued

References	Chemicals	Remarks
NGC 2281		
Gilroy (1989)	$^{12}C/^{13}C$	- M_{TO}=2.7 $M_\odot$; log(t)= 8.65
	Li	3 stars
NGC 2287		
Gilroy (1989)	$^{12}C/^{13}C$	- M_{TO}= 3.8 $M_\odot$; log(t)= 8.34
	Li	4 stars
NGC 2360		
Gilroy (1989)	$^{12}C/^{13}C$	- M_{TO}= 1.9 $M_\odot$; log(t)= 9.11
		1 star
Hamdani et al. (2000)	[Na/Fe]	- M_{TO}=1.98$M_\odot$
		4 stars
Smiljanic et al. (2009)	Na, C, N	- $M_{red,TO}$= 1.98 $M_\odot$; log(t)=9.06 ; [Fe/H]=0.04
	O	4 stars
Cr 140		
Gilroy (1989)	$^{12}C/^{13}C$	- M_{TO}= 6.0 $M_\odot$; log(t)= 7.70
	Li	1 star
NGC 2422		
Gilroy (1989)	$^{12}C/^{13}C$	- M_{TO}= 4.8 $M_\odot$; log(t)= 7.84
	Li	2 stars
NGC 2447		
Hamdani et al. (2000)	Na	-M_{TO}= 2.74 $M_\odot$
		3 stars
Smiljanic et al. (2009)	Na, C, N	- $M_{red,TO}$= 2.74 $M_\odot$; log(t)=8.65 ; [Fe/H]=-0.01
	O	3 stars
NGC 2451		
Gilroy (1989)	$^{12}C/^{13}C$	- M_{TO}= 5.0 $M_\odot$; log(t)= 7.81
	Li	1 star
NGC 2548		
Gilroy (1989)	$^{12}C/^{13}C$	- M_{TO}= 2.6 $M_\odot$; log(t)= 8.70
	Li	2 stars
NGC 5822		
Luck (1994)	C, O, N	- M_{TO}= 1.8 $M_\odot$; log(t)= 9.08
	$^{12}C/^{13}C$	3 stars
NGC 3532		
Smiljanic et al. (2009)	Na, C, N	- $M_{red,TO}$= 2.96 $M_\odot$; log(t)=8.55 ; [Fe/H]=0.04
	O, $^{12}C/^{13}C$	5 stars
Luck (1994)	C, O, N	- M_{TO}= 2.7 $M_\odot$; log(t)= 8.46
	$^{12}C/^{13}C$	14 stars
NGC 3960		
Prisinzano & Randich (2007)	Li	113 subgiant and giant stars
Praesepe		
Gilroy (1989)	$^{12}C/^{13}C$	- M_{TO}= 2.2 $M_\odot$; log(t)= 8.90
	Li	4 stars
UMa Group		
Gilroy (1989)	$^{12}C/^{13}C$	- M_{TO}= 2.9 $M_\odot$; log(t)= 8.54
	Li	3 stars
NGC 5822		
Smiljanic et al. (2009)	Na, C, N	- $M_{red,TO}$= 2.14 $M_\odot$; log(t)=8.95 ; [Fe/H]=0.04
	$^{12}C/^{13}C$	5 stars
NGC 6067		
Luck (1994)	C, O, N	- M_{TO}= 3.6 $M_\odot$; log(t)= 8.11
	$^{12}C/^{13}C$	8 stars
NGC 6087		
Luck (1994)	C, O, N	- M_{TO}= 5.5 $M_\odot$; log(t)= 7.85
	$^{12}C/^{13}C$	3 stars
NGC 6134		
Smiljanic et al. (2009)	Na, C, N	- $M_{red,TO}$= 2.31 $M_\odot$; log(t)=8.85 ; [Fe/H]=0.12
	$^{12}C/^{13}C$	3 stars
Mikolaitis et al. (2010)	C, N, O, Na	- $M_{red,TO}$= 2.31 $M_\odot$; log(t)=0.7.10^9
	Mg, $^{12}C/^{13}C$, C/N	6 clump stars

Open Cluster - continued

References	Chemicals	Remarks
NGC 6253		
Mikolaitis et al. (2012)	[C/Fe], [N/Fe], [O/Fe] C/N, ^{12}C/^{13}C	4 stars
Collinder 261		
Mikolaitis et al. (2012)	[C/Fe], [N/Fe], [O/Fe] C/N, ^{12}C/^{13}C	6 stars
NGC 6281		
Smiljanic et al. (2009)	Na, C, N	- $M_{red,TO}$= 3.09 $M_\odot$; log(t)=8.50 ; [Fe/H]=0.05
	O, ^{12}C/^{13}C	2 stars
NGC 6633		
Gilroy (1989)	^{12}C/^{13}C	- M_{TO}= 2.5 $M_\odot$; log(t)=8.74
	Li	4 stars.
Smiljanic et al. (2009)	Na, C, N	- $M_{red,TO}$= 2.74 $M_\odot$; log(t)=8.65 ; [Fe/H]=0.08
	O, ^{12}C/^{13}C	2 stars
NGC 6882/85		
Luck (1994)	C, O, N	- M_{TO}= 1.8 $M_\odot$; log(t)= 9.16
	^{12}C/^{13}C	2 stars
NGC 6939		
Jacobson et al. (2007)	Na, [O/Fe]	- M_{TO}=1.57 $M_\odot$
		9 stars
NGC 7142		
Jacobson et al. (2008)	Na, [O/Fe]	- M_{TO}=1.67 $M_\odot$
		4 stars
NGC 7789		
Pilachowski (1986)	Li	- 4 MS + 19 giant stars
Sneden & Pilachowski (1986)	^{12}C/^{13}C, Li	- 7 Giant stars
Tautvaišienė et al. (2005)	C, O, N	[Fe/H]=-0.04 + - 0.05
	Na, Mg, ^{12}C/^{13}C	9 stars (6 giants + 3 clump stars)
IC 4725		
Luck (1994)	C, O, N	- M_{TO}= 7.6 $M_\odot$; log(t)= 7.61
	^{12}C/^{13}C	5 stars
IC 4756		
Gilroy (1989)	^{12}C/^{13}C	- M_{TO}= 2.2 $M_\odot$; log(t)=8.90
	Li	7 stars
Jacobson et al. (2007)	Na, [O/Fe]	- 6stars
Smiljanic et al. (2009)	Na, C, N	- $M_{red,TO}$= 2.31 $M_\odot$; log(t)=8.85 ; [Fe/H]=0.04
	O, ^{12}C/^{13}C	5 stars
Luck (1994)	C, O, N	- M_{TO}= 2.0 $M_\odot$; log(t)= 8.92
	^{12}C/^{13}C	3 stars
IC 4651		
Randich et al. (2002)	Li, Be	3 stars
Pasquini et al. (2004b)	Li	- [Fe/H]=0.10±0.03
		22 stars MS, subgiant, and giant stars.
Smiljanic et al. (2010)	Li, Be	- Same stars than Pasquini et al. (2004).
Mikolaitis et al. (2011)	C/N	-$M_{red,TO}$= 1.69 $M_\odot$; log(t)=1.7.10^9
	^{12}C/^{13}C	3 stars
IC 2602		
Randich et al. (2001)	Li	12 stars
IC 2391		
Randich et al. (2001)	Li	18 stars
Randich et al. (2002)	Li	1 star
IC 2581		
Luck (1994)	C, O, N	- M_{TO}= 12.6 $M_\odot$; log(t)= 7.08
		1 star
IC 2714		
Smiljanic et al. (2009)	Na, C, N	- $M_{red,TO}$= 2.85 $M_\odot$; log(t)=8.60 ; [Fe/H]=0.12
		1 star

Table 3.3: Observations of chemical abundances for globular clusters from the literature.

Globular Cluster

References	Chemicals	Remarks
NGC 6397		
Bell et al. (1979)	C	5 stars
Briley et al. (1990)	C, N	25 giant stars
Lind et al. (2009)	Li, Na	
Koch et al. (2012)	Li	super Li-rich stars
M3		
Suntzeff (1981)	[C/Fe], [N/Fe]	29 RGB stars
NGC 6121 (M4)		
Smith & Suntzeff (1989)	^{12}C/^{13}C	7 stars
Brown et al. (1990)	^{12}C/^{13}C	4 stars
Brown et al. (1989)	C, N, O	4 stars
	^{12}C/^{13}C	
Suntzeff & Smith (1991)	^{12}C/^{13}C	32 stars
Brown & Wallerstein (1992)	Na, Mg	
	[O/Fe]	3 stars
Shetrone (2003)	^{12}C/^{13}C	- down to the bump luminosity
		16 stars
D'Orazi & Marino (2010)	Li	[Fe/H]=-1.18
		∼100 giants below and above bump luminosity
Mucciarelli et al. (2011)	Li	87 stars (in which 36 giants)
Monaco et al. (2012)	Li, Na	- 91 main sequence (MS)/sub-giant branch stars
M13		
Suntzeff (1981)	[C/Fe], [N/Fe]	35 RGB stars
M15		
Trefzger et al. (1983)	C, N	33 stars
NGC 6528		
Shetrone (2003)	^{12}C/^{13}C	- down to the bump luminosity
		9 stars
47 Tuc		
Shetrone (2003)	^{12}C/^{13}C	- down to the bump luminosity
		5 stars
Brown et al. (1990)	^{12}C/^{13}C	4 stars
Brown et al. (1989)	C, N, O	[Fe/H] is given
	^{12}C/^{13}C	4 stars
Bell et al. (1990)	^{12}C/^{13}C	4 stars
Brown & Wallerstein (1992)	Na, Mg	2 stars
	[O/Fe]	
D'Orazi et al. (2010)	Li, O, Na	∼90 stars
NGC 6553		
Shetrone (2003)	^{12}C/^{13}C	- down to the bump luminosity
		4 stars
NGC 6752		
Suntzeff & Smith (1991)	^{12}C/^{13}C	12 stars
Yong et al. (2005b)	Na, [O/Fe]	- 38 bright giants
Shen et al. (2010)	Li, O	- 112 stars
M22/NGC 6656		
Smith & Suntzeff (1989)	^{12}C/^{13}C	5 stars
Brown et al. (1990)	^{12}C/^{13}C	8 RGB stars
Brown et al. (1989)	C, N, O	7 stars
	^{12}C/^{13}C	
Brown & Wallerstein (1992)	Na, Mg	7 stars
	[O/Fe]	
Marino et al. (2012)	[C/Fe]	101 subgiant branch stars
M55		
Briley et al. (1990)	C	15 giant stars

Globular Cluster - continued

	M71	
Smith et al. (2007)	C, O, $^{12}C/^{13}C$	- Upper Red giant Branch stars 16 stars
Briley et al. (1994)	C, N, O Na, $^{12}C/^{13}C$	- 6 stars
Briley et al. (1997)	C, N, O $^{12}C/^{13}C$	- 10 stars
	M92	
Bell et al. (1979)	C	3 stars
Carbon et al. (1982)	C, N	- 45 stars
Langer et al. (1986)	[C/Fe]	- 41 stars
Pilachowski (1988)	[C/Fe],[N/Fe], [O/Fe]	6 G-stars
	ω Cen/NGC5139	
Brown & Wallerstein (1989)	$^{12}C/^{13}C$	6 RGB stars
Smith et al. (2002)	$^{12}C/^{13}C$, [C/Fe]	11 giant stars
	NGC1851	
Lardo et al. (2012)	C, N	64 MS and subgiant stars

Table 3.4: Observations of chemical abundances for field stars from the literature.

Field stars

References	Chemicals	Remarks
Day et al. (1973)	^{12}C/^{13}C	1 star
Luck (1977)	Li, ^{12}C/^{13}C	-19 G- and K- stars
Luck (1978)	C/N, O/N, C/O	19 G and K supergiant stars
	^{12}C/^{13}C	
Lambert et al. (1980)	Li	
Lambert & Ries (1981)	C, N , O	G- and K- giants
	^{12}C/^{13}C	32 stars
Luck & Lambert (1982)	Li	-31 M giants and supergiants
Wallerstein & Sneden (1982)	Li, C, N, O	- 1 K-giant star
	^{12}C/^{13}C	
Lambert & Sawyer (1984)	Li	9 G giant stars
Harris & Lambert (1984)	^{16}O/^{17}O, ^{16}O/^{18}O	- 7 giant stars
	^{17}O/^{18}O	
Smith & Lambert (1986)	Li	10 subgiant stars
Sneden et al. (1986)	C, N	[Fe/H] and log(g) are given
	^{12}C/^{13}C	19 stars ; $-0.8 \leq$[Fe/H]≤ -0.03
Cottrell & Sneden (1986)	C, N, O	- old disk giants, stellar mass and log(g) are given
	^{12}C/^{13}C	34 stars
Pallavicini et al. (1987)	Li	27 F-, G- and K- subgiant stars
Harris et al. (1988)	^{16}O/^{17}3O, ^{16}O/^{18}O	- 5 giant stars
	^{17}O/^{18}O	
Brown et al. (1989)	Li	- [Fe/H]
		644 G and K giants
Balachandran (1990)	Li	-140 MS stars
Pilachowski et al. (1993)	Li	79 halo subgiants
Shetrone et al. (1993)	Li,	- Old disc giants, [Fe/H] and stellar mass are given
	^{12}C/^{13}C	31 stars ; $-0.7\leq$[Fe/H]≤-0.2
Berdyugina & Savanov (1994)	Li, C, N, O	- Li rich stars
	^{12}C/^{13}C, C/N	10 stars ; $-0.25\leq$[Fe/H]≤0.23
Smith et al. (1995)	Li	-SMC & LMC
		112 stars
da Silva et al. (1995)	Li, C, N, O	- Li-rich stars
	^{12}C/^{13}C, ^{12}C/^{14}N	3 stars
Charbonnel et al. (1998b)	Li, C, N, O	7stars
	^{12}C/^{13}C	
Barrado y Navascues et al. (1997)	Li	- Stellar mass and age are given
		76 stars
Lèbre et al. (1999)	Li	- 120 F-, G-, and K-type Pop I subgiant stars.
		Rotational velocity
Mallik (1999)		-65 subgiant, giant and supergiant stars
Gratton et al. (2000)	Li, C, N, O	62 stars
	Na, ^{12}C/^{13}C	
Charbonnel & Balachandran (2000)	Li , ^{12}C/^{13}C	Li-rich stars
Drake et al. (2002)	Li, C, N, O	- Rapid rotating
	^{12}C/^{13}C	1 star ($\sim$ 1 $M_{\odot}$)
Reddy et al. (2002)	Li, C, N, O	K-giant star ; [Fe/H]=0.14
	^{12}C/^{13}C	1 star

Field stars - continued

References	Chemicals	Remarks
Reddy & Lambert (2005)	Li	- Stellar mass and [Fe/H] are given for each stars
	$^{12}C/^{13}C$	4 stars
Mishenina et al. (2006)	Li, C, N, O,	- Stellar mass, log(g) are given ; -0.69≤[Fe/H]≤0.27
	Mg, Na	177 clump giant stars of galactic disc
Luck & Heiter (2007)	Li, C, N, O	- 298 nearby giants
Uttenthaler et al. (2007)	Li	27 stars
Carlberg et al. (2010)	Li	Super Li-rich K-giant star
	$^{12}C/^{13}C$	1 star
Uttenthaler & Lebzelter (2010)	Li	-oxygen-rich AGB variables
		18 stars
Monaco et al. (2011)	Li, C, N,	- 824 thick-disk giants
	O, $^{12}C/^{13}C$	5 Li-rich stars
Kumar et al. (2011)	Li	-15 new Li-rich stars (including 4 super-Li-rich)
Palacios et al. (2012)	Li	-Weak G-band stars
Tautvaišienė et al. (2011)	[C/Fe], [N/Fe], [O/Fe]	
	$^{12}C/^{13}C$, C/N	1 star
Lebzelter et al. (2012)	Li	RGB stars in galactic bulge
		401 low-mass stars
Mucciarelli et al. (2012)	$^{12}C/^{13}C$, Li	- 17 halo lower RGB stars in range -3.4≤[Fe/H]≤-1.4

Chapter 4

Transport processes: From parametric to hydrodynamic computations.

Numerous spectroscopic observations provide compelling evidence for non-canonical processes that modify the surface abundances of low- and intermediate-mass stars which are not predicted by standard stellar theory (see Chapters 2 and 3). In this chapter, we will present different transport processes which have been proposed in the literature to explain abundance anomalies in giants.

4.1 Parametrized prescriptions for transport processes of nucleides

Parametric computations have been proposed to better understand the behaviour of chemical abundances at the stellar surface in low- and intermediate-mass stars. After showing that the Hot Bottom Burning (HBB) process, which was previously proposed by Cameron & Fowler (1971) to allow Li production in AGB stars, can explain the oxygen isotopic ratios in AGB stars with initial stellar mass between ∼4.5 and 7.0 $M_\odot$, Boothroyd et al. (1995) introduced the notion of Cool Bottom Processing (i.e., adhoc transport material from the cool bottom of stellar convective envelope to deeper and hotter radiative regions where nuclear reactions occur), to explain surface abundances of giant stars with masses $\lesssim$2.0 $M_\odot$ (see also Wasserburg et al. 1995; Boothroyd & Sackmann 1999; Sackmann & Boothroyd 1999).

Denissenkov & Weiss (1996) suggested like Wasserburg et al. (1995) the presence of non-standard mixing of unknown physical origin, between the hydrogen burning and the base of convective envelope after the bump to explain abundances anomalies in red giant stars. To understand variations of surface abundances of giant stars, they proposed a deep diffusive mixing (e.g. Denissenkov & Weiss 1996; Weiss et al. 1996; Denissenkov et al. 1998).

Nevertheless, these two propositions of extra-mixing are then not related to any physical mechanism to explain changes in surface abundances, and depend on free parameters.

4.2 Rotation-induced mixing

Rotation has been investigated as a possible source of mixing in RGB stars by several authors (Sweigart & Mengel 1979; Charbonnel 1995; Denissenkov & Tout 2000; Palacios et al. 2006; Chanamé et al. 2005). In this section, we will first briefly summarize the description of rotation-induced mixing and the physical prescription we use to compute our models for this study.

4.2.1 Physical description of rotation

Rotation drives the transport of angular momentum in radiative zone, which is induced by different processes :

- The stellar contraction or expansion. Due to the conservation of angular momentum, J $\propto r^2\Omega$=cst, when the star contracts or expands, angular velocity, Ω, increases or decreases.
- Turbulence shear. It occurs if a gradient of angular momentum exists between two adjacent layers. It acts like a diffusive process that smooth the angular velocity profiles inside the stars by promoting exchanges of angular momentum between adjacent layers.
- Meridional circulation. Rotating stars have hotter poles than their equator. This results in large scale motions, known as meridional circulation, which is created to transport heat and hence matter and angular momentum. Meridional circulation has advective nature. Therefore it acts to reinforce the angular velocity gradients, contrary to the shear which tends to smooth them out. The final angular velocity profiles thus depend on the delicate balance of these two processes in the phases of quasi hydrostatic equilibrium.

Transport of angular momentum

The hydrodynamics, meridional circulation and turbulent shear all concour to the transport of energy angular momentum and matter in a rotating star. This transport is modelled as follows in our approach.

Meridional circulation develops in radiative layers of rotating stars where it is generated by thermal imbalance induced by the breaking of spherical symmetry (Eddington 1925; Vogt 1926). In a uniformly rotating star, the equipotentials are closer to each other along the polar axis than along the equatorial axis. According to the Von Zeipel theorem, the heating on a equipotential is generally higher in the polar direction than in the equitorial direction, which thus drives a large scale circulation rising at the pole and descending at the equator. Indeed, in presence of rotation hydrostatic equilibrium and radiative thermal equilibrium cannot be simultaneously satisfied. This large scale circulation induces transports matter and advection of angular momentum. Meridional circulation favors the development of strong horizontal diffusion through different hydrostatic instabilities (e.g. Maeder & Meynet 2000), while vertical turbulence is inhibited due to the hight level of stratification in this direction. As a result of anisotropic turbulence, one can use the hypothesis of "shelullar rotation" (Zahn 1992). In this configuration, angular velocity Ω on the isobars is considered constant $\Omega \sim \Omega(\mathrm{P})$. Consequently, every quantity depends only on pressure and can be split into a mean value and its latitudinal perturbation :

$$f(\mathrm{P},\theta) = \bar{f}(\mathrm{P}) + \tilde{f}(\mathrm{P})\mathrm{P}_2(\cos\theta)$$

where $P_2(\cos\theta)$ is the Legendre polynomial order two.

For the shellular rotation, the transport of angular momentum in stellar radiative layers obeys an advection/diffusion equation

$$\underbrace{\rho\frac{\mathrm{d}(r^2\Omega)}{\mathrm{d}t}}_{\substack{\text{stellar}\\ \text{contraction/expansion}}} = \underbrace{\frac{1}{5r^2}\frac{\partial}{\partial r}(\rho r^4 \Omega U_r)}_{\substack{\text{advection of}\\ \text{angular momentum}\\ \text{by meridional circulation}}} + \underbrace{\frac{1}{r^2}\frac{\partial}{\partial r}\left(r^4 \rho \nu_v \frac{\partial\Omega}{\partial r}\right)}_{\substack{\text{diffusion effect of}\\ \text{shear-induced turbulence}}} \tag{4.1}$$

where r is the stellar radius, ρ the density, ν_v the vertical component of the turbulent viscosity, and Ω the angular velocity. The vertical component of meridional circulation velocity U is given by :

$$U(r) = \frac{P}{C_p\bar{\rho}\bar{T}\bar{g}[\nabla_{ad} - \nabla + \varphi/\delta\nabla_\mu]} \cdot \left[\frac{L}{M_\star}(E_\Omega + E_\mu) + \frac{C_p\bar{T}}{\delta}\frac{\partial\Theta}{\partial t}\right] \tag{4.2}$$

where L is the luminosity, $M_\star = M \cdot \left(1 - \frac{\Omega^2}{2\pi G\rho_m}\right)$ where M is the mass and ρ_m the mean density inside the shell with mass M, P the pressure, and C_P the specific heat at constant pressure, T the temperature, ∇_{ad}, ∇, and ∇_ν the adiabatic, radiative, and mean molecular weight gradients respectively (Maeder & Zahn 1998). g is the modulus of the effective gravity, defined by hydrostatic equilibrium equation :

$$\vec{g} = \vec{\nabla}\Phi + \frac{1}{2}\Omega^2\vec{\nabla}s^2 \tag{4.3}$$

$\varphi = (\partial ln\rho/\partial ln\mu)_{P,T}$ and $\delta = -(\partial ln\rho/\partial ln\mu)_{P,\mu}$ are coefficients issued from the equation of state (Kippenhahn & Weigert 1990).

E_Ω and E_μ depend respectively on the rotation profile and on the mean molecular weight as :

$$\begin{aligned}
E_\Omega = {} & 2\left[1 - \frac{\bar{\Omega}^2}{2\pi\bar{\rho}} - \frac{(\bar{\epsilon} + \bar{\epsilon}^{grav})}{\epsilon_m}\right]\frac{\tilde{g}}{\bar{g}} \\
& - \frac{\rho_m}{\bar{\rho}}\left\{\frac{r}{3}\frac{d}{dr}\left[H_T\frac{d}{dr}\left(\frac{\Theta}{\delta}\right) - \chi_T\left(\frac{\Theta}{\delta}\right) + \left(1 - \frac{1}{\delta}\right)\Theta\right] - \frac{2H_T}{r}\left(1 + \frac{D_h}{K}\right)\left(\frac{\Theta}{\delta}\right) + \frac{2}{3}\Theta\right\} \\
& - \frac{(\bar{\epsilon} + \bar{\epsilon}^{grav})}{\epsilon_m}\left[H_T\frac{d}{dr}\left(\frac{\Theta}{\delta}\right) + (f_\epsilon\epsilon_T - \chi_T)\left(\frac{\Theta}{\delta}\right) + \left(2 - f_\epsilon - \frac{1}{\delta}\right)\Theta - \frac{\bar{\Omega}^2}{2\pi G\bar{\rho}}\Theta\right] \\
& - \frac{\bar{\Omega}^2}{2\pi G\bar{\rho}}\Theta
\end{aligned} \tag{4.4}$$

and

$$\begin{aligned}
E_\mu = {} & \frac{\rho_m}{\bar{\rho}}\left\{\frac{r}{3}\frac{d}{dr}\left[H_T\frac{d}{dr}\left(\frac{\varphi}{\delta}\Lambda\right) - \left(\chi_\mu + \frac{\varphi}{\delta}\chi_T + \frac{\varphi}{\delta}\right)\Lambda\right] - \frac{2H_T}{r}\left(\frac{\varphi}{\delta}\Lambda\right)\right\} \\
& + \frac{(\bar{\epsilon} + \bar{\epsilon}^{grav})}{\epsilon_m}\left[H_T\frac{d}{dr}\left(\frac{\varphi}{\delta}\Lambda\right) + f_\epsilon\left(\epsilon_T + \frac{\varphi}{\delta}\epsilon_\mu\right) - \chi_\mu - \frac{\varphi}{\delta}(\chi_T + 1)\Lambda\right],
\end{aligned} \tag{4.5}$$

where H_T is the temperature scale height, K the thermal diffusivity and $f_\epsilon \equiv \bar{\epsilon}/(\bar{\epsilon} + \bar{\epsilon}^{grav})$, with $\bar{\epsilon}$ and $\bar{\epsilon}^{grav}$being respectively the mean nuclear and gravitational energy.

χ_μ and ϵ_μ are logarithmic derivatives of radiative conductivity χ and the total energy ϵ with respect to μ, while derivatives with respect to T are noted as χ_T and ϵ_T :

$$\chi_\mu = \left(\frac{\partial ln\chi}{ln\mu}\right)_{P,T,\mu}, \qquad \epsilon_\mu = \left(\frac{\partial ln\epsilon}{\partial ln\mu}\right)_{P,T,\mu} \tag{4.6}$$

$$\chi_T = \left(\frac{\partial ln\chi}{lnT}\right)_{P,\mu}, \qquad \epsilon_T = \left(\frac{\partial ln\epsilon}{\partial lnT}\right)_{P,\mu} \tag{4.7}$$

In these expressions, $\epsilon_m(r) \equiv L(r)/M(r)$ and ρ_m is the mean density inside the considered level surface. D$_h$ the horizontal diffusion coefficient (see Eq. 4.12). Θ and Λ are the relative variations over an isobar of density and mean molecular weight respectively, with

$$\Theta = \frac{\tilde{\rho}}{\bar{\rho}} = \frac{r^2}{3g}\frac{d\Omega^2}{dr} \quad \text{and} \quad \Lambda = \frac{\tilde{\mu}}{\mu} \tag{4.8}$$

Transport of chemical species

The transport of chemical elements is governed by a diffusion-advection equation like Eq. 4.1. However, since the horizontal component of the turbulent diffusion is large, the vertical advection of the elements (and not that of the angular momentum) can be treated as a simple diffusion (Chaboyer & Zahn 1992).

The advective transport is then parametrized by the effective diffusion coefficient :

$$\mathscr{D}_{\text{eff}} = \frac{|rU(r)|^2}{30\mathscr{D}_h} \tag{4.9}$$

where $\mathscr{D}_h$ is the diffusion coefficient associated to horizontal turbulence (see Eq. 4.12).

The vertical transport of a chemical species i of concentration c_i is described by a pure diffusion equation :

$$\frac{\mathrm{d}c_i}{\mathrm{d}t} = \underbrace{\dot{c_i}}_{\text{nuclear}} + \underbrace{\frac{1}{\rho r^2}\frac{\partial}{\partial r}\left(r^2\rho\mathscr{D}_{\text{tot}}\frac{\partial c_i}{\partial r}\right)}_{\text{diffusion processes}} \tag{4.10}$$

where $\dot{c_i}$ represents the variations of chemical composition due to nuclear reactions. The total diffusion coefficient $\mathscr{D}_{\text{tot}}$ for chemicals can be written as the sum of two coefficients:

$$\mathscr{D}_{\text{tot}} = \mathscr{D}_{\text{eff}} + \mathscr{D}_{\text{v}} \tag{4.11}$$

with D_{eff} the effective diffusion coefficient $\mathscr{D}_{eff} = \frac{|rU(r)|^2}{30D_h}$ by Zahn (1992); Chaboyer & Zahn (1992), and $\mathscr{D}_{\text{v}}$ (see Eq. 4.15) the vertical turbulent diffusion coefficient (Talon & Zahn 1997) Note that we do not include in our models microscopic diffusion.

The expression of the horizontal diffusion coefficient is taken from Zahn (1992), which is a formulation that prevents numerical diverge :

$$\mathscr{D}_h = \frac{r}{C_h}(|2V - \alpha U|^2 + U^2)^{1/2} \tag{4.12}$$

where C$_h$ is a free parameter of order unity (Zahn 1992) which describes the weakening effect of horizontal turbulence on the vertical transport of chemical species.

To develop the shear instability on stellar interior the matter must satisfy the Ridchardson criterion :

$$R_i = \frac{N^2}{(du/dz)^2} \leq R_{i_{crit}} \simeq \frac{1}{4} \tag{4.13}$$

with N the Brünt Vaïsälä frequency.

For the instability to grow, the Reynolds criterion has to be satisfied where the shear viscosity ν_v has to be higher than the microscopic viscosity ν :

$$\nu_v \leq \nu R_{e,crit} \tag{4.14}$$

where $R_{e,crit}$ is the critical Reynolds number.

Talon & Zahn (1997) gives a possible expression for the turbulent viscosity :

$$\nu_v = \frac{8}{5} \frac{R_{i,crit}\left(r\frac{d\Omega}{dr}\right)^2}{N_T^2/(K+D_h) + N_\mu^2/D_h} \tag{4.15}$$

where N_T and N_μ the thermal and chemical components of the Brünt Vaïsälä frequency :

$$N^2 = N_T^2 + N_\mu^2 = \frac{g}{H_P}[\delta(\nabla_{ad} - \nabla) + \varphi\nabla_\mu] \tag{4.16}$$

We assumed that the vertical turbulent diffusion coefficient D_v can be taken equal to the turbulent viscosity (D_v=ν_v, Talon & Zahn 1997), which remains valid as long as the turbulence is strong anisotropic.

4.2.2 Effect of rotation induced-mixing on chemical species

Rotation-induced mixing on the main sequence modifies internal and surface chemical abundances as extensively tested in previous papers. Maeder & Meynet (2000) (see their references) have also largely investigated stellar evolution with rotation in massive stars. It accounts nicely for the behaviour of lithium and beryllium at the surface of Population I main-sequence and subgiant low-mass stars (see § 4.1; Talon & Charbonnel 1998, 2010; Charbonnel & Talon 1999; Palacios et al. 2003; Pasquini et al. 2004a; Smiljanic et al. 2009; Charbonnel & Lagarde 2010b).

Rotation-induced mixing has also an impact on the internal abundance profiles of heavier chemicals involved in hydrogen-burning at higher temperatures than the fragile Li and Be. This can be seen at the moment of the turnoff in Fig. 4.1 for the 1.5 $M_\odot$ star computed for different initial rotation velocities.

In the rotating models, the abundance gradients are smoothed out compared to the standard case: ^{3}He, ^{13}C, ^{14}N, and ^{17}O diffuse outwards, while ^{12}C and ^{18}O diffuse inwards. However, rotation-induced mixing is not efficient enough to noticeably change the surface abundances of these elements on the main sequence for the 1.5 $M_\odot$ model[1], although it sets the scene for abundance variations in latter evolution phases. In particular the surface abundance variations during the first dredge-up are slightly strenghtened when rotation-induced mixing is accounted for, as shown in Fig. 4.2. For example, more ^{3}He is brought into the stellar envelope, and the post dredge-up ^{12}C/^{13}C and ^{16}O/^{17}O ratios are lower than in the non-rotating case. We note, however, that ^{16}O is not affected. These

---

[1] The only exception is ^{7}Li which is strongly depleted in the rotating case.

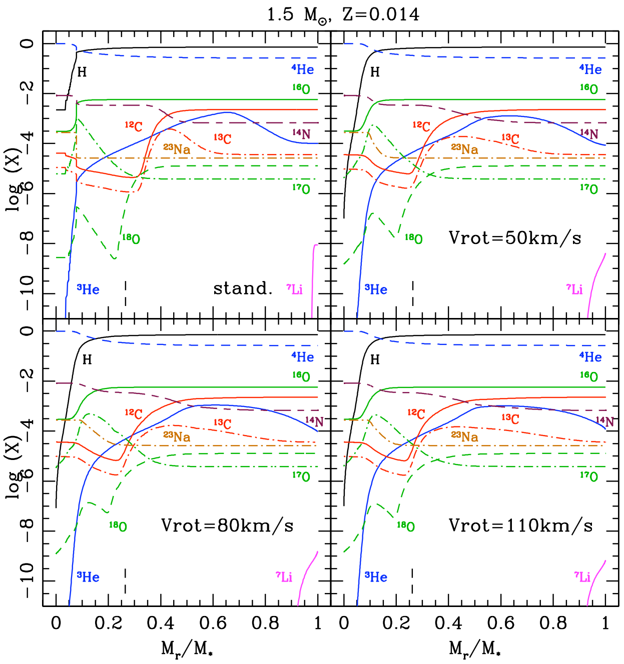

Figure 4.1: Chemical structure at the turnoff of the 1.5 $M_\odot$ star computed for different initial rotation velocities as indicated. The mass fractions are multiplied by 100 for ^{3}He, ^{12}C, and ^{14}N, by 2500 for ^{13}C, by 50, 900, and 5×10^4 for ^{16}O, ^{17}O, and ^{18}O respectively, and by 1500 for ^{23}Na. The vertical arrows show, in all cases, the maximum depth reached by the convective envelope at its maximum extent during the first dredge-up.

behaviors are dicussed in more details in Chapter 5 and in Charbonnel & Lagarde (2010a).

Nevertheless, Palacios et al. (2006, see also Chanamé et al. 2005) who studied the impact of rotation-induced mixing on the RGB for low-mass stars showed that the total transport coefficient of rotation at this phase is too low to imply abundances variation on the first ascent giant branch as requested by observations of RGB stars brighter than the bump (see Fig. 4.2). Another mechanism should be invoked to complement effects of rotation on giant branch.

4.3 Thermohaline instability

When the density of a fluid depends on variation of two components, a stably stratified system can undergo instability leading to significant vertical transport corresponding to thermohaline instability. We therefore studied effects of this mixing on the chemical properties of RGB stars. Thermohaline convection is a mixing process that corresponds to a double diffusive instability. Indeed, this instability evolves with two components, one of which is the stabilizing one (temperature), that diffuses faster than the other, whose stratification is unstable.

4.3.1 Physical mechanism in laboratory

Laboratory experiments were conducted on this double-diffusing fluid stabilized by the faster diffuser (T) and destabilized by the slower diffuser (S), the arrangement that leads to

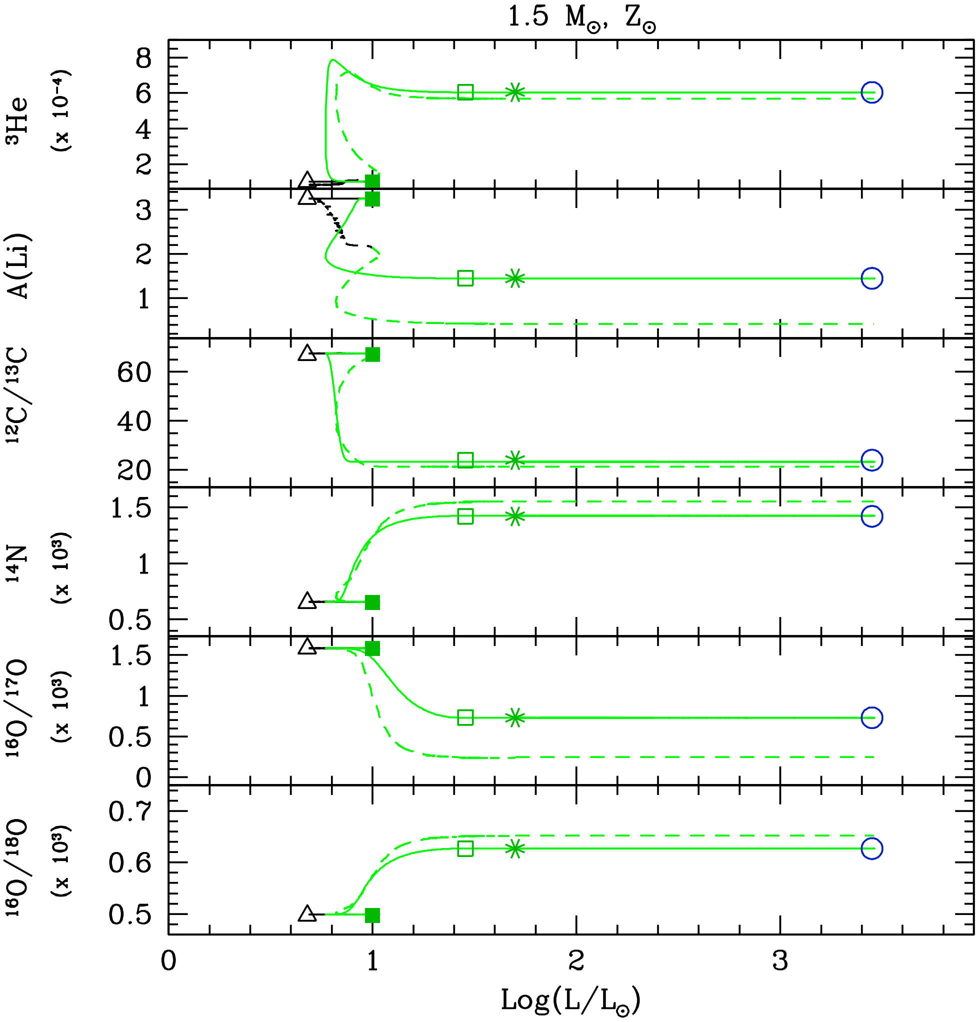

Figure 4.2: Same as Fig.2.15 : evolution of the surface abundances of ^{3}He and ^{14}N (in mass fraction), of A(Li), and of the carbon and oxygen isotopic ratios as a function of stellar luminosity. Predictions are shown for the 1.5 M$_\odot$ models at solar metallicity computed following standard prescriptions (solid line) and including rotation-induced mixing (V$_{ZAMS}$=110km/s, dashed line) from the ZAMS up to the RGB tip. Evolutionary phases are indicated by the same colors as in figure 2.2. Main evolution steps are pointed out with different symbols : ZAMS (open triangle), first dredge-up (start/end ; full/open squares), BUMP luminosity (asterisk).

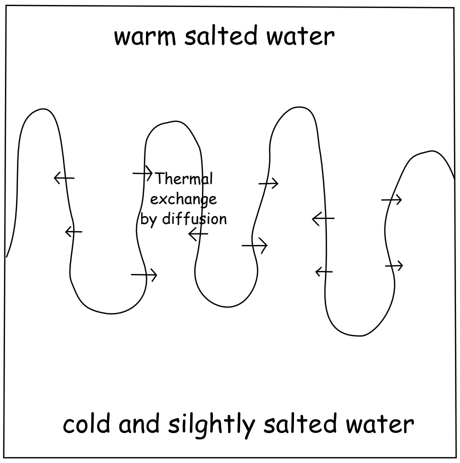

Figure 4.3: Schematic vue of thermohaline mixing

salt fingers. The word "**Thermohaline**" follows from gradient of temperature (**thermo-**) and salinity (**-haline**) which determines the density of salt water. The term of thermohaline convection was first used by Stern (1960). A well-known example is found in upper layers of the Earth's oceans.

In practice, as illustrated by figure 4.3, when a warm salted blob falls down in cold fresh water, the heat diffuses out more quickly than the salt. The blob continue to fall due to its weight until it mixes with surroundings.

We can define the density ratio R_ρ and the inverse Lewis number τ :

$$R_\rho = \frac{\alpha \nabla T}{\beta \nabla S} \quad ; \quad \tau = \frac{K_S}{K_T}$$

with K_T and K_S the thermal and saline diffusivities, $\alpha = -\frac{1}{\rho}(\frac{\partial \rho}{\partial T})_{S,P}$ and $\beta = \frac{1}{\rho}(\frac{\partial \rho}{\partial S})_{T,P}$. ∇T and ∇S the temperature and salinity gradients in the considered region.

For $R_\rho < 1$ the salt diffuses faster than the temperature, the blobs do not fall. There is no instability. So salt fingers grow for $R_\rho \geq 1$. On the other hand, they cannot form if R_ρ is larger than the ratio of thermal and salinity diffusivities, τ^{-1}. Salt fingers then can form and grow if the system follows this condition :

$$1 \leq R_\rho \leq \tau^{-1}$$

4.3.2 Thermohaline instability in astrophysical context

It is important to note that thermohaline instability has long been known to develop in stellar situations whenever inverted molecular-weight gradients are built.

To explain the metallicity excess observed in the central stars of planetary systems compared to other stars of the same spectral types, metal-rich planetisimal accretion onto explanet-host stars has been proposed by Gonzalez (1998). Effects of these planetisimal accretions onto solar-type stars, which happens during the process of planetary formation and migration in the early times of planetary systems, have been investigated by Vauclair

(2004), and Théado & Vauclair (2012). They showed that the dilution of metal-rich material in the surface convective envelope of young main sequence stars created an unstable μ-gradient. Thermohaline instability then develops at the transition of the convective and radiative zone, and drives this heavy elements inside the stars. At the end of the accretion/mixing period, they show that only a very small metallicity increase may remain (smaller than the overabundances observed in explanet-host stars). This discredits an accretion scenario of metal-rich matter to explain these overabundances and favours a significant dispersion in Li abundances .

Thermohaline mixing can be applied to carbon-enhanced metal poor (CEMP) stars. These stars with abundance anomalies are supposed to undergo some accretion of material coming from an AGB companion. Stancliffe et al. (2007) proposed that, in presence of accretion metal-rich matter, this accreted material falls down inside the star caused by thermohaline mixing, and the new matter should be mixed down over about 90% of the stellar mass. This could discredit an accretion episode. However, Thompson et al. (2008) and Stancliffe & Glebbeek (2008) underline that gravitational settling can inhibit thermohaline mixing. The main sequence stars could undergo helium and heavy element diffusion below its convective envelope, leading a stabilizing μ-gradient. Consequently, the accretion process between the star and its AGB companion is still valid.

On the other hand, effects of thermohaline instability should be taken into account in computation of iron accumulation which occurs in outer stellar layers due to atomic diffusion. Indeed, heavy-element accumulation creates an inverse μ-gradient, unstable for thermohaline mixing. Théado et al. (2009) presents effects of this transport process on abundance variation of A-F stars. Although iron accumulation remains, they showed that thermohaline mixing can reduce it.

Finally, thermohaline mixing has recently been identified as the mechanism that governs the photospheric composition of low-mass bright giants (Charbonnel & Zahn 2007b), which is interesting for the study on this thesis. In such stars, this double diffusive instability is induced by the molecular weight inversion created by the ^{3}He(^{3}He,2p)^{4}He reaction in the external wing of the hydrogen-burning shell (Eggleton et al. 2006, 2008). Indeed this peculiar reaction converts two particles into three and thus decreases the mean molecular weight, as already pointed out by Ulrich (1971) although in a different stellar context. The thermohaline instability is expected to set in after the first dredge-up when the star reaches the RGB luminosity bump. In terms of stellar structure, the RGB bump corresponds to the moment when the hydrogen-burning shell encounters the chemical discontinuity created inside the star by the convective envelope at its maximum extent during the first dredge-up. When the source shell (which provides the stellar luminosity on the RGB) reaches the border of the H-rich previously mixed zone, the corresponding decrease in molecular weight of the H-burning layers induces a drop in the total stellar luminosity, thereby creating a bump in the luminosity function since stars spend a relatively long time at this location (i.e., Fusi Pecci et al. 1990; Charbonnel 1994; Charbonnel et al. 1998a). Afterwards H-burning occurs in a region of uniform composition, allowing for the molecular weight inversion due to ^{3}He burning to show up and thus enabling the thermohaline instability to set in.

4.3.3 Thermohaline instability in stellar interior of RGB stars

Thermohaline mixing can also occur in stellar radiative zone in the presence of μ-gradients, when a layer has a mean molecular weight more important than a layer located below. In this study, we will focus on thermohaline mixing which occurs in radiative layers of bright RGB stars and which is induced by the mean molecular inversion created by the ^{3}He(^{3}He,2p)^{4}He reaction at the external layers of the Hydrogen Burning Shell (HBS, see more details in previous section). In the stellar case, the role of salt is playing by $\nabla_\mu = \frac{d\ln\mu}{d\ln P}$ while the difference between the adiabatic and radiative gradients, $\nabla_{ad} - \nabla$, plays the role of temperature gradient. When the destabilizing effect of μ-gradient is more important than the temperature gradient, the stellar region becomes unstable. Thermohaline mixing occurs (with $R_\rho > 1$) in a stable stratification that satisfies the Ledoux criterium for convective stability :

$$\nabla_{\rm ad} - \nabla + \frac{\varphi}{\delta}\nabla_\mu > 0$$

but where the mean molecular weight decreases with the depth :

$$\nabla_\mu = \frac{d\ln\mu}{d\ln \rm P} < 0,$$

we use the classical notations for $\nabla = \frac{\partial \rm lnT}{\partial \rm lnP}$, and

$$\varphi = (\partial\ln\rho/\partial\ln\mu)_{\rm P,T} \quad ,\text{and} \quad \delta = -(\partial\ln\rho/\partial\ln\mu)_{\rm P,\mu} \tag{4.17}$$

Thermohaline mixing occurs with $R_\rho < \tau^{-1}$,

$$\nabla_{\rm ad} - \nabla + \frac{\varphi}{\delta}\frac{\rm K_T}{\rm K_\mu}\nabla_\mu < 0$$

To better understand this instability, we can resolve the equations of motion, thermal energy, chemical composition, and for the mass conservation :

$$\rho_0\left(\frac{\partial\vec{u}}{\partial t} + (\vec{u}\cdot\vec{\nabla})\vec{u}\right) = -\vec{\nabla}p + \eta\nabla^2\vec{u} + \rho_1\vec{g} \tag{4.18}$$

$$\frac{\partial T}{\partial t} + \vec{u}\cdot\vec{\nabla}T = K_T\nabla^2 T \tag{4.19}$$

$$\frac{\partial \mu}{\partial t} + \vec{u}\cdot\vec{\nabla}\mu = K_\mu\nabla^2 \mu \tag{4.20}$$

$$\vec{\nabla}\cdot\vec{u} = \vec{0} \tag{4.21}$$

where $\vec{u}$ is the velocity ($\vec{u} = u\vec{e_x} + v\vec{e_y} + w\vec{e_z}$), ρ the density, p the pressure, g the gravity, η is the kinematical viscosity (ν =molecula viscosity=η/ρ), K$_T$ and K$_\mu$ represent the thermal and haline diffusivities respectively. One denote the unperturbed quantity and the fluctuation in a quantity (possibly modified by the fingers) by 0 and 1 repectively.

Assuming that, the relative deviations of ρ, T, and μ from their reference values in the initial unperturbed state (ρ_0, T$_0$, μ_0) are small, we use a linearized equation of state :

$$\frac{\rho_1}{\rho_0} = -\alpha T_1 + \beta\mu_1 \tag{4.22}$$

where the coefficients of thermal expansion and haline contraction are :

$$\alpha = -\frac{1}{T}\left(\frac{\partial ln\rho}{\partial lnT}\right)_P \quad \text{and} \quad \beta = \frac{1}{\mu}\left(\frac{\partial ln\rho}{\partial ln\mu}_P\right) \tag{4.23}$$

For the ideal gas law, which provides a good approximation to the equation of state in the radiative zone of a low-mass RGB star, we simply have $\alpha = \frac{1}{T}$ and $\beta = \frac{1}{\mu}$.

To simplify the analysis, Ulrich (1972) and Denissenkov (2010) proposed to neglect horizontal velocity components and we can also assume that $\nabla_h^2 = \partial^2/\partial^2 x + \partial^2/\partial_y^2$, because we study vertically elongated structures with a large ratio of the vertical to horizontal length scales.

As first derived by Stern (1960), in the context of Boussinesq approximation, we obtain the following equations for the vertical velocity, temperature and chemical composition, from equations 4.18, 4.19, 4.20, and 4.21:

$$\frac{\partial w}{\partial t} = g(\alpha T_1 - \beta\mu_1) + \nu\nabla_h^2 w \tag{4.24}$$

$$\frac{\partial T_1}{\partial t} + w\frac{\partial T}{\partial z} = K_T\nabla_h^2 T_1 \tag{4.25}$$

$$\frac{\partial \mu_1}{\partial t} + w\frac{\partial \mu}{\partial z} = K_\mu\nabla_h^2 \mu_1 \tag{4.26}$$

From these equations, Ulrich (1972) was the fist to derive an expression for the diffusion coefficient of thermohaline mixing apply to ^{3}He burning in stellar case (see his equation 31, and discussion about ^{3}He below) :

$$\mathscr{D}_{th} = \frac{8\pi^2\alpha^2}{3}\frac{4acT^3}{3\rho\kappa}\frac{1}{\rho C_P(\nabla_{ad} - \nabla)}\left(-\frac{\partial \text{ln}\mu}{\partial \text{lnP}}\right) \tag{4.27}$$

where the thermal diffusivity $K_T = \frac{4acT^3}{3\kappa C_P \rho^2}$, with a the radiation constant, c the speed of light, κ the Rosseland mean opacity, and C_P the specic heat at constant pressure, and α the aspect ratio of salt fingers.

$$\mathscr{D}_{th} = \alpha^2 K_T \mathscr{C}_t \frac{-\nabla_\mu}{(\nabla_{ad} - \nabla)} \tag{4.28}$$

with $\mathscr{C}_\text{t} = \frac{8\pi^2}{3}$.

Kippenhahn et al. (1980) use a different physical approach to derive a similar expression of the diffusion coefficient $\mathscr{D}_{th}$. Indeed, he defines the diffusion coefficient as the product between the vertical velocity v_μ at which the blob sinks and its vertical size l (Kippenhahn et al. 1980). Previously, Kippenhahn (1974), considering an homogeneous medium, defined v_μ :

$$v_\mu = \frac{\varphi}{\delta}\frac{H_P}{(\nabla_{ad} - \nabla)\tau_{KH}^\star}\frac{|D\mu|}{\mu} \tag{4.29}$$

where Dμ is the difference in molecular weight between the blob and the surroundings. φ and δ already defined in Eq. 4.17, H_P the pressure scale height and $\tau_{KH}^\star$ the local characteristic time of thermal adjustment given by Kippenhahn (1974) (his Eq. 7) :

$$\tau_{KH}^\star = \frac{C_P\kappa\rho^2 l^2}{16acT^3} = \frac{l^2}{12K_T} \tag{4.30}$$

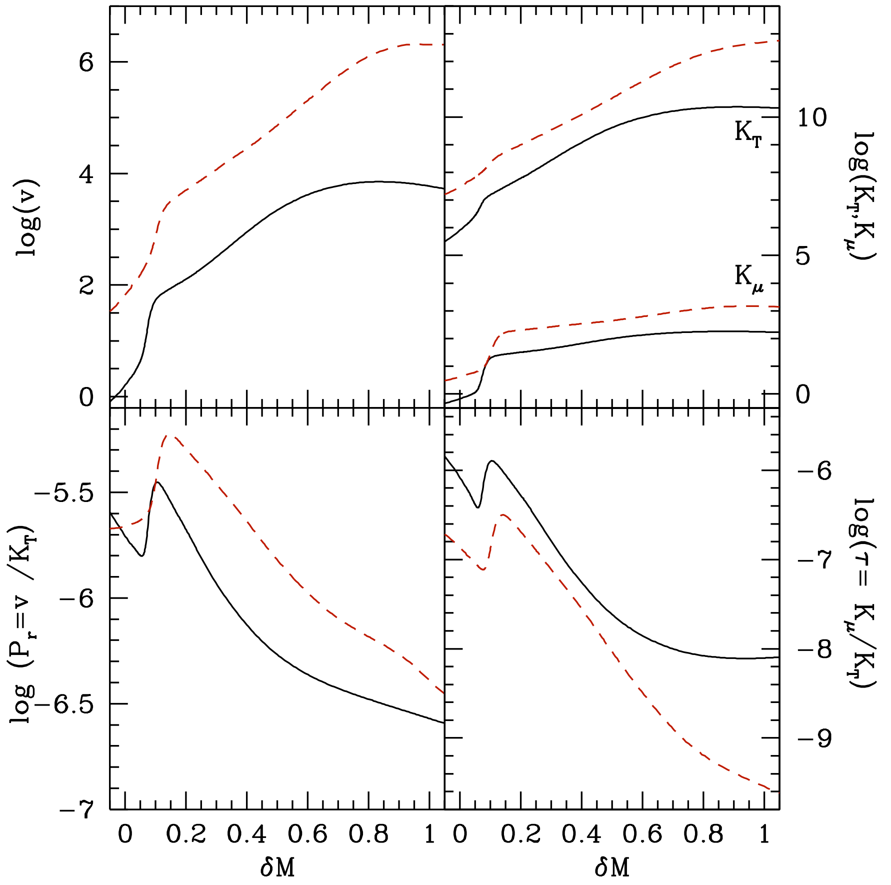

Figure 4.4: The viscosity, thermal and haline diffusivity, the prandtl number, and the inverse Lewis number for our 1.25 $M_\odot$ model at $Z_\odot$ as a function of δM. Predictions are shown just after the bump (at $\log(L/L_\odot)\sim1.8$) (black solid line) and close to the RGB tip (red dashed line).

So,

$$\mathscr{D}_{th} = v_\mu \cdot l = \frac{\varphi}{\delta}\frac{H_P l^2}{(\nabla_{ad}-\nabla)\tau^\star_{KH}}\left|\frac{dln\mu}{dr}\right| \tag{4.31}$$

$|d\ln\mu/dr|$=$|\nabla_\mu| = -\nabla_\mu$, because the mean molecular weight decreases with the depth :

$$\mathscr{D}_{th} = \mathscr{C}_T K_T \frac{\varphi}{\delta}\frac{-\nabla_\mu}{\nabla_{ad}-\nabla} \quad \text{with} \mathscr{C}_T = 12 H_P \tag{4.32}$$

Ulrich (1972), neglecting the influence of salt fingering on the thermal and molecular gradients, had obtained an expression for $\mathscr{D}_{thc}$ with the constant $\mathscr{C}_t$=$\frac{8\pi^2}{3}$, and depending on the aspect ratio of salt fingers (Eq. 4.28). Kippenhahn et al. (1980) gives a new expression of diffusion coefficient and he claims that the perturbed blobs of fluid did not have a chance to become salt fingers (i.e. with an high aspect ratio) due to their strong interactions with the surrounding medium. The value of α in actual stellar conditions was recently questioned by the results of 2D and 3D hydrodynamical simulations of thermohaline convection that favors α close to unity (see §4.3.4, Denissenkov 2010; Denissenkov & Merryfield 2011; Rosenblum et al. 2011; Traxler et al. 2011a).

Table 4.1: Comparison between ocean, hydrodynamic simulations and stellar parameters

Parameter	Ocean case		Hydrodynamic simulations	Stellar case (1.25 $M_\odot$ RGB star $Z_\odot$) at the Bump luminosity	
		value (cgs)	(Traxler et al. 2011a)		value (cgs)
Viscosity	ν	10^{-2}	-	ν	$1\text{-}\ 6.3{\cdot}10^{3}$
Thermal diffusivity	k_T	$1.4{\cdot}10^{-3}$	-	K_T	$3{\cdot}10^{5}\text{-}1.2{\cdot}10^{10}$
Haline diffusivity	k_S	$1.1{\cdot}10^{-5}$	-	K_μ	$0.6\text{-}1.7{\cdot}10^{2}$
Density ratio	R_ρ	1.6	1.025 to 20	$R_\rho = \frac{\nabla-\nabla_{ad}}{\nabla_\mu}$	$10^{5}\text{-}10^{7}$
Prantl number	$P_r = \frac{\nu}{k_T}$	7	1/30 to 1/3	$P_r = \frac{\nu}{K_T}$	$2.7{\cdot}10^{-7}\text{-}2.5{\cdot}10^{-6}$
Inverse Lewis number	$\tau = k_S/k_T$	$8{\cdot}10^{-3}$	1/30 to 1/3	$\tau = K_\mu/K_T$	$8{\cdot}10^{-9}\text{-}1.4{\cdot}10^{-6}$

In figure 4.4 we present the evolution along the RGB of stellar parameters involved in the description of thermohaline instability : thermal and haline diffusivities, the Pranldt number as well as the inverse Lewis number four our 1.25 $M_\odot$ model at $Z_\odot$ in region between the base of the convective envelope ($\delta M = 1$)[2], and the hydrogen burning shell ($\delta M = 0$). For comparison, Table 4.1 gives the correspondence between similar parameters in oceanic case and in stellar case. For oceanic case, we have used data from Kunze (2003), and for RGB case the data are taken from our 1.25 $M_\odot$ model at $Z_\odot$ close to the bump luminosity.

4.3.4 Hydrodynamic simulations of thermohaline mixing

Recently, the thermohaline mixing in both the oceans and the stellar interior has been studied using hydrodynamical simulations. We present it, in this part, and we compare different diffusion coefficients and their effects on surface abundances.

Denissenkov (2010) presents two-dimentional numerical simulations of thermohaline convection to determine if the salt fingering transport of chemical composition driven by ^{3}He burning is efficient enough to produce RGB extra-mixing. He analyses the linear stability of the Boussinesq equations (Equations 4.24, 4.25, and 4.26) with parameters set up to describe the growth of salt fingers driven by ^{3}He burning in the vinicity of the HBS in a low-mass RGB star above the bump luminosity. He derives the following expression for thermohaline diffusion coefficient :

$$\mathscr{D}_{th} = \mathscr{C}_t \frac{\nabla_\mu}{\nabla_{rad} - \nabla_{ad} - \nabla_\mu} \left(1 - \frac{\nu_{mol}}{K} \frac{\nabla_{rad} - \nabla_{ad}}{\nabla_\mu}\right) \alpha^2 K \tag{4.33}$$

where $\mathscr{C}_t$=$2\pi^2$, ν_{mol} and K are the molecular and thermal viscosities, and α is the aspect ratio. With his 2D numerical simulations of thermohaline convection for RGB parameter, he shows that the effective finger ratio (α in Eq. 4.33) does not exceed a value of ∼0.5 (Denissenkov 2010), which also results from 3D numerical simulations by Denissenkov & Merryfield (2011)

On the other hand, an other series of simulations have been made under oceanic conditions (Traxler et al. 2011b), and in physical conditions listed in table 4.1. (Traxler et al.

---

[2] The variable δM is a relative mass coordinate allowing for a blow-up of the radiative region above the HBS.

$$\delta M = \frac{M_r - M_{HBS}}{M_{BCE} - M_{HBS}}$$

is equal to 1 at the base of the convective envelope M_{BCE} (the Schwarzschild criterion allows us to define it) and to 0 at the base of the HBS M_{HBS} (which is chosen as the depth where the hydrogen mass fraction equals 10^{-10}).

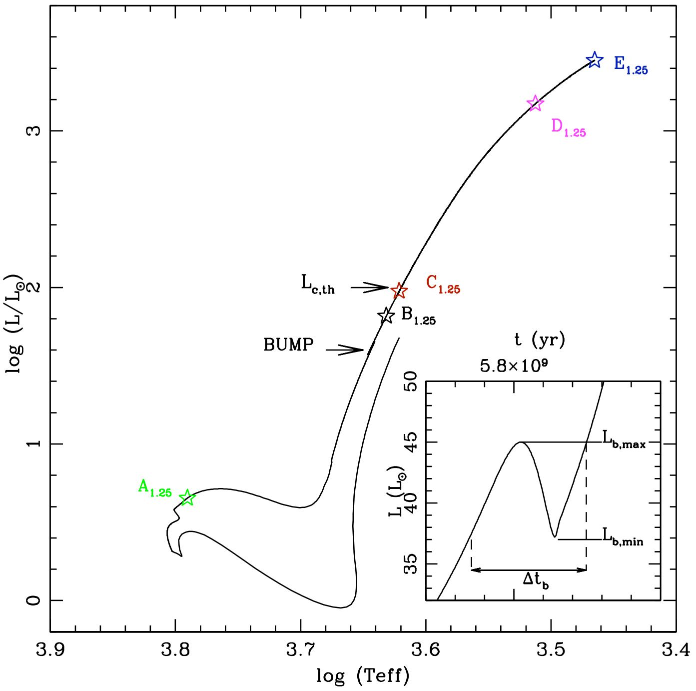

Figure 4.5: Evolutionary track (from the pre-main sequence up to the tip of the RGB) of the 1.25 $M_\odot$ model computed with thermohaline mixing. The minimum and maximum luminosity of the bump are indicated ($L_{b,min}$ and $L_{b,max}$ respectively) as well as the luminosity $L_{c,th}$ at which the thermohaline instability reaches the bottom of the convective envelope. The panel inserted on the right of the figure shows the evolution of the stellar luminosity around the bump as a function of time. Δt_b is the time spent by the star within the luminosity bump and equals to 3.9×10^7 yrs in the present case. *Figure from Charbonnel & Lagarde (2010a).*

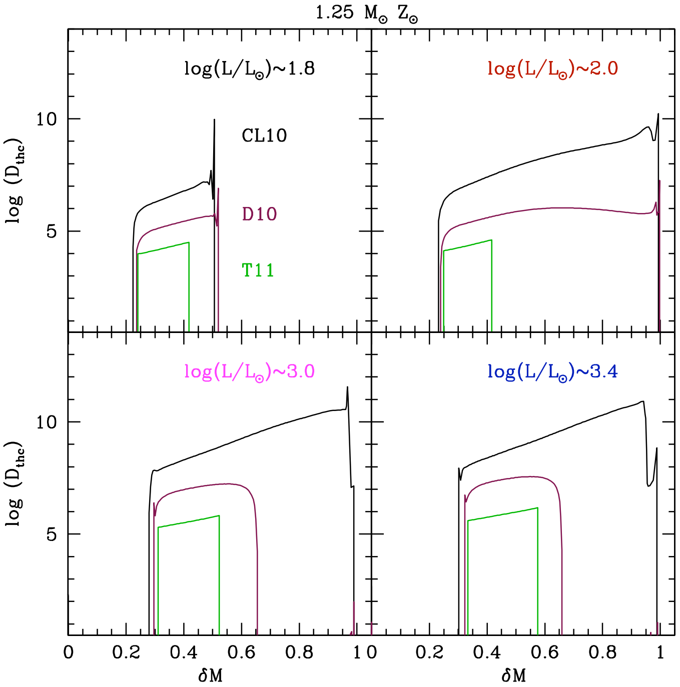

Figure 4.6: Diffusion coefficient of thermohaline convection as a function of δM at various evolution points on the RGB (see Fig 4.5) for different prescriptions : Charbonnel & Lagarde (2010a, CL10), Denissenkov (2010, D10), Traxler et al. (2011a, T11).

2011a). They find a diffusion coefficient for the transport by fingering convection :

$$\mathscr{D}_{th} = 101\sqrt{\kappa_\mu \nu} e^{-3.6r}(1-r)^{1.1} \tag{4.34}$$

where $r = (R_0^\star - 1)/(\tau^{-1} - 1)$ and $R_0^\star = \frac{\nabla - \nabla_{ad}}{\nabla_\mu}$.

However, these simulations are still far from the stellar regime. Indeed, even in the best case they are run at moderatly low values of the Prandtl number (1/3 to 1/30, Traxler et al. 2011a), which is several orders of magnitude away from stellar conditions (see table 4.1 and Fig. 4.6). In the outer radiative wing of the hydrogen-burning shell of a low-mass RGB star, the Prandtl number varies indeed from $\sim 3{\cdot}10^{-6}$ to $3{\cdot}10^{-7}$. The same difficulty arises when the density ratio assumed in the simulations is concerned (up to 7 maximum, compared to $\sim 6{\cdot}10^4$ in the RGB case). This casts some doubt on the accuracy and applicability in the stellar regime of the corresponding empirically determined transport laws.

4.3.5 Effect of different prescriptions on the diffusion coefficient

Figure 4.6 presents the temporal evolution of thermohaline instability diffusion coefficients computed with different prescriptions (Charbonnel & Lagarde 2010a; Denissenkov 2010; Traxler et al. 2011a) as a function of δM for 1.25 M$_\odot$ model at Z$_\odot$ at various evolution points along the RGB as indicated on HR diagram on figure 4.5). With prescription used for our study, thermohaline mixing is much more efficient than the other prescriptions.

Figure 4.7 depicts the temporal evolution along the RGB of the abundance profiles of H, ^{3}He and the diffusion coefficient $\mathscr{D}_{th}$ for models including thermohaline mixing following prescriptions by Denissenkov (2010) (solid lines) and Charbonnel & Lagarde (2010a)

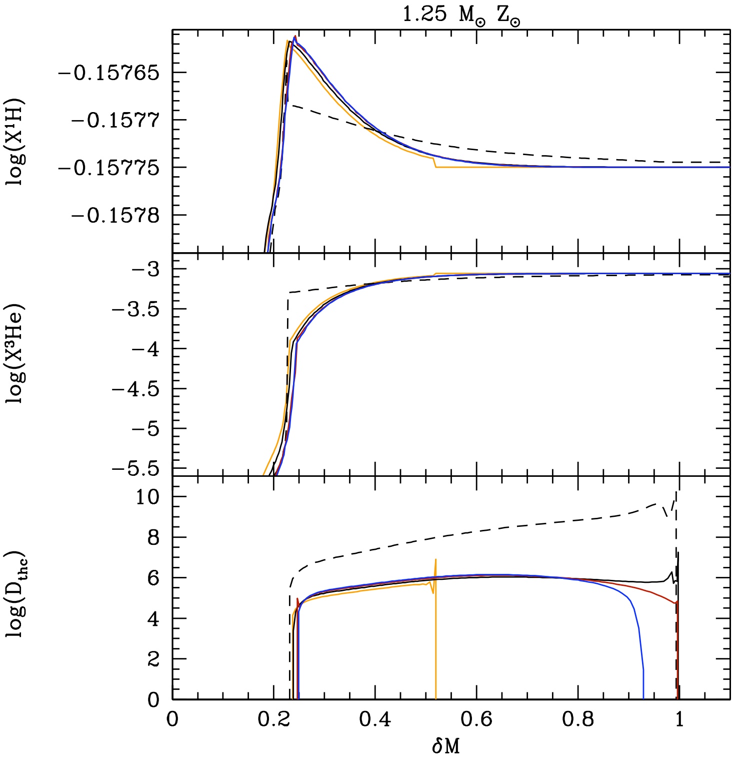

Figure 4.7: *From top to bottom :* Profiles of the abundances (in mass fraction) of H, ^{3}He and of thermohaline diffusion coefficient at various evolution points on the RGB (at L= 65, 94, 113, 123 L$_\odot$). The abscissa is the scaled mass coordinate δ M that allows a blow up of the region of interest (δM=0 at the base of the HBS and δM=1 at the base of the convective envelope). The solid lines correspond to prescription by Denissenkov (2010) (at at L=65, 94, 113, and 123 L$_\odot$ with orange, black, red, and blue line reaspectively) and the black dashed line to prescription by Charbonnel & Lagarde (2010a) at log L/L$_\odot$=2 (or L=94 L$_\odot$).

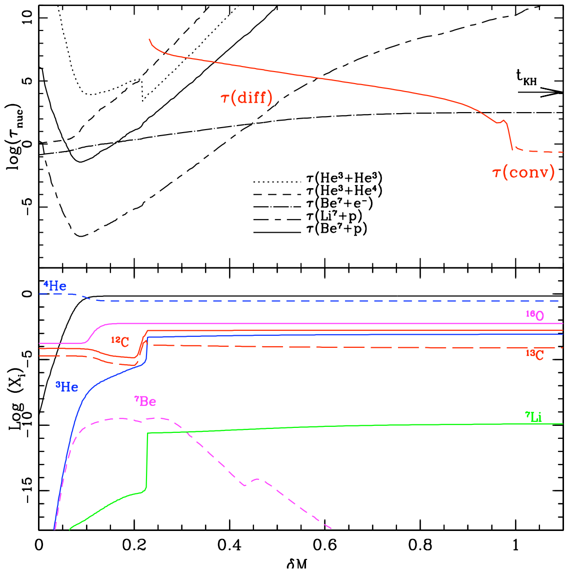

Figure 4.8: 1.25 $M_\odot$ model with thermohaline mixing (no rotation) following prescription presented in Charbonnel & Lagarde (2010a) at L=94 $L_\odot$(top) Lifetimes of ^{3}He, ^{7}Li, and ^{7}Be ; convective and thermohaline diffusive timescale (in years). The transition between the convective envelope and the radiative region occurs at δM=1. (bottom) Abundance profils (in mass fraction) of relevant species in the same region.

(black dashed line). The hydrogen profile shows a peak which maximum is located at the depth where the reaction ^{3}He(^{3}He,2p)^{4}He is faster than ^{3}He(^{4}He, γ)^{7}Be reaction (see figure 4.8 and 4.9 for CL10 and D10 prescriptions). As soon as the thermohaline instability sets in, fresh protons diffuse outwards, spreading out the molecular weight inversion and enlarging thermohaline region until it reaches the convective envelope. Silmultaneously ^{3}He diffuses from the convective envelope inwards where it is burn by pp chain and products new fresh protons. With prescription by D10, the diffusion coefficient is lower and it cannot diffuses as much fresh protons as prescription by CL10. The μ-gradient inversion occurs, and then at log(L/$L_\odot$)∼ 2 thermohaline mixing extends to convective envelope. At that phase, the time-scale of thermohaline mixing is slightly lower than the characteristic time-scale (t_{KH}, see Fig. 4.8 and 4.9). Although with prescriptions by D10, thermohaline connects the HBS with convective envelope, the diffusion coefficient remains too low to bring enough fresh protons to maintain this situation, and the time-scale of diffusion becomes higher than characteristic time.

However, it is important to underline that hydrodynamic simulations predict low value of the aspect ratio and are too far from stellar conditions. In our view, this urgently calls for a numerical exploration of low Péclet values ($P_e \propto 1/K_T$). Before this becomes available, we will keep to the analytical prescription that is able to describe the observational data on the RGB at all metallicities so well, and thus perform our computations with α=5 as in Charbonnel & Zahn (2007b) and as supported by laboratory experiments (Krishnamurti 2003).

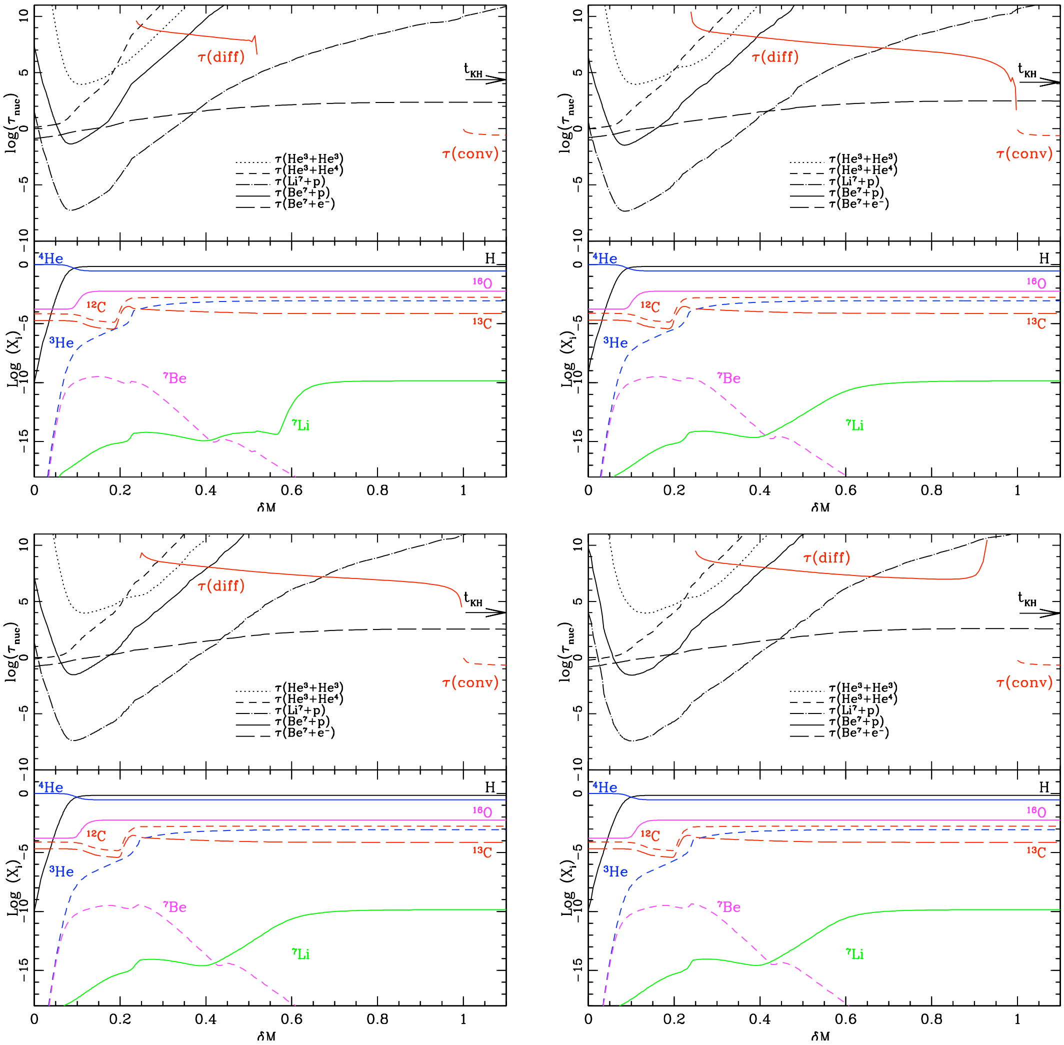

Figure 4.9: 1.25 $M_\odot$ model with thermohaline mixing (no rotation) following prescription of Denissenkov (2010) at L=65 $L_\odot$ (top left panel), at L=94 $L_\odot$ (top right panel), L=113$L_\odot$ (bottom left panel), L=123 $L_\odot$ (bottom right panel). For each panel : (top) Lifetimes of ^{3}He, ^{7}Li, and ^{7}Be ; convective and thermohaline diffusive timescale (in years). The transition between the convective envelope and the radiative region occurs at δM=1. (bottom) Abundance profils (in mass fraction) of relevant species in the same region.

4.3.6 Preliminary hydrodynamic study

Thermohaline mixing in the small-Péclet number approximation.

Lagarde N., Lignières F., and Zahn J.P.
2010 International Summer Institute for Modeling in Astrophysics - Proceeding -

As we presented in previous sections, it is important to derive prescriptions for thermohaline instability closer to stellar conditions, that can be implemented in stellar evolution code. The following proceeding presents work performed during the "2010 International Summer Institute for Modeling in Astrophysics", which discussed the formation of salt fingers on stable state for different perturbations when we use small Péclet number approximation. It represents a preliminary study of thermohaline instability under this approximation, which allowed me to familiarize myself with a hydrodynamic code and the equations of physics. This study will be continued after this thesis.

Thermohaline mixing in the small-Péclet number approximation.

Nadège Lagarde
in collaboration with François Lignières, and Jean-Paul Zahn

ISIMA 2010
- The International Summer Institute for Modeling in Astrophysics -

Abstract : Thermohaline mixing is the mechanism that governs the photospheric compostion of low- and intermediate-mass stars, and explain observations in these stars. It is important to study this instability with the hydrodynamic theory, and to derive prescriptions for the turbulent mixing that can be implemented in stellar codes. In this project, we discuss the formation of salt fingers on stable state, for different perturbations, when we use the small Péclet number approximation. The dominant mode of thermohaline mixing is different from the most unstable mode.

1 Introduction

Thermohaline mixing is well known in Oceans on Earth. In fact, the term thermohaline mixing refers to the part of the large-scale ocean circulation that is driven by global density gradients created by surface heat and cold water fluxes. The adjective thermohaline derives from thermo- referring to temperature and -haline referring to salt content, factors which together determine the density of sea water. In the polar regions (Arctic Ocean and Weddell Sea in particular), sea water turns into ice. Upon solidifying, the salts are rejected because the ice does not integrate them into its structure: liquid water is enriched in salts and the density increases, which begins a dive to the seabed and, eventually, large scale convection. So, this mixing is a double diffusive instability with two components : one stabilizing (temperature) diffuses faster than the other (Salt) whose stratification is unstable.

This instability has been already discussed in the literature : the first discussion by Stern (1960) ; Ulrich (1972) was the first to derive a prescription for this mehcanism ; Schmitt (1979) ; Kippenhahn et al. (1980) extended the Ulrich's prescription for the non-perfect gas, and Denissenkov (2010). In addition, in the laboratory, the instability takes the form of salt fingers (Krishnamurti 2003). Recently, thermohaline mixing has been identified as the mechanism that governs the photospheric composition of low- and intermediate mass stars (Charbonnel & Zahn 2007). In such stars, this double diffusive instability is induced by the inversion of mean molecular weight, created by the reaction $^3He(^3He,2p)^4He$ on the external wing of the hydrgen burning shell. In fact, this mixing can explain observed abundances in the red giant stars (Charbonnel & Lagarde 2010).

In addition, this instability appears in various other astrophysical situations, for instance when ^4He or C-rich material is deposited at the surface of a star in a mass transferring binary (Stothers & Simon 1969; Stancliffe et al. 2007), and when a star accretes heavy elements during planet formation (Vauclair 2004).

So it is very important to study this instability with the hydrodynamic theory, and to derive prescriptions for the turbulent mixing that can be implemented in stellar codes. As compared to oceans, a specificity of stellar fluid is its very high thermal diffusivity. This introduces scale separation effects that are difficult handle in numerical simulations. Here, we shall use the small-Pclet-approximation of the Boussinesq equations (Lignires 1999) that avoids this numerical difficulty but still enables to study the dynamics of an highly thermally diffusive atmosphere and in particular the thermohaline convection.

2 Equations for thermohaline instabilty with in small-Péclet number approximation

2.1 Boussinesq Equations with small-Péclet

We consider the Boussinesq equations for thermohaline instability :

$$\frac{\partial \vec{u}}{\partial t} + \vec{u}.\nabla\vec{u} = -\nabla p - \frac{\rho'}{\rho} g\vec{e}_z + \nu\nabla^2\vec{u} \tag{1}$$

$$\frac{\partial \theta}{\partial t} + \vec{u}.\nabla\theta = K_T\nabla^2\theta \tag{2}$$

$$\frac{\partial \mu}{\partial t} + \vec{u}.\nabla\mu = K_\mu\nabla^2\mu \tag{3}$$

$$\vec{\nabla}.\vec{u} = 0 \tag{4}$$

where, $\vec{u} = u\vec{e}_x + v\vec{e}_y + w\vec{e}_z$ is the velocity vector, p the pressure, θ the temperature, and μ the mean molecular weight. The z axis refers to the vertical direction, while x and y axis are the horizontal directions. K_T and $K\mu$ correspond to the thermal and haline diffusivity respectively. The vertical velocity, temperature and salinity perturbations are of the form $e^{\lambda t} sin(m\pi z) e^{i(kx+ly)}$, where λ is the growth rate. We note the wave number $a^2 = k^2 + l^2 + m^2\pi^2$, and $a_h^2 = k^2 + l^2$ the horizontal wave number. We consider the linear case, $\vec{u}.\nabla\vec{u} = 0$.

In stars, the thermal diffusivity largely exceeds the viscosity and the haline diffusivity. So with the expression of Péclet number given by (Lignières 1999) and his discussion, we can take small Péclet number in stellar radiative zones. In addition, the equation of state is $\frac{\rho'}{\rho} = -\alpha\theta + \sigma\mu$, where $\alpha = \frac{1}{T}$ is the coefficient of thermal expansion in stars, and $\sigma = \frac{1}{\mu}$ the coefficient of haline contraction in stars. In the context of Boussinesq approximation, with the small-Péclet number approximation and using this equation of state, we obtain the following equations for thermohaline mixing.

$$(\lambda - \nu\nabla^2)\nabla^2 w = g(\alpha\nabla_h^2\theta - \sigma\nabla_h^2\mu) \tag{5}$$

$$K_T\nabla^2\theta = -\beta_T w \tag{6}$$

$$(\lambda - K_\mu\nabla^2)\mu = -\beta_\mu w \tag{7}$$

where $\beta_T = -\frac{\partial T}{\partial z}$ and $\beta_\mu = \frac{\partial \mu}{\partial z}$ are thermal and salinity gradients respectively. Substituting equations (6) and (7) in (5) gives the following quadratic equation for λ :

$$\lambda^2 + B\lambda + C = 0 \tag{8}$$

with

$$B = \frac{\hat{a}^2 \nu}{L^2}\left[1 + \frac{K_\mu}{\nu} + \frac{\hat{a}_h^2}{\hat{a}^6} Ra_T\right] \tag{9}$$

and

$$C = \frac{\hat{a}^4 \nu K_\mu}{L^4}\left[1 + \frac{\hat{a}_h^2}{\hat{a}^6}\left(Ra_T - Ra_\mu\right)\right] \tag{10}$$

where the wavenumbers have been non-dimensionalized

$$\hat{a} = aL \qquad \hat{a}_h = a_h L \tag{11}$$

and where we have introduced the thermal and haline Rayleigh numbers

$$Ra_T = -\frac{g\alpha\beta_T L^4}{\nu K_T} \qquad Ra_\mu = \frac{g\sigma\beta_\mu L^4}{\nu K_\mu}. \tag{12}$$

2.2 Study of stability

For $C < 0$ the discriminant $\Delta = B^2 - 4C$ is positive, thus the quadratic equation has two real roots, of which one is positive, leading to exponential growth. This root vanishes for $C = 0$, namely when

$$Ra_\mu - Ra_T = \frac{\hat{a}^6}{\hat{a}_h^2}. \tag{13}$$

The minimum of $(Ra_\mu - Ra_T)$ is obtained for $\hat{a}_h^2 = m^2\pi^2/2$, which yields the instability condition at small Péclet number :

$$Ra_\mu - Ra_T > \frac{27}{4}\pi^4. \tag{14}$$

One retrieves the familiar condition for thermal convection when one ignores Ra_μ and changes the sign of Ra_T (since then $\beta_T < 0$).

3 2D Simulations in the non-linear regime : the dominant mode

In order to explore the non-linear regime, and know the dominant mode of the thermohaline instability, we use the code Balaitous. It is a 3D code that uses a pseudo-spectral Fourier method in the horizontal directions and compact finite differences in the vertical. We compute two dimensions simulations, with 101x128 grid points. The vertical extend of the domain is L and the horizontal one is $2\pi L$. In the horizontal direction the boundary conditions are periodic. At the bottom and top surfaces, the velocity satisfies stress-free impenetrable boundary conditions while the perturbations of mean molecular weight and temperature vanish there.

The initial conditions are inspired from the solution of the linear equations (5)- (7) ; for the velocity components ($\hat{w}$ and $\hat{u}$), and the mean molecular weight ($\hat{\mu}$). We take respectively :

$$\hat{w} = \hat{w_0}\sin(m\pi\hat{z})\cos(\hat{a}_h\hat{x}) \tag{15}$$

$$\hat{u} = -\frac{m}{2\hat{a}_h}\hat{w_0}\cos(m\pi\hat{z})\sin(\hat{a}_h\hat{x}) \tag{16}$$

$$\hat{\mu} = \frac{-K_\mu}{\nu R_{a_T}}\hat{w_0} \tag{17}$$

where $\hat{a_h}$ is an integer.

We take $R_{a_T} = 100$ and $R_{a_\mu} = 1000$. In these conditions, we find the most unstable mode for linear growth rate $a_h = 3.92$. In order to determine the dominant mode of thermohaline instability, we compute simulations with two perturbations which have two different horizontal wave numbers, and the same initial amplitude.

In table 1, we show the different models computed, with different horizontal wave numbers.

3.1 $a_h = 4$ and 2

Figure 1 shows the vertical velocity at $x = \frac{\pi}{4}$ as a function of time, for model computed with initial wavenumbers $a_h = 4$ and $a_h = 2$. The system tends towards a stable solution when $t = 30$. Figure 2 represents the mean molecular weight in grey, when the system is stable. The system tends directly towards a stable solution with the formation of two salt fingers. This fingers take the form of mushroom.

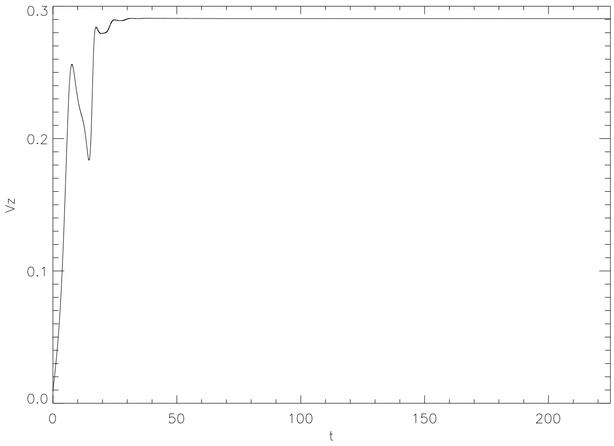

Figure 1: The vertical component of velocity as a function of time, for model with initial wavenumbers $a_h = 4$, $a_h = 2$.

3.2 $a_h = 4$ and 5

Figure 3 shows the vertical velocity at $x = \frac{\pi}{4}$ as a function of time, for model with initial wavenumbers $a_h = 4$ and $a_h = 5$. The system tends towards an intermediate solution when $t = 20$, and after a stable solution when $t > 200$.

Figure 4 represents the mean molecular weight in grey, when the system is in intermediate state (left panel) with four saltfingers, and stable state (right panel) with only two saltfingers.

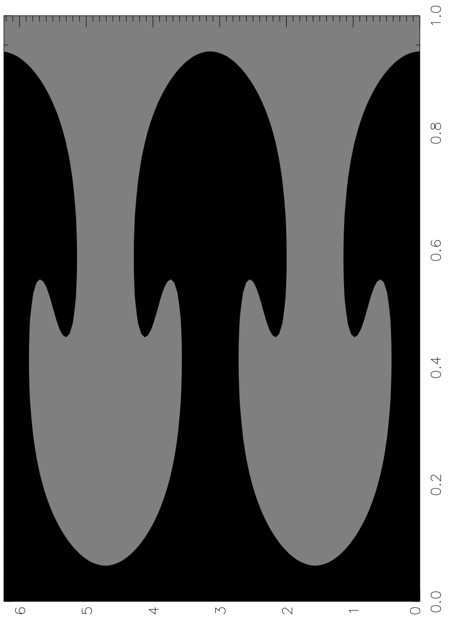

Figure 2: Salinity (in grey) at t=225, for model with initial wavenumbers $a_h = 4$, $a_h = 2$.

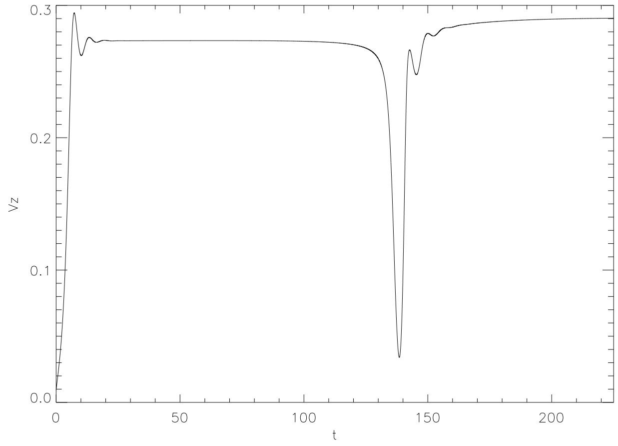

Figure 3: The vertical component of velocity as a function of time, for model with initial wavenumbers $a_h = 4$, $a_h = 5$.

3.3 $a_h = 5$ and 9

Figure 5 shows the vertical velocity at $x = \frac{\pi}{4}$ as a function of time. The system, as for previous model, tends towards an intermediate solution (t=20), and then into a stable solution (t ¿150). Figure 6 represents the mean molecular weight in grey, when the system is in intermediate state, and stable state respectively. The system forms five salt fingers on the intermediate state, and then three on stable solution.

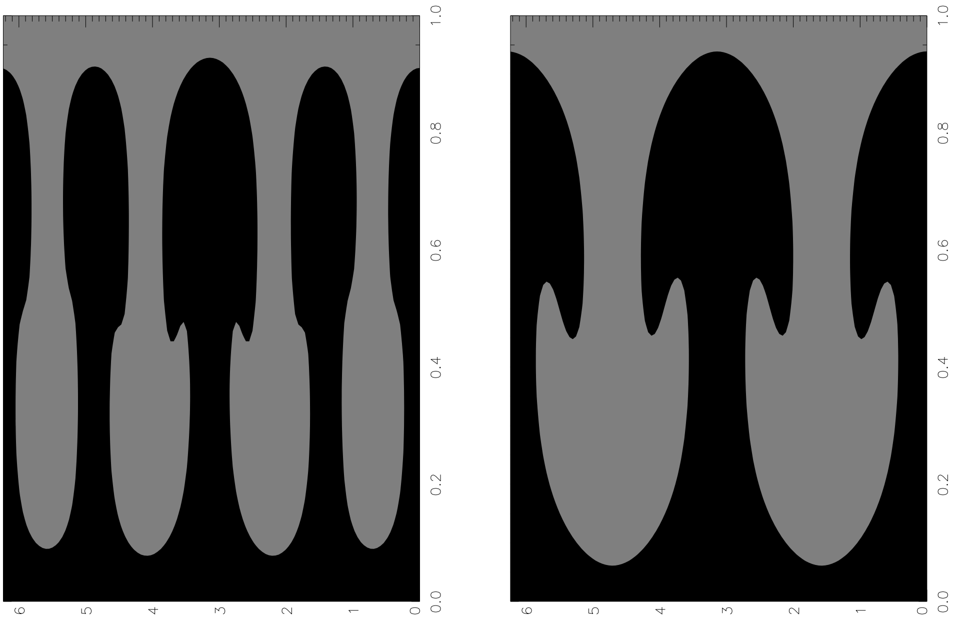

Figure 4: Salinity (in grey) at t=90s (left) and at t=225 (right), for model with initial wavenumbers $a_h = 4$, $a_h = 5$.

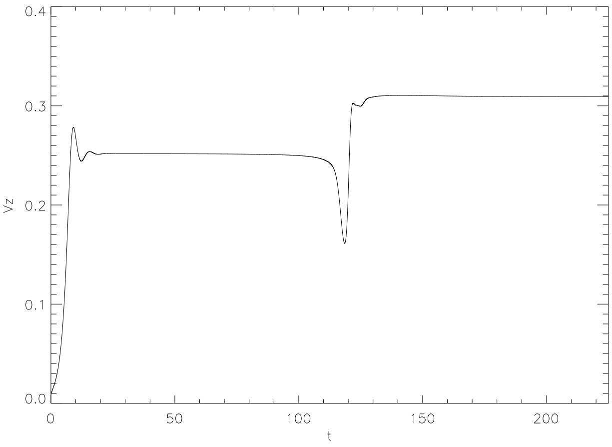

Figure 5: The vertical component of velocity as a function of time, for model with $a_h = 5$ $a_h = 9$.

4 Conclusions and future work

We applied the small-Péclet number approximation to the equations of thermohaline mixing. In these conditions, we have obtained a condition of thermohaline instablity, linked directly with the thermal and haline Rayleigh numbers. Then we have computed nine models with two perturbations which have two different horizontal wave numbers, in order to determine the dominant mode. We have shown that the dominant mode is different from the most unstable mode.

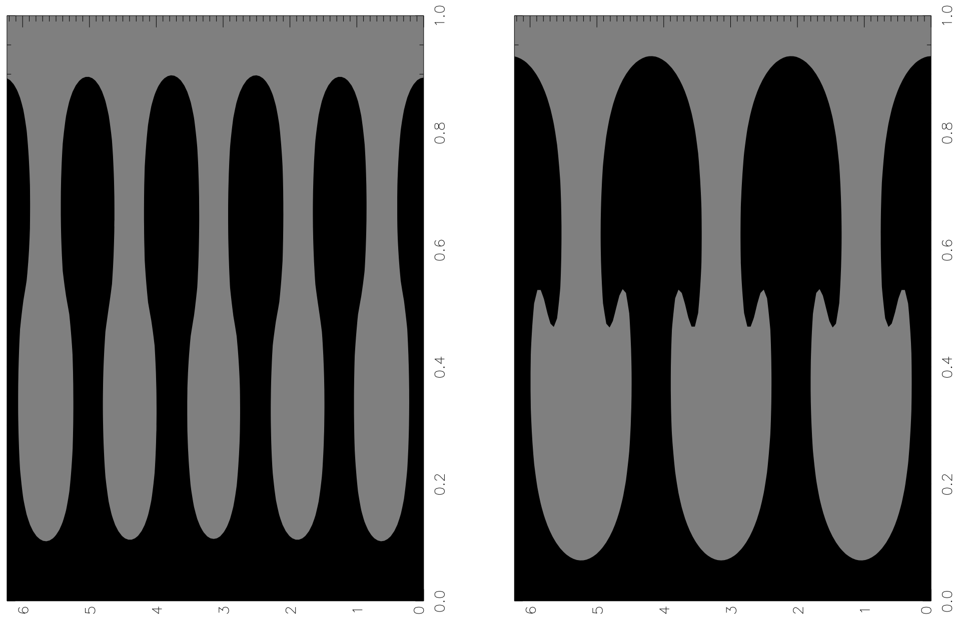

Figure 6: Salinity (in grey) at t=90s (left) and at t=225 (right), for model with $a_h = 4$ $a_h = 5$.

For all our models, the system tends towards a stable solution with two or three salt fingers. In addition, the table 1 shows two different evolutions. First, when the horizontal wave number is lower than the most unstable mode, the system tends directly to the stable mode. Second, when the horizontal wave number is higher than the most unstable mode, the system evolves to an intermediate state, and then to the final stable state.

The dominant mode of thermohaline mixing, in these conditions, is different from the most unstable mode.

In addition, we can study the aspect ratio of salt fingers. It is defined as the ratio between the length and width of fingers. In our conditions of computation, we obtain an aspect ratio equal to the normalized horizontal wavenumber. And we have seen that a_h is always superior to 1. In fact, the efficiency of mixing depends sensitively on this aspect ratio. The diffusive coefficient is given with the equation 18, where α is the aspect ratio of salt fingers, according to Ulrich (1972) :

$$D_t = \frac{8}{3}\pi^2\alpha^2 K(\frac{\phi}{\delta})\frac{-\nabla_\mu}{(\nabla_{ad} - \nabla)} \tag{18}$$

In future work, we must computed other simulations with different parameters in order to understand the effects on aspect ratio of salt fingers, and thus on the efficiency of thermohaline mixing, with two and three dimensions simulations

References

Charbonnel, C. & Lagarde, N. 2010, ArXiv e-prints

Models	a_h		intermediate state	stable state
M1	2	4	-	2
M2	2	6	-	2
M3	3	5	-	3
M4	3	6	-	3
M5	4	5	4	2
M6	5	8	5	3
M7	5	9	5	3
M8	6	10	6	2
M9	7	9	7	3

Table 1: Models computed with two different initial horizontal wave numbers (given in second column). The third and fourth columns give the number of saltfingers in the computational domain

Charbonnel, C. & Zahn, J.-P. 2007, A&A, 467, L15

Denissenkov, P. A. 2010, ArXiv e-prints

Kippenhahn, R., Ruschenplatt, G., & Thomas, H.-C. 1980, A&A, 91, 175

Krishnamurti, R. 2003, Journal of Fluid Mechanics, 483, 287

Lignières, F. 1999, A&A, 348, 933

Schmitt, R. 1979, Deep Sea Research Part I: Oceanographic Research, 26, 23

Stancliffe, R. J., Glebbeek, E., Izzard, R. G., & Pols, O. R. 2007, A&A, 464, L57

Stern, M. E. 1960, Tellus, 12, 172

Stothers, R. & Simon, N. R. 1969, ApJ, 157, 673

Ulrich, R. K. 1972, ApJ, 172, 165

Vauclair, S. 2004, in IAU Symposium, Vol. 224, The A-Star Puzzle, ed. J. Zverko, J. Ziznovsky, S. J. Adelman, & W. W. Weiss, 161–166

Chapter 5

Effects of thermohaline mixing and rotation-induced mixing.

As discussed in Chapters 2 and 3, low- and intermediate-mass stars exhibit at all stages of their evolution the signatures of complex physical process that requiere challenging modelling beyond canonical (or standard) stellar theory. Through several articles that we have included in this chapter, we studied the effects of rotation-induced mixing and thermohaline instability as described in chapter 4, on internal structure, stellar evolution, nucleosynthesis, as well as on the asteroseismic and chemical properties of low- and intermediate-mass stars at different metallicities (Smiljanic et al. 2010; Charbonnel & Lagarde 2010a; Lagarde et al. 2012a, 2010). In these papers, we also compared our models with observations of various kinds.

5.1 STAREVOL code and input physics of stellar models

During this thesis, I computed a grid of models in the initial mass range between 0.85 $M_\odot$ and 6.0 $M_\odot$ with four metallicities Z = 0.0001, 0.002, 0.004 and 0.014 ([Fe/H]= -2.16, -0.86, -0.56, and 0 respectively). For each mass and metallicity, models are computed with standard prescriptions (no mixing other than convection process), and both with thermohaline instability and rotational transport. For all masses the evolution is followed from the beginning of the pre-main sequence (along the Hayashi track) up to the early-AGB phase.

5.1.1 Basic inputs with STAREVOL

The models presented in this chapter, as well as the standard models presented in Chapter 2, were computed with the code STAREVOL, originally developed by Manuel Forestini. The models are computed with the lagrangian implicit stellar evolution code STAREVOL (v3.00. See Siess et al. 2000; Palacios et al. 2003, 2006; Decressin et al. 2009). In the lagrangain description, the equations of stellar internal structure are written with two independent variables, a temporal one t, and a spatial one m_r which represents the mass of a fluid element. With this description we can write equations to decribe the stellar structure as follow :

- Mass conservation

$$\frac{dr}{dm_r} = \frac{1}{4\pi r^2 \rho} \tag{5.1}$$

- Energy conservation

$$\frac{\partial L_r}{\partial m_r} = \epsilon_{nuc} - \epsilon_{\nu} + \epsilon_{grav} \tag{5.2}$$

  where ϵ_{nuc}, ϵ_{ν}, and ϵ_{grav} are the energies produced by the nuclear reactions, lost by neutrinos, and due to gravitational heating, respectively.

- Conservation of motion

$$\frac{\partial u}{\partial t} = -\left(4\pi r^2 \frac{\partial P}{\partial m_r} + \frac{G m_r}{r^2}\right) \tag{5.3}$$

  where P is the pressure given by the equation of state, and $u = \frac{\partial r}{\partial t}$.

- Heat transport

$$\frac{dT}{dm_r} = \frac{1}{\pi r^2}\left(g + \frac{du}{dt}\right)\frac{T}{P}\nabla \tag{5.4}$$

  where

$$\nabla = \frac{\partial lnT}{\partial lnP} = \begin{cases} \nabla_{rad} = \frac{3}{16\pi acG}\frac{\kappa L_r P}{m_r T^4} & \text{in radiative zones} \\ \nabla_{conv} & \text{in convective zones} \end{cases} \tag{5.5}$$

- Chemical species transport

$$\left(\frac{dY_i}{dt}\right) = \left(\frac{\partial Y_i}{\partial t}\right)_{nuc} + \frac{\partial}{\partial m_r}\left[(4\pi r^2 \rho)^2 \mathscr{D} \frac{\partial Y_i}{\partial m_r}\right] \tag{5.6}$$

where T is the temperature, ρ the density, L_r the luminosity, r the radius of the fluid, Y_i represents abundances of species i, and $\mathscr{D}$ the diffusion coefficient.

To solve this system, the following physical ingredients are required :

- Nuclear reaction rates are needed to follow the chemical changes inside burning sites, and to determine the production of energy by the nuclear reaction, ϵ_{nuc}, and the energy loss by neutrino, ϵ_{ν}. We follow stellar nucleosynthesis with a network including 185 nuclear reactions involving 54 stable and unstable species from ^{1}H to ^{37}Cl. Numerical tables for the nuclear reaction rates were generated from NACRE compilation (Arnould et al. 1999; Aikawa et al. 2005) with the NetGen web interface[1]. We mainly use reactions rates from NACRE or from Caughlan & Fowler (1988) when NACRE rates are not available. For proton captures on elements higher than Ne we follow rates from Iliadis et al. (2001) otherwise from Bao et al. (2000). The following reactions rates are computed by:

---

[1] `http://www.astro.ulb.ac.be/Netgen/form.html`

  - ^{3}He(D,p)^{4}He (Descouvemont et al. 2004)
  - ^{3}He($\alpha\alpha,\gamma$)^{12}C (Fynbo et al. 2005)
  - ^{8}B(β,ν)2^{4}He ; ^{13}N(β,ν)^{13}C ; ^{22}Na(β,ν)^{22}Ne ; ^{26}Alm(β,ν)^{26}Mg ; ^{26}Alg(β,ν)^{26}Mg (Horiguchi et al. 1996)
  - ^{14}C(p,γ)^{15}N (Wiescher et al. 1990)
  - ^{14}C(p,n)^{14}N (Koehler & O'brien 1989a)
  - ^{14}C(α,n)^{17}O ; ^{17}O(n,^{4}He)^{14}C (Schatz et al. 1993)
  - ^{14}C(α,γ)^{18}O (Funck & Langanke 1989)
  - ^{14}N(n,p)^{14}C (Koehler & O'brien 1989b)
  - ^{14}N(p,γ)^{15}O (Mukhamedzhanov et al. 2003)
  - ^{17}O(n,γ)^{18}O (Wagoner 1969)
  - ^{22}Ne(p,γ)^{23}Na (Hale et al. 2002)
  - ^{22}Ne(n,γ)^{23}Na (Beer et al. 2002)
  - ^{22}Na(n,γ)^{23}Na ; ^{23}Na(α,p)^{26}Mg ; ^{25}Mg(α,p)^{28}Si ; ^{26}Mg(α,p)^{29}Si ; ^{27}Al(α,p)^{30}Si (Hauser & Feshbach 1952)
  - ^{26}Alm(n,γ)^{27}Al ; ^{26}Alg(n,γ)^{27}Al (Woosley et al. 1978)[2]

- The screening factors are calculated with the formalism of Mitler (1977) for weak and intermediate screening conditions and of Graboske et al. (1973) for strong screening conditions.

- Opacities are required to compute the radiative gradient ∇_{rad} and the energy transport by radiative transfer. We generate opacity tables according to Iglesias & Rogers (1996) using the OPAL website[3] for $T > 8000K$ that accounts for C and O enrichments. At lower temperature ($T < 8000K$), we use the atomic and molecular opacities given by Ferguson et al. (2005).

- The equation of state relates the temperature, pressure, and density and thus provides different thermodynamic quantities ($\nabla_{\rm ad}$, $c_{\rm P}$,...). In STAREVOL we follow the formalism developed by Eggleton et al. (1973) and extended by Pols et al. (1995) that is based on the principle of Helmholtz free energy minimization (see Dufour 1999, and Siess et al. 2000 for detailed description and numerical implementation). It accounts for the non-ideal effects due to Coulomb interactions and pressure ionization.

- The treatment of convection is needed to compute the temperature gradient inside a convective zone. It is based on classical mixing length formalism with $\alpha_{MLT} = 1.6$, from solar-calibrated models without atomic diffusion nor rotation computed by Geneva models (see Ekström et al. 2012). We assume instantaneous convective mixing, except when hot-bottom burning occurs on the TP-AGB, which requires a time-dependent convective diffusion algorithm as developed in Forestini & Charbonnel (1997). The boundary between convective and radiative layers is defined with

---

[2] ^{26}Alm and ^{26}Alg represent the radioactive nuclide ^{26}Al in its two isomeric states.

[3] `http://adg.llnl.gov/Research/OPAL/opal.html`

the Schwarzschild criterion. An overshoot parameter $d_{\rm over}/H_{\rm p}$ is taken into account for the convective core. This parameter is set to 0.05 or to 0.10 respectively for stars with masses below or above 2.0 $M_\odot$ [4]. No overshoot is applied for stars with masses below 1.0 $M_\odot$

- We use a grey atmosphere where the photosphere is defined as the layer for which the optical depth τ is between 0.005 and 10. We define the effective temperature and radius at the layer where $\tau = 2/3$.

- For mass loss we use Reimers (1975) formula (with $\eta_R = 0.5$) from the ZAMS up to central helium exhaustion

$$\dot{M} = -3.98 \cdot 10^{-13} \eta_R \frac{LR}{M} {\rm M_\odot.yr^{-1}}. \tag{5.7}$$

On AGB we shift to the mass loss prescription by Vassiliadis & Wood (1993).

5.1.2 Transport processes in radiative zones

Thermohaline mixing

For the turbulent diffusivity related to the thermohaline instablity induced by ^{3}He burning, we use the prescription advocated in Chapter 4 (§4.3) based on Ulrich (1972) arguments with a value of 6 for the aspect ratio (length/width) of the salt fingers as supported by laboratory experiments (Krishnamurti 2003) and including Kippenhahn et al. (1980) correction for the case of a non-perfect gas. We note that this value is higher than obtained by current 2D and 3D numerical simulations (Denissenkov 2010; Denissenkov & Merryfield 2011; Rosenblum et al. 2011; Traxler et al. 2011a). Before a final word on this discrepancy comes from future numerical simulations in realistic stellar conditions, we adopt an aspect ratio (i.e., maximum length relative to their diameter) of 5, which nicely accounts for the observed chemical properties of red giant stars (see chap. 4).

Rotation-induced mixing

For the treatment of rotation-induced mixing we use the complete formalism developed by Zahn (1992) and Maeder & Zahn (1998) presented in Chap 4 (§4.1). Rotation is not included during the pre-main sequence, and solid-body rotation is assumed when the star arrives on the Zero Age Main Sequence (ZAMS). The initial rotation velocity of our models on the ZAMS is chosen at 45% of the critical velocity at that point, with $V_{\rm crit} = \left(\frac{2}{3}\right)^{\frac{3}{2}} \left(\frac{GM}{R}\right)^{\frac{1}{2}}$. Here we take R the stellar radius computed without considering the stellar deformation due to rotation ; if we were to take into account the deformation of the stellar radius as in Ekström et al. (2012), then our initial velocities would correspond to 30% of critical velocity. This choice of $V_{\rm ini}/V_{\rm crit} = 0.45$ fits well the mean value in the observed velocity distribution of low- and intermediate-mass stars in young open clusters.

From the ZAMS, the evolution of the internal angular momentum profile is accounted for with the complete formalism developed by Zahn (1992) and Maeder & Zahn (1998) that takes into account advection by meridional circulation and diffusion by shear turbulence.

---

[4] For small-sized core its mass extent is not allowed to be larger than $d_{\rm over}$ times the core mass.

5.2 Beryllium abundances in the open cluster IC 4651.

Beryllium abundances along the evolutionary sequence of the open cluster IC 4651 - A new test for hydrodynamical stellar models

R. Smiljanic, L. Pasquini, C. Charbonnel and N.Lagarde

A&A 510 A50 (2010)

In this article, we present beryllium abundances in stars along the whole evolutionary sequence of the open cluster IC 4651. This study complements previous analyzes of lithium in main sequence stars and especially the observations of Li in the same open cluster (Pasquini et al. 2004a). This is the first time Be abundances have been determined for stars along the whole evolutionary sequence of an open cluster including solar-type, Li-dip, turn-off, subgiant, and lower red giant stars. Our contribution to this paper consists on a detailed comparison of the observed behavior of Be and Li to theoretical predictions from our stellar models including rotation-induced mixing, internal gravity waves, and thermohaline mixing. Only rotation (not thermohaline mixing) can be tested because observed stars in this sample have an earlier evolutionnary phase than the bump luminosity.

Results

As discussed by Palacios et al. (2003), who have tested rotation-induced mixing with only Li abundances, this mixing acting on the main sequence enlarges the Li- and Be-free regions inside the stars, implying earlier (i.e., at higher Teff inside the Hertzsprung gap) Li and Be depletion at the surface of subgiant stars, as well as lower Li and Be values after dredge-up in giant stars. Otherwise, the Be abundances also present a significant dispersion. The dispersion of Li and Be abundances on the blue side of the dip and in evolved stars is very well explained by our models when accounting for a dispersion in the initial values of the stellar rotational velocities.

A&A 510, A50 (2010)
DOI: 10.1051/0004-6361/200912957

Astronomy & Astrophysics

Beryllium abundances along the evolutionary sequence of the open cluster IC 4651 – A new test for hydrodynamical stellar models[*]

R. Smiljanic[1,**], L. Pasquini[2], C. Charbonnel[3,4], and N. Lagarde[3]

[1] Universidade de São Paulo, IAG, Dep. de Astronomia, Rua do Matão 1226, São Paulo-SP 05508-090, Brazil
e-mail: `rsmiljan@eso.org`
[2] European Southern Observatory, Karl-Schwarzschild-Str. 2, 85748 Garching bei München, Germany
e-mail: `lpasquin@eso.org`
[3] Geneva Observatory, University of Geneva, chemin des Maillettes 51, 1290 Versoix, Switzerland
e-mail: `[Corinne.Charbonnel;Nadege.Lagarde]@unige.ch`
[4] LATT, CNRS UMR 5572, Université de Toulouse, 14 avenue Edouard Belin, 31400 Toulouse Cedex 04, France

Received 22 July 2009 / Accepted 5 November 2009

ABSTRACT

Context. Previous analyses of lithium abundances in main sequence and red giant stars have revealed the action of mixing mechanisms other than convection in stellar interiors. Beryllium abundances in stars with Li abundance determinations can offer valuable complementary information on the nature of these mechanisms.
Aims. Our aim is to derive Be abundances along the whole evolutionary sequence of an open cluster. We focus on the well-studied open cluster IC 4651. These Be abundances are used with previously determined Li abundances, in the same sample stars, to investigate the mixing mechanisms in a range of stellar masses and evolutionary stages.
Methods. Atmospheric parameters were adopted from a previous abundance analysis by the same authors. New Be abundances have been determined from high-resolution, high signal-to-noise UVES spectra using spectrum synthesis and model atmospheres. The careful synthetic modeling of the Be lines region is used to calculate reliable abundances in rapidly rotating stars. The observed behavior of Be and Li is compared to theoretical predictions from stellar models including rotation-induced mixing, internal gravity waves, atomic diffusion, and thermohaline mixing.
Results. Beryllium is detected in all the main sequence and turn-off sample stars, both slow- and fast-rotating stars, including the Li-dip stars, but is not detected in the red giants. Confirming previous results, we find that the Li dip is also a Be dip, although the depletion of Be is more modest than for Li in the corresponding effective temperature range. For post-main-sequence stars, the Be dilution starts earlier within the Hertzsprung gap than expected from classical predictions, as does the Li dilution. A clear dispersion in the Be abundances is also observed. Theoretical stellar models including the hydrodynamical transport processes mentioned above are able to reproduce all the observed features well. These results show a good theoretical understanding of the Li and Be behavior along the color-magnitude diagram of this intermediate-age cluster for stars more massive than 1.2 $M_{\odot}$.

Key words. stars: abundances – stars: evolution – rotation – open clusters and associations: individual: IC 4651

1. Introduction

The classical theory of stellar evolution, which only allows for mixing in stellar convective layers, fails to explain nearly all Li abundance patterns observed so far at the surface of low-mass stars. Indeed, in contradiction to the classical predictions, the vast majority of F- and early G-type stars (including the Sun) deplete, often quite severely, their surface Li abundance during their main-sequence lifetime, revealing transport processes beyond convection. A-type stars are also concerned, although in these objects the signatures of non-standard Li depletion, occurring in their interior during the main sequence, appear at their surface only when they cross the Hertzsprung gap and become subgiants.

Lithium depletion is seen both in field (e.g., Herbig 1965; Duncan 1981; Pasquini et al. 1994; Lèbre et al. 1999; Chen et al. 2001; Lambert & Reddy 2004, and references therein) and in open cluster stars (e.g. Wallerstein et al. 1965; Zappala 1972; Cayrel et al. 1984; Soderblom et al. 1990; Balachandran 1995; Jones et al. 1997; Pasquini et al. 2001; Sestito & Randich 2005, and references therein). As cluster stars have well-defined masses and, most important, share the same age and initial chemical composition, they are ideal targets for investigating mixing processes as a function of stellar mass and evolutionary status. They have therefore received considerable attention in the literature. Observations of the Li evolution along the color magnitude diagram (CMD) of open clusters have revealed a number of interesting features, such as the Li-dip (Wallerstein et al. 1965; Boesgaard & Tripicco 1986), the lack of abundance trends with

---

[*] Based on observations made with the ESO VLT, at Paranal Observatory, under programs 065.L-0427 and 067.D-0126.
[**] Current address: European Southern Observatory, Karl-Schwarzschild-Str. 2, 85748 Garching bei München, Germany.

age among A-type stars (Burkhart & Coupry 1998, 2000), the presence of a spread of Li among solar-type stars in relatively old clusters like M67 (Pasquini et al. 1997; Jones et al. 1999), and the Li variations with mass and evolutionary status as in the case of IC 4651 (Pasquini et al. 2004).

Many different physical mechanisms have been proposed to explain these observations: atomic diffusion (Michaud 1986; Michaud et al. 2004), mass loss (Hobbs et al. 1989; Swenson & Faulkner 1992), rotation-induced mixing (Charbonnel et al. 1992; Deliyannis & Pinsonneault 1997; Talon & Charbonnel 1998; Palacios et al. 2003; Théado & Vauclair 2003), mixing by internal gravity waves (Garcia Lopez & Spruit 1991; Montalbán & Schatzman 2000; Young et al. 2003), or a combination of some of these processes. So far, only the hydrodynamic stellar models that combine the effects of meridional circulation, shear turbulence, internal gravity waves, and atomic diffusion have been able to account for Li observations over a broad range of stellar masses, ages, and evolutionary status (Talon & Charbonnel 2003, 2005; Charbonnel & Talon 2005, 2008). These models, which use a prescription for the wave excitation that reproduces the solar-p modes (Goldreich et al. 1994), explain other observational constraints concomitantly, like the behavior of C, N, O, and Be across the Li dip in young clusters, such as the Hyades, or the internal rotation profile of the Sun (Charbonnel & Talon 2005).

Additional clues can help ascertain the nature and description of transport mechanisms of chemicals and angular momentum inside low-mass stars. In particular the simultaneous determination of Li and Be abundances in the same stars strengthens the constraints by performing a stellar tomography. Such a powerful diagnosis is possible because Li and Be burn at different temperatures (~2.5×10^6 K for Li and ~3.5×10^6 K for Be), which correspond to different depths in the stellar interior (see e.g. Deliyannis et al. 2000).

Although the simultaneous study of Li and Be in the same stars is a powerful tool, Be has been determined in far fewer stars than Li has. In particular, despite the advantages of cluster stars mentioned above, Be has been investigated in only a few open clusters (e.g. Boesgaard et al. 1977, 2004a; Garcia Lopez et al. 1995; Randich et al. 2002, 2007, and references therein), while field stars have been more extensively studied (e.g. Boesgaard 1976; Stephens et al. 1997; Santos et al. 2004; Boesgaard & Krugler Hollek 2009, and references therein).

Boesgaard and collaborators discovered a Be dip and a correlation between Li and Be depletion in mid F-stars in the field (Deliyannis et al. 1998) and also in the Hyades, Coma, and Praesepe clusters (Boesgaard & King 2002; Boesgaard et al. 2004a). They also show that for cooler G stars there is little or no Be depletion, even in Li-depleted objects up to ~5500 K (Boesgaard et al. 2004b, and references therein). For even cooler stars, below ~5500 K, Santos et al. (2004) show a Be decline correlated with decreasing temperature. These findings were confirmed by Randich et al. (2002, 2007), who investigated Li and Be in late F- and early G-type stars in some open clusters over a relatively broad age range (IC 2391 – 50 Myr, NGC 2516 – 150 Myr, Hyades – 600 Myr, IC 4651 – 1.7 Gyr, and M 67 – 4.5 Gyr).

To improve our understanding of the mixing processes, adding new Be data covering a large fraction of the color magnitude diagram of well-studied open clusters is important. The ambitious aim is to compare the observations with models for stars over as wide as possible a range of mass and evolutionary status. In this context, the open cluster IC 4651 is a very good test case. It has well-determined membership (Meibom et al. 2002), and precisely known metallicity and chemical composition ([Fe/H] = +0.11; Pasquini et al. 2004; Carretta et al. 2004; Pace et al. 2008). Age determinations for this cluster vary between 1.2 ± 0.2 Gyr (Biazzo et al. 2007) and 1.7 ± 0.15 Gyr (Meibom et al. 2002). A color magnitude diagram of IC 4651 is shown in Fig. 1.

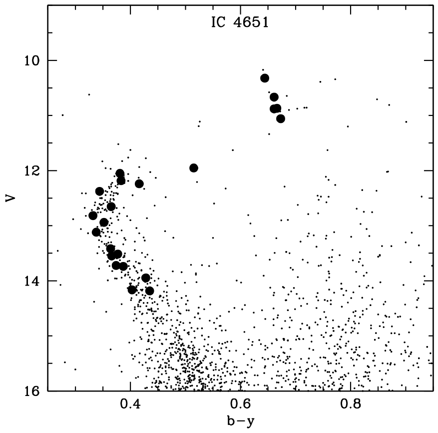

Fig. 1. Color magnitude diagram of IC 4651. Sample stars are shown as filled circles. The *ubvy* photometry is from Meibom (2000) and obtained by means of the WEBDA database.

Important is that the Li evolution along the CMD of this cluster has already been investigated in detail by Pasquini et al. (2004). Well-determined patterns have been found along its evolutionary sequence (see Fig. 3 by Pasquini et al. 2004). In a sequence of increasing stellar mass, the cluster indeed has an Li "plateau" around solar mass stars, followed by a well-determined Li dip, after which the maximum Li content is observed, at meteoritic value. A sudden Li drop follows along the Hertzsprung gap, possibly indicating the onset of dilution (the so-called first dredge-up). Some of the giants show noticeable differences in Li abundance while sharing other stellar characteristics. It has been shown that models of rotating stars by Charbonnel & Talon (1999) and Palacios et al. (2003) were able to reproduce the Li behavior both of main sequence stars lying on the blue side of the dip and of evolved stars.

In this work we present Be abundances for the same stars analyzed by Pasquini et al. (2004). This is the first time Be abundances have been determined for stars along the whole evolutionary sequence of an open cluster, including solar-type, Li-dip, turn-off, subgiant, and red giant stars. With these new results, the mixing processes in different stellar masses can be investigated in greater detail.

2. Observations and stellar parameters

Our sample is composed of 22 stars. Twenty one of them have been analyzed by Pasquini et al. (2004). To these we add one star of this same cluster analyzed by Randich et al. (2002), star T2105. The sample was selected to cover a large interval of the CMD from the Strömgren photometry obtained by Meibom (2000). The interested reader is referred to the work of Pasquini et al. (2004) for more details on the sample selection.

Spectra were obtained using UVES, the *Ultraviolet and Visual Echelle Spectrograph* (Dekker et al. 2000) fed by UT2 of the VLT. UVES is a cross-dispersed echelle spectrograph

Table 1. Observational data of the sample stars.

Star	v	$(b-y)$	obs. date	$t_{\rm exp}$ (s)	S/N
E3	12.05	0.38	10. May. 2001	2 × 2100	90
E5	12.82	0.33	09. May. 2001	2 × 3000	90
E7	14.17	0.40	26. Mar. 2000	4 × 3600	60
E14	13.12	0.34	09. May. 2001	2 × 3300	95
E15	13.52	0.38	10. Apr. 2001	2 × 4500	85
E19	12.24	0.42	08. Apr. 2001	2 × 2100	85
E34	13.42	0.36	11. May. 2001	2 × 4500	90
E45	14.18	0.44	29. Mar. 2000	3 × 3600	40
E56	12.18	0.38	08. Jun. 2001	2 × 2100	85
E64	13.72	0.37	06. Jun. 2001	2 × 4500	100
E79	13.55	0.37	09. Apr. 2001	2 × 4500	90
E86	13.74	0.39	06. Jun. 2001	2 × 4500	100
E95	11.95	0.52	08. Jun. 2001	2 × 2100	80
E99	12.38	0.34	08. Jun. 2001	2 × 2100	90
T1228	12.94	0.35	08. Jun. 2001	2 × 3300	90
E25	12.65	0.37	07. Jun. 2001	2 × 2100	85
T2105	13.95	0.43	Randich et al. (2002)		
E8	10.67	0.66	10. May. 2001	1500	50
E12	10.32	0.64	15. Apr. 2001	2 × 1200	75
E60	10.87	0.67	09. Apr. 2001	2 × 1800	70
E98	10.88	0.66	11. May. 2001	2 × 1800	65
T812	11.06	0.67	07. Jun. 2001	2 × 1800	70

Notes. The Strömgren photometry is from Meibom (2000). The S/N, per resolution element (4 pixels), was measured in the Be region. The five stars grouped at the end of this and the following tables are the red giants.

able to obtain spectra from the atmospheric cut-off at 300 nm to ~1100 nm. The reduction was conducted with the ESO UVES pipeline within MIDAS. The spectra have typical signal-to-noise (S/N) between 40 and 100 and $R \sim 45\,000$. The log book of the observations is given in Table 1. Stars with names starting with an "E" follow the numbering system of Eggen (1971). Stars with names starting with a "T" follow the numbering system of Anthony-Twarog et al. (1988).

The atmospheric parameters for the sample stars determined by Pasquini et al. (2004) were adopted. A first estimate of the effective temperature ($T_{\rm eff}$) was calculated using the calibrations of Alonso et al. (1996, 1999). A first estimate of the surface gravity was obtained using this $T_{\rm eff}$, a mass of 1.80 $M_\odot$ for the cluster turn-off, and the distance modulus determined by Meibom et al. (2002), $(m-M)_0 = 10.03$. Starting with these values, both the $T_{\rm eff}$ and the microturbulence velocity (ξ) were further constrained using Fe lines, eliminating trends with the excitation potential and the equivalent widths, respectively. The ionization equilibrium, on the other hand, was not adopted to constrain the gravity. While the other parameters were being varied, gravity was also varied by at most 0.30 dex to obtain as good an equilibrium as possible without departing much from the log g given by the star position at the CMD.

Using this method, Pasquini et al. (2004) had some difficulty constraining the parameters of the fast-rotating hot stars around the turn-off. The above-mentioned approach resulted in higher metallicities for these stars than the ones determined for the slow-rotating stars. This effect was likely caused by the blending of the Fe lines with other neighboring lines due to the rotational broadening. Thus, the measured equivalent widths were greater than they should be. As in these cases the spectroscopic parameters are likely not reliable, atmospheric parameters for the fast-rotating stars were calculated adopting the photometric temperatures. The spectroscopic temperatures were adopted for the remaining stars. The atmospheric parameters of the stars are given in Table 2. The mean metallicity of the cluster as determined by Pasquini et al. (2004) was adopted for all the stars, [Fe/H] = +0.11.

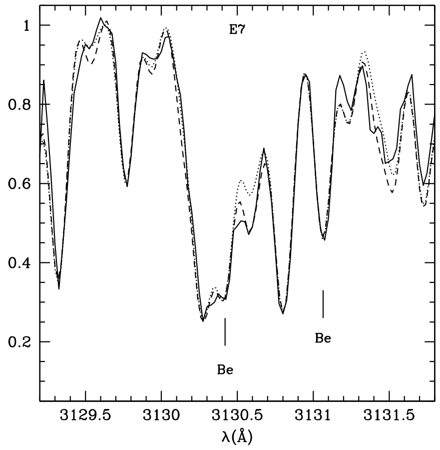

Fig. 2. Fit to the region of the Be lines in the main sequence star E7. The solid line represents the observed spectrum, the dotted line a synthetic one with solar abundance ratios, and the dashed line a synthetic spectrum with [O/Fe] = +0.25 and [C/Fe] = +0.10.

3. Be abundances

3.1. Synthetic spectra

For late-type stars, Be abundances can only be determined using the Be ^{2}S–^{2}P$_0$ resonance lines at 3131.065 Å and 3130.420 Å. This near-UV region is extremely crowded with atomic and molecular lines, some of them still lacking proper identification. Thus, determination of Be abundances needs to be conducted with spectrum synthesis taking all the blending nearby features into account.

To derive the Be abundances, synthetic spectra were calculated with the codes described in Coelho et al. (2005) and the grids of model atmospheres without overshooting calculated with the ATLAS9 program (Castelli & Kurucz 2003). These models assume local thermodynamic equilibrium, plane-parallel geometry, and hydrostatic equilibrium.

The line list is the same as used in Smiljanic et al. (2008, 2009b). In short, the molecular line list is described in Coelho et al. (2005) and the atomic line list is the one compiled by Primas et al. (1997). Log gf of −0.168 and −0.468 were adopted for the Be lines at 3131.065 Å and 3130.420 Å, respectively. The line list includes an Fe line in 3131.043 Å, with log $gf = -2.517$ and $\chi = 2.85$ eV, affecting the blue wing of the Be 3131 line. The parameters of this line were constrained using several stars of different parameters and metallicities (see Primas et al. 1997, for details). The proper identification of this line, however, remains controversial in the literature, and other choices have been made by different authors. As discussed in more detail by Randich et al. (2007), this choice has no significant effect on the calculation of Be abundances of stars with $T_{\rm eff} > 5400$ K.

Table 2. Stellar parameters and abundances of Li and Be.

Star	$T_{\rm eff}$ (K)	Spec. or Phot.	log g (dex)	ξ (km s^{-1})	v sin$i$ (km s^{-1})	A(Be) (dex)	A(Li) (dex)
E3	6550	Phot.	3.90	2.10	29.9	1.21	1.64
E5	6930	Phot.	4.20	2.00	23.9	1.36	3.47
E7	6300	Spec.	4.30	1.10	2.1	1.11	2.83
E14	6860	Phot.	4.20	1.90	34.1	0.76	≤2.07
E15	6540	Phot.	4.20	1.70	10.0	0.64	≤1.93
E19	6280	Phot.	3.90	2.10	32.1	0.41	≤1.66
E34	6640	Phot.	4.20	1.90	24.2	0.11	≤1.92
E45	6350	Spec.	4.30	1.10	4.2	1.08	2.80
E56	6520	Phot.	3.90	2.10	27.8	1.21	≤2.16
E64	6650	Spec.	4.30	1.70	9.2	0.76	2.24
E79	6620	Spec.	4.30	1.70	21.8	0.51	≤1.91
E86	6600	Spec.	4.30	1.70	14.0	0.96	2.20
E95	5800	Spec.	3.50	1.70	12.0	0.61	2.19
E99	6830	Phot.	4.00	2.00	28.1	1.21	≤2.38
T1228	6770	Phot.	4.20	1.70	5.7	1.21	3.18
E25	6680	Phot.	4.00	2.00	21.3	1.11	3.29
T2105	6110	Phot.	4.44	1.10	8.0	1.11	2.82
E8	4900	Spec.	2.70	1.30	0.1	–	≤0.09
E12	5000	Spec.	2.70	1.50	1.1	≤−0.70	≤0.35
E60	4900	Spec.	2.90	1.40	1.9	≤−0.70	0.42
E98	4900	Spec.	3.00	1.40	1.0	≤−0.50	0.72
T812	5000	Spec.	3.00	1.60	0.5	≤−0.70	≤0.38

3.2. The Sun and the slow-rotating stars

That some of the sample stars are fast rotators adds further difficulty to the analysis of the Be spectral region. Thus, we conducted a careful analysis, first modeling the slow-rotating stars and conducting a few tests to make certain any possible systematic effect affecting the modeling of the fast-rotating stars would be under control.

As the first step, with the line list described above, we fitted the Be lines in the solar UVES[1] spectrum, adopting the parameters: $T_{\rm eff}$ = 5777 K, log g = 4.44, and ξ = 1.00 km s^{-1}. An abundance of A(Be) = 1.10 was obtained. This abundance is in excellent agreement with the one found by Chmielewski et al. (1975), A(Be) = 1.15, usually adopted as the reference photospheric solar abundance.

The low photospheric solar Li abundance, depleted by a factor of ~160 with respect to the meteoritic value, has been known for a long time (see e.g. Müller et al. 1975). The photospheric Be abundance and its difference with respect to the meteoritic one have instead been a matter of debate. All analyses of the solar photospheric abundance obtain log(Be/H) ~1.15–1.25 (Chmielewski et al. 1975; Garcia Lopez et al. 1995; Randich et al. 2002), a factor of 2 less than what is measured in meteorites, log(Be/H) = 1.41 (Lodders 2003). This issue now seems settled to a large extent; the measured photospheric value is lower than the real one due to our inability of properly accounting all continuum opacity sources in the region around 313 nm, where the two Be resonance lines are located, when calculating model atmospheres (Balachandran & Bell 1998; Asplund 2004).

The second step was to fit the two main sequence slow-rotating stars E7 and E45. The cluster was found to have a solar abundance pattern by Pasquini et al. (2004). Thus, the solar abundance ratios[2] were adopted when calculating a first set of synthetic spectra. However, as shown in Fig. 2, when adopting a solar abundance pattern, an important molecular feature near the 3130 Å Be line is not properly fitted. A better fit is obtained when [O/Fe] is increased by +0.25 dex and [C/Fe] by +0.10 dex, in both E7 and E45. These apparent overabundances are likely not to be real but caused by shortcomings in the analysis, such as the neglect of effects caused by departures from the local thermodynamic equilibrium and/or by problems with the molecular and atomic data in this region.

Nevertheless, it is important to notice that properly fitting the neighboring molecular features in the slow-rotating stars is an important step toward analyzing the fast-rotating ones. In the last case, all these lines are blended into a single feature. As all the stars in the cluster are expected to have the same chemical composition (except for the giants), one may expect that the enhanced abundances of C and O are also needed to properly fit the spectra of the fast-rotating stars. We stress that this increase in the abundances of C and O has no effect on the calculated Be abundances of the slow-rotating stars. Thus, when fitting the fast rotators, C and O abundances were kept with these increased values, while the other elements were kept with a solar ratio. Only the Be abundance was varied from star to star. The derived Be abundances are listed in Table 2.

3.3. The fast-rotating stars

Before fitting the true fast-rotating stars, we conducted a test to better understand the effects of the broadening in the derived abundances. We artificially broadened the spectra of the two slow-rotating stars, E7 and E45, by convolving them with

---

[1] The spectrum is available for download at the ESO website: `www.eso.org/observing/dfo/quality/UVES/pipeline/solar_spectrum.html`

[2] The abundances recommended by Grevesse & Sauval (1998) were adopted for all elements except for oxygen, for which we adopted the abundance suitable for the 1D atmospheric models recommended by Allende Prieto et al. (2001), A(O) = 8.77, and for Be for which the abundance derived above from the solar spectrum was adopted.

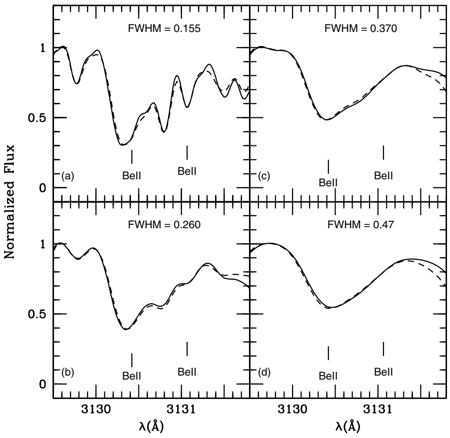

Fig. 3. Fit to the region of the Be lines in the main sequence star E7. The four panels show a sequence of larger broadening applied to the observed spectrum. In all panels the best-fitting synthetic spectrum has $A(\text{Be}) = 1.16$ dex.

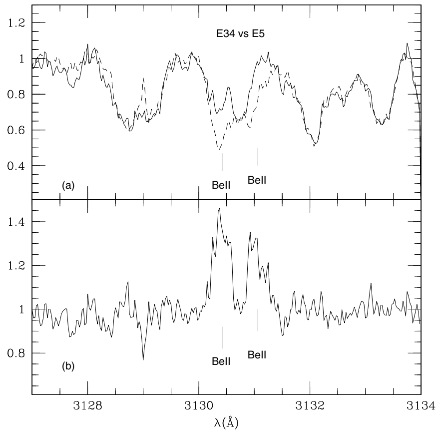

Fig. 4. a) Comparison between the observed spectra of stars E5 (dashed line) and E34 (solid line). The stars have similar rotational velocity and different Be abundances. **b)** The result of the division of the two spectra in the upper panel. The two residual features are located at 3130.41 and 3131.03 Å. These wavelengths are compatible with the difference being caused by different Be abundances.

Gaussian functions. In Fig. 3 we show the spectrum of the star E7 broadened with four different Gaussian functions. The Be abundance was then calculated for these broadened spectra.

In the four cases shown in Fig. 3, an abundance of $A(\text{Be}) = 1.16$ dex was derived for E7, while $A(\text{Be}) = 1.11$ dex was derived in the original unbroadened spectrum. Applying similar broadening to E45, we obtain $A(\text{Be}) = 1.15$ for all the broadened cases, while $A(\text{Be}) = 1.08$ dex was obtained for the original observed spectrum. Thus, we conclude that the abundances in a broadened spectrum are slightly overestimated. However, this small amount is well within the uncertainties (see below). Therefore, we are confident that it is possible to derive meaningful abundances for the fast-rotating stars with our method of analysis.

Beryllium abundances were then derived for all the fast-rotating main-sequence and turn-off stars. The stars were found to have a broad range in abundances, from 1.36 dex (E5) to 0.11 dex (E34). In Fig. 4 we plot the spectra of these two stars, which have similar $v \sin i$, to show that the difference in Be abundance obtained in the analysis is real. In the lower panel of this same figure we show the result of the division of these spectra. The structures left in the division have central wavelengths of 3130.41 and 3131.03 Å, arguing that the difference is really caused by the different Be abundances. Similarly, we compare in Fig. 5 the observed spectrum of star E34 and the spectrum of E7 artificially broadened to a $v \sin i$ similar to that of E34. It is clear from this figure that star E34 has a smaller Be abundance than E7. This comparison again shows that the difference in Be abundances detected in the stars is real.

Finally, we point out that Be was detected in all the sample of main sequence and turn-off stars. Most of the stars show signs of Be depletion, i.e., Be lower than the meteoritic value, but still have a detectable amount of Be in their photospheres. In Fig. 6 we show the observed spectra of E19 and E34, the two stars with smaller Be content. Also shown are a best-fit synthetic spectrum together with a spectrum calculated with no Be at all. As clearly seen, the spectra lacking Be show a marked difference when compared to the observed ones. This comparison argues that our Be abundances are actual detections and not upper-limits. The derived Be abundances are listed in Table 2.

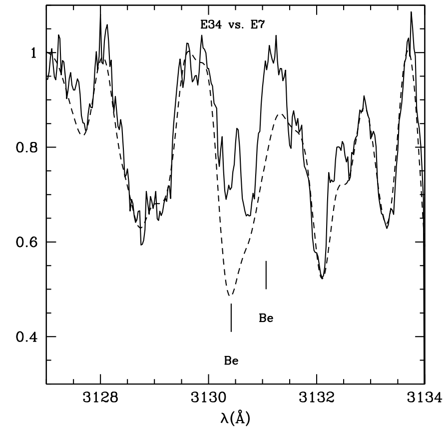

Fig. 5. Comparison between the observed spectrum of star E34 (solid line) and the spectrum of star E7 (dashed line) artificially broadened to a $v \sin i$ similar to the one of E34. It is clear the lower Be abundance of star E34 and that a higher abundance could be easily detected in our analysis.

3.4. The red giants

Fitting synthetic spectra in the Be region for the red giants proved to be even more challenging than fitting the fast-rotating stars. From this exercise it became clear that the line list used to fit the main sequence and turn-off stars is not fully adequate for red giants. Problems with the wavelengths and depths of the lines become clear. More work on the transitions affecting the near UV region is required.

In particular, the Fe line adopted as the blend affecting the 3131 Å Be line appears to be too strong here and with a wrong wavelength when compared to the observed spectra (see Fig. 7). For the dwarf stars, as discussed before, this blend has no significant effect. For metal-poor stars, such as the subgiants

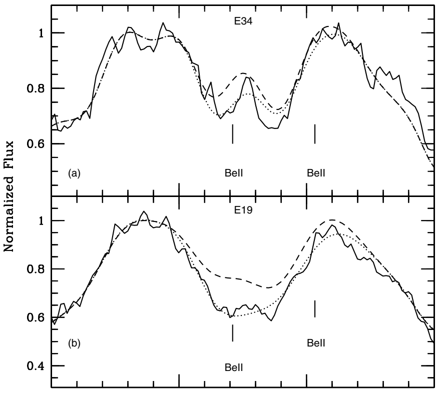

Fig. 6. **a)** Comparison between the observed spectrum of star E34 (solid line), the best synthetic fit (dotted line), and a synthetic spectrum calculated without Be (dashed line). **b)** Comparison between the observed spectrum of star E19, the best synthetic fit, and a synthetic spectrum calculated without Be. These two comparisons argue for both stars having detectable amounts of Be.

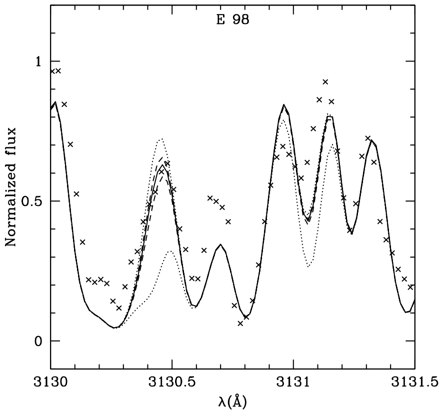

Fig. 7. Fitting the Be lines in the red giant E98. The crosses represent the observed spectrum, the solid line the best fit, the dashed lines represent variations of ±0.20 dex from the best fit, and the dotted lines represent a spectrum without Be and one with A(Be) = 1.21.

analyzed by García Pérez & Primas (2006), the blending feature is also not significant. For our metal-rich cool giants, however, it prevents reliable abundances from being derived from this Be line. In this case, we relied solely on the 3130.4 Å feature.

The 3130.4 Å line, however, is very weak (indicating that Be is strongly depleted or even absent in giants) and strongly blended. In Fig. 7 an example of fitting the Be region in a red giant is given. The Be line only affects the wing of a very strong and heavily blended feature. The best fit is found when the wing of this feature in the synthetic spectrum is brought to the level of the wing in the observed spectrum. The figure suggests that an abundance cannot be derived in this case with an uncertainty better than ±0.20 dex.

One should also note that the abundances in this case are strongly dependent on broadening, blending features (their inclusion and also on the right abundance for the given element), and on the determination of the continuum. Thus, one should be very careful when interpreting the abundances derived for the red giants. In this case we consider that only an upper limit on the Be abundance can be determined. In addition, the difficulties discussed above mean that one should be very careful not to push the comparison between dwarfs and giants too far. The Be upper limits for the red giants are listed in Table 2.

Of all these issues, the level of the continuum is of particular concern. Different solutions could bring the wing of the line up or down, changing the best fit. Finding the correct level of the continuum in the near UV region is at best a very difficult task. However, by adopting very similar solutions for all the stars that have very similar atmospheric parameters, we believe that at least a reliable differential scale can be obtained.

Regarding the abundances of other elements, it is expected that the first dredge-up would change C and N abundances of the stars on the red giant branch (RGB). This near UV region is affected by many CN, NH, and CH lines, so this change in abundances could be an important issue. We calculated a synthetic spectrum for star E60 by adopting typical post dredge-up values for these elements, [C/Fe] = −0.15 and [N/Fe] = +0.40 (see e.g. Smiljanic et al. 2009a). A comparison with the best fit obtained using unaltered abundances showed only very weak effects, well within the ±0.20 uncertainty of the fit.

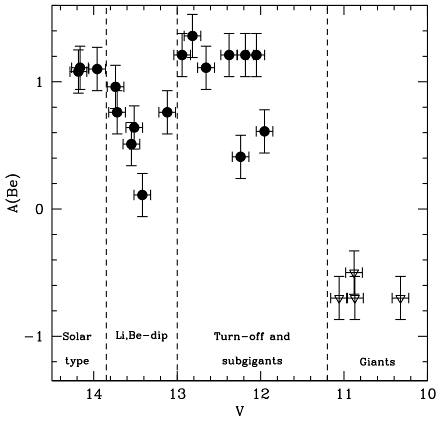

Fig. 8. The Be abundances of the sample stars, calculated in this work, as a function of the V magnitude. Abundance determinations are shown as solid circles and upper limits as open triangles. The Be dip is clearly seen.

The Be abundances of all sample stars are shown as a function of the V magnitude in Fig. 8. For comparison, we also show a plot of the Li abundances determined by Pasquini et al. (2004) as a function of V in Fig. 9. The evolutionary stages of the stars are indicated in the figures. It is clearly seen that the stars of the Li dip also define a clear Be dip.

3.5. Uncertainties and comparison with the literature

The determination of Be abundances is affected by the uncertainties of the atmospheric parameters and by the uncertainty in the determination of the pseudo-continuum during the spectrum fitting. To conduct the calculations of the errors, we adopted the same uncertainties of the atmospheric parameters determined by Pasquini et al. (2004), $\sigma_{T_{\rm eff}}$ = ± 100 K, $\sigma_{\log g}$ = ± 0.30 dex, σ_{ξ} = ± 0.30 km s^{-1}, and $\sigma_{\rm [Fe/H]}$ = ± 0.10 dex.

To estimate the effect of the atmospheric parameters, we can change each one by its own error, keeping the other ones with the

Table 3. The uncertainties of the Be abundance introduced by the uncertainties of the atmospheric parameters and by uncertainty of the fitting itself related to the level of the continuum and the S/N.

Star	$\sigma_{T_{\rm eff}}$	$\sigma_{\log g}$	σ_{ξ}	$\sigma_{\rm [Fe/H]}$	$\sigma_{\rm fitt.}$	$\sigma_{\rm total}$
E 7	±0.03	±0.10	±0.00	±0.00	±0.05	±0.12
E 86	±0.05	±0.10	±0.05	±0.05	± 0.10	±0.17
E 60	±0.15	±0.05	±0.03	±0.05	± 0.20	±0.26

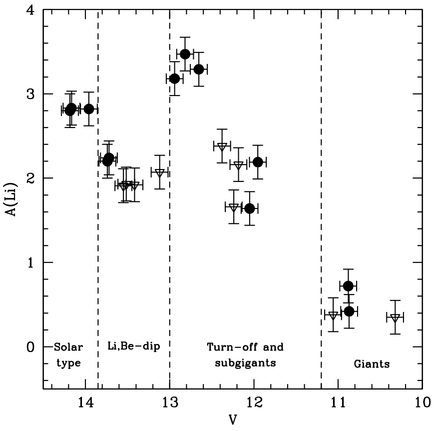

Fig. 9. The Li abundances of the sample stars, calculated in Pasquini et al. (2004), as a function of the V magnitude. Abundance determinations are shown as solid circles and upper limits as open triangles.

original adopted values, and recalculate the abundances. Thus, we measure what effect the variation of one parameter has on the abundances. We assume the uncertainties introduced by each parameter to be independent of the other ones. The uncertainty due to the continuum was determined by estimating the sensitivity of the derived Be abundance on the adopted continuum level. This uncertainty is mostly related to the S/N of the spectrum. These effects are listed in Table 3. The calculations were done for three representative stars, E7 as an example of slow-rotating star, E86 as an example of a fast-rotating star, and E60 as an example of a giant star. The Li and Be abundances derived for the star E5, which seem to be slightly above the solar values (see Table 2), seem to suggest that the uncertainty on its temperature is slightly higher than for the other stars. For these hot stars, the effective temperature is also important for determining Be abundances. We thus believe that its Li and Be abundances are slightly overestimated and should be interpreted with care.

As mentioned in Sect. 2, Randich et al. (2002) has analyzed three main sequence stars of IC 4651 and determined their Be abundances. Two of their stars, E7 and E45, are also analyzed here. The atmospheric parameters derived by Randich et al. (2002) are different from the ones adopted here. Randich et al. (2002) calculated temperatures of 6061 and 6016 K, while we adopted 6300 and 6350 K for stars E7 and E45, respectively. A gravity of log g = 4.44 was adopted by Randich et al. (2002) for all stars they analyzed, while a value of log g = 4.30 was calculated for both E7 and E45 in Pasquini et al. (2004) and adopted here. In spite of these differences, the Be abundances of the two stars as derived by Randich et al. (2002) agree with ours within the uncertainties; that is, Randich et al. (2002) derived A(Be) = 1.11 and 1.16 for stars E7 and E45, while we obtained A(Be) = 1.11 and 1.08, respectively.

4. Comparison with model predictions for rotating stars

4.1. Input physics of the hydrodynamical stellar models

4.1.1. Hot side of the Li dip

In Pasquini et al. (2004) the Li abundance patterns in IC 4651 were compared with model predictions for rotating stars by Charbonnel & Talon (1999) and Palacios et al. (2003). These models include atomic diffusion, as well as the transport of angular momentum and chemicals by meridional circulation and shear turbulence following the formalism by Zahn (1992), Talon & Zahn (1997), and Maeder & Zahn (1998) (for more details and references see the original papers as well as Decressin et al. 2009). They are adequate for stars that lie on or originate in the hot side of the dip and inside which angular momentum transport by internal gravity waves emitted by convective envelopes is inefficient (Talon & Charbonnel 2003). These models were found to explain the corresponding Li data for both main sequence and giant stars in the intermediate-age IC 4651 (see Pasquini et al. 2004), as they do for younger clusters like the Hyades, Coma Berenices, and Praesepe (see e.g. Charbonnel & Talon 2008).

Meanwhile new stellar models within the same mass range (i.e., for stars more massive than 1.2 $M_{\odot}$) were computed for other purposes with the stellar evolution code STAREVOL V3.1 (Charbonnel & Lagarde, in preparation) using the same prescriptions for the transport of angular momentum and chemicals by meridional circulation and shear turbulence as in the above-mentioned papers. Atomic diffusion is also included in the form of gravitational settling, as well as that related to thermal gradients, using the formulation by Paquette et al. (1986). As far as the input physics is concerned, the differences with the models by Charbonnel & Talon (1999) and Palacios et al. (2003) are the following: (1) the reference solar composition is the one derived by Asplund et al. (2006), except for Ne for which the recommendations by Cunha et al. (2006) are followed; (2) new OPAL opacity tables are used according to the chemical mixture; (3) thermohaline mixing is accounted for following Charbonnel & Zahn (2007), a process that only becomes efficient when the stars reach the so-called luminosity bump on the RGB (see Sect. 4.3).

Results of these recent computations for initial stellar masses of 1.3, 1.35, 1.4, 1.5, 1.8, and 2 $M_{\odot}$ for Z = 0.014 are presented. In view of the remaining uncertainty on the age of IC 4651, we provide in Table 4 relevant model characteristics at 1.2 and 1.7 Gyr for the stars that are still on the main sequence at that time. In all cases various initial rotation velocities on the zero-age main sequence were considered. (The 1.3, 1.35, 1.4, and 1.5 $M_{\odot}$ models are computed for $V_{\rm ZAMS}$ = 50, 80, and 110 km s^{-1}; the 1.8 $M_{\odot}$ models are computed for $V_{\rm ZAMS}$ = 80, 110, and 180 km s^{-1}, and the 2 $M_{\odot}$ models for $V_{\rm ZAMS}$ = 110, 180, and 250 km s^{-1}.) The efficiency of magnetic braking applied to stars arriving on the main sequence is determined according to the work of Gaigé (1993) following the braking law by Kawaler (1988) (for more details see Palacios et al. 2003). In practice, magnetic braking only has to be applied to the 1.3, 1.35, and 1.4 $M_{\odot}$ stars that have thicker convective envelopes than more massive stars. As in previous works, the aim was to reproduce the rotation velocity distribution observed at the age of the Hyades. Theoretical rotation velocities at the age of IC 4651 are given in Table 4 and span the velocity range of our sample

Table 4. Rotation velocity, effective temperature, and surface abundances of Li and Be predicted for the stellar models that are still on the main sequence at the age of IC 4651

M ($M_\odot$)	$V_{\rm ZAMS}$ (km s^{-1})	$V_{\rm Age}$ (km s^{-1})		$T_{\rm eff}$ (K)		A(Li)		A(Be)	
		1.2 Gyr	1.7 Gyr	1.2 Gyr	1.7 Gyr	1.2 Gyr	1.7 Gyr	1.2 Gyr	1.7 Gyr
1.3	50	19.4	16.9	6532	6507	2.05	1.51	1.02	0.77
	80	28.3	24.4	6535	6528	1.24	0.37	0.62	0.22
	110	36.2	30.9	6520	6483	0.47	−0.59	0.2	−0.29
1.35	50	30.3	27.6	6687	6663	2.69	2.33	1.26	1.10
	80	28.6	24.5	6683	6670	1.16	0.24	0.57	0.15
	110	36.6	31.5	6685	6676	0.43	−0.70	0.20	−0.35
1.4	50	42.7	41.4	6834	6762	3.24	3.22	1.41	1.41
	80	67.8	67.8	6824	6764	3.20	3.10	1.41	1.39
	110	96	95.2	6826	6781	3.12	2.94	1.39	1.33
1.5	50	40.5	37.5	7094	6857	3.23	3.18	1.41	1.40
	80	66.5	62.7	7174	6948	3.13	2.94	1.40	1.34
	110	92.2	87.8	7136	6900	2.97	2.66	1.35	1.21

Notes. Models by Charbonnel & Lagarde (in preparation). See text for more details.

stars. In all cases the surface rotation velocity also changes because of secular evolution, and it is reduced to only a few km s^{-1} when the models are on the subgiant branch due to the radius expansion.

4.1.2. Cool side of the Li dip

For less massive main-sequence stars lying on the cool side of the Li dip that have deeper convective envelopes, internal gravity waves are efficiently generated and participate in the extraction of internal angular momentum, along with meridional circulation and shear turbulence (Talon & Charbonnel 2003). In this case, the appropriate models are those by Talon & Charbonnel (2005) and Charbonnel & Talon (2005), which take all these effects into account. Unfortunately the 1.0 $M_\odot$ models of Charbonnel & Talon (2005) have an effective temperature at the age of the IC 4651 (i.e., 5597 K), lower than our cooler main sequence stars, and they cannot be used for comparison with the present sample. Obviously abundance determinations for such relatively cool objects would be extremely valuable for further tests of the models. Only the 1.2 $M_\odot$ model computed by Talon & Charbonnel (2005) is available for comparison purposes (see Sect. 4.2). It has an initial rotation velocity on the zero age main sequence of 50 km s^{-1}, and surface spin-down follows Kawaler (1988) as explained in Sect. 4.1.1.

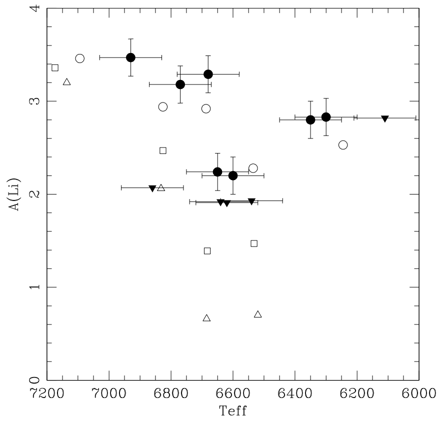

Fig. 10. Li abundances in IC 4651 main sequence and turnoff stars fainter than $V \sim 12.6$ (black points and triangles for actual determinations and upper limits, respectively). Open circles, squares, and triangles show model predictions for initial rotation velocities of 50, 80, and 110 km s^{-1}, respectively. For comparison purposes the theoretical Li points are increased by 0.16 dex to account for the difference between the meteoritic value and the highest Li abundance determined in our sample stars. See text for more details.

4.1.3. Initial values for Li and Be

In the following we compare the predictions of the hydrodynamical models described above with the observations of both Li and Be in IC 4651. Results are presented separately for the main sequence and turnoff stars (Sect. 4.2) and for more evolved stars (Sect. 4.3). In the following figures, we use the V magnitudes to divide the stars according to their evolutionary stages; stars fainter than V = 12.6 are at the main sequence, stars between 12.6 and 11.8 are at the upper turn-off or at the subgiant branch, and stars brighter than 11.8 are giants.

For the initial values of A(Li) and A(Be) used in our computations we chose the meteoritic abundances, i.e., 3.25 (Asplund et al. 2006) and 1.41 (Lodders 2003), respectively. This Li value is actually lower than the highest Li abundance determined among our sample stars, which induces an artificial shift within the comparison between predictions and data. For this reason we increase, within the figures, the theoretical Li points by 0.16 dex. This corresponds to assuming that the highest Li abundance derived among our sample stars (E5, A(Li) = 3.47 dex) is the initial abundance of the sample stars.

4.2. Comparisons with observed features on the main sequence

Figures 10 and 11 compare the predictions of the stellar models described in Sect. 4.1 to the Li and Be observed abundances of the main-sequence and turn-off stars of our IC 4651 sample as a function of the effective temperature. The models provide an estimate of the expected dispersion in surface abundances due to a dispersion in initial rotation velocities. On the cool side of the dip, only one theoretical point is available in the temperature range considered in the present study (1.2 $M_\odot$, $V_{\rm ZAMS}$ = 50 km s^{-1} model of Talon & Charbonnel 2005).

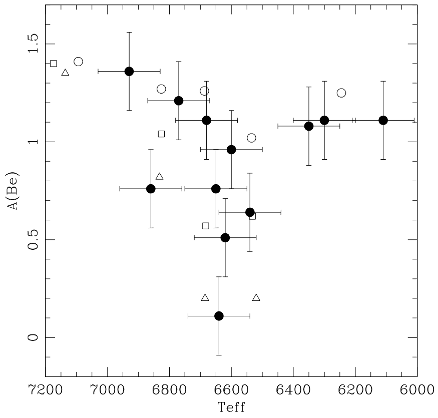

Fig. 11. Same as Fig. 10 for observed and theoretical Be abundances.

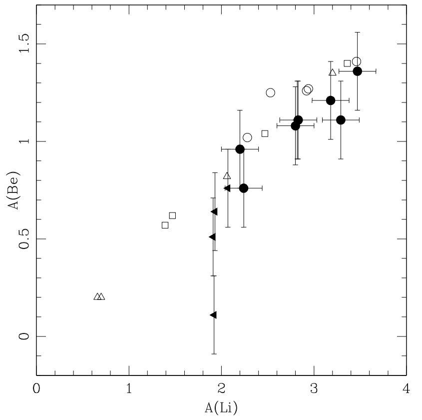

Fig. 12. Li and Be abundances in IC 4651 main sequence and turnoff stars fainter than $V \sim 12.6$ (black points and triangles for Li actual determinations and upper limits, respectively). Open circles, squares, and triangles show model predictions for initial rotation velocities of 50, 80, and 110 km s^{-1}, respectively. For comparison purposes the theoretical Li points are increased by 0.16 dex to account for the difference between the meteoritic value and the highest Li abundance determined in our sample stars. See text for more details.

It is possible to note on these graphs (see also Fig. 12) that the observational behavior of the Be abundances follows that of the Li abundances closely. The Li dip is also a Be dip, confirming previous literature results (Boesgaard & King 2002; Boesgaard et al. 2004a). In a narrow range in effective temperature centered on ~6650 K, stars present both an Li and a Be depletion. Important is that Li, which is more fragile (it burns indeed through proton-captures at $\sim 2.5 \times 10^6$ K compared to $\sim 3.5 \times 10^6$ K for Be), is more strongly depleted within the dip. In most of the stars lying in this region, only upper limits could be derived for Li, while Be is always detected.

The predictions of the models described in Sect. 4.1 successfully account for the Li patterns as a function of effective temperature, namely, the presence of a large fraction of stars with Li upper limits between ~6500 and 6800 K (i.e., within the dip) and the higher Li values on both the cool and hot sides of the dip (see Fig. 10). They also reproduce the Be behavior remarkably well in the whole effective temperature range considered (see Fig. 11). The success of the models is confirmed when plotting Be versus Li as shown in Fig. 12. As noted in Sect. 4.1.3, the theoretical Li values have been shifted by 0.16 dex to account for the difference between the meteoritic Li and the highest Li abundance determined in our sample stars; however, what really matters for constraining the models is the slope of the trend between Li and Be. As can be seen in Fig. 12, the theoretical and observational slopes are found to agree very nicely. Linear fits of the observational values, accounting for errors in both axes, have slopes of +0.58 ± 0.09, if all detections and upper limits are considered, of +0.45 ± 0.05 if we only exclude star E34 (the one with the smaller Be abundance), and of +0.35 ± 0.08 if we consider only the detections. For the theoretical values we calculate a slope of +0.45 considering all points. If we restrict the theoretical values to the ones with $A(\mathrm{Li}) > 2.0$, which is the range where the observational detections are, a slope of +0.33 is obtained. These values agree very well with the observed ones. Similar correlated depletions of Li and Be have also been observed in field and cluster stars by Deliyannis et al. (1998), Boesgaard et al. (2004b), and Randich et al. (2007).

On the cool side of the dip (i.e., below ~6400 K), we find no Be dispersion thus confirming previous results by Boesgaard et al. (2004b) and Randich et al. (2002, 2007). This provides further constraints to models of rotating low-mass (i.e., below $\sim 1.25\ M_{\odot}$) stars including the transport of angular momentum by gravity waves that should assume a range in initial rotation velocities (Charbonnel et al. in preparation)[3]. However, we can already note that models of solar-mass stars computed with a large range of initial angular momentum (V_{ini} from 15 to 110 km s^{-1}) and including the effects of internal gravity waves predict very small Li dispersion at the age of IC 4651 (see Charbonnel & Talon 2005), and thus even more modest Be dispersion. This is caused by internal gravity waves that dominate the transport of angular momentum in stars lying on the red side of the dip and enforce quasi solid-body rotation within the stellar interior. As a result, the surface Li and Be depletions are expected to almost be independent of the initial angular momentum distribution (i.e., of the initial rotation velocity), implying very low surface abundance variations from star to star. On the other hand, in more massive (i.e., higher than $\sim 1.25\ M_{\odot}$) stars the efficiency of internal gravity waves dramatically drops and internal differential rotation is expected to be maintained along the stellar life under the effects of meridional circulation and turbulence. Consistently, variations in the initial angular momentum from star to star lead to more Li and Be dispersion, as required by the observations.

4.3. Comparisons with features observed in subgiant and giant stars

Let us now focus on the post-main-sequence evolution. Figures 13 and 14 compare the Li and Be abundances of our

---

[3] Randich et al. (2002) compared the Li and Be abundances determined in early G-type stars in old clusters, among which IC 4651 with predictions of models including gravity waves by Montalbán & Schatzman (2000). In these models, rotation-induced processes are ignored, and waves are invoked as the only source of mixing for chemicals in the stellar radiative zone. This is very different from the view proposed by Charbonnel & Talon. In this case indeed gravity waves transport angular momentum, together with meridional circulation and turbulence, but the transport of chemicals is essentially caused by rotation-induced mixing. See the original papers for more detailed information.

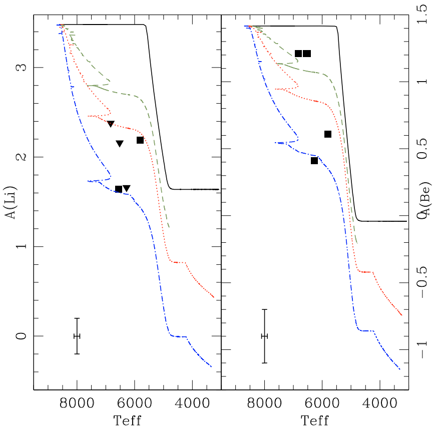

Fig. 13. Li and Be abundances in IC 4651 subgiant stars with $T_{\rm eff}$ between ~6830 and 5800 K and V between 12.6 and 11.8. Theoretical predictions for the surface Li and Be evolution are shown for the 1.8 $M_\odot$ star (see text for more details). The solid line is for the classical case, while the other lines present the results for the rotating models computed with different initial rotation velocities (80, 110, and 180 km s^{-1}, respectively, for dashed, dotted, and dot-dashed lines). The Li tracks are shifted by 0.16 dex as explained in the text.

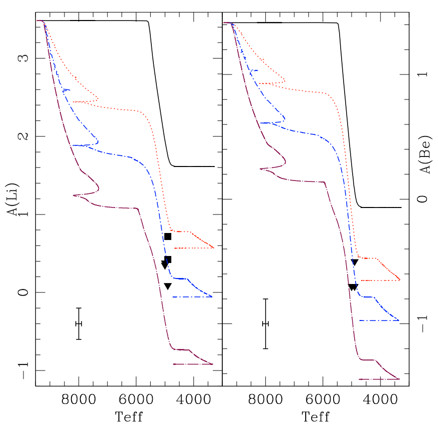

Fig. 14. Li and Be abundances in IC 4651 evolved stars brighter than V ~ 12.6. Predictions are shown for the 2 $M_\odot$ model. The solid line is for the classical case, while the other lines present the results for the rotating models computed with different initial rotation velocities (110, 180, and 250 km s^{-1} for dotted, and dot-dashed, and dot-long dashed lines, respectively). The Li tracks are shifted by 0.16 dex as explained in the text.

subgiant and giant sample stars, as a function of the effective temperature (which now depicts evolutionary stage), with predictions of our most massive models computed by assuming different initial rotation velocities. Standard (i.e., non-rotating) predictions are also shown. The subgiant stars (with $T_{\rm eff}$ between ~ 6830 and 5800 K) are compared with the 1.8 $M_\odot$ model predictions, while the relevant tracks for the giants (with $T_{\rm eff}$ at ~4900–5000 K) are the 2$M_\odot$ ones.

In the classical (non-rotating) case, the surface depletion of both Li and Be begins relatively late in $T_{\rm eff}$ within the Hertzsprung gap (i.e., at ~5500 K). This depicts dilution of the external layers with nuclear-processed material when the convective stellar envelope deepens in mass. However and as shown in Fig. 13, actual dilution starts earlier than predicted classically, as already revealed by Li data both in open clusters like IC 4651 (Pasquini et al. 2004) and NGC 3680 (Pasquini et al. 2001), but also in field stars (Alschuler 1975; Brown et al. 1989; Lèbre et al. 1999; Do Nascimento et al. 2000; Palacios et al. 2003). As can be seen in Fig. 13, the Be depletion also occurs earlier than predicted in the classical case. This simply means that the Li- and Be-free regions are larger in real main sequence stars than classically predicted.

This favors the complete hydrodynamical models, since rotation-induced mixing acting on the main sequence enlarges the Li- and Be-free regions inside the stars, implying earlier (i.e., at higher $T_{\rm eff}$ inside the Hertzsprung gap) Li and Be depletion at the surface of subgiant stars, as well as lower Li and Be values after dredge-up in giant stars (see also Palacios et al. 2003, for model comparison with Li data for field stars). The behavior of both elements predicted in the rotating case nicely matches the data for the subgiant and giant stars in IC 4651, and a dispersion in initial rotation velocity explains the observed abundance dispersion along the evolutionary sequence well.

Lithium abundances of the red giants of IC 4651 are discussed in detail by Pasquini et al. (2004). As can be seen from Table 2, Li was detected in only two giants, although all five of them have very similar atmospheric parameters. To explain this, Pasquini et al. (2004) suggests that the Li observed in these stars might have been produced in their interior after the first dredge-up. We can see, however, that this is not necessary, since in the corresponding stellar mass domain, differences in initial rotation velocities are expected to lead naturally to a significant dispersion (~1.6 dex for the range in initial rotation assumed here) in post-dredge-up Li values, accounting nicely for the observed data.

Pasquini et al. (2004) also discusses the issue of the evolutionary status of the giant stars in IC 4651. Their proper classification is based only on their position at the CMD and is not straightforward. These stars could indeed be either on the first ascent RGB or at the clump. As mentioned in Sect. 4.1.1, the new models presented here are computed to include thermohaline mixing following Charbonnel & Zahn (2007). This process only becomes efficient when the stars reach the bump on the RGB. It then leads to an additional decrease in both the Li and Be surface abundance at $T_{\rm eff}$ ~ 4250 K, as can be seen in Fig. 14. Clump stars are thus expected to have lower Li and Be surface abundances than their RGB counterparts. However, for a 2 $M_\odot$ star the effect is relatively modest (see also Charbonnel & Lagarde, in preparation), and the theoretical predictions cannot help us disentangling the evolutionary status of the giants.

5. Conclusions

Beryllium abundances were calculated for twenty-one main sequence, turn-off, subgiant, and giant stars belonging to the open cluster IC 4651. This is the first time that such an analysis has been carried out along the whole evolutionary sequence of an open cluster.

The Be abundances are found to closely follow the behavior of the Li abundances as determined by Pasquini et al. (2004). The coolest main sequence stars observed present no Be abundance dispersion, and a well-defined Be dip overlaps the well-documented Li dip for F-type stars. The Be abundances of post-main-sequence stars confirm that first-dredge up dilution starts earlier than the expected classically and present a significant dispersion. This is consistent with the Li behavior in evolved stars in IC 4651, in NGC 3680, and in the field.

Our observations are compared with theoretical predictions. For the main sequence and turnoff stars lying on the hot side of the Li-dip, as well as for the evolved stars, we compared the observations with results of new hydrodynamical stellar models calculated with STAREVOL V3.1 (Charbonnel & Lagarde, in preparation). These models include the effects of atomic diffusion, meridional circulation, shear turbulence, and thermohaline mixing. (Wave-induced transport is negligible in the case of these stars that have very narrow convective envelope while on the main sequence.) For the main sequence stars lying on the cool side of the Li dip, we compared the observations with the 1.2 $M_\odot$ model of Charbonnel & Talon (2005) which also includes the transport of angular momentum by internal gravity waves.

The models reproduce all the Li and Be features very nicely along the CMD of IC 4651. The dispersion of Li and Be abundances on the blue side of the dip and in evolved stars is very well explained when accounting for a dispersion in the initial values of the stellar rotational velocity as observed in young open clusters. On the other hand, the lack of abundance dispersion in lower mass stars is expected to be caused by the impact of internal gravity waves.

The success in explaining the Li and Be abundances along the whole evolutionary sequence of IC 4651 is very encouraging. It shows that important steps have been taken towards the proper understanding of the physical mechanisms acting during the stellar evolution.

Acknowledgements. This research has made use of the WEBDA database, operated at the Institute for Astronomy of the University of Vienna, of NASA's Astrophysics Data System, and of the Simbad database operated at CDS, Strasbourg, France. R.S. acknowledges FAPESP PhD (04/13667-4) and post-doc fellowships (08/55923-8). C.C. and N.L. acknowledge financial support from the FNS (Switzerland) and from the Programme National de Physique Stellaire of CNRS/INSU (France).

References

Allende Prieto, C., Lambert, D. L., & Asplund, M. 2001, ApJ, 556, L63
Alonso, A., Arribas, S., & Martinez-Roger, C. 1996, A&AS, 117
Alonso, A., Arribas, S., & Martínez-Roger, C. 1999, A&AS, 140, 261
Alschuler, W. R. 1975, ApJ, 195, 649
Anthony-Twarog, B. J., Mukherjee, K., Twarog, B. A., & Caldwell, N. 1988, AJ, 95, 1453
Asplund, M. 2004, A&A, 417, 769
Asplund, M., Grevesse, N., & Sauval, A. J. 2006, Nucl. Phys. A, 777, 1
Balachandran, S. 1995, ApJ, 446, 203
Balachandran, S. C., & Bell, R. A. 1998, Nature, 392, 791
Biazzo, K., Pasquini, L., Girardi, L., et al. 2007, A&A, 475, 981
Boesgaard, A. M. 1976, ApJ, 210, 466
Boesgaard, A. M., & King, J. R. 2002, ApJ, 565, 587
Boesgaard, A. M., & Krugler Hollek, J. 2009, ApJ, 691, 1412
Boesgaard, A. M., & Tripicco, M. J. 1986, ApJ, 302, L49
Boesgaard, A. M., Heacox, W. D., & Conti, P. S. 1977, ApJ, 214, 124
Boesgaard, A. M., Armengaud, E., & King, J. R. 2004a, ApJ, 605, 864
Boesgaard, A. M., Armengaud, E., King, J. R., Deliyannis, C. P., & Stephens, A. 2004b, ApJ, 613, 1202
Brown, J. A., Sneden, C., Lambert, D. L., & Dutchover, E. J. 1989, ApJS, 71, 293
Burkhart, C., & Coupry, M. F. 1998, A&A, 338, 1073
Burkhart, C., & Coupry, M. F. 2000, A&A, 354, 216
Carretta, E., Bragaglia, A., Gratton, R. G., & Tosi, M. 2004, A&A, 422, 951
Castelli, F., & Kurucz, R. L. 2003, in Proc. IAU Symp. 210, ed. N. Piskunov, W. W. Weiss, & D. F. Gray, A20
Cayrel, R., Cayrel de Strobel, G., Campbell, B., & Dappen, W. 1984, ApJ, 283, 205
Charbonnel, C., & Talon, S. 1999, A&A, 351, 635
Charbonnel, C., & Talon, S. 2005, Science, 309, 2189
Charbonnel, C., & Talon, S. 2008, in Proc. IAU Symp. 252, ed. L. Deng & K. L. Chan, 163–174
Charbonnel, C., & Zahn, J.-P. 2007, A&A, 467, L15
Charbonnel, C., Vauclair, S., & Zahn, J.-P. 1992, A&A, 255, 191
Chen, Y. Q., Nissen, P. E., Benoni, T., & Zhao, G. 2001, A&A, 371, 943
Chmielewski, Y., Brault, J. W., & Mueller, E. A. 1975, A&A, 42, 37
Coelho, P., Barbuy, B., Meléndez, J., Schiavon, R. P., & Castilho, B. V. 2005, A&A, 443, 735
Cunha, K., Hubeny, I., & Lanz, T. 2006, ApJ, 647, L143
Decressin, T., Mathis, S., Palacios, A., et al. 2009, A&A, 495, 271
Dekker, H., D'Odorico, S., Kaufer, A., Delabre, B., & Kotzlowski, H. 2000, in Optical and IR Telescope Instrumentation and Detectors, ed. M. Iye & A. F. Moorwood, Proc. SPIE, 4008, 534
Deliyannis, C. P., & Pinsonneault, M. H. 1997, ApJ, 488, 836
Deliyannis, C. P., Boesgaard, A. M., Stephens, A., et al. 1998, ApJ, 498, L147
Deliyannis, C. P., Pinsonneault, M. H., & Charbonnel, C. 2000, in Proc. IAU Symp. 198, ed. L. da Silva, R. De Medeiros, & M. Spite, 61
Do Nascimento, Jr., J. D., Charbonnel, C., Lèbre, A., de Laverny, P., & De Medeiros, J. R. 2000, A&A, 357, 931
Duncan, D. K. 1981, ApJ, 248, 651
Eggen, O. J. 1971, ApJ, 166, 87
Gaigé, Y. 1993, A&A, 269, 267
Garcia Lopez, R. J., & Spruit, H. C. 1991, ApJ, 377, 268
Garcia Lopez, R. J., Rebolo, R., & Perez de Taoro, M. R. 1995, A&A, 302, 184
García Pérez, A. E., & Primas, F. 2006, A&A, 447, 299
Goldreich, P., Murray, N., & Kumar, P. 1994, ApJ, 424, 466
Grevesse, N., & Sauval, A. J. 1998, Space Sci. Rev., 85, 161
Herbig, G. H. 1965, ApJ, 141, 588
Hobbs, L. M., Iben, I. J., & Pilachowski, C. 1989, ApJ, 347, 817
Jones, B. F., Fischer, D., Shetrone, M., & Soderblom, D. R. 1997, AJ, 114, 352
Jones, B. F., Fischer, D., & Soderblom, D. R. 1999, AJ, 117, 330
Kawaler, S. D. 1988, ApJ, 333, 236
Lambert, D. L., & Reddy, B. E. 2004, MNRAS, 349, 757
Lèbre, A., de Laverny, P., De Medeiros, J. R., Charbonnel, C., & da Silva, L. 1999, A&A, 345, 936
Lodders, K. 2003, ApJ, 591, 1220
Maeder, A., & Zahn, J.-P. 1998, A&A, 334, 1000
Meibom, S. 2000, A&A, 361, 929
Meibom, S., Andersen, J., & Nordström, B. 2002, A&A, 386, 187
Michaud, G. 1986, ApJ, 302, 650
Michaud, G., Richard, O., Richer, J., & VandenBerg, D. A. 2004, ApJ, 606, 452
Montalbán, J., & Schatzman, E. 2000, A&A, 354, 943
Müller, E. A., Peytremann, E., & de La Reza, R. 1975, Sol. Phys., 41, 53
Pace, G., Pasquini, L., & François, P. 2008, A&A, 489, 403
Palacios, A., Talon, S., Charbonnel, C., & Forestini, M. 2003, A&A, 399, 603
Paquette, C., Pelletier, C., Fontaine, G., & Michaud, G. 1986, ApJS, 61, 177
Pasquini, L., Liu, Q., & Pallavicini, R. 1994, A&A, 287, 191
Pasquini, L., Randich, S., & Pallavicini, R. 1997, A&A, 325, 535
Pasquini, L., Randich, S., & Pallavicini, R. 2001, A&A, 374, 1017
Pasquini, L., Randich, S., Zoccali, M., et al. 2004, A&A, 424, 951
Primas, F., Duncan, D. K., Pinsonneault, M. H., Deliyannis, C. P., & Thorburn, J. A. 1997, ApJ, 480, 784
Randich, S., Primas, F., Pasquini, L., & Pallavicini, R. 2002, A&A, 387, 222
Randich, S., Primas, F., Pasquini, L., Sestito, P., & Pallavicini, R. 2007, A&A, 469, 163
Santos, N. C., Israelian, G., Randich, S., García López, R. J., & Rebolo, R. 2004, A&A, 425, 1013
Sestito, P., & Randich, S. 2005, A&A, 442, 615
Smiljanic, R., Pasquini, L., Primas, F., et al. 2008, MNRAS, 385, L93
Smiljanic, R., Gauderon, R., North, P., et al. 2009a, A&A, 502, 267
Smiljanic, R., Pasquini, L., Bonifacio, P., et al. 2009b, A&A, 499, 103
Soderblom, D. R., Oey, M. S., Johnson, D. R. H., & Stone, R. P. S. 1990, AJ, 99, 595
Stephens, A., Boesgaard, A. M., King, J. R., & Deliyannis, C. P. 1997, ApJ, 491, 339
Swenson, F. J., & Faulkner, J. 1992, ApJ, 395, 654
Talon, S., & Charbonnel, C. 1998, A&A, 335, 959
Talon, S., & Charbonnel, C. 2003, A&A, 405, 1025
Talon, S., & Charbonnel, C. 2005, A&A, 440, 981
Talon, S., & Zahn, J.-P. 1997, A&A, 317, 749
Théado, S., & Vauclair, S. 2003, ApJ, 587, 795
Wallerstein, G., Herbig, G. H., & Conti, P. S. 1965, ApJ, 141, 610
Young, P. A., Knierman, K. A., Rigby, J. R., & Arnett, D. 2003, ApJ, 595, 1114
Zahn, J.-P. 1992, A&A, 265, 115
Zappala, R. R. 1972, ApJ, 172, 57

5.3 Low- and intermediate-mass solar metallicity stars up to the end of the AGB

Thermohaline instability and rotation-induced mixing
I - Low- and intermediate-mass solar metallicity stars up to the end of the AGB

C. Charbonnel and N.Lagarde
A&A 522, A10 (2010)

In this article we present the effects of thermohaline instability induced by ^{3}He-burning that sets in above the RGB bump, and rotation-induced mixing on the evolution and chemical properties of stars from the ZAMS to the AGB tip, in the 1-4 $M_\odot$ range at solar metallicity. In order to quantify precisely the impact of each transport process at the various evolutionary phases, we have computed models with the following assumptions: (1) Standard models (no mixing mechanism other than convection); (2) Models including thermohaline mixing only (rotation velocity V=0); (3) Models including thermohaline mixing and rotation-induced processes for different initial rotation velocities. Predictions are compared to data for lithium, $^{12}C/^{13}C$, [N/C], [Na/Fe], $^{16}O/^{17}O$, and $^{16}O/^{18}O$ for field and open cluster stars with well-defined masses and evolutionary status (RGB, clump, early-AGB, and planetary nebula phases).

Results

We find that non-standard theoretical and observational behaviours for these species are in very good agreement over the whole scrutinized mass range. Thermohaline mixing is confirmed to be the main physical process governing the surface abundances of ^{3}He, ^{7}Li, C, and N for stars more evolved than the RGB bump in all the models with initial masses below 2.2 $M_\odot$. Although its efficiency is increasing with decreasing initial stellar mass. In all cases ^{3}He decreases by a large fraction in the stellar yields compared to the standard models, although we find that low-mass stars remain net producers of ^{3}He (see Lagarde et al. 2011, and §5.3, for more details on this light element).

It is also found that thermohaline mixing leads to lithium production on the TP-AGB phase, as first shown by Stancliffe (2010) in the case of low-metallicity stars. However, the Li yields remain negative, and these stars are not expected to contribute to Galactic Li enrichment. In one 2.0 $M_\odot$ model computed up to the AGB tip thermohaline mixing was found to help initiating the occurrence of the third dredge-up during the TP-AGB phase.

On the other hand, rotation-induced mixing modifies the internal chemical structure of main sequence stars, although its signatures are revealed only later in the evolution when the first dredge-up occurs. Rotation is found to favour the occurrence of thermohaline mixing, in the mass range between $\sim$ 1.5 and 2.2 $M_\odot$ (in other words, in this mass range indeed, the thermohaline instability occurs earlier on the red giant branch than in non-rotating models). Finally, rotation accounts for the observed star-to-star abundance variations at a given evolutionary status, and is necessary to explain the features of CN-processed material in intermediate-mass stars. Overall, the present models account for the observational constraints very well over the whole mass range presently investigated.

A&A 522, A10 (2010)
DOI: 10.1051/0004-6361/201014432

Astronomy & Astrophysics

Thermohaline instability and rotation-induced mixing

I. Low- and intermediate-mass solar metallicity stars up to the end of the AGB

C. Charbonnel[1,2] and N. Lagarde[1]

[1] Geneva Observatory, University of Geneva, Chemin des Maillettes 51, 1290 Versoix, Switzerland
e-mail: `Corinne.Charbonnel@unige.ch`
[2] Laboratoire d'Astrophysique de Toulouse-Tarbes, CNRS UMR 5572, Université de Toulouse, 14 Av. E. Belin, 31400 Toulouse, France

Received 15 March 2010 / Accepted 21 June 2010

ABSTRACT

Context. Numerous spectroscopic observations provide compelling evidence for non-canonical processes that modify the surface abundances of low- and intermediate-mass stars beyond the predictions of standard stellar theory.
Aims. We study the effects of thermohaline instability and rotation-induced mixing in the 1–4 $M_\odot$ range at solar metallicity.
Methods. We present evolutionary models by considering both thermohaline and rotation-induced mixing in stellar interior. We discuss the effects of these processes on the chemical properties of stars from the zero age main sequence up to the end of the second dredge-up on the early-AGB for intermediate-mass stars and up to the AGB tip for low-mass stars. Model predictions are compared to observational data for lithium, ^{12}C/^{13}C, [N/C], [Na/Fe], ^{16}O/^{17}O, and ^{16}O/^{18}O in Galactic open clusters and in field stars with well-defined evolutionary status, as well as in planetary nebulae.
Results. Thermohaline mixing simultaneously accounts for the observed behaviour of ^{12}C/^{13}C, [N/C], and lithium in low-mass stars that are more luminous than the RGB bump, and its efficiency is increasing with decreasing initial stellar mass. On the TP-AGB, thermohaline mixing leads to lithium production, although the ^{7}Li yields remain negative. Although the ^{3}He stellar yields are much reduced thanks to this process, we find that solar-metallicity, low-mass stars remain net ^{3}He producers. Rotation-induced mixing is found to change the stellar structure so that in the mass range between ~1.5 and 2.2 $M_\odot$ the thermohaline instability occurs earlier on the red giant branch than in non-rotating models. Finally rotation accounts for the observed star-to-star abundance variations at a given evolutionary status, and is necessary to explain the features of CN-processed material in intermediate-mass stars.
Conclusions. Overall, the present models account for the observational constraints very well over the whole mass range presently investigated.

Key words. instabilities – stars: abundances – stars: interiors – stars: rotation – stars: evolution – hydrodynamics

1. Introduction

At all stages of their evolution, low- and intermediate-mass stars (LIMS) exhibit the signatures of complex physical processes that require challenging modelling beyond canonical (or standard) stellar theory[1]. The combined effects of rotation-induced mixing, atomic diffusion, and internal gravity waves, have been extensively studied and were shown to account self-consistently for observational patterns of light elements such as lithium and beryllium in main sequence and subgiant LIMS (see e.g. Charbonnel & Talon 2008; Smiljanic et al. 2009, and references therein). During the first dredge-up (1DUP, Iben 1967), the stellar surface chemical composition is further modified when the deepening convective envelope mixes the external layers with hydrogen-processed material. Dilution then changes the surface abundances of helium-3, lithium, beryllium, boron, carbon, nitrogen, and eventually sodium, with modification amplitudes that strongly depend on the initial stellar mass and metallicity (e.g. Sweigart et al. 1989; Charbonnel 1994; Boothroyd & Sackmann 1999). After the completion of the first dredge-up, both standard and recent rotating models (Chanamé et al. 2005; Palacios et al. 2006) predict no further variations in the surface abundance patterns until the stars start climbing the asymptotic giant branch (AGB).

Numerous observations provide, however, compelling evidence of a non-canonical mixing process that occurs when low-mass stars reach the so-called bump in the luminosity function on the red giant branch (RGB). At that phase, indeed, the surface carbon isotopic ratio drops, together with the abundances of lithium and carbon, while that of nitrogen increases slightly (Gilroy 1989; Gilroy & Brown 1991; Luck 1994; Charbonnel 1994; Charbonnel et al. 1998; Charbonnel & Do Nascimento 1998; Gratton et al. 2000; Tautvaišienė et al. 2000, 2005; Smith et al. 2002; Shetrone 2003; Pilachowski et al. 2003; Geisler et al. 2005; Spite et al. 2006; Recio-Blanco & de Laverny 2007; Smiljanic et al. 2009). Based on lithium observations, Charbonnel & Balachandran (2000) proposed that intermediate-mass stars suffer from a similar extra-mixing episode when they reach the equivalent of the bump on the early-AGB phase, after helium exhaustion.

Thermohaline mixing has recently been identified as the mechanism that governs the photospheric composition of

---

[1] By canonical we refer to the modelling of non-rotating, non-magnetic stars, in which convection is the only mechanism that drives mixing in stellar interiors.

low-mass bright[2] giants (Charbonnel & Zahn 2007b, hereafter CZ07). In such stars, this double diffusive instability is induced by the molecular weight inversion created by the ^{3}He(^{3}He, 2p)^{4}He reaction in the external wing of the hydrogen-burning shell. Indeed this peculiar reaction converts two particles into three and thus decreases the mean molecular weight, as already pointed out by Ulrich (1971) although in a different stellar context. The thermohaline instability is expected to set in after the first dredge-up when the star reaches the RGB luminosity bump. In terms of stellar structure, the RGB bump corresponds to the moment when the hydrogen-burning shell (hereafter HBS) encounters the chemical discontinuity created inside the star by the convective envelope at its maximum extent during the first dredge-up. When the source shell (which provides the stellar luminosity on the RGB) reaches the border of the H-rich previously mixed zone, the corresponding decrease in molecular weight of the H-burning layers induces a drop in the total stellar luminosity, thereby creating a bump in the luminosity function since stars spend a relatively long time at this location (i.e., Fusi Pecci et al. 1990; Charbonnel 1994; Charbonnel et al. 1998). Afterwards H-burning occurs in a region of uniform composition, allowing for the molecular weight inversion due to ^{3}He burning to show up and thus enabling the thermohaline instability to set in.

Actually it was Eggleton et al. (2006) who first drew attention to the destabilizing role of the mu-inversion due to ^{3}He-burning in a red giant. Their claim was based on a 3D simulation aimed at studying the core helium flash of low-mass red giants with the hydrodynamic code "Djehuty" and performed with a mu-profile drawn from a 1D evolutionary sequence (Dearborn et al. 2006), which fortuitously demonstrated what the authors called an "unexpected mixing"; they ascribed it to the well-known Rayleigh-Taylor instability (Eggleton et al. 2006, 2007). However CZ07 pointed out that in a star, as the inverse mu-gradient is gradually building up, the first instability to occur and to modify the mu-profile is the double-diffusive instability known in the literature under the generic name of thermohaline instability (Stern 1960). This important precision on the actual nature of the physical process operating in the star was acknowledged by Eggleton et al. (2008; see also Denissenkov & Pinsonneault 2008; and Cantiello & Langer 2010); it is not just a question of semantics, since these two instabilities – one dynamical and the other double diffusive – proceed on much different timescales. It is important to note that thermohaline instability has long been known to develop in other stellar situations whenever inverted molecular-weight gradients are built. This is the case for instance when helium- or carbon-rich material is deposited at the surface of a star in a mass-transferring binary (Stothers & Simon 1969; Stancliffe et al. 2007), when a star accretes heavy elements during planet formation (Vauclair 2004), or after the ignition of ^{4}He burning in a degenerate shell (i.e., core helium flash, see Thomas 1967, 1970). It also develops in stars where radiative levitation leads to the accumulation of heavy elements in outer stellar layers (Théado et al. 2009). Since the term "thermohaline" is long established in the literature, we see no reason to replace it by the expression "$\delta\mu$-mixing" as proposed by Eggleton et al. (2008).

CZ07 showed how nicely models including thermohaline mixing as described by the theoretical prescription advocated by Ulrich (1972, see Sect. 2.2) do account for the carbon isotopic ratio, as well as for the lithium, carbon, and nitrogen abundances in low-metallicity, low-mass bright giants (see also Stancliffe et al. 2009) and simultaneously reduce significantly the stellar yields of ^{3}He with respect to canonical models, as required by measurements of ^{3}He/H in Galactic HII regions (Balser et al. 1994, 1999; Bania et al. 1997, 2002; Tosi 1998; Dearborn et al. 1996; Charbonnel 2002; Chiappini et al. 2002; Romano et al. 2003).

Note that the connection between the so-called "helium-3 problem" and the behaviour of the carbon isotopes in RGB stars was long established. Indeed although it had not yet been identified, the mechanism responsible for the low ^{12}C/^{13}C values in bright giants was expected to lead to the destruction of ^{3}He by a large factor in the bulk of the stellar envelope as initially suggested by Rood et al. (1984; see also Hogan 1995; Charbonnel 1995; Wasserburg et al. 1995; Weiss et al. 1996; Sackmann & Boothroyd 1999; Eggleton et al. 2006; Balser et al. 2007). CZ07 results were confirmed by Eggleton et al. (2008) although with a simplistic phenomenological procedure to estimate the diffusion coefficient. Additionally, Cantiello & Langer (2008, 2010) reported that thermohaline instability can still occur during core helium-burning and beyond in stars that have kept a ^{3}He reservoir at these advanced phases. Finally Stancliffe et al. (2009) and Siess (2009) discussed the impact of this mechanism in low-metallicity intermediate-mass thermally pulsing AGB stars and in super-AGB stars respectively.

The signatures of thermohaline mixing induced by ^{3}He-burning have been observed in giants of both open and globular clusters, as well as in field stars including extremely metal-poor giants, and in stars belonging to extragalactic systems such as the Large Magellanic Cloud and the Sculptor galaxy (see references above). It appears thus to be a universal process that occurs independently of the stellar environment, although it may be inhibited in some rare RGB stars hosting strong fossil magnetic fields. Indeed Charbonnel & Zahn (2007a) examined the effect of a magnetic field on the thermohaline instability, and concluded that in a large fraction of the descendants of Ap stars thermohaline mixing should not occur. The relative number of such stars with respect to non-magnetic objects that undergo thermohaline mixing is very low (less than 5%, see i.e., Wolff 1968; North 1993; Power et al. 2007) and consistent with the statistical constraint coming from observations of the carbon isotopic ratio in evolved stars as estimated by Charbonnel & Do Nascimento (1998). It also reconciles the measurements of ^{3}He/H in Galactic HII regions with high values of ^{3}He observed in a couple of planetary nebulae (for more details see Charbonnel & Zahn 2007a).

However, the impact of thermohaline mixing on the stellar chemical properties appears to depend on the initial stellar mass and metallicity, as suggested by the observations of the carbon isotopic ratio (which is the most reliable signature of this mechanism) in giant stars over broad ranges in mass and metallicity (see references above). Until now, the theoretical background for these correlations is not firmly established (e.g., the mass range where thermohaline convection actually modifies the stellar surface composition), and the influence of other quantities such as the rotation history has never been investigated.

This is the aim of this series of papers where we investigate the occurrence and the impact of thermohaline mixing in stars of various initial masses and metallicities with non-canonical models, i.e., taking into account self-consistently this mechanism together with rotation-induced mixing. Here we focus on the solar metallicity case, with the main observational constraints coming from abundance determinations in evolved stars with well defined evolutionary status up to the early-AGB and belonging to open clusters with turnoff masses between ∼1 and 4 $M_{\odot}$ or to the field. We also use as observational constraints lithium abundance

---

[2] "Bright" refers here to stars that are more evolved than the RGB bump.

determinations in low-mass oxygen-rich AGB variables and carbon isotopic ratios in planetary nebulae. In Sect. 2 we present the input physics of our models. In Sect. 3 we discuss the predictions of our models computed with thermohaline mixing only, and then of our models that also include rotation-induced mixing. Theoretical predictions are compared to observations in Sect. 4 before we conclude in Sect. 5.

2. Input physics for the stellar models

We present models computed with the code STAREVOL (Siess et al. 2000; Palacios et al. 2003, 2006) at solar metallicity (with Asplund et al. 2005; chemical composition except for Ne for which we use the value derived by Cunha et al. 2006) for a range of initial stellar masses between 1 and 4 $M_\odot$. In order to quantify precisely the impact of each transport process at the various evolutionary phases, we will show predictions for models computed with the following assumptions: (1) standard models (no mixing mechanism other than convection); (2) models including thermohaline mixing only (rotation velocity $V = 0$); (3) models including thermohaline mixing and rotation-induced processes for different initial rotation velocities. All the models are computed up to the end of the second dredge-up on the early-AGB. Some of the low-mass models are followed along the TP-AGB up to the AGB tip.

2.1. Microphysics

We use the OPAL opacity tables (Iglesias & Rogers 1996) for $T > 8000$ K that account for C and O enrichments, and the Ferguson et al. (2005) data at lower temperatures. In both cases tables consistent with the assumed initial composition have been generated[3]. We follow the evolution of 53 chemical species from ^{1}H to ^{37}Cl using the nominal NACRE nuclear reaction rates (Angulo et al. 1999) by default and those given in Appendix A otherwise. The equation of state is described in details in Siess et al. (2000) and accounts for the non-ideal effects due to Coulomb interactions and pressure ionisation. The treatment of convection is based on the classical mixing length formalism with $\alpha_{\rm MLT} = 1.6$, and no convective overshoot is included. The mass loss rates are computed with Reimers (1975) formula (with $\eta_{\rm R} = 0.5$) up to the early-AGB phase, and with Vassiliadis & Wood (1993) prescription on the TP-AGB.

2.2. Thermohaline mixing

The thermohaline instability occurs in a stable stratification that satisfies the Ledoux criterion for convective instability:

$$\nabla_{\rm ad} - \nabla + \left(\frac{\varphi}{\delta}\right)\nabla_\mu > 0, \tag{1}$$

but where the molecular weight decreases with depth:

$$\nabla_\mu := \frac{{\rm d}\ln\mu}{{\rm d}\ln P} < 0 \tag{2}$$

with the classical notations for $\nabla = (\partial\ln T/\partial\ln P)$, $\varphi = (\partial\ln\rho/\partial\ln\mu)_{P,T}$ and $\delta = -(\partial\ln\rho/\partial\ln T)_{P,\mu}$, ∇_μ and $\nabla_{\rm ad}$ being respectively the molecular weight gradient and the adiabatic gradient.

For the turbulent diffusivity produced by the thermohaline instablity we use the prescription advocated by CZ07 based on Ulrich (1972) arguments for the aspect ratio α (length/width) of the salt fingers as supported by laboratory experiments Krishnamurti (2003) and including Kippenhahn et al. (1980) extended expression for the case of a non-perfect gas (including radiation pressure, degeneracy):

$$D_{\rm t} = C_{\rm t}\,K\left(\frac{\varphi}{\delta}\right)\frac{-\nabla_\mu}{(\nabla_{\rm ad}-\nabla)} \quad \text{for } \nabla_\mu < 0, \tag{3}$$

with K the thermal diffusivity.

$$C_{\rm t} = \frac{8}{3}\pi^2\alpha^2, \tag{4}$$

and with $\alpha = 5$ (Ulrich 1972) this coefficient is $C_{\rm t} = 658$. For consistency reasons we assume actually $C_{\rm t} = 1000$ as in CZ07.

2.3. Rotation-induced mixing

For the treatment of rotation-induced mixing we proceed as follows. Solid-body rotation is assumed when the star arrives on the zero age main sequence (ZAMS). Typical initial (i.e., ZAMS) rotation velocities are chosen depending on the stellar mass based on observed rotation distributions in young open clusters (Gaigé 1993). Surface braking by a magnetic torque is applied for stars with an effective temperature on the ZAMS lower than 6900 K that have relatively a thick convective envelope as discussed in Talon & Charbonnel (1998) and Charbonnel & Talon (1999); the adopted braking law follows the description of Kawaler (1988). From the ZAMS on the evolution of the internal angular momentum profile is accounted for with the complete formalism developed by Zahn (1992) and Maeder & Zahn (1998) that takes into account advection by meridional circulation and diffusion by shear turbulence (for a description of the implementation in STAREVOL, see Palacios et al. 2003, 2006; and Decressin et al. 2009). The transport of chemicals resulting from meridional circulation and both horizontal and vertical turbulence is computed as a diffusive process throughout the evolution. The complete treatment for the transport of angular momentum and chemicals is applied up to the RGB tip or up to the second dredge-up for the stars with initial masses below or above 2.0 $M_\odot$ respectively. The convective envelope is supposed to rotate as a solid body (uniform angular velocity) throughout the evolution; we discuss the implications of this assumption in Sect. 3.2.2. The transport of angular momentum by internal gravity waves (which is efficient only in main sequence stars with effective temperatures on the ZAMS lower than 6500 K, see Talon & Charbonnel 2003), is neglected.

In the present work the transport coefficients for chemicals associated to thermohaline and rotation-induced mixings are simply added in the diffusion equation and we do not consider the possible interactions between the two mechanisms, nor with magnetic diffusion. As a matter of fact under the present assumptions the thermohaline diffusion coefficient is several orders of magnitude higher than the total diffusion coefficient associated to rotation (see Sect. 3). This is confirmed by Cantiello & Langer (2010) who also show that magnetic diffusion in RGB stars is much less efficient than thermohaline mixing. However, we should keep an eye on future hydrodynamic calculations that are required to evaluate with confidence the possible interactions of thermohaline fingers with differential rotation and magnetic fields in red giants.

---

[3] `http://opalopacity.llnl.gov` and `http://webs.wichita.edu/physics/opacity`

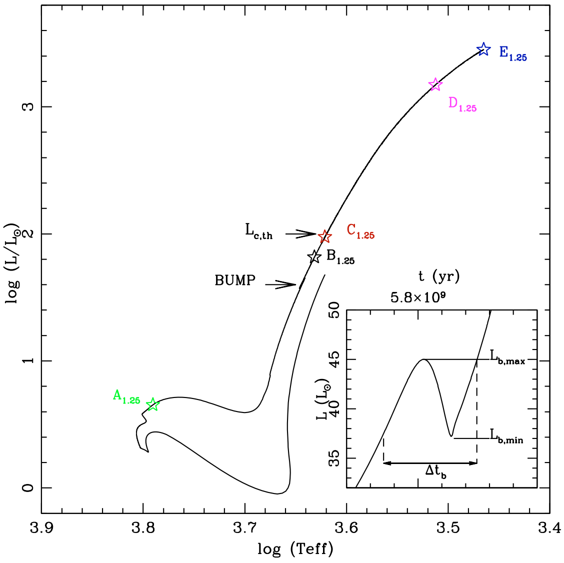

Fig. 1. Evolutionary track (from the pre-main sequence up to the tip of the RGB) of the 1.25 $M_\odot$ model computed with thermohaline mixing only. The minimum and maximum luminosity of the bump are indicated ($L_{\rm b,min}$ and $L_{\rm b,max}$ respectively) as well as the luminosity $L_{\rm c,th}$ at which the thermohaline instability reaches the bottom of the convective envelope. Open symbols labelled $A_{1.25}$ to $E_{1.25}$ correspond to evolution points for which some stellar properties are discussed in the text. The panel inserted on the right of the figure shows the evolution of the stellar luminosity around the bump as a function of time. $\Delta t_{\rm b}$ is the time spend by the star within the luminosity bump and equals to 3.9×10^7 yrs in the present case.

3. Theoretical predictions

We first consider the case of low-mass stars that ignite helium-burning by a flash at the tip of the RGB well above (in terms of luminosity) the bump. With the considered metallicity and input physics this corresponds to stars with initial masses below $\sim$2.2 $M_\odot$. We present detailed predictions for a 1.25 $M_\odot$ model computed without and with rotation (but with thermohaline mixing in both cases) in Sects. 3.1 and 3.2 respectively, and discuss the uncertainties on the thermohaline diffusivity in Sect. 3.3. Section 3.4 is devoted to the case of stars in the mass range 1.5–2.2 $M_\odot$. Then in Sect. 3.5 we shortly discuss the predictions for intermediate-mass stars.

3.1. 1.25 $M_\odot$ model with thermohaline mixing only

Figure 1 presents the evolutionary track in the Hertzsprung-Russell diagram (HRD) of the 1.25 $M_\odot$ model computed with thermohaline mixing only (no rotation). Several points are selected along the track in order to discuss the evolution of some relevant stellar properties. $A_{1.25}$ corresponds to the turnoff, when the hydrogen mass fraction in the stellar core is below 10^{-8}. $B_{1.25}$ is chosen at intermediate luminosity between the bump (which minimum and maximum luminosities, $L_{\rm b,min}$ and $L_{\rm b,max}$, are also shown) and the moment when the thermohaline zone "contacts" the convective envelope (see below). $C_{1.25}$ stands at the "contact" luminosity $L_{\rm c,th}$ where surface abundances start changing due to thermohaline mixing. $D_{1.25}$ and $E_{1.25}$ are close to and at the tip of the RGB (then the mass of the helium core is 0.428 and 0.486 $M_\odot$ respectively, for a total stellar mass of 1.14 and 1.03 $M_\odot$).

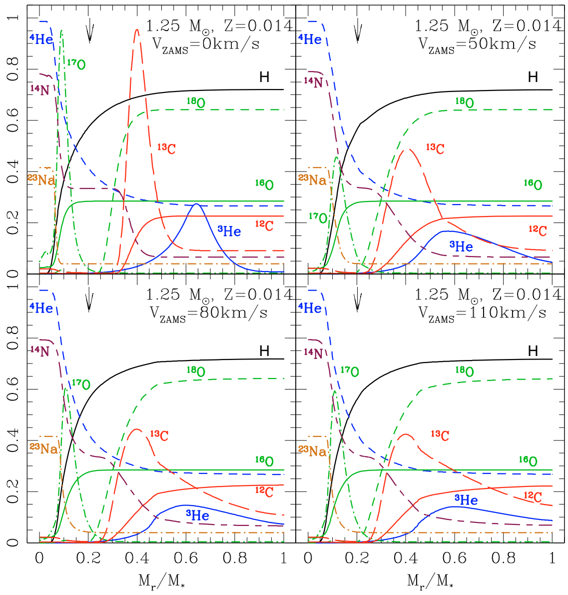

Fig. 2. Chemical structure at the turnoff of the 1.25 $M_\odot$ star computed for different initial rotation velocities as indicated. The mass fractions are multiplied by 100 for ^{3}He, ^{12}C, and ^{14}N, by 2500 for ^{13}C, by 50, 900, and 5×10^4 for ^{16}O, ^{17}O, and ^{18}O respectively, and by 1500 for ^{23}Na. The vertical arrows show, in all cases, the maximum depth reached by the convective envelope at its maximum extent during the first dredge-up.

Table 1. Luminosities of the bump ($L_{\rm b,min}$ and $L_{\rm b,max}$, see Fig. 1), of the evolution point when the thermohaline zone contacts the convective envelope ($L_{\rm c,th}$), and of the RGB tip ($L_{\rm tip}$), for the low-mass stars at various initial rotation velocities.

M ($M_\odot$)	$V_{\rm zams}$ (km s^{-1})	$L_{\rm b,min}$ ($L_\odot$)	$L_{\rm b,max}$ ($L_\odot$)	$L_{\rm c,th}$ ($L_\odot$)	$L_{\rm tip}$ ($L_\odot$)
1.25	0	37	45	94	2821
	50	25	25	64	2798
	80	15	16	72	2807
	110	16	17	72	2798
1.5	0	50	59	784	2903
	110	27	36	101	2869
1.8	0	74	83	1907	2995
	110	51	57	145	2768
2.0	0	79	87	1908	2994
	110	64	87	250	2872
	180	74	117	256	2670
	250	76	95	232	2416

3.1.1. Main sequence and subgiant branch

Figure 2 depicts the chemical structure of a 1.25 $M_\odot$ star at the end of central hydrogen-burning (point $A_{1.25}$; top left panel for the present case without rotation-induced mixing). The most fragile elements lithium, beryllium, and boron, which burn at relatively low-temperatures and are preserved only in the most external stellar layers, are not shown here. On the pre-main sequence, pristine deuterium is converted to ^{3}He, while on the

Table 2. Surface values of ^{12}C/^{13}C, [C/Fe], [N/Fe], [Na/Fe], N(Li) and N(Be) at the end of the first and second dredge-up (1DUP and 2DUP respectively) and at the RGB tip (RGB) for models computed under different assumptions: Standard (st, no thermohaline nor rotation-induced mixing), with thermohaline mixing only (th), and with both thermohaline and rotation-induced mixing (th+rot).

M		$V_{\rm ZAMS}$	^{12}C/^{13}C			[C/Fe]			[N/Fe]			N(Li)			N(Be)			[Na/Fe]		
($M_\odot$)		(km s^{-1})	1DUP	RGB	2DUP	1DUP	RGB	2DUP	1DUP	RGB	2DUP	1DUP	RGB	2DUP	1DUP	RGB	2DUP	1DUP	RGB	2DUP
1	st	0	28.8	28.8	25	–0.05	–0.05	–0.07	0.16	0.16	0.21	1.1	1.1	0.85	0.34	0.34	0.15	0	0	0
	th	0	28.8	8.1	7.7	–0.05	–0.09	–0.10	0.16	0.25	0.28	1.1	–1.3	–1.87	0.33	–1.65	–2.1	0	0	0
1.1	th	0	27.35	8.9	8.5	–0.07	–0.11	–0.12	0.22	0.28	0.33	1.34	–0.58	–0.97	0.27	–1.33	–1.63	0	0	0
1.25	st	0	25.74	25.78	–	–0.10	–0.10	–	0.27	0.27	–	1.46	1.46	–	0.18	0.18	–	0	0	–
	th	0	25.6	10.4	9.9	–0.10	–0.12	–0.14	0.37	0.31	0.33	1.45	0.07	–0.26	0.18	–0.97	–1.23	0	0	0
	th+rot	50	23.69	10	–	–0.12	–0.14	–	0.39	0.34	–	–4.35	–3.25	–	–2.12	–3.24	–	0	0	–
	th+rot	80	21.6	9.6	9.1	–0.13	–0.15	–0.16	0.31	0.35	0.36	–6.2	–3.2	–3.9	–3.7	–4.8	–5.3	0	0	0
	th+rot	110	18.6	9.1	8.5	–0.14	–0.16	–0.18	0.33	0.37	0.38	–6.87	–3.25	–3.94	–5.12	–6.21	–6.74	0	0	0
1.3	th	0	24.8	11	–	–0.11	–0.13	–	0.39	0.32	–	1.46	0.22	–	0.15	0.88	–	0	0	–
1.4	st	0	24.1	24.1	23.3	–0.13	–0.13	–0.14	0.31	0.31	0.32	1.46	1.46	1.37	0.01	0.01	0.03	0	0	0
	th	0	24.2	12.14	–	–0.13	–0.14	–	0.31	0.33	–	1.46	0.46	–	0.01	–0.73	–	0	0	–
1.5	st	0	23.2	23.2	22.6	–0.14	–0.14	–0.15	0.33	0.33	0.34	1.45	1.45	1.37	0.06	0.06	0	0	0	0
	th	0	23.3	15.3	–	–0.14	–0.15	–	0.33	0.34	–	1.45	1.03	–	0.06	–0.30	–	0	0	–
	th+rot	110	21.2	12.8	11.8	–0.16	–0.18	–0.18	0.36	0.38	0.39	0.43	–0.28	–0.87	–0.47	–1.06	–1.49	0.02	0.02	0.02
1.7	st	0	22.5	22.5	21.9	–0.16	–0.16	–0.17	0.36	0.36	0.37	1.41	1.41	1.34	–0.02	–0.02	–0.07	0	0	0
	th	0	22.6	18.6	16.7	–0.16	–0.17	–0.17	0.36	0.36	0.37	1.42	1.24	0.95	–0.004	–0.16	–0.39	0	0	0
1.8	th	0	22.2	19.9	–	–0.17	–0.18	–	0.37	0.37	–	1.41	1.32	–	–0.03	–0.11	–	0	0	–
	th+rot	110	20.04	15.24	–	–0.18	–0.19	–	0.31	0.31	–	0.59	0.19	–	–0.42	–0.75	–	0.15	0.15	–
1.9	th	0	21.9	20.2	18.7	–0.18	–0.18	–0.19	0.38	0.38	0.39	1.39	1.31	1.05	–0.062	–0.13	–0.32	0	0	0
2.0	st	0	21.8	21.8	21.3	–0.19	–0.19	–0.19	0.39	0.39	0.40	1.38	1.38	1.31	–0.07	–0.07	–0.11	0.04	0.04	0.04
	th	0	21.8	20.8	19.6	–0.19	–0.19	–0.20	0.40	0.39	0.40	1.37	1.31	1.10	–0.07	–0.12	–0.28	0	0	0
	th+rot	110	19.4	16.6	16.2	–0.22	–0.22	–0.23	0.47	0.47	0.47	0.55	0.33	0.16	–0.48	–0.65	–0.77	0.18	0.18	0.18
	th+rot	180	17.7	15.3	15	–0.23	–0.23	–0.24	0.47	0.48	0.48	–0.33	–0.54	–0.92	–0.86	–1.03	–1.21	0.18	0.18	0.18
	th+rot	250	14.8	13.4	13.2	–0.22	–0.23	–0.23	0.47	0.48	0.48	–0.96	–1.15	–1.3	–1.29	–1.44	–1.55	0.22	0.22	0.22
2.5	st	0	21.2	21.2	21.1	–0.21	–0.21	–0.21	0.45	0.45	0.45	1.34	1.34	1.25	–0.11	–0.11	–0.16	0	0.16	0.16
	th	0	21.2	21.4	20.9	–0.21	–0.27	–0.27	0.45	0.45	0.45	1.36	1.36	1.27	–0.01	–0.01	–0.14	0	0.16	0.16
	th+rot	300	17.2	14.7	13	–0.53	–0.53	–0.53	0.55	0.82	0.86	–4.99	–4.99	–5.12	–3.77	–3.77	–3.91	0	0.76	0.85
2.7	th+rot	110	19.3	19.3	19.1	–0.24	–0.24	–0.24	0.52	0.52	0.53	0.53	0.53	0.44	–0.49	–0.49	–0.54	0.28	0.28	0.28
	th+rot	250	16.4	16.4	–	–0.28	–0.28	–	0.56	0.56	–	–0.95	–0.95	–	–1.28	–1.28	–	0.32	0.32	–
	th+rot	300	18	15.1	–	–0.53	–0.53	–	0.83	0.84	–	–4.9	–4.9	–	–3.79	–3.79	–	0.76	0.76	–
3.0	th	0	20.85	20.84	20.55	–0.21	–0.21	–0.22	0.47	0.48	0.48	1.30	1.30	1.15	–0.15	–0.15	–0.23	0.031	0.22	0.23
4.0	st	0	20.48	20.48	19.94	–0.21	–0.21	–0.22	0.49	0.49	0.50	1.28	1.28	1.02	–0.16	–0.16	–0.33	0	0.26	0.28
	th	0	20.49	20.49	19.86	–0.20	–0.20	–0.22	0.49	0.49	0.51	1.29	1.29	1.03	–0.16	–0.16	–0.33	0.25	0.25	0.28
	th+rot	300	14	14	13.82	–0.31	–0.31	–0.32	0.61	0.61	0.62	–1.76	–1.77	–1.94	–1.77	–1.77	–1.87	0.4	0.4	0.42

main sequence H-burning through the pp-chains builds up a ^{3}He peak at $M_{\rm r}/M_* \sim 0.65$. Deeper inside the star the ^{13}C peak results from the competition between the ^{12}C(p, γ)^{13}N($\beta+\nu$)^{13}C and ^{13}C(p, γ)^{14}N reactions. ^{12}C and ^{16}O are partially converted into ^{14}N which abundance profile presents a double plateau. ON-cycling results in ^{18}O depletion and in the building up of a ^{17}O peak. In the very central regions, ^{23}Na is produced through proton capture by ^{22}Ne.

When the star moves towards the RGB its convective envelope deepens and engulfes most of the regions that have been nuclearly processed (1DUP). In Fig. 2 the maximum depth reached by the convective envelope is indicated by the vertical arrow. The so-called first dredge-up results in severe changes in the surface chemical properties of the star (see Fig. 6) since surface material is diluted with matter enriched in ^{3}He, ^{13}C, and ^{14}N, but depleted in ^{12}C and ^{18}O. In the standard models the surface abundances are not predicted to change anymore after the end of the first dredge-up until the star reaches the early-AGB. However, as we shall see below, thermohaline mixing induces a second modification of the stellar chemical appearance on the upper end of the RGB.

3.1.2. Predictions up to the RGB tip

As discussed in Sect. 1, the thermohaline instability induced by the ^{3}He(^{3}He, 2p)^{4}He reaction is able to set in on the RGB only after the star has reached the luminosity bump, when the HBS crosses the molecular weight barrier left behind by the convective envelope when it reached its maximum extent. In the case where thermohaline mixing is the only transport process considered within radiative regions (i.e., rotation-induced mixing being neglected), we find that for solar metallicity stars with initial mass lower or equal to 1.5 $M_\odot$, the thermohaline instability soon extends between the external wing of the HBS and the base of the convective envelope (see Table 1). This is shown for the 1.25 $M_\odot$ model in Fig. 3 where the thermohaline region is indicated in blue. For this model, the bump is located between $L_{\rm b,min} = 37\ L_\odot$ and $L_{\rm b,max} = 45\ L_\odot$, and the thermohaline instability contacts the convective envelope when the stellar luminosity is $L_{\rm c,th} \sim 94\ L_\odot$. As far as timescales are concerned, the 1.25 $M_\odot$ model spends 3.9×10^7 years in the bump (i.e., in the luminosity interval between $L_{\rm b,min}$ and $L_{\rm b,max}$, see Fig. 1), and then reaches $L_{\rm c,th}$ after 2.65×10^7 years.

Figure 4 depicts the temporal evolution along the RGB of the abundance profiles of H, ^{3}He, of the carbon isotopic ratio, and of the thermohaline diffusion coefficient $D_{\rm thc}$. The variable δM is a relative mass coordinate allowing for a blow-up of the radiative region above the HBS.

Namely,

$$\delta M = \frac{M_{\rm r} - M_{\rm HBS}}{M_{\rm BCE} - M_{\rm HBS}}.$$

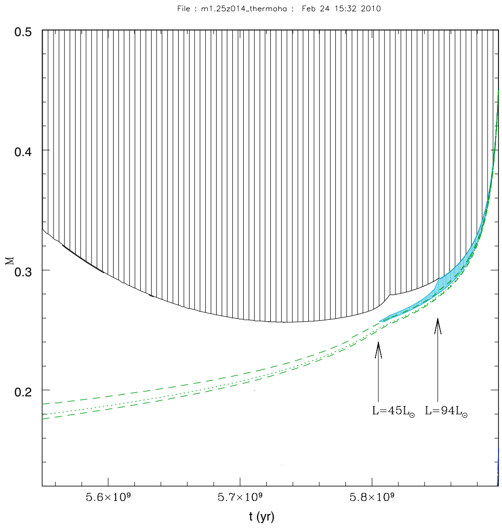

Fig. 3. Kippenhahn diagram for the 1.25 $M_\odot$ star computed with thermohaline mixing (no rotation-induced processes). Here we focus on the evolution phase around the RGB luminosity bump (located at a total stellar luminosity of $\sim$45 $L_\odot$ as indicated by the left arrow). Hatched area is the convective envelope. Green dotted lines delimit the hydrogen-burning shell above the degenerate helium core. The zone where the thermohaline instability develops is shown in hatched blue. The right arrow indicates the total stellar luminosity ($L_{\rm c,th} \sim 94$ $L_\odot$) at which the thermohaline region extends up to the convective envelope and thus when the surface chemical composition starts changing.

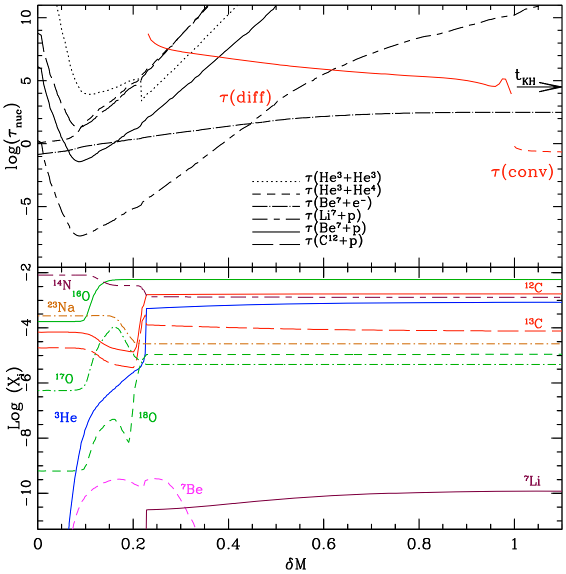

Fig. 5. 1.25 $M_\odot$ model with thermohaline mixing (no rotation) at the evolution point $C_{1.25}$ – (*top*) Lifetime of ^{3}He, ^{7}Li, ^{7}Be, and ^{12}C, and convective and thermohaline diffusive timescales (in years). The transition between the convective envelope and the radiative region occurs at $\delta M = 1$. (*Bottom*) Abundance profiles (in mass fraction) of relevant species in the same region.

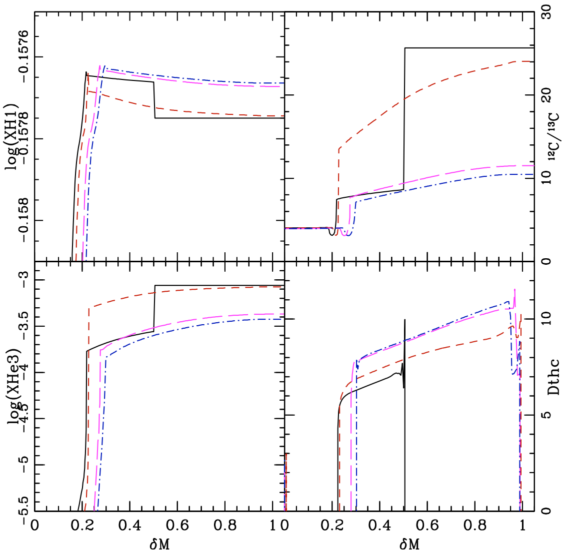

Fig. 4. Profiles of the abundances (in mass fraction) of H, ^{3}He, of the carbon isotopic ratio, and of the thermohaline diffusion coefficient at various evolution points on the RGB (see Fig. 1): slightly above the bump (point $B_{1.25}$, black solid line), at the luminosity of the contact (point $C_{1.25}$, red dashed line), close from the RGB tip (point $D_{1.25}$, magenta long dashed line), and at the RGB tip (point $E_{1.25}$, blue dot-dashed line). The abscissa is the scaled mass coordinate δM that allows a blow up of the region of interest ($\delta M = 0$ at the base of the HBS and $\delta M = 1$ at the base of the convective envelope).

It is equal to 1 at the base of the convective envelope $M_{\rm BCE}$ and to 0 at the base of the HBS $M_{\rm HBS}$ (which is defined as the depth where the hydrogen mass fraction equals 10^{-10}) . On each graph the black solid lines correspond to the evolution point $B_{1.25}$ on the HRD when the thermohaline region is still quenched in a very tiny region, while the other curves correspond to latter times (points $C_{1.25}$, $D_{1.25}$, and $E_{1.25}$) when the thermohaline instability has extended up to the base of the convective envelope. The maximum depth of the thermohaline unstable region corresponds to the layer where the ^{3}He(^{4}He, γ)^{7}Be reaction becomes faster than ^{3}He(^{3}He, 2p)^{4}He ($\delta M \sim 0.2$; see upper panel in Fig. 5). There the hydrogen profile shows a peak which maximum is located at the depth where the reaction ^{3}He(^{3}He, 2p)^{4}He is the fastest. As soon as the thermohaline instability sets in, fresh protons diffuse outwards, spreading out the molecular-weight inversion and enlarging the thermohaline region until it reaches the convective envelope. Simultaneously ^{3}He diffuses from the convective envelope inwards, which fuels the thermohaline instability. ^{12}C and ^{13}C diffuse respectively inwards and outwards, leading to a decrease of the surface carbon isotopic ratio. ^{14}N also diffuses outwards. Among the oxygen isotopes, only ^{18}O is affected, which leads to a slight increase of the ^{16}O/^{18}O surface ratio while ^{16}O/^{17}O does not change. Elements with higher atomic numbers such as ^{23}Na, which burn or are produced at higher temperature than that of the maximum depth of the thermohaline region, are unaffected. In Fig. 5 one can see also that in the external wing of the HBS below $\delta M \sim 0.6$, the thermohaline diffusion timescale τ(diff) is longer than both τ(^{7}Be + e$^-$) and τ(^{7}Li+p). As a consequence no fresh ^{7}Li shows up at the stellar surface on the RGB for the value of the coefficient C_t chosen for the computations. Rather, the surface ^{7}Li abundance decreases as this fragile element is drained from the convective

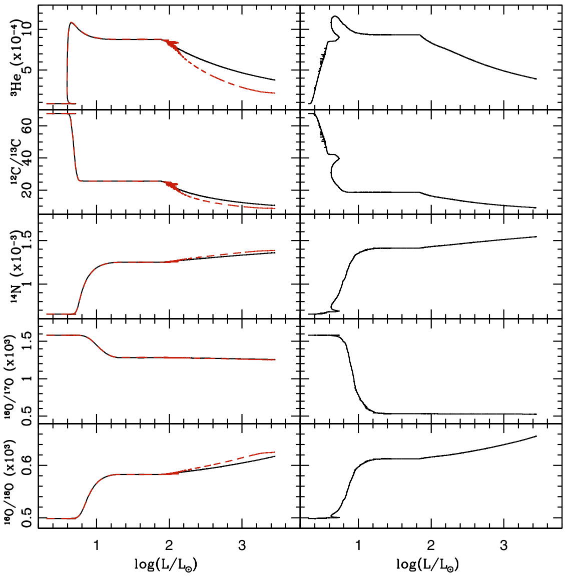

Fig. 6. Evolution of the surface abundances of ^{3}He and ^{14}N (in mass fraction) and of the carbon and oxygen isotopic ratios as a function of stellar luminosity for the 1.25 $M_\odot$ models computed without (*left*) and with rotation (initial rotation velocity of 110 km s^{-1}, *right*). Thermohaline instablity is accounted for in both cases. In *the left panels* the black and red lines correspond to $C_t = 10^3$ and 10^4 respectively, while in *the right panels* $C_t = 10^3$. Predictions are shown from the zero age main sequence up to the RGB tip. In the rotating case the first dredge-up starts at lower luminosity and ends at $\log(L/L_\odot) \sim 1$ with slightly stronger abundance modifications than in the standard case. Also, thermohaline mixing sets in slightly earlier on the RGB at $\log(L_{c,th}/L_\odot) \sim 1.9$ when rotation is accounted for.

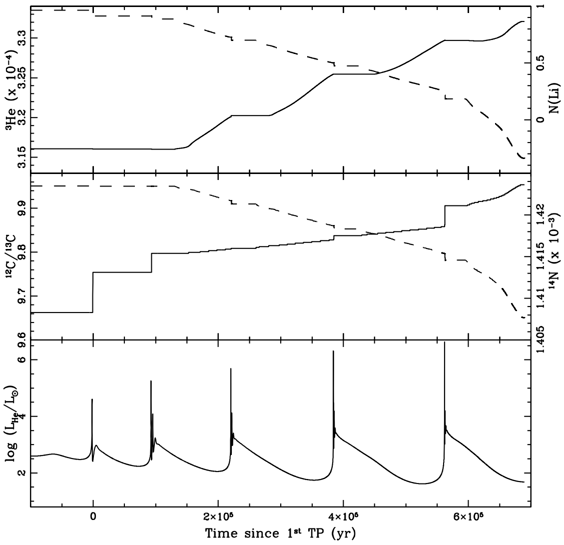

Fig. 7. Evolution of the surface abundances of ^{3}He and ^{7}Li (*top*, dashed and solid lines respectively), of ^{14}N and of the carbon isotopic ratio (*middle*, solid and dashed lines respectively), and of the helium-burning luminosity and total stellar mass (*bottom*, solid and dashed lines respectively) on the TP-AGB of the 1.25 $M_\odot$ model computed with thermohaline mixing only. The abscissa is the time since the first thermal pulse.

envelope downwards. For the 1.25 $M_\odot$ non-rotating model the value of N(Li)[4] at the RGB tip is ~0 (see Table 2 and Fig. 10 in Sect. 3.3).

The evolution of the surface abundances from the zero age main sequence up to the RGB tip is shown in Fig. 6 (left panels for the present case without rotation-induced mixing). One sees clearly the signatures of the first dredge-up at $\text{Log}(L/L_\odot) \sim 0.6$ that leads to an increase of the surface abundances of ^{3}He, ^{13}C, ^{14}N, and ^{17}O, and of the ^{16}O/^{18}O ratio, and to a decrease of ^{12}C, ^{18}O, of the ^{12}C/^{13}C and ^{16}O/^{17}O ratios as the convective envelope digs into the regions that have been nuclearly processed on the main sequence (see Fig. 2). Then all surface abundances level off while the star ascends the RGB up to the bump[5]. At $\log(L/L_\odot) \sim 2$, thermohaline mixing does lead to a second change in the stellar surface composition. It induces in particular a second drop of the carbon isotopic ratio and efficiently destroys ^{3}He and ^{7}Li (see Fig. 10) while ^{14}N and ^{16}O/^{18}O slightly increase. We note that the ^{3}He surface abundance at the tip of the RGB is much reduced compared to its value after the first dredge-up, although it remains higher than the initial value the star is born with. This is due to the combination of several factors related to the thermohaline diffusion timescale on one hand, and to the compactness of the HBS. More specifically, the final ^{3}He surface abundance can in principle decrease down to the value of ^{3}He at the bottom of the thermohaline unstable region (i.e., at $\delta M \sim 0.3$ in the 1.25 $M_\odot$ case; see Fig. 4). However, the timescale for thermohaline diffusion in this model is such that the surface ^{3}He at the RGB tip saturates at a higher value. In the case of low-mass, low-metallicity stars presented in CZ07, the thermohaline unstable region is more compact and has a steeper temperature gradient, resulting in a more efficient decrease of the surface ^{3}He abundance than in the present case. The same reasoning applies to the surface abundance changes in ^{12}C and ^{13}C so that the carbon isotopic ratio at the tip of the RGB saturates here to a value of the order of 10, while lower ratios closer from the equilibrium value are reached in low-mass, low-metallicity stars (see Figs. 3 and 4 of CZ07).

3.1.3. Predictions on the AGB

After helium ignition at the RGB tip, the total stellar luminosity drops down to the location of the clump (at $\text{Log}(L/L_\odot) \sim 1.7$ for the 1.25 $M_\odot$ model discussed here). A very modest decrease of the surface ^{7}Li and ^{12}C/^{13}C occurs when the star starts ascending the early-AGB due to a second deepening of the convective envelope (see Table 2). Also, ^{3}He (in mass fraction) decreases very slightly from 3.7×10^{-4} to 3.3×10^{-4}. In other words, some ^{3}He remains in the external convective layers when the star enters the thermal pulse phase on the AGB (TP-AGB) and is available to drive thermohaline mixing further as discussed below.

This 1.25 $M_\odot$ model was computed until the end of the superwind phase (at that point the total stellar mass is 0.567 $M_\odot$ and the mass of the envelope is 0.017 $M_\odot$). Meanwhile it has undergone five thermal pulses. In the present study we assume no convectively induced extra-mixing below the convective envelope

---

[4] N(Li) = log[n(Li)/n(H)] + 12.

[5] In the standard case without thermohaline mixing, the abundances obtained at the end of the first dredge-up remain unchanged until the convective envelope deepens for the second time on the early-AGB.

as usually required to induce the third dredge-up in low-mass TP-AGB models (Herwig et al. 1997; Herwig 2000; Herwig et al. 2007; Mowlavi 1999; Karakas et al. 2002; Karakas 2010). Consequently we do not expect our models to mimic carbon-rich stars (but see Sect. 3.4). Such a study is out of the scope of the present work and TP-AGB predictions based on the present computations but including also different overshoot prescriptions will be presented in a future paper.

Let us note, however, that we find that with the present assumptions thermohaline mixing is active during each interpulse and modifies the surface abundances as can be seen in Fig. 7. As on the RGB, thermohaline mixing changes, but in a very modest way, the abundances of ^{3}He, ^{12}C, ^{13}C, ^{14}N, ^{17}O, and ^{18}O, while heavier elements are unaffected.

Also and in contrast with what happened on the RGB, the surface abundance of ^{7}Li now increases (see Table 3). This is due to the mixing efficiency that allows the transport of fresh ^{7}Be outwards to regions cool enough for ^{7}Li to survive. In the present case the production of ^{7}Li is significant, and the surface N(Li) reaches a value of ∼0.9 (then the star has a total luminosity Log($L/L_\odot$) between ∼3.0 and 3.6). We thus confirm, but this time at solar metallicity, the finding by Stancliffe (2010) that thermohaline mixing does increase the surface Li abundance in low-mass TP-AGB stars. Whether these Li-rich objects can simultaneously be carbon-rich will require further investigation of the TP-AGB phase including parametric convective overshoot as mentioned before. As can be seen in Table 3, the total stellar yields for lithium remain negative.

3.2. 1.25 $M_\odot$ model with thermohaline and rotation-induced mixing

Let us now discuss the case of a 1.25 $M_\odot$ model that does take into account both thermohaline instability and rotation-induced mixing as described in Sects. 2.2 and 2.3.

3.2.1. Main sequence and subgiant branch

As described above, the thermohaline instability induced by ^{3}He-burning sets in only on the RGB after the bump. Before a star reaches that phase, the modifications of its internal and surface chemical abundances are thus driven by rotation-induced mixing on the main sequence and convective dilution during the first dredge-up episode on the subgiant branch and early-RGB. The predictions of our rotating models up to that phase have been extensively tested in previous papers. They account nicely for the behaviour of lithium and beryllium at the surface of Population I main-sequence and subgiant stars (see Sect. 4.1; Talon & Charbonnel 1998, 2010; Charbonnel & Talon 1999; Palacios et al. 2003; Pasquini et al. 2004; Smiljanic et al. 2009; Charbonnel & Lagarde 2010).

Rotation-induced mixing has also an impact on the internal abundance profiles of heavier chemicals involved in hydrogen-burning at higher temperatures than the fragile Li and Be. This can be seen at the moment of the turnoff in Fig. 2 for the 1.25 $M_\odot$ star computed for different initial rotation velocities.

In the rotating models, the abundance gradients are smoothed out compared to the standard case: ^{3}He, ^{13}C, ^{14}N, and ^{17}O diffuse outwards, while ^{12}C and ^{18}O diffuse inwards. However, rotation-induced mixing is not efficient enough to noticeably change the surface abundances of these elements while on the main sequence for the 1.25 $M_\odot$ model[6], although it sets the scene for abundance variations in latter evolution phases.

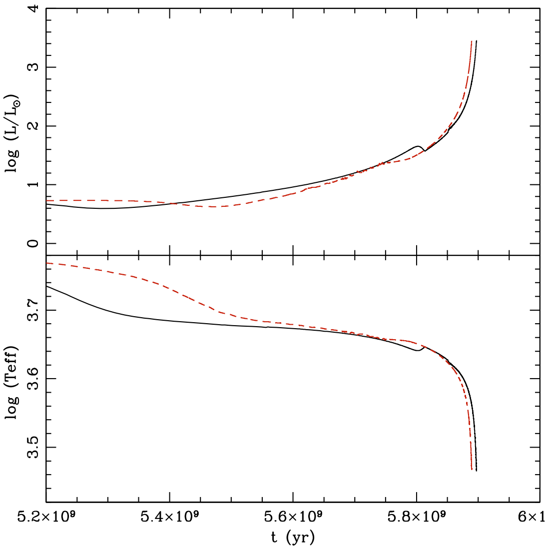

Fig. 8. Evolution with time along the RGB of the effective temperature and of the luminosity of the 1.25 $M_\odot$ models computed with thermohaline mixing only (black solid line) and with both thermohaline and rotation-induced mixing (initial rotation velocity of 110 km s^{-1}, red dotted line).

In particular the surface abundance variations during the first dredge-up are slightly strenghtened when rotation-induced mixing is accounted for, as shown in Fig. 6. For example, more ^{3}He is brought into the stellar envelope, and the post dredge-up ^{12}C/^{13}C and ^{16}O/^{17}O ratios are lower than in the non-rotating case. We note, however, that neither ^{16}O nor ^{23}Na are affected, and that no ^{23}Na enhancement is expected at the surface of such a low-mass star during the first dredge-up.

3.2.2. Red giant branch

The modifications of the internal abundances due to rotation-induced mixing that we just discussed for the 1.25 $M_\odot$ model do induce slight variations of the overal stellar structure and of the evolutionary track. In the case of such a low-mass star, the impact on the effective temperature and luminosity along the RGB is relatively modest as can be seen in Fig. 8. We note that in the case of the computation without rotation (black full line) the drop in luminosity at the RGB bump (that is associated with a slight increase in Teff at $\sim 5.8 \times 10^9$ years) is clearly noticeable. In the rotating case the inflexion in luminosity at the bump is less pronounced and occurs at slightly lower luminosity. Consequently, the stellar luminosity at which the thermohaline instability reaches the convective envelope is also slightly lower in the rotating case (see Table 1).

Figure 9 shows, at the evolution point C$_{1.25}$ for the 1.25 $M_\odot$ model computed with an initial rotation velocity of 110 km s^{-1}, the diffusion coefficient associated to the thermohaline instability, $D_{\rm thc}$ (Eq. (1) for $C_{\rm t} = 1000$), and the total diffusion coefficient associated to rotation, $D_{\rm rot}$, that characterizes the transport

---

[6] The only exception is ^{7}Li which is strongly depleted in the rotating case.

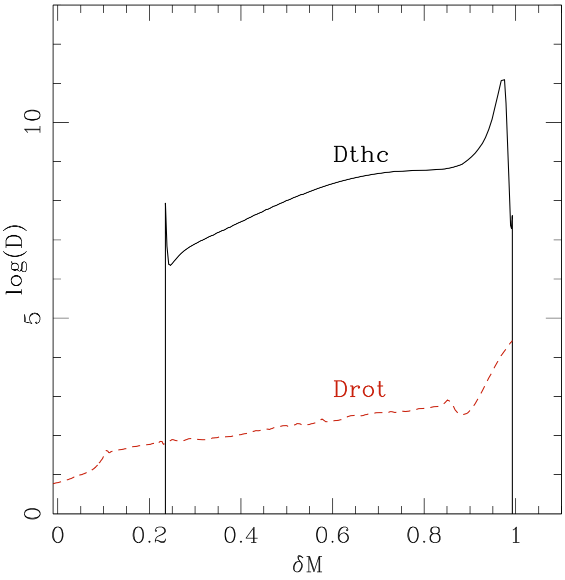

Fig. 9. Thermohaline diffusion coefficient $D_{\rm thc}$ (black solid line) and total rotation coefficient $D_{\rm rot}$ (red dashed line) as a function of δM for a 1.25 $M_\odot$ star (initial rotation velocity of 110 km s^{-1}) on the RGB at a total stellar luminosity of 105 $L_\odot$ (i.e., at the evolution point $C_{1.25}$). In the current model at this precise evolution point the size of the region between $\delta M = 0$ and 1 is 0.687696 $R_\odot$ while the thermohaline instability extends over 0.66136 $R_\odot$.

of chemicals through the interaction of meridional circulation and shear turbulence Zahn (1992; see e.g. Eqs. (5), (7) and (8) in Palacios et al. 2006). $D_{\rm thc}$ is five to six orders of magnitude higher than $D_{\rm rot}$, and this result is independent of the initial rotation velocity on the ZAMS.

This confirms the finding by Cantiello & Langer (2008, 2010) that in the relevant layers thermohaline mixing has much higher diffusion coefficients than rotational and magnetic instabilities[7]. It is also perfectly consistent with the results of Palacios et al. (2006; see also Chanamé et al. 2005) who studied the impact of rotation-induced mixing on the RGB for low-mass stars and showed that it cannot (with the present assumptions) account for the abundance anomalies observed in bright giants. These authors noted that assuming differential rotation (i.e., uniform specific angular momentum) instead of solid body rotation (i.e., uniform angular velocity) in the convective envelope along the RGB (see, i.e., Brun & Palacios 2009) does lead to higher efficiency of the rotation-induced processes below the convective envelope. However, even in that case, Palacios and collaborators showed that the total transport coefficient associated to rotation does not rise above 10^5 cm^2 s^{-1} in the outer HBS, which is still much lower than the thermohaline diffusion coefficient.

Thermohaline mixing thus governs the surface abundance variations on the upper half of the RGB as already discussed by CZ07. The corresponding predictions for the 1.25 $M_\odot$ model computed with an initial rotation velocity of 110 km s^{-1} can be seen in Fig. 6 (right panels).

3.2.3. AGB

The 1.25 $M_\odot$ model with an initial rotation velocity of 110 km s^{-1} was computed until the end of the superwind phase (total stellar mass and mass of the envelope being respectively equal to 0.566 $M_\odot$ and 0.014 $M_\odot$), and has undergone four thermal pulses. During the TP-AGB the behaviour of the surface abundances is similar to that discussed in Sect. 3.1.2. In the present case, the maximum N(Li) value reached at the end of the TP-AGB is ∼0.8 (instead of 0.9 in the 1.25 $M_\odot$ non-rotating model discussed in Sect. 3.1; see also Table 3). Again, predictions for carbon at that phase must be taken with caution since the impact of parametric convectively induced extra-mixing is not taken into account.

3.3. Uncertainties on the thermohaline diffusion coefficient

3.3.1. Size and shape of the thermohaline cells

CZ07 performed computations for various values of the coefficient $C_{\rm t}$ and discussed the uncertainties on the efficiency of the thermohaline mixing that are basically related to the size and shape of the thermohaline cells. Their prefered value for the aspect ratio $\alpha = 5$ (see Sect. 2.2) also used in the present computations corresponds to "fingers" rather than "blobs" whose shorter mixing length would translate into smaller value (by a factor of ∼50) for the coefficient $C_{\rm t}$. Crude as it may be, this choice first advocated by Ulrich (1972) is supported by laboratory experiments where the instability takes the form of salt fingers (Krishnamurti 2003). Also and contrary to the "blob assumption", the "finger prescription" leads to a very good description of the surface abundances in low-metallicity stars as shown in CZ07, as well as in solar-metallicity stars as will be discussed in Sect. 4. Unfortunatly and as mentionned by Eggleton et al. (2007) the 3D simulation by Eggleton et al. (2006) did not have the resolution to give clues on the aspect ratio of the fingers.

As a test we have however run a 1.25 $M_\odot$ model without rotation-induced mixing but with $C_{\rm t} = 10^4$ instead of the value of 10^3 used in all the other computations presented in the present paper. The predictions for the evolution of the surface abundances up to the RGB tip are shown in Fig. 6 (red lines in left panels) and 10. As expected, increasing the thermohaline diffusion coefficient by a factor of 10 leads to faster and substantially stronger processing of material on the RGB: at the RGB tip, the surface abundances of ^{3}He and of ^{7}Li are reduced respectively by a factor of 2 and by ∼1.5 dex compared to the $C_{\rm t} = 10^3$ assumption. The impact on the carbon and oxygen isotopic ratios and on the surface abundance of ^{14}N is more moderate.

Even in that case there remains enough ^{3}He to drive thermohaline mixing when the star is on the TP-AGB. The Li production during that phase is higher than in the $C_{\rm t} = 10^3$ case, with the final surface abundance N(Li) = 2 instead of 0.9. The final ^{3}He abundance and carbon isotopic ratio are 1.8×10^{-4} (in mass fraction) and 8 respectively (instead of 3.15×10^{-4} and 9.65).

3.3.2. Atomic diffusion

In the present computations we have not included the effects of atomic diffusion. In particular we do not consider radiative levitation that may lead to accumulation of heavy elements and thus to thermohaline instability in the outer layers of peculiar, slowly-rotating main sequence A-type stars (see Théado et al. 2009). This simplification has no effect on our conclusions, since the thermohaline instability induced by iron accumulation affects

---

[7] This conclusion on the magnetic diffusivity was obtained in the case of magnetic fields that are created in differentially rotating star and is not valid for magnetic stars that possess anomalous fossil fields such as the Ap star descendants discussed in Charbonnel & Zahn (2007a).

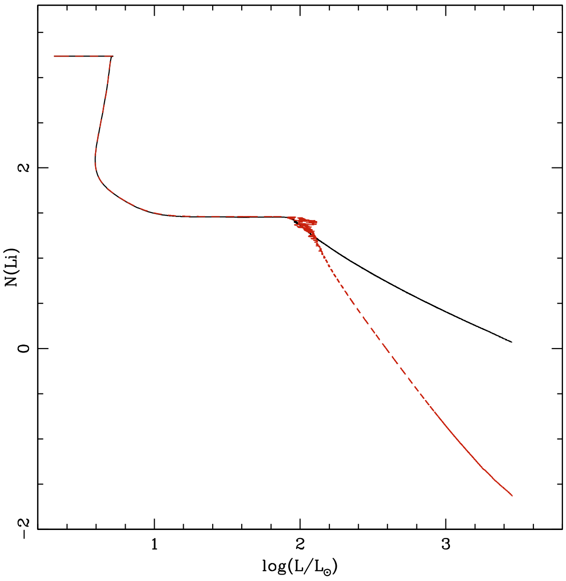

Fig. 10. Evolution of the surface abundance of ^{7}Li in the 1.25 $M_\odot$ star up to the RGB tip when considering thermohaline transport but no rotation-induced mixing. The black solid and red dashed curves correspond to computations performed with $C_t = 10^3$ and 10^4 respectively.

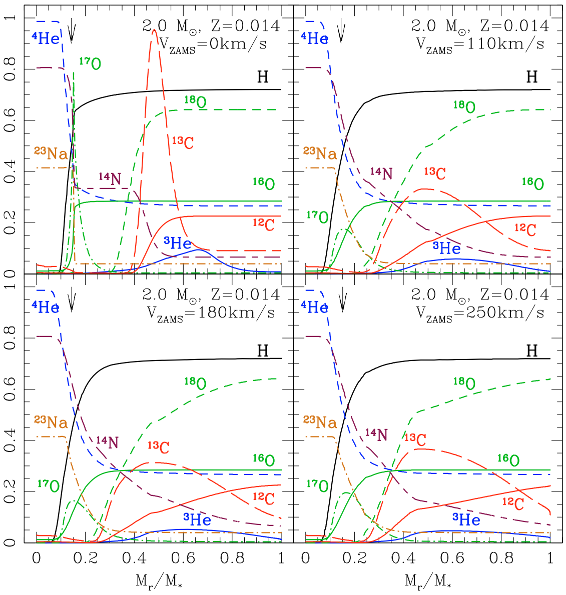

Fig. 11. Same as Fig. 2 for the 2.0 $M_\odot$ star computed for different initial rotation velocities, as indicated. The mass fractions are multiplied by 100 for ^{3}He, ^{12}C, and ^{14}N, by 2500 for ^{13}C, by 50, 1100, and 5×10^4 for ^{16}O, ^{17}O, and ^{18}O respectively, and by 1500 for ^{23}Na. The vertical arrows show, in all cases, the maximum depth reached by the convective envelope at its maximum extent during the first dredge-up.

only the very external regions of these atypical main sequence stars and has no direct impact on the nuclear burning occuring much deeper inside the star, nor on the RGB chemical properties.

We do not consider either the effect of atomic diffusion on the RGB, although Michaud et al. (2010) pointed out that at that phase ^{4}He gravitational settling may eventually lead to a larger μ-inversion than ^{3}He-burning on the outskirts of the HBS. In their computations, however, thermohaline mixing is not taken into account. Consequently the effects of concentration variations on μ they get from pure atomic diffusion are maximum compared to reality where thermohaline mixing (induced by ^{3}He-burning and eventually by ^{4}He-settling) counteracts atomic diffusion. Michaud and collaborators have estimated that a value of D$_{\rm thc}$ of the order of 10^7 cm^2 s^{-1} is able to substantially reduce (by a factor of 10) the small gradients of He caused by atomic diffusion on the RGB for a 0.95 $M_\odot$, $Z = 0.004$ model. Given that this number is smaller than D$_{\rm thc}$ obtained in our RGB models (see Figs. 4 and 9), we can safely assume that the effects of atomic diffusion must be wiped out by turbulence and that ^{3}He-burning is the dominating process inducing thermohaline instability between the HBS and the convective envelope in RGB stars. We are aware that some ^{4}He settling may remain even under the counteracting action of thermohaline mixing, although this should be confirmed by computations that are out of the scope of the present paper. One may note, however, that this should simply slightly re-inforce the μ-inversion induced by ^{3}He-burning (although to a much lower extent than in Michaud's computations), and thus strengthen the thermohaline transport compared to the present models.

3.4. Low-mass stars more massive than ∼1.5 $M_\odot$

Table 1 gives the luminosity of the bump as well as the luminosity $L_{\rm c,th}$ at which the thermohaline instability "contacts" the base of the convective envelope for all the low-mass stellar models computed both without and with rotation for the present study. As we have just seen, for RGB stars less massive than ∼1.5 $M_\odot$, thermohaline mixing starts changing the surface abundances soon after the bump. However, for RGB stars with initial mass higher than 1.5 $M_\odot$ computed without rotation-induced mixing, the thermohaline instability is long quenched into a very thin region, and is able to connect the external wing of the HBS with the convective envelope only when the star reaches already very high luminosity, close from the RGB tip. This is consistent with the finding by Cantiello & Langer (2008, 2010) of an upper mass limit for efficient thermohaline mixing in non-rotating low-mass RGB stars. However, as we shall see below, this conclusion does not hold anymore when one considers the impact of stellar rotation.

Let us now discuss indeed the case of a 2.0 $M_\odot$ star which interior chemical structure at the turnoff is shown in Fig. 11 for different initial velocities. As for the 1.25 $M_\odot$ models discussed before, rotation-induced mixing smoothes the abundance profiles inside the star and in the present case it already leads to variations of the surface abundances on the main sequence that are stronger for higher initial rotation velocities (this can be seen by looking at the abundance values at $M_r/M_* = 1$ in the various panels of Fig. 11; see also e.g. Meynet & Maeder 2002). Note also that the maximum value of ^{3}He at the peak is much lower than in the 1.25 $M_\odot$, because on the main sequence the 2.0 $M_\odot$ burns hydrogen mainly through the CNO cycle rather than through the pp-chains. The more massive star thus dredges less ^{3}He on the subgiant branch as can be seen by comparing Figs. 6 and 12.

Figure 12 shows the evolution of the surface abundances of ^{3}He, ^{7}Li, ^{14}N, and of the ^{12}C/^{13}C, ^{16}O/^{17}O, and ^{16}O/^{18}O ratios

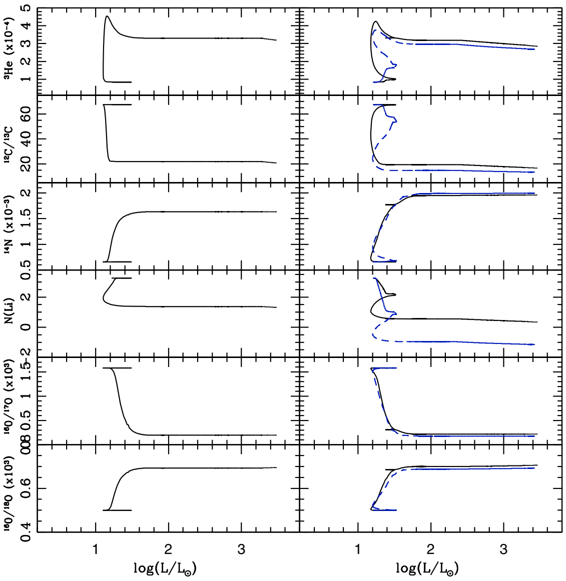

Fig. 12. Evolution of the surface abundances of ^{3}He, ^{7}Li, ^{14}N, and of the carbon and oxygen isotopic ratios for the 2.0 $M_{\odot}$ star from the zero age main sequence up to the RGB tip. (*Left*) Model including thermohaline mixing only. (*Right*) Models including thermohaline and rotation-induced mixing for different initial rotation velocities (110 and 250 km s^{-1}, solid black and dashed blue lines respectively). In all cases $C_t = 10^3$.

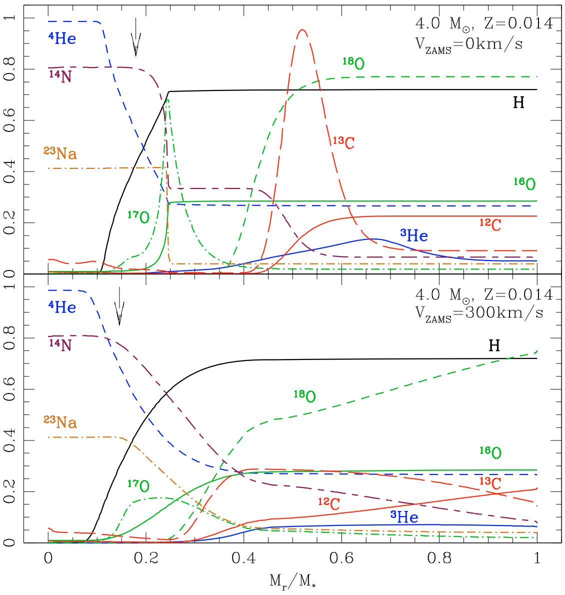

Fig. 13. Chemical structure at the turnoff of the 4.0 $M_{\odot}$ star computed without rotation and with rotation for an initial rotation velocity of 300 km s^{-1} (*top and bottom panels respectively*). The mass fractions are multiplied by 600 for ^{3}He, by 100 for ^{12}C and ^{14}N, by 2500 for ^{13}C, by 50, 5000, and 6×10^4 for ^{16}O, ^{17}O, and ^{18}O respectively, and by 1500 for ^{23}Na. The vertical arrows show, in both cases, the maximum depth reached by the convective envelope at its maximum extent during the first dredge-up.

as a function of luminosity up to the RGB tip in 2.0 $M_{\odot}$ models computed without or with rotation (left and right panels respectively). At this stellar mass some ^{23}Na produced during the main sequence is dredged-up (not shown in Fig. 12 but see Table 2). All these quantities at the end of the first dredge-up are slightly affected by rotation-induced mixing that changed the abundance profiles while the star was on the main sequence (e.g., the post dredge-up value of the carbon isotopic ratio is lower when faster rotation is accounted for). Furthermore, we note that the changes in surface abundances due to thermohaline mixing start at much lower luminosity (closer from the bump) on the RGB than in the non-rotating case (see also Table 1). Overall, the total abundance variations at the tip of the RGB are stronger for higher initial rotation velocity.

Thus and contrary to the conclusion by Cantiello et al. (2007) and Cantiello & Langer (2010), we find no mass limit (in the case of low-mass stars that ignite He in a degenerate core) for thermohaline mixing to change the surface abundances on the RGB. However, the global efficiency of this process increases when one considers less massive stars at a given metallicity, or more metal-poor stars at a given stellar mass. As discussed previously, this results from the combination of several factors like the thermohaline diffusion timescale compared to the secular timescale, the compactness of the HBS and of the thermohaline unstable region, and the amount of ^{3}He available to power the thermohaline instability.

In this mass range thermohaline mixing also leads to Li production during the TP-AGB (see Table 3). In the 2.0 $M_{\odot}$ model computed with an initial rotation velocity of 110 km s^{-1}, N(Li) increases from a value of 0.1 on the early AGB up to ~1.5 at the end of the TP-AGB (the envelope mass is then ~0.14 $M_{\odot}$, and the star has undergone 11 thermal pulses). Meanwhile the ^{3}He surface abundance has slightly decreased from 2.74×10^{-4} to 2.67×10^{-4}.

We wish to emphasize an interesting result obtained for the 2.0 $M_{\odot}$ model that was computed up to the AGB tip with thermohaline mixing but without rotation. This model did undergo 11 thermal pulses in total. After the 9th thermal pulse third dredge-up occurred, that slightly increased the ^{12}C surface abundance as well as the carbon isotopic ratio. During the following interpulse phase this ratio was slightly lowered under the effect of thermohaline mixing. Quantitatively, the carbon isotopic ratio increased from 19.6 to 21.33 between the end of the second dredge-up and the AGB tip (see also Fig. 18 and discussion in Sect. 4.2). This could indicate that thermohaline mixing does favour the occurrence of third dredge-up. This will be investigated further in a future paper.

3.5. Theoretical predictions for intermediate-mass stars

By definition, intermediate-mass stars are objects that ignite central helium-burning in a non-degenerate core at relatively low luminosity on the RGB, well before the HBS reaches the mean molecular weight discontinuity caused by the first dredge-up. In other words, these objects do not go through a bump on their short ascend of the RGB, and thus do not undergo thermohaline mixing at that phase.

We should note, however, that as in the previous cases, rotation-induced mixing can not be neglected from the whole picture. We refer to Eggenberger et al. (2010) for a discussion of the global effects of rotation on the evolution and asterosismic

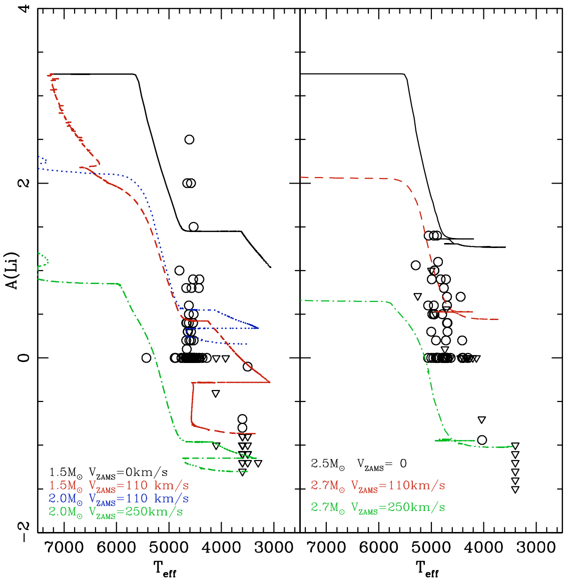

Fig. 14. Lithium data for field evolved stars from the sample by Charbonnel et al. (in prep., see the text) that are segregated according to their mass (*left and right panels* include respectively sample stars with masses lower and higher than 2 $M_\odot$; Li detections and upper limits are shown as circles and triangles respectively). Theoretical lithium evolution is shown from the ZAMS up to the end of the early-AGB. Various lines correspond to predictions for stellar models of different masses computed without or with rotation as indicated, and with thermohaline mixing in all cases (with $C_t = 10^3$).

properties of intermediate-mass red giants (see also e.g. Meynet & Maeder 2002). Its impact on the chemical structure of a 4.0 $M_\odot$ star at turnoff can be seen in Fig. 13. Note that in this mass range the base of the convective envelope reaches the ^{23}Na plateau during the first dredge-up, leading to an increase of the surface abundance of this element both in the non-rotating and rotating cases.

Overall rotation-induced mixing leads to stronger modifications of the stellar chemical properties when the star becomes a giant as its convective envelope dredges-up nuclearly processed material. At the end of the dredge-up for the 4 $M_\odot$ models, the surface ^{3}He abundance is 1.1×10^{-4} and 8.4×10^{-5} in the non-rotating and rotating (initial rotation velocity of 300 km s^{-1}) models respectively, while the carbon isotopic ratio is 20.5 or 14 respectively, and N(Li) is 1.3 or –1.8.

We computed the first 11 thermal pulses for the 4 $M_\odot$ models without and with rotation-induced mixing, including thermohaline mixing in both cases. A strong Li increase at the stellar surface is obtained during the first thermal pulses, and then lithium production levels off at a value of the order of N(Li) = 2.2. This agrees with Stancliffe (2010) predictions. Again, a detailed exploration of the TP-AGB phase for intermediate-mass stars is postponed to a further paper.

4. Comparison with observations

We now test the theoretical predictions of our models with respect to observations of relevant chemical elements in stars at different evolution stages. In Table 2 we give the surface carbon isotopic ratio as well as surface abundances of ^{7}Li, ^{9}Be, [C/Fe], [N/Fe], and [Na/Fe], at the end of the first dredge-up, at the RGB tip, and at the end of the second dredge-up, for each of the models we have computed. In this table and in the following figures all the predictions correspond to models computed with a value of $C_t = 10^3$ for thermohaline mixing (without or with rotation-induced mixing). As underlined in Sect. 3, we did not include parametric convectively induced extra-mixing during the TP-AGB phase so that our models are not expected to undergo third dredge-up and to mimic carbon-rich stars.

4.1. Lithium behaviour

4.1.1. Lithium destruction

As already mentioned the predictions of the present rotating models have been successfully compared to Li and Be observations along the whole evolutionary sequence of the Galactic open cluster IC 4651 (turnoff mass 1.8 $M_\odot$) by Smiljanic et al. (2010, see their Figs. 10 to 14). They account very nicely for all the Li and Be features observed in this cluster.

Here we use as additional constraints Li observations that we performed for a large sample of field red giant stars (subgiant, RGB, and early-AGB stars) with metallicities around solar. All sample stars have Hipparcos parallaxes so that their mass and evolutionary status could be relatively well determined (Charbonnel et al., in preparation). In Fig. 14 they are distinguished with respect to their mass (less or more massive than 2 $M_\odot$ in the left and right panels respectively).

Let us consider first the stars with initial masses lower than 2 $M_\odot$, whose Li properties are compared with predictions for the 1.5 and 2 $M_\odot$ models (left panel of Fig. 14). The theoretical Li behaviour is relatively straightforward. On the main sequence and on the early-RGB, rotation-induced mixing leads to stronger Li depletion than in the standard case (compare e.g. the red curve with the black one); in this mass range indeed standard models predict no Li depletion on the main sequence and a N(Li) of the order of 1.5 at the end of the first dredge-up, which is at odds with the data. After the end of the first dredge-up ($T_{\rm eff} \sim 4800$ K), the theoretical Li abundance remains temporarily constant as the convective envelope withdraws in mass. When thermohaline mixing becomes efficient ($T_{\rm eff} \sim 4200$ K), the theoretical Li abundance drops again in drastic manner (while it would stay constant in the standard case). After the star has reached the RGB tip its effective temperature increases (up to ~4800 K) as it settles on the clump, before decreasing again when the star starts climbing the early-AGB. The second dredge-up that occurs then leads to a final decrease of N(Li). On this graph we do not plot the Li increase that is predicted to occur during the TP-AGB phase at a Teff of ~3200 K due to thermohaline mixing, and which is discussed in Sect. 4.1.2. As can be seen in Fig. 14, the present predictions are in perfect agreement with the data all along the evolutionary sequence and explain very well the upper limits observed for the brightest sample giant stars. The observed Li dispersion at a given effective temperature reflects dispersion in the initial rotation velocity and in the initial stellar mass (see also Charbonnel & Talon 1999; Palacios et al. 2003; Smiljanic et al. 2010).

The case of the more massive stars, whose Li observational behaviour is compared to predictions for the 2.5 and 2.7 $M_\odot$ models (right panel of Fig. 14) is even more simple. In these objects indeed no thermohaline mixing occurs on the too short RGB, and rotation-induced mixing alone explains very well the data.

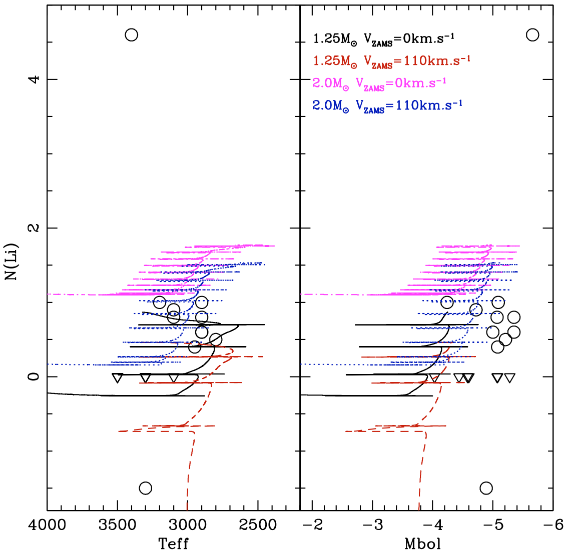

Fig. 15. Lithium observations in Uttenthaler & Lebzelter (2010) sample of oxygen-rich variables belonging to the Galactic disk (circles and triangles are for abundance determinations and upper limits respectively) as a function of effective temperature and bolometric magnitude. Typical error bars are indicated. The star with the highest Li abundance is W441 Cyg (see text). Theoretical lithium evolution is shown from the early-AGB up to the end of the TP-AGB. Various lines correspond to predictions for stellar models of different masses computed without or with rotation as indicated, and with thermohaline mixing in all cases (with $C_t = 10^3$).

Table 3. Surface lithium abundance after the second dredge-up and at the end of the TP-AGB phase, and total lithium yield.

M ($M_\odot$)		$V_{\rm zams}$ (km s^{-1})	N(Li) 2DUP	N(Li) tip AGB	Yield ($M_\odot$)
1.0	th	0	–1.86	–0.3	-5.17×10^{-9}
1.1	th	0	–0.97	0.25	-5.81×10^{-9}
1.25	th	0	–0.25	0.87	-6.75×10^{-9}
	th+rot	80	–3.93	0.46	-6.79×10^{-9}
	th+rot	110	–3.91	0.85	-6.79×10^{-9}
1.5	st	0	1.38	1.38	-8.25×10^{-9}
	th	0	0.63	1.49	-8.25×10^{-9}
	th+rot	110	–0.8	1.04	-8.35×10^{-9}
1.9	th	0	1.05	1.8	-1.0×10^{-8}
2.0	th	0	1.1	1.8	-1.12×10^{-8}
	th+rot	110	0.16	1.52	-1.14×10^{-8}

4.1.2. Lithium production

In all the models that we have computed along the TP-AGB, non negligible fresh lithium production is obtained, although the total stellar yields remain negative. Table 3 gives the final N(Li) value and the total Li yield for those models. In all cases thermohaline transport is responsible for this strong Li enrichment.

The evolution of the surface abundance along the TP-AGB is shown as a function of effective temperature and bolometric magnitude in Fig. 15 for the 1.25 and 2.0 $M_\odot$ models computed without and with rotation, and with thermohaline mixing in both cases (with $C_t = 10^3$). Li production starts at slightly higher effective temperature and luminosity for the more massive star.

Table 4. References for the abundance studies in Galactic open clusters used in the comparisons with model predictions.

Open cluster	$M_{\rm redTO}$ ($M_\odot$)	^{12}C/^{13}C	N/C	Na	Symbol colour
M 67	1.5	GB91	B87	Y05	black
NGC 752	2.0	G89	–	–	merlot
NGC 6939	1.57	–	–	J07	light green
NGC 7142	1.67	–	–	J08	yellow
NGC 3680	1.70	–	–	S09	pink
NGC 2141	1.73	–	–	J09	sauvignon
NGC 2360	1.98	S09	S09	S09	cyan
NGC 2158	2.04	–	–	J09	lime
NGC 1883	2.08	–	–	J09	grey
NGC 5822	2.14	S09	S09	S09	orange
IC 4756	2.31	S09	S09	J07, S09	green
NGC 6134	2.31	S09, M10	S09	S09, M10	red
NGC 2447	2.74	S09	S09	S09	olive
NGC 6633	2.74	S09	S09	H00	light blue
NGC 1817	2.82	–	–	J09	brown
IC 2714	2.85	S09	S09	S09	blue purple
NGC 3532	2.96	S09	S09	S09	blue
NGC 6281	3.09	S09	S09	S09	magenta

Notes. Brown (1987): B87; Gilroy (1989): G89; Gilroy & Brown (1991): GB91; Hamdani et al. (2000): H00; Jacobson et al. (2007, 2008, 2009): J07, J08, J09, J10; Mikolaitis et al. (2010): M10; Smiljanic et al. (2009): S09; Yong et al. (2005): Y05. The red turnoff masses given in the second column were estimated using the WEBDA database and Geneva isochrones (see text). Listed in the last column are the symbol colours used in Fig. 17 and Figs. 19 to 21.

Predictions are compared with lithium values in the sample of low-mass oxygen-rich AGB variables belonging to the Galactic disk studied by Uttenthaler & Lebzelter (2010). Theoretical Li production sets in above a lower luminosity limit which agrees with the observational Mbol threshold. Models are found to fit very nicely the lithium behaviour. However, they can not account for the very high Li abundance (3.1 to 4.6 depending on the model atmosphere) of the star V441 Cyg, which may rather be an intermediate-mass AGB star undergoing hot bottom burning (see discussion in Uttenthaler & Lebzelter 2010).

4.2. Carbon isotopic ratio

As discussed in the introduction, the behaviour of the carbon isotopic ratio is the best indicator of non-standard transport processes in evolved low-mass stars. This quantity has been determined in a large number of stars in Galactic open clusters. The references for the studies we consider here are listed in Table 4 where we also give the cluster red turnoff masses (see Meynet et al. 1993) derived from the WEBDA database when using the Geneva isochrones (Schaller et al. 1992).

Figure 16 displays observations of the ^{12}C/^{13}C ratio in subgiant, RGB, and clump stars of the open cluster M 67 (turnoff mass ∼1.2 $M_\odot$ according to Gilroy & Brown (1991), and 1.5 $M_\odot$ according to WEBDA, see above) by Gilroy & Brown (1991). The data are compared to the predictions of our 1.25 $M_\odot$ models computed for three different initial velocities and including thermohaline mixing (the non-rotating case is also shown). We see that the theoretical and observational behaviours are in complete agreement all along the evolutionary sequence. While the dispersion for stars that have not yet reached the RGB bump (i.e., with Log$(L/L)_\odot$ between ∼0.7 and 1.8) reflects only the dispersion in the initial rotation velocity, explaining the data for more

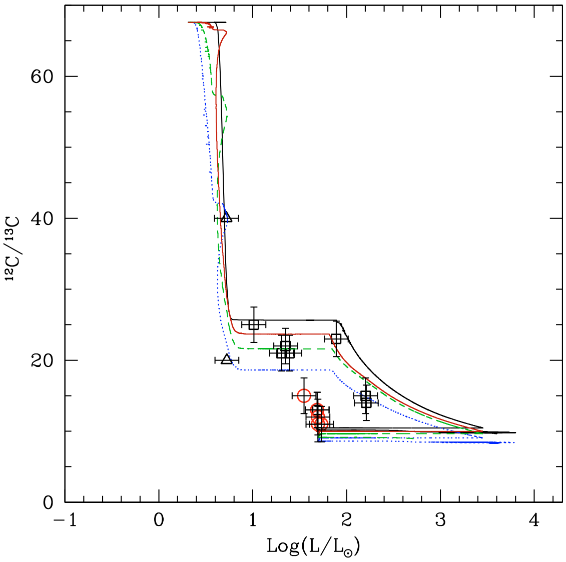

Fig. 16. Evolution of the surface ^{12}C/^{13}C value as a function of stellar luminosity for the 1.25 $M_\odot$ models including thermohaline instability and rotation-induced mixing (for initial rotation velocities of 50, 80, and 110 km s^{-1} shown as solid red, dashed green, and dotted blue lines respectively). The non rotating case is also shown (black solid line). Observations along the evolutionary sequence of the open cluster M 67 are from Gilroy & Brown (1991). The triangle is for a subgiant star for which only a lower value could be obtained, while black squares and red circles correspond respectively to RGB and clump stars.

evolved stars requires the occurrence of thermohaline mixing as predicted by the models.

We now compare the predictions of our models over the 1.0–4.0 $M_\odot$ range with carbon isotopic ratios in open clusters of different turnoff masses. The data shown in Fig. 17 are from Gilroy & Brown (1991) for M 67, from Gilroy (1989) for her open clusters with turnoff masses below 1.7 $M_\odot$ (i.e., NGC 752), from the more recent study by Smiljanic et al. (2009) for nine pen clusters with turnoff masses above 1.7 $M_\odot$ (IC 2714, IC 4756, NGC 2360, NGC 2447, NGC 3532, NGC 5822, NGC 6134, NGC 6281, NGC 6633), and from Mikolaitis et al. (2010) for NGC 6134. Individual stars are attributed the red turnoff mass of their host cluster determined as described above (see Table 4). Indications on their evolutionary status, when available, are given in the plot (squares, circles, and asteriscs are for RGB, clump, early-AGB stars respectively, while diamonds are for stars with uncertain evolutionary status). Model predictions are shown both at the tip of the RGB and at the end of the second dredge-up[8] (black and blue lines respectively) for different assumptions. Dotted lines correspond to standard models computed without thermohaline mixing nor rotation; those account only for the upper envelope of the data. Solid lines correspond to models computed with thermohaline mixing only. They reproduce very well the ^{12}C/^{13}C behaviour for stars with initial masses lower than ∼1.7 $M_\odot$. In this mass range rotation-induced mixing leads only to slightly lower values as shown by the long-dashed lines for an initial velocity of 110 km s^{-1}. Note that the squares at $M_{\rm turnoff}$ = 1.5 $M_\odot$ correspond to the M 67 stars that have not yet reached the RGB bump (see Fig. 16), which explains why they lie between the standard and the thermohaline curves. For stars with masses between ∼1.7 and 2.2 $M_\odot$ both thermohaline and rotation-induced mixing are required to fit the data. For more massive stars thermohaline mixing plays no role but the observational uncertainties allow the data to be well accounted for when rotation-induced mixing is taken into account (dot-dashed and dashed lines for initial velocities of 250 and 300 km s^{-1} respectively).

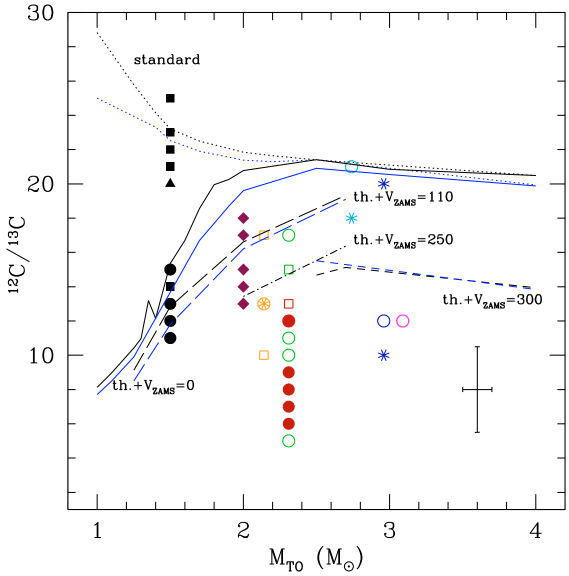

Fig. 17. Observations of ^{12}C/^{13}C in evolved stars of Galactic open clusters by Smiljanic et al. (2009, open symbols), Gilroy (1989), Gilroy & Brown (1991), and Mikolaitis et al. (2010) as a function of the turnoff mass of the corresponding host cluster that can be identified thanks to the colours of the symbols (see text and Table 4). Squares, circles, and asteriscs are for RGB, clump, and early-AGB stars respectively, while diamonds are for stars from Gilroy (1989) sample with doubtful evolutionary status; triangles are for lower limits. A typical error bar is indicated. Theoretical predictions are shown at the tip of the RGB and after completion of the second dredge-up (black and blue lines respectively). Standard models (no thermohaline nor rotation-induced mixing) are shown as dotted lines, models with thermohaline mixing only ($V_{\rm ZAMS} = 0$) as solid lines, and models with thermohaline and rotation-induced mixing for different initial rotation velocities as indicated as long-dashed, dot-dashed, and dashed lines.

Finally we compare in Fig. 18 our predictions for the carbon isotopic ratio to its determination in a sample of planetary nebulae obtained by means of millimeter wave observations of ^{12}CO and ^{13}CO (Palla et al. 2000). The abcissa is the progenitor mass derived by Palla and collaborators; this quantity is highly uncertain as shown by the error bars. Since the formation of the planetary nebula occurs at the AGB tip, the data should be compared to the model predictions at the end of the superwind phase as plotted in red. As explained in Sect. 3 only some of our low-mass models (with initial mass ≤2 $M_\odot$) were computed up to that phase. For these objects thermohaline mixing was found to slightly lower the carbon isotopic ratio during the thermal pulse phase, except in the 2 $M_\odot$ model with thermohaline mixing

---

[8] Note that with the present computations without parametric convective overshoot during the thermal pulses, the carbon isotopic ratio is only very slightly modified during the TP-AGB phase compared to its value at the end of the second dredge-up.

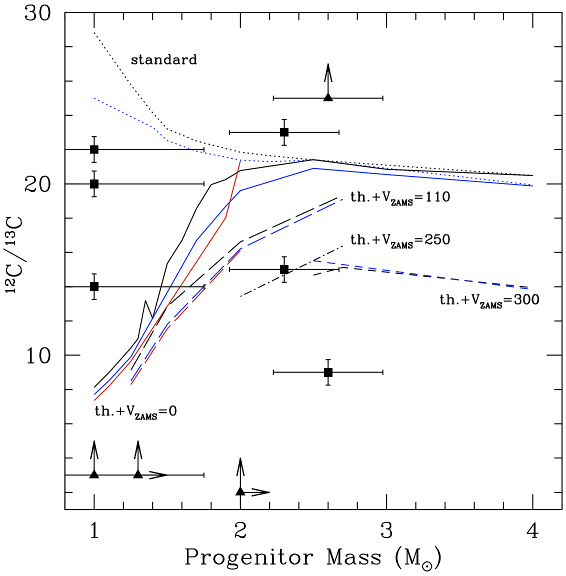

Fig. 18. Observations of $^{12}C/^{13}C$ in planetary nebulae as a function of the progenitor mass (Palla et al. 2000). Squares and triangles are respectively for actual determinations and lower limits of the carbon isotopic ratio. Black and blue theoretical lines have the same meaning as in Fig. 17, while red curves show the model predictions at the AGB tip for the low-mass models that were computed up to that phase (solid and dashed red curves are respectively for the models with thermohaline mixing only and for the models with thermohaline and rotation-induced mixing).

and no rotation that has undergone third dredge-up from the 9th pulse on (see Sect. 3.4); in that case the carbon isotopic ratio at the AGB tip is slightly higher than at the end of the second dredge-up. Overall the comparison between the models and the data turns out to be quite satisfactory. Two of the planetary nebulae with low-mass progenitors (namely NGC 6781 and M 1-17) actually exhibit relatively high carbon isotopic ratio. Although the uncertainty on the initial stellar mass of these objects allows the data to be well accounted for by the thermohaline models (both with and without rotation), it could also be that in this couple of stars thermohaline mixing was inhibited by strong fossil magnetic fields as suggested by Charbonnel & Zahn (2007a). In this context it would be extremely valuable to look for magnetic fields in these two possible "thermohaline deviant stars". On the other hand, computations are now needed to estimate the combined effect of third dredge-up, hot bottom burning, and thermohaline mixing during the TP-AGB phase for stars more massive than 2 $M_\odot$. This is work is in progress.

4.3. Nitrogen, sodium, and oxygen isotopes

[N/C] data for the open cluster sample listed in Table 4 is shown as a function of the cluster red turnoff mass and as a function of $^{12}C/^{13}C$ in Figs. 19 and 20 respectively.

During the first dredge-up, the convective envelope of intermediate mass-stars reaches the regions where ^{16}O has been partially converted into ^{14}N while the star was on the main sequence, while in the case of low-mass stars it reaches only the first ^{14}N step due to ^{13}C-burning (compare the position of the vertical arrows in Figs. 2, 11, and 13). Models thus predict an increase of the post dredge-up [N/C] value with initial stellar mass, in agreement with the observed behaviour. We note, however, that the lower envelope of the observational data lies slightly below the standard predictions, which might indicate that the models overestimate the first dredge-up. On the other hand, the corresponding offset may well be related to observational

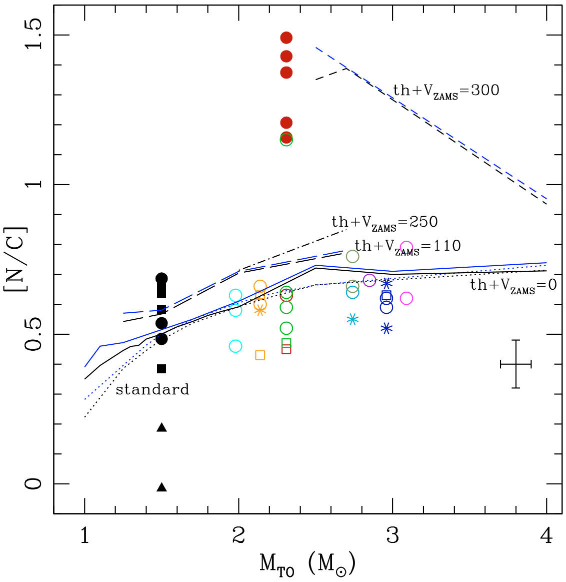

Fig. 19. [N/C] ratio as a function of turn-off mass of the host cluster for the Galactic open cluster sample by Smiljanic et al. (2009) and for M 67 by Brown (1987). Symbols and lines have the same meaning as in Fig. 17.

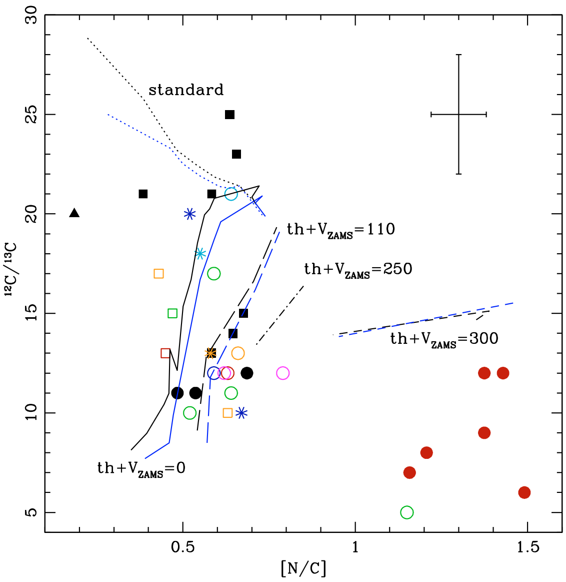

Fig. 20. $^{12}C/^{13}C$ as a function of [N/C]. See Table 4 for references. Symbols are the same as in Fig. 17.

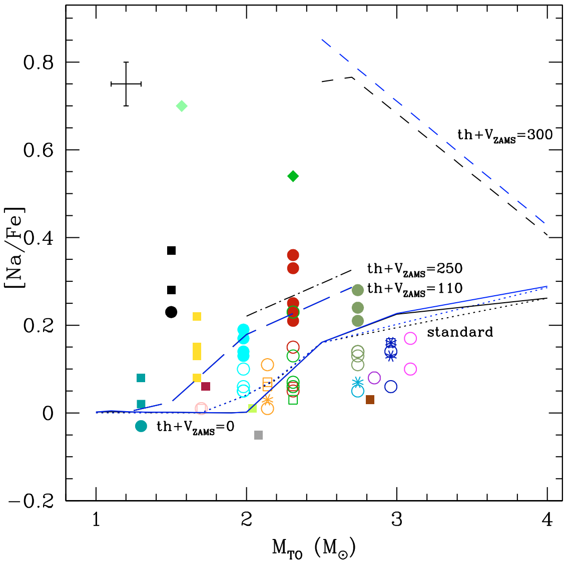

Fig. 21. [Na/Fe] ratio as a function of turn-off mass for the sample of Galactic open clusters listed in Table 4. Symbols and lines are the same as in Fig. 17. The green diamonds are the mean [Na/Fe] values given by Jacobson et al. (2007) for IC 4756 and NGC 6939.

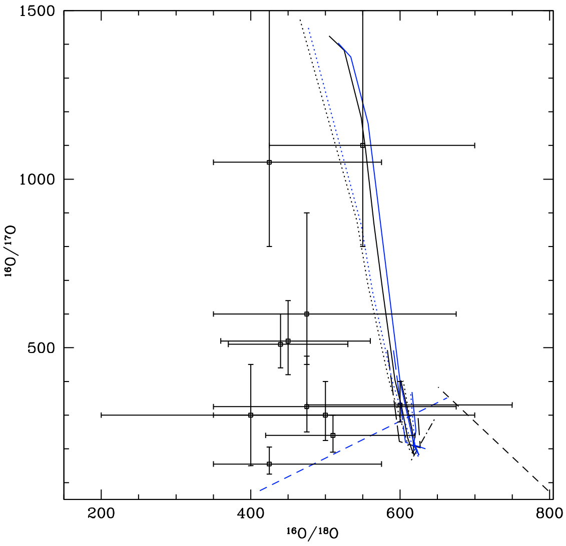

Fig. 22. $^{16}O/^{17}O$ versus $^{16}O/^{18}O$. Observations are from Harris & Lambert (1984), Harris et al. (1988) for stars in the 1–3 $M_\odot$ range. The line symbols are the same as in Fig. 17. The initial values assumed for $^{16}O/^{17}O$ and $^{16}O/^{18}O$ are 1490 and 445 respectively.

uncertainties. Over the whole mass range thermohaline mixing on one hand, and rotation-induced mixing on the other hand, lead to additional transport of CNO-cycled material, and thus further increase the [N/C] ratio with respect to the standard predictions. Given the observational error bars, one can conclude from Figs. 19 and 20 that the models account nicely for the observational constraints on C and N.

In Fig. 21 we plot the [Na/Fe] ratio for the open cluster sample listed in Table 4 as a function of cluster turnoff mass. Note that the observational data were reported to the solar Na value from Asplund et al. (2005) we assume in the initial composition of our models[9]. Both the predictions and observations show a positive correlation between [Na/Fe] values and stellar mass. Rotation-induced mixing leads to an increase of the amount of Na processed to the surface and allows an explanation for the observed dispersion. There is however an offset of about 0.1 dex between the data and the predictions as was already noticed by Smiljanic et al. (2009) who compared their observations with standard model predictions by Mowlavi (1999). As a matter of fact, very different observational Na abundances for giant stars have been reported in the literature. As can be seen in Fig. 21 some studies present [Na/Fe] values as high as +0.6 dex (Jacobson et al. 2007), some only a mild overabundance of +0.2 dex (Hamdani et al. 2000, see Fig. 21), and other solar values (Sestito et al. 2007). We refer to Smiljanic et al. (2009) for a discussion on the possible causes of these discrepancies. The present predictions for the stars more massive than ∼2 $M_\odot$ are actually in better agreement with the mild overabundance of [Na/Fe] measured by Hamdani et al. (2000).

Finally we show in Fig. 22 the $^{16}O/^{17}O$ vs. $^{16}O/^{18}O$ for the G and K giants by Harris & Lambert (1984) and Harris et al. (1988). Included in the figure are our predictions. As discussed in Sect. 3, thermohaline mixing affects only slightly the $^{16}O/^{18}O$ ratio, and leaves $^{16}O/^{17}O$ unaffected; on the other hand, rotation-induced mixing lowers the $^{16}O/^{17}O$ ratio, and helps account for the lowest $^{16}O/^{18}O$ values. Given the large observational uncertainties, the predictions are reasonably consistent with the O isotopic ratios measured in RGB stars.

5. Conclusions

In the present paper we have investigated the effects of the thermohaline instability induced by ^{3}He-burning that sets in above the RGB bump and of rotation-induced mixing on the evolution and chemical properties of low- and intermediate-mass stars (1 to 4 $M_\odot$) at solar metallicity. All the stellar models were computed up to the end of the second dredge-up on the early-AGB, and some of them up to the end of the TP-AGB phase. Predictions are compared to data for lithium, $^{12}C/^{13}C$, [N/C], [Na/Fe], $^{16}O/^{17}O$, and $^{16}O/^{18}O$ in giant stars with well-defined masses and evolutionary status on the RGB, clump, early-AGB, and planetary nebulae phases.

We find that the theoretical and observational behaviours for these species are in very good agreement over the whole scrutinized mass range. Thermohaline mixing is confirmed to be the main physical process governing the surface abundances of ^{3}He, ^{7}Li, C, and N for stars more evolved than the RGB bump in all the models with initial masses below 2.2 $M_\odot$, although its efficiency is increasing with decreasing initial stellar mass. In all cases ^{3}He decreases by a large fraction in the stellar yields compared to the standard models, although we find that low-mass stars remain net producers of ^{3}He (^{3}He yields for stellar models over a broad range in both mass and metallicity will be published

---

[9] Smiljanic et al. (2009) and Mikolaitis et al. (2010) adopted solar abundances recommended by Grevesse et al. (1993) (A(Na) = 6.33, A(Fe) = 7.50), while Jacobson et al. (2007, 2008, 2009) and Hamdani et al. (2000) used solar abundances given by Anders & Grevesse (1989) (A(Na) = 6.33). In Fig. 21 the observational data are reported to the solar abondances values we use in our computations (Asplund et al. 2005, A(Na) = 6.20, and A(Fe) = 7.45).

in a future paper). It is also found that thermohaline mixing leads to lithium production on the TP-AGB phase, as first shown by Stancliffe (2010) in the case of low-metallicity stars. However, the Li yields remain negative, and these stars are not expected to contribute to Galactic Li enrichment. In one 2.0 $M_\odot$ model computed up to the AGB tip thermohaline mixing was found to help initiating the occurrence of the third dredge-up during the TP-AGB phase.

On the other hand, rotation-induced mixing modifies the internal chemical structure of main sequence stars, although its signatures are revealed only later in the evolution when the first dredge-up occurs. It favours the occurrence of thermohaline mixing in RGB stars in the mass range between ∼1.5 and 2.2 $M_\odot$. It accounts for the observed dispersion of abundances in stars of similar mass and evolutionary status, and is necessary to explain the features of CN-processed material in intermediate-mass stars.

These results were obtained using the prescription for the turbulent diffusivity related to the thermohaline instability advocated first by Ulrich (1972) that is supported by laboratory experiments Krishnamurti (2003). The same prescription was shown by Charbonnel & Zahn (2007b) to nicely account for the photospheric composition of low-mass, low-metallicity giant stars.

Acknowledgements. We wish to thank Jean-Paul Zahn and Thibaut Decressin for helpful comments on our manuscript. We acknowledge financial support from the Swiss National Science Foundation (FNS) and the french Programme National de Physique Stellaire (PNPS) of CNRS/INSU. This research has made use of the VizieR catalogue access tool, CDS, Strasbourg, France.

Appendix A: Nuclear reaction rates

All reactions for hydrogen burning are computed with nominal NACRE reaction rates (Angulo et al. 1999), with the exception of:

^{14}C(p, γ)^{15}N (Wiescher et al. 1990); ^{14}C(p, n)^{14}N (Koehler & O'brien 1989); ^{14}C(p, α)^{11}B (Caughlan & Fowler 1988); ^{14}N(p, γ)^{15}O (Mukhamedzhanov et al. 2003); ^{21}Ne(p, γ)^{22}Na, ^{22}Na(p, γ)^{23}Na, ^{23}Na(p, α)^{20}Ne, and ^{23}Na(p, γ)^{24}Mg (Iliadis et al. 2001); ^{22}Ne(p, γ)^{23}Na (Hale et al. 2002).

References

Anders, E., & Grevesse, N. 1989, Geochim. Cosmochim. Acta, 53, 197
Angulo, C., Arnould, M., Rayet, M., et al. 1999, Nuclear Physics A, 656, 3
Asplund, M., Grevesse, N., & Sauval, A. J. 2005, in Cosmic Abundances as Records of Stellar Evolution and Nucleosynthesis, ed. T. G. Barnes III, & F. N. Bash, ASP Conf. Ser., 336, 25
Balser, D. S., Bania, T. M., Brockway, C. J., Rood, R. T., & Wilson, T. L. 1994, ApJ, 430, 667
Balser, D. S., Bania, T. M., Rood, R. T., & Wilson, T. L. 1999, ApJ, 510, 759
Balser, D. S., Rood, R. T., & Bania, T. M. 2007, Science, 317, 1171
Bania, T. M., Balser, D. S., Rood, R. T., Wilson, T. L., & Wilson, T. J. 1997, ApJS, 113, 353
Bania, T. M., Rood, R. T., & Balser, D. S. 2002, Nature, 415, 54
Boothroyd, A. I., & Sackmann, I.-J. 1999, ApJ, 510, 232
Brown, J. A. 1987, ApJ, 317, 701
Brun, A. S., & Palacios, A. 2009, ApJ, 702, 1078
Cantiello, M., & Langer, N. 2008, in IAU Symp. 252, ed. L. Deng & K. L. Chan, 103
Cantiello, M., & Langer, N. 2010, A&A, 521, A9
Cantiello, M., Hoekstra, H., Langer, N., & Poelarends, A. J. T. 2007, in Unsolved Problems in Stellar Physics: A Conference in Honor of Douglas Gough, ed. R. J. Stancliffe, G. Houdek, R. G. Martin, & C. A. Tout, AIP Conf. Ser., 948, 73
Caughlan, G. R., & Fowler, W. A. 1988, Atomic Data and Nuclear Data Tables, 40, 283
Chanamé, J., Pinsonneault, M., & Terndrup, D. M. 2005, ApJ, 631, 540
Charbonnel, C. 1994, A&A, 282, 811
Charbonnel, C. 1995, ApJ, 453, L41
Charbonnel, C. 2002, Nature, 415, 27
Charbonnel, C., & Balachandran, S. C. 2000, A&A, 359, 563
Charbonnel, C., & Do Nascimento, Jr., J. D. 1998, A&A, 336, 915
Charbonnel, C., & Lagarde, N. 2010, in IAU Symp. 268, ed. C. Charbonnel, M. Tosi, F. Primas, & C. Chiappini
Charbonnel, C., & Talon, S. 1999, A&A, 351, 635
Charbonnel, C., & Talon, S. 2008, in IAU Symp. 252, ed. L. Deng & K. L. Chan, 163
Charbonnel, C., & Zahn, J. 2007a, A&A, 476, L29
Charbonnel, C., & Zahn, J.-P. 2007b, A&A, 467, L15
Charbonnel, C., Brown, J. A., & Wallerstein, G. 1998, A&A, 332, 204
Chiappini, C., Renda, A., & Matteucci, F. 2002, A&A, 395, 789
Cunha, K., Hubeny, I., & Lanz, T. 2006, ApJ, 647, L143
Dearborn, D. S. P., Steigman, G., & Tosi, M. 1996, ApJ, 465, 887
Dearborn, D. S. P., Lattanzio, J. C., & Eggleton, P. P. 2006, ApJ, 639, 405
Decressin, T., Mathis, S., Palacios, A., et al. 2009, A&A, 495, 271
Denissenkov, P. A., & Pinsonneault, M. 2008, ApJ, 684, 626
Eggenberger, P., Miglio, A., Montalban, J., et al. 2010, A&A, 509, A72
Eggleton, P. P., Dearborn, D. S. P., & Lattanzio, J. C. 2006, Science, 314, 1580 ik
Eggleton, P. P., Dearborn, D. S. P., & Lattanzio, J. C. 2007, in IAU Symp. 239, ed. T. Kuroda, H. Sugama, R. Kanno, & M. Okamoto, 286
Eggleton, P. P., Dearborn, D. S. P., & Lattanzio, J. C. 2008, ApJ, 677, 581
Ferguson, J. W., Alexander, D. R., Allard, F., et al. 2005, ApJ, 623, 585
Fusi Pecci, F., Ferraro, F. R., Crocker, D. A., Rood, R. T., & Buonanno, R. 1990, A&A, 238, 95
Gaigé, Y. 1993, A&A, 269, 267
Geisler, D., Smith, V. V., Wallerstein, G., Gonzalez, G., & Charbonnel, C. 2005, AJ, 129, 1428
Gilroy, K. K. 1989, ApJ, 347, 835
Gilroy, K. K., & Brown, J. A. 1991, ApJ, 371, 578
Gratton, R. G., Sneden, C., Carretta, E., & Bragaglia, A. 2000, A&A, 354, 169
Grevesse, N., Noels, A., & Sauval, A. J. 1993, A&A, 271, 587
Hale, S. E., Champagne, A. E., Iliadis, C., et al. 2002, Phys. Rev. C, 65, 015801
Hamdani, S., North, P., Mowlavi, N., Raboud, D., & Mermilliod, J. 2000, A&A, 360, 509
Harris, M. J., & Lambert, D. L. 1984, ApJ, 285, 674
Harris, M. J., Lambert, D. L., & Smith, V. V. 1988, ApJ, 325, 768
Herwig, F. 2000, A&A, 360, 952
Herwig, F., Bloecker, T., Schoenberner, D., & El Eid, M. 1997, A&A, 324, L81
Herwig, F., Freytag, B., Fuchs, T., et al. 2007, in Why Galaxies Care About AGB Stars: Their Importance as Actors and Probes, ed. F. Kerschbaum, C. Charbonnel, & R. F. Wing, ASP Conf. Ser., 378, 43
Hogan, C. J. 1995, ApJ, 441, L17
Iben, Jr., I. 1967, ApJ, 147, 624
Iglesias, C. A., & Rogers, F. J. 1996, ApJ, 464, 943
Iliadis, C., D'Auria, J. M., Starrfield, S., Thompson, W. J., & Wiescher, M. 2001, ApJS, 134, 151
Jacobson, H. R., Friel, E. D., & Pilachowski, C. A. 2007, AJ, 134, 1216
Jacobson, H. R., Friel, E. D., & Pilachowski, C. A. 2008, AJ, 135, 2341
Jacobson, H. R., Friel, E. D., & Pilachowski, C. A. 2009, AJ, 137, 4753
Karakas, A. I. 2010, in IAU Symp. 266, ed. R. de Grijs, & J. R. D. Lépine, 161
Karakas, A. I., Lattanzio, J. C., & Pols, O. R. 2002, Publ. Astron. Soc. Austral., 19, 515
Kawaler, S. D. 1988, ApJ, 333, 236
Kippenhahn, R., Ruschenplatt, G., & Thomas, H.-C. 1980, A&A, 91, 175
Koehler, P. E., & O'brien, H. A. 1989, Phys. Rev. C, 39, 1655
Krishnamurti, R. 2003, J. Fluid Mech., 483, 287
Luck, R. E. 1994, ApJS, 91, 309
Maeder, A., & Zahn, J.-P. 1998, A&A, 334, 1000
Meynet, G., & Maeder, A. 2002, A&A, 390, 561
Meynet, G., Mermilliod, J., & Maeder, A. 1993, A&AS, 98, 477
Michaud, G., Richer, J., & Richard, O. 2010, A&A, 510, A104
Mikolaitis, Š., Tautvaišienė, G., Gratton, R., Bragaglia, A., & Carretta, E. 2010, MNRAS, 407, 1866
Mowlavi, N. 1999, A&A, 344, 617
Mukhamedzhanov, A. M., Bém, P., Brown, B. A., et al. 2003, Phys. Rev. C, 67, 065804
North, P. 1993, in Peculiar versus Normal Phenomena in A-type and Related Stars, ed. M. M. Dworetsky, F. Castelli, & R. Faraggiana, ASP Conf. Ser. 44, IAU Colloq., 138, 577
Palacios, A., Talon, S., Charbonnel, C., & Forestini, M. 2003, A&A, 399, 603
Palacios, A., Charbonnel, C., Talon, S., & Siess, L. 2006, A&A, 453, 261
Palla, F., Bachiller, R., Stanghellini, L., Tosi, M., & Galli, D. 2000, A&A, 355, 69

Pasquini, L., Bonifacio, P., Randich, S., Galli, D., & Gratton, R. G. 2004, A&A, 426, 651

Pilachowski, C., Sneden, C., Freeland, E., & Casperson, J. 2003, AJ, 125, 794

Power, J., Wade, G. A., Hanes, D. A., Aurier, M., & Silvester, J. 2007, in Physics of Magnetic Stars, 89

Recio-Blanco, A., & de Laverny, P. 2007, A&A, 461, L13

Reimers, D. 1975, in Mémoires, Société Royale des Sciences de Liège, 8, 369

Romano, D., Tosi, M., Matteucci, F., & Chiappini, C. 2003, MNRAS, 346, 295

Rood, R. T., Bania, T. M., & Wilson, T. L. 1984, ApJ, 280, 629

Sackmann, I., & Boothroyd, A. I. 1999, ApJ, 510, 217

Schaller, G., Schaerer, D., Meynet, G., & Maeder, A. 1992, A&AS, 96, 269

Sestito, P., Randich, S., & Bragaglia, A. 2007, A&A, 465, 185

Shetrone, M. D. 2003, ApJ, 585, L45

Siess, L. 2009, A&A, 497, 463

Siess, L., Dufour, E., & Forestini, M. 2000, A&A, 358, 593

Smiljanic, R., Gauderon, R., North, P., et al. 2009, A&A, 502, 267

Smiljanic, R., Pasquini, L., Charbonnel, C., & Lagarde, N. 2010, A&A, 510, A50

Smith, V. V., Hinkle, K. H., Cunha, K., et al. 2002, AJ, 124, 3241

Spite, M., Cayrel, R., Hill, V., et al. 2006, A&A, 455, 291

Stancliffe, R. J. 2010, MNRAS, 174

Stancliffe, R. J., Glebbeek, E., Izzard, R. G., & Pols, O. R. 2007, A&A, 464, L57

Stancliffe, R. J., Church, R. P., Angelou, G. C., & Lattanzio, J. C. 2009, MNRAS, 396, 2313

Stern, M. E. 1960, Tellus, 12, 172

Stothers, R., & Simon, N. R. 1969, ApJ, 157, 673

Sweigart, A. V., Greggio, L., & Renzini, A. 1989, ApJS, 69, 911

Talon, S., & Charbonnel, C. 1998, A&A, 335, 959

Talon, S., & Charbonnel, C. 2003, A&A, 405, 1025

Talon, S., & Charbonnel, C. 2010, in IAU Symp. 268, ed. C. Charbonnel, M. Tosi, F. Primas, & C. Chiappini

Tautvaišienė, G., Edvardsson, B., Tuominen, I., & Ilyin, I. 2000, A&A, 360, 499

Tautvaišienė, G., Edvardsson, B., Puzeras, E., & Ilyin, I. 2005, A&A, 431, 933

Théado, S., Vauclair, S., Alecian, G., & Le Blanc, F. 2009, ApJ, 704, 1262

Thomas, H. 1967, Z. Astrophys., 67, 420

Thomas, H. 1970, Ap&SS, 6, 400

Tosi, M. 1998, Space Sci. Rev., 84, 207

Ulrich, R. K. 1971, ApJ, 168, 57

Ulrich, R. K. 1972, ApJ, 172, 165

Uttenthaler, S., & Lebzelter, T. 2010, A&A, 510, A62

Vassiliadis, E., & Wood, P. R. 1993, ApJ, 413, 641

Vauclair, S. 2004, in The A-Star Puzzle, ed. J. Zverko, J. Ziznovsky, S. J. Adelman, & W. W. Weiss, IAU Symp., 224, 161

Wasserburg, G. J., Boothroyd, A. I., & Sackmann, I. 1995, ApJ, 447, L37

Weiss, A., Wagenhuber, J., & Denissenkov, P. A. 1996, A&A, 313, 581

Wiescher, M., Gorres, J., & Thielemann, F. 1990, ApJ, 363, 340

Wolff, S. C. 1968, PASP, 80, 281

Yong, D., Carney, B. W., & Teixera de Almeida, M. L. 2005, AJ, 130, 597

Zahn, J.-P. 1992, A&A, 265, 115

5.4 Grid of stellar models and asymptotic asteroseismic quantities

Thermohaline instability and rotation-induced mixing
III - Grid of stellar models and asymptotic asteroseismic quantities from the pre-main sequence up to the AGB for low- and intermediate-mass stars at various metallicities

N.Lagarde, T. Decressin, C. Charbonnel, P. Eggenberger, S. Ekström, and A. Palacios

arXiv 1204.5193 (2012 ; accepted for publication in A&A)

Stellar evolution and structure still have many unknown. For long theoretical predictions were tested only with respect to classical observations using spectroscopy, photometry, and interferometry, which give informations on the stellar surface properties : stellar luminosity, radius, effective temperature, surface gravity, or chemical abundances. Such observations probe only a thin shell at the stellar surface, while information on stellar interiors is needed to constrain better stellar models.

Like geologists who probe the internal structure of our planet with the propagation of seismic waves during earthquakes, asterosismologists use a similar method to study the inside of a star. After the blooming of heliseismology with e.g. a satellites such as *SOHO*, the satellite *CoRoT* allows to study with the same method the internal stellar structure of stars of various types, as well as the detection of several exoplanets. The *Kepler* spacecraft that was launched in 2009 can detect giants (Bedding et al. 2010), and to discover Earth-like planets orbiting other stars. Consequently, in recent years, a large number of asteroseismic data has been obtained for different kinds of stars, which allowed the detection and characterization of solar-like oscillations in a large number of red giants by space missions (e.g. De Ridder et al. 2009). This adds in valuable and independent constraints to current stellar models. In particular, the confrontation between models including a detailed description of transport processes in stellar interiors as those that we developed and these asteroseismic constraints opens a new promising path for our understanding of stars. In addition, these grids help to develop statistical studies of the seismic properties of stellar populations.

On the other hand grids of stellar models at different metallicities are obviously a key tool for various important astrophysical topics related to e.g., stellar evolution in clusters, stellar nucleosynthesis, or chemical evolution. They are available since a long time for standard stellar models (e.g. Schaller et al. 1992; Forestini & Charbonnel 1997; Yi et al. 2003; Cassisi et al. 2006), and have recently appeared in the literature for rotation-induced models (Brott et al. 2011, Ekström et al. (2012)). However, these latest studies focus more on the evolution of massive stars, and do not include thermohaline mixing nor study the TP-AGB phase for low- and intermediate-mass stars as do those we present here.

The aim of the present paper is to provide the relevant classical stellar parameters together with the global asteroseismic properties of low- and intermediate-mass stars all along their evolution. This is done from the pre-main sequence (along the Hayashi track) to the early-asymptotic giant branch (and along the TP-AGB for selected cases) for the grid of models computed for four metallicities spanning the range between Z = 0.0001 and Z = 0.014 and with initial masses between 0.85/1.0 $M_\odot$ and 6.0 $M_\odot$. This grid contains models computed with rotation-induced mixing and thermohaline instability, along with standard models without mixing outside convective regions for comparison purposes.

Results

We recall the various impacts of metallicity variations and rotation-induced mixing on the global stellar properties such as central temperature and density, surface luminosity, effective temperature, and lifetimes. Althougth, thermohaline mixing changes the surface abundances from the bump luminosity and must be included in stellar evolution models to understand the observed chemical properties of bright giant stars (already discussed in Charbonnel & Lagarde (2010a) and Lagarde et al. (2011)), this process does not change the global stellar parameters like luminosity and effective temperature. In addition, it does not affect the global seismic properties presented here.

We also computed for the whole grid in mass and metallicity the global asteroseismic parameters that can be directly obtained from global stellar properties using scaling relations, and we used the information on the internal structure of models to compute asymptotic relations. Therefore we provide for the first time for low- and intermediate-mass stars all along their evolution, including effects of thermohaline instability and rotation-induced mixing :

- The large separation, the frequency with the maximum amplitude $\nu_{\rm max}$, as well as the maximum amplitude $A_{\rm max}$ depending on stellar mass, radius, effective temperature and luminosity. These asteroseismic quantities are additional observational constraints to determine them. Moreover, these asteroseismic parameters help us to establish the evolutionary stages of two stars having the same luminosity and effective temperature.

- The total acoustic radius T, the acoustic radius at the base of convective evelope $t_{\rm BCE}$, the acoustic radius at the location of helium second-ionisation region $t_{\rm He}$, and the asymptotic period spacing of g-modes $\Delta\Pi_{(l=1)}$ give us information about stellar structure. Indeed, $t_{\rm BCE}$ and $t_{\rm He}$ allow us to locate the base of convective envelope and the He-ionisation zone, respectively. On the oher hand, the presence of convective core affects the domain where the g-modes are trapped and therefore the value of $\Delta\Pi_{(l=1)}$. We can then distinguish two stars that have the same luminosity one being at the RGB bump and the other at the clump undergoing central He-burning.

We show that rotation-induced mixing has an impact on these quantities, contrary to thermohaline mixing. While rotation changes the global properties of main sequence stars and has an impact on the global asteroseismic properties, thermohaline mixing does not affect the seismic properties analyzed here although it changes the surface abundances in the red giants.

In addition to spectrophotometric studies, we show that seismic studies allow to distinguish two stars with approximatively the same surface luminosity and effective temperature but with different evolutionary stages.

A&A 543, A108 (2012)
DOI: 10.1051/0004-6361/201118331

Astronomy & Astrophysics

Thermohaline instability and rotation-induced mixing

III. Grid of stellar models and asymptotic asteroseismic quantities from the pre-main sequence up to the AGB for low- and intermediate-mass stars of various metallicities[⋆]

N. Lagarde[1], T. Decressin[1], C. Charbonnel[1,2], P. Eggenberger[1], S. Ekström[1], and A. Palacios[3]

[1] Geneva Observatory, University of Geneva, Chemin des Maillettes 51, 1290 Versoix, Switzerland
e-mail: `Nadege.Lagarde@unige.ch`
[2] IRAP, UMR 5277 CNRS and Université de Toulouse, 14 Av. E. Belin, 31400 Toulouse, France
[3] LUPM, Université Montpellier II, CNRS, UMR 5299, Place E. Bataillon, 34095 Montpellier, France

Received 25 October 2011 / Accepted 13 April 2012

ABSTRACT

Context. The availability of asteroseismic constraints for a large sample of stars from the missions CoRoT and *Kepler* paves the way for various statistical studies of the seismic properties of stellar populations.

Aims. We evaluate the impact of rotation-induced mixing and thermohaline instability on the global asteroseismic parameters at different stages of the stellar evolution from the zero age main sequence to the thermally pulsating asymptotic giant branch to distinguish stellar populations.

Methods. We present a grid of stellar evolutionary models for four metallicities ($Z = 0.0001$, 0.002, 0.004, and 0.014) in the mass range from 0.85 to 6.0 $M_{\odot}$. The models are computed either with standard prescriptions or including both thermohaline convection and rotation-induced mixing. For the whole grid, we provide the usual stellar parameters (luminosity, effective temperature, lifetimes, ...), together with the global seismic parameters, i.e. the large frequency separation and asymptotic relations, the frequency corresponding to the maximum oscillation power $\nu_{\max}$, the maximal amplitude $A_{\max}$, the asymptotic period spacing of g-modes, and different acoustic radii.

Results. We discuss a signature of rotation-induced mixing on the global asteroseismic quantities, that can be detected observationally. Thermohaline mixing whose effects can be identified using spectroscopic studies cannot be characterized by the global seismic parameters studied here. However, we cannot exclude that individual mode frequencies or other well chosen asteroseismic quantities might help us to constrain this mixing.

Key words. asteroseismology – instabilities – stars: evolution – stars: interiors – stars: rotation

1. Introduction

Much effort has been devoted to improving our understanding of the physics of low- and intermediate-mass stars, and in particular explaining the abundance anomalies they exhibit during their lifetime. Rotation has been shown to change the internal dynamics of these stars, by means of the transport of both angular momentum and chemical species through the action of meridional circulation and shear turbulence, combined possibly with other processes induced by internal gravity waves or magnetic fields (see e.g. Zahn 1992; Zahn et al. 1997; Maeder & Zahn 1998; Talon & Charbonnel 1998; Eggenberger et al. 2005; Charbonnel & Talon 2005, 2008). Rotation-induced mixing results in variations of the stellar chemical properties that successfully explain many of the abundance patterns observed at the surface of these stars (Palacios et al. 2003; Charbonnel & Talon 2008; Smiljanic et al. 2010; Charbonnel & Lagarde 2010). In addition, thermohaline mixing driven by ^{3}He-burning has been proposed to be the most likely process modifying the photospheric compositions of bright low-mass red giant stars (Charbonnel & Zahn 2007b; for references on the abundance anomalies at that evolution phase, see Charbonnel & Lagarde 2010, hereafter Paper I; and Lagarde et al. 2011, hereafter Paper II). During the thermal-pulse phase on the asymptotic giant branch (TP-AGB), thermohaline mixing was found to lead to lithium production (Paper I; Stancliffe 2010), accounting for the Li abundances observed in oxygen-rich AGB variables of the Galactic disk (Uttenthaler & Lebzelter 2010). In summary and as discussed in Papers I and II of this series (see also Charbonnel & Zahn 2007b), the effects of both rotation-induced mixing and thermohaline instability as described presently do account very nicely for most of the spectroscopic observations of low- and intermediate-mass stars at various metallicities.

This has crucial consequences for the chemical evolution of the Galaxy (Paper II, and Lagarde et al., in prep.), and should also be taken into account in the other topical astrophysical domains that use stellar models as input physics. This is particiularly true as asteroseismic probes observe stars across the Hertzsprung-Russell (HR) diagram. Thanks to the development of dedicated satellites such as CoRoT and *Kepler*, the internal properties of stars on both the main sequence (e.g. Michel et al. 2008; Chaplin et al. 2010) and the giant branches (e.g. De Ridder et al. 2009; Bedding et al. 2010) have been revealed. Furthermore, owing to the large number of stars observed by these missions, statistical studies are possible through

---

[⋆] Results tables are only available at the CDS via anonymous ftp to `cdsarc.u-strasbg.fr (130.79.128.5)` or via
`http://cdsarc.u-strasbg.fr/viz-bin/qcat?J/A+A/543/A108`

the determination of global pulsation properties such as the frequency of maximum oscillation power and the large frequency separation (see e.g. Miglio et al. 2009; Chaplin et al. 2011a).

In this broad context, the aim of the present paper is to provide the relevant classical stellar parameters together with the global asteroseismic properties of low- and intermediate-mass stars throughout their evolution. This is done from the pre-main sequence (along the Hayashi track) to the early-AGB (and along the TP-AGB for selected cases) for the grid of models computed in Papers I and II for four metallicities spanning the range between $Z = 0.0001$ and $Z = 0.014$ and with initial masses between 0.85 $M_\odot$ and 6.0 $M_\odot$. This grid contains models computed with rotation-induced mixing and thermohaline instability, along with for comparison purposes standard models without mixing outside convective regions. The present work is a prerequisite to validating the current theoretical prescriptions for the non-standard mechanisms before we test them through detailed seismic analysis of individual stars.

Such a grid of stellar models at different metallicities is obviously a key tool for various important astrophysical topics related to e.g., stellar evolution in clusters, stellar nucleosynthesis, and chemical evolution. They have been available for a long time as part of standard stellar models (e.g. Schaller et al. 1992; Forestini & Charbonnel 1997; Yi et al. 2003; Cassisi et al. 2006), and have more recently appeared in the literature for rotation-induced models (Brott et al. 2011; Ekström et al. 2012). However, these latest studies focus more on the evolution of massive stars, and neitherinclude thermohaline mixing nor study the TP-AGB phase for low- and intermediate-mass stars as we do here.

The paper is organized as follows. In Sect. 2, we describe the physical inputs of the stellar evolution models. The table content of our grids is presented in Sect. 3. Section 4 includes a short discussion on the main properties of the models and a comparison with the solar metallicity models of Ekström et al. (2012). In Sect. 5, we present the asteroseismic parameters of models with and without rotation. Finally, our main results are summarized in Sect. 6.

2. Physical inputs

The models are computed with the implicit Lagrangian stellar-evolution code STAREVOL (v3.00. See Siess et al. 2000; Palacios et al. 2003, 2006; Decressin et al. 2009). In this section, we summarize the main physical ingredients used for the present grid.

2.1. Basic inputs

The description of the stellar structure rests on the hydrostatic and the continuity equations, and the equations for energy conservation and transport. To solve this system, the following physical ingredients are required:

- Nuclear reaction rates are needed to follow the chemical changes inside burning sites, and to determine the production of energy by the nuclear reaction, $\epsilon_{\rm nuc}$, and the energy loss by the neutrino, ϵ_ν. We follow stellar nucleosynthesis with a network including 185 nuclear reactions involving 54 stable and unstable species from ^{1}H to ^{37}Cl. Numerical tables for the nuclear reaction rates were generated from the NACRE compilation (Arnould et al. 1999; Aikawa et al. 2005) with the NetGen web interface[1]. We mainly use reactions rates from either NACRE or Caughlan & Fowler (1988) when NACRE rates are unavailable. For proton captures on elements higher then Ne, we follow rates from Iliadis et al. (2001) or otherwise Bao et al. (2000). The following reactions rates are computed by:
  - ^{3}He(D, p)^{4}He (Descouvemont et al. 2004);
  - ^{3}He($\alpha\alpha$, γ)^{12}C (Fynbo et al. 2005);
  - ^{8}B(β, ν)2^{4}He; ^{13}N(β, ν)^{13}C; ^{22}Na(β, ν)^{22}Ne; ^{26}Alm(β, ν)^{26}Mg; ^{26}Alg(β, ν)^{26}Mg (Horiguchi et al. 1996);
  - ^{14}C(p, γ)^{15}N (Wiescher et al. 1990);
  - ^{14}C(p, n)^{14}N (Koehler & O'brien 1989a);
  - ^{14}C(α, n)^{17}O; ^{17}O(n,^{4}He)^{14}C (Schatz et al. 1993);
  - ^{14}C(α, γ)^{18}O (Funck & Langanke 1989);
  - ^{14}N(n, p)^{14}C (Koehler & O'brien 1989b);
  - ^{14}N(p, γ)^{15}O (Mukhamedzhanov et al. 2003);
  - ^{17}O(n, γ)^{18}O (Wagoner 1969);
  - ^{22}Ne(p, γ)^{23}Na (Hale et al. 2002);
  - ^{22}Ne(n, γ)^{23}Na (Beer et al. 2002);
  - ^{22}Na(n, γ)^{23}Na; ^{23}Na(α, p)^{26}Mg; ^{25}Mg(α, p)^{28}Si; ^{26}Mg(α, p)^{29}Si; ^{27}Al(α, p)^{30}Si (Hauser & Feshbach 1952);
  - ^{26}Alm(n, γ)^{27}Al; ^{26}Alg(n, γ)^{27}Al (Woosley et al. 1978)[2].
- The screening factors are calculated with the formalism of Mitler (1977) for weak and intermediate screening conditions and Graboske et al. (1973) for strong screening conditions.
- Opacities are required to compute the radiative gradient $\nabla_{\rm rad}$ and the energy transport by radiative transfer. We generate opacity tables according to Iglesias & Rogers (1996) using the OPAL website[3] for $T > 8000$ K that account for C and O enrichments. At lower temperature ($T < 8000$ K), we use the atomic and molecular opacities given by Ferguson et al. (2005).
- The equation of state relates the temperature, pressure, and density and thus provides different thermodynamic quantities ($\nabla_{\rm ad}$, $c_{\rm P}$, ...). In STAREVOL, we follow the formalism developed by Eggleton et al. (1973) and extended by Pols et al. (1995), which is based on the principle of Helmholtz free energy minimization (see Dufour 1999; and Siess et al. 2000, for detailed description and numerical implementation): this accounts for the non-ideal effects of Coulomb interactions and pressure ionization.
- The treatment of convection is needed to compute the temperature gradient inside a convective zone. It is based on a classical mixing-length formalism with $\alpha_{\rm MLT} = 1.6$, recovered from solar-calibrated models that include neither atomic diffusion nor rotation and were computed using Geneva models (see Ekström et al. 2012). We assume instantaneous convective mixing, except when hot-bottom burning occurs on the TP-AGB, which requires a time-dependent convective diffusion algorithm as developed in Forestini & Charbonnel (1997). The boundary between convective and radiative layers is defined with the Schwarzschild criterion. An overshoot parameter $d_{\rm over}/H_{\rm p}$ is taken into account for the convective core. This parameter is set to 0.05 or 0.10 respectively for stars with masses below or above 2.0 $M_\odot$[4].
- We use a gray atmosphere where the photosphere is defined as the layer for which the optical depth τ is between 0.005

---

[1] `http://www.astro.ulb.ac.be/Netgen/form.html`

[2] ^{26}Alm and ^{26}Alg represent the radioactive nuclide ^{26}Al in its two isomeric states.

[3] `http://adg.llnl.gov/Research/OPAL/opal.html`

[4] For small cores its mass is not allowed to be higher than $d_{\rm over}$ times the core mass.

and 10. We define the effective temperature and radius at the layer where $\tau = 2/3$.

- For mass loss, we use Reimers (1975) formula (with $\eta_R = 0.5$) from the ZAMS up to central helium exhaustion

$$\dot{M} = -3.98\ 10^{-13}\eta_R \frac{LR}{M}\ M_\odot\ \mathrm{yr}^{-1}. \tag{1}$$

On the AGB, we adopt the mass-loss prescription of Vassiliadis & Wood (1993).

2.2. Transport processes in radiative zones

2.2.1. Thermohaline mixing

Thermohaline instability develops along the red giant branch (RGB) at the bump luminosity in low-mass stars and on the early-AGB in intermediate-mass stars, when the gradient of molecular weight becomes negative ($\nabla_\mu = \frac{\mathrm{d}\ln\mu}{\mathrm{d}\ln P} < 0$) in the external wing of the thin hydrogen-burning shell surrounding the degenerate stellar core (Charbonnel & Zahn 2007b,a; Siess 2009; Stancliffe et al. 2009; Charbonnel & Lagarde 2010). This inversion of molecular weight is created by the $^3\mathrm{He}(^3\mathrm{He}, 2p)^4\mathrm{He}$ reaction (Ulrich 1971; Eggleton et al. 2006, 2008).

The present grid of models is computed using the prescription advocated by Charbonnel & Zahn (2007b) and Papers I, II. It is based on Ulrich (1972) with an aspect ratio of instability fingers $\alpha = 6$, in agreement with laboratory experiments (Krishnamurti 2003). It includes the correction for non-perfect gas (including radiation pressure, degeneracy) in the diffusion coefficient for thermohaline mixing that is given by:

$$D_\mathrm{t} = C_\mathrm{t}\, K\left(\frac{\varphi}{\delta}\right)\frac{-\nabla_\mu}{(\nabla_\mathrm{ad} - \nabla)} \quad \text{for } \nabla_\mu < 0, \tag{2}$$

where K is the thermal diffusivity; $\varphi = (\partial\ln\rho/\partial\ln\mu)_{P,T}$; $\delta = -(\partial\ln\rho/\partial\ln\nu)_{P,\mu}$; and with the non-dimensional coefficient

$$C_\mathrm{t} = \frac{8}{3}\pi^2\alpha^2. \tag{3}$$

The value of α in actual stellar conditions was recently questionned by the results of two- and three-dimentional hydrodynamical simulations of thermohaline convection for which α is close to unity (Denissenkov 2010; Denissenkov & Merryfield 2011; Rosenblum et al. 2011; Traxler et al. 2011). However, these simulations are still far from the stellar regime, hence we decided to use in this series the prescription described above since it successfully reproduces the abundance data for evolved stars of various masses and metallicities (see Papers I and II for a more detailed discussion).

2.2.2. Rotation-induced mixing

Pre-main sequence evolution along the Hayashi track is computed in a standard way (i.e., without accounting for rotation-induced mixing), and solid-body rotation is assumed on the Zero Age Main Sequence (ZAMS). On the main sequence, the evolution of the internal angular momentum profile is accounted for using the complete formalism developed by Zahn (1992), Maeder & Zahn (1998), and Mathis & Zahn (2004), which takes into account advection by meridional circulation and diffusion by shear turbulence (see Palacios et al. 2003, 2006; Decressin et al. 2009, for a description of the implementation in STAREVOL). We do not take into account the inhibitory effects of μ gradients in the treatement of rotation.

We assume solid-body rotation in the convective regions, as we did in Papers I and II. In addition, we assume that the transport of angular momentum is dominated by the large amount of turbulence in these regions that instantaneously flattens out the angular velocity profile as it does for the abundance profiles. This hypothesis leads to a minimum shear-mixing approach in the underlying radiative layers, as discussed in Palacios et al. (2006) and Brun & Palacios (2009).

On the other hand, the transport of angular momentum in stellar radiative layers obeys the advection/diffusion equation

$$\rho\frac{\mathrm{d}(r^2\Omega)}{\mathrm{d}t} = \frac{1}{5r^2}\frac{\partial}{\partial r}(\rho r^4\Omega U_r) + \frac{1}{r}\frac{\partial}{\partial r}\left(r^4\rho\nu_v\frac{\partial\Omega}{\partial r}\right) \tag{4}$$

where ρ, r, and Ω have their usual meaning, U_r is the vertical component of meridional circulation velocity, and ν_v is the vertical component of the turbulence viscosity.

The transport of chemical species resulting from meridional circulation and both vertical and horizontal turbulence is computed as a diffusive process (Chaboyer & Zahn 1992). The vertical transport of a chemical species i of concentration c_i is described by a pure diffusion equation

$$\frac{\mathrm{d}c_i}{\mathrm{d}t} = \underbrace{\dot{c}_i}_{\text{nuclear}} + \underbrace{\frac{1}{\rho r^2}\frac{\partial}{\partial r}\left(r^2\rho D_\mathrm{tot}\frac{\partial c_i}{\partial r}\right)}_{\text{diffusion processes}}, \tag{5}$$

where $\dot{c}_i$ represents the variations in the chemical composition due to nuclear reactions. The total diffusion coefficient D_tot for chemicals can be written as the sum of three coefficients

$$D_\mathrm{tot} = D_\mathrm{th} + D_\mathrm{eff} + D_\mathrm{v} \tag{6}$$

with D_th the thermohaline coefficient (Sect. 2.2.1), D_eff the effective diffusion coefficient ($\propto 1/D_\mathrm{h}$), and D_v the vertical turbulent diffusion coefficient (Talon & Zahn 1997), the last of which is proportional to the horizontal diffusion coefficient Chaboyer & Zahn 1992). The expression of the horizontal diffusion coefficient is taken from Zahn (1992), with its expression that prevents numerical divergence

$$D_\mathrm{h} = \frac{r}{C_\mathrm{h}}\left(|2V - \alpha U|^2 + U^2\right)^{1/2}. \tag{7}$$

We do consider neither possible interactions between thermohaline and rotation-induced mixing, nor magnetic diffusion. Under the present assumptions, the thermohaline diffusion coefficient is several orders of magnitude higher than both the total diffusion coefficient related to rotation and the magnetic diffusivity in the advanced phases where the thermohaline instability develops (see e.g., Charbonnel & Lagarde 2010; Cantiello & Langer 2010, and Paper II).

The complete treatment is applied up to either the RGB tip or the second dredge-up for stars undergoing the helium-flash episode.

2.3. Initial rotation velocity

The initial rotation velocity of our models on the ZAMS is chosen at 45% of the critical velocity at that point, with $V_\mathrm{crit} = \left(\frac{2}{3}\right)^{\frac{3}{2}}\left(\frac{GM}{R}\right)^{\frac{1}{2}}$. Here we take R to be the stellar radius computed without considering the stellar deformation due to rotation; if we were to take into account the deformation of the stellar radius as in Ekström et al. (2012), then our initial velocities would correspond to 30% of the critical velocity. This choice

Table 1. Initial abundances in mass fraction for the models at different metallicities.

[Fe/H] Element	0 $Z = 0.014$	–0.56 $Z = 0.004$	–0.86 $Z = 0.002$	–2.16 $Z = 0.0001$
^{1}H	7.20×10^{-01}	7.42×10^{-01}	7.47×10^{-01}	7.52×10^{-01}
^{2}H	3.74×10^{-05}	3.86×10^{-05}	3.89×10^{-05}	3.91×10^{-05}
^{3}He	2.83×10^{-05}	2.69×10^{-05}	2.67×10^{-05}	2.64×10^{-05}
^{4}He	2.66×10^{-01}	2.53×10^{-01}	2.50×10^{-01}	2.48×10^{-01}
^{6}Li	6.35×10^{-10}	1.81×10^{-10}	9.07×10^{-11}	4.53×10^{-12}
^{7}Li	9.00×10^{-09}	2.16×10^{-09}	2.17×10^{-09}	2.18×10^{-09}
^{9}Be	1.69×10^{-10}	4.82×10^{-11}	2.41×10^{-11}	1.21×10^{-12}
^{10}B	8.09×10^{-10}	2.31×10^{-10}	1.16×10^{-10}	5.78×10^{-12}
^{11}B	3.94×10^{-09}	1.13×10^{-09}	5.63×10^{-10}	2.82×10^{-11}
^{12}C	2.27×10^{-03}	6.47×10^{-04}	3.24×10^{-04}	1.62×10^{-05}
^{13}C	3.63×10^{-05}	1.04×10^{-05}	5.19×10^{-06}	2.59×10^{-07}
^{14}N	6.56×10^{-04}	1.87×10^{-04}	9.38×10^{-05}	4.69×10^{-06}
^{15}N	2.34×10^{-06}	6.69×10^{-07}	3.35×10^{-07}	1.67×10^{-08}
^{16}O	5.69×10^{-03}	1.62×10^{-03}	8.13×10^{-04}	4.06×10^{-05}
^{17}O	3.82×10^{-06}	1.09×10^{-06}	5.46×10^{-07}	2.73×10^{-08}
^{18}O	1.28×10^{-05}	3.67×10^{-06}	1.83×10^{-06}	9.17×10^{-08}
^{19}F	5.38×10^{-07}	1.54×10^{-07}	7.69×10^{-08}	3.85×10^{-09}
^{20}Ne	1.79×10^{-03}	5.10×10^{-04}	2.55×10^{-04}	1.28×10^{-05}
^{21}Ne	5.70×10^{-06}	1.63×10^{-06}	8.14×10^{-07}	4.07×10^{-08}
^{22}Ne	2.40×10^{-04}	6.85×10^{-05}	3.42×10^{-05}	1.71×10^{-06}
^{23}Na	2.65×10^{-05}	7.58×10^{-06}	3.79×10^{-06}	1.89×10^{-07}
^{24}Mg	4.99×10^{-04}	1.42×10^{-04}	7.13×10^{-05}	3.57×10^{-06}
^{25}Mg	6.69×10^{-05}	1.91×10^{-05}	9.56×10^{-06}	4.78×10^{-07}
^{26}Mg	7.67×10^{-05}	2.19×10^{-05}	1.10×10^{-05}	5.48×10^{-07}
^{27}Al	4.94×10^{-05}	1.41×10^{-05}	7.05×10^{-06}	3.52×10^{-07}
^{28}Si	5.97×10^{-04}	1.71×10^{-04}	8.53×10^{-05}	4.27×10^{-06}
^{29}Si	6.65×10^{-05}	1.90×10^{-05}	9.50×10^{-06}	4.75×10^{-07}
^{30}Si	4.81×10^{-05}	1.38×10^{-05}	6.87×10^{-06}	3.44×10^{-07}
^{31}P	5.54×10^{-06}	1.58×10^{-06}	7.91×10^{-07}	3.96×10^{-08}
^{32}S	3.24×10^{-04}	9.26×10^{-05}	4.63×10^{-05}	2.31×10^{-06}
^{33}S	3.48×10^{-06}	9.95×10^{-07}	4.97×10^{-07}	2.49×10^{-08}
^{34}S	1.80×10^{-05}	5.15×10^{-06}	2.58×10^{-06}	1.29×10^{-07}
^{35}Cl	6.54×10^{-06}	1.87×10^{-06}	9.34×10^{-07}	4.67×10^{-08}
^{37}Cl	2.15×10^{-06}	6.14×10^{-07}	3.07×10^{-07}	1.53×10^{-08}
Others	1.47×10^{-03}	4.19×10^{-04}	2.09×10^{-04}	1.05×10^{-05}

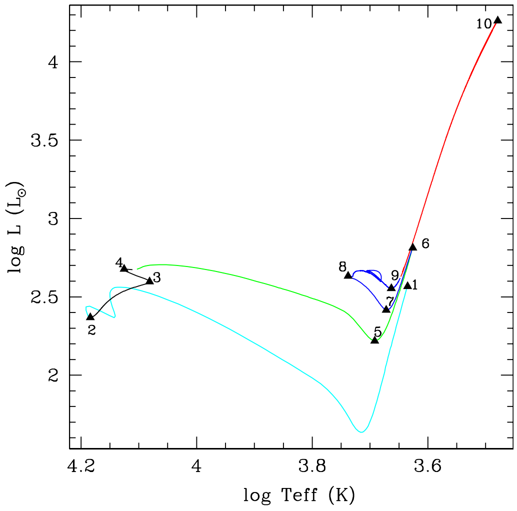

Fig. 1. Evolution track in the Hertzsprung-Russell diagram of the standard 4.0 $M_\odot$ model at solar metallicity. Each phase is indicated by a different color: pre-main sequence (cyan), main sequence (black), Hertzsprung gap and red giant branch (green), core helium-burning phase (blue), and asymptotic giant branch (red). Black triangles show the points that we have selected to describe the tracks (see Sect. 3.1)

of $V_{\rm ini}/V_{\rm crit} = 0.45$ closely agrees with the mean value of the observed velocity distribution for low- and intermediate-mass stars in young open clusters. This initial rotation rate leads to mean velocities on the main sequence of between 90 and 137 km s^{-1}.

We apply magnetic braking only to [1.25 $M_\odot$; $Z_\odot$] and [0.85 $M_\odot$; Z = 0.0001] following the description of Kawaler (1988) according to Talon & Charbonnel (1998) and Charbonnel & Talon (1999).

We neglect the transport by internal gravity waves, which is efficient only in main sequence stars with effective temperatures on the ZAMS lower than 6500 K (see Talon & Charbonnel 2003). We similarly account for neither dynamo processes nor the presence of fossil magnetic fields.

2.4. Initial abundances

Table 1 presents the initial abundances in mass fraction that we assume at different metallicities. We adopt the solar mixture of Asplund et al. (2009), except for Ne for which we use the value derived by Cunha et al. (2006). We use the ratio $\Delta Y/\Delta Z = 1.29$ derived by Ekström et al. (2012) to account for the enrichment in helium reported to enrichment in heavy elements in the Galaxy until the birth of the Sun. For the primordial abundances, we take the WMAP-SBBN value from Coc et al. (2004). To determine the initial composition of our models at a given metallicity Z, we use the scaling ($X_i = X_{i,\odot} \cdot \frac{Z}{Z_\odot}$) for all elements except for ^{7}Li, which is assumed to be constant (Li/H = 4.15×10^{-10}) for $\frac{Z}{X} < 7.8 \times 10^{-3}$. We assume that [$\alpha$/Fe] = 0 at all metallicities, which has a negligible impact in the present context[5].

3. Description of grids

3.1. Content of electronic tables

We provide files containing sets of relevant physical quantities as a function of time that characterize our models computed in the initial mass range between 0.85 $M_\odot$ and 6.0 $M_\odot$ with four metallicities Z = 0.0001, 0.002, 0.004, and 0.014 ([Fe/H] = −2.16, –0.86, –0.56, and 0, respectively). For each mass and metallicity, models are computed with standard prescriptions (no mixing other than that caused by convection), and for both thermohaline instability and rotational transport. For all masses, the evolution is followed from the beginning of the pre-main sequence (along the Hayashi track) up to the early-AGB phase. For each model, we selecte 500 points to allow a good description of the full raw tracks. We first established several key evolutionary points (see Fig. 1):

1. beginning of the pre-main sequence;

---

[5] Using [α/Fe] = +0.3 instead of 0 for our [1.5 $M_\odot$; Z = 0.0001] model leads to a decrease in the main-sequence lifetime by ~2%, and lowers the turnoff luminosity and effective temperature by 5% and 1% respectively. This is negligible compared to the effects of rotation.

2. the ZAMS defined as the time when the central hydrogen abundance X_c has decreased by 0.003 in mass fraction compared to its initial value;
3. turning point with the lowest $T_{\rm eff}$ on the main sequence;
4. end of core H-burning defined as the point beyond which X_c is smaller than 10^{-7};
5. bottom of the red giant branch (RGB);
6. the RGB-tip;
7. local minimum of luminosity during central helium-burning;
8. local maximum of $T_{\rm eff}$ during central helium-burning;
9. bottom of AGB: point with local minimum of luminosity after the loop on HB;
10. end of core helium-burning defined as the point beyond which Y_c is smaller than 10^{-4}.

The data in the tables are linearly interpolated within the results of each evolutionary model. We perform the interpolation as a function of time, of the central mass fraction of hydrogen or helium, or luminosity according to the evolutionary phase, and the final interpolated values are given at 499 points that we distribute as follows:

- 99 points evenly distributed in time that sample the pre-main sequence between points number 1 and 2;
- 110 points evenly distributed in terms of the central hydrogen mass fraction $X_{\rm C}$ that sample the main sequence with 85 points distributed between points number 2 and 3, and 25 points distributed between points number 3 and 4;
- 60 points evenly spaced in time sample the Herzsprung gap between points number 4 and 5;
- 80 points evenly distributed in terms of $\log L$ sample the RGB between points number 5 and 6;
- 20, 70 and 70 points evenly distributed in terms of $Y_{\rm C}$ respectively sample the central He burning phase between points number 6 and 7[6], 7 and 8 and, 8 and 9;
- finally, 50 points evenly spaced in $\log L$ are selected between points number 9 and 10.

For each model, we store the quantities given in Table 2 in a file that can be retrieved on the web page[7].

3.2. Comparisons between the models of Ekström et al. (2012, Geneva code) and our models (STAREVOL)

Ekström et al. (2012) computed a large grid of models taking into account rotation for stars of mass from 0.8 to 120 $M_\odot$ at solar metallicity with the Geneva stellar evolution code. The present grid is complementary to these models since the low-mass star models of Ekström et al. (2012) are computed only until the helium flash at the RGB tip and do not include thermohaline mixing. In addition, we presently explore asteroseismic diagnostics during the TP-AGB.

To offer this complementarity between the models of these two sets of giants, we were careful in choosing the same input physics and assumptions, although some differences remain that we describe below. Both codes adopt the same physical inputs for convection (Schwarzschild criterion and overshoot), opacities, mass loss, and nuclear reaction rates, and for the mass domain explored the different equations of state have a negligible impact on the stellar structures. The initial abundances of our models are similar, apart from the larger number of species considered by STAREVOL. STAREVOL has indeed a more extended network of nuclear reactions than the Geneva code, which allows us to follow in particular the evolution of unstable elements such as ^{13}N, ^{15}O, and ^{7}Be. As a consequence, the convective cores are smaller on the main sequence in STAREVOL models (by ~7% for the [4.0 $M_\odot$, $Z_\odot$] model), and the tracks in the HR-diagram are slightly less luminous ($L_{\rm TO}$ is ~10% lower for the [4.0 $M_\odot$, $Z_\odot$] model). This results in a difference in the lifetime on the main sequence of 4% for the [4.0 $M_\odot$, $Z_\odot$] model. This is the main difference we could identify when comparing standard models computed with the two codes.

For the rotational transport, both codes follow the advection by meridional circulation and the diffusion by shear turbulence. We carefully checked that the use of a different prescription for the turbulent diffusion coefficient D_v (Talon & Zahn 1997, in STAREVOL; and Maeder 1997, in Geneva code) has no impact in the mass domain we explore, as the mixing above the convective core is dominated by $D_{\rm eff}$. Both codes use prescriptions from Zahn (1992) for the horizontal diffusion coefficient, $D_{\rm h}$. However, in STAREVOL we always use Eq. (7) that is given by Zahn (1992) to avoid the divergence in the effective diffusion coefficient ($\propto \frac{1}{D_{\rm h}}$), while in the Geneva code the original Eq. (2.29) of Zahn (1992) is used. Surprisingly, Eq. (7) implies higher values of $D_{\rm h}$ at the edge of the convective core (by about a factor of four in the [4.0 $M_\odot$, $Z_\odot$] model on the main sequence), which leads to less mixing in these central regions. Combined with the STAREVOL models having a lower initial rotation velocity on the ZAMS, this results in a shorter lifetime and lower luminosity (the maximum difference being 15% for the [4.0 $M_\odot$, $Z_\odot$] model).

4. Global properties of the models

The effects of rotation-induced mixing and thermohaline instability on the surface chemical properties of the grid stars were extensively discussed in Papers I and II. Here we focus on the global properties of the models.

4.1. Hertzsprung-Russell diagrams and $\log T_c$ versus $\log \rho_c$

The evolutionary tracks in the HR diagram are shown in Fig. 2 for all the models computed in this study, with and without rotation. We also present the evolution of the central temperature and density in Fig. 3 for the solar-metallicity case.

4.1.1. Metallicity effects

We first recall the impact of metallicity as already reported in the literature (e.g. Schaller et al. 1992; Schaerer et al. 1993; Charbonnel 1994; Heger & Langer 2000; Maeder 2009). For a given stellar mass, one notes the following effects when metallicity decreases, owing to a decrease in the radiative opacity:

- the ZAMS is shifted to the blue, and both the stellar luminosity and effective temperature are higher at that phase than for solar metallicity models;
- the positions of the RGB and the AGB are shifted to the blue, and the ignition of helium (in degenerate conditions or not) occurs at a lower luminosity at the tip of the RGB ($L = 21\,308\,L_\odot$ and $21\,252\,L_\odot$ for models [1.5 $M_\odot$, $Z = 0.014$ and $Z = 0.002$], respectively);

---

[6] For low-mass stars below 2.0 $M_\odot$ in which a helium-flash occurs, we do not include table points between evolutionary points number 6 and 7.

[7] `http://obswww.unige.ch/Recherche/evol/-Database-`

Table 2. Description of table containing the results of our evolutionary models, both in the standard case and when including rotation and thermohaline mixing.

Stellar parameters	Surface abundances	Central abundances
- Model number	^{1}H ^{2}H	^{1}H
- Maximum of temperature $T_{\rm max}$ (K)	^{3}He ^{4}He	^{3}He ^{4}He
- Mass coordinate of $T_{\rm max}$ ($M_\odot$)	^{6}Li ^{7}Li	
- Effective temperature $T_{\rm eff}$ (K)	^{7}Be ^{9}Be	
- Surface luminosity L ($L_\odot$)	^{10}B ^{11}B	
- Photospheric radius radius $R_{\rm eff}$ ($R_\odot$)	^{12}C ^{13}C ^{14}C	^{12}C ^{13}C ^{14}C
- Photospheric density $\rho_{\rm eff}$ (g cm^{-3})	^{14}N ^{15}N	^{14}N
- Density at the location of $T_{\rm max}$, $\rho_{\rm max}$ (g cm^{-3})	^{16}O ^{17}O ^{18}O	^{16}O ^{17}O ^{18}O
- Stellar mass M ($M_\odot$)	^{19}F	^{19}F
- Mass-loss rate ($M_\odot$ yr^{-1})	^{20}Ne ^{21}Ne ^{22}Ne	^{20}Ne ^{21}Ne ^{22}Ne
- Age t (yr)	^{23}Na	^{23}Na
- Photospheric gravity log($g_{\rm eff}$) (log(cgs))	^{24}Mg ^{25}Mg ^{26}Mg	^{24}Mg ^{25}Mg ^{26}Mg
- Central temperature $T_{\rm c}$ (K)	^{26}Al ^{27}Al	^{26}Al ^{27}Al
- Central pressure $P_{\rm c}$	^{28}Si	^{28}Si
- Surface velocity $\upsilon_{\rm surf}$ (km s^{-1})		
- Mass at the base of convective envelope ($M_\odot$)		
- The large separation from scaling relation $\Delta\nu_{\rm scale}$ (νHz)		
- The large separation from asymptotic relation $\Delta\nu_{\rm asymp}$ (νHz)		
- The frequency with the maximum amplitude $\nu_{\rm max}$		
- The maximum amplitude $A_{\rm max}$		
- The asymptotic period spacing of g-modes $\Delta\Pi$ (s)		
- The total acoustic radius T (s)		
- The acoustic radius at the base of the convective envelope $t_{\rm BCE}$ (s)		
- The acoustic radius at the location of helium second-ionisation region $t_{\rm He}$ (s)		

- central helium-burning occurs at a higher effective temperature, and more extended blue loops are obtained.

4.1.2. Impact of rotation-induced mixing and thermohaline instability

- As has been known for a long time (see e.g. Maeder & Meynet 2000) and shown in Fig. 2, rotation-induced mixing affects the evolution tracks in the HR diagram. On the main sequence, rotational mixing brings fresh hydrogen fuel into the longer-lasting convective core, and transports H-burning products outwards. This results in more massive helium cores at the turnoff than in the standard case and shifts the tracks toward higher effective temperatures and luminosities throughout their evolution (Ekström et al. 2012; Heger & Langer 2000; Maeder & Meynet 2000; Meynet & Maeder 2000). The right panel of Fig. 3 shows the central conditions in standard and rotating models for selected masses at solar metallicity. Rotating models behave as stars with higher masses throughout their evolution.
- Thermohaline mixing induced by ^{3}He-burning becomes efficient only on the RGB at the bump luminosity (Charbonnel & Zahn 2007b; Charbonnel & Lagarde 2010). Beyond this point, the double-diffusive instability develops in a very thin region located between the hydrogen-burning shell and the convective envelope, and has a negligible effect on the stellar structure. It does not modify the evolutionary tracks in the HR diagram nor the $\log T_{\rm c}$ versus $\log \rho_{\rm C}$ diagram.

4.2. Lifetimes

The theoretical lifetimes are shown in Fig. 4 for the main phases of evolution as a function of the initial stellar mass and for the four metallicities considered, with the effects of rotation being clearly illustrated. We recall the main points:

- The duration of all the evolutionary phases decreases when the initial stellar mass increases and when the metallicity decreases (Schaller et al. 1992; Schaerer et al. 1993; Charbonnel 1994), which is consistent with the above-mentioned luminosity and effective-temperature differences.
- After the bump luminosity, the thermohaline mixing does not affect the lifetimes on the RGB and on the early-AGB phases.
- The lifetimes of rotating models on the main sequence are longer than those of the standard models. Indeed rotation-induced mixing brings fresh hydrogen fuel into the stellar core during that phase. As a consequence, the exhaustion of hydrogen in the central region is delayed and the lifetime on the main sequence lengthens; in addition, the mass of the helium-core is larger at the end of the main sequence when rotation is accounted for (Ekström et al. 2012; Heger & Langer 2000; Maeder & Meynet 2000; Meynet & Maeder 2000).
- As a consequence of having a more massive core at the end of the main sequence due to rotation, the models that undergo the helium-flash spend a shorter time on the RGB (see Fig. 4). As for the Main Sequence (MS), all rotating models have a longer lifetime during the quiescent central He burning phase.
- Lifetimes on the early-AGB are longer in rotating models than in standard models, owing to their more massive core. This remains unchanged if we add the lifetime on the TP-AGB (1.1×10^{6} yr for [1.5 $M_\odot$, $Z_\odot$] and 2×10^{6} yr for [3 $M_\odot$, $Z_\odot$]) to the early-AGB, as the total lifetime on the AGB is only increased by a few percent.

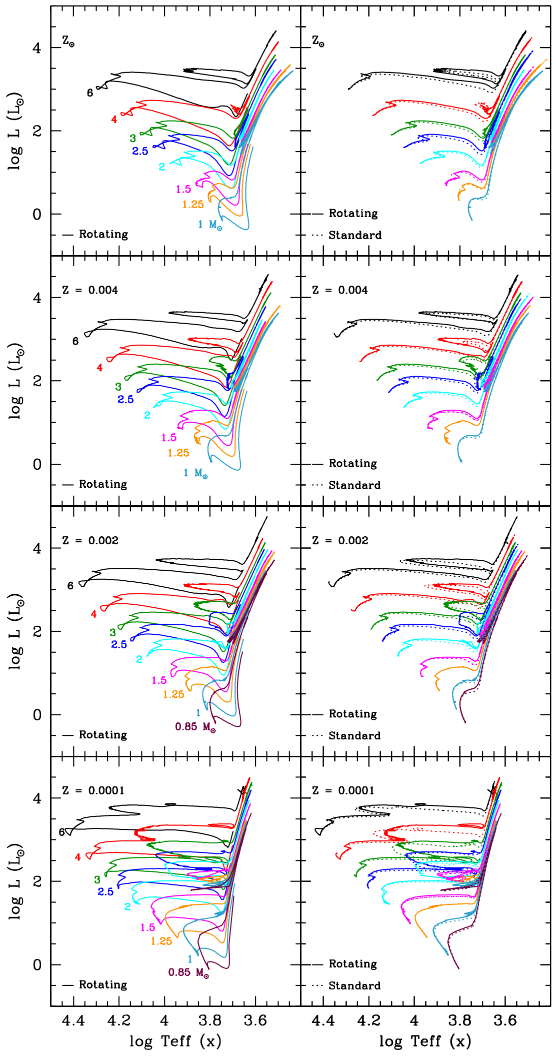

Fig. 2. Theoretical evolution tracks in the HR diagram for the ensemble of calculated models for all metallicities ($Z_{\odot}$, $Z = 0.004$, $Z = 0.002$, and $Z = 0.0001$, from top to bottom). In the *left panels*, the tracks are shown for the rotating models from the pre-main sequence on. In the *right panels*, both standard and rotating predictions are shown (dashed and solid lines respectively) from the ZAMS and beyond.

- As seen in previous subsections, thermohaline mixing has a negligible impact on the stellar structure, and modifies neither the stellar evolutionary tracks nor lifetimes.

5. Global asteroseismic quantities

A large number of asteroseismic observations have been obtained for different kinds of stars. In particular, the detection and characterization of solar-like oscillations in a large number of red giants by space missions (e.g. De Ridder et al. 2009) promises to provide valuable and independent constraints of current stellar models. The comparison of models including a detailed description of transport processes in stellar interiors and these asteroseismic constraints promises to help us improve our understanding of stars.

Rotation is one of a number of key processes that change all outputs of stellar models (see Sect. 4) with a significant impact on asteroseismic observables. In the case of main-sequence solar-type stars, rotation is found to shift the evolutionary tracks to the blue part of the HR diagram resulting in higher values of the large frequency separation for rotating models than for non-rotating ones at a given evolutionary stage (Eggenberger et al. 2010a). For red giants, rotating models are found to decrease the determined value of the stellar mass of a star located at a given luminosity in the HR diagram and to increase the value of its age. Consequently, the inclusion of rotation significantly changes the fundamental parameters determined for a star by performing an asteroseismic calibration (Eggenberger et al. 2010b).

5.1. Scaling relations and asymptotic quantities provided for the present grid

For this new grid of standard and rotating models, we now provide the values of different asteroseismic parameters (see Table 2) that can be directly computed from global stellar properties using scaling relations. We also use the information on the internal structure of models to compute asymptotic relations. These scaling relations are particularly useful for constraining stellar parameters and obtaining additional information about stellar evolution without the need to perform a full asteroseismic analysis (see e.g. Stello et al. 2009; Miglio et al. 2009; Hekker et al. 2009; Mosser et al. 2010; Chaplin et al. 2011b; Beck et al. 2011; Bedding et al. 2011). Although solar-like oscillations are expected to be excited in relatively cool stars (main sequence, as well as red giant stars), these global asteroseismic quantities are provided for all models of our grid and not only for models with a significant convective envelope.

The first global asteroseismic quantity we provide is the large frequency separation $\Delta\nu$, which is expected to be proportional to the square root of the mean stellar density (e.g. Ulrich 1986)

$$\Delta\nu_{\rm scale} = \Delta\nu_{\odot} \left(\frac{M}{M_{\odot}}\right)^{0.5} \left(\frac{R}{R_{\odot}}\right)^{-1.5}, \quad (8)$$

with the solar large-frequency separation $\Delta\nu_{\odot} = 134.9\,\mu$Hz.

Belkacem et al. (2011) proved that the frequency $\nu_{\rm max}$ at which the oscillation modes reach their strongest amplitudes is approximatively proportional to the acoustic cut-off frequency, as suspected by Brown et al. (1991) and Kjeldsen & Bedding (1995), such that

$$\nu_{\rm max} = \nu_{\rm max,\odot} \left(\frac{M}{M_{\odot}}\right) \left(\frac{R}{R_{\odot}}\right)^{-2} \left(\frac{T_{\rm eff}}{T_{\rm eff,\odot}}\right)^{-0.5}, \quad (9)$$

for the solar value $\nu_{\rm max,\odot} = 3150\,\mu$Hz.

Finally, the value of maximum oscillation amplitude relative to that of the Sun ($A_{\rm max}/A_{\rm max,\odot}$) is computed using the relation (e.g. Huber et al. 2011)

$$A_{\rm max}/A_{\rm max,\odot} = \frac{(L/L_{\odot})^{s}}{(M/M_{\odot})^{t}} \left(\frac{T_{\rm eff}}{T_{\rm eff,\odot}}\right)^{-r}, \quad (10)$$

for the solar value from *Kepler* $A_{\rm max,\odot} = 2.5$ ppm.

Following Huber and collaborators, we adopt $s = 0.838$ and $t = 1.32$. A value of $r = 2$ is adopted as advocated by Kjeldsen & Bedding (1995). We note that we simply assume that these relations hold for the different models computed here and that we do

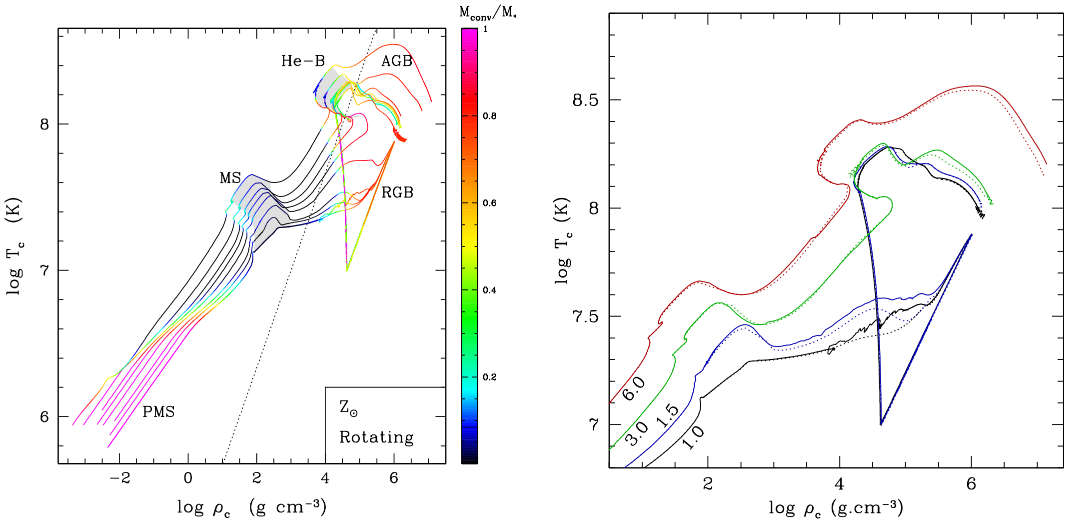

Fig. 3. *Left panel*: central density as a function of central temperature for the rotating $Z_{\odot}$ models. Colours indicate the mass of convective regions (convective core and convective envelope) over the total stellar mass. Shaded regions indicate the phases of central hydrogen-burning (MS) and helium-burning (He-B). *Right panel*: central density as a function of central temperature for standard and rotating models (dashed and solid lines respectively) for four initial stellar masses from the ZAMS beyond.

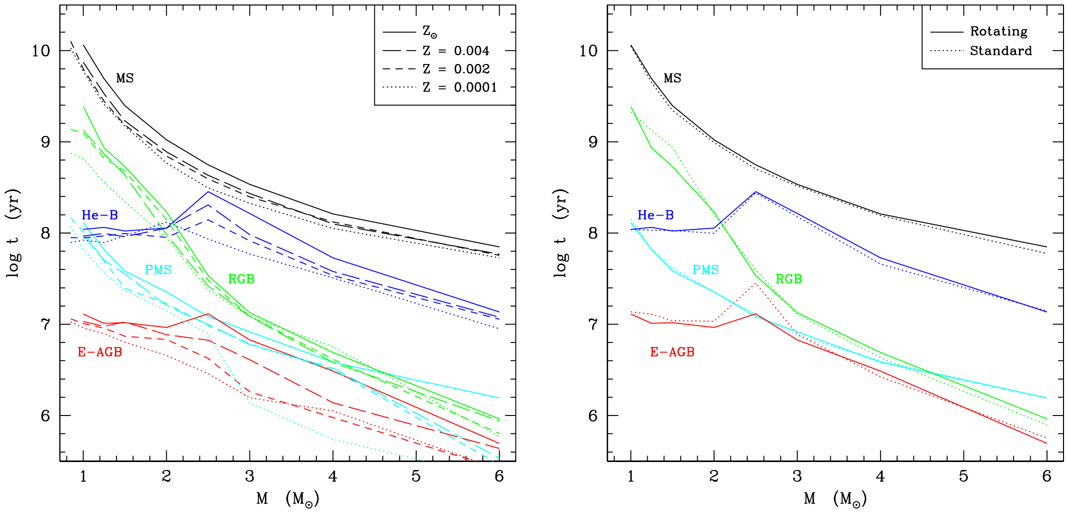

Fig. 4. Duration of the different evolution phases as a function of the initial stellar mass. *(Left)* Effects of metallicity in the standard models. *(Right)* Effects of rotation at solar metallicity.

not test the validity of the scaling relations. Preliminary studies suggest that these simple scaling relations hold reasonably well for main sequence and RGB stars (e.g. Stello et al. 2009; White et al. 2011).

In addition to the asteroseismic observables deduced from scaling relations, asymptotic asteroseismic quantities are also provided.

The asymptotic large frequency separation is given by

$$\Delta\nu_{\mathrm{asymp}} = \left(2\int_0^R \frac{\mathrm{d}r}{c_{\mathrm{s}}}\right)^{-1}, \tag{11}$$

where R is the stellar radius and c_{s} is the sound speed.

The total acoustic radius T is directly related to the large frequency separation, such that

$$T = \int_0^R \frac{\mathrm{d}r}{c_{\mathrm{s}}} = \frac{1}{2\cdot\Delta\nu_{\mathrm{asymp}}}. \tag{12}$$

The acoustic radius at the base of convective envelope (t_{BCE}) and the location of the helium second-ionisation region[8] (t_{He})

---

[8] The Schwarzschild citerion allows us to define the base of the convective envelope. The mininum in Γ_1, the adiabatic exponent, corresponding to He-II defines the location of the helium second-ionisation region.

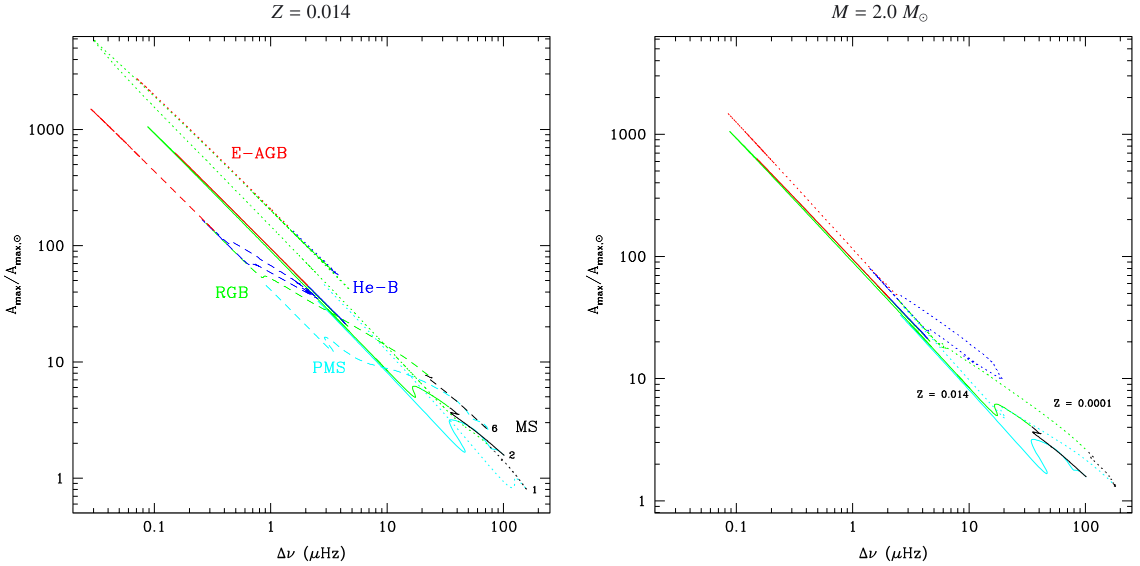

Fig. 5. Maximal amplitude compared to solar as a function of the large separation: (*left panel*) at solar metallicity for 1.25 $M_\odot$, 2.0 $M_\odot$, and 6.0 $M_\odot$ rotating models, and (*right panel*) at two metallicities $Z = 0.014$ (solid lines) and $Z = 0.0001$ (dotted-lines) for a 2.0 $M_\odot$ rotating model. Evolutionary phases are color-labeled: pre-main sequence (cyan), main sequence (black), RGB (green), helium-burning (blue), and AGB (red).

are determined with the relations

$$t_{\rm BCE} = \int_0^{r_{\rm BCE}} \frac{{\rm d}r}{c_{\rm s}},\quad t_{\rm He} = \int_0^{r_{\rm He}} \frac{{\rm d}r}{c_{\rm s}}, \tag{13}$$

where $r_{\rm BCE}$ and $r_{\rm He}$ represent the stellar radius at the base of convective envelope and the location of the helium second-ionization zone, respectively.

The period spacing of gravity modes for $\ell = 1$ and different acoustic radii can be determined with the asymptotic relation

$$\Delta\Pi(\ell = 1) = \frac{2^{\frac{1}{2}} \cdot \pi^2}{\int_{r_1}^{r_2} N \cdot \frac{{\rm d}r}{r}}, \tag{14}$$

where N is the Brunt-Väisälä frequency, and r_1 and r_2 define the domain (in radius) where the g modes are trapped. Within this region, the mode frequency (ω) must satisfy the conditions

$$\omega^2 < N^2 \tag{15}$$

and

$$\omega^2 < S_1^2 = \frac{l(l+1)c_{\rm s}^2}{r^2} \tag{16}$$

where S_1 is the Lamb frequency.

In the following discussions, we use the large separation determined with the scaling relation $\Delta\nu_{\rm scale}$(noted $\Delta\nu$ in the following sections). We have compared the large separation estimates $\Delta\nu_{\rm scale}$ (Eq. (8)) and $\Delta\nu_{\rm asymp}$ (Eq. (11)) to evaluate the difference between both expressions. On the main sequence, this difference varies between 3% and 5% for a 1.0 $M_\odot$ model at solar metallicity. We find that the relative error obtained when using either Eqs. (8) or (11) depends on the stellar mass (i.e. 3–8% for [2.0 $M_\odot$, $Z_\odot$] MS model), the metallicity (i.e. 10–12% for the [2.0 $M_\odot$, $Z = 10^{-4}$] MS model), and the evolutionary phase (i.e. <15% on RGB, <10% on He-B both for [1.0 $M_\odot$, $Z_\odot$] model). In a future paper, we propose to interpret these differences and investigate how they compare to White et al. (2011).

5.2. Evolution of the asteroseismic observables

We now describe the global asteroseismic properties of low- and intermediate-mass stars during their evolution, and discuss the effects of varying the stellar mass, metallicity, and the non-standard mixing mechanisms. We illustrate our discussion in Figs. 5 to 10. In Fig. 5, we present the maximal oscillation amplitude as a function of the large frequency separation throughout the stellar evolution from the pre-main sequence to the AGB phase for three different initial stellar masses at solar metallicity (left panel) and for a 2 $M_\odot$ star between the lowest ($Z = 0.0001$) and the highest ($Z = 0.014$) metallicities explored here (right panel). The line colors change with the stellar evolution phases: cyan corresponds to the pre-main sequence, black to the main sequence, green to the red giant branch, blue to core helium-burning, and red to the AGB. Figure 6 presents the same quantities for all the stellar masses considered at solar metallicity, for both the standard and the rotating cases (dashed and solid lines, respectively), each evolutionary phase being presented singly.

5.2.1. Trends for a given stellar mass and metallicity – the case of the 2.0 $M_\odot$, $Z_\odot$ models

We now describe the evolution of the seismic properties of a star of 2.0 $M_\odot$ at solar metallicity as depicted by the solid line in Fig. 5 and the black line in Fig. 6. Although this 2 $M_\odot$ star is not expected to undergo solar-like oscillations during the main sequence owing to its too high surface temperature, it represents a typical model of a red giant exhibiting solar-like oscillations. Moreover, the discussion in the changes of the asteroseismic quantities during the main sequence remains globally valid for less-massive main-sequence stars (the main difference being the value of the ratio of the acoustic radius at the base of the convective envelope to the total acoustic radius, see Fig. 8).

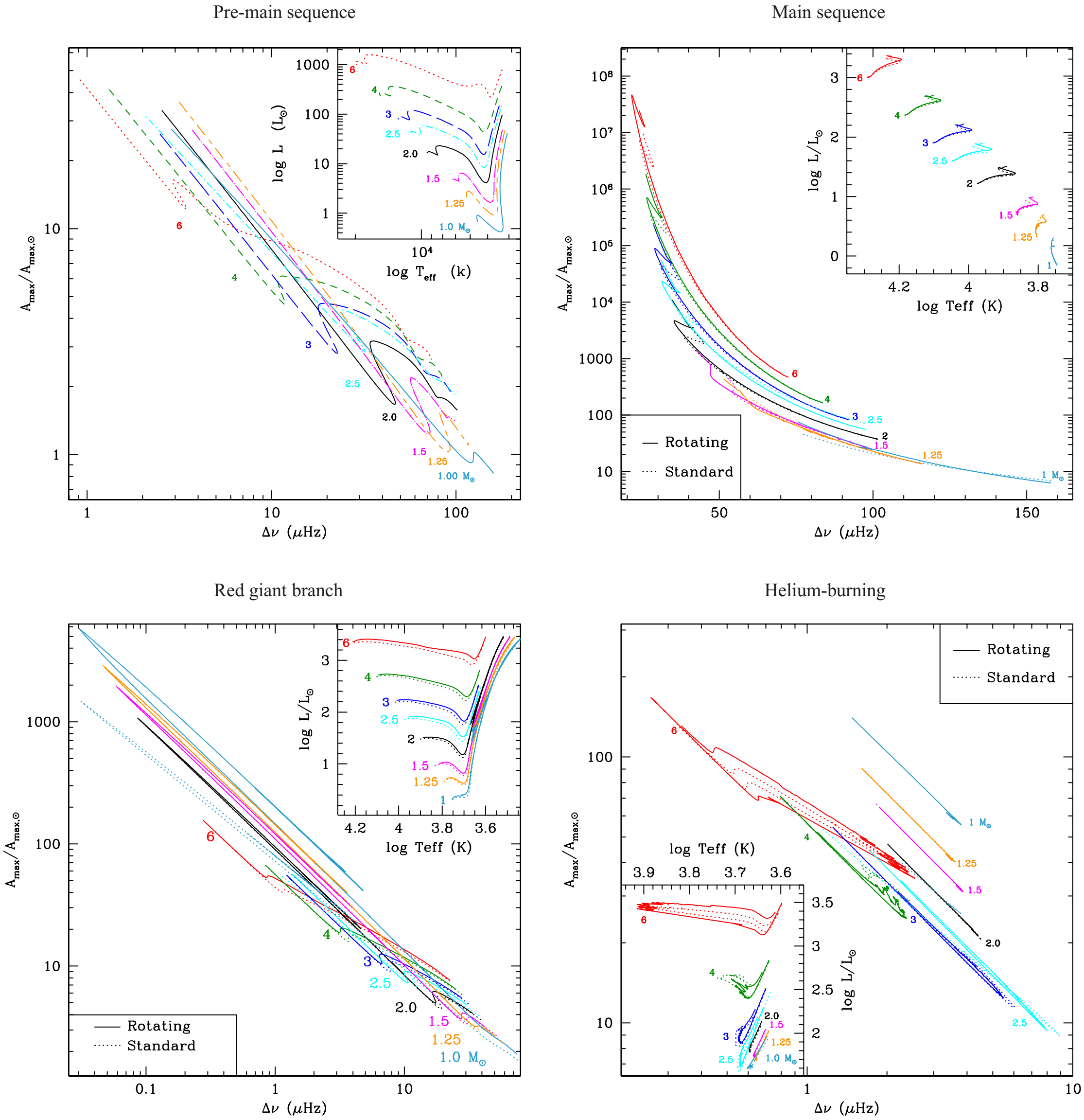

Fig. 6. Maximal amplitude compared to solar as a function of the larger separation for models at $Z_\odot$. *Top-left panel*: on the pre-main sequence; *top-right panel*: on the main sequence; *bottom-left panel*: on the red giant branch; *bottom-right panel:* on helium-burning phase. Standard models and rotating models are shown with dashed and solid lines respectively except for pre-main sequence. The corresponding evolution in the Hertzsprung-Russell diagram is shown on the right corner of each panel.

The large separation $\Delta\nu$ increases along the pre-main sequence because of its inverse dependence on stellar radius, which decreases during that phase (see Eq. (14)). On the other hand, the simultaneous decrease in maximal amplitude $A_{max}/A_{max,\odot}$ results from the decrease in luminosity and from the rise in effective temperature (see Eq. (10)).

On the main sequence, $A_{max}/A_{max,\odot}$ rises because of its dependence on both luminosity and the inverse of the effective temperature. In addition, the expansion of the stellar radius causes $\Delta\nu$ to increase. The radius increase also causes the large separation to drop significantly as the model evolves on the RGB, while the maximum amplitude increases during this phase as a result of the luminosity increase and the effective temperature decrease.

After the helium-flash at the tip of the RGB, the luminosity and the stellar radius dwindle with a rise in effective temperature, implying that the maximum of the amplitude wanes as the large separation increases. Throughout the helium-burning

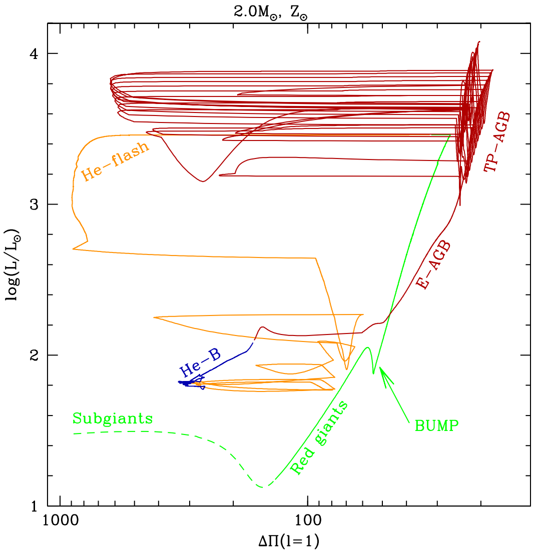

Fig. 7. The stellar luminosity as a function of the asymptotic period spacing of g-modes for the standard 2.0 $M_\odot$ model at solar metallicity. Evolutionary phases are color-labeled: subgiant (green dashed), red giant (green solid), helium-flash episode (orange), helium-burning (blue), and asymptotic giant branch (red).

phase, the luminosity and stellar radius increase, while the effective temperature and stellar mass decrease. Consequently, a gain in $A_{\rm max}$ is obtained, while the large separation reduces.

Figure 7 presents the asymptotic period spacing of gravity modes $\Delta\Pi(\ell = 1)$ for the standard model of 2.0 $M_\odot$ at solar metallicity. As proposed by Bedding et al. (2011) and Mosser et al. (2011), this quantity allows us to distinguish two stars that have the same luminosity, one being at the RGB bump and the other one being at the clump undergoing central He burning. At $\log(L/L_\odot) \sim 2.0$, we indeed find that $\Delta\Pi(\ell = 1) = 55$ s at the RGB bump, and $\Delta\Pi(\ell = 1) = 190$ s in the clump. As the stellar structure, and more particularly the presence of the convective core affects the domain where the g-modes are trapped, $\Delta\Pi(\ell = 1)$ is larger in clump stars than in RGB stars (Christensen-Dalsgaard 2011). Large variations in $\Delta\Pi(\ell = 1)$ are observed during the thermal pulses and helium-flash phase because of the formation of an intermediate convective zone during the helium-flashes and thermal pulses. We assume that the modes are trapped in the outermost radiative zone leading to a large value of $\Delta\Pi(\ell = 1)$ (Bildsten et al. 2012).

Figure 8 shows the acoustic radius at the bases of convective envelope ($t_{\rm BCE}$) and helium-ionization zone ($t_{\rm He}$), both over the total acoustic radius as a function of luminosity, for the standard (black line) 1.0 $M_\odot$ (left panel) and 2.0 $M_\odot$ (right panel) models at solar metallicity from the main sequence to helium-burning phase. As the extent (in radius) of the convective envelope decreases with increasing stellar mass on the main sequence, the difference between $t_{\rm He}$ and $t_{\rm BCE}$ becomes smaller.

As the convective envelope deepens inside the star with the first dredge-up, the acoustic radius $t_{\rm BCE}$ decreases during the subgiant branch. During this phase, the acoustic radius at the base of He II ionization zone follows the variation in effective temperature and $t_{\rm He}$ increases while $T_{\rm eff}$ decreases. In addition, the total acoustic radius increases because of its dependence on the stellar radius, which increases during this phase. Consequently, $t_{\rm He}/T$ decreases from 0.8 to 0.68 and from 0.9 to 0.7 for [1.0 $M_\odot$, $Z_\odot$] and [2.0 $M_\odot$, $Z_\odot$] models, respectively. As the star ascends the RGB, $t_{\rm BCE}$ follows the convective envelope and the acoustic radius $t_{\rm He}/T$ decreases to 0.2 for the 2.0 $M_\odot$ model until the RGB tip is reached (at $\log L/L_\odot \sim 3.5$). When the stellar luminosity decreases after the RGB tip, the convective envelope radius decreases, and the effective temperature increases as the star contracts. Therefore, $t_{\rm BCE}/T$ and $t_{\rm He}/T$ increase until the central temperature is sufficient to ignite helium. At the end of the He burning phase, the surface layers expand and the convective envelope deepens as the effective temperature decreases. During this phase, $t_{\rm BCE}/T$ and $t_{\rm He}/T$ in 2.0 $M_\odot$ model decrease slowly from ~0.62 and ~0.1 to ~0.55 and ~0.05, respectively.

Although we do not include this phase in the files presented in Sect. 3.1, we discuss the evolution of the asteroseismic parameters during the TP-AGB. Figure 10 shows the evolution of the stellar parameters (L, $T_{\rm eff}$, and M), and asteroseismic parameters ($\Delta\nu$, $\nu_{\rm max}$, and $A_{\rm max}$) as a function of time from the first thermal pulse for a 2.0 $M_\odot$ model at $Z_\odot$.

Between each thermal pulse, the stellar radius increases. The mass slowly decreases by steps at this phase, remaining almost constant during the inter-pulses. The large separation then decreases between each thermal pulse as well as $\nu_{\rm max}$ despite the slight decrease in effective temperature. The maximal amplitude increases as a result of the luminosity increase and the decrease in the effective temperature and total stellar mass. The strong increase in $A_{\rm max}$ during the interpulses is due to the large mass loss at this phase, which can be moreclearly seen in the last pulse shown in Fig. 10.

5.2.2. Effects of metallicity

Although the current asteroseismic missions focus on solar metallicity stars, we present the effects of metallicity on the global asteroseismic parameters in Fig. 5 (right panel) for a 2.0 $M_\odot$ model.

As discussed in Sect. 4.1.1, at lower metallicity the main sequence is shifted to both the blue and higher luminosity on the HR diagram. Therefore, the track in the $A_{\rm max}$ vs. $\Delta\nu$ plot is moved to lower $A_{\rm max}/A_{{\rm max},\odot}$ values. In addition, the luminosity of the helium-ignition at the RGB tip occurs at lower $A_{\rm max}/A_{{\rm max},\odot}$ when the metallicity is lower. The evolutionary track in the $A_{\rm max}$ vs. $\Delta\nu$ plot is shifted to the right (toward higher $\Delta\nu$ values) when the metallicity decreases. This is a direct consequence of a more metal-poor star behaving as a more massive star.

5.2.3. Effects of stellar mass

As the mass increases, the ZAMS (point at higher $\Delta\nu$ and lower $A_{\rm max}$) is shifted to lower $\Delta\nu$ and higher $A_{\rm max}$ (see Fig. 5 and top panels of Fig. 6). Indeed, the large frequency separation at the point of ZAMS decreases because of its dependence on the mean stellar density. As in the case of the Hayashi tracks during the pre-main sequence, stars with different masses tend to join together in the $A_{\rm max}$ vs. $\Delta\nu$ plot during the RGB and early-AGB phase (see green and red lines, respectively in Fig. 5). As stellar mass increases, stars follow more extended blue loops during the central helium-burning phase. As shown in Fig. 6 (bottom right panel), blue loops range over high $\Delta\nu$ and low $A_{\rm max}/A_{{\rm max},\odot}$.

Figure 9 shows the theoretical evolution of the stellar acoustic radius at the base of the helium-ionization zone and the asymptotic period spacing of g-modes along the evolutionary

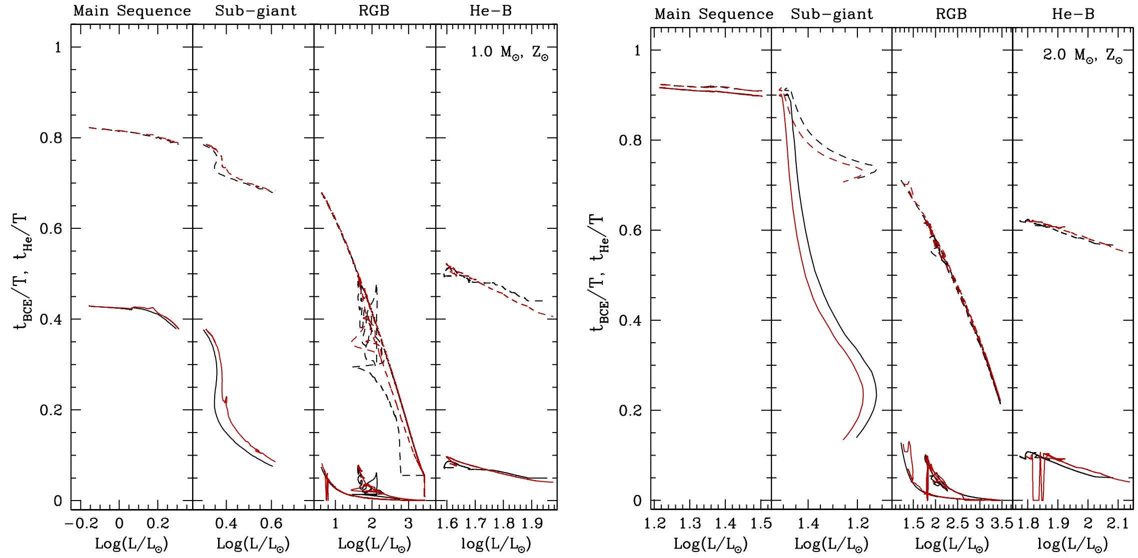

Fig. 8. Acoustic radius at the base of the convective envelope ($t_{\rm BCE}$, solid line) and at the base of helium-ionization zone ($t_{\rm He}$, dashed line) compared to total acoustic radius T as a function of the stellar luminosity for (*left panel*) 1.0 and (*right panel*) 2.0 $M_\odot$ models at solar metallicity following standard (black line) and rotating prescriptions (red line); (*from left to right*) on the main sequence, the sub-giant branch, red giant branch, and helium burning phase.

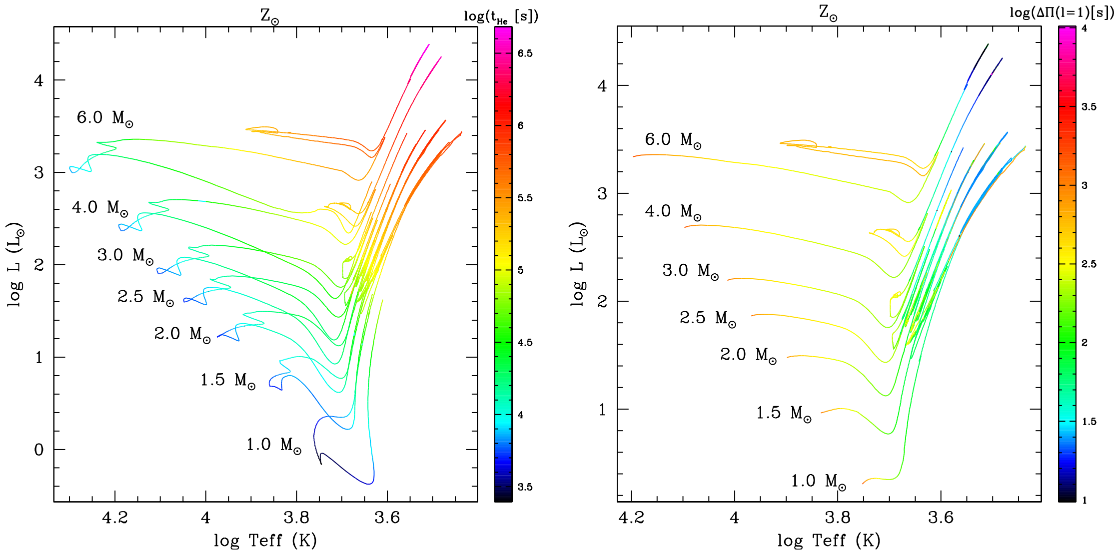

Fig. 9. Color-coded HR diagram for all the masses in the grid at solar metallicity. The color code represents the values (in seconds) of the acoustic radius at the base of the ionization of He II $t_{\rm He}$ (*left panel*) and of the asymptotic period spacing of g-modes $\Delta\Pi(\ell = 1)$ (*right panel*). The values increase from blue to red in both cases as shown on the scales on the right of the plots.

tracks in the HR diagram for models of different masses at solar metallicity. The variations in both quantities are expressed in seconds. Evolution is shown from the pre-main sequence to the early-AGB phase and from the subgiant branch to the early-AGB phase for $t_{\rm He}$ and $\Delta\Pi$, respectively. At a given evolutionary phase, higher stellar mass implies larger acoustic radius at the base of the helium-ionization zone. The same is true for $\Delta\Pi$.

5.2.4. Impact of rotation on the evolution within the amplitude vs. $\Delta\nu$ diagram

We now focus on the effect of accounting for rotational mixing on the global asteroseismic parameters. As thermohaline mixing solely affects the abundance at both the surface and the external layers of HBS pattern during the giant phase, without modifying

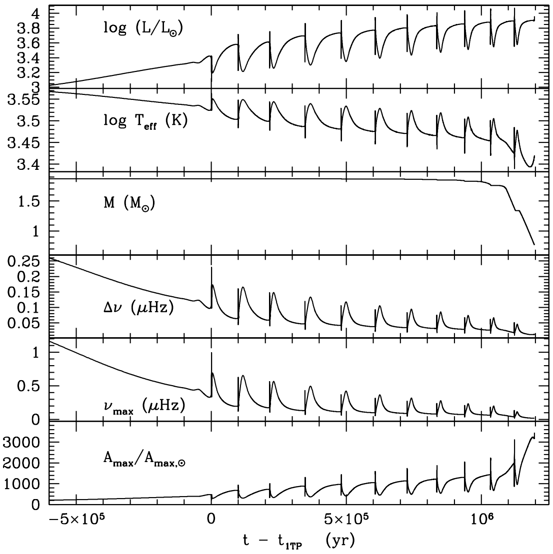

Fig. 10. *From top to bottom:* evolution of global stellar properties (luminosity L, effective temperature $T_{\rm eff}$ and total stellar mass M) and asteroseismic parameters ($\Delta\nu$, and $\nu_{\rm max}$, $A_{\rm max}/A_{{\rm max},\odot}$) on the TP-AGB of the [2.0 $M_\odot$, $Z_\odot$] model computed with rotation up to the RGB tip and thermohaline mixing all along the evolution. The abscissa is the time since the first thermal pulse.

the temperature, radius, luminosity, or mass of the models, this process has no impact on the global asteroseismic parameters. It is nevertheless not excluded that well-chosen asteroseismic parameters might help to constrain the thermohaline mixing.

As discussed in Sect. 4, rotation modifies the position of the evolutionary tracks in the HR diagram (see Fig. 2). Consequently, there are differences in both the maximal amplitude and the large separation, between the standard and rotating models. This effect clearly shows up at the end of the main sequence owing to the larger width of the main sequence in rotating models.

On the subgiant branch, rotating models then evolve to higher luminosities than their standard counterparts, which is indicative of a higher maximal amplitude. The rotation has no impact on the ratios $t_{\rm BCE}/T$ and $t_{\rm He}/T$ as seen in Fig. 8. In this figure, the effect of rotation on the stellar luminosity during the subgiant phase is also shown.

When the stars reach the RGB, the differences in effective temperature and luminosity between standard and rotating models become marginal, hence the tracks are almost identical in Fig. 6 (bottom left panel).

Rotation affects the extension and width of the blue loops. As a consequence, the differences in the asteroseismic parameters appear during the combustion phase of He, as illustrated in Fig. 6 (bottom right panel).

5.3. Same position in HR-diagram, same asteroseismic parameters?

Figure 11 shows how asteroseismic parameters can help us to distinguish between two stars with the same effective temperature and luminosity. In the left panel, we show the 1.5 $M_\odot$ and 2.0 $M_\odot$ tracks in the HR diagram with the intersection indicated by the black dot. At this point, the 1.5 $M_\odot$ star evolves within the HR gap and has the same effective temperature and luminosity as the 2.0 $M_\odot$ star evolving on the pre-main sequence. This black dot corresponds to two different points in the $A_{\rm max}$ vs. $\Delta\nu$ plot shown in the right panel. As we can see, the larger separation of the 1.5 $M_\odot$ model is smaller than that of the 2.0 $M_\odot$ model, while the maximal amplitude is higher. These stars have neither the same mean stellar density, and nor same $\Delta\nu$. On the other hand, both the total stellar mass and the maximal amplitude are different at this point.

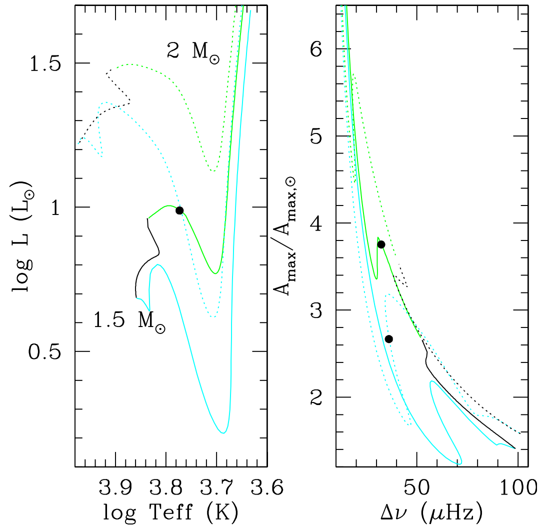

Fig. 11. *Left panel*: evolutionary tracks in Hertzsprung-Russell diagram of 1.5 and 2.0 $Z_\odot$(solid and dotted lines respectively) stars at solar metallicity. *Right panel*: maximal amplitude over Sun value as a function of the large separation for the same models. As in Fig. 5, the lines color indicates the evolutionary.

6. Conclusions

We have presented a grid of single-star evolution models in the mass range between 0.85 $M_\odot$ and 6.0 $M_\odot$, for four metallicities, including the impact of rotation and thermohaline mixing, along with standard models. All data detailed in Table 2 are available on a website[9], for all the models computed (i.e., standard on the one hand, and with rotation-induced mixing and thermohaline instability on the other hand).

We recall the various impacts of metallicity variations and rotation-induced mixing on the stellar properties that were previously discussed in literature. Thermohaline mixing does not change stellar parameters such as luminosity and effective temperature, and indeed any of the seismic properties analyzed here. However and as discussed in Papers I and II, it changes the surface abundances from the bump luminosity on, and has to be taken into account to explain the observed chemical properties of bright giant stars.

Last but not least, we also present the evolution of global asteroseismic parameters for all the models in our grid. The large frequency separation $\Delta\nu$, the frequency $\nu_{\rm max}$, and the maximum oscillation amplitude $A_{\rm max}$ are computed using scaling relations. Asymptotic asteroseismic quantities are also computed,

---

[9] `http://obswww.unige.ch/Recherche/evol/-Database-`

namely: $\Delta\nu_{\mathrm{asympt}}$, another estimate or the large frequency separation; t_{BCE}, the acoustic radius at the base of convective envelope; t_{He}, the acoustic radius at the base of the HeII ionization zone; T, the total acoustic radius; and $\Delta\Pi(\ell = 1)$, the period spacing of gravity modes.

We show that rotation-induced mixing has an impact on these quantities, in contrast to thermohaline mixing. While rotation changes the global properties of main sequence stars and has an impact on the global asteroseismic properties, thermohaline mixing is negligible in these aspects, although it does change the surface abundances in the red giants. In addition to spectrophotometric studies, seismic studies allow us to distinguish two stars with approximately the same luminosity and effective temperature but at different evolutionary stages.

Acknowledgements. We wish to thank the referee and Benoit Mosser for helpful comments on our manuscript. We acknowledge financial support from the Swiss National Science Foundation (FNS), from ESF-Euro Genesis, and the French Programme National de Physique Stellaire (PNPS) of CNRS/INSU.

References

Aikawa, M., Arnould, M., Goriely, S., Jorissen, A., & Takahashi, K. 2005, A&A, 441, 1195
Arnould, M., Goriely, S., & Jorissen, A. 1999, A&A, 347, 572
Asplund, M., Grevesse, N., Sauval, A. J., & Scott, P. 2009, ARA&A, 47, 481
Bao, Z. Y., Beer, H., Käppeler, F., et al. 2000, in AIP Conf. Ser. 529 (Santa Fe, New Mexico: AIP), 706
Beck, P. G., Bedding, T. R., Mosser, B., et al. 2011, Science, 332, 205
Bedding, T. R., Huber, D., Stello, D., et al. 2010, ApJ, 713, L176
Bedding, T. R., Mosser, B., Huber, D., et al. 2011, Nature, 471, 608
Beer, H., Sedyshev, P. V., Rochow, W., Mohr, P., & Oberhummer, H. 2002, Nucl. Phys. A, 705, 239
Belkacem, K., Goupil, M. J., Dupret, M. A., et al. 2011, A&A, 530, A142
Bildsten, L., Paxton, B., Moore, K., & Macias, P. J. 2012, ApJ, 744, L6
Brott, I., de Mink, S. E., Cantiello, M., et al. 2011, A&A, 530, A115
Brown, T. M., Gilliland, R. L., Noyes, R. W., & Ramsey, L. W. 1991, ApJ, 368, 599
Brun, A. S., & Palacios, A. 2009, ApJ, 702, 1078
Cantiello, M., & Langer, N. 2010, A&A, 521, A9
Cassisi, S., Pietrinferni, A., Salaris, M., et al. 2006, Mem. Soc. Astron. It., 77, 71
Caughlan, G. R., & Fowler, W. A. 1988, At. Data Nucl. Data Tab., 40, 283
Chaboyer, B., & Zahn, J.-P. 1992, A&A, 253, 173
Chaplin, W. J., Appourchaux, T., Elsworth, Y., et al. 2010, ApJ, 713, L169
Chaplin, W. J., Kjeldsen, H., Bedding, T. R., et al. 2011a, ApJ, 732, 54
Chaplin, W. J., Kjeldsen, H., Christensen-Dalsgaard, J., et al. 2011b, Science, 332, 213
Charbonnel, C. 1994, A&A, 282, 811
Charbonnel, C., & Lagarde, N. 2010, A&A, 522, A10 (Paper I)
Charbonnel, C., & Talon, S. 1999, A&A, 351, 635
Charbonnel, C., & Talon, S. 2005, Science, 309, 2189
Charbonnel, C., & Talon, S. 2008, in IAU Symp. 252, eds. L. Deng, & K. L. Chan (Sanya: CUP), 163
Charbonnel, C., & Zahn, J. 2007a, A&A, 476, L29
Charbonnel, C., & Zahn, J.-P. 2007b, A&A, 467, L15
Christensen-Dalsgaard, J. 2011 [`arXiv:1106.5946`]
Coc, A., Vangioni-Flam, E., Descouvemont, P., Adahchour, A., & Angulo, C. 2004, ApJ, 600, 544
Cunha, K., Hubeny, I., & Lanz, T. 2006, ApJ, 647, L143
De Ridder, J., Barban, C., Baudin, F., et al. 2009, Nature, 459, 398
Decressin, T., Mathis, S., Palacios, A., et al. 2009, A&A, 495, 271
Denissenkov, P. A. 2010, ApJ, 723, 563
Denissenkov, P. A., & Merryfield, W. J. 2011, ApJ, 727, L8
Descouvemont, P., Adahchour, A., Angulo, C., Coc, A., & Vangioni-Flam, E. 2004, At. Data Nucl. Data Tab., 88, 203
Dufour, E. 1999, Ph.D. Thesis, Université Joseph Fourier – Grenoble I
Eggenberger, P., Maeder, A., & Meynet, G. 2005, A&A, 440, L9
Eggenberger, P., Meynet, G., Maeder, A., et al. 2010a, A&A, 519, A116
Eggenberger, P., Miglio, A., Montalban, J., et al. 2010b, A&A, 509, A72
Eggleton, P. P., Faulkner, J., & Flannery, B. P. 1973, A&A, 23, 325
Eggleton, P. P., Dearborn, D. S. P., & Lattanzio, J. C. 2006, Science, 314, 1580
Eggleton, P. P., Dearborn, D. S. P., & Lattanzio, J. C. 2008, ApJ, 677, 581
Ekström, S., Georgy, C., Eggenberger, P., et al. 2012, A&A, 537, A146
Ferguson, J. W., Alexander, D. R., Allard, F., et al. 2005, ApJ, 623, 585
Forestini, M., & Charbonnel, C. 1997, A&AS, 123, 241
Funck, C., & Langanke, K. 1989, ApJ, 344, 46
Fynbo, H. O. U., Diget, C. A., Bergmann, U. C., et al. 2005, Nature, 433, 136
Graboske, H. C., Dewitt, H. E., Grossman, A. S., & Cooper, M. S. 1973, ApJ, 181, 457
Hale, S. E., Champagne, A. E., Iliadis, C., et al. 2002, Phys. Rev. C, 65, 015801
Hauser, W., & Feshbach, H. 1952, Phys. Rev., 87, 366
Heger, A., & Langer, N. 2000, ApJ, 544, 1016
Hekker, S., Kallinger, T., Baudin, F., et al. 2009, A&A, 506, 465
Horiguchi, T., Tachibana, T., & Katakura, J. 1996, Nuclear Data Center, Japan Atomic Energy Research Institute, Ibaraki
Huber, D., Bedding, T. R., Stello, D., et al. 2011, ApJ, 743, 143
Iglesias, C. A., & Rogers, F. J. 1996, ApJ, 464, 943
Iliadis, C., D'Auria, J. M., Starrfield, S., Thompson, W. J., & Wiescher, M. 2001, ApJS, 134, 151
Kawaler, S. D. 1988, ApJ, 333, 236
Kjeldsen, H., & Bedding, T. R. 1995, A&A, 293, 87
Koehler, P. E., & O'brien, H. A. 1989a, Phys. Rev. C, 39, 1655
Koehler, P. E., & O'brien, H. A. 1989b, Phys. Rev. C, 39, 1655
Krishnamurti, R. 2003, J. Fluid Mech., 483, 287
Lagarde, N., Charbonnel, C., Decressin, T., & Hagelberg, J. 2011, A&A, 536, A28 (Paper II)
Maeder, A. 1997, A&A, 321, 134
Maeder, A. 2009, Physics, Formation and Evolution of Rotating Stars (Berlin Heidelberg: Springer)
Maeder, A., & Meynet, G. 2000, ARA&A, 38, 143
Maeder, A., & Zahn, J.-P. 1998, A&A, 334, 1000
Mathis, S., & Zahn, J.-P. 2004, A&A, 425, 229
Meynet, G., & Maeder, A. 2000, A&A, 361, 101
Michel, E., Baglin, A., Auvergne, M., et al. 2008, Science, 322, 558
Miglio, A., Montalbán, J., Baudin, F., et al. 2009, A&A, 503, L21
Mitler, H. E. 1977, ApJ, 212, 513
Mosser, B., Belkacem, K., Goupil, M.-J., et al. 2010, A&A, 517, A22
Mosser, B., Barban, C., Montalbán, J., et al. 2011, A&A, 532, A86
Mukhamedzhanov, A. M., Bém, P., Brown, B. A., et al. 2003, Phys. Rev. C, 67, 065804
Palacios, A., Talon, S., Charbonnel, C., & Forestini, M. 2003, A&A, 399, 603
Palacios, A., Charbonnel, C., Talon, S., & Siess, L. 2006, A&A, 453, 261
Pols, O. R., Tout, C. A., Eggleton, P. P., & Han, Z. 1995, MNRAS, 274, 964
Reimers, D. 1975, Mem. Soc. Roy. Sci. Liege, 8, 369
Rosenblum, E., Garaud, P., Traxler, A., & Stellmach, S. 2011, ApJ, 731, 66
Schaller, G., Schaerer, D., Meynet, G., & Maeder, A. 1992, A&AS, 96, 269
Schaerer, D., Meynet, G., Maeder, A., & Schaller, G. 1993, A&AS, 98, 523
Schatz, H., Kaeppeler, F., Koehler, P. E., Wiescher, M., & Trautvetter, H.-P. 1993, ApJ, 413, 750
Siess, L. 2009, A&A, 497, 463
Siess, L., Dufour, E., & Forestini, M. 2000, A&A, 358, 593
Smiljanic, R., Pasquini, L., Charbonnel, C., & Lagarde, N. 2010, A&A, 510, A50
Stancliffe, R. J. 2010, MNRAS, 174
Stancliffe, R. J., Church, R. P., Angelou, G. C., & Lattanzio, J. C. 2009, MNRAS, 396, 2313
Stello, D., Chaplin, W. J., Bruntt, H., et al. 2009, ApJ, 700, 1589
Talon, S., & Charbonnel, C. 1998, A&A, 335, 959
Talon, S., & Charbonnel, C. 2003, A&A, 405, 1025
Talon, S., & Zahn, J.-P. 1997, A&A, 317, 749
Traxler, A., Garaud, P., & Stellmach, S. 2011, ApJ, 728, L29
Ulrich, R. K. 1971, ApJ, 168, 57
Ulrich, R. K. 1972, ApJ, 172, 165
Ulrich, R. K. 1986, ApJ, 306, L37
Uttenthaler, S., & Lebzelter, T. 2010, A&A, 510, A62
Vassiliadis, E., & Wood, P. R. 1993, ApJ, 413, 641
Wagoner, R. V. 1969, ApJS, 18, 247
White, T. R., Bedding, T. R., Stello, D., et al. 2011, ApJ, 742, L3
Wiescher, M., Gorres, J., & Thielemann, F. 1990, ApJ, 363, 340
Woosley, S. E., Fowler, W. A., Holmes, J. A., & Zimmerman, B. A. 1978, At. Data Nucl. Data Tab., 22, 371
Yi, S. K., Kim, Y.-C., & Demarque, P. 2003, ApJS, 144, 259
Zahn, J.-P. 1992, A&A, 265, 115
Zahn, J.-P., Talon, S., & Matias, J. 1997, A&A, 322, 320

Chapter 6

Cosmic evolution of ^{3}He from the Big Bang to present day

In the previous chapter, we described the effects of thermohaline instability and rotation-induced mixing on the surface abundances of low- and intermediate-mass stars at different metallicity. In Chap. 5 we also showed that these processes change the surface abundances in low- and intermediate-mass giant stars. As we shall discuss in this chapter, they also lead to a drastic reduction of ^{3}He production in low-mass stars.

The predictions of these new stellar models can be tested against galaxy evolution. In particular, the resulting evolution of the light elements Deuterium (D), ^{3}He and ^{4}He can be compared with their primordial values inferred from the Wilkinson Microwave Anisotropy Probe data and with the abundances derived from observations of different Galactic regions. Indeed, D, ^{3}He, and ^{4}He are all synthesized in astrophysical relevant quantities during the Big Bang Nucleosynthesis (BBN; Peebles 1966; Wagoner et al. 1967). The galactic abundance of D, in the absence of any other realistic production channel (Epstein et al. 1976; Prodanović & Fields 2003), has been continuously decreasing as this element is only destroyed in stellar nucleosynthesis. On the other hand, ^{3}He and ^{4}He have a more complex history since they are both produced and destroyed inside stars.

6.1 The "^{3}He problem"

The classical theory of stellar evolution predicts a very simple Galactic destiny to ^{3}He, dominated by the production of this isotope during Standard Big Bang Nucleosynthesis (SBBN) and in stars with initial mass lower than ~ 3 M$_\odot$ (see Lagarde et al. 2011, 2012b, , Chap. 5). In these objects, ^{3}He is produced first through D-processing on the pre-main sequence and then through the pp-chain on the main sequence. This fresh ^{3}He is then engulfed in the stellar envelope during the so-called first dredge-up (Iben 1967), and according to classical stellar modelling it survives the following evolution phase before being released in the interstellar matter through stellar wind and planetary nebula ejection (Rood et al. 1976; Vassiliadis & Wood 1993; Dearborn et al. 1996b; Weiss et al. 1996; Forestini & Charbonnel 1997). In chapter 3, we showed that two planetary nebulae, namely NGC 3242 and J320, have been found to "behave classically". Slightly more massive than the Sun, they are presently expelling into the interstellar matter freshly synthesized elements among which ^{3}He with the amount predicted by classical stellar

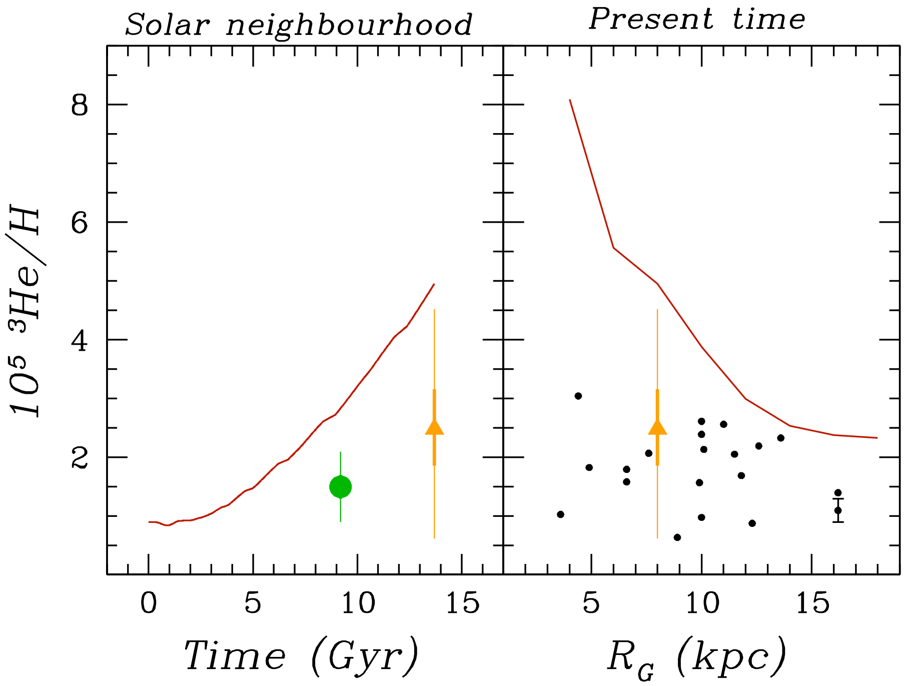

Figure 6.1: Standard galactic evolution of ^{3}He/H in the solar neighborhood (left panel) and its distribution along the galactic disc predicted by the standard prescription at the present time (right panel). Data for the protosolar cloud (PSC, green) and local interstellar medium (LISM, orange) are from Geiss & Gloeckler (1998) and Gloeckler & Geiss (1996) respectively. 1σ and $3\ \sigma$ are shown with thick and thin lines respectively. The black dots are HII regions data from Bania et al. (2002) and triangle at R_G=8 kpc is LISM data from Gloeckler & Geiss (1996). Error bar for S209 is shown in black at R_G =16.2kpc from Bania et al. (2002).

models (Balser et al. 1997, 1999a, 2006; Galli et al. 1997).

As a consequence, one expects with time a large increase of ^{3}He in the Galaxy (see Fig. 6.1, left panel) with respect to its primordial abundance (see e.g. Wilson & Rood 1994), this latest quantity is well constrained thanks to accurate determination of the baryon density of the Universe by recent cosmic microwave background experiments, most particularly from WMAP (Bennett et al. 2003; Spergel et al. 2003), which has led to an unprecedented precision on the yields of SBBN. Galactic HII regions should in particular be highly enriched in ^{3}He since their matter content chronicles the result of billion years of chemical evolution since the Milky Way formation. Additionally the ^{3}He/H abundance ratio is expected to be higher in the central regions of the Galaxy where there has been more substantial stellar processing than in the solar neighborhood (see Fig. 6.1, right panel). However, the ^{3}He abundance in HII regions sampling a large volume of the Galactic disk is found to be very homogeneous (Rood et al. 1979; Balser et al. 1994, 1999a; Bania et al. 1997, 2002, 2010), similar to that of the Sun at the epoch of its formation (for references see Geiss & Gloeckler 2010), and only slightly higher than the WMAP+SBBN primordial abundance. No observational evidence is thus found for strong enrichment of this element along Galactic history contrary to expectations of all chemical evolution models that take into account ^{3}He yields from classical stellar models (e.g. Galli et al. 1995; Olive et al. 1995; Tosi 1996).

This is the well-known "^{3}He problem" that could be solved if only $\sim$ 10 % or less of the low-mass stars were actually releasing ^{3}He as predicted by the classical stellar theory (Tosi 1998, 2000; Palla et al. 2000; Romano et al. 2003), among which NGC 3242 and J320. In other words, the lack of increase of the Galactic ^{3}He abundance can be accounted for if most ($\geq$ 90 %) low-mass stars consume most of the ^{3}He they produce during the main sequence before it can be released in the interstellar medium. This calls for a physical process that is ignored by the classical theory of stellar evolution, but which spectroscopic signatures have been revealed long ago at the surface of relatively bright low-mass red giants (see Chapter 3). As discuss in chapter 5 (Smiljanic et al. 2010; Charbonnel & Lagarde 2010a, see also), thermohaline instability and rotation-induced mixing can explain these abundances anomalies along the red giant branch.

6.2 Yields of ^{3}He for low- and intermediate-mass stars

Thermohaline instability and rotation-induced mixing
II - Yields of ^{3}He for low- and intermediate-mass stars

N.Lagarde, C. Charbonnel, T. Decressin, and J. Hagelberg
A&A 536, A28 (2011)

In this article, we quantify the effects of thermohaline and rotation-induced mixings on the production and destruction of ^{3}He over the lifetime of low- and intermediate-mass stars, which are classical considered to be net ^{3}He producers. The stellar evolutionary models in the mass range 1 to 6 M$_\odot$ for four metallicities (Z=0.014, 0.004, 0.002, and 0.0001), are described in detail in Lagarde et al. (2012a). Then, we discuss the effects of these processes on internal and surface abundances of ^{3}He and on the net yields.

Results

As seen in previous article (Charbonnel & Lagarde 2010a, , see Chap. 5 §5.2), rotation-induced mixing modifies the internal structure and the abundance patterns in the main sequence stars. Over the whole mass and metallicity range investigated, it lowers the ^{3}He content at the end of the main sequence. In addition, the change of stellar structure favours a deeper first dredge-up, and therefore lowers the post dredge-up value of ^{3}He when rotation is accounted for compared to the standard case. Consequently, rotation-induced mixing lowers the ^{3}He production, as well as the upper mass limit at which stars destroy ^{3}He.

For low-mass stars (M<2-2.2 M$_\odot$) that produce large quantities of this light element through the pp chains on the main sequence, thermohaline mixing on both the RGB and the TP-AGB is dominant in reducing the final ^{3}He yield. These stars remain net producers of ^{3}He however, although their contribution to the Galactic evolution of this light element is strongly reduced compared to the standard framework.
In addition, in stars with initial masses lower than, or equal to 2 and 1.5 M$_\odot$ for Z=Z$_\odot$ and Z=0.0001 respectively, the ^{3}He abundance continues to decrease at the stellar surface between the end of central helium burning and the second dredge up episode through

thermohaline mixing.

For intermediate-mass stars, thermohaline mixing does not operate on the shorter RGB, because these stars ignite central He burning before reaching the RGB bump. For those with masses between 2-2.2 and 3-4 $M_\odot$, thermohaline mixing leads however to modest ^{3}He depletion during the TP-AGB phase, associated with lithium production. Contrary to low-mass stars, the dominating process is the rotation to decrease ^{3}He on early-AGB. In more massive stars, ^{3}He is not abundant enough to drive thermohaline mixing during the thermal pulses. Nevertheless, it is strongly reduced through the action of rotation that lowers the upper mass limit for stars that are net ^{3}He producers, and is additionally destroyed through hot-bottom burning while they climb the TP-AGB. In these objects Li is produced through the classical Cameron-Fowler mechanism.

These new yields of ^{3}He have been included in Galactic evolution code, to quantify impact of thermohaline mixing and rotation-induced mixing on the evolution of ^{3}He in the Milky Way ; we also followed the evolution of deuterium and helium-4 using our non standard yields.

A&A 536, A28 (2011)
DOI: 10.1051/0004-6361/201117739

Astronomy & Astrophysics

Thermohaline instability and rotation-induced mixing

II. Yields of ^{3}He for low- and intermediate-mass stars

N. Lagarde[1], C. Charbonnel[1,2], T. Decressin[1], and J. Hagelberg[1]

[1] Geneva Observatory, University of Geneva, Chemin des Maillettes 51, 1290 Versoix, Switzerland
e-mail: `nadege.lagarde@unige.ch`
[2] IRAP, UMR 5277 CNRS and Université de Toulouse, 14, Av. E. Belin, 31400 Toulouse, France

Received 21 July 2011 / Accepted 13 September 2011

ABSTRACT

Context. The ^{3}He content of Galactic HII regions is very close to that of the Sun and the solar system, and only slightly higher than the primordial ^{3}He abundance as predicted by the standard Big Bang nucleosynthesis. However, the classical theory of stellar evolution predicts a high production of ^{3}He by low-mass stars, implying a strong increase of ^{3}He with time in the Galaxy. This is the well-known "^{3}He problem".

Aims. We study the effects of thermohaline and rotation-induced mixings on the production and destruction of ^{3}He over the lifetime of low- and intermediate-mass stars at various metallicities.

Methods. We compute stellar evolutionary models in the mass range 1 to 6 $M_\odot$ for four metallicities, taking into account thermohaline instability and rotation-induced mixing. For the thermohaline diffusivity we use the prescription based on the linear stability analysis, which reproduces red giant branch (RGB) abundance patterns at all metallicities. Rotation-induced mixing is treated taking into account meridional circulation and shear turbulence. We discuss the effects of these processes on internal and surface abundances of ^{3}He and on the net yields.

Results. Over the whole mass and metallicity range investigated, rotation-induced mixing lowers the ^{3}He production, as well as the upper mass limit at which stars destroy ^{3}He. For low-mass stars, thermohaline mixing occuring beyond the RGB bump is the dominant process in strongly reducing the net ^{3}He yield compared to standard computations. Yet these stars remain net ^{3}He producers.

Conclusions. Overall, the net ^{3}He yields are strongly reduced compared to the standard framework predictions.

Key words. stars: evolution – stars: abundances – stars: low-mass – stars: rotation – Galaxy: abundances – primordial nucleosynthesis

1. Introduction

The classical theory of stellar evolution predicts a very simple Galactic destiny for ^{3}He, dominated by the production of this isotope during the Big Bang nucleosynthesis (BBN) and in stars with initial masses lower than ~3 $M_\odot$. In these objects, ^{3}He is produced first through D-processing on the pre-main sequence and then through the pp-chain on the main sequence. This fresh ^{3}He is then engulfed in the stellar convective envelope during the so-called first dredge-up when the stars move towards the red giant branch (Iben 1967). According to classical modelling[1], it survives the following stellar evolution phases before it is released in the interstellar matter through stellar wind and planetary nebula ejection (Rood et al. 1976; Vassiliadis & Wood 1993; Dearborn et al. 1996; Weiss et al. 1996; Forestini & Charbonnel 1997). Two planetary nebulae, namely NGC 3242 and J320, whose estimated initial masses were slightly higher than that of the Sun, have been found to "behave classically": they are presently expelling freshly synthesized elements among which is ^{3}He with the amount predicted by classical stellar models (Balser et al. 1997, 1999, 2006; Galli et al. 1997).

As a consequence, one expects a steep increase of ^{3}He with time in the Galaxy with respect to its primordial abundance (see e.g. Wilson & Rood 1994), this latest quantity being well constrained through accurate determination of the baryon density of the Universe by recent cosmic microwave background experiments, most particularly from WMAP (Spergel et al. 2003; Dunkley et al. 2009), which has led to an unprecedented precision on the yields of standard BBN (Coc et al. 2004; Cyburt et al. 2008). Galactic HII regions in particular should be highly enriched in ^{3}He because their matter content chronicles the result of billion years of chemical evolution since the Milky Way formation. Additionally, the present ^{3}He/H abundance ratio is expected to be higher in the central regions of the Galaxy, where there has been more substantial stellar processing than in the solar neighbourhood. However, the ^{3}He abundance in HII regions that sample a large volume of the Galactic disk is found to be relatively homogeneous (Rood et al. 1979; Balser et al. 1994, 1999; Bania et al. 1997, 2002, 2010); its average value is similar to that of the Sun at the epoch of its formation (for references see Geiss & Gloeckler 2010), and only slightly higher than the WMAP+SBBN primordial abundance[2]. No observational evidence is therefore found for the strong enrichment of this element in the Galactic history, contrary to expectations from all chemical evolution models that take into account ^{3}He yields from classical stellar models (e.g. Galli et al. 1995; Olive et al. 1995; Tosi 1996).

This is the well-known "^{3}He problem" that could be solved if only ~10% or less of all low-mass stars were actually

---

[1] Classical (or standard) stellar models consider convection as the only mixing mechanism inside stars, and neglect all possible transport processes in stellar radiative regions.

[2] The average abundance in Galactic HII regions is ^{3}He/H = (1.9 ± 0.6) × 10^{-5} (Bania et al. 2002). The protosolar and SBBN-WMAP values are ^{3}He/H = (1.5 ± 0.2) × 10^{-5} (Geiss & Gloeckler 1998) and ^{3}He/H = (1.04 ± 0.04) × 10^{-5} (Coc et al. 2004).

releasing ^{3}He, as predicted by the classical stellar theory (Tosi 1998, 2000; Palla et al. 2000; Chiappini et al. 2002; Romano et al. 2003), among which are NGC 3242 and J320. In other words, the lack of increase of the Galactic ^{3}He abundance can be accounted for if most ($\geq$90%) low-mass stars consume most of the ^{3}He they produce during the main sequence before it can be released into the interstellar medium. This calls for a physical process that is ignored by the classical theory of stellar evolution, but whose spectroscopic signatures have been revealed long ago at the surface of relatively bright low-mass red giants. In particular, one observes a sudden drop of the surface ^{12}C/^{13}C ratio as low-mass stars evolve beyond the so-called luminosity bump on the red giant branch (RGB) well after the end of the first dredge-up (Gilroy 1989; Gilroy & Brown 1991; Charbonnel 1994; Charbonnel et al. 1998; Gratton et al. 2000; Tautvaišiene et al. 2000, 2005; Shetrone 2003; Pilachowski et al. 2003; Spite et al. 2006; Recio-Blanco & de Laverny 2007; Charbonnel & Lagarde 2010b). This behaviour, which is not predicted by standard stellar modelling, appears to be almost universal. Indeed, about 96% of all low-mass bright red giant stars exhibit unexpectedly low ^{12}C/^{13}C, regardless of whether they belong to the field, to open or globular clusters (Charbonnel & Do Nascimento 1998), or even to external galaxies (Smith et al. 2002; Geisler et al. 2005).

This high number satisfies the Galactic requirements for the evolution of the ^{3}He abundance because the mechanism responsible for the low values of ^{12}C/^{13}C is also expected to lead to the depletion of ^{3}He by a large factor in the stellar envelopes, as initially suggested by Rood et al. (1984; see also Charbonnel 1995; Hogan 1995; Sackmann & Boothroyd 1999; Eggleton et al. 2006). This correlation was recently confirmed by Charbonnel & Zahn (2007b) and Eggleton et al. (2008), who included the transport of chemicals caused by thermohaline mixing in stellar models (see also Stancliffe et al. 2009; Charbonnel & Lagarde 2010a). In red giant stars, this double diffusive instability (also called "fingering convection"), is induced by the mean molecular weight inversion created by the ^{3}He(^{3}He, 2p)^{4}He reaction in the region between the hydrogen-burning shell and the convective envelope (Charbonnel & Zahn 2007b)[3]. It sets in naturally as soon as stars reach the so-called luminosity bump on the RGB. However, and importantly in the ^{3}He context, Charbonnel & Zahn (2007a) proposed that thermohaline mixing can be inhibited by a fossil magnetic field in red giant stars that are the descendants of Ap stars. As a consequence, these "stubborn" objects are expected to enrich the ISM with ^{3}He as predicted by standard models and as observed in very rare planetary nebulae. Their relative number is low (of the order of 2–5% of all A-type stars, see references in Charbonnel & Zahn 2007a), which helps in principle to reconcile the long-standing problem of ^{3}He overproduction on Galactic timescales with the measurements of ^{3}He/H in planetary nebulae like NGC 3242 and J320.

In order to validate the whole picture quantitatively, one needs to compute ^{3}He yields for stars of various masses and metallicities that contributed to the chemical evolution of the Galaxy, taking into account the various processes that may modify stellar nucleosynthesis. This is the aim of the present work. In Paper I (Charbonnel & Lagarde 2010a) we presented evolution models for low- and intermediate-mass solar metallicity stars including the effects of both thermohaline and rotation-induced mixing. This study extended the former calculations by Charbonnel & Zahn (2007b) that focussed on low-metallicity stars and confirmed that thermohaline mixing is potentially the universal process that governs the photospheric composition of low-mass[4] bright giant stars. In both papers we showed that when described with the prescription adopted by Charbonnel & Zahn (2007b, see Sect. 2.2) this mechanism, whose efficiency on the RGB increases with decreasing initial stellar mass and metallicity, accounts very nicely for the observed behaviour of ^{12}C/^{13}C, [N/C], and Li while efficiently lowering the ^{3}He content in low-mass bright RGB stars of various metallicities. On the other hand, we also showed in Paper I that rotation-induced mixing on the main sequence changes the stellar structure so that it slightly re-enforces the effects of the thermohaline instability in low-mass stars and explains the observed features of CN-processed material in more massive evolved stars that do not undergo thermohaline mixing on the RGB. Last but not least, in Paper I thermohaline mixing was found to lead to additional ^{3}He depletion associated to Li production in all the solar-metallicity models that we computed along the thermal pulse phase on the asymptotic giant branch (TP-AGB), confirming the previous findings by Stancliffe (2010) for low-metallicity low-mass stars. This accounts beautifully for the Li behaviour in Galactic oxygen-rich AGB variables.

Based on these successes we presently extend the computations at different metallicities within the same framework to quantify the impact of thermohaline and rotation-induced mixings on the yields of ^{3}He in low- and intermediate-mass stars that are classicaly considered to be net producers of ^{3}He. In Sect. 2 we briefly recall the assumptions and input physics of our stellar models. In Sect. 3 we present the theoretical predictions for ^{3}He nucleosynthesis both in standard (or classical) models and in models where thermohaline and rotation-induced instabilities are taken into account. The corresponding yields of ^{3}He are given and discussed in Sect. 4. The impact of our new ^{3}He yields on Galactic chemical evolution will be presented in a separate paper.

2. Input physics of the stellar models

2.1. Basic assumptions

We present predictions for stellar models computed with the code STAREVOL (V3.00) for a range of initial masses between 0.85 and 6 $M_{\odot}$[5] and for four metallicities Z = 0.0001, 0.002, 0.004, and 0.14, which correspond to [Fe/H] = −2.16, −0.86, −0.56, and 0[6]. For each given stellar mass and metallicity, models are computed from the beginning of the pre-main sequence

---

[3] Attention to the local depression of μ occurring in RGB stars was drawn by Eggleton et al. (2006), although the peculiarity of this nuclear reaction that converts two particles into three was already pointed out by Ulrich (1971) in a different stellar context.

[4] We define low-mass stars as those that climb the red giant branch with a degenerate helium core; their initial mass is typically lower than 2–2.2 $M_{\odot}$ depending on metallicity. Intermediate-mass stars are those that ignite central helium-burning in a non-degenerate core at relatively low luminosity on the RGB, and finish their lives as C-O white dwarfs.

[5] We do not compute models for more massive stars (i.e., with initial mass higher than ~6 $M_{\odot}$) that are anyway considered as net ^{3}He destroyers within the standard framework since a large amount of their material is processed at temperatures high enough to burn any present ^{3}He to ^{4}He or beyond (Dearborn et al. 1986).

[6] The ratio measuring the enrichment in ^{4}He reported to the enrichment in heavy elements in the Galaxy until the birth of the Sun is taken equal to $\Delta Y/\Delta Z$ = 1.29 (see Lagarde et al., Paper III, in prep.). We assume [α/Fe] = 0 at all metallicities, which has a negligible impact on the final yields of ^{3}He. Indeed, for the [1.5 $M_{\odot}$; Z = 0.0001] models the ^{3}He yields are only ~4.6–4.7% (standard and thermohaline cases respectively) higher when [α/Fe] is increased to 0.3.

(along the Hayashi track) up to the end of the second dredge-up on the early-AGB with different assumptions: (1) standard (no mixing mechanism other than convection), (2) with thermohaline mixing only, and (3) with both thermohaline and rotation-induced mixing. Selected models are pursued along the TP-AGB up to the end of the superwind phase (see Sects. 2.3 and 3 for details). The general evolution and detailed characteristics of the ensemble of our models are presented in Paper III (Lagarde et al., in prep.) of this series.

We refer to Charbonnel & Lagarde (2010a) and to Paper III for a detailed description of the physical ingredients of the models. For the primordial D/H at all Z we assumed the WMAP-SBBN value of 2.6×10^{-5} (Coc et al. 2004), which is higher than the protosolar value $2.1 \pm 0.5 \times 10^{-5}$ (Geiss & Gloeckler 1998). In addition, the initial value of ^{3}He/H is assumed to vary with the metallicity from $^3\mathrm{He/H} = 1.17 \times 10^{-5}$ for $Z = 0.0001$ to $^3\mathrm{He/H} = 1.31 \times 10^{-5}$ for $Z = 0.014$.

For the nuclear reactions involving ^{3}He we used the nominal rates from NACRE compilation (Angulo et al. 1999); the corresponding uncertainties are less than 6% (except for D(H, γ)^{3}He, for which it amounts to 40%) and are therefore not affecting our conclusions. Convection was treated within the standard mixing length theory with an α-parameter taken equal to 1.6, and no overshooting or semi-convection was included. We assumed instantaneous convective mixing, except when hot-bottom burning occurs, which requires a time-dependent convective diffusion algorithm as developed in Forestini & Charbonnel (1997). The treatment of transport processes in radiative regions is described in Sect. 2.2. For mass loss we used the Reimers (1975) formula (with $\eta_R = 0.5$) up to central helium exhaustion and then shifted to the Vassiliadis & Wood (1993) prescription on the AGB.

2.2. Transport processes in radiative regions

2.2.1. Thermohaline instability

For the thermohaline diffusivity we used the prescription advocated by Charbonnel & Zahn (2007b) that beautifully reproduces RGB abundance patterns at all metallicities (see Sect. 1). It is based on the linear stability analysis by Ulrich (1972) of the Boussinesq equations that describe motion in a nearly incompressible stratified viscous fluid, and includes the Kippenhahn et al. (1980) terms for a non-perfect gas (for more details see Charbonnel & Zahn 2007b; Charbonnel & Lagarde 2010a). The corresponding favoured geometry of the instability cells is that of long thin fingers with the aspect ratio (i.e., maximum length relative to their diameter, $\alpha = l/d = 5$ to 6) first obtained by Ulrich (1972) and supported by the Krishnamurti (2003) laboratory experiments. Although it is quite successful in reproducing the abundance data for evolved stars over a wide range in both mass and metallicity as shown in our previous studies (see also Denissenkov 2010), this value for α turns out to be ~5−10 times higher than that obtained by current 2D and 3D numerical simulations of thermohaline convection (Denissenkov 2010; Denissenkov & Merryfield 2011; Rosenblum et al. 2011; Traxler et al. 2011). However, these simulations are still far from the stellar regime. Indeed, even in the "best" case they are run at moderately low values of the Prandtl number (1/3 to 1/30 Traxler et al. 2011), which is several orders of magnitude away from stellar conditions. In the outer radiative wing of the hydrogen-burning shell of a low-mass RGB star, the Prandtl number varies indeed from $\sim 3 \times 10^{-6}$ to 3×10^{-7}. The same difficulty arises when the density ratio assumed in the simulations is concerned (up to 7 maximum, compared to $\sim 2 \times 10^3$ in the RGB case). This casts some doubt on the accuracy and applicability in the stellar regime of the corresponding empirically determined transport laws. Additionally (and not surprisingly), the use in stellar models of the corresponding low α values precludes surface abundance variations on the RGB as shown by Wachlin et al. (2011). In our view, this urgently calls for a numerical exploration of low Péclet values. Before this becomes available, we keep to the analytical prescription that is able to describe the observational data on the RGB at all metallicities so well, and thus perform our computations with $\alpha = 6$ as in Charbonnel & Zahn (2007b) and Charbonnel & Lagarde (2010a).

2.2.2. Rotation-induced mixing

Rotation-induced mixing is treated as in Charbonnel & Lagarde (2010; see also Decressin et al. 2009) using the complete formalism developed by Zahn (1992) and Maeder & Zahn (1998) that takes into account the evolution of angular momentum and chemicals under the combined action of meridional circulation and shear turbulence. This complete treatment is applied up to the RGB tip or up to the second dredge-up for stars with masses below or above 2 $M_\odot$, respectively.

For all rotating models the initial rotation velocity on the zero age main sequence, V_{ZAMS}, is chosen equal to 45% of the critical rotation velocity of the corresponding model at that evolution point, V_{crit}. This corresponds to the mean observed values for these stars (see more details in Paper III and Ekström et al., submitted). A couple of models were computed with higher initial rotation velocities to quantify the impact on the ^{3}He yields (see the values in Tables 1 and 4 and Sects. 3 and 4 for a discussion).

2.3. Computation of the ^{3}He yields

Except in a few cases that will be discussed in detail in Sect. 3, the standard computations were stopped at the end of the second dredge-up on the early-AGB (label A in the last column of Tables 1 to 4), and the net ^{3}He yields are extrapolated as described below. For some of the non-standard models, however, we pursued the computations on the TP-AGB including the effects of thermohaline instability. For rotating stars and for one classical star (6.0 $M_\odot$) that currently undergoes a hot-bottom burning process (HBB), models were computed until the complete consumption of ^{3}He in the stellar envelope if it is reached on the TP-AGB phase (label B in Tables 1 to 4). For non-standard models that do not undergo HBB, we stopped the computations either at the end of the second dredge-up on early AGB or at the end of the superwind phase at the AGB tip (labels A and C in Tables 1 to 4).

In cases A and B the net ^{3}He yields have to be extrapolated from the ^{3}He content of the convective envelope in the last model computed along the corresponding evolutionary sequence. To estimate the mass lost from that point up to the AGB tip, we used the relation by Dobbie et al. (2006) between the initial stellar mass and the mass of the white dwarfs ($M_{\mathrm{final}} = 0.289\, M_{\mathrm{initial}} + 0.133$). In addition, we assume that the ^{3}He abundance does not change at the stellar surface and consequently in the stellar wind during the final evolution on the TP-AGB. This assumption is reasonable for stars with initial masses lower than, or equal to ~3 $M_\odot$ that do not undergo hot-bottom burning on the TP-AGB, and in which the thermohaline instability leads only to very modest ^{3}He depletion during that phase, as

Table 1. Model results for metallicity of $Z = 0.0001$.

M ($M_\odot$)		$V_{\rm ZAMS}/V_{\rm crit}$^{a}	$V_{\rm ZAMS}$^{a} (km s^{-1})	Life time at TO^b (yr)	Mass fraction ^{3}He^c		Yield ^{3}He^d ($M_\odot$)	^{e}
					1DUP	2DUP		
0.85	stand.	-	-	1.06×10^{10}	1.38×10^{-03}	9.25×10^{-04}	4.39×10^{-04}	A
	thermoh	-	-	1.06×10^{10}	1.39×10^{-03}	1.40×10^{-04}	5.95×10^{-05}	A
	th. +rot.	0.45	115	1.08×10^{10}	1.79×10^{-03}	1.56×10^{-04}	7.17×10^{-05}	A
	th. +rot. ($K = 10^{31}$)	0.45	115	1.08×10^{10}	1.99×10^{-03}	1.57×10^{-04}	6.89×10^{-05}	A
1.0	stand.	-	-	5.93×10^{09}	9.38×10^{-04}	7.03×10^{-04}	3.99×10^{-04}	A
	thermoh	-	-	5.93×10^{09}	9.38×10^{-04}	1.67×10^{-04}	8.54×10^{-05}	A
	th. +rot.	0.45	116	6.06×10^{09}	1.13×10^{-03}	2.06×10^{-04}	1.10×10^{-04}	A
1.25	thermoh	-	-	2.70×10^{09}	5.74×10^{-04}	1.95×10^{-04}	1.31×10^{-04}	A
	th. +rot.	0.45	125	2.65×10^{09}	5.30×10^{-04}	2.02×10^{-04}	1.36×10^{-04}	A
1.5	stand.	-	-	1.46×10^{09}	3.98×10^{-04}	3.16×10^{-04}	2.71×10^{-04}	A
	thermoh	-	-	1.48×10^{09}	3.98×10^{-04}	1.95×10^{-04}	1.60×10^{-04}	A
	th. +rot.	0.45	134	1.52×10^{09}	3.53×10^{-04}	2.13×10^{-04}	1.76×10^{-04}	A
2.0	stand.	-	-	5.70×10^{08}	2.26×10^{-04}	1.85×10^{-04}	2.57×10^{-04}	A
	thermoh	-	-	5.69×10^{08}	2.26×10^{-04}	1.85×10^{-04}	2.05×10^{-04}	A
	th. +rot.	0.45	150	6.08×10^{08}	1.81×10^{-04}	1.51×10^{-04}	1.61×10^{-04}	A
	th. +rot.	0.90	300	6.08×10^{08}	1.39×10^{-04}	1.17×10^{-04}	1.18×10^{-04}	A
2.5	stand.	-	-	3.08×10^{08}	9.73×10^{-05}	1.79×10^{-04}	2.50×10^{-04}	A
	thermoh	-	-	3.08×10^{08}	9.63×10^{-05}	1.76×10^{-04}	2.47×10^{-04}	A
	th. +rot.	0.45	162	3.24×10^{08}	2.13×10^{-04}	1.31×10^{-04}	1.73×10^{-04}	A
3.0	stand.	-	-	2.06×10^{08}	8.46×10^{-05}	1.33×10^{-04}	2.13×10^{-04}	A
	thermoh	-	-	2.06×10^{08}	8.46×10^{-05}	1.32×10^{-04}	2.11×10^{-04}	A
	th. +rot.	0.45	170	2.15×10^{08}	1.47×10^{-04}	9.51×10^{-05}	1.37×10^{-04}	A
4.0	stand.	-	-	1.08×10^{08}	2.63×10^{-05}	8.01×10^{-05}	-	A
	thermoh	-	-	1.08×10^{08}	2.63×10^{-05}	8.09×10^{-05}	-	A
	th. +rot.	0.45	152	1.13×10^{08}	1.08×10^{-04}	6.18×10^{-05}	-7.1×10^{-05}	B
	th.+rot.	0.90	304	1.18×10^{08}	9.48×10^{-05}	4.90×10^{-05}	-	A
6.0	stand.	-	-	5.15×10^{07}	3.26×10^{-05}	4.65×10^{-05}	-	A
	thermoh	-	-	5.16×10^{07}	3.26×10^{-05}	4.68×10^{-05}	-	A
	th. +rot.	0.45	175	5.35×10^{07}	8.26×10^{-05}	3.18×10^{-05}	-1.08×10^{-4}	B

Notes. Each row contains entries for different assumptions: standard (without thermohaline or rotation-induced mixing); thermohaline mixing only; thermohaline and rotation-induced mixing. $^{(a)}$ The initial rotation on the ZAMS. $^{(b)}$ Life time at turn-off. $^{(c)}$ Mass fraction of ^{3}He at the stellar surface after first and second dredge-up. $^{(d)}$ Yields of ^{3}He. $^{(e)}$ The phase where the computations are stopped is given in the last column: Case A: model computed until the end of the second dredge-up on the early-AGB. Case B: model computed along the TP-AGB until the mass fraction of ^{3}He at the surface is below $\sim 10^{-5}$ due to the HBB process. Case C: model computed until the end of the superwind phase. In that former case we also give the extrapolated A yield value (in brackets, A).

will be discussed below. The impact of these hypotheses will be quantified in Sects. 3 and 4.

3. ^{3}He nucleosynthesis and surface abundance

3.1. Standard predictions for the production and destruction of ^{3}He in low- and intermediate-mass stars

3.1.1. STAREVOL standard predictions

While on the pre-main sequence, low- and intermediate-mass stars are converting pristine D into ^{3}He via proton-capture at relatively low temperatures ($\geq 6 \times 10^5$ K) within their contracting interior. Then on the main sequence a peak of fresh ^{3}He builds up in these objects as a result of the competition within the pp-chain between the production reactions (namely p(p, D) followed by D(p, ^{3}He)) and the destruction ones (i.e., ^{3}He(^{3}He, ^{4}He), ^{3}He(^{4}He, 7Be)). The position and size of the peak depends on the stellar mass and metallicity, as can be seen in Fig. 1 (left panels for the standard models). Lower initial stellar mass at a given metallicity as well as higher metallicity at a given stellar mass both result in a higher ^{3}He abundance outside the regions of complete pp-processing caused by a longer main-sequence lifetime and by the dominance of the pp-chains with respect to the CNO-cycle. Additionally, lower initial mass and higher metallicity imply a more extended and deeper (in mass) ^{3}He-rich region owing to lower temperatures at given depths as well as flatter dT/dM_r gradients within the stellar interior during the evolution on the main sequence. Consequently, the net production of ^{3}He during that phase increases with decreasing stellar mass and increasing metallicity.

When stars move towards the RGB, their convective envelope deepens until they reach the region indicated by the vertical lines in Fig. 1, and engulfs all or part of the fresh ^{3}He peak. The first dredge-up efficiency (in terms of maximum penetration depth of the convective envelope) decreases with decreasing metallicity as shown in Fig. 2 (at $Z = 10^{-4}$, no first dredge-up occurs for stars more massive than $\sim 3.0\ M_\odot$). As a consequence, the surface abundance of ^{3}He increases by a factor that depends on the initial stellar mass as well as on the metallicity, as can be seen in Figs. 3–5[7].

---

[7] The evolution of the ^{3}He abundance at the surface of 6 $M_\odot$ standard models depicted in Fig. 4 for the two extreme Z values shows a couple of peculiarities compared to the case of low-mass stars. For such a relatively massive star, the base of the convective envelope withdraws very quickly on the pre-main sequence, precluding any increase of the surface ^{3}He during that phase. However, because of mass loss, the layers enriched in ^{3}He by pristine D-burning appear at the surface later on. In addition, no first dredge-up occurs in the lowest Z 6 $M_\odot$ model (see also Fig. 5).

Table 2. Same as Table 1 for Z = 0.002.

M ($M_\odot$)		$V_{\rm ZAMS}/V_{\rm crit}$	$V_{\rm ZAMS}$ (km s^{-1})	Life time at TO (yr)	Mass fraction ^{3}He 1DUP	2DUP	Yield ^{3}He ($M_\odot$)	
0.85	stand.	-	-	1.24×10^{10}	1.63×10^{-03}	1.33×10^{-03}	6.40×10^{-04}	A
	thermoh	-	-	1.24×10^{10}	1.62×10^{-03}	1.64×10^{-04}	7.69×10^{-05}	A
	th. +rot.	0.45	114	1.23×10^{10}	1.89×10^{-03}	1.76×10^{-04}	9.20×10^{-05}	A
1.0	stand	-	-	6.72×10^{09}	1.15×10^{-03}	9.84×10^{-04}	(5.82×10^{-04}, A) 5.66×10^{-04}	C
	thermoh	-	-	6.72×10^{09}	1.15×10^{-03}	1.84×10^{-04}	(1.19×10^{-04}, A) 1.06×10^{-04}	C
	th. +rot.	0.45	112	6.92×10^{09}	1.27×10^{-03}	2.26×10^{-04}	1.32×10^{-04}	A
1.25	thermoh	-	-	2.88×10^{09}	7.12×10^{-04}	2.43×10^{-04}	1.71×10^{-04}	A
	th. +rot.	0.45	115	2.90×10^{09}	6.30×10^{-04}	2.45×10^{-04}	1.72×10^{-04}	A
1.5	stand	-	-	1.59×10^{09}	5.03×10^{-04}	4.55×10^{-04}	(4.16×10^{-04}, A) 4.02×10^{-04}	C
	thermoh	-	-	1.52×10^{09}	4.90×10^{-04}	2.56×10^{-04}	2.18×10^{-04}	A
	th. +rot.	0.45	123	1.57×10^{09}	4.59×10^{-04}	2.53×10^{-04}	2.15×10^{-04}	A
2.0	stand.	-	-	7.14×10^{08}	2.95×10^{-04}	2.79×10^{-04}	3.26×10^{-04}	A
	thermoh	-	-	7.14×10^{08}	2.95×10^{-04}	2.28×10^{-04}	(2.80×10^{-04}, A) 2.62×10^{-04}	C
	th. +rot.	0.45	137	7.21×10^{08}	2.61×10^{-04}	2.13×10^{-04}	2.40×10^{-04}	A
2.5	stand	-	-	3.91×10^{08}	2.0×10^{-04}	1.90×10^{-04}	2.70×10^{-04}	A
	thermoh	-	-	3.91×10^{08}	1.95×10^{-04}	1.87×10^{-04}	2.65×10^{-04}	A
	th. +rot.	0.45	146	4.03×10^{08}	1.66×10^{-04}	1.56×10^{-04}	2.13×10^{-04}	A
3.0	stand.	-	-	2.48×10^{08}	1.57×10^{-04}	1.45×10^{-04}	2.37×10^{-04}	A
	thermoh	-	-	2.48×10^{08}	1.57×10^{-04}	1.44×10^{-04}	2.35×10^{-04}	A
	th. +rot.	0.45	153	2.57×10^{08}	1.26×10^{-04}	1.17×10^{-04}	1.80×10^{-04}	A
4.0	stand.	-	-	1.28×10^{08}	1.18×10^{-04}	9.79×10^{-05}	1.93×10^{-04}	A
	thermoh	-	-	1.28×10^{08}	1.19×10^{-04}	1.00×10^{-4}	1.99×10^{-4}	A
	th. +rot.	0.45	163	1.33×10^{08}	8.80×10^{-05}	7.52×10^{-05}	-7.05×10^{-05}	B
6.0	stand.	-	-	5.53×10^{07}	8.17×10^{-05}	5.71×10^{-05}	-	A
	thermoh	-	-	5.53×10^{07}	8.19×10^{-05}	5.72×10^{-05}	-	A
	th. +rot.	0.45	170	5.72×10^{07}	6.0×10^{-05}	4.40×10^{-05}	-1.01×10^{-04}	B

Table 3. Same as Table 1 for Z = 0.004.

M ($M_\odot$)		$V_{\rm ZAMS}/V_{\rm crit}$	$V_{\rm ZAMS}$ (km s^{-1})	Life time at TO (yr)	Mass fraction ^{3}He 1DUP	2DUP	Yield ^{3}He ($M_\odot$)	
1.0	stand	-	-	7.64×10^{09}	1.23×10^{-03}	1.09×10^{-03}	(6.39×10^{-04}, A) 6.29×10^{-04}	C
	thermoh	-	-	7.64×10^{09}	1.23×10^{-03}	2.02×10^{-04}	(1.35×10^{-04}, A) 1.25×10^{-04}	C
	th. +rot.	0.45	112	7.69×10^{09}	1.40×10^{-03}	2.45×10^{-04}	1.50×10^{-04}	A
1.25	thermoh	-	-	3.19×10^{09}	7.64×10^{-04}	2.72×10^{-04}	1.96×10^{-04}	A
	th. +rot.	0.45	111	3.49×10^{09}	7.27×10^{-04}	2.81×10^{-04}	2.04×10^{-04}	A
1.5	stand	-	-	1.66×10^{09}	5.25×10^{-04}	4.97×10^{-04}	4.41×10^{-04}	A
	thermoh	-	-	1.66×10^{09}	5.25×10^{-04}	2.61×10^{-04}	(2.44×10^{-04}, A) 2.26×10^{-04}	C
	th. +rot.	0.45	119	1.76×10^{09}	4.67×10^{-04}	2.69×10^{-04}	2.31×10^{-04}	A
2.0	stand.	-	-	7.54×10^{08}	3.06×10^{-04}	2.96×10^{-04}	3.47×10^{-04}	A
	thermoh	-	-	7.54×10^{08}	3.06×10^{-04}	2.52×10^{-04}	(3.11×10^{-04}, A) 2.93×10^{-04}	C
	th. +rot.	0.45	123	7.98×10^{08}	2.78×10^{-04}	2.35×10^{-04}	2.68×10^{-04}	A
2.5	stand	-	-	4.22×10^{08}	2.05×10^{-04}	2.00×10^{-04}	2.85×10^{-04}	A
	thermoh	-	-	4.22×10^{08}	2.06×10^{-04}	2.00×10^{-04}	2.85×10^{-04}	A
	th. +rot.	0.45	141	4.43×10^{08}	1.80×10^{-04}	1.76×10^{-04}	2.45×10^{-04}	A
3.0	stand.	-	-	2.69×10^{08}	1.57×10^{-04}	1.50×10^{-04}	2.46×10^{-04}	A
	thermoh	-	-	2.68×10^{08}	1.57×10^{-04}	1.49×10^{-04}	2.43×10^{-04}	A
	th. +rot.	0.45	147	2.80×10^{08}	1.32×10^{-04}	1.26×10^{-04}	1.98×10^{-04}	A
4.0	stand.	-	-	1.25×10^{08}	1.11×10^{-04}	1.03×10^{-04}	2.05×10^{-04}	A
	thermoh	-	-	1.25×10^{08}	1.11×10^{-04}	1.02×10^{-04}	2.04×10^{-04}	A
	th. +rot.	0.44	147	1.30×10^{08}	8.81×10^{-05}	7.90×10^{-05}	-6.13×10^{-05}	B
6.0	stand.	-	-	5.69×10^{07}	7.38×10^{-05}	5.98×10^{-05}	-	A
	thermoh	-	-	5.68×10^{07}	7.40×10^{-05}	5.99×10^{-05}	-	A
	th. +rot.	0.45	167	5.88×10^{07}	5.60×10^{-05}	4.59×10^{-05}	-9.77×10^{-05}	B

During the subsequent evolution on the RGB that proceeds on shorter timescales compared to the main-sequence lifetime, H-burning is concentrated in a very small (both in mass and radius) radiative shell that surrounds the degenerate helium core and is dominated by the CNO-cycle. There is thus no significant further ^{3}He production inside evolved stars. In addition, the temperature in their convective envelope remains always low enough to preserve the freshly dredged-up ^{3}He.

Table 4. Same as Table 1 for $Z = 0.014$.

M ($M_\odot$)		$V_{\rm ZAMS}/V_{\rm crit}$	$V_{\rm ZAMS}$ (km s^{-1})	Life time at TO (yr)	Mass fraction ^{3}He		Yield ^{3}He ($M_\odot$)	
					1DUP	2DUP		
1.0	stand	-	-	1.15×10^{10}	1.45×10^{-03}	1.28×10^{-03}	7.73×10^{-04}	A
	thermoh	-	-	1.15×10^{10}	1.44×10^{-03}	2.79×10^{-04}	(1.97×10^{-04}, A) 1.92×10^{-04}	C
1.25	thermoh	-	-	4.70×10^{09}	8.74×10^{-04}	3.33×10^{-04}	(2.61×10^{-04}, A) 2.54×10^{-04}	C
	th. +rot.	0.45	110	5.04×10^{09}	9.33×10^{-04}	2.93×10^{-04}	(2.43×10^{-04}, A) 2.39×10^{-04}	C
1.5	stand	-	-	2.29×10^{09}	6.04×10^{-04}	5.85×10^{-04}	(5.21×10^{-04}, A) 5.20×10^{-04}	C
	thermoh	-	-	2.29×10^{09}	6.04×10^{-04}	3.77×10^{-04}	(3.53×10^{-04}, A) 3.43×10^{-04}	C
	th. +rot.	0.45	110	2.56×10^{09}	5.68×10^{-04}	2.95×10^{-04}	(2.70×10^{-04}, A) 2.64×10^{-04}	C
2.0	stand.	-	-	1.01×10^{09}	3.40×10^{-04}	3.33×10^{-04}	(3.93×10^{-04}, A) 3.92×10^{-04}	C
	thermoh	-	-	9.61×10^{08}	3.40×10^{-04}	3.06×10^{-04}	3.62×10^{-04}	A
	th. +rot.	0.40	110	1.08×10^{09}	3.19×10^{-04}	2.73×10^{-04}	(3.18×10^{-04}, A) 3.12×10^{-04}	C
	th. +rot.	0.91	250	1.08×10^{09}	2.96×10^{-04}	2.6×10^{-04}	2.97×10^{-04}	A
2.5	stand	-	-	5.22×10^{08}	2.19×10^{-04}	2.18×10^{-04}	3.12×10^{-04}	A
	thermoh	-	-	5.22×10^{08}	2.19×10^{-04}	2.19×10^{-04}	3.14×10^{-04}	A
	th. +rot.	0.45	130	5.76×10^{08}	2.03×10^{-04}	2.02×10^{-04}	(2.86×10^{-04}, A) 2.80×10^{-04}	C
3.0	stand.	-	-	3.37×10^{08}	1.63×10^{-04}	1.61×10^{-04}	2.65×10^{-04}	A
	thermoh	-	-	3.21×10^{08}	1.60×10^{-04}	1.58×10^{-04}	2.59×10^{-04}	A
	th. +rot.	0.45	136	3.52×10^{08}	1.48×10^{-04}	1.46×10^{-04}	(2.35×10^{-04}, A) 2.30×10^{-04}	C
4.0	stand.	-	-	1.61×10^{08}	1.07×10^{-04}	1.04×10^{-04}	2.04×10^{-04}	A
	thermoh	-	-	1.61×10^{08}	1.07×10^{-04}	1.03×10^{-04}	2.04×10^{-04}	A
	th. +rot.	0.45	144	1.67×10^{08}	9.41×10^{-05}	9.18×10^{-05}	1.72×10^{-04}	A
	th. +rot.	0.93	300	1.68×10^{08}	8.41×10^{-05}	8.23×10^{-05}	1.46×10^{-04}	A
6.0	stand.	-	-	6.16×10^{07}	6.80×10^{-05}	5.92×10^{-05}	-1.05×10^{-04}	B
	thermoh	-	-	6.16×10^{07}	6.75×10^{-05}	5.89×10^{-05}	-	A
	th. +rot.	0.45	156	7.24×10^{07}	5.78×10^{-05}	5.04×10^{-5}	-5.37×10^{-05}	B

Consequently and as far as standard models are concerned, there is no other change in the ^{3}He surface abundance until the stars undergo the second dredge-up on the early-AGB. During this short episode the convective envelope deepens again (see Fig. 2) and reaches ^{3}He-free regions, which induces a slight decrease of the surface abundance of this element (see Figs. 3–5).

Except in the few cases discussed below (see Tables 1 to 4), we stopped our standard computations at that phase. For low-mass stars the standard models published in the literature predict that the ^{3}He stored in the stellar convective envelope survives the TP-AGB phase before it is injected into the ISM by stellar wind and planetary nebula ejection (see references in Sect. 3.1.2). This agrees with our standard [1.5, 2 $M_\odot$; $Z_\odot$], [1.0; $Z = 0.004$], and [1.0, 1.5 $M_\odot$; $Z = 0.002$] models that we computed up to the AGB tip and for which surface ^{3}He abundance remains constant during the TP-AGB phase. Note, however, that in stars with initial masses higher than ~3.5−4 $M_\odot$, hot-bottom burning during the TP-AGB phase induces ^{3}He-burning at the base of the convective envelope and thus reduces the abundance of this element in the whole envelope and at the stellar surface (Sackmann & Boothroyd 1992; Weiss et al. 1996; Forestini & Charbonnel 1997; Sackmann & Boothroyd 1999). Because of this process ^{3}He can even be completely destroyed at the AGB tip in the most massive intermediate-mass stars (see the standard [6 $M_\odot$; $Z_\odot$] model in Fig. 4), so that the corresponding net yields are negative. This will be discussed in more detail in Sect. 3.2, where we present the computations up to the TP-AGB tip for complete models including the effects of thermohaline and rotation-induced mixing.

3.1.2. Surface abundances prior to the TP-AGB and comparison with standard models from the litterature

In Fig. 5 we present the standard predictions for the surface abundance of ^{3}He after both first and second dredge-up episodes (solid and dashed lines respectively) as a function of initial stellar mass for the four considered metallicity values. Note that the 3 to 6 $M_\odot$ models at $Z = 0.0001$ do not undergo the first dredge-up (see Fig. 2). In this case we show the ^{3}He surface abundance at the end of the main sequence and after second dredge-up (solid and dashed).

The assumed initial ^{3}He abundance as well as the total initial D+^{3}He are also indicated in Fig. 5. This confirms that in the standard case, stars with an initial mass lower than ~3.5−4 $M_\odot$ that do not undergo hot-bottom burning are expected to strongly enrich the Universe with ^{3}He. The mass dependency described above also clearly shows up.

In this figure we also compare our standard predictions with those by Weiss et al. (1996) and Sackmann & Boothroyd (1999) at solar metallicity on one hand, and those by Sackmann & Boothroyd (1999) for $Z = 10^{-4}$ on the other hand. An excellent agreement is found with these standard theoretical models.

3.2. Models including rotation-induced mixing and thermohaline instability

In Paper I we discussed at length the impact of both rotation-induced mixing and thermohaline instability on the structure and chemical properties of low- and intermediate-mass stars at various phases of their evolution. Here we only briefly summarize the main points, focusing on ^{3}He.

Note that in low-mass stars, thermohaline mixing induced by the molecular-weight inversion due to the ^{3}He(^{3}He, 2p)^{4}He reaction sets in only at the RGB bump. Up to that phase, predictions for models including only this process (i.e., not including rotation-induced effects) are therefore similar to the standard ones described above (in particular the predictions are the same for ^{3}He surface values caused by first dredge-up), and they start differing only on the upper RGB. In the case of intermediate-mass stars, thermohaline mixing starts playing a role even later,

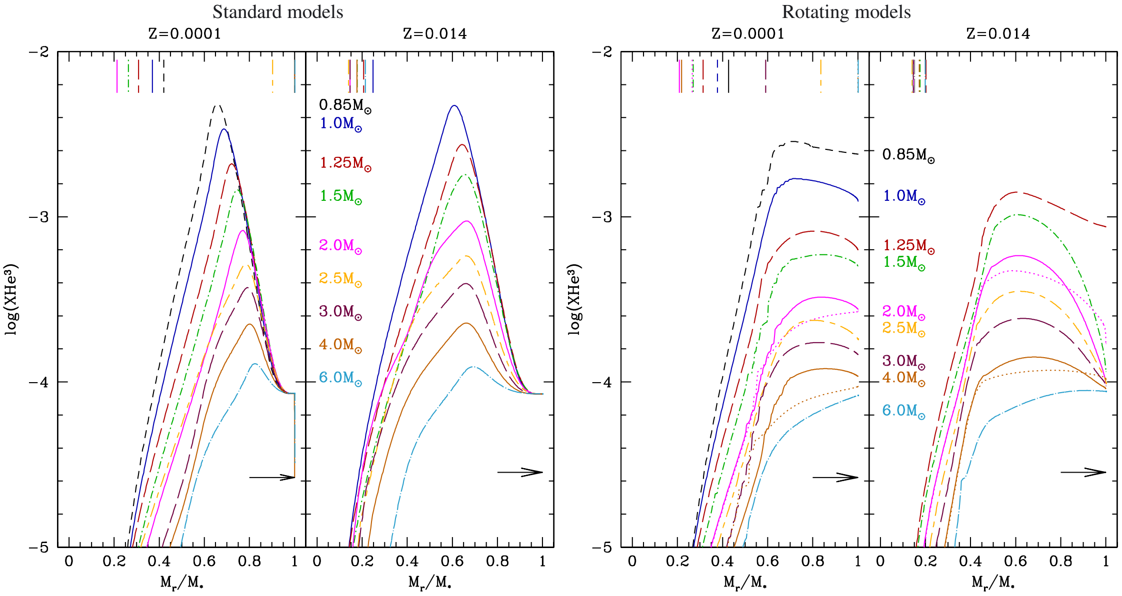

Fig. 1. ^{3}He profile (in mass fraction) at the main-sequence turnoff for models of various masses as indicated and for two values of the metallicity ($Z = 10^{-4}$ and $Z_\odot$ in the left and right subpanels respectively). The horizontal arrows indicate the initial ^{3}He content assumed at stellar birth. The vertical lines show, in each case, the maximum depth reached by the convective envelope during the first dredge-up. *(Left)* Standard models. *(Right)* Models including rotation-induced mixing, assuming an initial rotation velocity equal to 45% of the critical velocity on the zero age main sequence; for the [2, 4 $M_\odot$; $Z_\odot$ and $Z = 10^{-04}$] rotating models, the dotted curves correspond to predictions assuming $V_{\rm ZAMS}/V_{\rm crit} \sim 0.90$.

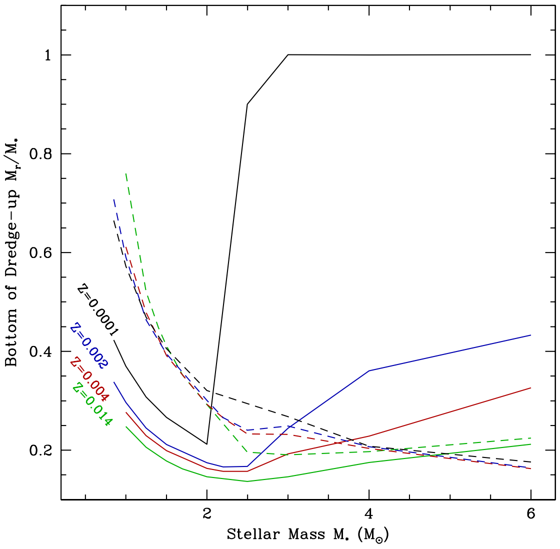

Fig. 2. Maximum depth in mass of the convective envelope relative to the total stellar mass reached during first and second dredge-up (solid and dashed lines respectively) as a function of initial stellar mass and for the different metallicities, as indicated by the colours of the curves.

i.e., on the TP-AGB phase. However, rotation-induced mixing has an impact already in the earlier phases for all stellar masses, as described below.

3.2.1. Main-sequence abundance profiles and first dredge-up

As known for a long time (see references in Paper I), rotation-induced mixing modifies the internal structure of main-sequence stars, and smoothes out the abundance gradients with respect to the standard case. Consequently, the ^{3}He production is moderatly affected by the slightly higher temperature in the rotating models compared to the standard case for a given stellar mass and metallicity during central H-burning. But more importantly, the ^{3}He peak is spread out and fresh ^{3}He is expected to reach the stellar surface during the main-sequence lifetime. The resulting profiles at turnoff are shown in Fig. 1 and can be compared to the standard ones (left and right panels respectively). At that evolution point, the total ^{3}He content for a star of given initial stellar mass and metallicity is slightly lower in the rotating case. As can be seen in Fig. 1, the higher the initial rotation velocity, the stronger the effect.

Additionally, the structural and chemical changes caused by rotation on the main sequence favour a slightly deeper penetration of the convective envelope during the subsequent first dredge-up episode (because the mass of the He-core is slightly larger at the end of the main sequence in the rotating case), which leads to the engulfment of larger ^{3}He-free regions that lie below the peak. As a consequence, post dredge-up ^{3}He values are lower when rotation is accounted for than in the standard models, as can be seen in Figs. 3–5, and in Tables 1 to 4. The effects are stronger for increasing stellar mass and decreasing metallicity.

3.2.2. Red giant branch

In the advanced evolution phases the total diffusion coefficient associated to rotation is too low to induce abundance changes

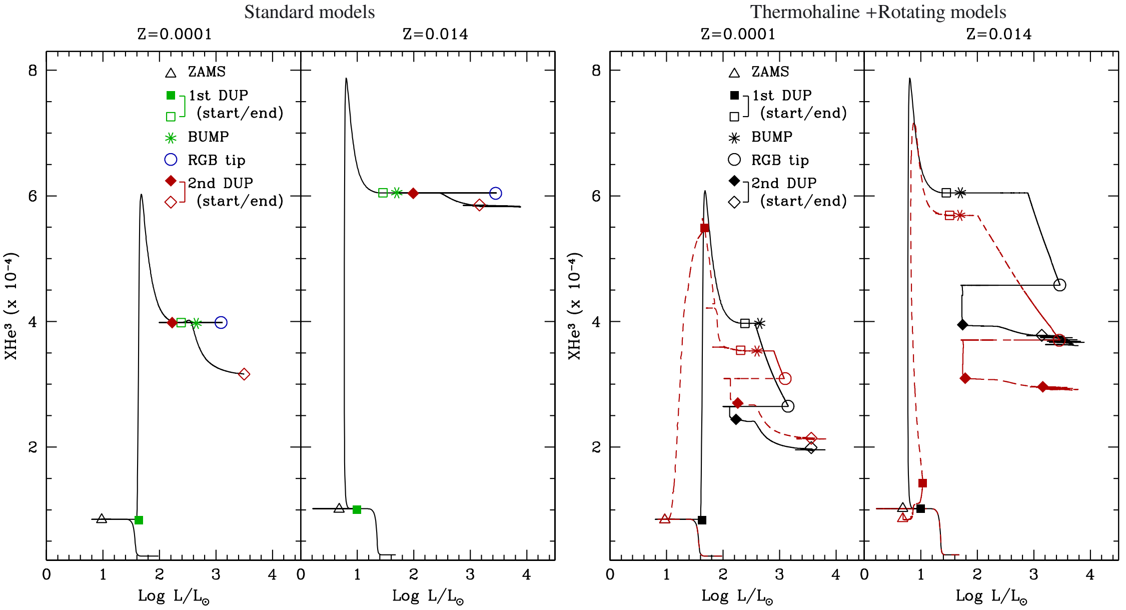

Fig. 3. Evolution of the surface abundance of ^{3}He as a function of stellar luminosity for 1.5 $M_\odot$ models with $Z = 10^{-4}$ and $Z_\odot$ as indicated. Main evolution steps are pointed out with different symbols. *(Left)* Standard case computed up to the end of the second dredge-up only. *(Right)* Models including either thermohaline mixing only (black solid lines), or both thermohaline and rotation-induced mixing (red dashed lines; $V_{\rm ZAMS}/V_{\rm crit} = 0.45$); at $Z_\odot$ the non-standard models are both computed up to the AGB tip.

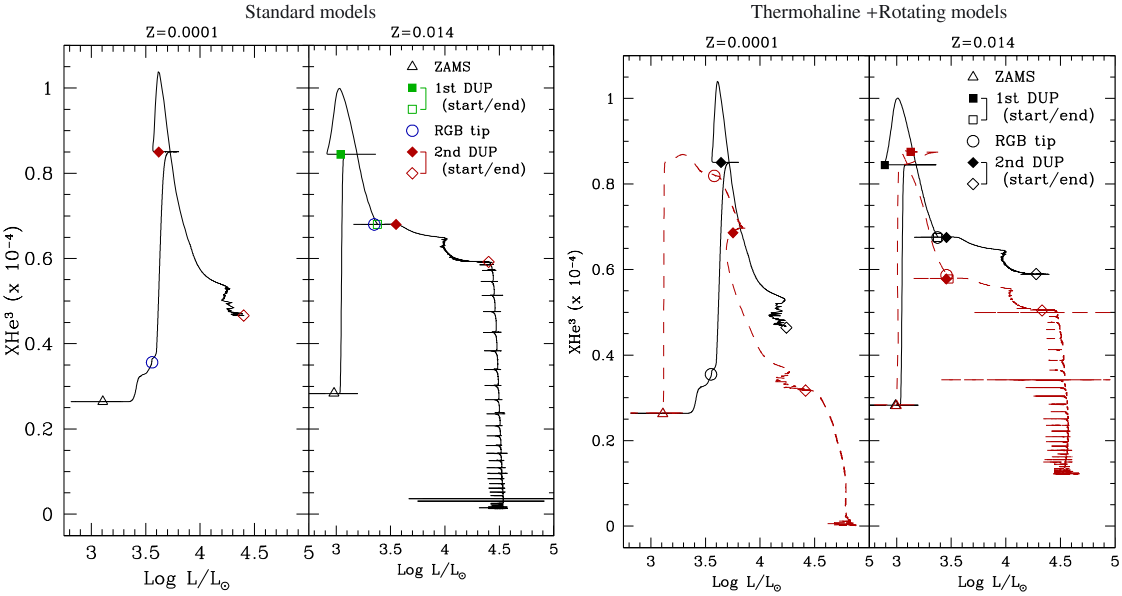

Fig. 4. Same as Fig. 3 for 6 $M_\odot$ models (but with different ordinate). *(Left)* Standard case. The low-metallicity model is computed up to the end of second dredge-up only, while the $Z_\odot$ one is carried out until the AGB tip. *(Right)* Models including thermohaline mixing only (black solid lines), and including both thermohaline and rotation-induced mixings (red dashed lines; $V_{\rm ZAMS}/V_{\rm crit} = 0.45$). These rotating models are computed until the AGB tip.

at the stellar surface (see below, and also Chanamé et al. 2005; Palacios et al. 2006; Cantiello & Langer 2008, 2010; and Paper I) However, for low-mass stars the surface abundances change after the RGB bump with respect to the post dredge-up values, because of thermohaline mixing induced by the molecular weight inversion created by the ^{3}He(^{3}He, 2p)^{4}He reaction in the outer

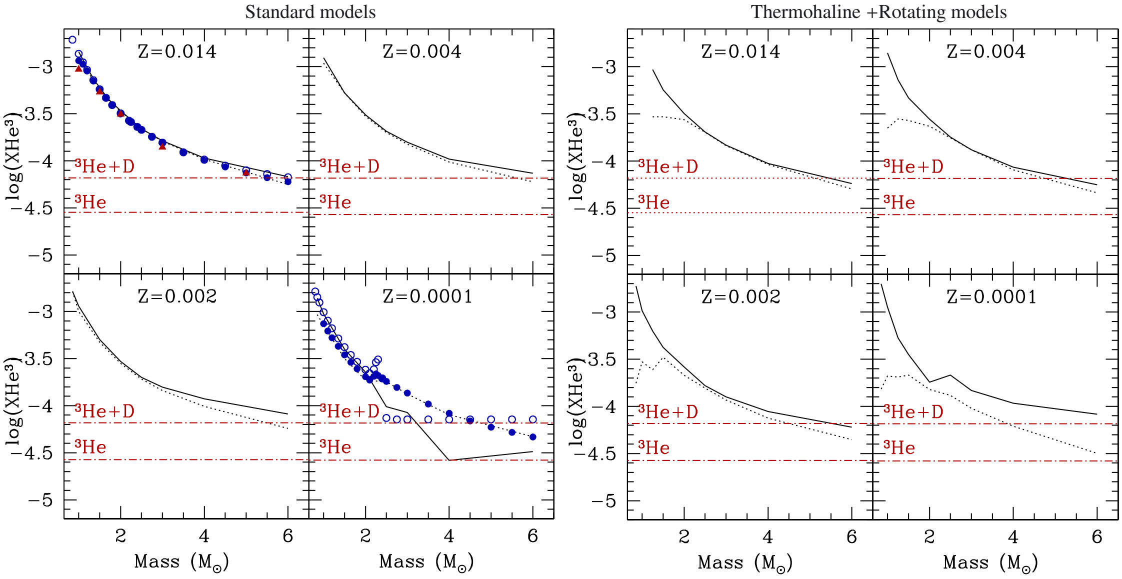

Fig. 5. Surface abundance of ^{3}He (in mass fraction) at the end of first and second dredge-up episodes (solid and dashed black lines respectively) as a function of initial stellar mass and for the four metallicities considered (for the 3 to 6 $M_\odot$ standard models at $Z = 0.0001$ that do not undergo first dredge-up, we show instead the ^{3}He surface abundance at the main-sequence turnoff). Red dotted curves indicate the initial ^{3}He abundance and total D+^{3}He assumed at stellar birth. *(Left)* Standard models. Full red triangles correspond to the predictions by Weiss et al. (1996) at the end of 1DUP for $Z_\odot$; blue circles (open and full at the end of 1DUP and 2DUP respectively) are predictions by Sackmann & Boothroyd (1999) for $Z_\odot$ and $Z = 10^{-4}$. *(Right)* Models including thermohaline and rotation-induced mixings.

wing of the hydrogen-burning shell. Figure 6 compares the diffusion coefficient associated to the thermohaline instability, $D_{\rm thc}$, for a 1.25 $M_\odot$ star at different metallicities, to the total diffusion coefficient associated to rotation, $D_{\rm rot}$, that characterizes the transport of chemicals caused by meridional circulation and shear turbulence. For each model these quantities are shown at the evolution point on the RGB when the surface abundances start changing because of thermohaline mixing (this refers to the evolution point $C_{1.25}$ in Fig. 1 of Paper I) . In all cases, $D_{\rm thc}$ is at least 2 to 3 orders of magnitude higher than $D_{\rm rot}$ (see also Paper I; and Cantiello & Langer 2008, 2010).

As discussed in detail in Paper I and in Charbonnel & Zahn (2007b), the present prescription for the thermohaline diffusivity accounts for the observed behaviour of ^{12}C/^{13}C, [N/C], and lithium in low-mass stars that are more luminous than the RGB bump. It simultaneously leads to strong ^{3}He depletion in the stellar envelope, as can be seen in Fig. 3 (see also e.g. Charbonnel & Zahn 2007b). However, ^{3}He is not completely destroyed at the RGB tip, and therefore it can drive the thermohaline instability in the latter evolution phases, as discussed below.

3.2.3. Early-AGB and ^{3}He surface abundances after the second dredge-up

In stars with initial masses lower than, or equal to 2 and 1.5 $M_\odot$ for $Z = Z_\odot$ and $Z = 0.0001$ respectively (with intermediate values for the upper mass limit for the intermediate metallicities), the ^{3}He abundance continues to decrease at the stellar surface between the end of central helium burning and the second dredge-up episode through thermohaline mixing, as can be seen in Fig. 3. On the other hand, in more massive stars rotation induces a decrease of the ^{3}He surface abundance during central

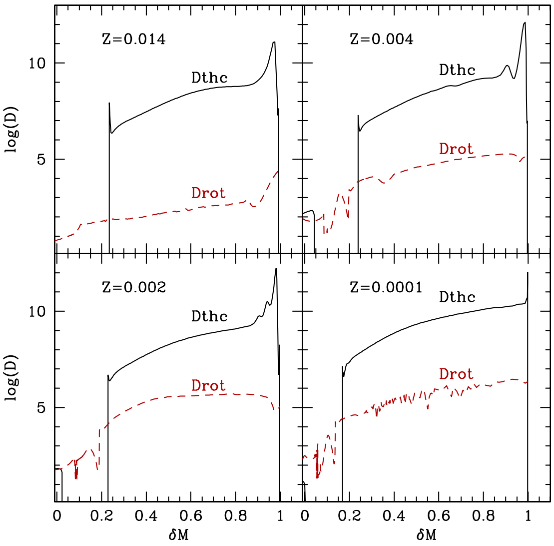

Fig. 6. Thermohaline diffusion coefficient, $D_{\rm thc}$, and total rotation diffusion coefficient, $D_{\rm rot}$, (solid and dashed lines respectively) as a function of reduced stellar mass, δM ($\delta M = \frac{M_r - M_{\rm HBS}}{M_{\rm BCE} - M_{\rm HBS}} = 0$ at the base of the hydrogen-burning shell, $M_{\rm HBS}$; $\delta M = 1$ at the base of the convective envelope, $M_{\rm BCE}$) for 1.25 $M_\odot$ models at different metallicities. In each case the evolution point is chosen at the luminosity when thermohaline mixing connects the hydrogen-burning shell with the convective envelope (see text).

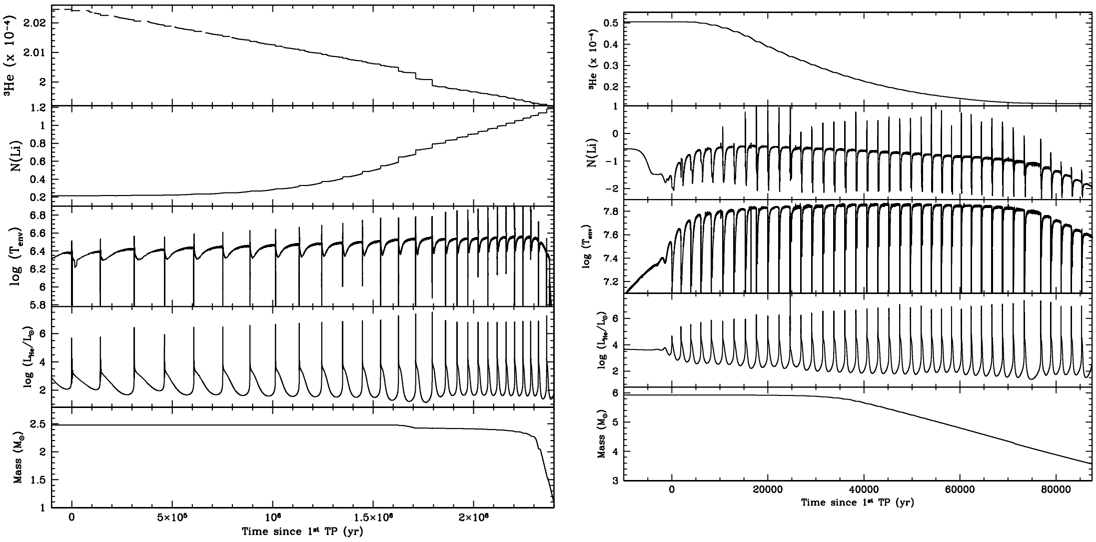

Fig. 7. *(From top to bottom)* Evolution along the TP-AGB of the surface abundance of ^{3}He, of N(Li), of the temperature at the base of convective envelope, of the helium-burning luminosity, and of the total stellar mass. The abscissa is the time since the first thermal pulse. *Left and right respectively:* 2.5 and 6 $M_\odot$ at $Z_\odot$ models computed with thermohaline and rotation-induced mixings.

helium burning and on the early-AGB (see Fig. 4) before they undergo the second dredge-up (Fig. 2). When integrated over the whole evolution, changing $V_{\rm ZAMS}/V_{\rm crit}$ from 0.45 to ~0.9 leads to a decrease of the ^{3}He surface abundance after the second dredge-up of ~5, 11.5, and 22, 23% in the [2 $M_\odot$; $Z_\odot$], [4 $M_\odot$; $Z_\odot$], and [2 $M_\odot$; Z = 10^{-04}], [4 $M_\odot$; Z = 10^{-04}] models respectively (see Table 4).

The resulting surface ^{3}He values after second dredge-up are shown in Fig. 5 (right panels) for the non-standard models over the whole mass and metallicity range. In summary, compared to the standard case (left panels), one finds that the thermohaline instability dominates in reducing the ^{3}He content of low-mass stars, while the dominating process is rotation for intermediate-mass stars. The impact of both mechanisms increases with decreasing metallicity.

3.2.4. TP-AGB

After the second dredge-up, ^{3}He remains in sufficient quantity to drive thermohaline mixing during the TP-AGB in stars that do not undergo hot-bottom burning (i.e., with initial mass below ~3 $M_\odot$). As discussed in Paper I (see also Cantiello & Langer 2010; Stancliffe 2010), this leads to even greater (although modest) depletion of ^{3}He associated to ^{7}Li production during that phase. This is depicted in Fig. 7 as a function of time since the first thermal pulse for a rotating [2.5 $M_\odot$; $Z_\odot$] model computed with thermohaline mixing up to the AGB tip (left panels). This figure also shows the temperature at the base of the convective envelope, the helium-burning luminosity, and the total stellar mass. When compared to the [1.25 $M_\odot$; $Z_\odot$] model discussed in Fig. 7 of Paper I, a slight difference shows up. In the 2.5 $M_\odot$ and from pulse number four on, the convective envelope deepens immediately after each pulse inside the thermohaline region, re-inforcing the thermohaline effect modifying the surface abundances, as can be seen in Fig. 8 (which focusses on pulses number 7 to 9). Note, however, that the decrease of ^{3}He at the stellar surface owing to the whole process along the TP-AGB is modest, and that ^{3}He is not completely destroyed when these

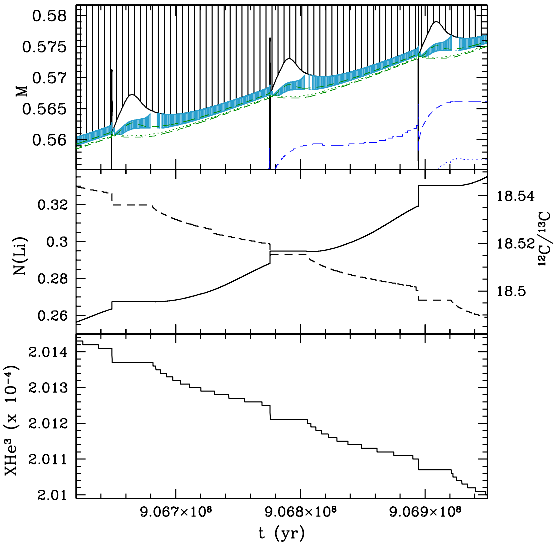

Fig. 8. Zoom on the effect of thermohaline mixing between the thermal pulses number 7 and 9 for the 2.5 $M_\odot$ rotating model at $Z_\odot$. *(Bottom)* Kippenhahn diagram. The hatched zone is the convective envelope; the blue shaded region corresponds to the layers where the thermohaline instability develops; the green and blue dashed lines surround the hydrogen and the helium burning shell respectively (in both cases, the dotted lines show the region of maximum nuclear energy production). *(Middle)* Evolution of the surface ^{7}Li abundance (full line) and ^{12}C/^{13}C ratio (dashed line). *(Bottom)* Evolution of the surface ^{3}He abundance (in mass fraction).

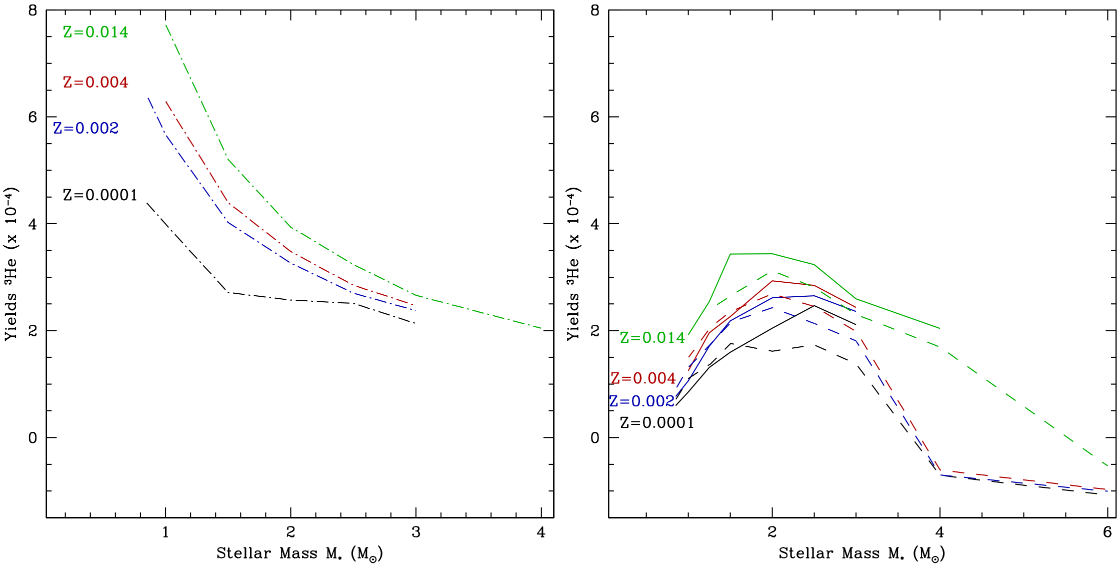

Fig. 9. Yields of ^{3}He as a function of stellar mass, at different metallicities. *(Left)* Predictions for standard models. *(Right)* Predictions including thermohaline mixing only (solid lines) and including both thermohaline and rotation-induced mixings (dashed lines, for models computed up to the AGB tip or to ^{3}He exhaustion).

stars reach the TP-AGB tip (see also Tables 1 to 3). In this framework low-mass stars accordingly remain net ^{3}He producers.

Figure 7 also shows the evolution during TP-AGB of ^{3}He and ^{7}Li abundances at the surface of the non-standard [6.0 $M_\odot$, $Z_\odot$] model. For such a relatively massive star ^{3}He is not abundant enough to drive thermohaline mixing during thermal pulses. However, the temperature at the base of the convective envelope is sufficient to engage hot-bottom burning. As a consequence, the surface abundance of ^{3}He decreases very rapidly, until complete destruction. The simultaneous ^{7}Li enrichment at the stellar surface is caused in this case by the Cameron & Fowler (1971) process.

4. Yields of ^{3}He and conclusions

We can now summarize our study by quantifying in terms of yields the impact of thermohaline instability and rotation-induced mixing on the production and destruction of ^{3}He by low- and intermediate-mass stars at various metallicities. The net yields of ^{3}He are shown in Fig. 9 for all our models and are also given in Tables 1 to 4. There one can find for selected models comparisons between the yields obtained when computing the models until the end of second dredge-up only (case A), or up to the AGB tip (case C). Because the decrease of ^{3}He caused by thermohaline mixing during the TP-AGB is very modest for low-mass stars compared to what happens on the RGB, the difference between the extrapolated yields (A) and the ones obtained from the full computations (C) is below ~12% only.

Our main results may be summarized as follows:

- Over the whole mass and metallicity range considered, the total ^{3}He content is lowered when rotation-induced mixing is accounted for compared to the standard case.
- For low-mass stars ($M < 2$–$2.2\ M_\odot$) that produce large quantities of this light element through the pp-chains on the main sequence, thermohaline mixing on both the RGB and the TP-AGB is dominant in reducing the final ^{3}He yield. These stars remain net producers of ^{3}He however, although their contribution to the Galactic evolution of this light element is strongly reduced compared to the standard framework.
- For intermediate-mass stars thermohaline mixing does not operate on the shorter RGB (these stars ignite central He-burning before reaching the RGB bump).
- For those with masses between 2–2.2 and 3–4 $M_\odot$, thermohaline mixing leads however to modest ^{3}He depletion during the TP-AGB phase, associated with lithium production.
- In more massive intermediate-mass stars, ^{3}He is strongly reduced through the action of rotation that lowers the upper mass limit for stars that are net ^{3}He producers, and is additionally destroyed through hot-bottom burning while they climb the TP-AGB. In these objects Li is produced through the classical Cameron-Fowler mechanism.

The impact on Galactic evolution predictions of these new ^{3}He yields will be presented in a forthcoming paper.

Acknowledgements. We thank J.-P. Zahn, C. Chiappini, D. Romano, M. Tosi, T. Bania, R. T. Rood and D. Balser for fruitful discussions on the ^{3}He problem over the years. We acknowledge financial support from the Swiss National Science Foundation (FNS), from ESF-Euro Genesis, and the french Programme National de Physique Stellaire (PNPS) of CNRS/INSU.

References

Angulo, C., Arnould, M., Rayet, M., et al. 1999, Nucl. Phys. A, 656, 3
Balser, D. S., Bania, T. M., Brockway, C. J., Rood, R. T., & Wilson, T. L. 1994, ApJ, 430, 667
Balser, D. S., Bania, T. M., Rood, R. T., & Wilson, T. L. 1997, ApJ, 483, 320
Balser, D. S., Bania, T. M., Rood, R. T., & Wilson, T. L. 1999, ApJ, 510, 759
Balser, D. S., Goss, W. M., Bania, T. M., & Rood, R. T. 2006, ApJ, 640, 360
Bania, T. M., Balser, D. S., Rood, R. T., Wilson, T. L., & Wilson, T. J. 1997, ApJS, 113, 353
Bania, T. M., Rood, R. T., & Balser, D. S. 2002, Nature, 415, 54

Bania, T. M., Rood, R. T., & Balser, D. S. 2010, in IAU Symp. 268, ed. C. Charbonnel, M. Tosi, F. Primas & C. Chiappini, 81

Cameron, A. G. W., & Fowler, W. A. 1971, ApJ, 164, 111

Cantiello, M., & Langer, N. 2008, in IAU Symp. 252, ed. L. Deng & K. L. Chan, 103

Cantiello, M., & Langer, N. 2010, A&A, 521, A9

Chanamé, J., Pinsonneault, M., & Terndrup, D. M. 2005, ApJ, 631, 540

Charbonnel, C. 1994, A&A, 282, 811

Charbonnel, C. 1995, ApJ, 453, L41

Charbonnel, C., & Do Nascimento, Jr., J. D. 1998, A&A, 336, 915

Charbonnel, C., & Lagarde, N. 2010a, A&A, 522, A10

Charbonnel, C., & Lagarde, N. 2010b, in IAU Symp. 268, ed. C. Charbonnel, M. Tosi, F. Primas & C. Chiappini

Charbonnel, C., & Zahn, J. 2007a, A&A, 476, L29

Charbonnel, C., & Zahn, J.-P. 2007b, A&A, 467, L15

Charbonnel, C., Brown, J. A., & Wallerstein, G. 1998, A&A, 332, 204

Chiappini, C., Renda, A., & Matteucci, F. 2002, A&A, 395, 789

Coc, A., Vangioni-Flam, E., Descouvemont, P., Adahchour, A., & Angulo, C. 2004, ApJ, 600, 544

Cyburt, R. H., Fields, B. D., & Olive, K. A. 2008, J. Cosmology Astropart. Phys., 11, 12

Dearborn, D. S. P., Schramm, D. N., & Steigman, G. 1986, ApJ, 302, 35

Dearborn, D. S. P., Steigman, G., & Tosi, M. 1996, ApJ, 465, 887

Decressin, T., Mathis, S., Palacios, A., et al. 2009, A&A, 495, 271

Denissenkov, P. A. 2010, ApJ, 723, 563

Denissenkov, P. A., & Merryfield, W. J. 2011, ApJ, 727, L8

Dobbie, P. D., Napiwotzki, R., Burleigh, M. R., et al. 2006, MNRAS, 369, 383

Dunkley, J., Komatsu, E., Nolta, M. R., et al. 2009, ApJS, 180, 306

Eggleton, P. P., Dearborn, D. S. P., & Lattanzio, J. C. 2006, Science, 314, 1580

Eggleton, P. P., Dearborn, D. S. P., & Lattanzio, J. C. 2008, ApJ, 677, 581

Forestini, M., & Charbonnel, C. 1997, A&AS, 123, 241

Galli, D., Palla, F., Ferrini, F., & Penco, U. 1995, ApJ, 443, 536

Galli, D., Stanghellini, L., Tosi, M., & Palla, F. 1997, ApJ, 477, 218

Geisler, D., Smith, V. V., Wallerstein, G., Gonzalez, G., & Charbonnel, C. 2005, AJ, 129, 1428

Geiss, J., & Gloeckler, G. 1998, Space Sci. Rev., 84, 239

Geiss, J., & Gloeckler, G. 2010, in IAU Symp. 268, ed. C. Charbonnel, M. Tosi, F. Primas & C. Chiappini, 71

Gilroy, K. K. 1989, ApJ, 347, 835

Gilroy, K. K., & Brown, J. A. 1991, ApJ, 371, 578

Gratton, R. G., Sneden, C., Carretta, E., & Bragaglia, A. 2000, A&A, 354, 169

Hogan, C. J. 1995, ApJ, 441, L17

Iben, Jr., I. 1967, ApJ, 147, 624

Kippenhahn, R., Ruschenplatt, G., & Thomas, H.-C. 1980, A&A, 91, 175

Krishnamurti, R. 2003, J. Fluid Mech., 483, 287

Maeder, A., & Zahn, J.-P. 1998, A&A, 334, 1000

Olive, K. A., Rood, R. T., Schramm, D. N., Truran, J., & Vangioni-Flam, E. 1995, ApJ, 444, 680

Palacios, A., Charbonnel, C., Talon, S., & Siess, L. 2006, A&A, 453, 261

Palla, F., Bachiller, R., Stanghellini, L., Tosi, M., & Galli, D. 2000, A&A, 355, 69

Pilachowski, C., Sneden, C., Freeland, E., & Casperson, J. 2003, AJ, 125, 794

Recio-Blanco, A., & de Laverny, P. 2007, A&A, 461, L13

Reimers, D. 1975, Mem. Soc. Roy. Sci. Liege, 8, 369

Rood, R. T., Steigman, G., & Tinsley, B. M. 1976, ApJ, 207, L57

Rood, R. T., Wilson, T. L., & Steigman, G. 1979, ApJ, 227, L97

Romano, D., Tosi, M., Matteucci, F., & Chiappini, C. 2003, MNRAS, 346, 295

Rood, R. T., Bania, T. M., & Wilson, T. L. 1984, ApJ, 280, 629

Rosenblum, E., Garaud, P., Traxler, A., & Stellmach, S. 2011, ApJ, 731, 66

Sackmann, I., & Boothroyd, A. I. 1992, ApJ, 392, L71

Sackmann, I., & Boothroyd, A. I. 1999, ApJ, 510, 217

Shetrone, M. D. 2003, ApJ, 585, L45

Smith, V. V., Hinkle, K. H., Cunha, K., et al. 2002, AJ, 124, 3241

Spergel, D. N., Verde, L., Peiris, H. V., et al. 2003, ApJS, 148, 175

Spite, M., Cayrel, R., Hill, V., et al. 2006, A&A, 455, 291

Stancliffe, R. J. 2010, MNRAS, 174

Stancliffe, R. J., Church, R. P., Angelou, G. C., & Lattanzio, J. C. 2009, MNRAS, 396, 2313

Tautvaišiene, G., Edvardsson, B., Tuominen, I., & Ilyin, I. 2000, A&A, 360, 499

Tautvaišienė, G., Edvardsson, B., Puzeras, E., & Ilyin, I. 2005, A&A, 431, 933

Tosi, M. 1996, in From Stars to Galaxies: the Impact of Stellar Physics on Galaxy Evolution, ed. C. Leitherer, U. Fritze-von-Alvensleben & J. Huchra, APS Conf. Ser., 98, 299

Tosi, M. 1998, Space Sci. Rev., 84, 207

Tosi, M. 2000, in The Light Elements and their Evolution, ed. L. da Silva, R. de Medeiros & M. Spite, IAU Symp., 198, 525

Traxler, A., Garaud, P., & Stellmach, S. 2011, ApJ, 728, L29

Ulrich, R. K. 1971, ApJ, 168, 57

Ulrich, R. K. 1972, ApJ, 172, 165

Vassiliadis, E., & Wood, P. R. 1993, ApJ, 413, 641

Wachlin, F. C., Miller Bertolami, M. M., & Althaus, L. G. 2011, A&A, 533, A139

Weiss, A., Wagenhuber, J., & Denissenkov, P. A. 1996, A&A, 313, 581

Wilson, T. L., & Rood, R. 1994, ARA&A, 32, 191

Zahn, J.-P. 1992, A&A, 265, 115

6.3 Evolution of light elements in the Galaxy

Effects of thermohaline instability and rotation-induced mixing on the evolution of light elements in the Galaxy : D, ^{3}He and ^{4}He

N. Lagarde, D. Romano, C. Charbonnel, M. Tosi, C. Chiappini, and F. Matteucci

arXiv 1204.2266 (2012 ; accepted for publication in A&A)

In this section, we deal with the evolution of D, ^{3}He, and ^{4}He in the solar vicinity, as well as their distributions across the Galactic disc. The production of ^{3}He is strictly related to the destruction of D and the production of ^{4}He. Therefore, these elements are considered all together. The main novelty of the work presented in the next article is the new nucleosynthesis prescriptions for the synthesis of ^{3}He and ^{4}He in low-mass stars (masses below 6 $M_\odot$). We present, for the first time, chemical evolution models for ^{3}He computed with stellar yields from non-standard stellar models that include both rotation-induced and thermohaline mixing (Charbonnel & Zahn 2007a; Charbonnel & Lagarde 2010a; Lagarde et al. 2011). These yields bring chemical evolution model predictions into agreement with the Galactic ^{3}He data without the necessity of assuming "ad hoc" fractions of extra-mixing among low-mass stars.

Galactic chemical evolution code

For this study we use the galactic chemical evolution code developed by D. Romano, C. Chiappini, M. Tosi, and F. Matteucci (Matteucci & Francois 1989; Chiappini et al. 1997; Matteucci 2001; Chiappini et al. 2001). We present in this paragraph the main ingredients necessary to build models of chemical evolution of spiral galaxy like the Milky Way. Some assumptions of physical process are requiered to build a good model of Galactic chemical evolution which must predict the evolution of the abundances of the most common chemical elements with the space and the time :

- The first is the star formation caracterized by the stellar birthrate, which is divided into two independent functions, the star formation rate (only a function of time, SFR) and the initial mass function (only a function of mass, IMF). In our galactic chemical evolution models, we use the IMF given by Kroupa et al. (1993).
- The second is the infall rate. The adopted model for the chemical evolution of the Galaxy assumes that the Milky Way forms two main accretion episodes almost completely disentangled (Chiappini et al. 1997, 2001). During the first one, the primordial gas collapses very quickly and forms the spheroidal components, halo and bulge. During the second one, the thin-disc forms, mainly by accretion of matter of primordial chemical composition. Chiappini et al. (1997) adopted a double low for the halo-thick and thin-disk :

  $$\mathrm{IR} = \mathrm{A(R)} \cdot e^{-t/\tau_H} + \mathrm{B(R)} \cdot e^{-(t-t_{max})/\tau_D(\mathrm{R})},$$

  where τ_H and τ_D(R) are the timesacales for the halo-thick and thin-disk formation, respectively. The dependence of τ_D on the Galactocentric distance is a linear function (see Chiappini et al. 1997). The disc is built-up in the framework of the inside-out scenario of Galaxy formation, which ensures the formation of abundance gradients along the disc (Larson 1976; Matteucci & Francois 1989). The Galactic disc is approximated by several independent rings, 2 kpc wide, without exchange of matter between them.

- The third is the stellar nucleosynthesis. The nucleosynthesis prescriptions for metals (elements heavier than ^{4}He) are from Paper II (Lagarde et al. 2011) for low- and intermediate-mass stars (M $\leq$ 6 M$_\odot$). As for massive stars and Type Ia supernovae, we adopt the same nucleosynthesis prescriptions as in Romano et al. (2010), their model 6, namely:
  - Yields for core-collapse supernovae are taken from Kobayashi et al. (2006), except for carbon, nitrogen and oxygen, for which the adopted yields are from Meynet & Maeder (2002); Hirschi et al. (2005); Hirschi (2007); Ekström et al. (2008).
  - Yields for Type Ia supernovae are from Iwamoto et al. (1999).

  For our models (analysed below §6.4) we use standard prescriptions from Dearborn et al. (1996a) in the 6 to 100 M$_\odot$ mass range for D and ^{3}He and yields by Meynet & Maeder (2002); Hirschi et al. (2005); Hirschi (2007); Ekström et al. (2008) for ^{4}He. For low- and intermediate-mass stars (M $\leq$ 6 M$_\odot$) we use the yields from Charbonnel & Lagarde (2010a); Lagarde et al. (2011) and we compute three different models described in the article below. Linear interpolations in mass and metallicity are used to fill the gaps in the computed grids of yields (see Romano et al. 2010 for a discussion of the potential spurious effects introduced by this procedure).

Results

We model the time-behavior of D, ^{3}He and ^{4}He in the solar neighbourhood, as well as in the inner and outer disc. The predictions of our stellar models including thermohaline instability and rotation-induced mixing are compared to the predictions of models adopting standard nucleosynthesis prescriptions and to the most recent relevant observations.

As discussed in the previous section (§6.2), thermohaline mixing induces significant depletion of ^{3}He in low- and intermediate-mass stars. Indeed, in low-mass stellar models (Lagarde et al. 2011, , chap. 5) including thermohaline mixing, ^{3}He is destroyed from the bump luminosity on the RGB during shell hydrogen burning and during the early AGB. Although these stars remain net producers of ^{3}He, their contribution to the Galactic evolution of this element is highly reduced compared to classical theory. As a consequence, our Galactic Chemical Evolution (GCE) models including thermohaline mixing reproduce the observations of ^{3}He in the proto-solar cloud (PSC), local interstellar medium (LISM) and HII regions, while ^{3}He is overproduced on a Galactic scale with standard models. On the other hand, in the inner regions of the Galactic disk, where the star formation was stronger, the contribution of low- and intermediate-mass stars to the ^{3}He enrichment of the ISM is more important. Although the contribution of low-mass stars in the inner regions is significantly reduced in our model including thermohaline instability and rotation-induced mixing, a negative gradient of ^{3}He/H is still predicted, contrary to observations in HII regions which show a gradient close to zero. Nevertheless, it would be very useful if future work could provide a sound estimate of the errors associated to ^{3}He determinations across the Galactic disk, to better constrain both stellar and galactic evolution studies. Inhibition of thermohaline instability by a fossil magnetic field (Charbonnel & Zahn 2007a) in the rare red giant stars that are descendants of Ap stars does reconcile the measurements of ^{3}He/H in Galactic HII regions with high values of ^{3}He in a couple of planetary nebulae.

Then again, rotation has an impact on the stellar yields of H and ^{4}He. Whether GCE models including rotation fit better the Galactic ^{4}He data than standard models can not be said, because of the uncertainties on the actual solar chemical composition. However, they are consistent with the relatively high value of $(D/H)_{\rm LISM}$ proposed by Prodanović et al. (2010).

We conclude that GCE models taking into account the stellar yields including both thermohaline mixing and rotation-induced mixing reproduce satisfactorily well all the available data on D, ^{3}He and, possibly, ^{4}He abundances in the Milky Way, within the errors. In addition, thermohaline mixing is the only physical mechanism known so far able to solve the so-called "^{3}He problem" plaguing in the literature since many years.

A&A 542, A62 (2012)
DOI: 10.1051/0004-6361/201219132

Astronomy & Astrophysics

Effects of thermohaline instability and rotation-induced mixing on the evolution of light elements in the Galaxy: D, ^{3}He and ^{4}He

N. Lagarde[1], D. Romano[2], C. Charbonnel[1,3], M. Tosi[2], C. Chiappini[4], and F. Matteucci[5,6]

[1] Geneva Observatory, University of Geneva, Chemin des Maillettes 51, 1290 Versoix, Switzerland
e-mail: Nadege.Lagarde@unige.ch
[2] INAF – Bologna Observatory, via Ranzani 1, 40127 Bologna, Italy
[3] IRAP, CNRS UMR 5277, Université de Toulouse, 14, Av. E.Belin, 31400 Toulouse, France
[4] Leibniz – Institut für Astrophysik Potsdam (AIP), An der Sternwarte 16, 14482 Potsdam, Germany
[5] Physics Department, Trieste University, via Tiepolo 11, 34143 Trieste, Italy
[6] INAF-Trieste Observatory, via Tiepolo 11, 34143 Trieste, Italy

Received 28 February 2012 / Accepted 8 April 2012

ABSTRACT

Context. Recent studies of low- and intermediate-mass stars show that the evolution of the chemical elements in these stars is very different from that proposed by standard stellar models. Rotation-induced mixing modifies the internal chemical structure of main sequence stars, although its signatures are revealed only later in the evolution when the first dredge-up occurs. Thermohaline mixing is likely the dominating process that governs the photospheric composition of low-mass red giant branch stars and has been shown to drastically reduce the net ^{3}He production in these stars. The predictions of these new stellar models need to be tested against galaxy evolution. In particular, the resulting evolution of the light elements D, ^{3}He and ^{4}He should be compared with their primordial values inferred from the *Wilkinson* Microwave Anisotropy Probe data and with the abundances derived from observations of different Galactic regions.

Aims. We study the effects of thermohaline mixing and rotation-induced mixing on the evolution of the light elements in the Milky Way.

Methods. We compute Galactic evolutionary models including new yields from stellar models computed with thermohaline instability and rotation-induced mixing. We discuss the effects of these important physical processes acting in stars on the evolution of the light elements D, ^{3}He, and ^{4}He in the Galaxy.

Results. Galactic chemical evolution models computed with stellar yields including thermohaline mixing and rotation fit better observations of ^{3}He and ^{4}He in the Galaxy than models computed with standard stellar yields.

Conclusions. The inclusion of thermohaline mixing in stellar models provides a solution to the long-standing "^{3}He problem" on a Galactic scale. Stellar models including rotation-induced mixing and thermohaline instability reproduce also the observations of D and ^{4}He.

Key words. Galaxy: evolution – galaxies: abundances – galaxies: formation

1. Introduction

Understanding the evolution of the light elements deuterium (D), helium-3 (^{3}He), and helium-4 (^{4}He) hinges on the comprehension of several astrophysical processes and links together different branches of physics and cosmology. D, ^{3}He, and ^{4}He are all synthesized in astrophysically relevant quantities during Big Bang nucleosynthesis (BBN; Peebles 1966; Wagoner et al. 1967). In the absence of any other realistic production channel (Epstein et al. 1976; Prodanović & Fields 2003), the abundance of D in galaxies smoothly decreases in time as gas cycles through stars. ^{3}He and ^{4}He, instead, have a more complex history, since they are both produced and destroyed in stars.

The sensitivity of the predicted BBN abundance of D, $(D/H)_P$, to the baryon-to-photon ratio, η_B, coupled with its straightforward galactic evolution, has long made this element be the "baryometer" of choice (Reeves et al. 1973). In the nineties, the controversial assessment of the primordial abundance of D from observations of high-redshift clouds (e.g. Songaila et al. 1994; Burles & Tytler 1998), probing an almost unevolved medium, led researchers to resort to detailed Galactic chemical evolution (GCE) modelling in order to constrain the pre-Galactic D abundance and, hence, the value of η_B. It was shown that any reasonable GCE model results in moderate local D astration, by less than a factor of three (Steigman & Tosi 1992; Edmunds 1994; Galli et al. 1995; Dearborn et al. 1996; Prantzos 1996; Tosi et al. 1998; Chiappini et al. 2002). Assuming that the local present-day abundance of D is well known, this provided a stringent bound to $(D/H)_P$ and, hence, a test for BBN theories. Chemical evolution models able to reproduce the majority of the observational constraints for the Milky Way firmly ruled out the highest values of $(D/H)_P$ by Songaila et al. (1994). In particular, the values of $(D/H)_P$ and η_B suggested by Tosi (2000) and Chiappini et al. (2002) turned out to be in very good agreement with the ones determined from the analysis of the first *Wilkinson* Microwave Anisotropy Probe (WMAP) data (Bennett et al. 2003; Spergel et al. 2003).

Indeed, the first release of results from WMAP made us enter a new precision era for cosmology – η_B is now known with exquisite accuracy. Converging measurements of D abundances in remote gas clouds lead to $(D/H)_P = (2.8 \pm 0.2) \times 10^{-5}$ (Pettini et al. 2008), a value consistent, within the errors, with the

Table 1. Abundances of deuterium, ^{3}He, and ^{4}He at different epochs.

Chemicals	Units	SBBN+WMAP (t = 0 Gyr)	Protosolar cloud (t = 9.2 Gyr)	Local intestellar medium (Present time)
D	10^{5} (D/H)	2.49 ± 0.17[a] $2.60\,^{+0.19}_{-0.17}$[b]	2.1 ± 0.5[c]	2.31 ± 0.24[d] 0.98 ± 0.19[e] 2.0 ± 0.1[f]
^{3}He	10^{5} (^{3}He/H)	1.00 ± 0.07[a] 1.04 ± 0.04[b]	1.5 ± 0.2[c]	2.4 ± 0.7[g]
^{4}He	Y	0.2486 ± 0.0002[a] $0.2479\,^{+0.0004}_{-0.0005}$[b]	0.2703[h]	

References. (a) Cyburt et al. (2008); (b) Coc et al. (2004); (c) Geiss & Gloeckler (1998); (d) Linsky et al. (2006); (e) Hébrard et al. (2005); (f) Prodanović et al. (2010); (g) Gloeckler & Geiss (1996); (h) Asplund et al. (2009).

primordial D abundance predicted by the standard model of cosmology with parameters fixed by WMAP data (e.g. Cyburt et al. 2008; Coc et al. 2004, see Table 1). The remarkable homogeneity of D abundances at high redshifts, however, clashes with the unexpectedly large scatter in D/H revealed by determinations of relatively local D abundances (Vidal-Madjar et al. 1998; Jenkins et al. 1999; Sonneborn et al. 2000; Hébrard et al. 2002; Oliveira & Hébrard 2006). The observed dispersion can be reconciled with the predictions on D evolution from standard GCE models by taking into account two short-term, small-scale phenomena: D depletion onto dust grains and localized infall of primordial gas (Romano et al. 2006; Steigman et al. 2007; Romano 2010).

As far as ^{3}He is concerned, Iben (1967) and Truran & Cameron (1971) first showed that large amounts of this element are produced by low-mass stars ($M \simeq 1$–$3\ M_{\odot}$) in the ashes of hydrogen burning by the p-p cycle on the main sequence. Problems arised soon, when Rood et al. (1976) incorporated these yields in models of GCE and came out with predicted ^{3}He abundances orders of magnitude higher than the observed ones in the Galaxy. Indeed, the nearly constancy of the ^{3}He abundance with both time and position within the Galaxy (e.g. Bania et al. 2002) rather implies a negligible production of this element in stars, at variance with predictions from standard stellar models. It was then advocated that some non-standard mechanisms are acting in a major fraction of low-mass stars, which prevents the fresh ^{3}He from surviving and being ejected in the interstellar medium (ISM; Rood et al. 1984). For instance, extra mixing was also invoked in order to explain other abundance anomalies like the carbon isotopic ratio in red giants (Charbonnel 1995; Hogan 1995; Charbonnel & Do Nascimento 1998; see also Eggleton et al. 2006, 2008). The first ^{3}He stellar yields for low-mass stars computed with "ad hoc" extra-mixing (i.e., not related to a physical mechanism, see Sect. 2.2.2) became available with the work of Boothroyd & Sackmann (1999). Galli et al. (1997); Palla et al. (2000); Chiappini et al. (2002) implemented those yields, accounting for the dependency of the helium-3 production/destruction on the stellar mass, metallicity and initial D abundances. It was shown that chemical evolution models which account for about 90% of low-mass stars undergoing extra-mixing led to a good agreement with the Proto Solar Cloud (PSC) observations as well as with the observed gradient along the disk.

The physical process responsible for the extra-mixing has possibly been recently identified. Charbonnel & Zahn (2007b) have shown indeed that thermohaline instability, when modelled with a simple prescription based on linear stability analysis, leads to a drastic reduction of ^{3}He production in low-mass, low-metallicity red giant stars. However a couple of planetary nebulae, namely NGC 3242 and J320, have been found to behave classically (see Bania et al. 2010): slightly more massive than the Sun, they are currently returning fresh ^{3}He to the ISM, in agreement with standard predictions (Rood et al. 1992; Galli et al. 1997; Balser et al. 1999, 2006). To reconcile the ^{3}He/H measurements in Galactic HII regions with the high values of ^{3}He in NGC 3242 and J320, Charbonnel & Zahn (2007a) proposed that thermohaline mixing is inhibited by a fossil magnetic field in red giant branch (RGB) stars that are descendants of Ap stars. The percentage of such stars is about 2–10% of all A-type objects. This number agrees with the fact that about 4% of low-mass evolved stars (including NGC 3242) exhibit standard suface abundances as depicted by their carbon isotopic ratios (Charbonnel & Do Nascimento 1998). Grids of ^{3}He yields from stellar models taking into account thermohaline instability, as well as rotational mixing, are presented in Lagarde et al. (2011). These are suitable for use in GCE studies such as the one presented here.

The scarce determinations of reliable ^{4}He abundances in the Galaxy (Balser et al. 2010; Peimbert et al. 2010), together with the steadiness of GCE model predictions on the evolution of ^{4}He when adopting different stellar yields (e.g. Chiappini et al. 2002; Romano et al. 2010), have given this element little attention in GCE studies.

In this paper, we deal with the evolution of D, ^{3}He, and ^{4}He in the solar vicinity, as well as their distributions across the Galactic disc. The production of ^{3}He is strictly related to the destruction of D and the production of ^{4}He. Therefore, these elements are considered all together. The main novelty of the present work is the new nucleosynthesis prescriptions for the synthesis of ^{3}He and ^{4}He in low-mass stars (masses below 6 $M_{\odot}$). Here we present, for the first time, chemical evolution models for ^{3}He computed with stellar yields from non-standard stellar models that include both rotation-induced and thermohaline mixing (Charbonnel & Zahn 2007a; Charbonnel & Lagarde 2010; Lagarde et al. 2011). As we will show in the next sections, these yields bring chemical evolution model predictions into agreement with the Galactic ^{3}He data without the necessity of assuming "ad hoc" fractions of extra-mixing among low-mass stars.

The layout of the paper is as follows. In Sect. 2 we discuss the production/destruction channels of D, ^{3}He, and ^{4}He in stars in light of new generation stellar models that take into account rotation-induced mixing and thermohaline instability. A comparison with stellar yields predictions from the literature is presented. In Sect. 3 we describe the adopted GCE model. In Sect. 4

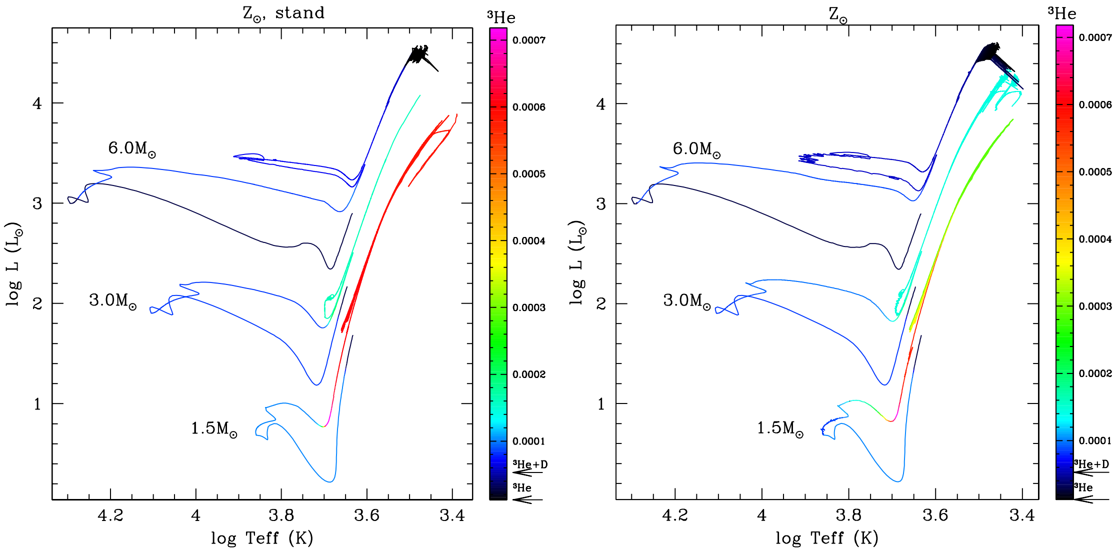

Fig. 1. Theoretical evolutionary tracks in the HR diagram for the 1.5 $M_\odot$, 3.0 $M_\odot$, and 6.0 $M_\odot$ models at solar metallicity following the standard prescription (*left panel*); and including rotation-induced mixing and thermohaline instability (*right panel*), from the pre-main sequence up to the end of the TP-AGB phase. Colours depict the mass fraction of ^{3}He at the stellar surface as indicated on the right, with the arrows showing the initial ^{3}He and ^{3}He+^{2}H content assumed at birth.

we discuss our results on the evolution of the light elements in the Galaxy. In particular, we try to put constraints on the uncertain parameters of stellar evolution through a comparison of the model predictions with the relevant data. We draw our conclusions in Sect. 5.

2. Stellar nucleosynthesis of light elements from new generation models for low- and intermediate-mass stars

In a series of papers (Charbonnel & Lagarde 2010; Lagarde et al. 2011, 2012, hereinafter Papers I, II and III, respectively; see also Charbonnel & Zahn 2007b,a), we discuss the impact of rotation-induced mixing and thermohaline instability on the structure, evolution, nucleosynthesis and yields, as well as on the asteroseismic and chemical properties of low- and intermediate-mass stars at various metallicities. A detailed description of the input physics of the models is given in Paper III. Rotation-induced mixing is treated using the complete formalism developed by Zahn (1992) and Maeder & Zahn (1998) (see for more details, Papers I, II, III). In these stellar models, we consider that thermohaline instability develops as long thin fingers with the aspect ratio consistent with predictions by Ulrich (1972) and confirmed by the laboratory experiments (Krishnamurti 2003). We note that this value is higher than obtained by current 2D and 3D numerical simulations (Denissenkov 2010; Denissenkov & Merryfield 2011; Rosenblum et al. 2011; Traxler et al. 2011). Before a final word on this discrepancy comes from future numerical simulations in realistic stellar conditions, we adopt an aspect ration (i.e., maximum length relative to their diameter) of 5, which nicely accounts for the observed chemical properties of red giant stars. These new generation stellar models account very nicely for main-sequence and RGB abundance patterns observed in field and open cluster stars over the mass and metallicity range covered, as shown in Paper I and in Charbonnel & Zahn (2007b). In this section we briefly summarize their characteristics as far as the nucleosynthesis of light elements is concerned.

2.1. Deuterium

Deuterium burns by proton-captures at low temperature during the pre-main sequence (Reeves et al. 1973). Therefore, it is totally destroyed in stellar interiors and the corresponding net yields are negative whatever the mass and metallicity of the star, as in the case of standard stellar models.

2.2. Helium-3

2.2.1. Impact of rotation-induced mixing and thermohaline instability on model predictions

Paper II describes in detail the behaviour of ^{3}He both in the standard case and in our models including thermohaline instability and rotation-induced mixing. Figure 1 shows the theoretical evolution of the ^{3}He surface abundance along the evolutionary tracks in the HR diagram for the models of 1.5, 3.0, and 6.0 $M_\odot$ at solar metallicity that take into account these two processes. The colour coding in mass fraction is given on the right, with the initial values of ^{3}He and D+^{3}He indicated by the arrows. Evolution is shown from the pre-main sequence along the Hayashi track up to the end of the thermally-pulsing asymptotic giant branch (TP-AGB) phase. We see the changes in ^{3}He surface abundance due to D-burning on the pre-main sequence except in the 6.0 $M_\odot$ model whose convective envelope withdraws very quickly at the beginning of that phase allowing to the preservation of pristine D in a very thin external layer. ^{3}He is then produced in low- and intermediate-mass stars during the main sequence through the pp-chains and subsequently dredged-up when the stars move towards the RGB. On the 1.5 $M_\odot$ track one sees the effect of rotation-induced mixing that already brings fresh ^{3}He towards the stellar surface while the star is on the main

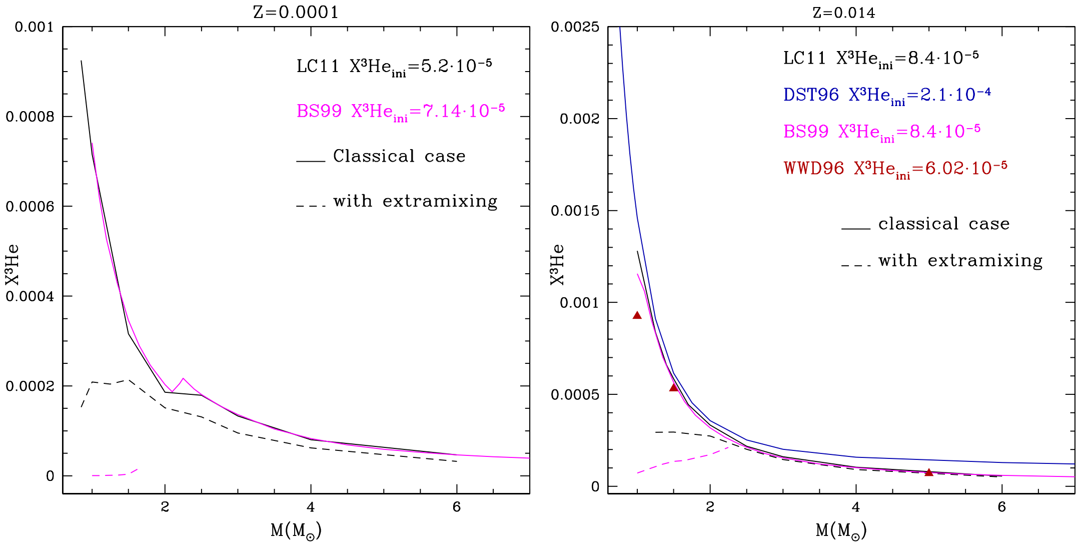

Fig. 2. Mass fraction of ^{3}He at the stellar surface at the end of the second dredge-up as a function of initial stellar mass in standard models (solid lines and triangles) and in models including various prescriptions for mixing in the radiative regions (dashed lines), at two metallicities ($Z = 0.0001$ and $Z = 0.014$; left and right panels, respectively). The predictions are from Dearborn et al. (1996, DST96, blue line), Boothroyd & Sackmann (1999, BS99, at the RGB tip, magenta lines), Weiss et al. (1996, WWD96, red triangles), and Lagarde et al. (2011, LC11, black lines). The initial abundances of ^{3}He adopted at the zero age main sequence by the different authors are given on the top right corner of each panel.

sequence (on the contrary, in the standard case the surface abundance of ^{3}He remains constant on the main sequence and starts changing only at the very base of the RGB due to the first dredge-up). However, as discussed in Paper II rotation-induced mixing is found to lower the total ^{3}He production compared to the standard case over the whole mass and metallicity range scrutinized, and to decrease the upper mass limit at which stars destroy this element (see Fig. 5 in Paper II). Additionally, for low-mass stars ($M \leq 2$–$2.2\ M_\odot$) thermohaline mixing occurring during the RGB phase beyond the bump and on the TP-AGB leads to the destruction of part of the freshly produced ^{3}He while accounting for the observed surface abundance anomalies of other chemicals (i.e., lithium and nitrogen, as well as carbon isotopic ratio; see also Charbonnel & Zahn 2007b); the associated decrease of surface ^{3}He is clearly seen for the 1.5 $M_\odot$ model in Fig. 1 (right panel). Therefore, although low-mass stars remain net ^{3}He producers, their contribution to the Galactic evolution of this element is much lower than in the standard case. It was also shown in Paper II that thermohaline mixing leads to ^{3}He depletion during the TP-AGB phase for stars with masses up to ~4 $M_\odot$ (see the 3 $M_\odot$ track in the figure). In more massive intermediate-mass stars, ^{3}He is further destroyed through hot-bottom burning on the TP-AGB. Finally, this figure shows that the lower the mass of the star, the higher the surface abundance of ^{3}He at the end of the TP-AGB. The global impact of rotation-induced mixing and thermohaline instability on the net ^{3}He yields from low- and intermediate-mass stars of various metallicities is summarized in Fig. 9 and in Tables 1 to 4 of Paper II (see also Fig. 2 discussed below).

2.2.2. Comparison with other stellar models

In Fig. 2 we show the mass fraction of ^{3}He at the end of the second dredge-up as a function of the initial stellar mass at two metallicities ($Z = 0.0001$ and 0.014; left and right panels, respectively) from our models (black lines; see Paper II). A comparison is made with model predictions from the literature (coloured lines and filled triangles).

Our standard predictions (full lines) are in very good agreement with those from Dearborn et al. (1996), Boothroyd & Sackmann (1999), and Weiss et al. (1996). For the reasons given in Sect. 2.2.1 they are higher than in the case including rotation-induced mixing and thermohaline instability (dashed black lines). Let us note that thermohaline mixing on the TP-AGB leads to further decrease of the ^{3}He mass fraction at the stellar surface (reduction of 64, 83, and 19% in the [1.25 $M_\odot$, $Z_\odot$], [0.85 $M_\odot$, $Z = 0.0001$], and [2.0 $M_\odot$, $Z_\odot$ and $Z = 0.0001$] models, respectively; see Paper II).

In Fig. 2 we also plot the predictions at the end of the second dredge-up for the models of Boothroyd & Sackmann (1999, hereafter BS99) that include parametric mixing below the base of the convective envelope of RGB stars (the so-called "conveyor-belt" circulation and the associated "cool bottom processing", CBP; dashed magenta lines). In BS99 post-processing computations, the mixing is not related to any physical mechanism. Rather, the depth of the mixed zone is a free parameter that corresponds to the difference $\Delta \log T$ between the temperature at the base of the hydrogen-burning shell and that at the base of the assumed mixed zone. BS99 assumed that the value of $\Delta \log T$ remains constant along the RGB, and this free parameter was calibrated in order to reproduce the observed carbon isotopic ratio of clump stars in M 67. We note that the fixed $\Delta \log T$ value used by BS99 leads to shallower mixing just after the RGB bump than what we get when considering thermohaline instability as the physical mixing mechanism. As a consequence BS99 prescription leads to a slow and gradual theoretical decrease of the ^{12}C/^{13}C ratio up to the RGB tip; this behaviour disagrees with the sudden drop of this quantity that is observed after the RGB bump and that is well reproduced by our models that include thermohaline mixing (see Paper I and Charbonnel & Zahn 2007b). However, due to the higher compactness of the hydrogen-burning shell when the stars reach higher luminosities on the RGB, the fixed $\Delta\log T$ value adopted by BS99 leads to deeper mixing close to the RGB tip. The second free parameter is the stream mass flow rate, $\dot{M}_{\rm p}$. Contrary to thermohaline mixing, for which the stream mass flow rate[1] decreases along the RGB from $\sim 10^{-2.5}$ to $\sim 10^{-5}$ $M_{\odot}$ yr^{-1}, BS99 assumed that the value of $\dot{M}_{\rm p}$ stays constant along the RGB ($\dot{M}_{\rm p} = 10^{-4}$ $M_{\odot}$ yr^{-1}). This difference in the mixing efficiency at the end of the RGB explains the difference between BS99's models and ours on the final ^{3}He surface mass fraction. Another drawback of such models was also that a physical reason was missing to explain why only 7% of the low mass stars would produce ^{3}He following the standard predictions.

2.3. Helium-4

2.3.1. Standard predictions

Changes in the surface ^{4}He abundance result from the dredge-up episodes undergone by the stars along their evolution, that eventually lead to the partial engulfment of the ashes of central- and shell-H-burning by the convective envelopes. The efficiency of the successive dredge-up events depends both on stellar mass and metallicity (see e.g. Paper II), as depicted in Fig. 3 where we present our standard predictions (upper panels) for the surface abundance of ^{4}He, adjusted to its initial value, in mass fraction, after the first and the second dredge-up (solid and dashed lines, respectively) as a function of the initial stellar mass, for our two extreme metallicities ($Z_{\odot}$ and $Z = 0.0001$). For solar metallicity, the surface abundance of ^{4}He increases during the first dredge-up over the whole mass range investigated, while for the lowest metallicity ($Z = 10^{-4}$) only stars with $M \leq 2.5$ $M_{\odot}$ are affected. On the other hand, the second dredge-up leads to an increase of the ^{4}He surface abundance only for the upper part of the considered mass range (i.e., for stars with masses higher than ~ 2.5 $M_{\odot}$). Finally, the third dredge-up, which occurs in stars with mass ≥ 6.0 $M_{\odot}$ for $Z_{\odot}$ and 2.5 $M_{\odot}$ for $Z = 10^{-4}$ during the TP-AGB phase, allows to increase the ^{4}He abundance at the surface of these stars (not shown here). This increase is $\sim 1\%$ for [6.0 $M_{\odot}$, $Z_{\odot}$], and [4.0 $M_{\odot}$, $Z = 0.0001$] models[2].

2.3.2. Impact of rotation-induced mixing and thermohaline instability on model predictions

Thermohaline instability has no significant impact on the surface abundance of ^{4}He since it develops only in the upper wing of the hydrogen-burning shell (see e.g. Paper I for more details)[3]. However, rotation-induced mixing smoothes the internal abundance gradients compared to the standard case, leading freshly produced ^{4}He to diffuse outwards. This can be seen in Fig. 4 where we show the abundance profile of ^{4}He at the end of the main sequence for two stellar masses and metallicities in the standard and the rotating cases (black full and red dashed lines, respectively; the vertical bars indicate the depth reached by the convective envelope at its maximum extent during the first dredge-up). This results in stronger ^{4}He abundance variations at the end of the first dredge-up when rotation-induced mixing is accounted for, as seen in Fig. 3 (bottom panels). For the same reasons, the effect of the second dredge-up is also strengthened in the rotating models. Overall, the impact of rotation increases with decreasing metallicity (see Paper I, and references therein).

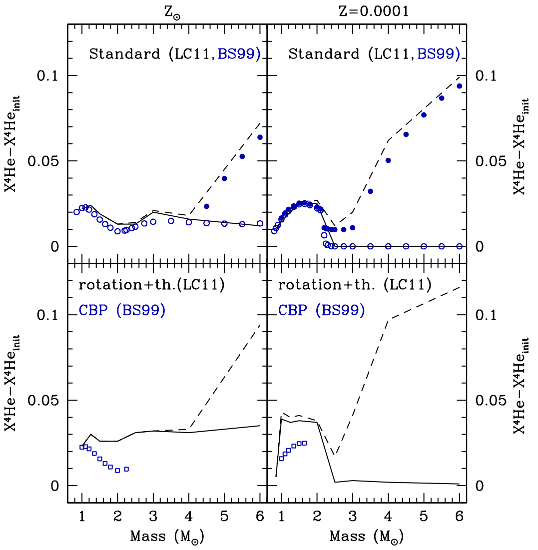

Fig. 3. Relative enrichment of the surface abundance of ^{4}He with respect to its initial value (in mass fraction) for Paper I models at the end of the first and second dredge-up (solid and dashed black lines, respectively) as a function of the initial stellar mass and for two metallicities ($Z_{\odot}$ and $Z = 0.0001$; left and right panels, respectively). *Top panels*: our standard predictions are compared with those of BS99 (blue circles; open and full at the end of the first and second dredge-up, respectively). *Bottom panels*: our models including both rotation-induced mixing and thermohaline instability are compared with the "cool-bottom processing" predictions by BS99 at the RGB tip (blue squares).

Consequently, the yields of ^{4}He are higher in the models including rotation-induced mixing than in the standard case (see Tables 3 to 6). And at the same time, the fraction of H is decreased.

Figure 5 summarizes all the effects described above on the surface abundance of ^{4}He along the evolution of standard and rotating stars with different initial masses at solar metallicity. The tracks are shown from the zero age main sequence up to the end of the TP-AGB, with the colour coding given on the right scale.

---

[1] To translate the thermohaline diffusion coefficient of our models into a stream mass flow rate as used by BS99, we compute:

$$\dot{M}_{\rm p} = \frac{4\pi r^2 \rho \mathcal{D}}{l_{\rm mix}}$$

with r and ρ the radius and the density at the base of the region where the thermohaline instability develops, $l_{\rm mix}$ the size of this mixing zone, and $\mathcal{D}$ the mean diffusion coefficient along the mixing zone.

[2] Note that we did not include additional mechanisms to force the third dredge-up in our models, as required in the literature for reproducing the carbon-star luminosity function (e.g. Frogel et al. 1990; Costa & Frogel 1996; Groenewegen 1998; Marigo et al. 1999). Hence, we do not attempt any comparison of the model predictions with available data for C and N isotopes. However this has no impact on the galactic chemical evolution of the light elements we focus on.

[3] Thermohaline mixing leads to an increase of the surface abundance of ^{4}He during the RGB by $\sim 0.1\%$ in the 1.25 $M_{\odot}$ models independently of the stellar metallicity.

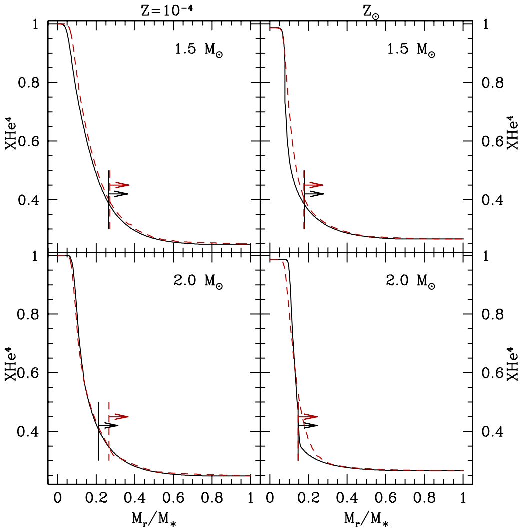

Fig. 4. Abundance profile of ^{4}He at the end of the main sequence for the 1.5 $M_\odot$ and 2.0 $M_\odot$ models at two metallicities (Z = 0.0001 and Z = 0.014, left and right panel, respectively) in the standard case (solid black line), and when including the effects of rotation (red dashed line). Models are from Paper II. The maximum depth reached by the convective envelope during the first dredge-up is shown with the vertical bars and arrows.

2.3.3. Comparison with other stellar models

In Fig. 3 we compare our predictions with those of Boothroyd & Sackmann (1999). We note a very good agreement as far as the standard models are concerned (upper panels). On the other hand, neither the thermohaline instability nor BS99 “cool bottom processing” do affect the ^{4}He surface abundances. The differences that appear in the lower panels result essentially from the effects of rotation-induced mixing.

3. Chemical evolution model

3.1. Basic assumptions

The adopted model for the chemical evolution of the Galaxy assumes that the Milky Way forms out of two main accretion episodes almost completely disentangled (Chiappini et al. 1997, 2001). During the first one, the primordial gas collapses very quickly and forms the spheroidal components, halo and bulge. During the second one, the thin-disc forms, mainly by accretion of matter of primordial chemical composition. The disc is built-up in the framework of the inside-out scenario of Galaxy formation, which ensures the formation of abundance gradients along the disc (Larson 1976; Matteucci & Francois 1989). The Galactic disc is approximated by several independent rings, 2 kpc wide, without exchange of matter between them.

3.2. Nucleosynthesis prescriptions

The nucleosynthesis prescriptions for metals (elements heavier than ^{4}He) are from Paper II for low- and intermediate-mass stars ($M \leq 6\ M_\odot$). As for massive stars and Type Ia supernovae, we adopt the same nucleosynthesis prescriptions as in Romano et al. (2010), their model 6, namely:

- yields for core-collapse supernovae are taken from Kobayashi et al. (2006), except for carbon, nitrogen and oxygen, for which the adopted yields are from Meynet & Maeder (2002); Hirschi et al. (2005); Hirschi (2007); Ekström et al. (2008);
- yields for Type Ia supernovae are from Iwamoto et al. (1999).

Table 2. Description of different models computed with yields from Lagarde et al. (2011) for stars below 6 $M_\odot$.

Models	Stellar mass	
	$M \leq 2.5\ M_\odot$	$M > 2.5\ M_\odot$
A	100% standard	100% standard
B	96% th. + rot[1] 4% standard	100% th.+ rot
C	100% th.+ rot	100% th.+ rot

Notes. (1) th. + rot means that we use yields including thermohaline instability and rotation induced mixing.

As far as the nucleosynthesis prescriptions for D, ^{3}He and ^{4}He are concerned, we use standard prescriptions from Dearborn et al. (1996) in the 6 to 100 $M_\odot$ mass range for D and ^{3}He and yields by Meynet & Maeder (2002); Hirschi et al. (2005); Hirschi (2007); Ekström et al. (2008) for ^{4}He. For low- and intermediate-mass stars ($M \leq 6\ M_\odot$) we use the yields from Papers II and III[4] and we compute three different models with the following assumptions (summarized in Table 2):

- In Model A we consider the standard yields for all stars with masses below 6.0 $M_\odot$.
- In Model B we consider the yields including thermohaline instability and rotation-induced mixing for 100% of the intermediate-mass stars ($M > 2.5\ M_\odot$) and 96% of the low-mass stars ($M \leq 2.5\ M_\odot$). The remaining 4% of the low-mass stars are assumed to release the yields as predicted by the standard theory. This allows us to account for the fact that some rare planetary nebulae (J320, NGC 3242) exhibit ^{3}He as predicted by the standard models (see e.g. Balser et al. 2007, and references therein).
- In Model C we assume the yields including thermohaline instability and rotation-induced mixing for all the low- and intermediate-mass stars. Obviously the outcome of Models B and C are expected to be very similar.

Linear interpolations in mass and metallicity are used to fill the gaps in the computed grids of yields (see Romano et al. 2010, for a discussion of the potential spurious effects introduced by this procedure).

4. Evolution of the light elements in the Milky Way

In the following sections we discuss the evolution of the light elements in the Galaxy within the framework described in Sect. 3 when taking into account the yields from our non-standard stellar models, and compare the predictions with different observations. The relevant data are presented in Table 1.

4.1. Evolution of deuterium

In this paper we assume (D/H)$_\mathrm{P}$ = 2.6 × 10^{-5} for consistency with the initial value adopted by the stellar models. However, we note that our GCE model gives a better fit to the data when

---

[4] ^{3}He stellar yields are presented in Tables 1 to 4 of Paper II. ^{4}He stellar yields are shown in Tables 3 to 6.

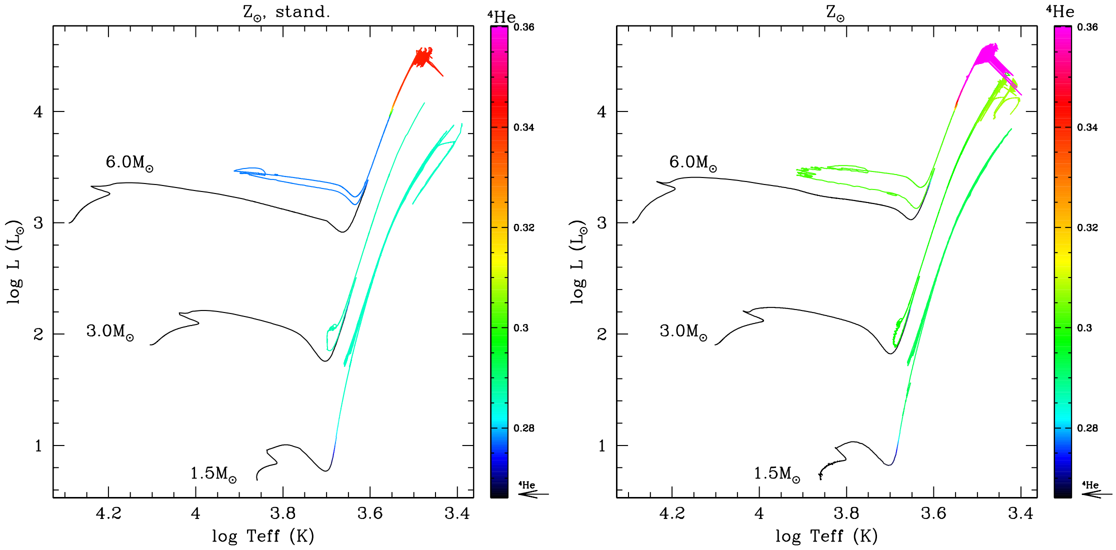

Fig. 5. Same as Fig. 1 for ^{4}He from the zero age main sequence to the end of the TP-AGB.

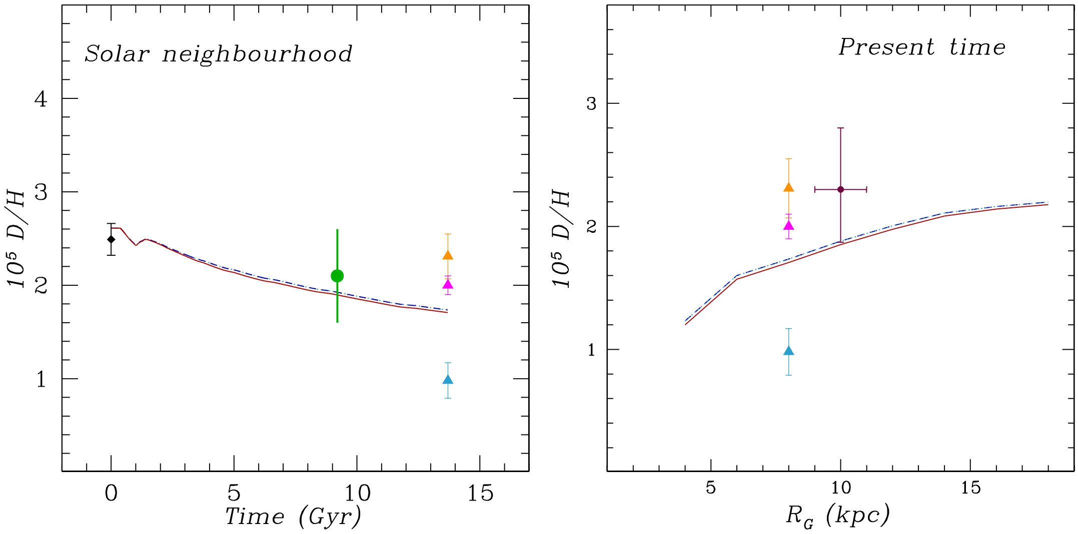

Fig. 6. Evolution of D/H in the solar neighborhood (*left panel*) and distribution of D/H along the Galactic disc at the present time (*right panel*). The predictions of Models A and B are shown (red solid and dashed blue lines, respectively). At $t = 0$ Gyr, we plot the WMAP value (filled black diamond). The PSC data by Geiss & Gloeckler (1998) are shown (filled green circle). The local interstellar medium (LISM) data are from Linsky et al. (2006), Hébrard et al. (2005) and Prodanović et al. (2010) (filled orange, light blue, and magenta triangles, respectively). The data for the outer disc ($R_G = 10$ kpc) are from Rogers et al. (2005, filled bordeaux circle).

a value of $(\mathrm{D/H})_\mathrm{P} = 2.8 \times 10^{-5}$ as observed in quasar spectra (Pettini et al. 2008) is adopted instead (see Fig. 3 of Romano 2010).

Figure 6 (left panel) shows the data for deuterium from the Big Bang (WMAP value, filled black diamond) to the present day (local interstellar medium, LISM, filled triangles). The determinations of primordial and PSC (filled green circle, Geiss & Gloeckler 1998, according with Geiss & Reeves 1972, 1981) deuterium abundances underline a small depletion from the Big Bang ($t = 0$ Gyr) to the solar-system formation ($t = 9.2$ Gyr). Analyses of Far Ultraviolet Spectroscopic Explorer (FUSE) observations have allowed measurements of D/H in the LISM for many lines of sight. These observations have revealed a large variation of the local D abundances, which complicates the interpretation in the context of standard GCE models (Linsky et al. 2006; Linsky 2010). Hébrard et al. (2005) and Linsky et al. (2006) proposed that either the lowest ($\mathrm{D/H} = 0.98 \times 10^{-5}$) or the highest ($\mathrm{D/H} = 2.31 \times 10^{-5}$) observed value is indicative of the true LISM value reflecting the process of D astration through successive stellar generations during the whole Galaxy's

Table 3. Model results for metallicity of $Z = 0.0001$.

M ($M_\odot$)		$V_{\rm ZAMS}/V_{\rm crit}$ ^{1}	$V_{\rm ZAMS}$ ^{1} (km s^{-1})	Yield ^{4}He^2 ($M_\odot$)
0.85	stand.	–	–	5.22×10^{-03}
	th. +rot.	0.45	115	1.29×10^{-02}
1.0	stand.	–	–	9.41×10^{-03}
	th. +rot.	0.45	116	2.42×10^{-02}
1.25	th. +rot.	0.45	125	2.98×10^{-02}
1.5	stand.	–	–	2.44×10^{-02}
	th. +rot.	0.45	134	3.74×10^{-02}
2.0	stand.	–	–	3.38×10^{-02}
	th. +rot.	0.45	150	4.89×10^{-02}
2.5	stand.	–	–	1.90×10^{-02}
	th. +rot.	0.45	162	2.77×10^{-02}
3.0	stand.	–	–	3.99×10^{-02}
	th. +rot.	0.45	170	8.21×10^{-02}
4.0	stand.	–	–	1.67×10^{-02}
	th. +rot.	0.45	152	2.75×10^{-02}
6.0	stand.	–	–	4.09×10^{-02}
	th. +rot.	0.45	175	4.79×10^{-02}

Notes. Each row contains entries for different assumptions: standard (without thermohaline or rotation-induced mixing); thermohaline mixing only; thermohaline and rotation-induced mixing. $^{(1)}$ The initial rotation on the ZAMS. $^{(2)}$ Yields of ^{4}He.

Table 4. Same as Table 3 for $Z = 0.002$.

M ($M_\odot$)		$V_{\rm ZAMS}/V_{\rm crit}$	$V_{\rm ZAMS}$ (km s^{-1})	Yield ^{4}He ($M_\odot$)
0.85	stand.	–	–	7.47×10^{-03}
	th. +rot.	0.45	114	1.61×10^{-02}
1.0	stand.	–	–	1.18×10^{-02}
	th. +rot.	0.45	112	2.68×10^{-02}
1.25	th. +rot.	0.45	115	2.90×10^{-02}
1.5	stand.	–	–	3.13×10^{-02}
	th. +rot.	0.45	123	4.20×10^{-02}
2.0	stand.	–	–	2.13×10^{-02}
	th. +rot.	0.45	137	4.71×10^{-02}
2.5	stand.	–	–	2.15×10^{-02}
	th. +rot.	0.45	146	5.84×10^{-02}
3.0	stand.	–	–	9.84×10^{-03}
	th. +rot.	0.45	153	5.76×10^{-02}
4.0	stand.	–	–	1.28×10^{-01}
	th. +rot.	0.45	163	2.28×10^{-01}
6.0	stand.	–	–	3.92×10^{-01}
	th. +rot.	0.45	170	4.30×10^{-01}

Table 5. Same as Table 3 for $Z = 0.004$.

M ($M_\odot$)		$V_{\rm ZAMS}/V_{\rm crit}$	$V_{\rm ZAMS}$ (km s^{-1})	Yield ^{4}He ($M_\odot$)
1.0	stand.	–	–	1.24×10^{-02}
	th. +rot.	0.45	112	$2 \times 10 \times 10^{-02}$
1.25	th. +rot.	0.45	111	2.84×10^{-02}
1.5	stand.	–	–	1.95×10^{-02}
	th. +rot.	0.45	119	2.83×10^{-02}
2.0	stand.	–	–	1.90×10^{-02}
	th. +rot.	0.45	123	3.33×10^{-02}
2.5	stand.	–	–	2.94×10^{-02}
	th. +rot.	0.45	141	5.62×10^{-02}
3.0	stand.	–	–	2.03×10^{-02}
	th. +rot.	0.45	147	6.75×10^{-02}
4.0	stand.	–	–	7.83×10^{-02}
	th. +rot.	0.45	147	1.93×10^{-01}
6.0	stand.	–	–	3.49×10^{-01}
	th. +rot.	0.45	167	4.14×10^{-01}

Table 6. Same as Table 3 for $Z = 0.014$.

M ($M_\odot$)		$V_{\rm ZAMS}/V_{\rm crit}$	$V_{\rm ZAMS}$ (km s^{-1})	Yield ^{4}He ($M_\odot$)
1.0	stand.	–	–	1.29×10^{-02}
1.25	th. +rot.	0.45	110	2.27×10^{-02}
1.5	stand.	–	–	2.79×10^{-02}
	th. +rot.	0.45	110	2.45×10^{-02}
2.0	stand.	–	–	1.65×10^{-02}
	th. +rot.	0.45	110	3.36×10^{-02}
2.5	stand.	–	–	2.35×10^{-02}
	th. +rot.	0.45	130	5.36×10^{-02}
3.0	stand.	–	–	4.08×10^{-02}
	th. +rot.	0.45	136	8.09×10^{-02}
4.0	stand.	–	–	4.80×10^{-02}
	th. +rot.	0.45	144	8.98×10^{-02}
6.0	stand.	–	–	3.07×10^{-01}
	th. +rot.	0.45	156	3.84×10^{-01}

evolution. Hébrard et al. (2005) suggest a value of the true local deuterium abundance lower than the one measured in the local bubble. On the other hand, Linsky et al. (2006) give a lower bound to the true local deuterium abundance very close to the primordial abundance, pointing to a deuterium astration factor smaller than predicted by standard GCE models. More recently, Prodanović et al. (2010) have applied a statistical Bayesian method to determine the true local D abundance. They propose a value very close to the D abundance at the time of the formation of the Sun (see Table 1). GCE models that fulfil all the major observational constraints available for the solar neighbourhood and for the Milky Way disc can explain the LISM D abundance suggested by Prodanović et al. (2010) as a result of D astration during Galactic evolution; lower and higher values can only be explained as due to small-scale, transient phenomena, such as D depletion on to dust grains and localized infall of gas of primordial chemical composition (Romano et al. 2006; Steigman et al. 2007; Romano 2010, and references therein).

Our predictions for the evolution of deuterium with time in the solar neighborhood and for the present deuterium abundance profile along the Milky Way disc are shown in Fig. 6 (left and right panels, respectively). The very modest shift between the predictions of Models A and B is due to the slight difference in the H yields when stellar rotation is accounted for compared to the standard case. Since pristine deuterium burns entirely in stars independently of their mass and metallicity, the predicted trends depend only on the total astration assumed in the GCE model. The present predictions fit well the PSC deuterium data and favour the local abundance of deuterium suggested by Prodanović et al. (2010).

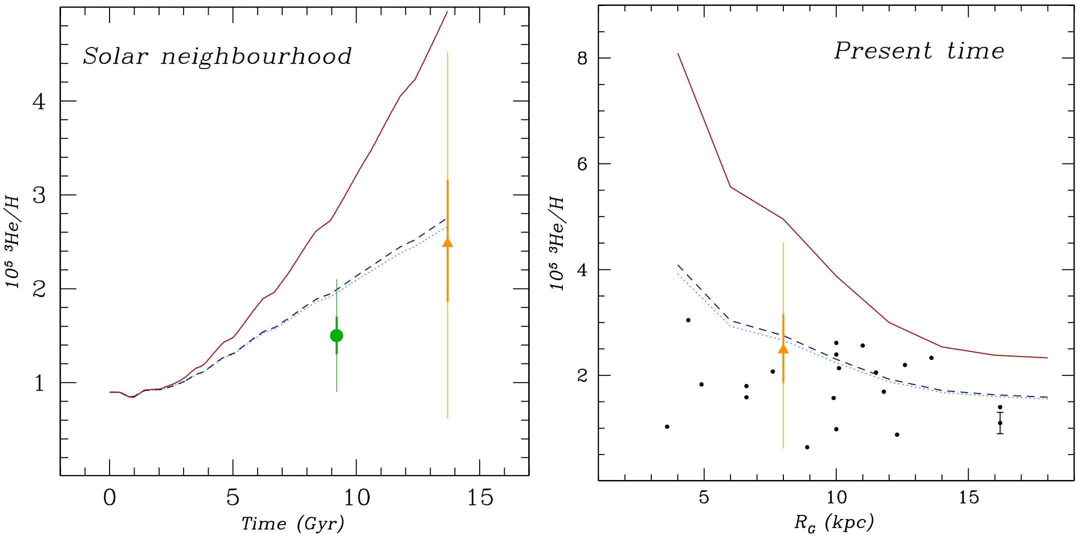

Fig. 7. *Left panel*: evolution of ^{3}He/H with time in the solar neighborhood. Data for the PSC (green filled circle) and local interstellar medium (LISM, orange filled triangle) are from Geiss & Gloeckler (1998) and Gloeckler & Geiss (1996), respectively. 1-σ and 3-σ error bars are shown with thick and thin lines, respectively. *Right panel*: radial distribution of ^{3}He/H at the present time. The dots are HII regions data from Bania et al. (2002) (error bars are shown only for S209; see text for discussion). The triangle at R_G = 8 kpc represents LISM data from Gloeckler & Geiss (1996). The predictions from Models A, B and C are shown in both panels by the red full, blue dashed and cyan dotted lines respectively.

4.2. Evolution of ^{3}He

Figure 7 (left panel) shows the evolution of ^{3}He/H in the solar neighborhood as predicted by Models A, B, and C (see Sect. 3.2). As already discussed in the literature (see Sect. 1), standard stellar models strongly overestimate the production of ^{3}He by low-mass stars.

According to standard predictions, ^{3}He is produced on the main sequence during the core hydrogen burning and it is not destroyed during later phases. Consequently, when adopting standard predictions ^{3}He is overproduced in the course of Galactic evolution (Model A, red solid line). In low-mass stellar models including thermohaline mixing, ^{3}He is destroyed from the bump luminosity on the RGB during shell hydrogen burning and during the early AGB. When low-mass stars are assumed to experience this extra-mixing, GCE models do not overproduce ^{3}He (Fig. 7, Model C, cyan dotted line). Model B (dashed blue line) shows the effect of inhibiting the thermohaline mixing in 4% of low-mass stars (see Sect. 3.2), that thus follow the standard prescriptions. As can be seen in Fig. 7, negligible differences are found between Model B and Model C predictions. The PSC and local ^{3}He abundances (Geiss & Gloeckler 1998; Gloeckler & Geiss 1996) are reproduced by the models (at 3- and 1-sigma level, respectively).

The present-day ^{3}He abundance distribution along the Galactic disk is shown in Fig. 7 (right panel). Model A, adopting standard ^{3}He yields for low-mass stars, predicts too much ^{3}He at all Galactocentric distances. In the inner regions, where the star formation was stronger, the contribution of low- and intermediate-mass stars to the ^{3}He enrichment of the ISM is more important. As a consequence, Model A predicts a large negative gradient of ^{3}He/H. Although the contribution of low-mass stars in the inner regions is significantly reduced in Model B, it still predicts a negative gradient. In Fig. 7, we compare the predictions of Models A and B with observations of ^{3}He in HII regions from Bania et al. (2002) and with the local ^{3}He abundance from Gloeckler & Geiss (1996). Contrary to what is predicted by classical theory, the observations in HII regions show a gradient close to zero. Bania et al. (2002) derived meaningful error estimates only for one source [S209: ^{3}He/H = $(1.1 \pm 0.2) \times 10^{-5}$) and pointed our the riskiness of basing one's conclusion on only one object. In order to better constrain both stellar and galactic evolution studies, it would be very useful if future work could provide a sound estimate of the errors associated to ^{3}He determinations across the Galactic disk. Nevertheless, we can conclude that thermohaline and rotating mixing are required to fit currently available measurements of ^{3}He in Galactic HII regions. In addition, the ^{3}He gradient is $\mathrm{d}\log(^3\mathrm{He/H})/\mathrm{d}R_G \sim -0.04$ and -0.028 dex/kpc for Models A and B, respectively, consistent with that predicted by Chiappini et al. (2002), $-0.04 < \mathrm{d}\log(^3\mathrm{He/H})/\mathrm{d}R_G < -0.03$ dex/kpc.

Tosi (2000) showed that GCE models including the CBP (Boothroyd & Sackmann 1999) also fit the relevant Galactic ^{3}He data, provided the primordial abundance of D is sufficiently low (see also Chiappini et al. 2002; Romano et al. 2003). However, CBP destructs ^{3}He too quickly and is not a physical mechanism (see Sect. 2.2). Therefore, it does not provide a reliable physical explanation of the ^{3}He observations in HII regions.

4.3. Evolution of ^{4}He

Figure 8 shows the temporal (left panel) and the spatial (right panel) evolution of the helium isotopic ratio (^{3}He/^{4}He) in the solar neighborhood and along the Galactic disk at the present time, respectively. Only the predictions of Models A and B are shown in the right panel. The PSC and LISM data are from Geiss & Gloeckler (1998) and Gloeckler & Geiss (1996), respectively. The standard theory predicts a significant evolution of the helium isotopic ratio in the Galaxy, and a strong gradient across the Galactic disc. When the thermohaline mixing – which destroys

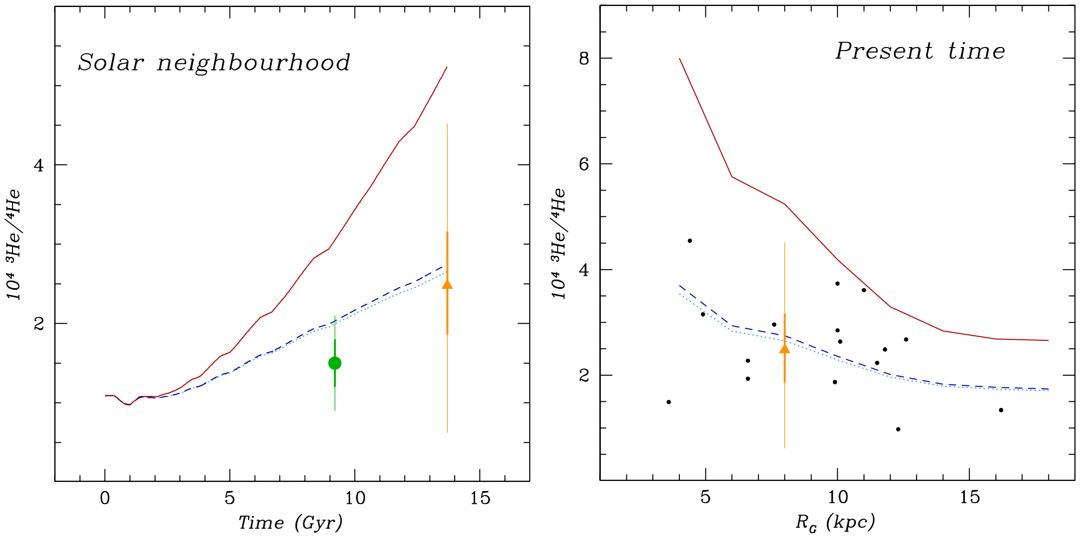

Fig. 8. Temporal (*left panel*) and spatial (*right panel*) variation of helium isotopic ratio in the solar neighborhood and along the galactic disk at the present time, respectively. Models are the same as in Fig. 7. Data are from Geiss & Gloeckler (1998) for the PSC (green filled circle), Bania et al. (2002) for Galactic HII regions (black dots), and Gloeckler & Geiss (1996) for the LISM (orange filled trangle). 1-σ and 3-σ errors are also shown as thick and thin lines, respectively.

^{3}He in the stellar interior – and the rotation-induced mixing – which increases ^{4}He at the stellar surface (see Sect. 3.3) – are taken into account, lower helium isotopic ratios are obtained (cf. the dashed versus solid lines in Fig. 8). Consequently, the gradient of the helium isotopic ratio across the Galactic disc decreases and the observations in HII regions can be reproduced.

Figure 9 presents the predictions for Y versus [Fe/H] in the solar neighborhood. The model predictions are compared with the initial abundance of ^{4}He in the Sun derived by Serenelli (2010) from full standard solar models computed for different sets of solar abundances. When the solar abundances from Grevesse & Sauval (1998) and a metal to hydrogen ratio in the solar photosphere of $(Z/X)_{\rm ph} = 0.0229$ are adopted, a value of $Y_i = 0.2721$ is obtained, which results in good agreement with the predictions of chemical evolution models including rotation-induced mixing and thermohaline mixing (green Sun symbol and dashed and dotted lines in Fig. 9, respectively). On the other hand, choosing the solar abundances from Asplund et al. (2009) and $(Z/X)_{\rm ph} = 0.0178$ result in $Y_i = 0.2653$, which is better fitted by models including standard stellar nucleosynthesis (orange Sun symbol and solid line in Fig. 9). Since the actual solar chemical composition is matter of debate, we can not discriminate between our models basing on the results for Y.

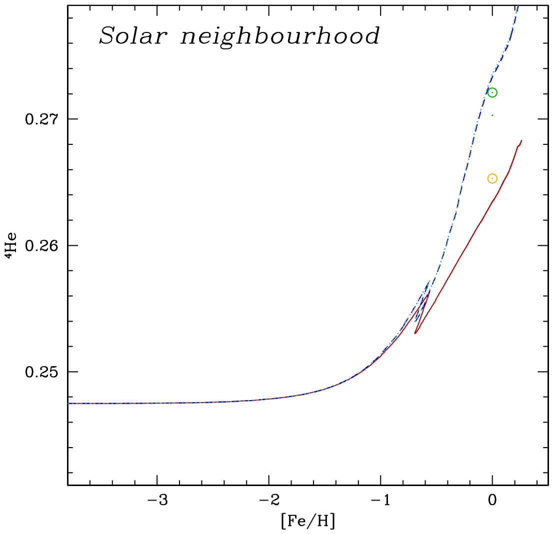

Fig. 9. Y versus [Fe/H] in the solar neighborhood predicted by models including yields computed with standard prescriptions (Model A; solid line) and with thermohaline mixing and rotation-induced mixing (Models B and C; dashed and dotted lines, respectively). Model predictions are compared with the protosolar values given by Serenelli (2010).

5. Conclusions

In this article, we have described the results for the Galactic evolution of the primordial elements D, ^{3}He and ^{4}He in the light of new stellar models including the effects of thermohaline instability and rotation-induced mixing on the stellar structure, evolution and nucleosynthesis. The new stellar models are presented and discussed at length in Charbonnel & Lagarde (2010) and Lagarde et al. (2011). We model the time-behavior of D, ^{3}He and ^{4}He in the solar neighbourhood, as well as in the inner and outer disc. The predictions of our models including thermohaline instability and rotation-induced mixing are compared to the predictions of models adopting standard nucleosynthesis prescriptions and to the most recent relevant observations.

We have seen that the CBP proposed before by Boothroyd & Sackmann (1999) is not a physical mechanism, and yields deduced do not take into account phases beyond the RGB. As discussed in the literature (Charbonnel & Zahn 2007b; Charbonnel & Lagarde 2010; Lagarde et al. 2011), thermohaline mixing can induces significant depletion of ^{3}He in low- and intermediate-mass stars. Although these stars remain net producers of ^{3}He, their contribution to the Galactic evolution of this element is highly reduced compared to classical theory. Indeed, our GCE models including thermohaline mixing reproduce the observations of ^{3}He in the PSC, LISM and HII regions, while ^{3}He is overproduced on a Galactic scale with standard models. Thermohaline mixing is the only physical mechanism known so far able to solve the so-called "^{3}He problem" plaguing in the literature since many years. Importantly, its inhibition by a fossil magnetic field in red giant stars that are descendants of Ap stars does reconcile the measurements of ^{3}He/H in Galactic HII regions with high values of ^{3}He in a couple of planetary nebulae.

On the other hand, rotation has an impact on the stellar yields of H and ^{4}He. Whether GCE models including rotation fit better the Galactic ^{4}He data than standard models can not be said, because of the uncertainties on the actual solar chemical composition. However, they are consistent with the relatively high value of $(D/H)_{\rm LISM}$ proposed by Prodanović et al. (2010).

We conclude that GCE models including both thermohaline mixing and rotation-induced mixing reproduce satisfactorily well all the available data on D, ^{3}He and, possibly, ^{4}He abundances in the Milky Way, within the errors. However, the additional data on HII regions and better refining of their interpolation would be crucial to assess how good our fit actually is.

Acknowledgements. We dedicate this paper to Robert T. Rood: the scientist to whom the stellar evolution and ^{3}He communities owe so much, and the friend whom we will miss for ever. We thank T. Bania, D. Balser, and H. Reeves for fruitful discussions. We are thankful to our referee, Dr Achim Weiss, for his interesting and constructive remarks on our article. C.C., D.R., and M.T. gratefully acknowledge the enlightening and fascinating conversations with Johannes Geiss and his hospitality at the International Space Science Institute (ISSI) in Bern (CH). We acknowledge financial support from the Swiss National Science Foundation (FNS) and the french Programme National de Physique Stellaire (PNPS) of CNRS/INSU.

References

Asplund, M., Grevesse, N., Sauval, A. J., & Scott, P. 2009, ARA&A, 47, 481
Balser, D. S., Bania, T. M., Rood, R. T., & Wilson, T. L. 1999, ApJ, 510, 759
Balser, D. S., Goss, W. M., Bania, T. M., & Rood, R. T. 2006, ApJ, 640, 360
Balser, D. S., Rood, R. T., & Bania, T. M. 2007, Science, 317, 1171
Balser, D., Rood, T. R., & Bania, T. M. 2010, in IAU Symp. 268, ed. C. Charbonnel, M. Tosi, F. Primas, & C. Chiappini, 101
Bania, T. M., Rood, R. T., & Balser, D. S. 2002, Nature, 415, 54
Bania, T. M., Rood, R. T., & Balser, D. S. 2010, in IAU Symp. 268, ed. C. Charbonnel, M. Tosi, F. Primas, & C. Chiappini, 81
Bennett, C. L., Halpern, M., Hinshaw, G., et al. 2003, ApJS, 148, 1
Boothroyd, A. I., & Sackmann, I.-J. 1999, ApJ, 510, 232
Burles, S., & Tytler, D. 1998, ApJ, 507, 732
Charbonnel, C. 1995, ApJ, 453, L41
Charbonnel, C., & Do Nascimento Jr., J. D. 1998, A&A, 336, 915
Charbonnel, C., & Lagarde, N. 2010, A&A, 522, A10
Charbonnel, C., & Zahn, J. 2007a, A&A, 476, L29
Charbonnel, C., & Zahn, J.-P. 2007b, A&A, 467, L15
Chiappini, C., Matteucci, F., & Gratton, R. 1997, ApJ, 477, 765
Chiappini, C., Matteucci, F., & Romano, D. 2001, ApJ, 554, 1044
Chiappini, C., Renda, A., & Matteucci, F. 2002, A&A, 395, 789
Coc, A., Vangioni-Flam, E., Descouvemont, P., Adahchour, A., & Angulo, C. 2004, ApJ, 600, 544
Costa, E., & Frogel, J. A. 1996, AJ, 112, 2607
Cyburt, R. H., Fields, B. D., & Olive, K. A. 2008, J. Cosmology Astropart. Phys., 11, 12
Dearborn, D. S. P., Steigman, G., & Tosi, M. 1996, ApJ, 465, 887
Denissenkov, P. A. 2010, ApJ, 723, 563
Denissenkov, P. A., & Merryfield, W. J. 2011, ApJ, 727, L8
Edmunds, M. G. 1994, MNRAS, 270, L37
Eggleton, P. P., Dearborn, D. S. P., & Lattanzio, J. C. 2006, Science, 314, 1580
Eggleton, P. P., Dearborn, D. S. P., & Lattanzio, J. C. 2008, ApJ, 677, 581
Ekström, S., Meynet, G., Chiappini, C., Hirschi, R., & Maeder, A. 2008, A&A, 489, 685
Epstein, R. I., Lattimer, J. M., & Schramm, D. N. 1976, Nature, 263, 198
Frogel, J. A., Mould, J., & Blanco, V. M. 1990, ApJ, 352, 96
Galli, D., Palla, F., Ferrini, F., & Penco, U. 1995, ApJ, 443, 536
Galli, D., Stanghellini, L., Tosi, M., & Palla, F. 1997, ApJ, 477, 218
Geiss, J., & Gloeckler, G. 1998, Space Sci. Rev., 84, 239
Geiss, J., & Reeves, H. 1972, A&A, 18, 126
Geiss, J., & Reeves, H. 1981, A&A, 93, 189
Gloeckler, G., & Geiss, J. 1996, Nature, 381, 210
Grevesse, N., & Sauval, A. J. 1998, Space Sci. Rev., 85, 161
Groenewegen, M. A. T. 1998, Ap&SS, 255, 379
Hébrard, G., Lemoine, M., Vidal-Madjar, A., et al. 2002, ApJS, 140, 103
Hébrard, G., Tripp, T. M., Chayer, P., et al. 2005, ApJ, 635, 1136
Hirschi, R. 2007, A&A, 461, 571
Hirschi, R., Meynet, G., & Maeder, A. 2005, A&A, 433, 1013
Hogan, C. J. 1995, ApJ, 441, L17
Iben, Jr., I. 1967, ApJ, 147, 624
Iwamoto, K., Brachwitz, F., Nomoto, K., et al. 1999, ApJS, 125, 439
Jenkins, E. B., Tripp, T. M., Woźniak, P. R., Sofia, U. J., & Sonneborn, G. 1999, ApJ, 520, 182
Kobayashi, C., Umeda, H., Nomoto, K., Tominaga, N., & Ohkubo, T. 2006, ApJ, 653, 1145
Krishnamurti, R. 2003, J. Fluid Mech., 483, 287
Lagarde, N., Charbonnel, C., Decressin, T., & Hagelberg, J. 2011, A&A, 536, A28
Lagarde, N., Decressin, T., Charbonnel, C., et al. 2012, A&A, in press, DOI:10.1051/0004-6361/201118331
Larson, R. B. 1976, MNRAS, 176, 31
Linsky, J. L. 2010, in IAU Symp. 268, ed. C. Charbonnel, M. Tosi, F. Primas, & C. Chiappini, 53
Linsky, J. L., Draine, B. T., Moos, H. W., et al. 2006, ApJ, 647, 1106
Maeder, A., & Zahn, J.-P. 1998, A&A, 334, 1000
Marigo, P., Girardi, L., & Bressan, A. 1999, A&A, 344, 123
Matteucci, F., & Francois, P. 1989, MNRAS, 239, 885
Meynet, G., & Maeder, A. 2002, A&A, 390, 561
Oliveira, C. M., & Hébrard, G. 2006, ApJ, 653, 345
Palla, F., Bachiller, R., Stanghellini, L., Tosi, M., & Galli, D. 2000, A&A, 355, 69
Peebles, P. J. E. 1966, ApJ, 146, 542
Peimbert, M., Peimbert, A., Carigi, L., & Luridiana, V. 2010, in IAU Symp. 268, ed. C. Charbonnel, M. Tosi, F. Primas, & C. Chiappini, 91
Pettini, M., Zych, B. J., Murphy, M. T., Lewis, A., & Steidel, C. C. 2008, MNRAS, 391, 1499
Prantzos, N. 1996, A&A, 310, 106
Prodanović, T., & Fields, B. D. 2003, ApJ, 597, 48
Prodanović, T., Steigman, G., & Fields, B. D. 2010, MNRAS, 406, 1108
Reeves, H., Audouze, J., Fowler, W. A., & Schramm, D. N. 1973, ApJ, 179, 909
Rogers, A. E. E., Dudevoir, K. A., Carter, J. C., et al. 2005, ApJ, 630, L41
Romano, D. 2010, in IAU Symp. 268, ed. C. Charbonnel, M. Tosi, F. Primas, & C. Chiappini, 431
Romano, D., Tosi, M., Matteucci, F., & Chiappini, C. 2003, MNRAS, 346, 295
Romano, D., Tosi, M., Chiappini, C., & Matteucci, F. 2006, MNRAS, 369, 295
Romano, D., Karakas, A. I., Tosi, M., & Matteucci, F. 2010, A&A, 522, A32
Rood, R. T., Steigman, G., & Tinsley, B. M. 1976, ApJ, 207, L57
Rood, R. T., Bania, T. M., & Wilson, T. L. 1984, ApJ, 280, 629
Rood, R. T., Bania, T. M., & Wilson, T. L. 1992, Nature, 355, 618
Rosenblum, E., Garaud, P., Traxler, A., & Stellmach, S. 2011, ApJ, 731, 66
Serenelli, A. M. 2010, Ap&SS, 328, 13
Songaila, A., Cowie, L. L., Hogan, C. J., & Rugers, M. 1994, Nature, 368, 599
Sonneborn, G., Tripp, T. M., Ferlet, R., et al. 2000, ApJ, 545, 277
Spergel, D. N., Verde, L., Peiris, H. V., et al. 2003, ApJS, 148, 175
Steigman, G., & Tosi, M. 1992, ApJ, 401, 150
Steigman, G., Romano, D., & Tosi, M. 2007, MNRAS, 378, 576
Tosi, M. 2000, in The Light Elements and their Evolution, ed. L. da Silva, R. de Medeiros, & M. Spite, IAU Symp., 198, 525
Tosi, M., Steigman, G., Matteucci, F., & Chiappini, C. 1998, ApJ, 498, 226
Traxler, A., Garaud, P., & Stellmach, S. 2011, ApJ, 728, L29
Truran, J. W., & Cameron, A. G. W. 1971, Ap&SS, 14, 179
Ulrich, R. K. 1972, ApJ, 172, 165
Vidal-Madjar, A., Lemoine, M., Ferlet, R., et al. 1998, A&A, 338, 694
Wagoner, R. V., Fowler, W. A., & Hoyle, F. 1967, ApJ, 148, 3
Weiss, A., Wagenhuber, J., & Denissenkov, P. A. 1996, A&A, 313, 581
Zahn, J.-P. 1992, A&A, 265, 115

Chapter 7

Conclusions and perspectives

7.1 Results

Numerous spectroscopic observations have provided compelling evidences for a non-canonical process that modifies the surface abundances of low- and intermediate-mass stars beyond the predictions of standard stellar theory.

In this thesis, we computed, for the first time, a grid of stellar models with various masses and metallicities following standard prescriptions and including thermohaline instability and rotation-induced mixing all along the evolution. We studied the impacts of thermohaline instability and rotation-induced mixing on stellar structure and surface abundance of low- and intermediate-mass stars, by means of models computed with the code STAREVOL from the pre-main sequence to the TP-AGB phase. By comparison of our models with chemical abundance determinations in open clusters and in field stars, we underlined the following conclusions :

- Thermohaline instability occurs when low- and intermediate-mass stars reach the so-called bump in the luminosity function on the Red Giant Branch (RGB). At this phase, the double diffusive instability is induced by ^{3}He(^{3}He,2p)^{4}He reaction that creates an inversion of mean molecular weight. We showed that its efficiency increases with the decrease of the initial stellar mass.

- During this phase thermohaline mixing induces the changes of surface abundances of ^{3}He, ^{7}Li, C and N for stars brighter than the bump luminosity. Our model predictions are compared to observational data for lithium, ^{12}C/^{13}C, [N/C], [Na/Fe], ^{16}O/^{17}O, and ^{16}O/^{18}O in Galactic open clusters and in field stars with well-defined evolutionary status, as well as in planetary nebulae. Thermohaline mixing simultaneously reproduce the observed behaviour of ^{12}C/^{13}C, [N/C], and lithium in low-mass stars that are more luminous than the RGB bump.

- Moreover, the ^{3}He is strongly depleted by thermohaline mixing on the RGB, although low-mass stars remain net ^{3}He producers. As a result, the contribution of low-mass stars to the Galactic evolution of the ^{3}He is strongly reduced compared to the standard framework.

- For intermediate-mass stars, thermohaline mixing leads to Li production with modest ^{3}He depletion during the thermal pulses phase. However, Li yields remain negative and these stars are not expected to contribute to Galactic lithium enrichment.

- Rotation-induced mixing modifies the internal chemical structure of main sequence stars so that in the mass range ∼1.5 and 2.2 $M_\odot$ the thermohaline instability occurs earlier on the red giant branch than in the non-rotating models.
- The dispersion of chemicals surface abundances in evolved stars is very well explained when accounting for a dispersion in the initial values of the stellar rotational velocity as observed in young open clusters.

We concluded that thermohaline mixing is the dominating chemical transport process in low-mass red giant stars ($M \lesssim 2.0\ M_\odot$), which governs their photospheric composition, while rotation-induced mixing with different initial velocities, explain surface abundances in more massive stars ($M>2.0\ M_\odot$). These results were presented in Smiljanic et al. (2010), Charbonnel & Lagarde (2010a), Lagarde et al. (2011), and Lagarde et al. (2012a). In the future, new observations of the oxygen isotopic ratios in open clusters, determined by R. Smiljanic, could be compared with our models and allow us to better understand evolution of these isotopes, and the influence of transport processes on the evolution of oxygen isotopic ratio.

During this thesis, we have included in the galactic chemical evolution code (Matteucci & Francois 1989; Chiappini et al. 1997; Matteucci 2001; Chiappini et al. 2001), new stellar yields of ^{3}He as well as ^{4}He and D taking into account effects of thermohaline instability and rotation-induced mixing. We have compared these new prescriptions with their primordial values and abundances derived from observations of different galactic regions. The inclusion of thermohaline instability in stellar models provides a solution to the long standing "^{3}He problem" on Galactic scale. In addition, stellar models including rotation and thermohaline instability reproduce very well observations of D and ^{4}He in our Galaxy. These results were discussed in Lagarde et al. (2012b).

Asteroseismic observations with *CoRoT* and *Kepler* pave the way for various statistical studies of seismic properties of stellar populations. In this context, we have evaluated the impact of thermohaline mixing and rotation-induced mixing using our new stellar evolution models, on global asteroseismic quantities (Lagarde et al. 2012a). We showed a net signature of rotation-induced mixing on the global asteroseismic parameters discussed in chapter 5. Thermohaline instability cannot be characterized by these asteroseismic parameters, although it can be identified by its effects on spectroscopic studies. Our of grid stellar models is enables to study effects of stellar mass, metallicity and transport processes (rotation and thermohaline instability) in the asteroseismic quantities related to stellar structure ($\Delta\Pi$; acoustic radii). This allows us to distinguish, along the asymptotic giant branch, stars which undergo a thermal pulse, or are in the interpulse. Moreover, many observations of red giant stars are available with *CoRoT* and *Kepler* missions, and could be compared with these new models. Effects of different physical processes as overshoot, differential rotation, and atomic diffusion could also be tested with these new large samples from spatial asteroseismic missions.

7.2 Future perspectives

During the last decade, the modelisation and study of physical processes which induce modifications of stellar structure, nucleosynthesis, and evolution have become more and more performing with the development of hydrodynamic simulations (in 1D, 2D or 3D).

Since several years, magneto-hydrodynamic simulations treated : the transport of internal angular momentum (e.g. Denissenkov 2010); the fossil and dynamo magnetic fields to understand their role in convective envelope and in radiative zones (e.g. Duez & Mathis 2009; Duez et al. 2010; Duez & Mathis 2010); the transport of angular momentum by the internal gravity waves (e.g. Mathis 2009) and their interaction with magnetic fields in stellar interior (e.g. Rogers & MacGregor 2010, 2011); and finally thermohaline instability (e.g. Denissenkov 2010; Denissenkov & Merryfield 2011; Rosenblum et al. 2011; Traxler et al. 2011a, see chapter 4), and a possible magneto-thermohaline mixing (Denissenkov et al. 2009).

Although our models including thermohaline mixing are quite successful in reproducing the abundance data for evolved stars over a wide range in both mass and metallicity, the aspect ratio value of salt fingers, which determines the efficiency of the mixing, remains uncertain. Recently, some hydrodynamic simulations tried to model thermohaline instability under different conditions, which remains still far from stellar regime. To better constrain this parameter and its effects on the efficiency of thermohaline mixing, hydrodynamic simulations close to stellar conditions will be useful. In this aim, I plan to continue simulations of thermohaline mixing in 3D with the hydrodynamic code, *BALAÏTOUS* (IRAP, Toulouse). Moreover, the effects of rotation process and atomic diffusion on the value of this aspect ratio are essential to better understand physical processes inside low- and intermediate-mass stars. That's why, I plan to study effects of these physical processes on the efficiency of thermohaline instability.

On the other hand, *CoRoT* and *Kepler* missions and spectropolarimetry with *NARVAL* and *ESPADON*, provide an insight on magnetic activity for very large sample of red giants stars. This constitutes an unique opportunity to study magnetic field of subgiant and giant stars which will improve our understanding of the dynamo mechanisms and how they evolve in stars. Our grid of stellar models will be useful for understanding the interplay of magnetic field and stellar evolution. Indeed various parameters as turn-over times computed at different places in the convective envelope as well as Rossby number from our models will be compared with observations from asteroseismic data and spectropolarimeters *NARVAL* or *ESPADON* (Charbonnel et al. 2012, in prep. ; Aurière et al. 2012, in prep.).

Furthermore, *CoRoT* and *Kepler* missions have detected solar-like oscillations in thousands of red giant stars (De Ridder et al. 2009; Bedding et al. 2010) which will add valuable and independent constraints on current stellar models. These observations sampling in different regions of the Galaxy, promises to improve our understanding on the Milky Way's constituents. To complete, and compare statistical analysis of red giant stars based on asteroseismic properties (Miglio et al. 2009), we will use our stellar grid to develop stellar population synthesis. In addition, to exploit all potential of asteroseismic data from *CoRoT* and *Kepler* missions, it would be crucial to combine them with spectroscopic constraints, which should be available in the future with the large spectroscopic survey such as *SDSS-APOGEE*, and *GAIA* mission (∼ 1 billion stars essentially in the Milky Way). Meanwhile, we will compare our model predictions with some stars for which spectroscopic studies have been done, to better constrain theoretical stellar evolution and effects of transport processes.

Conference's proceedings

Proceeding SF2A (2009) - Oral contribution -

Thermohaline instability and rotation-induced mixing in low and intermediate-mass stars.

N.Lagarde and C. Charbonnel

Abstract:

The classical theory of stellar evolution predicts that low-mass stars are strong producers of ^{3}He, in contradiction with abundance observations of this element in Galactic HII regions and in the protosolar nebula. However in 2007, Charbonnel & Zahn showed that thermohaline mixing drastically reduces the yields of ^{3}He producted by low-mass red giants. Simultaneously this mechanism changes the surface of carbon isotopic ratio as well as the abundances of lithium, carbon and nitrogen. In this paper, we present and discuss models computed with the code STAREVOL that include the transport of chemical species in the radiative regions due to thermohaline instability and to rotational mixing. We compare our theorical predictions with recent observations.

SF2A 2009
M. Heydari-Malayeri, C. Reylé and R. Samadi (eds)

THERMOHALINE INSTABILITY AND ROTATION-INDUCED MIXING IN LOW AND INTERMEDIATE-MASS STARS.

Lagarde, N.[1] and Charbonnel, C.[1, 2]

Abstract. The classical theory of stellar evolution predicts that low-mass stars are strong producers of ^3He, in contradiction with abundance observations of this element in Galactic HII regions and in the protosolar nebula. However in 2007, Charbonnel & Zahn showed that thermohaline mixing drastically reduces the yields of ^3He producted by low-mass red giants. Simultaneously this mechanism changes the surface of carbon isotopic ratio as well as the abundances of lithium, carbon and nitrogen. In this paper, we present and discuss models computed with the code STAREVOL that include the transport of chemical species in the radiative regions due to thermohaline instability and to rotational mixing. We compare our theorical predictions with recent observations.

1 Introduction

During the first dredge-up, the standard theory predicts that the convective envelope deepens in mass, and engulfes hydrogen-processed material. This induces a decrease of the surface $^{12}C/^{13}C$, Li, or ^{12}C abundances, while ^{14}N and ^3He abundances increase. After the first dredge-up, the convective envelope retracts and the hydrogen burning shell moves outward (in mass). The standard theory predicts ^3He is present and does not change further. The observations in open clusters and in galactic field are agree with standard theory at the first dredge-up. However, a second change in the surface abundance is observed latter, on RGB, more precisely at the BUMP luminosity. Eggleton et al. (2006) have proposed that the inversion of molecular weight created by $^3He(^3He, 2p)^4He$ reaction may be at the origin of mixing on the red giant branch, for low-mass stars. Charbonnel & Zahn showed that this inversion sets of the so-called thermohaline mixing. Which is a double diffusive instability. In following sections, we present some results obtained with the code STAREVOL, including thermohaline mixing and rotation-induced mixing, at solar metallicity.

2 Models and results

We discuss in this section the effects of rotation-induced mixing and thermohaline mixing in a low-mass star ($M = 1.25M_\odot$) and in a intermediate-mass star ($M = 2.0M_\odot$).

2.1 *Low-mass star,* $M = 1.25M_\odot$

In figure 1, we present a Kippenhahn diagram for a $M = 1.25M_\odot$ star, with thermohaline mixing and rotation with $V_{ZAMS} = 110km/s$. We note that the thermohaline zone (blue) extends between the convective envelope (CE, in black hatching) and the external wing of the hydrogen burning shell (HBS) at the luminosity near the BUMP luminosity. In figure 1, we present also the evolution of surface carbon isotopic ratio for the same star. Due to thermohaline mixing, $^{12}C/^{13}C$ decreases at the BUMP luminosity contrary to the standard theory. We note that the value after the first dredge-up is lower with rotation. Due to rotation-induced mixing on the main sequence (see Palacios, A. et al. 2003, 2006). We note that the luminosity where thermohaline mixing connect the CE and HBS is the same in both cases. In addition, the value of $^{12}C/^{13}C$ at the end of RGB is also very similar in all cases.

---

[1] Geneva Observatory, 51 chemin des Maillettes, 1290 Sauverny, Switzerland
[2] LATT, CNRS UMR 5572, Universite de Toulouse, 14 avenue Edouard Belin, F-31400 Toulouse Cedex 04, France

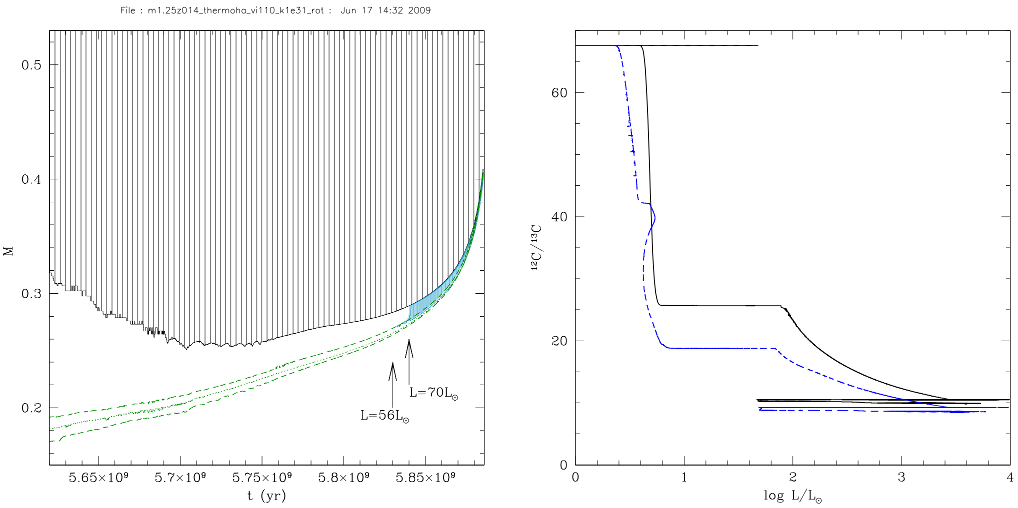

Fig. 1. Left : Kippenhahn diagram for a $M = 1.25M\odot$, $Z_\odot$ star, computed with thermohaline mixing and rotation-induced mixing ($V_{ZAMS} = 110km/s$). Thermohaline zone (between HBS and CE) is shown as blue hatching zone. **Right**: The evolution of surface carbon isotopic ratio as a function of luminosity. The solid line represents the standard model, and the dashed line represents the model computed with rotation $V_{ZAMS} = 110km/s$. Thermohaline mixing is present in both cases.

2.2 Intermediate-mass star : $M = 2.0M_\odot$

In figure 2, we present a Kippenhahn diagram for $M = 2.0M_\odot$, $Z_\odot$ star, with and without rotation. When the rotation is not included (left pannel), the thermohaline zone connects the CE with HBS at the end of RGB. So, it has not an effect on the surface abundance, as shown in figure 3. However, when the rotation is included (right pannel, fig 2), the thermohaline zone connects CE and HBS earlier in luminosity than in the model without rotation. In fact, the rotation changes the stellar structure on the main sequence, and favors the thermohaline mixing, in intermediate-mass stars. So, the evolution of $^{12}C/^{13}C$ for this star changes on the RGB. As can be seen in fig 3, the value of $^{12}C/^{13}C$ after the first drege-up decreases when the initial rotation velocity increases. Otherwise, the value of $^{12}C/^{13}C$ at the end of RGB decreases when the initial velocity increases. So the rotation favors the effect of thermohaline mixing on the RGB in the intermediate-mass star.

2.3 Comparison with observations

We compare our predictions with the observations in M67 by Gilroy & Brown (1991), and in 10 open clusters by Smiljanic et al. (2008) (see Smiljanic et al. 2009 (in press) for other comparisons). The standard theory does not explain the lower value of $^{12}C/^{13}C$ observed in the open clusters. For low-mass stars ($M \leq 1.7M_\odot$), thermohaline mixing explains well the observed carbon isotopic ratio, and the value of $^{12}C/^{13}C$ with rotation is approximatly the same, as discussed above. However, for interdiate-mass stars ($M \geq 1.7M_\odot$), rotation-induced mixing favors the effect of thermoaline mixing on the RGB.

3 Conclusion

An inversion of molecular weight created by the $^{3}He(^{3}He,2p)^{4}He$ reaction is at the origin of thermohaline mixing in RGB stars brighter than the BUMP luminosity. This mixing connects the convective envelope with the external wing of hydrogen burning shell and induces surface abundance modifications. The introduction of this process in models of rotating stars allows us to explain the carbon isotopic ratio anomalies in giant stars

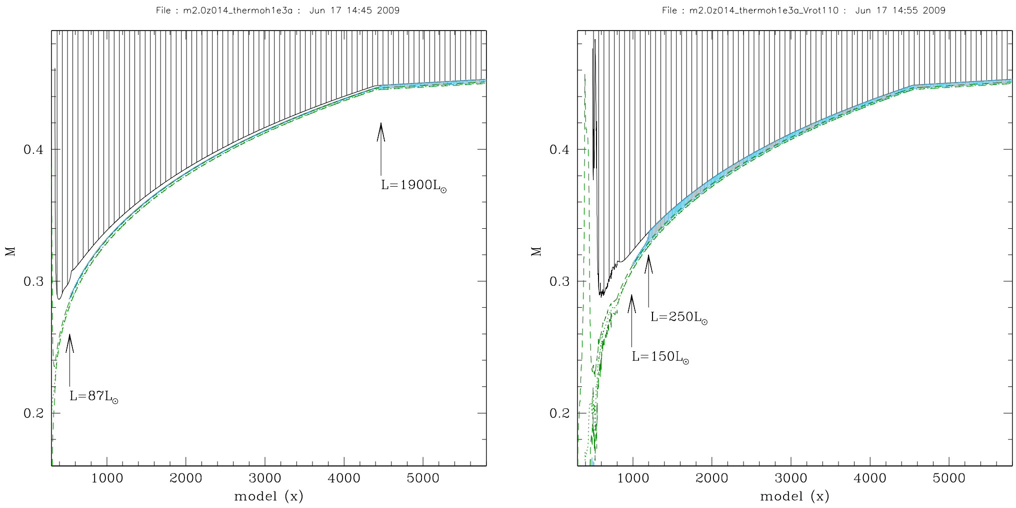

Fig. 2. Kippenhahn diagram for $M = 2.0M_\odot$, $Z_\odot$ star computed without rotation (**Left**), and with rotation (**Right**). In both cases, thermohaline mixing is included, and the region where it developsis represented with blue hatching between CE (black hachting) and HBS (green zone). The luminosity of BUMP and the luminosity when the thermohaline mixing connects CE and HBS are indicated.

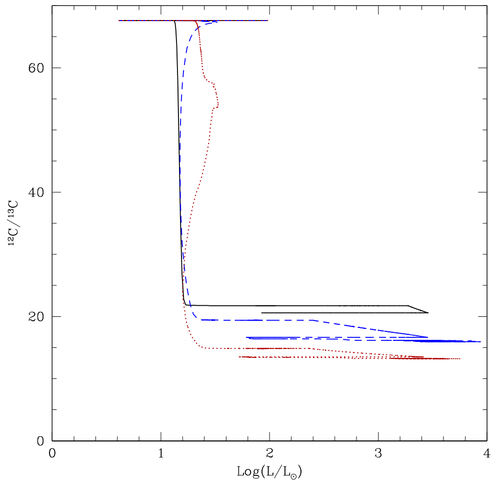

Fig. 3. The evolution of surface carbon isotopic ratio as a function of luminosity for a $M = 2.0M_\odot$, $Z_\odot$ star. Thermohaline mixing is present in all cases. The solid line is for the model without rotation, the dashed line for the model with $V_{ZAMS} = 110km/s$, and the dotted line for the model with $V_{ZAMS} = 180km/s$.

of open clusters over a broad range of turn-off.

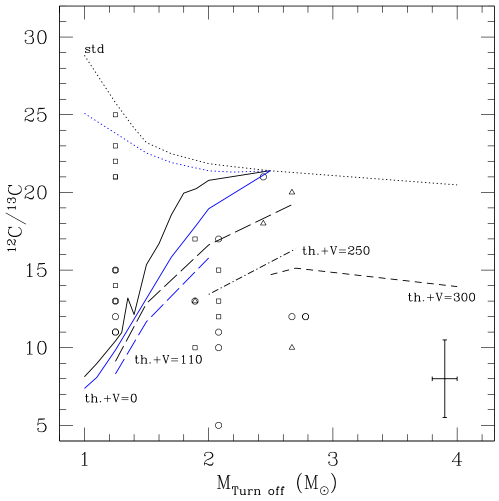

Fig. 4. Theorical predictions compared with observations of the carbon isotopic ratio, $^{12}C/^{13}C$, as a function of the open cluster turn-off mass. Our theorical values of $^{12}C/^{13}C$ as a function of the initial stellar mass : the standard models is shown as dotted lines ; the thermohaline models is shown as a solid line ; and the rotational models are shown as a long dashed lines for $V_{ZAMS} = 110km/s$; as a dot-dashed lines for $V_{ZAMS} = 250km/s$; and as a short dashed lines for $V_{ZAMS} = 300km/s$. For all theoricals models, values at the tip-RGB are shown in black and values at the tip-AGB are shown in blue. Observations of $^{12}C/^{13}C$ in open cluster by Smiljanic et al. (2008) and Gilroy & Brown (1991) : possible RGB stars are shown as open square, clump giants as open triangle, and possible early-AGB as open circle. For observations a typical error bar is shown.

References

Charbonnel, C., & Zahn, J.P., 2007, A&A, 467, L15-L18.
Eggleton, P.P., Dearborn, D.S.P., Lattanzio, J.C., 2006, Science, 314, 1580
Gilroy, K.K., Brown, J.A., 1991, ApJ, 371, 578-583
Palacios, A., Talon, S., Charbonnel, C., Forestini, M., 2003, A&A, 399, 603-616
Palacios, A., Charbonnel, C., Talon, S., Siess, L., 2006, A&A, 453, 261-278
Smiljanic, R., Gauderon, R., North, P., Barbuy, B., Charbonnel, C., Mowlavi, N, 2008, A&A, 502, 267-282
Smiljanic, R., Pasquini, L., Charbonnel C., Lagarde,N. , 2009, in press

Proceeding IAU Symposium 265 (2009)

"Chemical Abundances in the Universe : Connecting First Stars to Planets"

Thermohaline instability in stars and the long-standing ^{3}He problem.

C. Charbonnel and N.Lagarde

Abstract:

Thermohaline mixing has been recently identified as the dominating process that governs the photospheric composition of low-mass bright giant stars (Charbonnel & Zahn 2007). Here we present the predictions of stellar models computed with the code STAREVOL taking into account this mechanism together with rotational mixing and atomic diffusion. We compare our theorical predictions with recent observations and discuss how the corresponding yields for ^{3}He are compatible with the observed behaviour of this light element in our Galaxy.

Chemical Abundances in the Universe:
Connecting First Stars to Planets
Proceedings IAU Symposium No. 265, 2009
K. Cunha, M. Spite & B. Barbuy, eds.

doi:10.1017/S1743921310000554

Thermohaline mixing in stars and the long-standing ^{3}He problem

Corinne Charbonnel[1,2] **and Nadège Lagarde**[1]

[1]Geneva Observatory, University of Geneva
Chemin des Maillettes 51, 1290 Versoix, Switzerland
email: `Corinne.Charbonnel@unige.ch, Nadege.Lagarde@unige.ch`
[2]CNRS UMR 5572, Toulouse University
14, av.E.Belin, 31400 Toulouse, France

Abstract. Thermohaline mixing has been recently identified as the dominating process that governs the photospheric composition of low-mass bright giant stars (Charbonnel & Zahn 2007). Here we present the predictions of stellar models computed with the code STAREVOL taking into account this mechanism together with rotational mixing and atomic diffusion. We compare our theorical predictions with recent observations and discuss how the corresponding yields for ^{3}He are compatible with the observed behaviour of this light element in our Galaxy.

Keywords. hydrodynamics, instabilities, stars: abundances, evolution, rotation, Galaxy: abundances

1. Introduction

The classical theory of stellar evolution predicts a very simple Galactic destiny to ^{3}He, dominated by a large production of this isotope by low-mass stars (Iben 1967; Rood 1972; Rood *et al.* 1976; Dearborn *et al.* 1996; Weiss *et al.* 1996). As a consequence, one expects a large increase of ^{3}He with time in the Galaxy with respect to its primordial abundance (e.g., Tosi 1996). However, the ^{3}He content of Galactic HII regions (Balser *et al.* 1994, 1999a; Bania *et al.* 1997, 2002) is similar to that of the Sun and the solar system (Geiss & Reeves 1972; Geiss 1993, Mahaffy *et al.* 1998), and very close to the BBN value (Coc *et al.* 2004; Cyburt 2004; Serpico *et al.* 2004). This is the so-called "^{3}He problem" that could be resolved if only ∼10 % or less of the low-mass stars were releasing ^{3}He as predicted by classical stellar theory (Tosi 1998, 2000; Palla *et al.* 2000; Romano *et al.* 2003).

In 2007, Charbonnel & Zahn showed that thermohaline mixing drastically reduces the ^{3}He production in low-mass, low-metallicity stars. Simultaneously, this mechanism changes the surface carbon isotopic ratio as well as the abundances of lithium, carbon and nitrogen.

2. Stellar models including thermohaline convection, rotation-induced mixing, and atomic diffusion

Here we present the predictions of new stellar models computed with the code STAREVOL for solar metallicity. Computations include the transport of chemical species in the radiative regions due to thermohaline instability, rotational mixing, and atomic diffusion. For thermohaline transport we use the diffusion coefficient advocated by Charbonnel & Zahn (2007) that is supported by laboratory experiments (Krishnamurti 2003). The evolution of the internal angular momentum profile and the resulting transport of

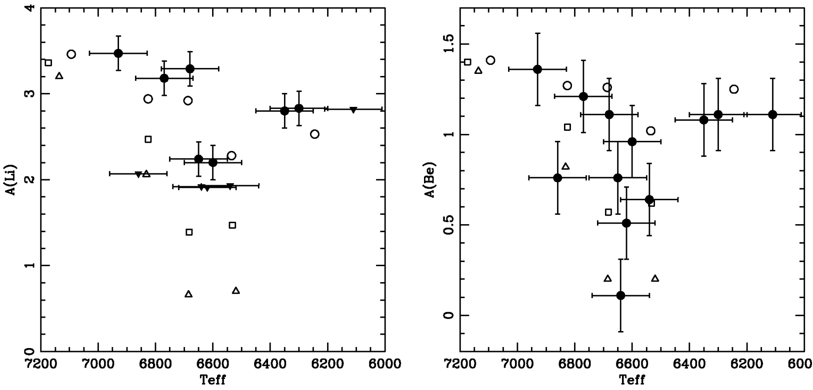

Figure 1. Li and Be abundances in IC 4651 main sequence and turnoff stars (black points and triangles for actual determinations and upper limits respectively). Open circles, squares, and triangles show model predictions for initial rotation velocities of 50, 80, and 110 km s^{-1} respectively. On the cool side of the Li and Be dip the model with Teff∼6250 K is from Talon & Charbonnel (2005) and takes into account additional transport of angular momentum by internal gravity waves. Figures from Smiljanic *et al.* (2009)

chemicals are accounted for with the complete formalism developed by Zahn(1992) and Maeder & Zahn (1998) that takes into account advection by meridional circulation and diffusion by shear turbulence (see Palacios *et al.* 2003, 2006 and Decressin *et al.* 2009 for a description of the implementation in STAREVOL). Typical initial (i.e., ZAMS) surface rotation velocities are chosen for all the models depending on the stellar mass. We assume magnetic braking on the early main sequence for the stars with Teff on the ZAMS lower than ∼ 6900 K that have relatively thick convective envelopes. The adopted braking law follows the description of Kawaler (1988). Rotational velocity further decreases when the stars evolve on the subgiant branch due to radius expansion. Atomic diffusion is included in the form of gravitational settling as well as that related to thermal gradients, using the formulation of Paquette *et al.* (1986).

3. Model predictions for the surface abundances

The model predictions for the evolution of the surface abundances of various species have been validated all along the evolutionary sequence. They reproduce for example very well the surface abundances of Li and Be in main sequence stars as shown in Fig. 1 in the case of data for the open cluster IC 4651, as well as in subgiant and giant stars (see Smiljanic *et al.* 2009 for more details).

Predictions for the evolution of the surface carbon isotopic ratio are shown in Fig. 2 for models of 1.25 and 2 $M_\odot$ stars, and compared with observations in the open cluster M67 (turnoff mass ∼1.2 $M_\odot$). We note that rotation-induced mixing on the main sequence slightly lowers the post-dredge-up $^{12}C/^{13}C$ value compared to the classical case. At the luminosity of the bump ($\log(L/L_\odot)\sim2$ for the 1.25 $M_\odot$ star), thermohaline mixing leads to further decrease of the carbon isotopic ratio, in excellent agreement with M67 data (see Charbonnel & Zahn 2007 for comparisons with low-metallicity stars). In the case of the 2 $M_\odot$ star, thermohaline mixing becomes efficient at the bump in the luminosity function only when rotation in earlier phases is accounted for.

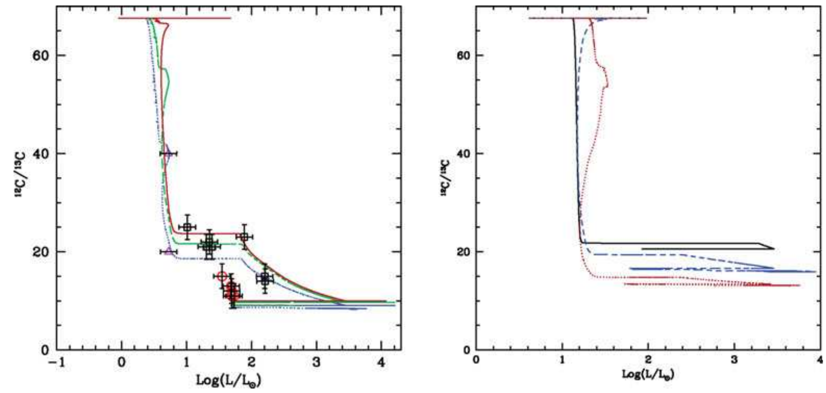

Figure 2. Evolution of the surface ^{12}C/^{13}C value as a function of stellar luminosity for the 1.25 and 2 M$_\odot$ models (left and right respectively). Different tracks correspond to different initial rotation velocities (50, 80, and 110 km.s^{-1} for the 1.25 M$_\odot$, and 0, 110, and 250 km.s^{-1} for the 2 M$_\odot$). Observations for M67 stars by Gilroy & Brown (1991) are also shown (triangle, squares, and circles for subgiant, RGB, and clump stars respectively; turnoff mass of M67 ∼1.2 M$_\odot$). Figures from Lagarde & Charbonnel (in preparation)

4. Model predictions for ^{3}He

On the main sequence, a ^{3}He peak builds up due to pp-reactions inside the low-mass stars, and is engulfed in the stellar envelope during the first dredge-up. As a consequence the surface abundance of ^{3}He strongly increases on the lower RGB as can be seen in Fig. 3 for stars of different masses. Its value reaches a maximum when the whole peak is engulfed. After the first dredge-up, the temperature at the base of the convective envelope is too low for ^{3}He to be nuclearly processed. As a result in canonical models ^{3}He stays constant at the surface until the ejection of the planetary nebula and its final value is strongly increased with respect to the initial one (this is the value before thermohaline mixing sets in at the bump).

In the present models however, thermohaline mixing sets in at the bump, and brings ^{3}He from the convective envelope down to the hydrogen-burning shell. This leads to a rapid decrease of the surface abundance of this element as can be seen in Fig. 3, and as already shown by Charbonnel & Zahn (2007) for low-metallicity stars. This confirms the early suggestion by Rood *et al.* (1984) that the variations of the carbon isotopic ratio and of ^{3}He are strongly connected (see also Charbonnel 1995 and Eggleton *et al.* 2006). It is important to note that in the models presented here ^{3}He decreases by a large factor in the ejected material with respect to the canonical evolution predictions but that low-mass stars remain net ^{3}He producers (while far much less efficient than in the canonical case).

Computations for a larger grid in stellar masses and metallicities are now being performed in order to quantify the actual contribution of low-mass stars to Galactic ^{3}He in the framework proposed here. We are confident that the corresponding ^{3}He yields will help reconciling the primordial nucleosynthesis with measurements of ^{3}He/H in Galactic HII regions (Charbonnel 2002).

Acknowledgements

We acknowledge financial support from IAU, from the French “Programme National de Physique Stellaire” of CNRS/INSU, and from the Swiss National Science Foundation.

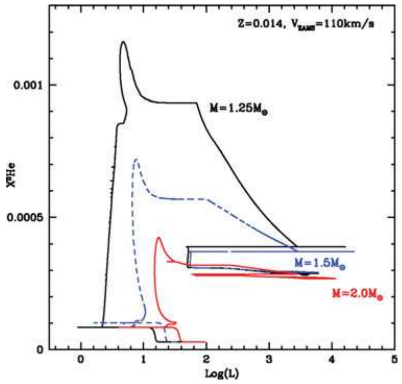

Figure 3. Evolution of the surface abundance of ^{3}He (in mass fraction) for solar metallicity stars of various initial masses. Figure from Lagarde & Charbonnel (in preparation)

References

Balser, D. A., Bania, T. M., Brockway, C. J., Rood, R. T., & Wilson, T. L., 1994, *ApJ*, 430, 667

Balser, D. A., Bania, T. M., Rood, R. T., & Wilson, T. L., 1999a, *ApJ*, 510, 759

Bania, T. M., Balser, D. A., Rood, R. T., Wilson, T. L., & Wilson, T. J., 1997, *ApJS*, 113, 353

Bania, T. M., Rood, R. T., & Balser, D. A., 2002, *Nature*, 415, 54

Charbonnel, C. 1995, *ApJ*, 453, L41

Charbonnel, C. 2002, *Nature*, 415, 27

Charbonnel, C. & Zahn, J. P. 2007, *A&A Letters*, 467, L15

Coc, A., Vangioni-Flam, E., Descouvemont, *et al.* 2004, *ApJ*, 600, 544

Cyburt, R. H. 2004, *Phys.Rev.D*, 70, 023 505

Dearborn, D. S. P., Steigman, G., & Tosi, M., 1996, *ApJ*, 465, 887

Decressin, T., Mathis, S., Palacios, A., *et al.* 2009, *A&A*, 495, 271

Eggleton, P. P., Dearborn, D. S. P., & Lattanzio, J. C 2006 *Science*, 314, 5805, 1580

Geiss, J. & Reeves, H., 1972, *A&A* 18, 126

Geiss, J., 1993, in Origin and evolution of the elements, eds. N.Prantzos *et al.*, p.89

Gilroy, K. K. & Brown, J. A. 1991, *ApJ*, 371, 578

Iben, I., 1967, *ApJ*, 143, 642

Kawaler, S. D., 1988, *ApJ*, 333, 236

Krishnamurti, R. 2003, *J. Fluid Mech.*, 483, 287

Maeder, A. & Zahn, J. P. 1998, *A&A*, 334, 1000

Mahaffy, P. R., Donahue, T. M., Atreya, S. K.,*et al.*, 1998, *Space Sci. Rev.*, 84, 251

Palacios, A., Charbonnel, C., Talon, S., & Forestini, M. 2003, *A&A*, 399, 603

Palacios, A., Charbonnel, C., Talon, S., & Siess, L. 2006, *A&A*, 453, 261

Palla, F., Bachiller, R., Stanghellini, L., Tosi, M., & Galli, D., 2000, *A&A*, 355, 69

Paquette, C., Pelletier, C., Fontaine, G., & Michaud, G., 1986, *ApJS*, 61,177

Rood, R. T., 1972, *ApJ*, 177, 681

Rood, R. T., Steigman, G., & Tinsley, B. M., 1976, *ApJ*, 207, L57

Rood, R. T., Bania, T. W., & Wilson, T. L. 1984, *ApJ*, 280, 629

Romano, D., Tosi, M., Matteucci, F., & Chiappini, C. 2003, *MNRAS*, 346, 295

Serpico, P. D., Esposito, S., Iocco, F., *et al.* 2004, *JCAP*, 12, 10S

Smiljanic, R., Pasquini, L., Charbonnel, C., & Lagarde, N. 2009, *A&A*, in press, astro-ph 0910.4399

Talon, S. & Charbonnel, C 2005, *A&A*, 440, 981

Tosi, M., 1996, *ASP Conference Series*, Vol. 98, 299

Tosi, M., 1998, *Space Science Reviews*, Vol.84, 207

Tosi, M., 2000, IAUS 198, 525

Weiss, A., Wagenhuber, J., & Denissenkov, P. A., 1996, *A&A*, 313, 581

Zahn, J. P. 1992, *A&A*, 265, 115

Proceeding IAU symposium 268 (2010) - Poster -

"Light Elements in the Universe"

Beryllium abundances along the evolutionary sequence of the open cluster IC 4651

R. Smiljanic, L. Pasquini, C. Charbonnel, and N. Lagarde

Abstract:

The simultaneous investigation of Li and Be in stars is a powerful tool in the study of the evolutionary mixing processes. Here, we present beryllium abundances in stars along the whole evolutionary sequence of the open cluster IC 4651. This cluster has a metallicity of [Fe/H] = +0.11 and an age of 1.2 or 1.7 Gyr. Abundances have been determined from highresolution, high signal-to-noise UVES spectra using spectrum synthesis and model atmospheres. Lithium abundances for the same stars were determined in a previous work. Confirming previous results, we find that the Li dip is also a Be dip. For post-main-sequence stars, the Be dilution starts earlier within the Hertzsprung gap than expected from classical predictions, as does the Li dilution. Theoretical hydrodynamical models are able to reproduce well all the observed features.

Light Elements in the Universe
Proceedings IAU Symposium No. 268, 2009
C. Charbonnel, M. Tosi, F. Primas & C. Chiappini, eds.

doi:10.1017/S174392131000445X

Beryllium abundances along the evolutionary sequence of the open cluster IC 4651

Rodolfo Smiljanic[1,2], **L. Pasquini**[2], **C. Charbonnel**[3,4], **and N. Lagarde**[3]

[1]IAG, University of São Paulo, Brazil, [2]ESO, Germany,
email: `rsmiljan@eso.org`
[3]Geneva Observatory, Switzerland, [4]LATT, CNRS, Université de Toulouse, France

Abstract. The simultaneous investigation of Li and Be in stars is a powerful tool in the study of the evolutionary mixing processes. Here, we present beryllium abundances in stars along the whole evolutionary sequence of the open cluster IC 4651. This cluster has a metallicity of [Fe/H] = +0.11 and an age of 1.2 or 1.7 Gyr. Abundances have been determined from high-resolution, high signal-to-noise UVES spectra using spectrum synthesis and model atmospheres. Lithium abundances for the same stars were determined in a previous work. Confirming previous results, we find that the Li dip is also a Be dip. For post-main-sequence stars, the Be dilution starts earlier within the Hertzsprung gap than expected from classical predictions, as does the Li dilution. Theoretical hydrodynamical models are able to reproduce well all the observed features.

Keywords. Stars: abundances, evolution, rotation – Open clusters and associations: individual: IC 4651

1. Introduction

In contradiction with standard stellar evolution models, where convection is the only mechanism driving mixing episodes, field and cluster F- and early G-type stars (including the Sun) deplete Li abundances during the main sequence (Lambert & Reddy 2004; Sestito & Randich 2005, and references therein). Different physical mechanisms have been proposed to explain these observations: atomic diffusion, mass loss, rotation-induced mixing, internal gravity waves, or combinations of these (see Charbonnel & Talon 2008 and references therein).

As Li and Be burn at different temperatures (2.5×10^6 K for Li and 3.5×10^6 K for Be), i.e. at different depths in the stellar interior, they help in constraining the transport mechanisms by performing a stellar tomography. In the study of mixing processes as a function of mass and evolutionary status cluster stars are ideal because they have well defined masses and share the same age and initial chemical composition. We derived Be abundances along the whole evolutionary sequence of the open cluster IC 4651, including solar-type, Li-dip, turn-off, subgiant, and red giant stars. With these new results, we investigate in detail the mixing processes in different stellar masses.

2. Discussion

The sample analyzed here is composed of 22 stars; 21 with atmospheric parameters and Li abundances from Pasquini *et al.* (2004) and 1 from Randich *et al.* (2002). The spectra have $40 \leqslant \mathrm{S/N} \leqslant 100$ (per resolution element) and R $\sim$ 45000.

Be abundances were determined using synthetic spectra and the same codes and line lists used in Smiljanic *et al.* (2009a). As some of the sample stars are fast rotators, we first carefully modeled the slow-rotating stars and tested the effects in the abundances

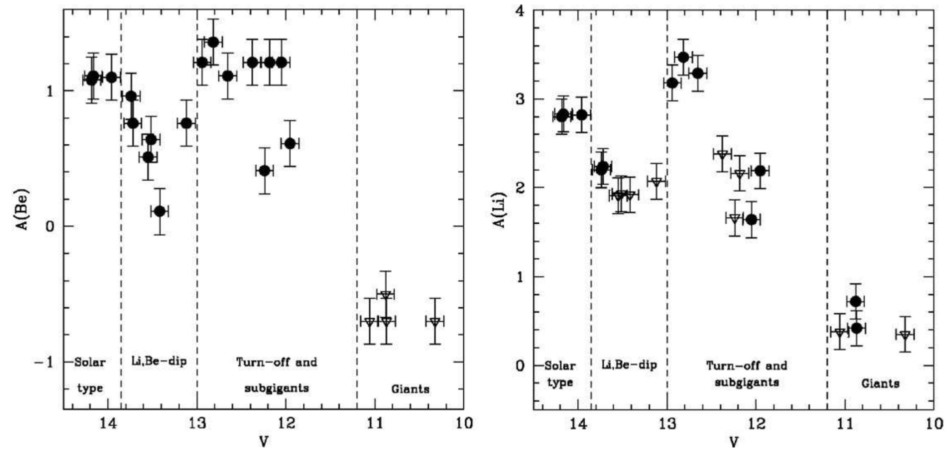

Figure 1. Abundances of Be (left panel) and Li (right panel) as a function of the V magnitude. Detections are shown as full circles and upper limits as open triangles.

of artificially broadening the spectra (see Smiljanic *et al.* 2009b for details). Beryllium was detected in all the sample stars except for the giants.

New evolutionary models for stars on the hot side of the dip, including atomic diffusion, meridional circulation, and shear turbulence, were calculated with STAREVOL V3.1 by Lagarde & Charbonnel (in preparation, see also Charbonnel & Lagarde this volume) for a range of stellar masses and initial rotation velocities. For stars on the cool side of the Li dip we use the 1.2 $M_\odot$ model computed by Talon & Charbonnel (2005) which has an initial rotation velocity of 50 km s^{-1}.

Beryllium abundances are found to follow closely the behavior of the Li abundances (Fig. 1). In a sequence of increasing mass we have first the coolest main-sequence stars that do not present a Be abundance dispersion. This is expected to be due to the impact of internal gravity waves. After that, a well-defined Be dip is seen. This confirms previous results that the Li dip is also a Be dip (Boesgaard & King 2002, Boesgaard *et al.* 2004). For post-main-sequence stars we confirm that Be dilution starts earlier than the expected classically. The Be abundances also present a significant dispersion.

The dispersion of Li and Be abundances on the blue side of the dip and in evolved stars is very well explained by the models when accounting for a dispersion in the initial values of the stellar rotational velocities. The models reproduce all the Li and Be features along the CMD of IC 4651. The success in explaining the Li and Be abundances along the whole evolutionary sequence shows that important steps have been taken towards the proper understanding of the physical mechanisms acting during the stellar evolution.

References

Boesgaard, A. M., Armengaud, E., & King, J. R. 2004, *ApJ*, 605, 864
Boesgaard, A. M. & King, J. R. 2002, *ApJ*, 565, 587
Charbonnel, C. & Talon, S. 2008, in Proceedings of IAUS 252, 163
Lambert, D. L. & Reddy, B. E. 2004, *MNRAS*, 349, 757
Pasquini, L., Randich, S., Zoccali, M. *et al.* 2004, *A&A*, 424, 951
Randich, S., Primas, F., Pasquini, L. *et al.* 2002, *A&A*, 387, 222
Sestito, P. & Randich, S. 2005, *A&A*, 442, 615
Smiljanic, R., Pasquini, L., Bonifacio, P., *et al.* 2009a, *A&A*, 499, 103
Smiljanic, R., Pasquini, L., Charbonnel, C., & Lagarde, N. 2009b, arXiv:0910.4399, *A&A*, in press
Talon, S. & Charbonnel, C. 2005, *A&A*, 440, 981

Proceeding IAU symposium 268 (2010) **- Oral contribution -**

"Light Elements in the Universe"

Thermohaline mixing in stars : solving the long-standing ^{3}He problem

C. Charbonnel and N.Lagarde

Abstract:

Thermohaline mixing has been recently identified as the dominating process that governs the photospheric composition of low-mass bright giant stars (Charbonnel & Zahn 2007a). Here we present the predictions of stellar models computed with the code STAREVOL that takes into account this mechanism together with rotational mixing and atomic diffusion. We compare our theorical predictions with recent observations and discuss how the corresponding yields for ^{3}He are compatible with the observed behaviour of this light element in our Galaxy.

Light Elements in the Universe
Proceedings IAU Symposium No. 268, 2009
C. Charbonnel, M. Tosi, F. Primas & C. Chiappini, eds.

doi:10.1017/S1743921310004606

Thermohaline mixing in stars : solving the long-standing ^{3}He problem

Corinne Charbonnel[1,2] **and Nadège Lagarde**[1]

[1]Geneva Observatory, University of Geneva
Chemin des Maillettes 51, 1290 Versoix, Switzerland
email: `Corinne.Charbonnel@unige.ch, Nadege.Lagarde@unige.ch`

[2]CNRS UMR 5572, Toulouse University
14, av.E.Belin, 31400 Toulouse, France

Abstract. Thermohaline mixing has been recently identified as the dominating process that governs the photospheric composition of low-mass bright giant stars (Charbonnel & Zahn 2007a). Here we present the predictions of stellar models computed with the code STAREVOL that takes into account this mechanism together with rotational mixing and atomic diffusion. We compare our theorical predictions with recent observations and discuss how the corresponding yields for ^{3}He are compatible with the observed behaviour of this light element in our Galaxy.

Keywords. Hydrodynamics, instabilities, Stars: abundances, evolution, rotation, Galaxy: abundances

1. The "^{3}He problem"

The classical theory of stellar evolution predicts a very simple Galactic destiny to ^{3}He, dominated by a large production of this isotope by low-mass stars (Iben 1967; Rood 1972; Rood *et al.* 1976; Dearborn *et al.* 1996; Weiss *et al.* 1996). As a consequence, one expects a large increase of ^{3}He with time in the Galaxy with respect to its primordial abundance (e.g., Tosi 1996). However, the ^{3}He content of Galactic HII regions (Balser *et al.* 1994, 1999; Bania *et al.* 1997, 2002) is very similar to that of the Sun and solar system (Geiss & Reeves 1972; Geiss 1993, Mahaffy *et al.* 1998), and very close to the BBN value (Coc *et al.* 2004; Cyburt 2004; Serpico *et al.* 2004). This is the so-called "^{3}He problem" that could be resolved if only ∼10 % or less of the low-mass stars were releasing ^{3}He as predicted by classical stellar theory (Tosi 1998, 2000; Palla *et al.* 2000; Charbonnel 2002; Romano *et al.* 2003).

Charbonnel & Zahn (2007a) showed that thermohaline mixing drastically reduces the ^{3}He production in low-mass, low-metallicity stars. Simultaneously, this mechanism changes the surface carbon isotopic ratio as well as the abundances of lithium, carbon and nitrogen.

2. Stellar models including thermohaline convection, rotation-induced mixing, and atomic diffusion

Here we present the predictions of new stellar models computed with the code STAREVOL for solar metallicity and stellar masses between 1 and 4 $M_\odot$. Computations include the transport of chemical species in the radiative regions due to thermohaline instability, rotational mixing, and atomic diffusion. For thermohaline transport we use the diffusion coefficient advocated by Charbonnel & Zahn (2007a) based on Ulrich (1972) arguments for the aspect ratio of the salt fingers as supported by laboratory experiments

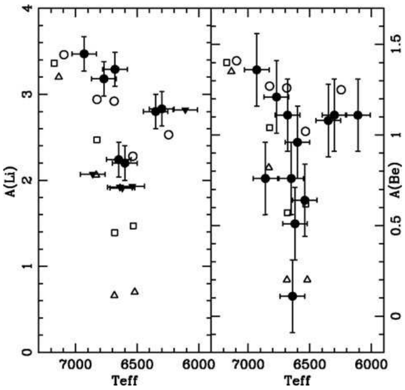

Figure 1. Li and Be abundances in IC 4651 main sequence and turnoff stars (black points and triangles for actual determinations and upper limits respectively). Open circles, squares, and triangles show model predictions for initial rotation velocities of 50, 80, and 110 km s^{-1} respectively. On the cool side of the Li and Be dip the model with Teff∼6250 K is from Talon & Charbonnel (2005) and takes into account additional transport of angular momentum by internal gravity waves. Adapted from Smiljanic *et al.* (2009b)

(Krishnamurti 2003) and on Kippenhahn *et al.* (1980) extended expression for the case of a non-perfect gas. The evolution of the internal angular momentum profile and the associated transport of chemicals are accounted for with the complete formalism developed by Zahn (1992) and Maeder & Zahn (1998) that takes into account advection by meridional circulation and diffusion by shear turbulence (see Palacios *et al.* 2003, 2006, and Decressin *et al.* 2009 for a description of the implementation in STAREVOL). Typical initial (i.e., ZAMS) surface rotation velocities are chosen for all the models depending on the stellar mass. We assume magnetic braking on the early main sequence for the stars with Teff on the ZAMS lower than ∼ 6900 K that have relatively thick convective envelopes (Talon & Charbonnel 1998). The adopted braking law follows the description of Kawaler (1988). Rotational velocity further decreases when the stars evolve on the subgiant branch due to radius expansion. Atomic diffusion is included in the form of gravitational settling as well as that related to thermal gradients, using the formulation of Paquette *et al.* (1986).

3. Model predictions for the surface abundances

The model predictions for the evolution of the surface abundances of various species have been validated all along the evolutionary sequence. They reproduce for example very nicely the surface abundances of Li and Be along the colour-magnitude diagram of the open cluster IC 4651 as shown in Fig.1 and 2. Note that thermohaline mixing is efficient only when RGB stars reach the so-called bump in the luminosity function, which is located at Teff ∼ 4200 K in the present case. For stars less evolved than the bump as those shown in both figures, the Li and Be behaviours are thus dictaded by rotation-induced mixing (see Smiljanic *et al.* 2009b for more details and Smiljanic *et al.*, this volume; see also Charbonnel & Talon 1999 and Palacios *et al.* 2003).

Predictions for the evolution of the surface carbon isotopic ratio are shown in Fig. 3 for models of 1.25 and 2 $M_\odot$ stars, and compared with observations in the open cluster M67 (turnoff mass ∼1.2 $M_\odot$). We note that rotation-induced mixing on the main sequence slightly lowers the post-dredge-up $^{12}C/^{13}C$ value compared to the classical case (i.e., no rotation, diffusion, nor thermohaline mixing). At the luminosity of the bump ($\log(L/L_\odot)\sim2$ for the 1.25 $M_\odot$ star), thermohaline mixing leads to further decrease of

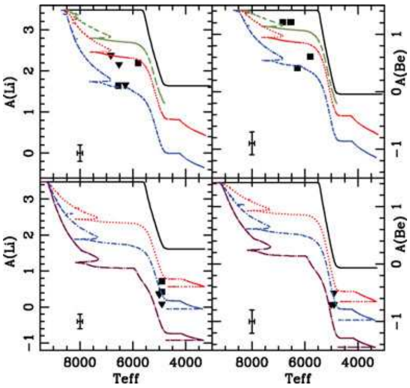

Figure 2. Li and Be abundances in IC 4651 evolved stars. Theoretical predictions for 1.8 and 2 M$_\odot$ models are compared to observations of subgiant and giant stars (upper and lower pannels resectively). Solid lines are for the classical case. Other lines correspond to different initial rotation velocities (80, 110, and 180 km s^{-1} for the 1.8 M$_\odot$ star; 110, 180, and 250 km s^{-1} for the 2.0 M$_\odot$ star). Adapted from Smiljanic *et al.* (2009b)

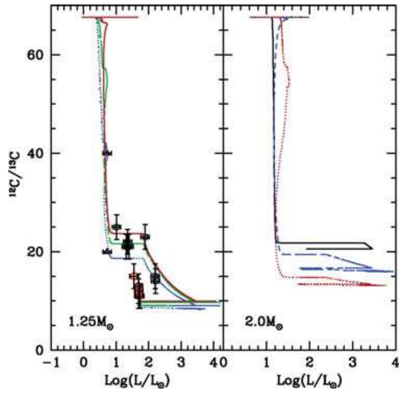

Figure 3. Evolution of the surface ^{12}C/^{13}C value as a function of stellar luminosity for models of 1.25 and 2 M$_\odot$ stars (left and right respectively). Different tracks are for different initial rotation velocities (50, 80, and 110 km.s^{-1} for the 1.25 M$_\odot$ star, and 0, 110, and 250 km.s^{-1} for the 2 M$_\odot$ star). Observations by Gilroy & Brown (1991) in evolved stars of the open cluster M67 (turnoff mass ∼1.2 M$_\odot$) are also shown (triangle, squares, and circles for subgiant, RGB, and clump stars respectively). Adapted from Lagarde & Charbonnel (in preparation)

the carbon isotopic ratio, in excellent agreement with M67 data. In the case of the 2 M$_\odot$ star, thermohaline mixing becomes efficient at the bump in the luminosity function only when rotation in earlier phases is accounted for. Importantly we note that at solar metallicity, the ^{12}C/^{13}C values reached when thermohaline mixing ceases are higher than in the case of metal-poor stars where the carbon isotopic ratios almost always reach the equilibrium value (see Fig. 3 of Charbonnel & Zahn 2007a). This metallicity-dependence is in perfect agreement with the observational behaviour (see Fig. 1 of Charbonnel & Do Nascimento 1998).

In Fig. 4 we show the predictions for the ^{12}C/^{13}C surface ratio at the tip of the RGB and of the AGB for our models over the whole considered mass range and compare them with observations in stars belonging to open clusters of various turnoff masses. We see that in models for stars with masses below $\sim$ 1.7 M$_\odot$, thermohaline mixing is the main physical process governing the photospheric composition of evolved giants, while rotation plays only a minor role on the red giant branch (see Palacios *et al.* 2006). In fact, the

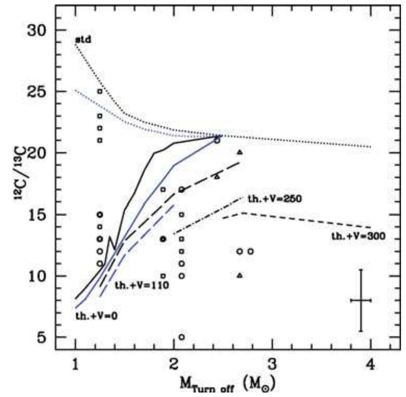

Figure 4. Theoretical predictions compared with observations of ^{12}C/^{13}C in open clusters spanning a large turnoff mass range. Data are from Smiljanic *et al.* (2009a) and Gilroy & Brown (1991). Squares, triangles and circles are for RGB, clump, and early-AGB stars respectively. Typical observational errors are indicated. Classical models (i.e., non-rotating and without thermohaline mixing) are shown as dotted lines. The solid lines are for models including thermohaline mixing only, while all the other models include rotation-induced mixing (with initial rotation velocities as indicated), thermohaline convection, and atomic diffusion. Black and blue lines correspond to model predictions at the tip of the RGB and AGB respectively. Adapted from Lagarde & Charbonnel (in preparation)

thermohaline diffusion coefficient at the RGB bump is several order of magnitudes higher than the total rotation-induced diffusion coefficient.

For more massive stars, thermohaline mixing occurs in the advanced phases when rotation-induced mixing is accounted for, but in a much less efficient manner. In this case, the final carbon isotopic ratio depends mainly on rotation-induced mixing on the main sequence that modifies the abundance profiles, and in particular the ^{13}C peak inside the stars, before the occurrence of the first dredge-up. Overal, the present models explain very well the observed abundance patterns over the considered mass range.

4. Model predictions for ^{3}He

On the main sequence, a ^{3}He peak builds up due to pp-reactions inside low-mass stars (Iben 1967), and is engulfed in the stellar envelope during the first dredge-up. As a consequence the surface abundance of ^{3}He strongly increases on the lower RGB as can be seen in Fig. 5 for various stellar masses. Its value reaches a maximum when the whole peak is engulfed. After the first dredge-up, the temperature at the base of the convective envelope is too low for ^{3}He to be nuclearly processed. As a result in canonical models this fresh ^{3}He is preserved until the ejection of the planetary nebula when it is released into the interstellar matter. This classical view is however contradicted by observations and chemical evolution models as discussed in § 1.

After the bump however, thermohaline mixing brings ^{3}He from the convective envelope down to the hydrogen-burning shell where it burns. This leads to a rapid decrease of the surface abundance (and thus of the corresponding yield) of this element as can be seen in Fig. 5, and as already shown by Charbonnel & Zahn (2007a) for low-metallicity stars. This confirms the early suggestion by Rood *et al.* (1984) that the variations of the carbon isotopic ratio and of ^{3}He are strongly connected (see also Charbonnel 1995; Charbonnel & Do Nascimento 1998; Eggleton *et al.* 2006). It is important to note that in the models presented here ^{3}He decreases by a large factor in the ejected material with respect to the canonical evolution predictions, but that low-mass stars remain net producers (while

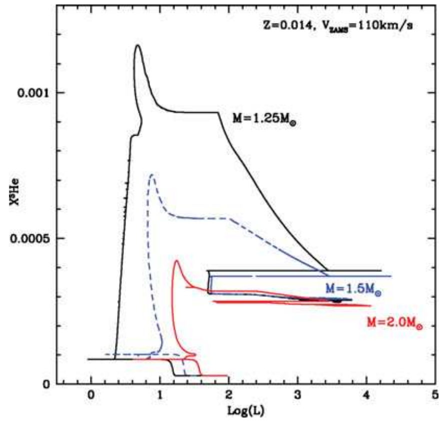

Figure 5. Evolution of the surface abundance of ^{3}He (in mass fraction) for stars of various initial masses and solar metallicity. Figure from Lagarde & Charbonnel (in preparation)

far much less efficient than in the canonical case) of ^{3}He. As already depicted by the ^{12}C/^{13}C behaviour that traces the dependance of the thermohaline mixing efficiency with metallicity, the destruction of fresh ^{3}He by this process is much more efficient in low-metallicity stars (see Fig. 4 of Charbonnel & Zahn 2007a).

Computations for a larger grid in stellar masses and metallicities are now being performed in order to quantify the actual contribution of low-mass stars to Galactic ^{3}He in the framework proposed here (Lagarde *et al.*, in preparation). We are confident that the corresponding ^{3}He yields will help reconciling the primordial nucleosynthesis with measurements of ^{3}He/H in Galactic HII regions (Charbonnel 2002).

5. The peculiar case of "thermohaline deviant stars": Ap star descendants?

However a couple of planetary nebulae, namely NGC 3242 and J320, have been found to behave "classically" (see Bania, this volume): slightly more massive than the Sun, they are currently returning fresh ^{3}He to the interstellar medium, in the amount predicted by classical stellar models (Rood *et al.* 1992; Galli *et al.* 1997; Balser *et al.* 1999, 2006).

To reconcile the ^{3}He/H measurements in Galactic HII regions with the high values of ^{3}He in NGC 3242 and J320, Charbonnel & Zahn (2007b) proposed that thermohaline mixing is inhibited by a fossil magnetic field in RGB stars that are descendants of Ap stars. They obtained a threshold for the magnetic field of 10^4-10^5 Gauss, above which it inhibits thermohaline mixing in red giant stars located at or above the L-bump. Fields of that order are expected in the descendants of Ap stars, taking into account the contraction of their core when they become red giants.

Charbonnel & Zahn (2007b) thus concluded that in a large fraction of descendants of Ap stars thermohaline mixing does not occur. As a consequence these objects should produce ^{3}He as predicted by the standard stellar theory and as observed in the planetary nebulae NGC 3242 and J320. The relative number of such stars with respect to non-magnetic objects that undergo thermohaline mixing is consistent with the statistical constraint coming from observations of the carbon isotopic ratio in red giant stars (Charbonnel & Do Nascimento 1998). It satisfies also the Galactic requirements for the evolution of the ^{3}He abundance.

Acknowledgements

We acknowledge financial support from IAU, from the French "Programme National de Physique Stellaire" of CNRS/INSU, and from the Swiss National Science Foundation.

References

Balser, D. A., Bania, T. M., Brockway, C. J., Rood, R. T., & Wilson, T. L., 1994, *ApJ*, 430, 667

Balser, D. A., Bania, T. M., Rood, R. T., & Wilson, T. L., 1999, *ApJ*, 510, 759

Balser, D. A., Goss, W. M., Bania, T. M., & Rood, R. T., 2006, *ApJ*, 640, 360

Bania, T. M., Balser, D. A., Rood, R. T., Wilson, T. L., & Wilson, T.J., 1997, *ApJS*, 113, 353

Bania, T. M., Rood, R. T., & Balser, D. A., 2002, *Nature*, 415, 54

Charbonnel, C. 1995, *ApJ*, 453, L41

Charbonnel, C. 2002, *Nature*, 415, 27

Charbonnel, C. & Do Nascimento, J. D. 1998, *A&A*, 336, 915

Charbonnel, C. & Talon, S. 1999, *A&A*, 351, 635

Charbonnel, C. & Zahn, J. P. 2007a, *A&A Letters*, 467, L15

Charbonnel, C. & Zahn, J. P. 2007b, *A&A Letters*, 476, L29

Coc, A., Vangioni-Flam, E., Descouvemont, P., Adahchour, A., & Angulo, C. 2004, *ApJ*, 600, 544

Cyburt, R. H. 2004, *Phys. Rev.D*, 70, 023 505

Dearborn, D. S. P., Steigman, G., & Tosi, M., 1996, *ApJ*, 465, 887

Decressin, T., Mathis, S., Palacios, A., *et al.* 2009, *A&A*, 495, 271

Eggleton, P. P., Dearborn, D. S. P., & Lattanzio, J. C 2006 *Science*, 314, 5805, 1580

Galli, D., Stanghellini, L., Tosi, M., & Palla, F. 1997, *ApJ*, 477, 218

Geiss, J. & Reeves, H., 1972, *A&A* 18, 126

Geiss, J., 1993, in Origin and evolution of the elements, eds. N. Prantzos *et al.*, p. 89

Gilroy, K. K. & Brown, J. A. 1991, *ApJ*, 371, 578

Iben, I., 1967, *ApJ*, 143, 642

Kawaler, S. D., 1988, *ApJ*, 333, 236

Kippenhahn, R., Ruschenplatt, G., & Thomas, H. C. 1980, *A&A*, 91, 175

Krishnamurti, R. 2003, *J. Fluid Mech.*, 483, 287

Maeder, A. & Zahn, J. P. 1998, *A&A*, 334, 1000

Palacios, A., Charbonnel, C., Talon, S., & Forestini, M. 2003, *A&A*, 399, 603

Palacios, A., Charbonnel, C., Talon, S., & Siess, L. 2006, *A&A*, 453, 261

Palla, F., Bachiller, R., Stanghellini, L., Tosi, M., Galli, D., 2000, *A&A*, 355, 69

Paquette, C., Pelletier, C., Fontaine, G., & Michaud, G., 1986, *ApJS*, 61,177

Rood, R. T., 1972, *ApJ*, 177, 681

Rood, R. T., Steigman, G., & Tinsley, B. M., 1976, *ApJ*, 207, L57

Rood, R. T., Bania, T. W., & Wilson, T. L. 1984, *ApJ*, 280, 629

Rood, R. T., Bania, T. W., & Wilson, T. L. 1992, *Nature*, 355, 618

Romano, D., Tosi, M., Matteucci, F., & Chiappini, C. 2003, *MNRAS*, 346, 295

Smiljanic, R., Gauderon, R., North, P., Barbuy, B., Charbonnel, C., & Mowlavi, N. 2009a, *A&A* 502, 267

Smiljanic, R., Pasquini, L., Charbonnel, C., & Lagarde, N. 2009b, *A&A*, in press, astro-ph 0910.4399

Talon, S. & Charbonnel, C 1998, *A&A*, 335, 959

Talon, S. & Charbonnel, C 2005, *A&A*, 440, 981

Tosi, M. 1996, *ASP Conference Series*, Vol. 98, 299

Tosi, M. 1998, *Space Science Reviews*, Vol. 84, 207

Tosi, M. 2000, IAUS 198, 525

Ulrich, R. K. 1972, *ApJ*, 172, 165

Weiss, A., Wagenhuber, J., & Denissenkov, P. A., 1996, *A&A*, 313, 581

Zahn, J. P. 1992, *A&A*, 265, 115

Proceedings IAU Symposium 268 (2010) - Poster -

"Light Elements in the Universe"

Li survey in giant stars : probing non-standard stellar physics

N.Lagarde, C. Charbonnel, G. Jasniewicz, P. North, M. Shetrone, J. Hollek, and V. V. Smith

Abstract:

Lithium has long been known to be a good tracer of non-standard mixing processes occurring in stellar interiors. Here we present the results of a large survey aimed at determining the surface Li abundance in a sample of about 800 giant (RGB and AGB) stars with accurate Hipparcos parallaxes. We compare the observed Li behaviour with that predicted by stellar models including rotation and thermohaline mixing.

Light Elements in the Universe
Proceedings IAU Symposium No. 268, 2009
C. Charbonnel, M. Tosi, F. Primas & C. Chiappini, eds.

doi:10.1017/S1743921310004564

Li survey in giant stars : probing non-standard stellar physics

N. Lagarde[1], C. Charbonnel[1,2], G. Jasniewicz[3], P. North[4], M. Shetrone[5], J. Hollek[5], and V. V. Smith[6]

[1]Geneva Observatory, University of Geneva , Switzerland
email: `Nadege.Lagarde@unige.ch`
[2]CNRS UMR 5572, Université de Toulouse, France
[3]Université de Montpellier II, CNRS/UM2 UMR 5024, France
[4]Laboratoire d'astrophysique, Ecole Polytechnique Fédérale de Lausanne, Switzerland
[5]University of Texas, McDonald Observatory, USA
[6]National Optical Astronomy Observatory, Tucson, USA

Abstract. Lithium has long been known to be a good tracer of non-standard mixing processes occurring in stellar interiors. Here we present the results of a large survey aimed at determining the surface Li abundance in a sample of about 800 giant (RGB and AGB) stars with accurate Hipparcos parallaxes. We compare the observed Li behaviour with that predicted by stellar models including rotation and thermohaline mixing.

Keywords. Hydrodynamics, instabilities, Stars: abundances, evolution, rotation

1. Introduction

Red giant stars present surface abundance anomalies that are not explained by classical stellar evolution models and that reveal the existence of extra-mixing (i.e., non convective) processes inside stellar interiors. Thermohaline mixing (Charbonnel & Zahn 2007) has been recently identified as the dominating process that governs the photospheric composition of low-mass bright giant stars, affecting in particular the surface Li abundances in red giants more luminous than the RGB bump. In order to test this assessment we present Li observations in a large sample of about 800 giant stars with Hipparcos parallaxes and compare our data for the solar-metallicity subsample with models computed with the evolutionary code STAREVOL and including thermohaline mixing and rotation-induced processes (see Charbonnel & Lagarde, this volume).

Observations were carried out with: (1) Standiford Cassegrain Echelle Spectrometer on the T2.1m at McDonald Observatory (2) Fiber-fed Extended Range Optical Spectrograph (FEROS) on the T1.52m at ESO ; (3) AURELIE spectrometer on the T1.52m at Haute-Provence Observatory.

2. Solar metallicity subsample

In Fig. 1 we compare our observations with the predictions of the solar metallicity models described in Charbonnel & Lagarde (this volume) and Lagarde & Charbonnel (in preparation) that were computed with the code STAREVOL taking into account (1) rotation-induced processes following the formalism by Zahn (92) and Maeder & Zahn (98), (2) thermohaline mixing as described by Charbonnel & Zahn (07), and (3) atomic diffusion. We also use these models to determine the mass and evolutionary status of each sample star.

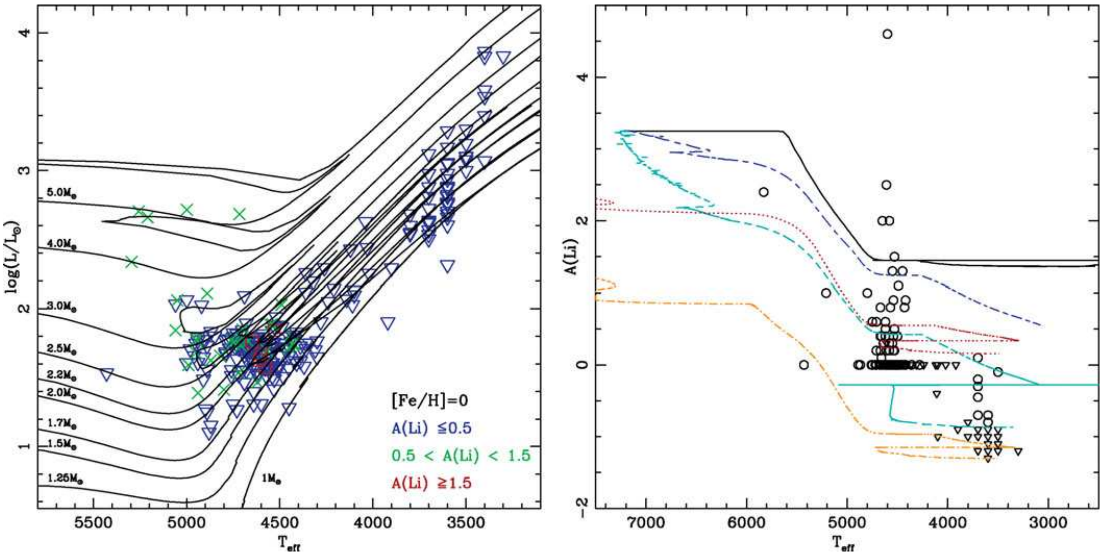

Figure 1. Comparison between models and data for the solar metallicity subsample. (Left:) HR diagram with indications on the surface Li abundance. Triangles : $A(Li) \leqslant 0.5$, square : $0.5 < A(Li) < 1.5$, crosses : $A(Li) \geqslant 1.5$. (Right:) Lithium as a function of Teff for stars with masses lower than $2M_{\odot}$ (Circles and triangles for actual determinations and upper limits respectively). Solid line, short dashed - long dashed line, and dashed line represent$1.5M_{\odot}$ stars in standard model, with thermohaline mixing and rotation $V_{ZAMS} = 50km/s$ and $V_{ZAMS} = 110km/s$ respectively. Dotted line and dot - short dashed line represent $2.0M_{\odot}$ with thermohaline mixing and rotation $V_{ZAMS} = 110km/s$ and $V_{ZAMS} = 250km/s$ respectively.

On the main sequence and early-RGB, rotation-induced processes lead to stronger Li depletion than in the standard case, in agreement with observations, and the observed Li dispersion reflects dispersion in the initial rotation velocity (see also Charbonnel & Talon 1999, Palacios *et al.* 2003, Smiljanic *et al.* 2009). After the end of the first dredge-up (Teff$\sim 4800K$), the Li abundance remains temporarily constant. When thermohaline mixing becomes efficient at the bump in the luminosity function (which corresponds here to Teff$\sim 4200K$), the Li abundance is predicted to drop again in drastic manner, explaining very well the Li upper limits obtained for the brightest RGB and AGB sample stars.

References

Charbonnel, C. & Zahn, J. P. 2007, *A&A*, 467, L15

Charbonnel, C. & Talon, S. 1999, *A&A*, 351, 635

Maeder, A. & Zahn, J. P. 1998, *A&A*, 334, 1000

Palacios, A., Talon, S., Charbonnel, C., & Forestini, M. 2003, *A&A*, 399, 603

Smiljanic, R., Pasquini, L., Charbonnel, C., & Lagarde, N. 2009, *A&A*,in press, astro-ph 0910.4399

Zahn, J. P. 1992, *A&A*, 265, 115

Proceeding SF2A (2010) - Oral contribution -

Thermohaline instability and rotation-induced mixing in low- and intermediate-mass stars

N.Lagarde and C. Charbonnel

Abstract:

Thermohaline mixing was recently identied as the dominating process that governs the photospheric composition of low-mass bright giant stars (Charbonnel & Zahn 2007a). Here we present the predictions of our stellar models computed with the code STAREVOL, taking into account this mechanism together with rotational mixing. We compare the predictions for the surface abundances with recent observations in evolved stars, and discuss the corresponding ^{3}He yields in the context of Galactic chemical evolution.

SF2A 2010
S. Boissier, M. Heydari-Malayeri, R. Samadi and D. Valls-Gabaud (eds)

THERMOHALINE INSTABILITY AND ROTATION-INDUCED MIXING IN LOW- AND INTERMEDIATE-MASS STARS

N. Lagarde[1] and C. Charbonnel [1,2]

Abstract. Thermohaline mixing was recently identified as the dominating process that governs the photospheric composition of low-mass bright giant stars (Charbonnel & Zahn 2007a). Here we present the predictions of our stellar models computed with the code STAREVOL, taking into account this mechanism together with rotational mixing. We compare the predictions for the surface abundances with recent observations in evolved stars, and discuss the corresponding ^{3}He yields in the context of Galactic chemical evolution.

Keywords: hydrodynamics, instabilities, stars: abundances, evolution, rotation, Galaxy: abundances

1 Introduction

At all stages of their evolution, low- and intermediate-mass stars (LIMS) exhibit the signatures of complex physical processes that require challenging modelling beyond canonical (or standard) stellar theory (by canonical we refer to the modelling of non-rotating, non-magnetic stars, in which convection is the only mechanism that drives mixing in stellar interiors). Charbonnel & Zahn (2007, hereafter CZ07) identified thermohaline mixing as the process that governs the surface abundances of LIMS evolving on the upper end of the red giant branch (RGB). In these stars, this double-diffusive instability is induced by the mean molecular weight inversion created by the $^3He(^3He, 2p)^4He$ reaction in the radiative layers between the convective envelope and the hydrogen burning shell (Eggleton et al. 2006). Here we focuss on the case of LIMS of solar-metallicity. We discuss the cumulated impact of thermohaline and rotation-induced mixings on the surface abundances, based on models computed with the code STAREVOL (see e.g. Decressin et al. 2009). Details on the assumptions and computations can be found in Charbonnel & Lagarde (2010), together with a more complete comparison with observations in Galactic open clusters.

2 Models and results

In order to quantify precisely the impact of each transport process at the various evolutionary phases, we have computed models with the following assumptions: (1) Standard models (no mixing mechanism other than convection); (2) Models including thermohaline mixing only (rotation velocity V=0); (3) Models including thermohaline mixing and rotation-induced processes for different initial rotation velocities.

For the turbulent diffusivity produced by the thermohaline instablity, we use the prescription advocated by CZ07 based on Ulrich (1972) arguments for the aspect ratio α (length/width) of the salt fingers as supported by laboratory experiments (Krishnamurti 2003) and including Kippenhahn et al. (1980) extended expression for the case of a non-perfect gas. For the treatment of rotation-induced mixing we proceed as follows. Solid-body rotation is assumed when the star arrives on the zero age main sequence (ZAMS). Typical initial (i.e., ZAMS) rotation velocities are chosen depending on the stellar mass based on observed rotation distributions in young open clusters (Gaigé 1993). Surface braking by a magnetic torque is applied for stars with an effective temperature on the ZAMS lower than 6900 K that have relatively a thick convective envelope as discussed in Talon & Charbonnel (1998); the adopted braking law follows the description of Kawaler (1988). From the ZAMS on, the evolution of the internal angular momentum profile is accounted for with the complete formalism developed by Zahn (1992) and Maeder & Zahn (1998) that takes into account advection by meridional circulation and diffusion by shear turbulence.

---

[1] Geneva Observatory, University of Geneva, Chemin des Maillettes 51, 1290 Versoix, Switzerland
[2] LATT, CNRS UMR 5572, Toulouse University, 14, av. E.Belin, 31400 Toulouse, France

2.1 Models predictions for $^{12}C/^{13}C$

In figure 1, we present observations of carbon isotopic ratio in evolved stars belonging to different Galactic open clusters, as a function of cluster's turn off mass. The data are compared with our theoritical predictions at solar metallicity. For low-mass stars ($M < 1.7M_{\odot}$), thermohaline mixing on the RGB appears to be the main mecanism explaining the low-carbon isotopic ratios observed. On the other hand, rotation-induced mixing is found to change the stellar structure so that in the mass range between $\sim$ 1.5 and 2.2 $M_{\odot}$ the thermohaline instability occurs earlier on the red giant branch than in non-rotating models. Finally, rotation accounts for the observed star-to-star abundance variations at a given evolutionary status, and is necessary to explain the features of CN-processed material in intermediate-mass stars.

2.2 Models predictions for Lithium on TP-AGB

In all the models that we have computed along the TP-AGB, thermohaline transport leads to non negligible fresh lithium production, as shown in figure 2. There we present the evolution of the surface lithium abundance N(Li) as a function of effective temperature and bolometric magnitude for TP-AGB models of 1.25 and 2.0$M_{\odot}$ stars. Theoritical predictions are compared with observations in the sample of low-mass oxygen-rich AGB variables belonging to the Galactic disk studied by Uttenthaler & Lebzelter (2010). Let us note that despite this strong Li production at that phase, the total stellar Li yields remain negative.

2.3 Models predictions for ^{3}He

In figure 3, we present the evolution of ^{3}He mass fraction at the surface of 1$M_{\odot}$ model at solar metallicity in the standard case and in the case with thermohaline mixing (black solid and red dotted lines respectively). Thermohaline mixing induces a strong decrease of ^{3}He at the bump luminosity, and the mass fraction of ^{3}He at the AGB tip is strongly reduced when thermohaline mixing is accounted for compared to the standard predictions. As a consequence, the overal ^{3}He yields are also strongly affected, as shown in 4. As will be discussed elsewhere (Lagarde et al., in preparation), this helps reconciling the theoretical Galactic evolution of ^{3}He with observations of this element in Galactic HII regions (i.e Balser et al. 1994, 1999; Bania et al. 1997, 2002).

3 Conclusions

An inversion of molecular weight created by the $^{3}He(^{3}He, 2p)^{4}He$ reaction is at the origin of thermohaline mixing in low- and intermediate-mass stars brighter than the luminosity of the bump on the RGB (see e.g. CZ07). Models including the transport of chemical induced by this double-diffusive instability explain very well the observations of ^{12}C/^{13}C in low-mass stars in Galactic open clusters. Rotation-induced mixing allows us to explain the ^{12}C/^{13}C anomalies in giant stars with a mass higher than $1.7M_{\odot}$. Thermohaline mixing has also an effect during TP-AGB, where it allows the production of lithium, in agreement with observations in oxygen-rich variables. Finaly, it can help reconciling the theoretical ^{3}He yields with the behaviour of this primordial element in the Galaxy.

References

Balser, D. S., Bania, T. M., Brockway, C. J., Rood, R. T., & Wilson, T. L. 1994, ApJ, 430, 667
Balser, D. S., Bania, T. M., Rood, R. T., & Wilson, T. L. 1999, ApJ, 510, 759
Bania, T. M., Balser, D. S., Rood, R. T., Wilson, T. L., & Wilson, T. J. 1997, ApJS, 113, 353
Bania, T. M., Rood, R. T., & Balser, D. S. 2002, Nature, 415, 54
Charbonnel, C. & Lagarde, N. 2010, ArXiv e-prints
Charbonnel, C. & Zahn, J.-P. 2007, A&A, 467, L15
Decressin, T., Mathis, S., Palacios, A., et al. 2009, A&A , 495, 271
Eggleton, P. P., Dearborn, D. S. P., & Lattanzio, J. C. 2006, Science, 314, 1580
Gaigé, Y. 1993, A&A, 269, 267
Gilroy, K. K. 1989, ApJ, 347, 835

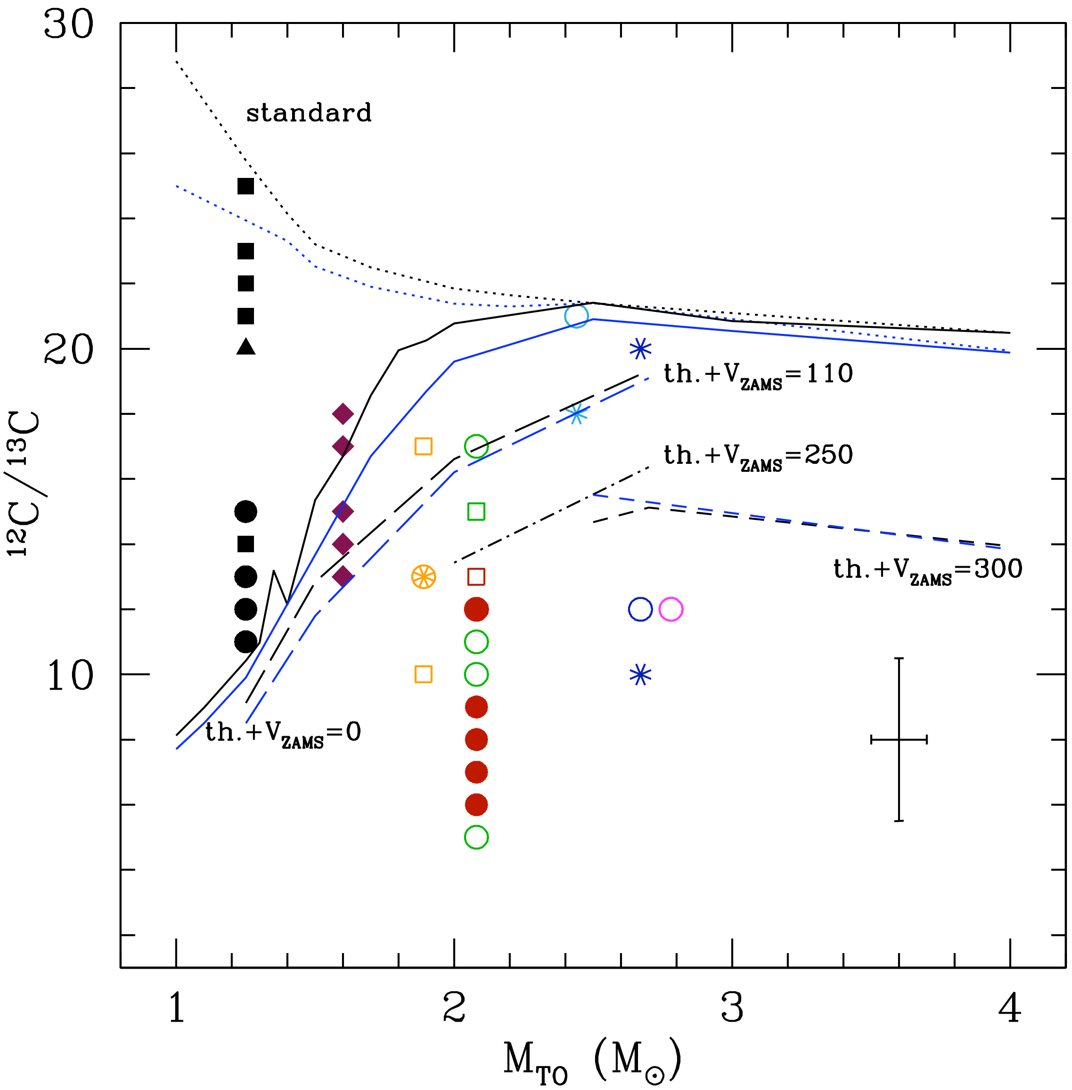

Fig. 1. Observations of $^{12}C/^{13}C$ in evolved stars of Galactic open clusters by Smiljanic et al. (2009, open cluster), Gilroy (1989), Gilroy & Brown (1991), and Mikolaitis et al. (2010) as a function of the turnoff mass of the corresponding host cluster. Squares, circles, and asteriscs are for RGB, clump, and early-AGB stars respectively, while diamonds are for stars from Gilroy (1989) sample with doubtful evolutionary status; triangles are for lower limits. A typical error bar is indicated. Theoretical predictions are shown at the tip of the RGB and after completion of the second dredge-up (black and blue lines respectively). Standard models (no thermohaline nor rotation-induced mixing) are shown as dotted lines, models with thermohaline mixing only (V_{ZAMS}=0) as solid lines, and models with thermohaline and rotation-induced mixing for different initial rotation velocities as indicated as long-dashed, dot-dashed, and dashed lines. Figure from Charbonnel & Lagarde (2010).

Gilroy, K. K. & Brown, J. A. 1991, ApJ, 371, 578

Kawaler, S. D. 1988, ApJ, 333, 236

Kippenhahn, R., Ruschenplatt, G., & Thomas, H.-C. 1980, A&A, 91, 175

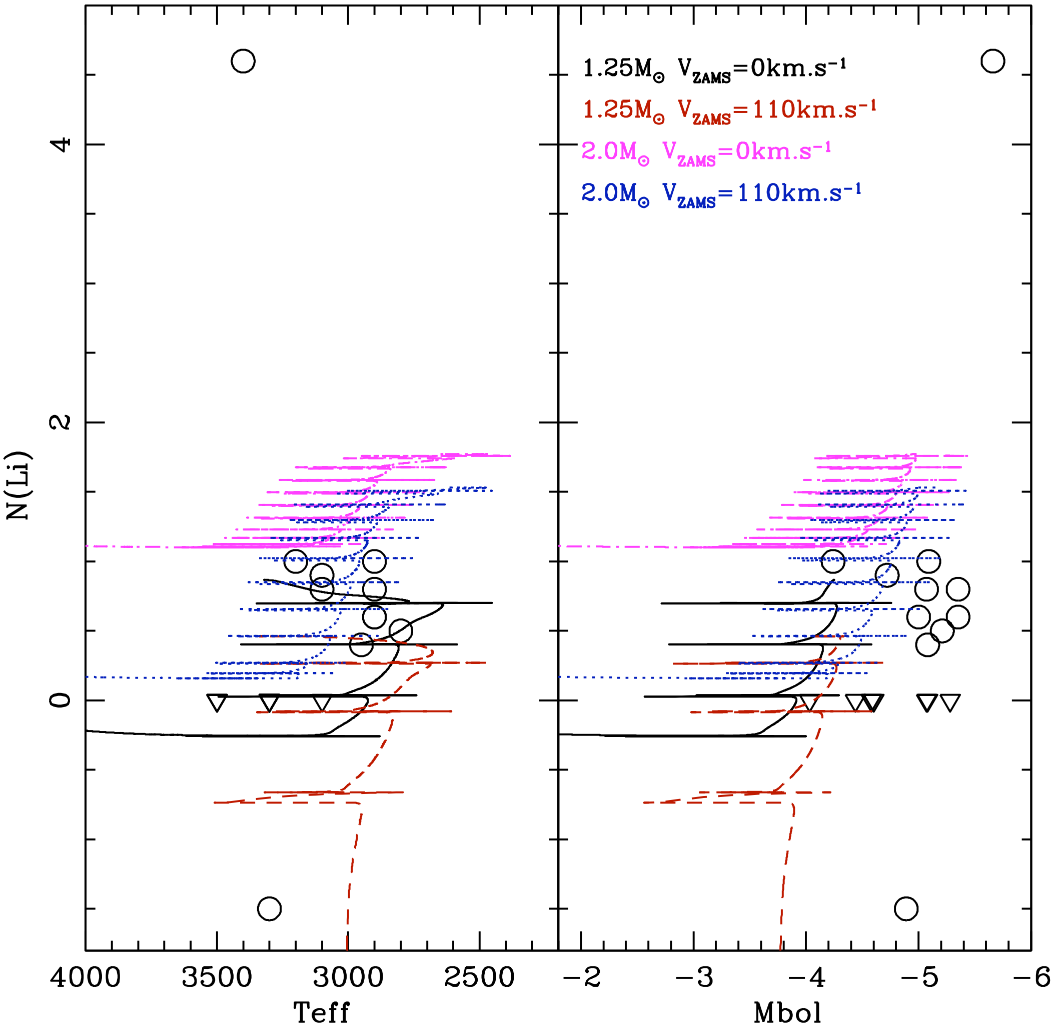

Fig. 2. Lithium observations in oxygen-rich variables belonging to the Galactic disk (Uttenthaler & Lebzelter 2010); circles and triangles are for abundance determinations and upper limits respectively) as a function of effective temperature and bolometric magnitude. Theoretical lithium evolution is shown from the early-AGB up to the end of the TP-AGB. Various lines correspond to predictions for stellar models of different masses computed without or with rotation as indicated, and with thermohaline mixing in all cases. Figure from Charbonnel & Lagarde (2010).

Krishnamurti, R. 2003, Journal of Fluid Mechanics, 483, 287

Maeder, A. & Zahn, J.-P. 1998, A&A, 334, 1000

Mikolaitis, Š., Tautvaišienė, G., Gratton, R., Bragaglia, A., & Carretta, E. 2010, MNRAS, 407, 1866

Smiljanic, R., Gauderon, R., North, P., et al. 2009, A&A, 502, 267

Talon, S. & Charbonnel, C. 1998, A&A, 335, 959

Ulrich, R. K. 1972, ApJ, 172, 165

Uttenthaler, S. & Lebzelter, T. 2010, A&A, 510, A62+

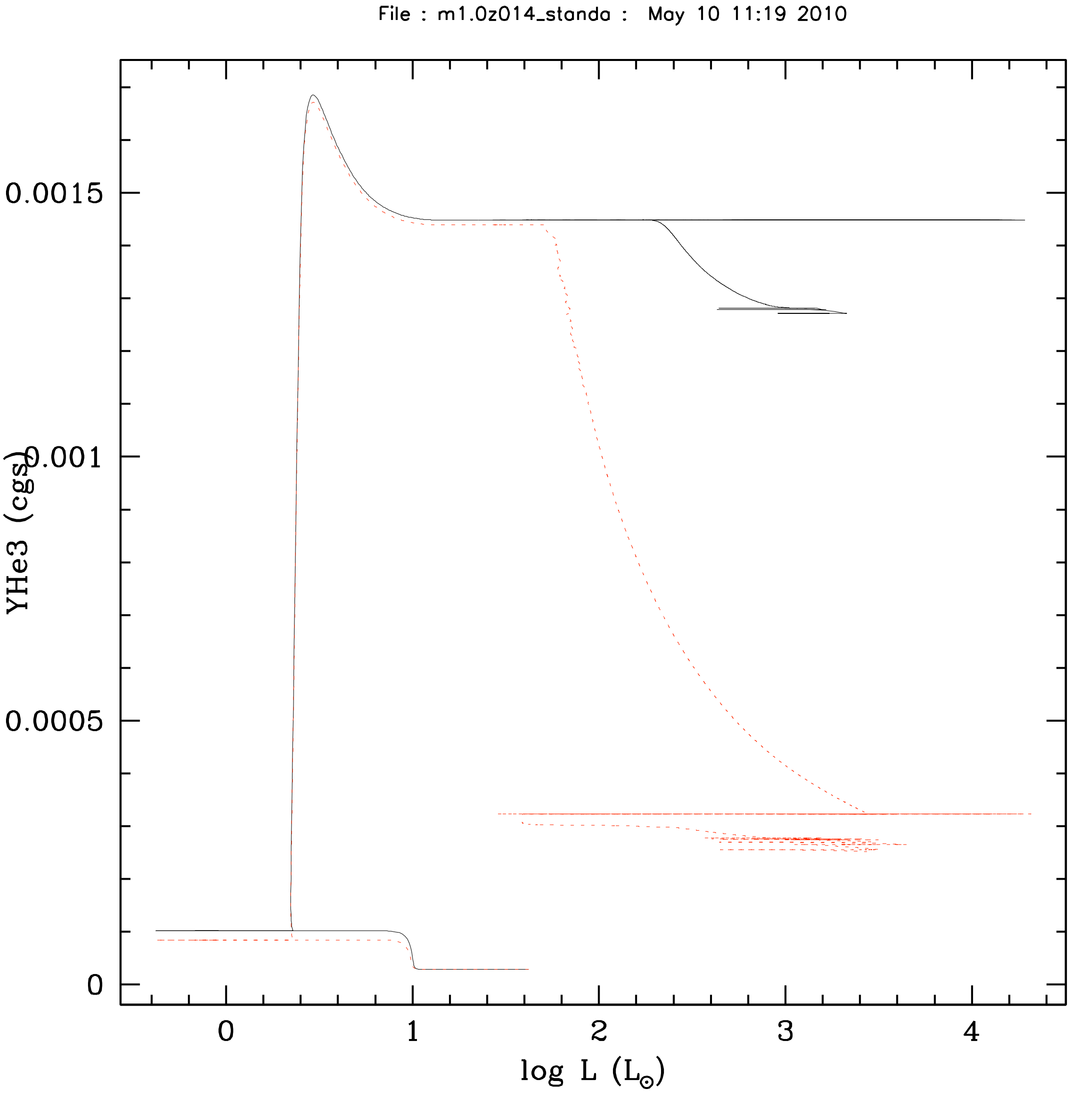

Fig. 3. Evolution of the surface abundance of ^{3}He (in mass fraction) from the pre-main sequence up to the AGB tip for $1M_\odot$ models at solar metallicity. The black solid line and the red dotted-line correspond to the standard and thermohaline cases respectively.

Zahn, J.-P. 1992, A&A, 265, 115

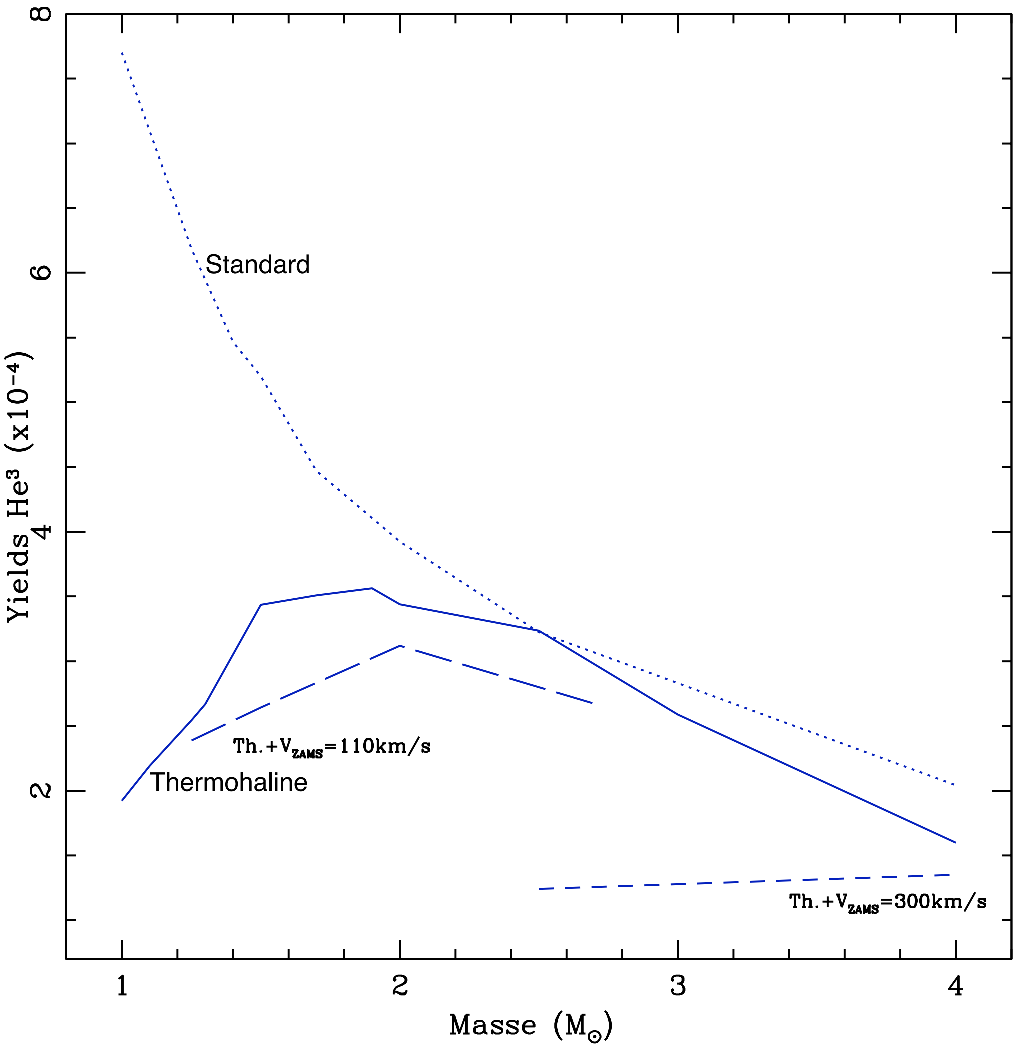

Fig. 4. Theoretical ^{3}He yields at solar metallicity as a function of initial stellar mass. The standard predictitions are shown by the dotted line; the thermohaline predictions are shown by the solid line; and the rotation+thermohaline models are shown as a long dashed lines for $V_{ZAMS} = 110 km/s$ and as a short dashed lines for $V_{ZAMS} = 300 km/s$. Figure from Lagarde et al. (in prep.)

Proceeding of the workshop (2011) :

"Red Giants as Probes of the Structure and Evolution of the Milky Way"

Impact of rotational mixing on the global and asteroseismic properties of red giants.

P. Eggenberger, N. Lagarde and C. Charbonnel

Abstract:

The influence of rotational mixing on the global parameters and asteroseismic properties of red giant stars is reviewed. While red giants are generally characterised by low surface rotational velocities, theymay have been rotating much more rapidly during the main sequence, so that the rotational history of a star has a large impact on its properties during the red giant phase. For stars massive enough to ignite helium burning in non-degenerate conditions, rotationalmixing leads to a significant increase of the stellar luminosity and shifts the location of the core helium burning phase to a higher luminosity in the HR diagram. This results in a change of the seismic properties of red giants and of the fundamental parameters of a red giant star as determined by performing an asteroseismic calibration. For red giants with a lower mass that undergo the helium flash, rotational mixing decreases the luminosity of the bump at solar metallicity changing thereby the global and asteroseismic properties of these stars.

Impact of rotational mixing on the global and asteroseismic properties of red giants

Patrick Eggenberger, Nadège Lagarde and Corinne Charbonnel

Abstract The influence of rotational mixing on the global parameters and asteroseismic properties of red giant stars is reviewed. While red giants are generally characterised by low surface rotational velocities, they may have been rotating much more rapidly during the main sequence, so that the rotational history of a star has a large impact on its properties during the red giant phase. For stars massive enough to ignite helium burning in non-degenerate conditions, rotational mixing leads to a significant increase of the stellar luminosity and shifts the location of the core helium burning phase to a higher luminosity in the HR diagram. This results in a change of the seismic properties of red giants and of the fundamental parameters of a red giant star as determined by performing an asteroseismic calibration. For red giants with a lower mass that undergo the helium flash, rotational mixing decreases the luminosity of the bump at solar metallicity changing thereby the global and asteroseismic properties of these stars.

P. Eggenberger
Observatoire de Genève, Université de Genève, 51 ch. des Maillettes, CH-1290 Sauverny
e-mail: `patrick.eggenberger@unige.ch`

N. Lagarde
Observatoire de Genève, Université de Genève, 51 ch. des Maillettes, CH-1290 Sauverny
e-mail: `nadege.lagarde@unige.ch`

C. Charbonnel
Observatoire de Genève, Université de Genève, 51 ch. des Maillettes, CH-1290 Sauverny
Laboratoire d’Astrophysique de Toulouse-Tarbes, CNRS UMR 5572, Université de Toulouse, 14 av. E. Belin F-31400 Toulouse
e-mail: `corinne.charbonnel@unige.ch`

1 Introduction

The wealth of information obtained about the internal structure of the Sun by the observation and interpretation of solar oscillation modes stimulated various attempts to detect solar-like oscillations on other stars. Consequently, many instruments have been recently developed to perform such asteroseismic studies. From the ground, the stabilized spectrographs have reached the accuracy needed to detect and characterise solar-like oscillations on stars other than the Sun, while space missions have been recently designed to perform very high accuracy photometric measurements of these oscillation modes. Solar-like oscillations are not restricted to solar-type stars, but are expected in any star exhibiting a convective envelope able to stochastically excite pressure modes of oscillations. In the case of red giants, solar-like oscillations have been first detected for a few stars (see e.g. Frandsen et al., 2002; Barban et al., 2004; De Ridder et al., 2006; Barban et al., 2007), while clear identifications of non-radial oscillations have then been obtained for a large number of red giant stars with the CoRoT space mission (De Ridder et al., 2009) and the *Kepler* satellite (Bedding et al., 2010). These observations stimulated population studies aiming at reproducing the distribution of global asteroseismic properties of red giant stars (Miglio et al., 2009a,b), as well as the theoretical study of the asteroseismic properties of red giants and of the effects of various physical processes on the modelling of these stars (Dupret et al., 2009; Eggenberger et al., 2010c; Montalbán et al., 2010). Rotation being one of the key processes that has an important impact on stellar physics and evolution (Maeder, 2009), we briefly review here its effects on the global and asteroseismic properties of red giants.

2 Effects of rotation on evolutionary tracks

Stellar models computed with and without the inclusion of shellular rotation (Zahn, 1992) are compared in order to discuss the influence of rotation on the evolution and global properties of red giant stars. We discuss first the evolution of stars massive enough to start helium burning in non-degenerate conditions, and then the evolution of low mass red giants undergoing the helium flash.

2.1 Intermediate-mass stars

The effects of rotation on the global properties of red giants massive enough to ignite He burning in non-degenerate conditions are illustrated by computing the evolution of a $3\,M_{\odot}$ star with and without rotation using the Geneva stellar evolution code (Eggenberger et al., 2008). The solar chemical composition given by Grevesse & Noels (1993) is used together with a solar calibrated value for the mixing-length parameter. No overshooting from the convective core into the surrounding radiatively stable layers is included. Figure 1 compares the evolutionary track of the non-rotating model with that of a rotating model computed with exactly the same input parameters except for an initial velocity of 150 km s^{-1} on the zero age main sequence (ZAMS).

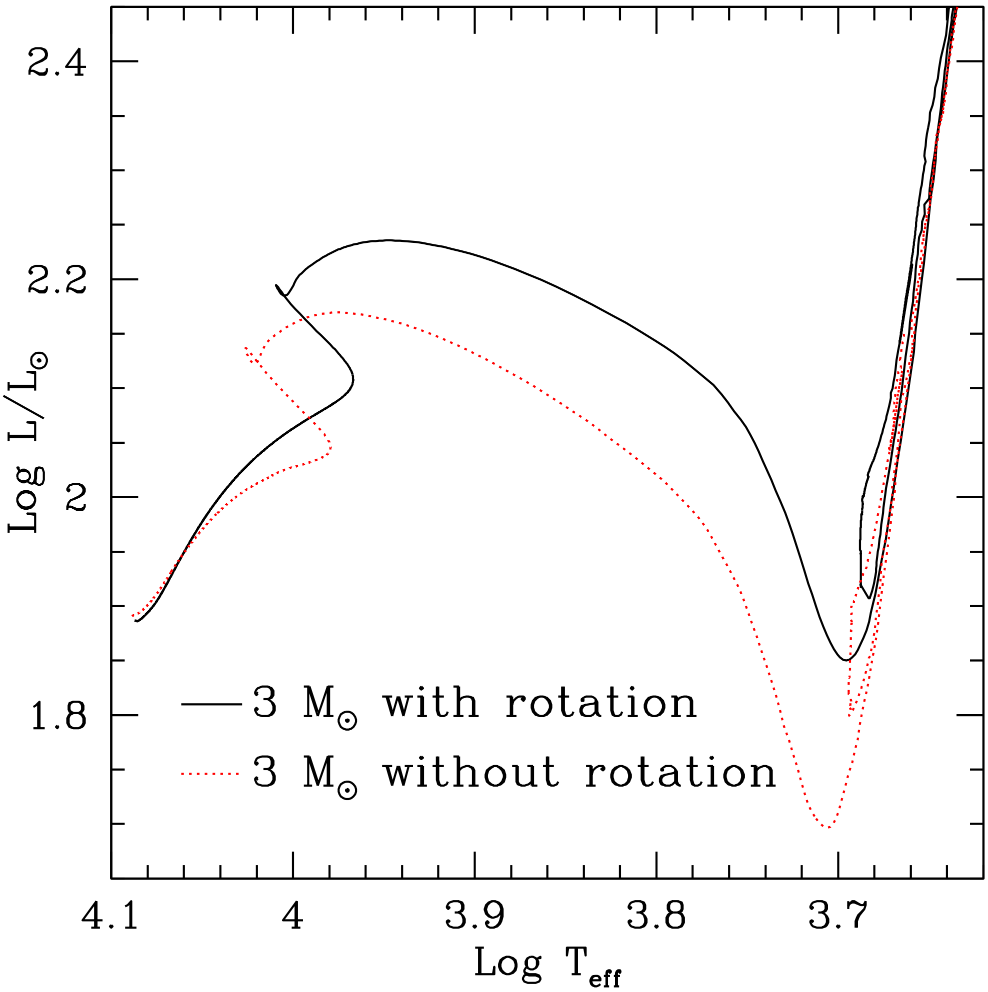

Fig. 1 Evolutionary tracks in the HR diagram for 3 M$_\odot$ models computed with (continuous line) and without (dotted line) shellular rotation.

We see that evolutionary tracks in the HR diagram are significantly affected when rotational effects are taken into account. During the main sequence, we first note a slight decrease of the luminosity for the rotating model compared to the model without rotation at the beginning of the main-sequence evolution, while the increase of the luminosity of the rotating model becomes more and more pronounced as evolution proceeds. In particular, the model including rotation has a larger luminosity than the standard one during the post-main sequence phase of evolution. The location of the core helium-burning phase, which is the phase during which the star spends most of its lifetime as a red giant, is then shifted to larger luminosity when rotational effects are included.

We recall here that rotational effects can be basically divided in two main categories: (1) the effects resulting from changes in the chemical and internal structure induced by rotational mixing and (2) the effects resulting from hydrostatic corrections due to the centrifugal force. At the beginning of the main sequence, only hydrostatic effects of rotation are observed. The effective gravity of the rotating model is then slightly reduced compared to the non-rotating model so that the resulting evolutionary track is similar to the one of a non-rotating star computed with a slightly lower initial mass. This explains the small decrease in luminosity and effective temperature observed near the ZAMS for the model including rotation in Fig. 1. As the star evolves on the main sequence, the effects related to rotational mixing plays however a more and more important role by bringing fresh hydrogen fuel in the stellar core and transporting helium and other H-burning products in the radiative zone. Rotational mixing thus increases the size of the convective core and changes the chemical composition profiles in the radiative zone. This induces an increase of the luminosity together with a widening of the main sequence when rotation is included in the computation (see Fig. 1). The changes observed in the tracks are thus mainly due to rotational mixing with only a very limited contribution from the effects of the centrifugal force at the very beginning of the main sequence. This can be explained by recalling that the kinetic rotational energy of the $3\,\mathrm{M}_\odot$ star is much lower than its gravitational energy.

Rotational mixing has also an important influence on stellar ages. The value of the central abundance of hydrogen at a given age is indeed larger for the rotating model than for the non-rotating one. This is due to the transport of hydrogen in the deep stellar layers, which leads to an enhancement of the main-sequence lifetime for rotating models compared to standard models. For the $3\,\mathrm{M}_\odot$ model considered here with an initial velocity of $150\,\mathrm{km\,s^{-1}}$, this corresponds to an increase of the age of about 10 %.

As far as the evolution of the surface rotational velocity is concerned, a slow decrease is first obtained during the main sequence; starting with an initial velocity of $150\,\mathrm{km\,s^{-1}}$ on the ZAMS, a velocity of $115\,\mathrm{km\,s^{-1}}$ is reached at the end of the main sequence for the $3\,\mathrm{M}_\odot$ star presented here. A very rapid decrease of the surface velocity then occurs when the star crosses the Hertzsprung gap. The exact value of the surface velocity during the red giant phase is sensitive to the assumption made on the rotation law in the extended convective envelope of the star. By assuming solid body rotation or uniform specific angular momentum in the external convective zone, a mean value of the surface rotational velocity of about 6 and $0.3\,\mathrm{km\,s^{-1}}$ is respectively found during the red giant phase. For both limiting assumptions on the rotation law in the external convective zone, a model computed with a significant value for the initial rotational velocity on the ZAMS thus exhibits a low surface rotational velocity as a red giant. This shows that a slowly rotating red giant may have been rotating much more rapidly during the main sequence and that its global properties depend on its rotational history.

2.2 Low-mass stars

The impact of rotational mixing on low-mass red giants that undergo the helium flash at the RGB tip is now briefly discussed by comparing 1.25 $M_\odot$ models with and without rotation. These models are computed with the evolution code STAREVOL (Charbonnel & Lagarde, 2010) at solar metallicity, with an initial velocity on the ZAMS of 110 $\mathrm{km\,s^{-1}}$ for the rotating case. The corresponding evolutionary tracks are shown in Fig. 2.

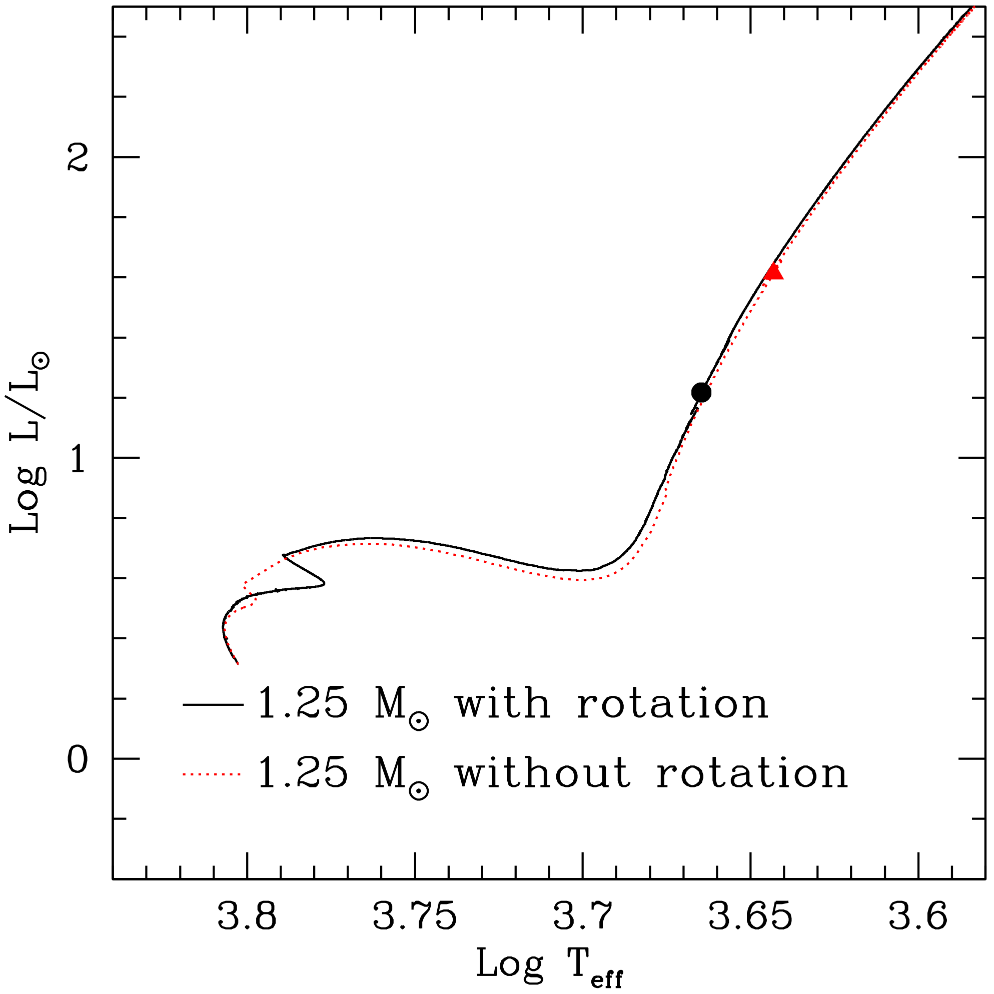

Fig. 2 Evolutionary tracks in the HR diagram for 1.25 $M_\odot$ models computed with (continuous line) and without (dotted line) shellular rotation. The dot and triangle indicate the location of the bump for the rotating and non-rotating model, respectively.

During the evolution on the main sequence, the inclusion of rotational effects results in slightly larger effective temperatures and luminosities. For these models with a lower mass and a small convective core, this shift is mainly due to the fact that rotational mixing counteracts the effects of atomic diffusion in the external layers of the star (Eggenberger et al., 2010b). Larger values of helium abundance are then found at the surface of models including rotation, which leads to a decrease of the opacity in the external layers of the star. As for the more massive $3\,\mathrm{M}_{\odot}$ models described above, the influence of rotational mixing is not restricted to the external layers of the star, since the properties of the central layers are changed due to the transport of fresh hydrogen fuel into the stellar core. Consequently, the main-sequence lifetime is larger when rotation is accounted for. Contrary to the case of intermediate-mass red giants discussed in Sect. 2.1, the location in the HR diagram of the core helium burning phase is now very similar for models computed with and without rotational effects. However, rotational mixing has a large impact on the location of the bump. At solar metallicity, the inclusion of rotation leads indeed to a significant decrease of the luminosity of the star at the bump and to an increase of its effective temperature (see Fig. 2 and Charbonnel & Lagarde, 2010).

3 Effects of rotation on asteroseismic properties of red giants

Red giant stars are characterised by deep convective envelopes and dense cores. From an asteroseismic point of view, the large density near the center of the star leads to huge values of the Brunt-Väisälä frequency in the central layers. Consequently, oscillation modes of mixed p-mode and g-mode properties are expected. In addition to purely acoustic radial modes, a large number of non-radial modes are then found, which are in most cases dominated by the g-mode behaviour and have therefore a high inertia. However, for non-radial modes trapped in the acoustic cavity the inertia becomes similar to the one of radial modes. For $\ell = 2$ modes, the separation between the p- and g-mode region is sufficient to obtain oscillation modes which in terms of inertia are very similar to purely acoustic modes. This results in trapped $\ell = 2$ modes with a dominant amplitude close to every radial mode, which define the small separation between $\ell = 0$ and $\ell = 2$ modes (see e.g. Christensen-Dalsgaard, 2004). This basic description of the properties of oscillation modes in red giant stars is solely based on inertia consideration and does not take into account the problem of excitation and damping of these modes (see e.g. Dziembowski et al., 2001; Dupret et al., 2009).

3.1 *Intermediate-mass stars*

We now discuss the effects of rotation on the properties of the oscillation modes of these stars. This is first done by comparing the asteroseismic properties of rotating and non-rotating models at the same evolutionary phase computed with the same input parameters (except for the inclusion of shellular rotation). A rotating model of $3\,\mathrm{M}_{\odot}$ computed with an initial velocity of $150\,\mathrm{km\,s^{-1}}$ on the ZAMS and situated in the middle of the core helium-burning phase ($\mathrm{Y_c} = 0.355$) is then compared to the corresponding non-rotating red-giant model. The theoretical low-ℓ frequencies of both models are computed and the values of the large and small frequency separations are obtained. The values of the large separation are calculated from the radial modes, while the small separations between $\ell = 0$ and $\ell = 2$ modes are determined by considering only $\ell = 2$ modes well trapped in the acoustic cavity.

Rotational effects lead to a significantly lower value of the mean large separation. The rotating model exhibits indeed a mean large separation that is about 20% lower that the one of the non-rotating model. The mean large separation being mainly proportional to the square root of the star's mean density, this difference is directly related to the larger radius of the rotating model (both models share the same mass of $3\,\mathrm{M}_{\odot}$). This larger radius is a direct consequence of the significant increase of the luminosity discussed in the preceding sections when rotational mixing is included in the computation. The value of the mean small frequency separation between radial modes and $\ell = 2$ modes trapped in the acoustic cavity of the star is also found to be significantly reduced when rotational effects are taken into account. For stars evolving on the main sequence, the ratio of the small to large separation is sensitive to the conditions in the central regions of the star (Roxburgh & Vorontsov, 2003; Roxburgh, 2005). In the case of red giant models, the decrease of the values of the small and large separation when rotation is included is similar, so that the ratio between the small and large separation remains approximately the same for rotating and non-rotating models. This shows that the decrease of the small separation between $\ell = 0$ and trapped $\ell = 2$ modes observed for rotating models is mainly due to the change of the global stellar properties and not to a change in the structure of the central regions of the star (Eggenberger et al., 2010c; Montalbán et al., 2010).

In addition to the comparison between rotating and non-rotating models computed with the same initial parameters, it is also interesting to discuss the impact of rotation on the determination of the fundamental stellar parameters and asteroseismic properties for red giants sharing the same location in the HR diagram. This is done by computing another model with approximately the same luminosity as the non-rotating red giant stars of $3\,\mathrm{M}_{\odot}$ during the core helium-burning phase. Since rotational mixing increases the stellar luminosity, such a rotating model is obtained for a lower mass of $2.7\,\mathrm{M}_{\odot}$. The lower initial mass of models including rotation leads to a large increase of the age determined for a red giant. This illustrates how rotational mixing changes the global stellar parameters needed to reach the same location in the HR diagram for core helium-burning stars.

The change of the global stellar parameters induced by rotation also results in differences in the asteroseismic properties between rotating and non-rotating models of red giants sharing the same location in the HR diagram. The rotating $2.7\,\mathrm{M}_{\odot}$ model is then characterised by a lower value of the mean large separation than the $3\,\mathrm{M}_{\odot}$ non-rotating model. This directly reflects the different masses of both models, which lead to different mean densities and hence mean large frequency separations. The mean small frequency separation between radial and $\ell = 2$ modes trapped in the acoustic cavity of the star is also found to decrease when rotational effects are taken into account. As mentioned above, this is mainly due to the change of the global stellar properties (the stellar mass in this case) for models computed with rotation compared to non-rotating models and not to differences in the structure of the central stellar layers.

3.2 Low-mass stars

The global asteroseismic properties of a rotating (initial velocity of $110\,\mathrm{km\,s^{-1}}$ on the ZAMS) $1.25\,\mathrm{M}_{\odot}$ red-giant model at the bump and the corresponding non-rotating model situated at the same evolutionary stage are finally compared. As noted above, the values of the large separation are calculated from the radial modes, while the small separations between $\ell = 0$ and $\ell = 2$ modes are determined by considering only $\ell = 2$ modes well trapped in the acoustic cavity of the star. For low-mass red giants at the bump, the inclusion of rotation results in a large increase of the mean value of the large separation, which is directly related to the smaller radius of the rotating model. As seen in Sect. 2.2, a rotating model of $1.25\,\mathrm{M}_{\odot}$ at solar metallicity is characterised by a lower luminosity and a larger effective temperature at the bump than a model without rotation. This leads to a smaller radius and hence a larger mean density and large frequency separation when rotational effects are taken into account. As for more massive red giant models, this change of the global stellar properties also results in a change of the mean small frequency separation between radial modes and trapped $\ell = 2$ modes with a significant increase of the small separation for rotating red giants.

4 Summary

The surface rotation velocity of a red giant star is generally low, but the star may have been rotating much more rapidly during the main sequence. The evolution in the red giant phase is then sensitive to the rotational history of the star, because rotation significantly changes its internal structure and global properties during the main sequence. Rotational mixing is the main driver of the changes of the evolutionary tracks in the HR diagram, with only a very limited contribution from hydrostatic corrections induced by rotation. For red giants massive enough to ignite He burning in non-degenerate conditions, rotational mixing shifts the location of the core helium burning phase to higher luminosity in the HR diagram, while for low-mass red giants undergoing the helium flash the luminosity at the bump is significantly reduced when rotation is included in the computation. This of course results in different global asteroseismic properties for red giant models with and without rotation and changes the values of the fundamental stellar parameters (in particular the mass and age of the star) determined from an asteroseismic calibration. In addition to these effects of rotation on the global asteroseismic properties, it will be interesting to study in detail the effects of rotational mixing on asteroseismic observables that are more sensitive to changes in the structure near the central core like the small separation between radial and dipole modes (Montalbán et al., 2010). Asteroseismic data coming from ground-based observations and space missions are thus particularly valuable to provide us with new insight into transport processes in stellar interiors like rotation, magnetic fields (e.g. Eggenberger et al., 2010a), and internal gravity waves (e.g. Charbonnel & Talon, 2005).

Acknowledgements Part of this work is supported by the Swiss National Science Foundation and by the French Programme National de Physique Stellaire (PNPS) of CNRS/INSU.

References

Barban, C., de Ridder, J., Mazumdar, A., et al. 2004, in ESA Special Publication, Vol. 559, SOHO 14 Helio- and Asteroseismology: Towards a Golden Future, ed. D. Danesy, 113
Barban, C., Matthews, J. M., de Ridder, J., et al. 2007, A&A , 468, 1033
Bedding, T. R., Huber, D., Stello, D., et al. 2010, ApJ , 713, L176
Charbonnel, C. & Lagarde, N. 2010, A&A , 522, A10
Charbonnel, C. & Talon, S. 2005, Science, 309, 2189
Christensen-Dalsgaard, J. 2004, Sol. Phys., 220, 137
De Ridder, J., Barban, C., Baudin, F., et al. 2009, Nature, 459, 398
De Ridder, J., Barban, C., Carrier, F., et al. 2006, A&A , 448, 689
Dupret, M., Belkacem, K., Samadi, R., et al. 2009, A&A , 506, 57
Dziembowski, W. A., Gough, D. O., Houdek, G., & Sienkiewicz, R. 2001, MNRAS , 328, 601
Eggenberger, P., Maeder, A., & Meynet, G. 2010a, A&A , 519, L2
Eggenberger, P., Meynet, G., Maeder, A., et al. 2008, Ap&SS , 316, 43
Eggenberger, P., Meynet, G., Maeder, A., et al. 2010b, A&A , 519, A116
Eggenberger, P., Miglio, A., Montalban, J., et al. 2010c, A&A , 509, A72
Frandsen, S., Carrier, F., Aerts, C., et al. 2002, A&A , 394, L5
Grevesse, N. & Noels, A. 1993, in Origin and evolution of the elements: proceedings of a symposium in honour of H. Reeves, held in Paris, June 22-25, 1992. Edited by N. Prantzos, E. Vangioni-Flam and M. Casse. Published by Cambridge University Press, Cambridge, England, 1993, p.14, ed. N. Prantzos, E. Vangioni-Flam, & M. Casse, 14
Maeder, A. 2009, Physics, Formation and Evolution of Rotating Stars (Springer Berlin Heidelberg)
Miglio, A., Montalbán, J., Baudin, F., et al. 2009a, A&A , 503, L21
Miglio, A., Montalbán, J., Eggenberger, P., Hekker, S., & Noels, A. 2009b, in American Institute of Physics Conference Series, Vol. 1170, American Institute of Physics Conference Series, ed. J. A. Guzik & P. A. Bradley, 132–136
Montalbán, J., Miglio, A., Noels, A., Scuflaire, R., & Ventura, P. 2010, ApJ , 721, L182
Roxburgh, I. W. 2005, A&A , 434, 665
Roxburgh, I. W. & Vorontsov, S. V. 2003, A&A , 411, 215
Zahn, J.-P. 1992, A&A , 265, 115

Proceeding of the workshop (2011) :

”Red Giants as Probes of the Structure and Evolution of the Milky Way”

Effects of rotation and thermohaline mixing in red giant stars

C. Charbonnel, N. Lagarde and P. Eggenberger

Abstract:

Thermohaline mixing has been recently identified as the probable dominating process that governs the photospheric composition of low-mass bright giant stars (Charbonnel & Zahn, 2007). Here we present the predictions of stellar models computed with the code STAREVOL including this mechanism together with rotational mixing.We compare our theoretical predictions with recent observations.

Effects of rotation and thermohaline mixing in red giant stars

Corinne Charbonnel, Nadège Lagarde & Patrick Eggenberger

Abstract Thermohaline mixing has been recently identified as the probable dominating process that governs the photospheric composition of low-mass bright giant stars (Charbonnel & Zahn, 2007). Here we present the predictions of stellar models computed with the code STAREVOL including this mechanism together with rotational mixing. We compare our theoretical predictions with recent observations.

1 Introduction

The standard theory of stellar evolution predicts that the convective envelope of low-mass stars deepens in mass during the contraction of the degenerate He-core after the main sequence turnoff, and engulfes hydrogen-processed material (the so-called first dredge-up, hereafter 1dup). This induces a decrease of the surface ^{12}C/^{13}C ratio and of the Li and ^{12}C abundances, while ^{14}N and ^{3}He abundances increase. After the 1dup, the convective envelope retracts and the hydrogen burning shell (HBS) moves outward (in mass). According to the standard theory, no further change of the surface chemical properties is expected after the 1dup on the Red Giant Branch (RGB). However, spectroscopic observations (Gilroy, 1989; Gilroy & Brown, 1991;

C. Charbonnel
Observatoire de Genève, Université de Genève, 51 ch. des Maillettes 1290 Versoix (Switzerland), Laboratoire d'Astrophysique de Toulouse-Tarbes, CNRS UMR 5572, Université de Toulouse, 14 av. E.Belin F-31400 Toulouse,
e-mail: `Chabonnel.Corinne@unige.ch`

N. Lagarde
Observatoire de Genève, Université de Genève, 51 ch. des Maillettes 1290 Versoix (Switzerland),
e-mail: `Lagarde.Nadege@unige.ch`

P. Eggenberger.
Observatoire de Genève, Université de Genève, 51 ch. des Maillettes 1290 Versoix (Switzerland),
e-mail: `Patrick.Eggenberger@unige.ch`

Luck, 1994; Gratton et al., 2000; Tautvaišiene et al., 2000; Tautvaišienė et al., 2005; Smith et al., 2002; Shetrone, 2003; Pilachowski et al., 2003; Geisler et al., 2005; Spite et al., 2006; Recio-Blanco & de Laverny, 2007; Smiljanic et al., 2009) show clear signatures of "extra-mixing" on the upper RGB in low-mass stars, when the HBS crosses the discontinuity left behind by the 1dup at the bump luminosity. More specifically, the carbon isotopic ratio and the C and Li abundances drop again as the stars move across the bump. Different processes have been proposed to explain these abundance anomalies. Here we recall the potential impact of rotation-induced mixing and thermohaline instability on the RGB.

2 Rotation-induced mixing

Rotation-induced mixing has an impact on the internal abundance profiles of chemicals involved in hydrogen-burning while the stars are on the main sequence (Talon & Charbonnel, 1998, 2010; Charbonnel & Talon, 1999; Palacios et al., 2003; Pasquini et al., 2004; Smiljanic et al., 2009; Charbonnel & Lagarde, 2010). This can be seen in Fig. 1 where we present the chemical structure at the end of the main sequence for $1.25\,M_\odot$ stellar models computed assuming different initial rotation velocities. In the rotating models, the abundance gradients are smoothed out compared to the standard (i.e., non-rotating) case: ^{3}He, ^{13}C, ^{14}N, and ^{17}O diffuse outwards, while ^{12}C and ^{18}O diffuse inwards. After the turnoff , this reflects in different post-dredge up predictions for the surface abundances that agree well with observations in low-luminosity red giant stars (see Fig.2). However, rotation-induced mixing does not explain the abundance anomalies observed in low-mass red giants brighter than the bump (Chanamé et al., 2005; Palacios et al., 2006).

3 Thermohaline mixing

Charbonnel & Zahn (2007) identified thermohaline mixing as the process that governs the photospheric composition of low-mass stars above the bump on the RGB. At this evolutionary phase, this double diffusive instability is induced by the ^{3}He(^{3}He; 2p)^{4}He reaction (Eggleton et al., 2006) that creates an inversion of mean molecular weight (Ulrich, 1971). Here we use the following prescription for the turbulent diffusivity coefficient (Ulrich, 1972; Kippenhahn et al., 1980) :

$$\mathrm{D_t} = \mathrm{C_t}\,\mathrm{K}\left(\frac{\varphi}{\delta}\right)\frac{-\nabla_\mu}{(\nabla_{\mathrm{ad}} - \nabla)} \quad \text{for } \nabla_\mu < 0, \tag{1}$$

$$\mathrm{C_t} = \frac{8}{3}\pi^2\alpha^2, \tag{2}$$

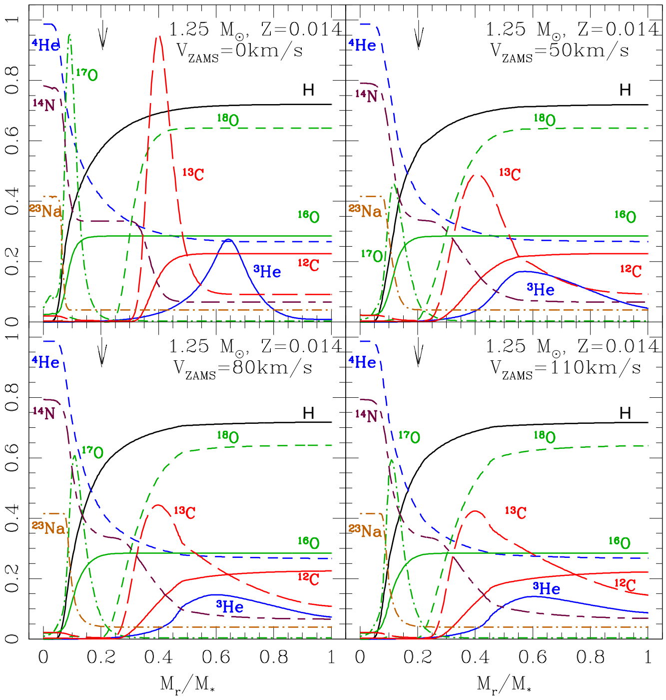

Fig. 1 Chemical structure at the turnoff of a 1.25 M$_\odot$ star computed for different initial rotation velocities as indicated. The mass fractions are multiplied by 100 for ^{3}He, ^{12}C, and ^{14}N, by 2500 for ^{13}C, by 50, 900, and 5×10^4 for ^{16}O, ^{17}O, and ^{18}O respectively, and by 1500 for ^{23}Na. The vertical arrows show, in all cases, the maximum depth reached by the convective envelope at its maximum extent during the 1dup. Figure from Charbonnel & Lagarde (2010).

with K the thermal diffusivity and $\alpha = 5$ the aspect ratio of salt fingers (Ulrich, 1972). At the RGB bump and above, the thermohaline diffusion coefficient is several order of magnitudes higher than the total diffusion coefficient related to rotation-induced processes (Charbonnel & Lagarde, 2010).

4 Model predictions and comparisons to observations.

The results shown in this section are presented and discussed in detail in Charbonnel & Lagarde (2010) and have been computed with the code STAREVOL including rotation-induced processes and thermohaline mixing. Here we briefly discuss the effects of rotation-induced mixing and thermohaline mixing on carbon isotopic ratio, lithium and ^{3}He.

4.1 Carbon isotopic ratio

In Fig.2 we compare the evolution of the theoretical surface carbon isotopic ratio for 1.25 $M_\odot$ models with observations in M67 stars by Gilroy & Brown (1991). We note that rotation-induced mixing on the main sequence slightly lowers the post-dredge-up ^{12}C/^{13}C value (see §2). On the other hand, thermohaline mixing leads to further decrease of the carbon isotopic ratio at the luminosity of the bump ($\log(L/L_\odot) \sim 2$), in excellent agreement with M67 data.

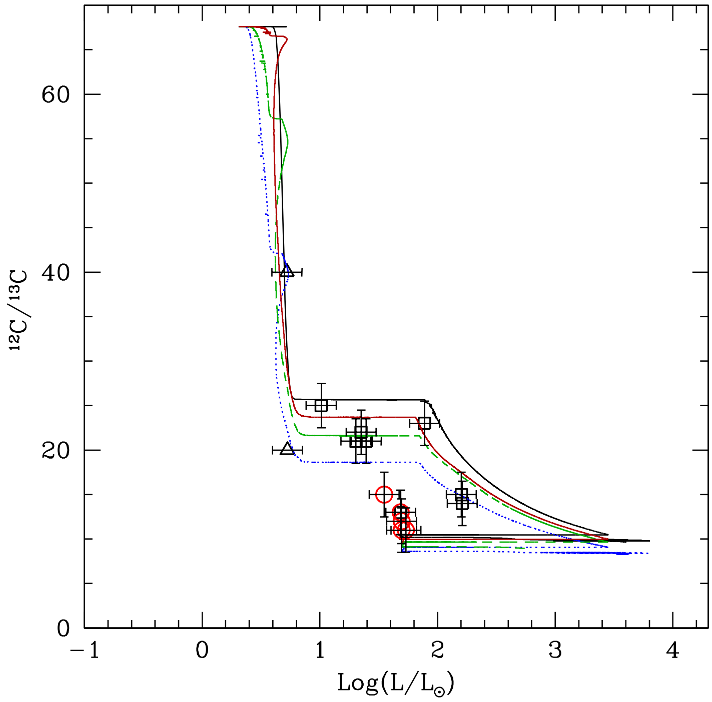

Fig. 2 Evolution of the surface ^{12}C/^{13}C ratio as a function of stellar luminosity for models of 1.25 M$_\odot$ stars. Different tracks are for different initial rotation velocities (non-rotating case, 50, 80, and 110 km.s^{-1} respectively in black, red, green, and blue). Observations by Gilroy & Brown (1991) in evolved stars of the open cluster M67 (turnoff mass ∼1.2 M$_\odot$) are also shown (triangle, squares, and circles for subgiant, RGB, and clump stars respectively). Figure from Charbonnel & Lagarde (2010).

In Fig.3 we show the predictions for the surface ^{12}C/^{13}C ratio at the tip of the RGB and at the end of second dredge-up (black and blue lines respectively) for models over a large mass range and compare them with observations in stars belonging to open clusters of various turnoff masses. We see that in stars with masses below ∼2M$_\odot$, thermohaline mixing is the main physical process governing the photospheric composition of evolved giants, although the final carbon isotopic ratio also slightly depends on rotation-induced mixing on the main sequence. In intermediate-mass stars that do not reach the bump on the RGB and do not undergo thermohaline mixing at that phase, rotation is necessary to explain the data and accounts for star-to-star abundance variations at a given evolutionary status. Overall, the present models explain very well the observed abundance patterns over the considered mass range.

4.2 Lithium

In Fig.4 we present lithium data for field red giant stars with metallicities around solar and precise determination of their evolutionary status, and compare them to predictions for models of various masses. Contrary to the standard case, rotation-induced mixing leads to Li depletion on the main sequence (see e.g. Talon & Charbonnel,

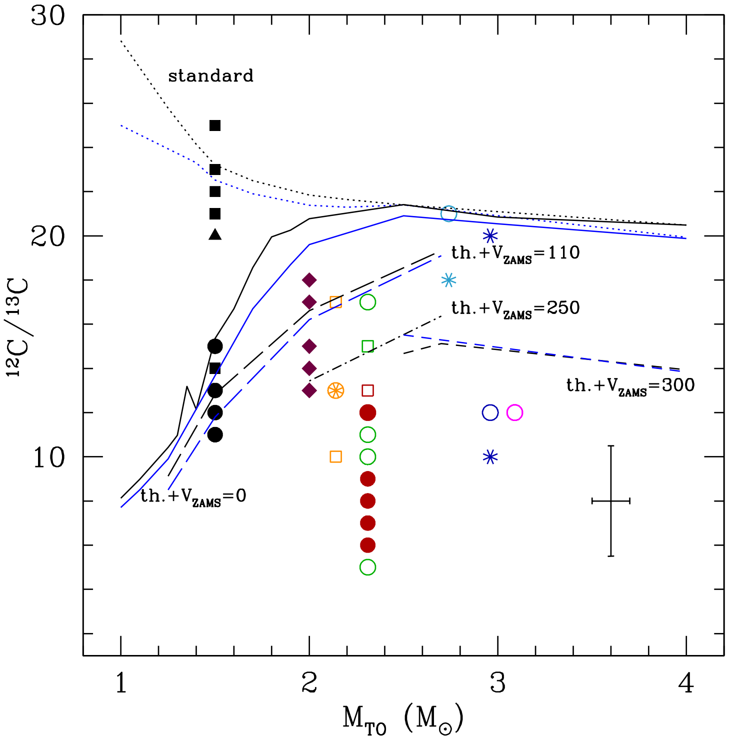

Fig. 3 Observations of $^{12}C/^{13}C$ in evolved stars of Galactic open clusters by Smiljanic et al. (2009), Gilroy (1989), Gilroy & Brown (1991), and Mikolaitis et al. (2010) as a function of the turnoff mass of the corresponding host cluster. Squares, circles, and asteriscs are for RGB, clump, and early-AGB stars respectively, while diamonds are for stars from Gilroy (1989) sample with doubtful evolutionary status; triangles are for lower limits. A typical error bar is indicated. Theoretical predictions are shown at the tip of the RGB and after completion of the second dredge-up (black and blue lines respectively). Standard models (no thermohaline nor rotation-induced mixing) are shown as dotted lines, models with thermohaline mixing only (V_{ZAMS}=0) as solid lines, and models with thermohaline and rotation-induced mixing for different initial rotation velocities as indicated as long-dashed, dot-dashed, and dashed lines. Figure from Charbonnel & Lagarde (2010).

1998, 2010; Palacios et al., 2003). After the 1dup, the surface Li abundance remains constant until the stars reach the bump luminosity where thermohaline mixing becomes efficient and destroys Li. Later on the star reaches the RGB tip, and finally the second dredge-up decreases again Li at the surface. Models are in perfect agreement with observations.

We have computed a few models along the TP-AGB, and found that thermohaline mixing leads to non negligible fresh lithium production, as shown in Fig.5. There we present the evolution of the surface lithium abundance as a function of both effective temperature and bolometric magnitude for TP-AGB models of 1.25 and 2.0$M_\odot$ stars. Theoretical predictions are compared with observations of the sample of low-mass oxygen-rich AGB variables belonging to the Galactic disk studied by Uttenthaler & Lebzelter (2010), and are found to fit very nicely the observed Li

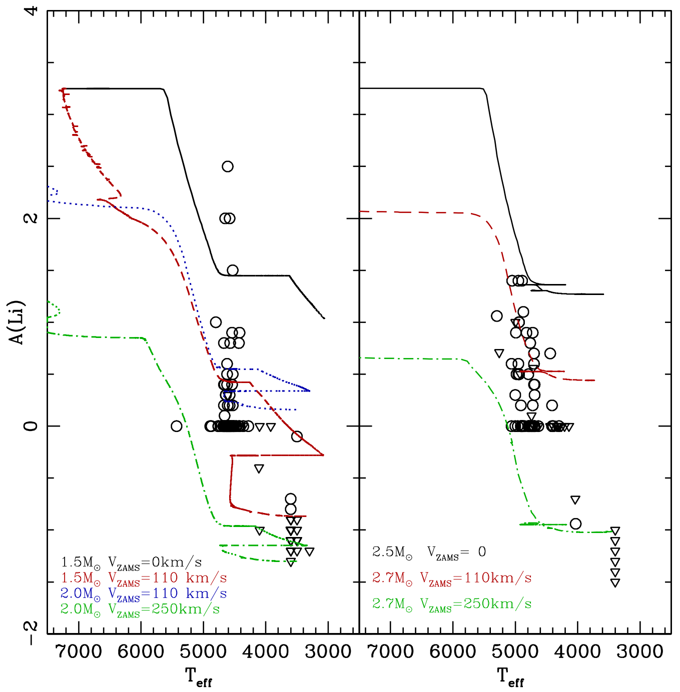

Fig. 4 Lithium data for field evolved stars from the sample by Charbonnel et al. (in prep.) that are segregated according to their mass (left and right panels include respectively sample stars with masses lower and higher than 2 $M_\odot$; Li detections and upper limits are shown as circles and triangles respectively). Theoretical lithium evolution is shown from the ZAMS up to the end of the early-AGB. Various lines correspond to predictions for stellar models of different masses computed without or with rotation as indicated, and with thermohaline mixing in all cases.

behaviour. Let us note that despite the strong production of fresh Li at that phase, the total stellar yields remain negative for this element.

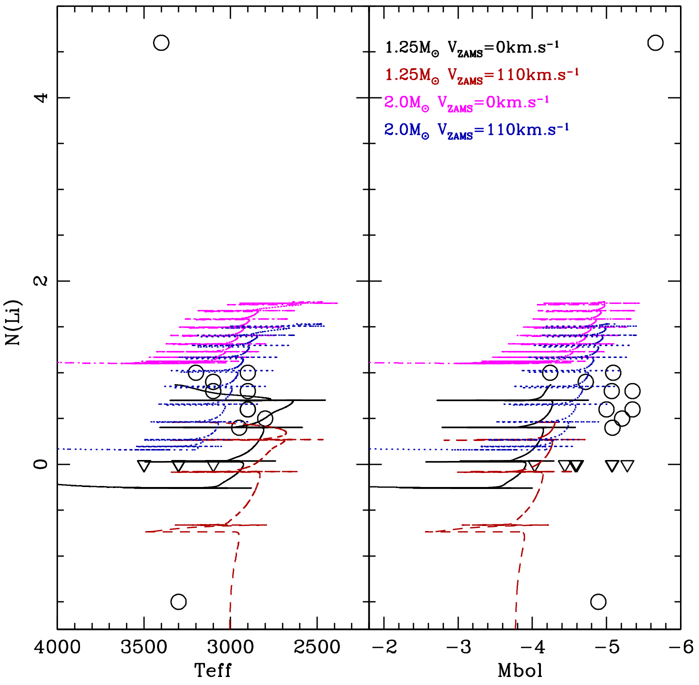

Fig. 5 Lithium observations in oxygen-rich variables belonging to the Galactic disk as a function of effective temperature and bolometric magnitude (Uttenthaler & Lebzelter, 2010); circles and triangles are for abundance determinations and upper limits respectively. Theoretical lithium evolution is shown from the early-AGB up to the end of the TP-AGB. Various lines correspond to predictions for stellar models of different masses computed without or with rotation as indicated, and with thermohaline mixing in all cases. Figure from Charbonnel & Lagarde (2010).

4.3 Helium 3

On the main sequence, a ^{3}He peak builds up due to pp-reactions inside low-mass stars (Iben, 1967), and is engulfed in the stellar envelope during the 1dup. As a consequence the surface abundance of ^{3}He strongly increases on the lower RGB as can be seen in Fig.6 which presents the evolution of ^{3}He mass fraction at the surface of 1 $M_\odot$ model at solar metallicity in the standard case and in the case with thermohaline mixing (black solid and red dotted lines respectively). After the bump, thermohaline mixing transports ^{3}He from the convective envelope down to the hydrogen-burning shell where it burns. This leads to a rapid decrease of the surface abundance (and thus of the corresponding yield) of this element as can be seen in Fig.6. We are presently computing similar stellar models over a large range in stellar mass and metallicity in order to quantify the actual contribution of low-mass stars to Galactic ^{3}He (Lagarde et al., in preparation). We are confident that the corresponding ^{3}He yields will help reconciling the primordial nucleosynthesis with measurements of ^{3}He/H in Galactic HII regions (Charbonnel, 2002).

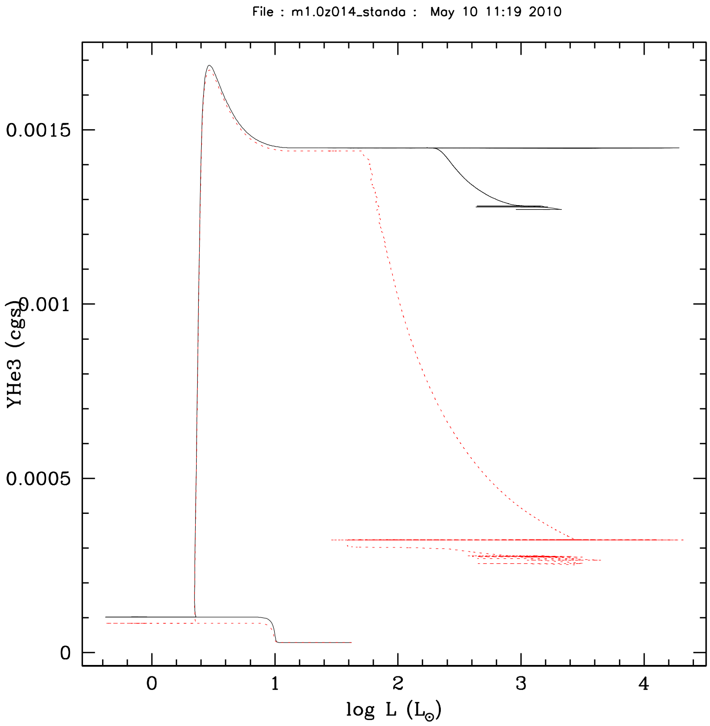

Fig. 6 Evolution of the surface abundance of ^{3}He (in mass fraction) from the pre-main sequence up to the AGB tip for 1M$_\odot$ models at solar metallicity. The black solid line and the red dotted-line correspond to the standard and thermohaline cases respectively.

5 Conclusions

An inversion of molecular weight created by the ^{3}He(^{3}He; 2p)^{4}He reaction is at the origin of thermohaline instability in low-mass RGB stars brighter than the bump. The associated mixing explains very well observations of ^{12}C/^{13}C and Li in these objects. Rotation-induced mixing, coupled with thermohaline mixing, allows us to explain the ^{12}C/^{13}C and Li data in giant stars over a large mass range. Thermohaline mixing has also an effect during the TP-AGB phase, where it leads to fresh lithium production. Finally, this process helps reconciling stellar yields predictions with the Galactic evolution of ^{3}He as constrained by the data in Galactic HII regions.

Acknowledgements We acknowledge financial support from the Swiss National Science Foundation (FNS) and from the french Programme National Program (PNPS) of CNRS/INSU.

References

Chanamé, J., Pinsonneault, M., & Terndrup, D. M. 2005, ApJ, 631, 540
Charbonnel, C. 2002, Nature, 415, 27
Charbonnel, C. & Lagarde, N. 2010, A&A, 522, A10
Charbonnel, C. & Talon, S. 1999, A&A, 351, 635
Charbonnel, C. & Zahn, J.-P. 2007, A&A, 467, L15
Eggleton, P. P., Dearborn, D. S. P., & Lattanzio, J. C. 2006, Science, 314, 1580
Geisler, D., Smith, V. V., Wallerstein, G., Gonzalez, G., & Charbonnel, C. 2005, AJ, 129, 1428
Gilroy, K. K. 1989, ApJ, 347, 835
Gilroy, K. K. & Brown, J. A. 1991, ApJ, 371, 578
Gratton, R. G., Sneden, C., Carretta, E., & Bragaglia, A. 2000, A&A, 354, 169
Iben, Jr., I. 1967, ApJ, 147, 624
Kippenhahn, R., Ruschenplatt, G., & Thomas, H.-C. 1980, A&A, 91, 175
Luck, R. E. 1994, ApJS, 91, 309
Mikolaitis, Š., Tautvaišienė, G., Gratton, R., Bragaglia, A., & Carretta, E. 2010, MNRAS, 407, 1866
Palacios, A., Charbonnel, C., Talon, S., & Siess, L. 2006, A&A, 453, 261
Palacios, A., Talon, S., Charbonnel, C., & Forestini, M. 2003, A&A, 399, 603
Pasquini, L., Bonifacio, P., Randich, S., Galli, D., & Gratton, R. G. 2004, A&A, 426, 651
Pilachowski, C., Sneden, C., Freeland, E., & Casperson, J. 2003, AJ, 125, 794
Recio-Blanco, A. & de Laverny, P. 2007, A&A, 461, L13
Shetrone, M. D. 2003, ApJ, 585, L45
Smiljanic, R., Gauderon, R., North, P., et al. 2009, A&A, 502, 267
Smith, V. V., Hinkle, K. H., Cunha, K., et al. 2002, AJ, 124, 3241
Spite, M., Cayrel, R., Hill, V., et al. 2006, A&A, 455, 291
Talon, S. & Charbonnel, C. 1998, A&A, 335, 959
Talon, S. & Charbonnel, C. 2010, in IAU Symposium, Vol. 268, IAU Symposium, ed. C.Charbonnel, M.Tosi, F.Primas & C.Chiappini
Tautvaišienė, G., Edvardsson, B., Puzeras, E., & Ilyin, I. 2005, A&A, 431, 933
Tautvaišiene, G., Edvardsson, B., Tuominen, I., & Ilyin, I. 2000, A&A, 360, 499
Ulrich, R. K. 1971, ApJ, 168, 57
Ulrich, R. K. 1972, ApJ, 172, 165
Uttenthaler, S. & Lebzelter, T. 2010, A&A, 510, A62

Bibliography

Aikawa, M., Arnould, M., Goriely, S., Jorissen, A., & Takahashi, K. 2005, A&A, 441, 1195

Anders, E. & Grevesse, N. 1989, Geochim. Cosmochim. Acta, 53, 197

Anthony-Twarog, B. J., Deliyannis, C. P., Twarog, B. A., Croxall, K. V., & Cummings, J. D. 2009, AJ, 138, 1171

Arnould, M., Goriely, S., & Jorissen, A. 1999, A&A, 347, 572

Asplund, M., Grevesse, N., & Sauval, A. J. 2005, in Astronomical Society of the Pacific Conference Series, Vol. 336, Cosmic Abundances as Records of Stellar Evolution and Nucleosynthesis, ed. T. G. Barnes III & F. N. Bash, 25–+

Aurière, M., Konstantinova-Antova, R., Petit, P., et al. 2011, A&A, 534, A139

Baglin, A., Auvergne, M., Boisnard, L., et al. 2006, in 36th COSPAR Scientific Assembly, Vol. 36, 3749

Balachandran, S. 1990, in Astronomical Society of the Pacific Conference Series, Vol. 9, Cool Stars, Stellar Systems, and the Sun, ed. G. Wallerstein, 357

Balser, D. S., Bania, T. M., Brockway, C. J., Rood, R. T., & Wilson, T. L. 1994, ApJ, 430, 667

Balser, D. S., Bania, T. M., Rood, R. T., & Wilson, T. L. 1997, ApJ, 483, 320

Balser, D. S., Bania, T. M., Rood, R. T., & Wilson, T. L. 1999a, ApJ, 510, 759

Balser, D. S., Goss, W. M., Bania, T. M., & Rood, R. T. 2006, ApJ, 640, 360

Balser, D. S., Rood, R. T., & Bania, T. M. 1999b, ApJ, 522, L73

Bania, T. M., Balser, D. S., Rood, R. T., Wilson, T. L., & Wilson, T. J. 1997, ApJS, 113, 353

Bania, T. M., Rood, R. T., & Balser, D. S. 2002, Nature, 415, 54

Bania, T. M., Rood, R. T., & Balser, D. S. 2010, in IAU Symposium, Vol. 268, IAU Symposium, ed. C. Charbonnel, M. Tosi, F. Primas, & C. Chiappini, 81–90

Bao, Z. Y., Beer, H., Käppeler, F., et al. 2000, in American Institute of Physics Conference Series, Vol. 529, American Institute of Physics Conference Series (Santa Fe, New Mexico: AIP), 706–709

Barisevičius, G., Tautvaišienė, G., Berdyugina, S., Chorniy, Y., & Ilyin, I. 2010, Baltic Astronomy, 19, 157

Barisevičius, G., Tautvaišienė, G., Berdyugina, S., Chorniy, Y., & Ilyin, I. 2011, Baltic Astronomy, 20, 53

Barrado y Navascues, D., Fernandez-Figueroa, M. J., Garcia Lopez, R. J., de Castro, E., & Cornide, M. 1997, A&A, 326, 780

Beck, P. G., Montalban, J., Kallinger, T., et al. 2012, Nature, 481, 55

Bedding, T. R., Huber, D., Stello, D., et al. 2010, ApJ, 713, L176

Beer, H., Sedyshev, P. V., Rochow, W., Mohr, P., & Oberhummer, H. 2002, Nuclear Physics A, 705, 239

Bell, R. A., Briley, M. M., & Smith, G. H. 1990, AJ, 100, 187

Bell, R. A. & Dickens, R. J. 1980, ApJ, 242, 657

Bell, R. A., Dickens, R. J., & Gustafsson, B. 1979, ApJ, 229, 604

Bennett, C. L., Halpern, M., Hinshaw, G., et al. 2003, ApJS, 148, 1

Berdyugina, S. V. & Savanov, I. S. 1994, Astronomy Letters, 20, 639

Boothroyd, A. I. & Sackmann, I.-J. 1999, ApJ, 510, 232

Boothroyd, A. I., Sackmann, I.-J., & Wasserburg, G. J. 1995, ApJ, 442, L21

Borucki, W. J., Koch, D., Basri, G., et al. 2010, Science, 327, 977

Briley, M. M., Bell, R. A., Hoban, S., & Dickens, R. J. 1990, ApJ, 359, 307

Briley, M. M., Smith, G. H., & Claver, C. F. 2001, AJ, 122, 2561

Briley, M. M., Smith, V. V., King, J., & Lambert, D. L. 1997, AJ, 113, 306

Briley, M. M., Smith, V. V., & Lambert, D. L. 1994, ApJ, 424, L119

Brott, I., de Mink, S. E., Cantiello, M., et al. 2011, A&A, 530, A115+

Brown, J. A. 1987, ApJ, 317, 701

Brown, J. A., Sneden, C., Lambert, D. L., & Dutchover, Jr., E. 1989, ApJS, 71, 293

Brown, J. A. & Wallerstein, G. 1989, AJ, 98, 1643

Brown, J. A. & Wallerstein, G. 1992, AJ, 104, 1818

Brown, J. A., Wallerstein, G., & Oke, J. B. 1990, AJ, 100, 1561

Cameron, A. G. W. & Fowler, W. A. 1971, ApJ, 164, 111

Canto Martins, B. L., Lèbre, A., Palacios, A., et al. 2011, A&A, 527, A94

Carbon, D. F., Romanishin, W., Langer, G. E., et al. 1982, ApJS, 49, 207

Carlberg, J. K., Smith, V. V., Cunha, K., Majewski, S. R., & Rood, R. T. 2010, ApJ, 723, L103

Carretta, E., Bragaglia, A., Gratton, R. G., & Tosi, M. 2004, A&A, 422, 951

Carretta, E., Gratton, R. G., & Sneden, C. 2000, A&A, 356, 238

Cassisi, S., Pietrinferni, A., Salaris, M., et al. 2006, Mem. Soc. Astron. Italiana, 77, 71

Caughlan, G. R. & Fowler, W. A. 1988, Atomic Data and Nuclear Data Tables, 40, 283

Cayrel, R., Cayrel de Strobel, G., Campbell, B., & Dappen, W. 1984, ApJ, 283, 205

Chaboyer, B. & Zahn, J.-P. 1992, A&A, 253, 173

Chanamé, J., Pinsonneault, M., & Terndrup, D. M. 2005, ApJ, 631, 540

Charbonnel, C. 1994, A&A, 282, 811

Charbonnel, C. 1995, ApJ, 453, L41+

Charbonnel, C. & Balachandran, S. C. 2000, A&A, 359, 563

Charbonnel, C., Brown, J. A., & Wallerstein, G. 1998a, A&A, 332, 204

Charbonnel, C., Brown, J. A., & Wallerstein, G. 1998b, A&A, 332, 204

Charbonnel, C. & Do Nascimento, Jr., J. D. 1998, A&A, 336, 915

Charbonnel, C. & Lagarde, N. 2010a, A&A, 522, A10+

Charbonnel, C. & Lagarde, N. 2010b, in IAU Symposium, Vol. 268, IAU Symposium, ed. C.Charbonnel, M.Tosi, F.Primas & C.Chiappini

Charbonnel, C. & Talon, S. 1999, A&A, 351, 635

Charbonnel, C. & Zahn, J. 2007a, A&A, 476, L29

Charbonnel, C. & Zahn, J.-P. 2007b, A&A, 467, L15

Chiappini, C., Matteucci, F., & Gratton, R. 1997, ApJ, 477, 765

Chiappini, C., Matteucci, F., & Romano, D. 2001, ApJ, 554, 1044

Cottrell, P. L. & Sneden, C. 1986, A&A, 161, 314

da Silva, L., de La Reza, R., & Barbuy, B. 1995, ApJ, 448, L41

Day, R. W., Lambert, D. L., & Sneden, C. 1973, ApJ, 185, 213

De Ridder, J., Barban, C., Baudin, F., et al. 2009, Nature, 459, 398

Dearborn, D. S. P., Steigman, G., & Tosi, M. 1996a, ApJ, 465, 887

Dearborn, D. S. P., Steigman, G., & Tosi, M. 1996b, ApJ, 465, 887

Decressin, T., Mathis, S., Palacios, A., et al. 2009, A&A, 495, 271

Denissenkov, P. A. 2010, ApJ, 723, 563

Denissenkov, P. A., Da Costa, G. S., Norris, J. E., & Weiss, A. 1998, A&A, 333, 926

Denissenkov, P. A. & Merryfield, W. J. 2011, ApJ, 727, L8+

Denissenkov, P. A., Pinsonneault, M., & MacGregor, K. B. 2009, ApJ, 696, 1823

Denissenkov, P. A. & Tout, C. A. 2000, MNRAS, 316, 395

Denissenkov, P. A. & Weiss, A. 1996, A&A, 308, 773

Descouvemont, P., Adahchour, A., Angulo, C., Coc, A., & Vangioni-Flam, E. 2004, Atomic Data and Nuclear Data Tables, 88, 203 do Nascimento, Jr., J. D., Charbonnel, C., Lèbre, A., de Laverny, P., & De Medeiros, J. R. 2000, A&A, 357, 931

D'Orazi, V., Lucatello, S., Gratton, R., et al. 2010, ApJ, 713, L1

D'Orazi, V. & Marino, A. F. 2010, ApJ, 716, L166

Drake, J. J., Ball, B., Eldridge, J. J., Ness, J.-U., & Stancliffe, R. J. 2011, AJ, 142, 144

Drake, N. A., de la Reza, R., da Silva, L., & Lambert, D. L. 2002, AJ, 123, 2703

Duez, V., Braithwaite, J., & Mathis, S. 2010, ApJ, 724, L34

Duez, V. & Mathis, S. 2009, ArXiv e-prints

Duez, V. & Mathis, S. 2010, A&A, 517, A58

Dufour, E. 1999, PhD thesis, Université Joseph Fourier – Grenoble I

Eddington, A. S. 1925, The Observatory, 48, 73

Eggleton, P. P., Dearborn, D. S. P., & Lattanzio, J. C. 2006, Science, 314, 1580

Eggleton, P. P., Dearborn, D. S. P., & Lattanzio, J. C. 2008, ApJ, 677, 581

Eggleton, P. P., Faulkner, J., & Flannery, B. P. 1973, A&A, 23, 325

Ekström, S., Georgy, C., Eggenberger, P., et al. 2012, A&A, 537, A146

Ekström, S., Meynet, G., Chiappini, C., Hirschi, R., & Maeder, A. 2008, A&A, 489, 685

Epstein, R. I., Lattimer, J. M., & Schramm, D. N. 1976, Nature, 263, 198

Ferguson, J. W., Alexander, D. R., Allard, F., et al. 2005, ApJ, 623, 585

Forestini, M. & Charbonnel, C. 1997, A&AS, 123, 241

Funck, C. & Langanke, K. 1989, ApJ, 344, 46

Fusi Pecci, F., Ferraro, F. R., Crocker, D. A., Rood, R. T., & Buonanno, R. 1990, A&A, 238, 95

Fynbo, H. O. U., Diget, C. A., Bergmann, U. C., et al. 2005, Nature, 433, 136

Galli, D., Palla, F., Ferrini, F., & Penco, U. 1995, ApJ, 443, 536

Galli, D., Stanghellini, L., Tosi, M., & Palla, F. 1997, ApJ, 477, 218

García, R. A., Mathur, S., Salabert, D., et al. 2010, Science, 329, 1032

Geiss, J. & Gloeckler, G. 1998, Space Sci. Rev., 84, 239

Geiss, J. & Gloeckler, G. 2010, in IAU Symposium, Vol. 268, IAU Symposium, ed. C. Charbonnel, M. Tosi, F. Primas, & C. Chiappini, 71–79

Gilroy, K. K. 1989, ApJ, 347, 835

Gilroy, K. K. & Brown, J. A. 1991, ApJ, 371, 578

Gloeckler, G. & Geiss, J. 1996, Nature, 381, 210

Gonzalez, G. 1998, A&A, 334, 221

Graboske, H. C., Dewitt, H. E., Grossman, A. S., & Cooper, M. S. 1973, ApJ, 181, 457

Gratton, R. G., Sneden, C., Carretta, E., & Bragaglia, A. 2000, A&A, 354, 169

Grevesse, N., Noels, A., & Sauval, A. J. 1993, A&A, 271, 587

Hale, S. E., Champagne, A. E., Iliadis, C., et al. 2002, Phys. Rev. C, 65, 015801

Hamdani, S., North, P., Mowlavi, N., Raboud, D., & Mermilliod, J. 2000, A&A, 360, 509

Harris, M. J. & Lambert, D. L. 1984, ApJ, 285, 674

Harris, M. J., Lambert, D. L., & Smith, V. V. 1988, ApJ, 325, 768

Hauser, W. & Feshbach, H. 1952, Physical Review, 87, 366

Hirschi, R. 2007, A&A, 461, 571

Hirschi, R., Meynet, G., & Maeder, A. 2005, A&A, 433, 1013

Horiguchi, T., Tachibana, T., & Katakura, J. 1996, Nuclear Data Center, Japan Atomic Energy Research Institute, Ibaraki

Iben, Jr., I. 1967, ApJ, 147, 624

Iglesias, C. A. & Rogers, F. J. 1996, ApJ, 464, 943

Iliadis, C., D'Auria, J. M., Starrfield, S., Thompson, W. J., & Wiescher, M. 2001, ApJS, 134, 151

Iwamoto, K., Brachwitz, F., Nomoto, K., et al. 1999, ApJS, 125, 439

Jacobson, H. R., Friel, E. D., & Pilachowski, C. A. 2007, AJ, 134, 1216

Jacobson, H. R., Friel, E. D., & Pilachowski, C. A. 2008, AJ, 135, 2341

Jacobson, H. R., Friel, E. D., & Pilachowski, C. A. 2009, AJ, 137, 4753

King, C. R., Da Costa, G. S., & Demarque, P. 1985, ApJ, 299, 674

Kippenhahn, R. 1974, in IAU Symposium, Vol. 66, Late Stages of Stellar Evolution, ed. R. J. Tayler & J. E. Hesser, 20

Kippenhahn, R., Ruschenplatt, G., & Thomas, H.-C. 1980, A&A, 91, 175

Kippenhahn, R. & Weigert, A. 1990, Stellar Structure and Evolution (Kippenhahn, R. & Weigert, A.)

Kobayashi, C., Umeda, H., Nomoto, K., Tominaga, N., & Ohkubo, T. 2006, ApJ, 653, 1145

Koch, A., Lind, K., Thompson, I. B., & Rich, R. M. 2012, ArXiv e-prints

Koehler, P. E. & O'brien, H. A. 1989a, Phys. Rev. C, 39, 1655

Koehler, P. E. & O'brien, H. A. 1989b, Phys. Rev. C, 39, 1655

Krishnamurti, R. 2003, Journal of Fluid Mechanics, 483, 287

Kroupa, P. 2001, MNRAS, 322, 231

Kroupa, P., Tout, C. A., & Gilmore, G. 1993, MNRAS, 262, 545

Kumar, Y. B., Reddy, B. E., & Lambert, D. L. 2011, ApJ, 730, L12

Kunze, E. 2003, Progress in Oceanography, 56, 399

Lagarde, N., Charbonnel, C., Decressin, T., & Hagelberg, J. 2011, A&A, 536, A28

Lagarde, N., Charbonnel, C., Jasniewicz, G., et al. 2010, in IAU Symposium, Vol. 268, IAU Symposium, ed. C. Charbonnel, M. Tosi, F. Primas, & C. Chiappini, 423–424

Lagarde, N., Decressin, T., Charbonnel, C., et al. 2012a, ArXiv e-prints

Lagarde, N., Romano, D., Charbonnel, C., et al. 2012b, ArXiv e-prints

Lambert, D. L., Dominy, J. F., & Sivertsen, S. 1980, ApJ, 235, 114

Lambert, D. L. & Ries, L. M. 1981, ApJ, 248, 228

Lambert, D. L. & Sawyer, S. R. 1984, ApJ, 283, 192

Langer, G. E., Kraft, R. P., Carbon, D. F., Friel, E., & Oke, J. B. 1986, PASP, 98, 473

Lardo, C., Milone, A. P., Marino, A. F., et al. 2012, ArXiv e-prints

Larson, R. B. 1976, MNRAS, 176, 31

Lèbre, A., de Laverny, P., de Medeiros, J. R., Charbonnel, C., & da Silva, L. 1999, A&A, 345, 936

Lebzelter, T., Uttenthaler, S., Busso, M., Schultheis, M., & Aringer, B. 2012, A&A, 538, A36

Lind, K., Primas, F., Charbonnel, C., Grundahl, F., & Asplund, M. 2009, A&A, 503, 545

Luck, R. E. 1977, ApJ, 218, 752

Luck, R. E. 1978, ApJ, 219, 148

Luck, R. E. 1994, ApJS, 91, 309

Luck, R. E. & Heiter, U. 2007, AJ, 133, 2464

Luck, R. E. & Lambert, D. L. 1982, ApJ, 256, 189

Luhman, K. L., Rieke, G. H., Young, E. T., et al. 2000, ApJ, 540, 1016

Maeder, A. & Meynet, G. 2000, ARA&A, 38, 143

Maeder, A. & Zahn, J.-P. 1998, A&A, 334, 1000

Mallik, S. V. 1999, A&A, 352, 495

Marino, A. F., Milone, A. P., Sneden, C., et al. 2012, A&A, 541, A15

Mathis, S. 2009, A&A, 506, 811

Matteucci, F. 2001, in Astronomical Society of the Pacific Conference Series, Vol. 230, Galaxy Disks and Disk Galaxies, ed. J. G. Funes & E. M. Corsini, 337–344

Matteucci, F. & Francois, P. 1989, MNRAS, 239, 885

Meynet, G. & Maeder, A. 2002, A&A, 390, 561

Miglio, A., Montalbán, J., Baudin, F., et al. 2009, A&A, 503, L21

Mikolaitis, Š., Tautvaišienė, G., Gratton, R., Bragaglia, A., & Carretta, E. 2010, MNRAS, 407, 1866

Mikolaitis, Š., Tautvaišienė, G., Gratton, R., Bragaglia, A., & Carretta, E. 2011, MNRAS, 295

Mikolaitis, Š., Tautvaišienė, G., Gratton, R., Bragaglia, A., & Carretta, E. 2012, ArXiv e-prints

Mishenina, T. V., Bienaymé, O., Gorbaneva, T. I., et al. 2006, A&A, 456, 1109

Mitler, H. E. 1977, ApJ, 212, 513

Monaco, L., Villanova, S., Bonifacio, P., et al. 2012, A&A, 539, A157

Monaco, L., Villanova, S., Moni Bidin, C., et al. 2011, A&A, 529, A90

Mosser, B., Barban, C., Montalbán, J., et al. 2011, A&A, 532, A86

Mucciarelli, A., Salaris, M., & Bonifacio, P. 2012, MNRAS, 419, 2195

Mucciarelli, A., Salaris, M., Lovisi, L., et al. 2011, MNRAS, 412, 81

Mukhamedzhanov, A. M., Bém, P., Brown, B. A., et al. 2003, Phys. Rev. C, 67, 065804

Olive, K. A., Rood, R. T., Schramm, D. N., Truran, J., & Vangioni-Flam, E. 1995, ApJ, 444, 680

Palacios, A. 2002, Thesis

Palacios, A., Charbonnel, C., Talon, S., & Siess, L. 2006, A&A, 453, 261

Palacios, A., Parthasarathy, M., Bharat Kumar, Y., & Jasniewicz, G. 2012, A&A, 538, A68

Palacios, A., Talon, S., Charbonnel, C., & Forestini, M. 2003, A&A, 399, 603

Palla, F., Bachiller, R., Stanghellini, L., Tosi, M., & Galli, D. 2000, A&A, 355, 69

Pallavicini, R., Cerruti-Sola, M., & Duncan, D. K. 1987, A&A, 174, 116

Pasquini, L., Bonifacio, P., Randich, S., Galli, D., & Gratton, R. G. 2004a, A&A, 426, 651

Pasquini, L., Randich, S., & Pallavicini, R. 2001, A&A, 374, 1017

Pasquini, L., Randich, S., Zoccali, M., et al. 2004b, A&A, 424, 951

Peebles, P. J. E. 1966, ApJ, 146, 542

Pilachowski, C. 1986, ApJ, 300, 289

Pilachowski, C., Saha, A., & Hobbs, L. M. 1988, PASP, 100, 474

Pilachowski, C. A. 1988, ApJ, 326, L57

Pilachowski, C. A., Sneden, C., & Booth, J. 1993, ApJ, 407, 699

Pols, O. R., Tout, C. A., Eggleton, P. P., & Han, Z. 1995, MNRAS, 274, 964

Prisinzano, L. & Randich, S. 2007, A&A, 475, 539

Prodanović, T. & Fields, B. D. 2003, ApJ, 597, 48

Prodanović, T., Steigman, G., & Fields, B. D. 2010, MNRAS, 406, 1108

Randich, S., Pallavicini, R., Meola, G., Stauffer, J. R., & Balachandran, S. C. 2001, A&A, 372, 862

Randich, S., Primas, F., Pasquini, L., & Pallavicini, R. 2002, A&A, 387, 222

Reddy, B. E. & Lambert, D. L. 2005, AJ, 129, 2831

Reddy, B. E., Lambert, D. L., Hrivnak, B. J., & Bakker, E. J. 2002, AJ, 123, 1993

Reimers, D. 1975, Memoires of the Societe Royale des Sciences de Liege, 8, 369

Rogers, T. M. & MacGregor, K. B. 2010, MNRAS, 401, 191

Rogers, T. M. & MacGregor, K. B. 2011, MNRAS, 410, 946

Romano, D., Karakas, A. I., Tosi, M., & Matteucci, F. 2010, A&A, 522, A32

Romano, D., Tosi, M., Matteucci, F., & Chiappini, C. 2003, MNRAS, 346, 295

Rood, R. T. 1972, ApJ, 177, 681

Rood, R. T., Bania, T. M., & Wilson, T. L. 1992, Nature, 355, 618

Rood, R. T., Steigman, G., & Tinsley, B. M. 1976, ApJ, 207, L57

Rood, R. T., Wilson, T. L., & Steigman, G. 1979, ApJ, 227, L97

Rosenblum, E., Garaud, P., Traxler, A., & Stellmach, S. 2011, ApJ, 731, 66

Sackmann, I. & Boothroyd, A. I. 1999, ApJ, 510, 217

Salpeter, E. E. 1955, ApJ, 121, 161

Scalo, J. M. 1986, Fund. Cosmic Phys., 11, 1

Schaller, G., Schaerer, D., Meynet, G., & Maeder, A. 1992, A&AS, 96, 269

Schatz, H., Kaeppeler, F., Koehler, P. E., Wiescher, M., & Trautvetter, H.-P. 1993, ApJ, 413, 750

Shen, Z.-X., Bonifacio, P., Pasquini, L., & Zaggia, S. 2010, A&A, 524, L2

Shetrone, M. D. 2003, ApJ, 585, L45

Shetrone, M. D., Sneden, C., & Pilachowski, C. A. 1993, PASP, 105, 337

Siess, L., Dufour, E., & Forestini, M. 2000, A&A, 358, 593

Smiljanic, R. 2012, ArXiv e-prints

Smiljanic, R., Gauderon, R., North, P., et al. 2009, A&A, 502, 267

Smiljanic, R., Pasquini, L., Charbonnel, C., & Lagarde, N. 2010, A&A, 510, A50+

Smith, G. H., Shetrone, M. D., & Strader, J. 2007, PASP, 119, 722

Smith, V. V., Hinkle, K. H., Cunha, K., et al. 2002, AJ, 124, 3241

Smith, V. V. & Lambert, D. L. 1986, ApJ, 303, 226

Smith, V. V., Plez, B., Lambert, D. L., & Lubowich, D. A. 1995, ApJ, 441, 735

Smith, V. V. & Suntzeff, N. B. 1989, AJ, 97, 1699

Sneden, C. & Pilachowski, C. A. 1986, ApJ, 301, 860

Sneden, C., Pilachowski, C. A., & Vandenberg, D. A. 1986, ApJ, 311, 826

Spergel, D. N., Verde, L., Peiris, H. V., et al. 2003, ApJS, 148, 175

Stancliffe, R. J. 2010, MNRAS, 174

Stancliffe, R. J. & Glebbeek, E. 2008, MNRAS, 389, 1828

Stancliffe, R. J., Glebbeek, E., Izzard, R. G., & Pols, O. R. 2007, A&A, 464, L57

Stern, M. E. 1960, Tellus, 12, 172

Suntzeff, N. B. 1981, ApJS, 47, 1

Suntzeff, N. B. & Smith, V. V. 1991, ApJ, 381, 160

Sweigart, A. V., Greggio, L., & Renzini, A. 1989, ApJS, 69, 911

Sweigart, A. V. & Mengel, J. G. 1979, ApJ, 229, 624

Talon, S. & Charbonnel, C. 1998, A&A, 335, 959

Talon, S. & Charbonnel, C. 2010, in IAU Symposium, Vol. 268, IAU Symposium, ed. C.Charbonnel, M.Tosi, F.Primas & C.Chiappini

Talon, S. & Zahn, J.-P. 1997, A&A, 317, 749

Tautvaišienė, G., Barisevičius, G., Berdyugina, S., Chorniy, Y., & Ilyin, I. 2010a, Baltic Astronomy, 19, 95

Tautvaišienė, G., Barisevičius, G., Berdyugina, S., Ilyin, I., & Chorniy, Y. 2011, Astronomische Nachrichten, 332, 925

Tautvaišienė, G., Edvardsson, B., Puzeras, E., Barisevičius, G., & Ilyin, I. 2010b, MNRAS, 409, 1213

Tautvaišienė, G., Edvardsson, B., Puzeras, E., & Ilyin, I. 2005, A&A, 431, 933

Tautvaišiene, G., Edvardsson, B., Tuominen, I., & Ilyin, I. 2000, A&A, 360, 499

Théado, S. & Vauclair, S. 2012, ApJ, 744, 123

Théado, S., Vauclair, S., Alecian, G., & Le Blanc, F. 2009, ApJ, 704, 1262

Thompson, I. B., Ivans, I. I., Bisterzo, S., et al. 2008, ApJ, 677, 556

Tosi, M. 1996, in Astronomical Society of the Pacific Conference Series, Vol. 98, From Stars to Galaxies: the Impact of Stellar Physics on Galaxy Evolution, ed. C. Leitherer, U. Fritze-von-Alvensleben, & J. Huchra, 299–+

Tosi, M. 1998, Space Science Reviews, 84, 207

Tosi, M. 2000, in IAU Symposium, Vol. 198, The Light Elements and their Evolution, ed. L. da Silva, R. de Medeiros, & M. Spite, 525–+

Traxler, A., Garaud, P., & Stellmach, S. 2011a, ApJ, 728, L29+

Traxler, A., Stellmach, S., Garaud, P., Radko, T., & Brummell, N. 2011b, Journal of Fluid Mechanics, 677, 530

Trefzger, D. V., Langer, G. E., Carbon, D. F., Suntzeff, N. B., & Kraft, R. P. 1983, ApJ, 266, 144

Ulrich, R. K. 1971, ApJ, 168, 57

Ulrich, R. K. 1972, ApJ, 172, 165

Uttenthaler, S. & Lebzelter, T. 2010, A&A, 510, A62+

Uttenthaler, S., Lebzelter, T., Palmerini, S., et al. 2007, A&A, 471, L41

Vassiliadis, E. & Wood, P. R. 1993, ApJ, 413, 641

Vauclair, S. 2004, in IAU Symposium, Vol. 224, The A-Star Puzzle, ed. J. Zverko, J. Ziznovsky, S. J. Adelman, & W. W. Weiss, 161–166

Vogt, H. 1926, Astronomische Nachrichten, 227, 325

Wagoner, R. V. 1969, ApJS, 18, 247

Wagoner, R. V., Fowler, W. A., & Hoyle, F. 1967, ApJ, 148, 3

Wallerstein, G., Herbig, G. H., & Conti, P. S. 1965, ApJ, 141, 610

Wallerstein, G. & Sneden, C. 1982, ApJ, 255, 577

Wasserburg, G. J., Boothroyd, A. I., & Sackmann, I. 1995, ApJ, 447, L37+

Weiss, A., Wagenhuber, J., & Denissenkov, P. A. 1996, A&A, 313, 581

Wiescher, M., Gorres, J., & Thielemann, F. 1990, ApJ, 363, 340

Wilson, T. L. & Rood, R. 1994, ARA&A, 32, 191

Woosley, S. E., Fowler, W. A., Holmes, J. A., & Zimmerman, B. A. 1978, Atomic Data and Nuclear Data Tables, 22, 371

Yi, S. K., Kim, Y.-C., & Demarque, P. 2003, ApJS, 144, 259

Yong, D., Carney, B. W., & Teixera de Almeida, M. L. 2005a, AJ, 130, 597

Yong, D., Grundahl, F., Nissen, P. E., Jensen, H. R., & Lambert, D. L. 2005b, A&A, 438, 875

Zahn, J.-P. 1992, A&A, 265, 115

Zappala, R. R. 1972, ApJ, 172, 57